

# Agronomy Research

Established in 2003 by the Faculty of Agronomy, Estonian Agricultural University

## **Aims and Scope:**

*Agronomy Research* is a peer-reviewed international Journal intended for publication of broad-spectrum original articles, reviews and short communications on actual problems of modern biosystems engineering incl. crop and animal science, genetics, economics, farm- and production engineering, environmental aspects, agro-ecology, renewable energy and bioenergy etc. in the temperate regions of the world.

## **Copyright:**

Copyright 2009 by Estonian University of Life Sciences, Latvia University of Life Sciences and Technologies, Vytautas Magnus University Agriculture Academy, Lithuanian Research Centre for Agriculture and Forestry. No part of this publication may be reproduced or transmitted in any form, or by any means, electronic or mechanical, incl. photocopying, electronic recording, or otherwise without the prior written permission from the Estonian University of Life Sciences, Latvia University of Life Sciences and Technologies, Vytautas Magnus University Agriculture Academy, Lithuanian Research Centre for Agriculture and Forestry.

## ***Agronomy Research* online:**

*Agronomy Research* is available online at: <http://agronomy.emu.ee/>

## **Acknowledgement to Referees:**

The Editors of *Agronomy Research* would like to thank the many scientists who gave so generously of their time and expertise to referee papers submitted to the Journal.

## **Abstracted and indexed:**

SCOPUS, EBSCO, CABI Full Paper and Thompson Scientific database: (Zoological Records, Biological Abstracts and Biosis Previews, AGRIS, ISPI, CAB Abstracts, AGRICOLA (NAL; USA), VINITI, INIST-PASCAL).

## **Subscription information:**

Institute of Technology, EULS  
St. Kreutzwaldi 56, 51014 Tartu, ESTONIA  
E-mail: [timo.kikas@emu.ee](mailto:timo.kikas@emu.ee)

## **Journal Policies:**

Estonian University of Life Sciences, Latvia University of Life Sciences and Technologies, Vytautas Magnus University Agriculture Academy, Lithuanian Research Centre for Agriculture and Forestry, and Editors of *Agronomy Research* assume no responsibility for views, statements and opinions expressed by contributors. Any reference to a pesticide, fertiliser, cultivar or other commercial or proprietary product does not constitute a recommendation or an endorsement of its use by the author(s), their institution or any person connected with preparation, publication or distribution of this Journal.

**ISSN 1406-894X**

# CONTENTS

**P. Alao, M. Tobias, H. Kallakas, T. Poltimäe, J. Kers and D. Goljandin**

Development of hemp hurd particleboards from formaldehyde-free resins ..... 679

**R.R. Andrade, I.F.F. Tinôco, F.A. Damasceno, M. Barbari, D.A. Valente,  
M.O. Vilela, C.F. Souza, L. Conti and G. Rossi**

Lighting and noise levels in compost dairy barns with natural and forced  
ventilation..... 689

**C.B. Aramian, F.B.A. Colonia, F.C. Silva, D. Cecchin, A.R.G. Azevedo and  
D.F. Carmo**

Sustainability indicators in cooperative management of recyclable materials ..... 699

**O. Bolotnikova, J. Bazarnova, E. Aronova and T. Bolotnikova**

Study of transhydrogenase systems features in the mutants of the yeast *pachysolen  
tannophilus* for the production of ethanol and xylitol from agricultural wastes ..... 720

**J. Brovkina, G. Shulga, J. Ozolins, B. Neiberte, A. Verovkins and V. Lakevics**

The advanced application of the wood-originated wastewater sludge..... 729

**V. Bulgakov, S. Nikolaenko, Z. Ruzhylo, I. Fedosiy, J. Nowak and J. Olt**

Theoretical study on motion of potato tuber on surface of separator..... 742

**M. Daneček, M. Havrlík, V. Beránek, J. Šafránková, M. Libra, V. Poulek,  
J. Sedláček and R. Belza**

Design and data comparison of the photovoltaic power plants in the southern  
and northern hemispheres..... 755

**A. Dastpak, B.P. Wilson and M. Lundström**

Investigation of the anticorrosion performance of lignin coatings after crosslinking  
with triethyl phosphate and their adhesion to a polyurethane topcoat ..... 762

<b>V. Denisova, K. Tihomirova, J. Neilands, K. Gruskevica, L. Mezule and T. Juhna</b>	
Comparison of phosphorus removal efficiency of conventional activated sludge system and sequencing batch reactors in a wastewater treatment plant .....	771
<b>L. Dubova, N. Strunnikova, N. Cielava, I. Alsina, O. Kassien and A. Bekker</b>	
Thermal decontamination of sewage sludge .....	781
<b>B. Fagundes, F.A. Damasceno, R.R. Andrade, J.A.O. Saraz, M. Barbari, F.A.O. Vega and J.A.C. Nascimento</b>	
Comparison of airflow homogeneity in Compost Dairy Barns with different ventilation systems using the CFD model .....	788
<b>P.F.P. Ferraz, R.F. Mendes, G.A.S. Ferraz, V.R. Carvalho, M.R.C. Avelino, C.R.P. Narciso, T.M.C. Eugênio, V.C. Gonzalez and G. Bambi</b>	
Thermal analysis of cement panels with lignocellulosic materials for building .....	797
<b>P.F.P. Ferraz, R.F. Mendes, G.A.S. Ferraz, F.A. Damasceno, I.M.A. Silva, L.E.V.S.B. Vaz, L.M. Mendes, D. Cecchin and J.O. Castro</b>	
Comparison between the thermal properties of cement composites using infrared thermal images.....	806
<b>P.F.P. Ferraz, R.F. Mendes, G.A.S. Ferraz, G. Rossi, L. Conti and M. Barbari</b>	
Chemical analyses of lignocellulosic materials residue for cement panels reinforcement.....	815
<b>M. Gailis, J. Rudzitis, M. Madisoo and J. Kreicbergs</b>	
Research on energy efficiency of pneumatic cylinder for pneumatic vehicle motor .....	823
<b>P. Hnízdil, R. Chotěborský and J. Kuře</b>	
Utilization of fused deposition method 3D printing for evaluation of discrete element method simulations .....	842

<b>A.G. Ipatov, A.B. Spiridonov, R.R. Shakirov, A.V. Kostin, S.N. Shmykov and V.S. Kukhar</b>	
Physico-mechanical properties of modified antifriction coatings based on babbitt B83 .....	852
<b>H. Kaletnik, V. Mazur, I. Gunko, V. Ryaboshapka, V. Bulgakov, V. Raide, R. Ilves and J. Olt</b>	
Study on performance of compression engine operated by biodiesel fuel .....	862
<b>M. Khrapova, M. Růžicka and V. Trnka</b>	
Recognition of retroreflective traffic signs by a vehicle camera system.....	888
<b>N.F. Luiz, D. Cecchin, A.R.G. Azevedo, J. Alexandre, M.T. Marvila, F.C. Da Silva, A.L.C. Paes, V.D. Pinheiro, D.F. Do Carmo, P.F.P Ferraz, C.M. Hüther, V.M.F. Da Cruz and M. Barbari</b>	
Characterization of materials used in the manufacture of ceramic tile with incorporation of ornamental rock waste.....	904
<b>D. Maksimov, H. Kalkis, Y. Perevoschikov and Z. Roja</b>	
Qualimetry as productivity criteria in metal-cutting operations .....	915
<b>V. Mitrofanovs, I. Boiko and Ē. Geriņš</b>	
New approach for recycling spare parts, components and assemblies.....	923
<b>F.A. Obando Vega, A.P. Montoya Rios, F.A. Damasceno, J.A. Osorio Saraz and J.A. Costa Do Nascimento</b>	
Airflow profile study of a compost dairy barn using a low-cost 3D-printed anemometer network.....	931
<b>D. Pastare, Z. Roja, H. Kalkis and I. Roja</b>	
Psychosocial risks analysis for employees in public administration.....	945
<b>H. Pihlap, A. Annuk, M. Lehtonen, S. Muiste, A. Tooming and A. Allik</b>	
A control method for increasing the heat usage efficiency of nearly-zero-energy buildings with heat pumps.....	958



**A. Ryabchikov, M. Kiviste, S.-M. Udras, M. Lindpere, A. Vassiljev and N. Korb**

The experimental investigation of the mechanical properties of steel fibre-reinforced concrete according to different testing standards ..... 969

**E.O. Samuilova, A.V. Podshivalov, M.I. Fokina, V.S. Chursina, I.E. Strelnikova and M.V. Uspenskaya**

Tensile properties of wood plastic composites based on plant-filled polyvinyl chloride/poly(3-hydroxybutyrate-co-3-hydroxyhexanoate) matrices ..... 980

**T. Schlechter, R. Froschauer and A. Bronowicka-Schlechter**

Towards a business and production engineering concept for individual beer brewing applying digitalization methodologies..... 989

**L. Šenfelde, D. Kairiša and D. Bārzdiņa**

Effect of concentrate feeding technology on nutrient digestibility in Latvian Dark-Head lambs ..... 1000

**T. Seregina, O. Chernikova, Yu. Mazhaysky and L. Ampleeva**

Features of the influence of copper nanoparticles and copper oxide on the formation of barley crop..... 1010

**K.L. Silva-Martínez, L. Cruz-Rivero, A. Arrieta-González and R. Purroy-Vasquez**

Non-Invasive measurer for methane and carbone dioxide emissions in bovine cattle through TRIZ ..... 1018

**R. Šmigins, V. Pīrs and D. Berjoza**

Investigation in fuel consumption of a hybrid and conventional vehicle..... 1027

**J. Sosnowski, K. Jankowski, M. Truba, J. Novák, E. Zdun and J. Skrzyczyńska**

Morpho-physiological effects of Stymjod foliar application on *Dactylis glomerata* L. .... 1036

**I. Tipans, J. Viba, M. Irbe and S.K. Vutukuru**

Investigation of dual varying area flapping actuator of a robotic fish with energy recovery ..... 1046

**A. Traumann, V. Urbane, J. Ievinš and P. Tint**

The co-influence of noise and carbon dioxide on humans in the work and living environment..... 1056

**M.O. Vilela, R.S. Gates, S. Zolnier, M. Barbari, C.G.S. Teles Junior, R.R. Andrade, K.S.O. Rocha, I.F.F. Tinôco, C.F. Souza, L. Conti and G. Rossi**

Variable velocity system for evaluating effects of air velocity on Japanese quail ..... 1068

**J. Vošahlík and J. Hart**

Reliability of camera systems to recognize facial features for access to specialized production areas..... 1082

**V. Vtoryi, S. Vtoryi and V. Gordeev**

Hydrogen sulfide emissions from cattle manure: experimental study ..... 1090

**A.R.P.P. Weerasuriya Arachchige, L. Mezule and T. Juhna**

Separation of reducing sugars from lignocellulosic hydrolysate: Membrane experiments & system dynamic modelling ..... 1099

## Development of hemp hurd particleboards from formaldehyde-free resins

P. Alao<sup>1,\*</sup>, M. Tobias<sup>1</sup>, H. Kallakas<sup>1</sup>, T. Poltimäe<sup>1</sup>, J. Kers<sup>1</sup> and D. Goljandin<sup>2</sup>

<sup>1</sup>Laboratory of Wood Technology, Department of Material and Environmental Technology, Ehitajate tee 5, EE19086 Tallinn, Estonia

<sup>2</sup>Department of Mechanical and Industrial Engineering, Tallinn University of Technology, Ehitajate tee 5, EE19086 Tallinn, Estonia

\*Correspondence: percy.alao@taltech.ee

**Abstract.** Low density of hemp hurd (*Cannabis Sativa* L), better end of life impact, performance comparable to wood chips and low energy requirement for cultivation make it a suitable alternative raw material for particleboards (Pb). However, due to concerns about sustainability and formaldehyde emissions, it is essential to develop the new bio-based resins from renewable resources. In this research, the mechanical and physical properties of Pb produced from hemp hurds (HH) and a variety of resins: Urea-formaldehyde (UF), formaldehyde-free acrylic resin (Acrodur®) and bio-based soy resin (Soyad™) were compared to those of wood particles (WP) bonded with UF. The results indicate that boards from HH are generally lighter than WP with a 5.6% variation between HH+UF and WP+UF. Hemp boards based on soy-resin showed higher tensile performance, with an average of 0.43 MPa compared to the 0.28 MPa and 0.24 MPa of (HH+UF) and (WP+UF) respectively. Nevertheless, thickness swelling (TS) of HH+UF (27%) was the least, while there was no significant difference in the water absorption (WA) compared to HH+Soyad4740, both were still lower than that of WP+UF. The overall outcome shows that bio-based soy resin can be a suitable alternative to UF as a binder in Pb production.

**Key words:** bio-resin, hemp hurd, mechanical properties, particleboard, urea-formaldehyde.

## INTRODUCTION

In the 21st century, maintaining sustainability in resources and the environment is the main challenge. The rapid increase in growth and imbalance between consumption and limited resources are of essential concern (S. Islam & Bhat, 2019). Therefore, a major trend is to develop new materials and solutions (Latif et al., 2015). One of such directions is related to particleboards from wood. However, this has caused a shortage of wood supply, increased deforestation and over-harvesting, especially in most developing countries (Mirski et al., 2017). As a result, it is more desirable to use non-traditional forest resources like hemp, flax and sisal since they offer comparable performance (Khazaeian et al., 2015). This will further enhance cleaner production, reduction in the consumption or over dependence on a raw material and positive climatic impact (Muizniece, Vilcane & Blumberga, 2015).

*Cannabis Sativa* L. is one of human's earliest cultivated industrial crops (Tobias, 2019). It requires low input for cultivation, it is easily diversified and requires no fertilizer or herbicides; moreover, it is environmentally friendly (Liu et al., 2017). Additionally, it is one of the strongest and stiffest natural woody materials, with its structure consisting of crystalline cellulose (55–72 wt. %), hemicellulose (8–19 wt. %), lignin (2–5 wt. %), waxes, and oils (Islam et al., 2010). Hemp is obtained by planting the hemp seed. When cultivated, CO<sub>2</sub> is trapped from the atmosphere causing a reduction in global warming and increasing air purification (Green Building, 2018). There is no particular soil preference for cultivation and the plant has a fast growth rate, reaching a height of about 4 m in just 100 days (Insulation-info.co.uk, 2019). Europe, China and Canada are the biggest producers of hemp. Natural fibres from hemp are being used to substitute conventional materials and synthetic fibres like glass in thermal insulation and as reinforcement for composites (Lühr, Pecenka & Gusovius, 2015).

For the production of wooden structural elements, such as trusses, plywood, particleboards, fibreboards and furniture, synthetic adhesives based on urea-formaldehyde, polyurethane, polyvinyl acetate, polyester and epoxides are commonly used because they provide excellent adhesive properties, high rigidity, and dimensional stability. However, wastewater from the production of these resins are found to contain a high amount of compounds that are toxic to aquatic life (Łebkowska et al., 2017). Furthermore, there are concerns about human and animal health due to the emission of volatile organic compounds (VOCs) from formaldehyde that is carcinogenic when inhaled and causes asthma, irritation of the eyes, nose, and respiration during hot pressing. Other problem stems from the fact that most synthetic adhesives are obtained from the production of hydrocarbons, which considerably affects air and environmental pollution (Alao et al., 2019). These and many more have led to a surge in research towards deriving appropriate substitutes (M.S. Islam & Miao, 2014).

Bio-based sustainable alternatives studied as potential substitutes are from natural materials like oilseeds and soybean. They are cheap, renewable, and biodegradable and applied in the past to substitute petroleum-based products (Hamarneh, 2010). Tannings, lignin, carbohydrates, and unsaturated oils are the other resins considered as possible replacements. Lately, commercial manufacturing companies have shown increasing interest in developing formaldehyde-free/bio-based adhesives for particleboards and other similar panel products. As an example, M. S. Islam & Miao (2014) focusing on the optimization of the processing conditions of flax fabric used Acrodur that is a product of BASF. It is an aqueous formaldehyde-free resin obtained by the dispersion of the polyester of polycarboxylic acid and polyalcohol in water. According to their results, the resin has the specific tensile strength of 57.9 MPa-cm<sup>3</sup>g<sup>-1</sup> and Young's modulus of 5.5 GPa-cmg<sup>-1</sup>. In the automotive industry, wooden and natural fibre products for cars have been moulded using this adhesive.

The purpose of this research is to develop particleboards from hemp hurd and to ascertain the feasibility of using formaldehyde-free resins as alternatives to urea-formaldehyde. The objectives are: to substitute UF with Acrodur® /Soyad™ resins for hemp hurd particleboards; to investigate the mechanical properties, physical properties and air permeability; to compare and analyse the properties with wood particleboards bonded with conventional resin (UF).

## MATERIALS AND METHODS

### Hemp hurd (HH) and wood particle (WP) board

Hempson OÜ supplied hemp hurd (HH) and we obtained wood particles from AS Repo Vabrikud. The particleboards were made using the same process, but, for the hemp Pb, the HH was first manually cleaned. The board target density of 600 kg m<sup>-3</sup> was chosen for this research (based on EN 314-4 for boards of thickness 13–20 mm) and the dimension was 400×400 mm. The Pb was produced from single-layer 1,200 g of hemp hurd/wood chips (7% average moisture content (MC)) and resin (11% wt. of the hemp hurd or wood particles dry matter), see Eq. (1) for the MC calculation. The adhesives were Urea-formaldehyde (UF), formaldehyde-free acrylic resin (Acrodur® 3510 and 3558 from BASF) and bio-based soy resin (Soyad™ CA4740EU and CA1025). The mixture was stirred in a labor mixer for 3 min, following slow application of the resins to the hemp hurds/wood chips then formed in a frame with a thickness of 15 mm. The blends were hot-pressed at a temperature of 140 °C and pressure of 2 MPa for 5 min. Table 1 shows the properties of the resins, while Fig. 1 shows a schematic of the process of board production.

$$MC = \frac{w_2 - w_3}{w_2 - w_1} \times 100\% \quad (1)$$

where  $w_1$  – weight of container with a lid;  $w_2$  – weight of container with a lid and sample before drying; and  $w_3$  – weight of container with a lid and sample after drying.

**Table 1.** Properties of the adhesives used (Tobias, 2019)

Description	Synthetic resin	Formaldehyde free acrylic resin: Acrodur®		Bio-based (Cationic) resin; Soyad™	
	Casco UF	3510	3558	CA1025	CA4740EU
Colour/Physical state	white-hazy liquid	yellowish liquid	yellowish liquid	golden, liquid	golden, liquid
Solid content (%)	61	50	50	25	48
pH value	7.2–8.4	3–4	3–4	2.8	3.5
Density (gcm <sup>-3</sup> )	1.27–1.30	1.2	1.2	1.07	1.13
Viscosity (mPa.s @23 °C)	100–340	150–300	300–1,500	175	175
Density (g cm <sup>-3</sup> )	1.3	1.2	1.2	1.07	1.13
For board production					
Adhesive					
(wt.% of hemp mass)	11	11	11	11	11
resin					
(wt.% of solid content)	61	50	50	23	48
Hardener (g)	40.25	–	–	58.89	51.69
Amount of water required	–	–	–	56.80	–

### Determination of board density

The density of the specimens was determined based on EVS-EN 323. The specimens were cut to test sizes of 50×50 mm, weighed using the Mettler Toledo B2002-S balance ( $d = 0.01$  g, max weight = 2,100 g) and measured with a digital calliper ( $d = 0.01$  mm). The width, length and thickness of the specimens were measured at three points to the nearest 0.5 mm. We rounded up the average measurements to the nearest 1 mm. The density in kg m<sup>-3</sup> was calculated from the weighed mass and volume.

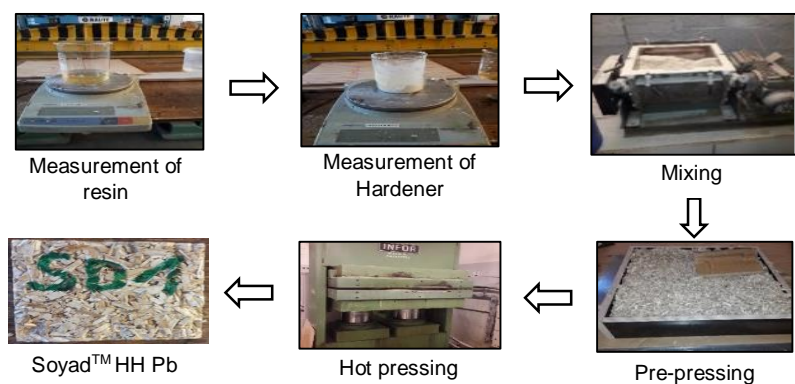


**Figure 1.** The particleboard production process (Tobias, 2019).

### Mechanical tests

The resistance to tension perpendicular to the surface of the test specimen (50×50 mm) was determined by applying the tensile force until the rupture occurs in accordance with EVS-EN 319. The bending strength was evaluated according to EVS-EN 310 by placing a load on the centre of the test specimen (50×250 mm) supported at two points. We used EVS-EN 320 to investigate axial withdrawal of screws by measuring the force required to withdraw a defined screw from the test piece (65×50 mm). All these tests were performed at room temperature (23 °C) using the Instron 5866 machine.

### Water absorption and thickness swelling

The thickness swelling and water absorption were determined by immersing the specimens (50×50 mm) in water at  $20 \pm 2$  °C and relative humidity of  $65 \pm 5\%$  for 24 hr according to EVS-EN 317. After the test, the specimens were drained, weighed and re-measured. The percentage change in mass (water absorption (WA)) and dimension (thickness swelling (TS)) were calculated using the following equations:

$$WA = \frac{m_2 - m_1}{m_1} \times 100\%, \quad (2)$$

where  $m_1$  is the mass of the test specimen, in grams (g), after initial drying and before immersion;  $m_2$  is the mass of the test specimen, in grams (g), after immersion.

$$TS = \frac{t_2 - t_1}{t_1} \times 100\% \quad (3)$$

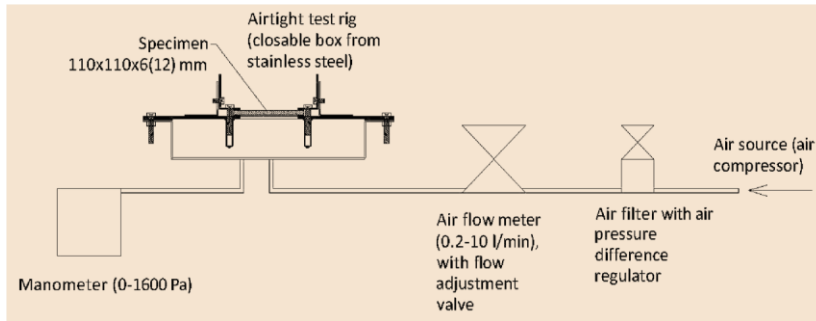
where  $t_1$  is the average thickness of the test specimen (mm), after initial drying and before immersion;  $t_2$  is the average thickness of the test specimen (mm) after immersion.

### Air permeability test

A fabricated test apparatus was used to expose the test specimens (100×100 mm) to two stages of predefined pressure, see Fig. 2. The test was performed to evaluate the insulation properties of the boards by determining the airflow resistivity following EVS-EN12114. The samples were sealed at the edges with tesa tape to prevent air passage during the test. The pressures in the second stage were calculated using the equation below.

$$\Delta p_i = 10^i \frac{\log \Delta p_{max} - \log \Delta p_{min}}{N} + \log \Delta p_{min} \quad (4)$$

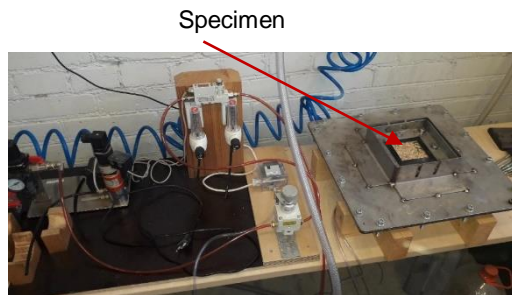
where  $\Delta p$  – pressure difference, Pa;  $N$  – total number of pressure steps; and  $i$  – number of pressure steps.



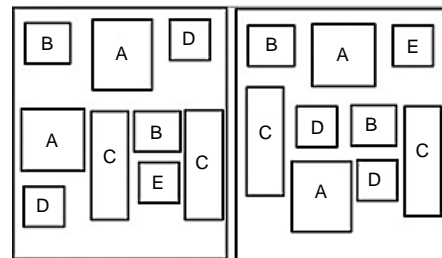
**Figure 2.** Set-up of air permeability test equipment. Source: (Kukk et al., 2017).

Fig. 3 shows the test specimen placed in the airtight test rig and held in place using metal screws. The pressure was applied from a small pipe at the bottom of the box. The maximum pressure difference ( $\Delta p_{max}$ ) was 550 Pa while the minimum ( $\Delta p_{min}$ ) was 50 Pa. In the first stage, three pulses of  $\Delta p_{max}$  were used for about 2 min. The specimens that were airtight at that stage were not subjected to further testing. For specimens with continued airflow,  $\Delta p_i$  was applied until the estimated minimum pressure.

Below (Fig. 4) presents the cutting layout for all the test pieces. Six (6) Pb variants were produced based on the resins and particle material.



**Figure 3.** Air resistivity testing of a specimen under the apparatus.



**Figure 4.** Cut plan for the air permeability (A), axial withdrawal of screw (B), bending (C) tensile strength (D) and density/thickness swelling/water absorption (E) (Tobias, 2019).

## RESULTS AND DISCUSSION

### Density

Fig. 5 reveals the average density results of all the boards. The values ranged from  $477 \text{ kg m}^{-3}$  (HH+ Soyad™ CA1025) to  $581 \text{ kg m}^{-3}$  (WP+UF) with the 5.6% difference between HH+UF and WP+UF linked to low density and the porous structure of hemp (Kallakas et al., 2018). A comparison of HH boards shows that the properties of the adhesives also influence the finite Pb density. For instance, according to Table 1, Soyad

CA1025 has a low solid content (25%) and requires water in preparation, some of which evaporates, causing a decrease in the final density. The 9.3% increase by HH+Soyad CA4740EU confirms this. Interestingly, there was a decrease of 6.8% by HH+Acrodur compared to HH + Soyad CA4740EU, which may be because Acrodur® is a water-based acrylic binder that already, exists in the liquid form. However, its value was still slightly higher than that of HH+Soyad CA1025. The variation of 1% between HH+Acrodur may be due to the processing inconsistency from the laboratory scale process, which is also noted in previous research. Therefore, it was impossible to achieve the target density of  $600 \text{ kg m}^{-3}$  for all the boards (Valarelli et al., 2014).

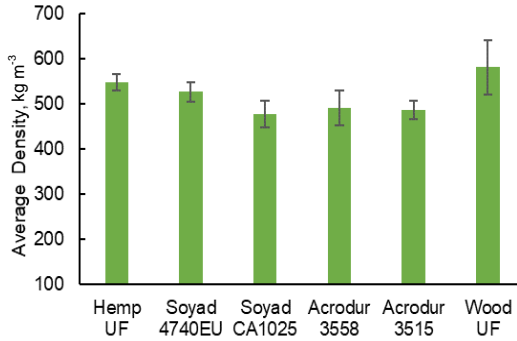


**Figure 5.** Average density values of test specimens.

### Tensile strength

Fig. 6 shows the results of average tensile strengths. Despite the low density of the soy-based hemp Pb, their tensile performance was the highest,  $0.43 \pm 0.07 \text{ MPa}$  (Soyad CA1025) and  $0.44 \pm 0.1 \text{ MPa}$  (Soyad 4740), there was no significant difference. But, there was an increase of approximately 17% in strength for the HH+UF in comparison to WP+UF, which suggest strong interfacial interaction between the hemp hurds and the resin, and improved adhesion (Kallakas et al., 2018); (Kallakas et al., 2019). Overall, HH+Acrodur 3558 had the lowest value ( $0.22 \pm 0.04 \text{ MPa}$ ) that may be because of the high viscosity (300–1,500 MPa.s) of the resin that prevents proper flow and filling of the cavities in the hemp particles. EN 312 stipulates the minimum standard value for tensile strength perpendicular to the plane of the particleboards as 0.24 MPa and from the obtained results, only HH+Acrodur 3558 did not meet this standard.

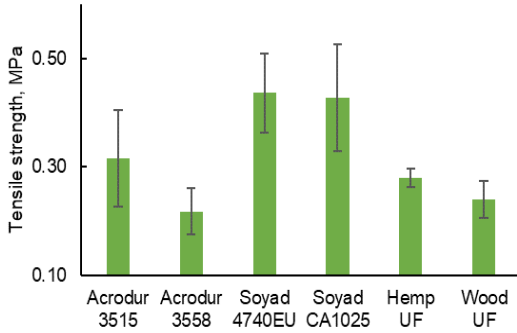


**Figure 6.** Tensile strength perpendicular to the plane of the boards.

### Bending strength

Fig. 7. presents the bending properties of all the test specimens. HH+Soyad CA4740 has the best result in bending (13.9 MPa), which corresponds to a 12% and 78% increase compared to HH+Soyad CA1025 ( $12 \pm 2 \text{ MPa}$ ) and HH+UF ( $3 \pm 0.4 \text{ MPa}$ ) respectively. All the HH Pb performed better than the WP+UF. Furthermore, the comparison of the hemp boards shows that soy-resin hemp Pb demonstrated better modulus of elasticity (MOE), which could be due to the increase in compactness of the



board, caused by the good interfacial interaction between the resin and the hemp hurds (Akinyemi et al., 2019). However, WP+UF showed the best MOE ( $650 \pm 100$  MPa) due to the high density of the board, see Fig. 8. General-purpose boards for use in dry conditions are required to have a maximum bending strength of 11.5 MPa according to EN312, but only the soy-based hemp boards meet this standard.

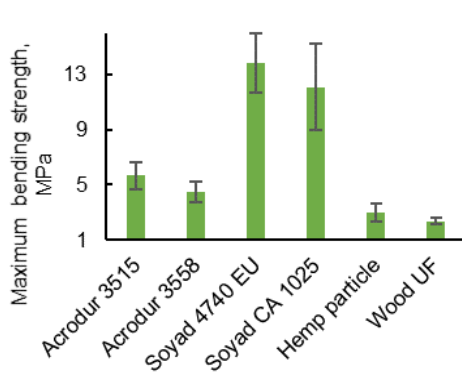


**Figure 7.** Bending strength of the boards.

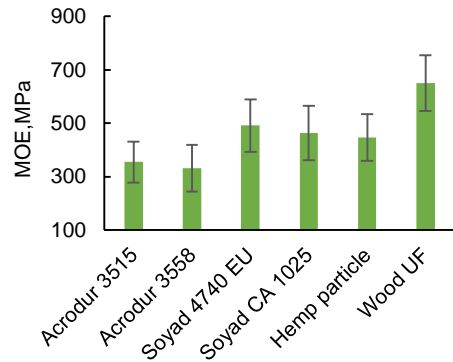


**Figure 8.** Modulus of elasticity of the boards.

### Resistance to axial withdrawal of screws

Ten specimens were tested for the resistance to axial withdrawal of screws. Fig. 9 presents the average results. The Hemp-based boards generally showed better properties than the wood particleboard. The highest axial screw withdrawal strength,  $21.6 \pm 2.7$  N mm<sup>-1</sup> was obtained for the HH+Soyad 4740 at 45.8%, exceeding UF bonded HH and WP. A similar performance of 11.7 N mm<sup>-1</sup> was obtained for UF bonded HH and WP boards. However, if a strong bond exist between the WP and adhesive, the high density of wood compared to hemp should always enhance resistance against the withdrawal of screws, because of the added stiffness of the board (Joščák et al., 2014). Although insignificant, the low margin of correction (0.3 N mm<sup>-1</sup>) of WP+UF in comparison to HH+UF (1.9 N mm<sup>-1</sup>), may be considered as a partial confirmation here. However, none of the particleboards meets the stipulated standard given by EN 622-4.

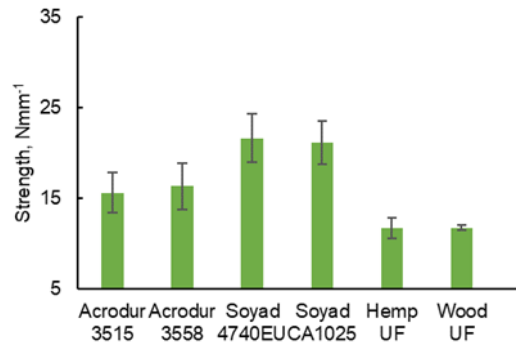


**Figure 9.** Resistance to axial withdrawal of screws.

### Water absorption and thickness swelling

All the test specimens gained mass and showed dimensional changes after the 24-hour immersion, see Fig. 10. The best TS ( $27 \pm 8\%$ ) corresponding to WA of ( $128 \pm 9\%$ )

was by HH+UF. This is an improvement of 40% and 14% in comparison to UF bonded WP respectively, even though HH general have high porosity than WP. The results show that the interaction of the resin with the HH is a more important determinant of dimensional stability and moisture resistance than the porosity or density of the final board. The soy-resin hemp boards also produced better results than WP+UF, however, Acrodur bonded hemp boards had the most affinity for moisture because the WA and TS outcomes were higher than the other samples. Considering our experimental procedure (EVS-EN 317), there is no standard maximum value given by EN 312 for particleboards WA, but the TS values for non-load bearing boards for use in dry and humid conditions are 15% & 14% respectively. None of the boards from this study achieved the required standard. This outcome may not be surprising, giving that there was no prior modification of the particles or coating of the finished boards with water repellent chemical. Earlier research observed that the board-density influences the TS and WA. (Akinyemi et al., 2019). Yet, this effect is not clear in this study because the high-density WP+UF gives a better result compared to the low-density HH+Acrodur, but different outcome to HH bonded UF and Soyad™.

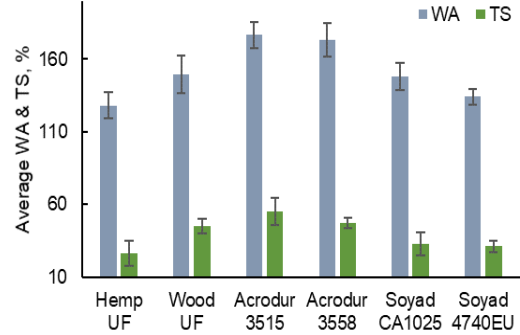


**Figure 10.** Water absorption and thickness swelling of all boards after 24-hour immersion.

### Air permeability

The HH boards were all airtight at the first stage pressure (550 MPa); hence, the results presented in Table 2 only show the outcome for the WP with an average value of 1.84 L s<sup>-1</sup> m<sup>2</sup>.

Although research on this topic is insufficient, the outcome is comparable to (Kallakas et al., 2018) where 1.73 L s<sup>-1</sup> m<sup>2</sup> was reported. This result confirms that the interaction between the resins and hemp hurds is stronger than that between the wood particle and the UF resin.

**Table 2.** Air permeability of the wood particleboard

Pressure steps	Pressure, Pa	Average Air permeability, L s <sup>-1</sup> m <sup>2</sup> L min <sup>-1</sup>	Air flow, L s <sup>-1</sup> m <sup>2</sup>
2 <sup>nd</sup>	50	0.29	0.48
	73	0.41	0.67
	108	0.56	0.98
	158	0.82	1.40
	232	1.12	2.03
	341	1.66	2.77
	500	2.45	4.08
1 <sup>st</sup>	550	2.67	4.13

## CONCLUSIONS

This study examined the possibility to use formaldehyde-free resin with hemp hurds to produce particleboards. The use of hemp hurds bonded with bio-based resin resulted in enhanced mechanical properties of the particleboard. However, the poor outcome in the TS and WA shows that prior modification of the hemp particles or the use of water repellent additives should be considered for wet application. Although the

airtightness was excellent, evaluations on a larger scale, vis-à-vis conventional insulation materials, are needed. Finally, it is required to compare the performance of the wood particleboards, especially for better justification, those bonded with soy-based resins with the HH particleboard.

ACKNOWLEDGEMENTS. The European Union, financed by the regional development fund and ASTRA 'TUT Institutional Development Programme for 2016-2022' Graduate School of Functional Materials and Technologies '(2014–2020.4.01.16-0032)'.

## REFERENCES

- Akinyemi, B.A., Olamide, O. & Oluwasogo, D. 2019. Formaldehyde free particleboards from wood chip wastes using glutaraldehyde modified cassava starch as binder. *Case Studies in Construction Materials*, **11**.
- Alao, P.F., Kallakas, H., Poltimäe, T. & Kers, J. 2019. Effect of hemp fibre length on the properties of polypropylene composites. *Agronomy Research* **17**(4), 1517–1531.
- EVS-EN 323:2002. Wood-based panels - Determination of density, Eesti Standardikeskus.
- EVS-EN 317:2000. Particleboards and fibreboards - Determination of swelling in thickness after immersion in water, Eesti Standardikeskus.
- EVS-EN 320:2011. Particleboards and fibreboards - Determination of resistance to axial withdrawal of screws, Eesti Standardikeskus
- EVS-EN 319:2000. Particleboards and fibreboards - Determination of tensile strength perpendicular to the plane of the board, Eesti Standardikeskus.
- EVS-EN 310:2002. Wood-based panels - Determination of modulus of elasticity in bending and bending strength, Eesti Standardikeskus.
- EVS-EN 12114:2000. Thermal performance of buildings - Air permeability of building components and building elements - Laboratory test method, Eesti Standardikeskus.
- EVS-EN 312:2010. Particleboards - Specifications - Part 4: Requirements for soft boards, Eesti Standardikeskus.
- Green Building. 2018. Hemp Insulation Comes to North America. 1–7. Retrieved from <https://www.greenbuildingadvisor.com/article/hemp-insulation-comes-to-north-america>.
- Hamaneh, A.I., Heeres, H.J., Broekhuis, A.A., Sjollem, K.A., Zhang, Y. & Picchioni, F. 2010. Use of soy proteins in polyketone-based wood adhesives. *International Journal of Adhesion and Adhesives* **30**(7), 626–635.
- Islam, S. & Bhat, G. 2019. Environmentally friendly thermal and acoustic insulation materials from recycled textiles. *Journal of Environmental Management* **251**, 109536.
- Islam, M.S. & Miao, M. 2014. Optimising processing conditions of flax fabric reinforced Acrodur biocomposites. *Journal of Composite Materials* **48**(26), 3281–3292.
- Islam, M.S., Pickering, K.L. & Foreman, N.J. 2010. Influence of alkali treatment on the interfacial and physico-mechanical properties of industrial hemp fibre reinforced polylactic acid composites. *Composites Part A: Applied Science and Manufacturing* **41**(5), 596–603.
- Joščák, P., Langová, N., Tvrdošský, M. 2014. Withdrawal resistance of wood screw in wood-based materials. *Annals of Warsaw University of Life Sciences–SGGW Forestry and Wood Technology*, Warsaw, **96**, 90–96.
- Kallakas, H., Liblik, J., Alao, P.F., Poltimäe, T., Just, A. & Kers, J. 2019. Fire and Mechanical Properties of Hemp and Clay Boards for Timber Structures. *IOP Conference Series: Earth and Environmental Science*, Prague, Czech Republic **290**(1).
- Kallakas, H., Närep, M., Närep, A., Poltimäe, T. & Kers, J. 2018. Mechanical and physical properties of industrial hemp-based insulation materials. *Proceedings of the Estonian Academy of Sciences*, Tallinn, Estonia, **67**(2), pp. 183–192.

- Khazaeian, A., Ashori, A. & Dizaj, M.Y. 2015. Suitability of sorghum stalk fibers for production of particleboard. *Carbohydrate Polymers* **120**, pp. 15–21.
- Kukk, V., Horta, R., Püssa, M., Luciani, G., Kallakas, H., Kalamees, T. & Kers, J. 2017. Impact of cracks to the hygrothermal properties of CLT water vapour resistance and air permeability. *Energy Procedia* **132**, 741–746.
- Latif, E., Ciupala, M.A., Tucker, S., Wijeyesekera, D.C. & Newport, D.J. 2015. Hygrothermal performance of wood-hemp insulation in timber frame wall panels with and without a vapour barrier. *Building and Environment* **92**, 122–134.
- Łebkowska, M., Załęska-Radziwiłł, M. & Tabernacka, A. 2017. Adhesives based on formaldehyde – environmental problems. *Biotechnologia* **98**(1), 53–65.
- Liu, M., Thygesen, A., Summerscales, J. & Meyer, A.S. 2017. Targeted pre-treatment of hemp bast fibres for optimal performance in biocomposite materials: A review. *Industrial Crops and Products* **108**, 660–683.
- Lühr, C., Pecenka, R. & Gusovius, H.-J. 2015. Production of high quality hemp shives with a new cleaning system. *Agronomy Research* **13**(1), 130–140.
- Mirski, R., Boruszewski, P., Trociński, A. & Dziurka, D. 2017. The Possibility to Use Long Fibres from Fast Growing Hemp (*Cannabis sativa L.*) for the Production of Boards for the Building and Furniture Industry. *BioResources* **12**(2), 3521–3529.
- Muizniece, I., Vilcane, L. & Blumberga, D. 2015. Laboratory research of granulated heat insulation material from coniferous forestry residue. *Agronomy Research* **13**(3), 690–699.
- Tobias, M.O. 2019. *Development of hemp hurdboard from formaldehyde-free resins*. MSc Thesis, Tallinn University of Technology, Tallinn, Estonia, 62 pp.
- Valarelli, I.D.D., Battistelle, R.A.G., Bueno, M.A.P., Bezerra, B.S., de Campos, C.I. & Alves, M.C.d.S. 2014. Physical and mechanical properties of particleboard bamboo waste bonded with urea formaldehyde and castor oil based adhesive. *Revista Materia* **19**(1), 1–2.

## **Lighting and noise levels in compost dairy barns with natural and forced ventilation**

R.R. Andrade<sup>1,\*</sup>, I.F.F. Tinôco<sup>1</sup>, F.A. Damasceno<sup>2</sup>, M. Barbari<sup>3,\*</sup>, D.A. Valente<sup>1</sup>,  
M.O. Vilela<sup>1</sup>, C.F. Souza<sup>1</sup>, L. Conti<sup>3</sup> and G. Rossi<sup>3</sup>

<sup>1</sup>Federal University of Viçosa, Department of Agricultural Engineering, Av. Peter Henry Rolfs, s/n Campus University of Viçosa, BR 36570-900, Viçosa, Minas Gerais, Brazil

<sup>2</sup>Federal University of Lavras, Department of Engineering, BR37200-000 Lavras, Minas Gerais, Brazil

<sup>3</sup>University of Florence, Department of Agriculture, Food, Environment and Forestry, Via San Bonaventura, 13, 50145 Firenze, Italy

\*Correspondence: [matteo.barbari@unifi.it](mailto:matteo.barbari@unifi.it), [rafaella.andrade@ufv.br](mailto:rafaella.andrade@ufv.br)

**Abstract.** The housing system, called compost barn, is attracting the interest of several farmers. It allows dairy cows to remain in free movement inside a shed without any containment partitions like those used in freestall barns. In Brazil the compost barns with open sides are very common, but recently some closed barns with climatic control systems have been implemented. The objective of this work was to evaluate and compare lighting and noise levels in an open compost barn with natural ventilation and in a closed compost barn with a climate control system. The latter one is based on tunnel ventilation: inlet of air through evaporative cellulose panels and exit through fans placed on the opposite wall. Through analysis of the collected data it was observed that the sound pressure recorded inside both analysed buildings did not exceed the ranges of noise discomfort recommended for the rearing of animals. However, the sound pressure amplitude inside the barn with climate control system was greater than in the open barn. The light intensity was significantly lower in the closed barn when compared to the open barn (84.96 and 1,413.58 lx, respectively). The artificial lighting system distributed throughout the closed barn was not sufficient to maintain brightness within the recommended range for lactating cows. In addition, it was found that in the closed building with forced ventilation, the highest brightness values are located near the exhaust fans.

**Key words:** animal facility, dairy cows, compost-bedded pack barn, light intensity.

## **INTRODUCTION**

Intensive milk production systems are commonly adopted by large producers around the world. In such systems care must be taken to ensure to the animals the appropriate environment throughout the year, that is one of the main challenges to win (Leão et al., 2015). Facilities used for dairy cows must be well designed to promote maximum animal comfort and mitigate the effects of climatic and physical factors that may interfere with the quality of production.

Compost bedded pack barns, generally known as compost barns, are alternative housing systems for dairy cows (Leso et al., 2013; Leso et al., 2019), attracting global interest. Compost barn is a housing system in which cows remain in free circulation within a covered shed (Eckelkamp et al., 2016; Leso et al., 2020). The system consists of confining the animals in facilities with a wide bedding area realized with organic matter substrates. The main purpose of bed materials is to absorb animal excreta and favour aerobic composting (Janni et al., 2007).

In naturally ventilated systems the facilities must be located in open areas to ensure natural ventilation to work well (Damasceno, 2012). The facility must be located with a slight elevation from the surrounding terrain to prevent the pack from getting wet during rainy periods, which would raise its humidity to undesirable levels (Janni et al., 2007).

When natural ventilation is not enough to improve the internal environment of the facility, it is necessary to use fans placed over both bedding area and feeding alley, aiming to reduce the heat load and improve air quality in the environment, besides to promote drying of the upper layer of the pack (Lobeck et al., 2012).

In Brazil, it is observed that many compost dairy barns are open on the sides, but recently some closed compost barns with climate control systems have been built. Currently, there is little information on the performance of completely closed compost dairy barns.

Fully enclosed facilities rely on mechanical ventilation and typically use evaporative cooling to reduce the temperature during the warmer months. In addition, some fully enclosed facilities for milk production install baffles, made of metal or canvas, to redirect airflow and to increase air speed to the space where the cows are located. The lower part of the baffles cannot interfere with the normal operation of machineries used to handle the bedding (Sheffield et al., 2007).

In this case, the way the system is built and the adaptation to hot weather conditions may allow the ideal temperature and air velocity to be maintained. The enclosed confinement system requires special attention in controlling environmental parameters that influence animal comfort and performance such as air temperature, relative humidity, air velocity, gas concentration, and dust (Damasceno et al., 2019). However, other factors, such as artificial lighting and fan noise, are important variables for the influence on livestock environment quality.

Several researchers investigated the effect of light day duration and light intensity on the main factors influencing the productive and reproductive performance in dairy cattle farms. Light is an essential component of farm animal environment. The lighting of facilities is necessary for a very important element of animal welfare that is the contact with other animals of the group (Phillips & Schofield, 1989; Dahl et al., 2000; Penev et al., 2014)

The physiological effect of light on dairy cows is well reported in the literature. Light intensity and the photoperiod influence the physiological response of dairy cows, impacting on growth, reproduction, and lactation. (Dahl et al., 2012).

Philips et al. (2000) tried to apply different levels of the light intensity (from 0 to 250 lx) in a cubicle passageway where cows walked to receive a food reward. They found that the optimum illumination for dairy cow locomotion could be considered between 39 and 119 lx.

Dahl et al. (2000) stated that to stimulate milk production the lighting system has to provide values of 150 lx of illuminance throughout the barn and 16–18 hours of continuous light.

The recommended illuminance levels for dairy livestock facilities, summarized by ASABE 2006 on several data collected in literature (MWPS, 1992; NFEC, 1993; Leech & Person, 1993), are the following: parlour, pit and near udder, 500 lx; parlour, stalls and return lanes, 200 lx; parlour, holding area, 100 lx; milking room, general, 200 lx; milking room, washing, 750–1,000 lx; stall barn, manger alley, 100 lx; stall barn, milking alley, 200 lx; drive-through, feed alley, 200 lx.

Lobeck et al. (2012) compared low profile cross-ventilated freestall and compost bedded pack barns for dairy cows. The authors observed that in the fully closed and air-conditioned freestall system the light intensity inside the facility was significantly lower than in compost barns and presented values close to the minimum for the light intensity recommended for cows during the lactation period.

The sensitivity of cattle to sound, and the levels to which they are exposed, has been reviewed by many authors. Thresholds for discomfort of cattle are indicated at 90–100 dB, with physical damage to the ear occurring at 110 dB (Phillips, 2009). Several studies show that sudden and unexpected sounds seem to have an impact on animal behaviour more than continuous high noise (Grandin, 1998; Arnold et al., 2007; Brouček & Slovak, 2014).

Oliveira et al. (2019), evaluating compost dairy barns with different ventilation systems, observed that the highest noise levels were observed close to fans or in the line of action of fans, as well as at the entrance to the feeding alley. The high noise levels were caused both by the presence of mechanical ventilation and by the presence of animals.

The objective of this work was to evaluate and compare the lighting and noise levels in a naturally ventilated compost dairy barn and in a compost barn with a climate control system by forced ventilation.

## **MATERIALS AND METHODS**

### **General considerations**

The survey was conducted in two compost dairy barns with different ventilation systems: climate controlled (CBC) and natural ventilation (CBN). The facilities are located on the same farm, in the city of Cajuri (Minas Gerais, Brazil), at 670 m altitude, coordinates 20° 46' 41" S and 42° 48' 57" W. The region's climate according to the Köppen classification is tropical in altitude, with rainy summers and cold and dry winters (Silva et al., 2004).

### **Evaluated treatments**

a) The climate controlled compost barn (CBC) was built in May 2017. The dimensions of the CBN barn are 55.0 m × 26.4 m. It is oriented northwest-southeast. The feeding alley has a concrete floor and is 4 m wide. The feeding alley, which includes the waterers, is separated from the pack by a low concrete wall (1.2 m). The building has a concrete structure and is covered with metal sheets. The eave height is 5 m and eave overhang is 0.8 m. Throughout the barn, five baffles are installed, placed 3 m above the floor and spaced every 11 m. The colour of the baffles is light blue.

Five LED lamps (100W) are distributed along the bedding area and feeding alley.

During the trials the CBC barn was bedded with a mix of wood shavings and coffee shells. The depth of the bed was approximately 0.50 m. The pack (dimensions 55.0 m × 16.0 m) was aerated twice a day using a chisel with roller, coupled to a tractor, while the cows were milked. The pack was aerated to a depth of 0.20. This barn was not cleaned out during the year.

On the southeast side of the building, porous cellulose panels with dimensions 18.0×3.5 m are used for evaporative cooling. The panels are moistened by dripping to cool the air before entering the CBC. A temperature sensor located inside the CBC monitors environmental conditions and allows the system to remain on if the air temperature is above 21 °C and the relative humidity below 75%.

On the northwest side the facility has five exhaust fans (BigFan®, 3.5 m diameter, six propellers, air volume 150,000 m<sup>3</sup> h<sup>-1</sup> volume and power of 2.0 HP). The five exhaust fans remain on continuously, 24 hours a day.

In the experimental period the CBC housed 88 lactating Holstein cows (600 kg) with a stock density of 10 m<sup>2</sup> cow<sup>-1</sup>. The milk production per cow was 25 kg day<sup>-1</sup>.

b) The natural ventilation compost barn (CBN) was built in July 2019. The dimensions of the CBN barn are 60.0 m × 24.0 m. The feeding alley is paved with concrete and is 4 m wide. The feeding alley, which includes the waterers, is separated from the pack by a low concrete wall (1.2 m). The structure of the building is in concrete. The roof is realized with metal sheets. The eave height is 6 m and eave overhang is 0.5 m.

A low concrete wall is present around the perimeter of the barn and wire cables are placed above the wall to prevent cows from falling or jumping onto feeding alley.

During the trials the CBN barn was bedded with a mix of wood shavings. The depth of the bed was approximately 0.30 m. The pack (dimensions 60.0 m × 14.0 m) was aerated twice a day using a chisel with roller, coupled to a tractor, while the cows were milked. The pack was aerated to a depth of 0.20. This barn was not cleaned out during the year. The barn has completely open sides to allow natural ventilation.

In the experimental period the CBN housed 63 lactating Holstein cows (600 kg) with a stock density of 13.3 m<sup>2</sup> cow<sup>-1</sup>. The milk production per cow was 30 kg day<sup>-1</sup>.

### **Data collection**

The study was carried out during the month of August 2019, that is winter season in the southern hemisphere. The variables illuminance (lx) and noise (dB) were recorded inside the two compost barns in the morning shift.

The evaluated data were collected into a rectangular grid containing 54 equidistant points, placed over the bedding area and feeding alley. Therefore, the data were collected in the area of 60 m × 18 m (CBN) and 55 m × 20 m (CBC). The collection of illuminance and noise data in each barn occurred on the same day and time. The procedures for data collection for both facilities were similar. The variables were collected at a height of 1.5 m.

A portable digital lx meter (MINIPA, model MLM-1011, range from 0 to 100,000 lx with 4.0% accuracy) was used for the illuminance measurements. For noise level measurements, a digital sound pressure level meter (Instrutherm®, ITDEC 4,000 model, accurate to ± 1.5 dB, measuring filter: A) was used.



**Statistical analysis**

Descriptive statistics was used to determine the mean, standard error, median, coefficient of variation, kurtosis, minimum and maximum values for each of the variables analysed in both facilities.

The conditions of noise level and lighting verified inside each of the compost dairy barn studied were compared statistically by means of the Mann–Whitney test at the level of 5% of significance.

Subsequently, from the data collected, descriptive maps of lighting and noise were generated (data is interpolated into a grid for contour plots).

The SigmaPlot® 12.0 software was used as a tool statistics for all analyses performed.

**RESULTS AND DISCUSSION**

**Illuminance (lx)**

According to Table 1, the average light intensity results were 1,413.58 lx (286.67–4,523.33 lx) for the CBN system and 84.96 lx (3.0–492.67 lx) for the CBC system. According to the values mentioned above, it is observed that average light intensity (84.96 ± 18.39 lx) recorded in the CBC was below the ranges considered ideal for lactating cows. The variation coefficients showed high variability for the barns, being higher inside the CBC.

**Table 1.** Values of mean, standard error (SE), median, coefficient of variation (CV), minimum value (Min.), and maximum value (Max.) illuminance (lx), in climate controlled compost dairy barn (CBC) and natural ventilation compost dairy barn (CBN)

	Mean ± SE	Median	CV (%)	Min.	Max.
Illuminance (lx)					
CBN	1,413.58 ± 139.82	998.33	73	286.67	4,523.33
CBC	84.96 ± 18.39	24.66	159	3.0	492.67

Lighting is an important factor in the milk production sector and regulates the health and welfare of animals. Studies have shown that to observe an efficient production response in lactating cows, the recommended light intensity is about 160 lx (Buyserie et al., 2001; Dahl, 2001). With regard to lactation, increasing light exposure to 16 to 18 h d<sup>-1</sup> (long-day photoperiod) with intensity of 200 lx enhances milk production on average (Dahl & Petitclerc, 2003).

According to NBR 5413 (1992), in places where general lighting is used continuously or areas with simple visual tasks (example in the region of the pack) the illuminance has to be from 100 to 200 lx. For the feeding alley, a minimum light level of 200 lx is recommended (House, 2015).

The lighting in the barns is also desired for inspecting animals and handling dairy cows. Cows move more easily through uniformly lit entrances and exits (Damasceno, 2012).

Fig. 1 shows the distribution of the light intensity based on data collected in the two facilities. A statistically significant difference was found between the data observed in the CBN and CBC barns.

The highest average values found in the CBN in comparison to those observed in the CBC are within the expected range, because the intensity of the CBN light depends mainly on the external conditions.

In a study by Lobeck et al. (2012) who evaluated and compared the light intensity in a closed installation with mechanical ventilation, low profile cross-ventilated freestall (CV), open compost barn (CB) and naturally ventilated freestall (NV), the results showed that light intensity was significantly lower in CV system than in CB and NV (111, 480 and 392 lx, respectively). The results were similar to those found in this study.

The CBC barn showed values of light intensity below that recommended for lactating dairy cows until the end of the study. It is observed that the closed barn had influence on the luminous intensity values, indicating that modifications need to be made in order to improve the lighting conditions inside. Lobeck et al. (2012) recommend that producers who build compost barns install additional lighting because the efficiency of the lamps decreases over time and due to the presence of dust.

For the CBN and CBC facilities, results on the lighting intensity showed that there was variation of this variable inside the facility, with greater amplitude for the CBN (Fig. 2, a, b).

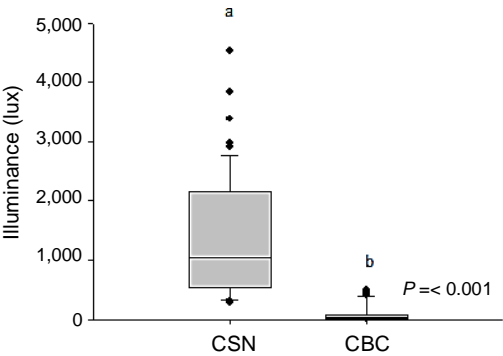


**Figure 1.** Distribution charts for illuminance data, in lux, during the winter period, in climate controlled compost barn (CBC) and natural ventilation compost barn (CBN). Averages followed by the same letters do not differ from each other at the 5% probability level by the Mann-Whitney test.

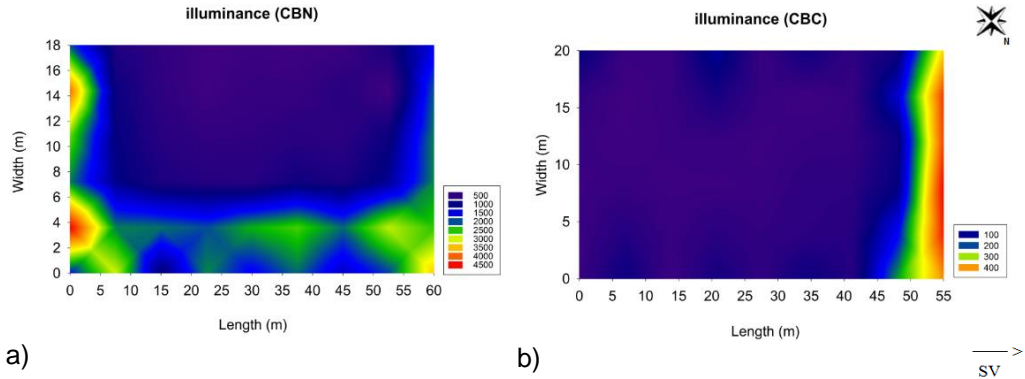


**Figure 2.** Maps of illuminance, in lx, during the winter period, in in climate controlled compost barn (CBN) and natural ventilation compost barn (CBC). SV – sense of ventilation.

It is observed that the CBN (Fig. 2, a) had a huge amplitude, and a pattern of higher light intensity concentration in the northwest, southwest and southeast faces of the house. It was observed that the presence of the overshoot ridge, from the data collected in the

morning, contributed to the greater passage of light in parts of the facility, which could be observed near the southwest face of the installation.

The lamps were not evenly arranged within the CBC barn (Fig. 2, b), so a variation in illuminance values was expected. In addition, in CBC the light intensity presented the highest values in the region near the hoods, which occurs due to its large diameter, allowing a greater passage of light.

**Noise Levels**

According to Table 2, the average noise levels present a mean value of 51.58 dBA (48.13–53.63 dBA) for the CBN system and of 54.45 (49.57–62.87 dBA) for the CBC system. It is observed that the maximum noise level values found in both facilities did not exceed the noise discomfort ranges, indicating a comfortable sound condition, resulting in tranquillity for the animals. Phillips (2010) classifies the range for hearing discomfort in cows between 90 and 100 dB, with physical damage occurring close to 110 dB.

**Table 2.** Values of mean, standard error (SE), median, coefficient of variation (CV), minimum value (Min.), and maximum value (Max.) noise (dBA), in climate controlled compost barn (CBC) and natural ventilation compost barn (CBN)

	Mean ± SE	Median	CV (%)	Min.	Max.
Noise (dBA)					
CBN	51.58 ± 0.16	51.61	2.3	48.13	53.63
CBC	54.45 ± 0.49	53.31	6.6	49.57	62.87

The variation coefficients showed low variability for the barns, being higher inside the CBC.

The distribution of the noise level data verified in the two facilities is presented in Fig. 3. A statistically significant difference was found between the data observed in the CBN and CBC.

CBN presented lower average values than CBC, with a more uniform distribution when compared to CBC. The results found in this study were similar to those presented by Damasceno et al. (2019). The lower values of sound pressure observed in CBN are mainly due to the vocalization of animals, the management operations and external sources.

For the CBN and CBC facilities, the results on the noise levels showed that there was variation of this variable inside the installation, with greater amplitude for the CBC (Fig. 4, a, b).

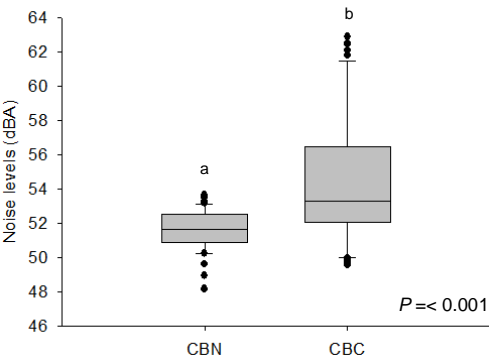


**Figure 3.** Distribution charts for noise level data, in dBA, during the winter period, in climate controlled compost barn (CBC) and natural ventilation compost barn (CBN). Averages followed by the same letters do not differ from each other at the 5% probability level by the Mann-Whitney test.

The results found in this study are similar to those presented by Garcia (2017), in which closed freestall facilities with climate control and open facilities were compared for the confined dairy cattle. The authors observed that the closed facilities presented greater amplitude (26.26 dB) in the sound pressure levels in relation to the open installations (7.8 dB) in trials carried out during the autumn, in the morning period. In this study, the sound pressure recorded in the confinement sheds also did not exceed the ranges of noise discomfort.

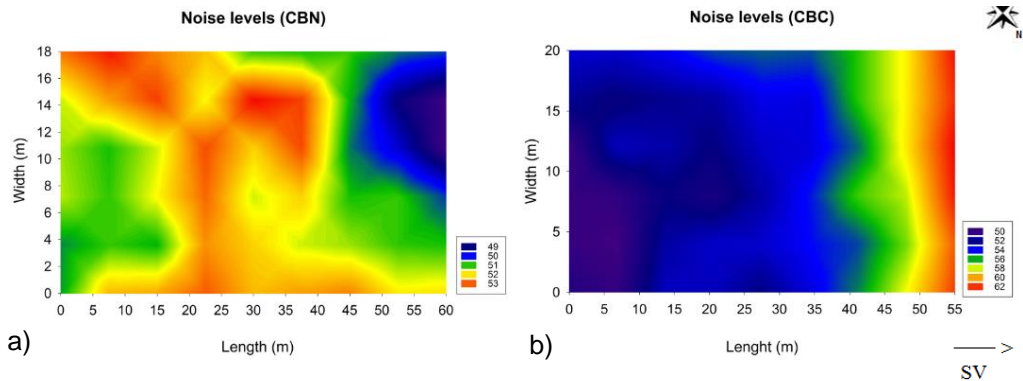


**Figure 4.** Maps of noise levels, in dBA, during the winter period, in climate controlled compost barn (CBC) and natural ventilation compost barn (CNB). SV – sense of ventilation.

The results showed (Fig. 4, b) the increase of noise in the region near the exhaust fans (62 dBA) in the CBC installation, being the highest values observed in the face where they were located, allowing to state that its occurrence is due to the characteristic noise caused by the rotation of the exhaust fans. On the opposite side of the CBC, close to the evaporative cooling plates, mean sound pressure values of 50 dB A were found.

The results are in agreement with other authors. Smith & Harner (2007) evaluated a cross-ventilated facility and found average noise levels below 65 dB, regardless of the number of fans in operation. In another study Damasceno et al. (2019), in CBC barn, found noise level values from 45 to 70 dB. The highest values were observed in the area immediately next to the face where the fans were located, due to their rotation.

### CONCLUSIONS

The natural ventilation compost barn presented, as expected, more light intensity when compared to climate controlled compost barn. In the latter, the artificial lighting system distributed throughout the facility was not sufficient to maintain the light intensity within the range recommended for lactating cows.

The sound pressure recorded inside the compost barn did not exceed the ranges of noise discomfort recommended for the rearing of animals in both the two facilities analysed. The facilities with artificial climatic control systems had average noise values below 62 dBA.

ACKNOWLEDGEMENTS. The authors are thankful to the Federal University of Viçosa (UFV–Brazil) and AMBIAGRO. This work was carried out with the support of CNPq, National Council for Scientific and Technological Development – Brazil, FAPEMIG and CAPES.

## REFERENCES

- Arnold, N.A., Kim, T.N., Jongman, E.C. & Hemsworth, P.H. 2007. The behavioural and physiological responses of dairy heifers to taperecorded milking facility noise with and without a pre-treatment adaptation phase. *Appl. Anim. Behav. Sci.* **106**, 13–25.
- ASABE STANDARDS 2006. Lighting Systems for Agricultural Facilities ASAE EP344.3 Jan 2005, 685–697.
- Brouček, J. & Slovak, J. 2014. Effect of noise on performance, stress, and behaviour of animals. *Anim. Sci.* **47**(2), 111–123.
- Buyserie, A.C., Dahl, G.E. & Gamroth, M.J. 2001. [https://ir.library.oregonstate.edu/concern/administrative\\_report\\_or\\_publications/xd07gt17](https://ir.library.oregonstate.edu/concern/administrative_report_or_publications/xd07gt17). Accessed 18.03.2020.
- Dahl, G.E. 2001. Photoperiod control improves production and profit of dairy cows. In: *Proc. 5<sup>th</sup> Western Dairy Management Conference*, Las Vegas, Nevada, pp. 27–30.
- Dahl, G.E. & Petitclerc, D. 2003. Management of photoperiod in the dairy herd for improved production and health. *J. Anim. Sci.* **81**, 11–17.
- Dahl, G.E., Buchanan, B.A. & Tucker, H.A. 2000. Photoperiodic effects on dairy cattle: A review. *J. Dairy Sci.* **83**, 885–893.
- Dahl, G.E., Tao, S. & Thompson, I.M. 2012. Lactation biology symposium: Effects of photoperiod on mammary gland development and lactation. *J. Anim. Sci.* **90**, 755–760.
- Damasceno, F.A. 2012. Compost bedded pack barns system and computational simulation of airflow through naturally ventilated reduced model. *Thesis*, Universidade Federal de Viçosa, Brazil, 404 pp.
- Damasceno, F.A., Oliveira, C.E.A., Ferraz, G.A.S., Nascimento, J.A.C., Barbari, M. & Ferraz, P.F.P. 2019. Spatial distribution of thermal variables, acoustics and lighting in compost dairy barn with climate control system. *Agronomy Research* **17**, 385–395.
- Eckelkamp, E.A., Taraba, J.L., Akers, K.A., Harmon, R.J. & Bewley, J.M. 2016. Understanding compost bedded pack barns: Interactions among environmental factors, bedding characteristics, and udder health. *Livestock Science* **190**, 35–42.
- Garcia, P.R. 2017. Low-Profile Cross-Ventilated freestall: thermal, zootechnical and animal welfare performance. *Thesis*, University of São Paulo, Brazil 150 pp. (in Portuguese).
- Grandin, T. 1998. The feasibility of using vocalization scoring as an indicator of poor welfare during cattle slaughter. *Appl. Anim. Behav. Sci.* **56**, 121–128.
- House, H.K. 2004. Lighting for More Milk. Free Stall Housing Manual. <http://www.omafra.gov.on.ca/english/engineer/facts/15-011.htm#1>. Accessed 27.03.2020.
- Janni, K.A., Endres, M.I., Reneau, J.K. & Schoper, W.W. 2007. Compost dairy barn layout and management recommendations. *Appl. Eng. Agric.* **23**, 97–102.
- Leão, J.M., Lima, J.A.M., Pôssas, F.P. & Pereira, L.G.R. 2015. Use of infrared thermography in precision livestock. *Embrapa Gado de Leite* **79**, 97–109 (in Portuguese).
- Leech, J.F. & Person, H.L. 1993. Housing for Horses (HIH 320). In American Youth Horse Council (ed): *Horse Industry Handbook*, Lexington, KY, pp. 1–9.
- Leso, L., Uberti, M., Morshed, W. & Barbari, M. 2013. A survey of Italian compost dairy barns. *J. Agr. Eng.* **44**, 120–124.
- Leso, L., Pellegrini, P. & Barbari, M. 2019. Effect of two housing systems on performance and longevity of dairy cows in Northern Italy. *Agronomy Research* **17**, 574–581.
- Leso, L., Barbari, M., Lopes, M.A., Damasceno, F.A., Galama, P., Taraba, J.L. & Kuipers, A. 2020. Invited review: Compost-bedded pack barns for dairy cows. *J. Dairy Sci.* **103**(2), 1072–1099.

- Lobeck, K.M., Endres, M.I., Janni, K.A., Godden, S.M. & Fetrow, J. 2012. Environmental characteristics and bacterial counts in bedding and milk bulk tank of low profile cross-ventilated, naturally ventilated, and compost bedded pack dairy barns. *Appl. Eng. Agric.* **28**, 117–128.
- NBR, ABNT. 5413. 1992. Interior illuminance. Brazilian Association of Technical Standards. Rio de Janeiro, 13 pp. (in Portuguese).
- NFEC. 1993. *Agricultural Wiring Handbook*. National Food and Energy Council, 409 Vandiver West, Suite 202, Columbia, Missouri 65202, 113 pp.
- MWPS. 1992. *Farm Buildings Wiring Handbook*. MWPS-28. Midwest Plan Service, Ames IA 50011, 96 pp.
- Oliveira, C.E.A., Damasceno, F.A., Ferraz, P.F.P., Nascimento, J.A.C., Ferraz, G.A.S. & Barbari, M. 2019. Geostatistics applied to evaluation of thermal conditions and noise in compost dairy barns with different ventilation systems. *Agronomy Research* **17**, 783–796.
- Penev, T., Radev, V., Slavov, T., Kirov, V., Dimov, D., Atanassov, A. & Marinov, I. 2014. Effect of lighting on the growth, development, behaviour, production and reproduction traits in dairy cows. *Int. J. Curr. Microbiol. App. Sci.* **3**(11), 798–810.
- Phillips, C.J.C. 2009. Housing, handling and the environment for cattle. In: *Principles of cattle production*. CABI, Wallingford, UK, pp. 95–128.
- Phillips, C.J.C. 2010. *Principles of Cattle Production Systems*. 2<sup>a</sup> ed. CABI, Wallingford, UK. 256 pp.
- Phillips, C.J.C. & Schofield, S.A. 1989. The effect of supplementary light on the production and behaviour of dairy cows. *Animal Production* **48**, 293–303.
- Phillips, C.J.C, Morris, I.D, Lomas, C.A, & Lockwood, S.J. 2000. The Locomotion of Dairy Cows in Passageways with Different Light Intensities. *Animal Welfare* **9**(4), 421–431.
- Sheffield, R.E., de Haro Marti, M., Smith, J.F. & Harner, J.P. 2007. Air emissions from a low-profile cross-ventilated dairy barn. In: *International Symposium on Air Quality and Waste Management for Agriculture*. Broomfield, Colorado, pp. 80–86.
- Sigma Plot 12. 2010. Sysstat Software Inc, San Jose, CA.
- Silva, N.R.S., Martins, S.V., Neto, M., Alves, J.A. & Souza, A.L.D. 2004. Floristic composition and structure of a seasonal semideciduous montane forest in Viçosa, MG, Brazil. *Revista Árvore*, **28**, 397–405.
- Smith, J.P. & Harner, J.F. 2007. <https://dairy-cattle.extension.org/comprehensive-evaluation-of-a-low-profile-cross-ventilated-free-stall-barn>. Accessed 13.12.2019.

## **Sustainability indicators in cooperative management of recyclable materials**

C.B. Aramian, F.B.A. Colonia, F.C. Silva, D. Cecchin, A.R.G. Azevedo and D.F. Carmo \*

Federal Fluminense University (UFF), Engineering school, Department of Agricultural Engineering and Environment, Street Passo da Pátria, n. 156, postal code: BR24210-240, Niterói, Rio de Janeiro, Brazil

\*Correspondence: [dirlanefc@id.uff.br](mailto:dirlanefc@id.uff.br)

**Abstract.** Following the promulgation of the National Solid Waste Policy in 2010, legal provisions, government programs and sectoral agreements have been implemented, but without the expected efficiency in relation to recycling. It should be noted that Cooperatives of Recyclable Material Pickers (CRMP) should play a leading role in this regard, but they do not have adequate management to be economically, socially and environmentally sustainable, depending on assistance to maintain the activity. Aiming to elucidate this issue, in this paper was made an institutional diagnosis of the category of waste pickers using the Gramacho region in the city of Duque de Caxias (Rio de Janeiro) as a case study. It was carried out an evaluation of the historical context of the neighbourhood, and it was drawn up a semi-structured questionnaire in 12 of the 18 cooperatives in the region. The data were interpreted through a SWOT matrix and the Venn diagram. A matrix was proposed and elaborated with 15 sustainability indicators specific to the CRMC reality in order to evaluate and monitor the management of cooperatives. After collecting the primary data, it was possible to validate the matrix of indicators with indexes of cultural, economic, political and ecological sustainability of the cooperatives. It was found that the matrix of indicators facilitated the understanding of the data and the comparison between the indicators. This tool can help decision-making, creation of action plans and identification of demands by the cooperative waste pickers themselves, without the presence of an analyst or technician.

**Key words:** matrix of indicators, planning, pickers, solid waste.

### **INTRODUCTION**

In Brazil, 62.78 million tons of solid waste were collected in 2018, but of this volume, the mass of recyclable waste collected selectively was only 1.7 million tons (Brasil, 2019). Thus, 75.6% of the waste was disposed of in landfills, while 24.4% was improperly disposed of in dumps and controlled landfills (Brasil, 2019). The use of strategies and indicators can help to find effective alternatives for waste disposal (Chotovinský & Altmann, 2018), either for collection or for the best destination (Mimra et al., 2016; Chotovinský & Altmann, 2017).

No Brazil, the integrated management of Solid Waste (SW) recommended by the National Solid Waste Policy – PNRS, law number 12305 (Brasil, 2010a) involves different stakeholders: public sector, private sector, consumers and pickers' cooperatives.

The Decree number 7404 (Brasil, 2010b) regulated the management of solid waste, which underwent profound changes. In this sense, legal provisions, public policies and sectoral agreements included recyclable material pickers, which, before the PNRS, were ignored.

The challenge after the enactment of the PNRS is how to include waste pickers in the recycling market, ensuring autonomy, competitiveness and financial and / or administrative independence.

The survey of basic sanitation data in Brazil (Brasil, 2019) points out that the lack of knowledge about the performance of waste pickers' cooperatives is not rare among municipalities in the country. Even so, with the government, in a formal partnership, the pickers were responsible for 30.7% of the total tons collected selectively in 2018 (Brasil, 2019).

Even with the technical and financial support invested in hundreds of cooperatives throughout Brazil, a balanced and effective development pattern for the category has not yet been established. When only investment plans focused on acquired rights are implemented, without the prerogative of any counterpart or results on the part of the cooperatives, the efficiency of the project is compromised. For that, clear notions about the main conditions that involve the organization and development of Cooperatives of Recyclable Material Pickers (CRMP) are needed, in an accessible and flexible way to local demands. Sustainability indicators can assist in the provision and interpretation of data for both the self-management of CCMPs and it can support in feeding and interpreting data for the National Solid Waste Plan (MMA, 2016)

According to Fiksel, Eason & Frederickson (2012) a sustainability indicator can be defined as an aspect of the economic, environmental and social systems that can be measured, thus assisting to monitor changes that may occur in the characteristics of these systems that are relevant to maintaining human and environmental well-being. Thereby, Garrett & Latawiec (2015) emphasize that of indicators should be simple, measurable, feasible, flexible, dynamic and user-inspired.

The definition of a management strategy developed in stages, generating a Matrix of Indicators that can be used autonomously and continuously by the cooperatives, in addition to facilitating decision making, helps in the identification of objectives and goals, allowing to compare different projects and diagnoses. This methodology can also be applied in other enterprises, rural or urban, that seek to implement a matrix of indicators for monitoring.

It should be noted that the National Information System on Solid Waste Management (SINIR) is based on public data sources, considering states and municipalities, as mentioned in its objectives: 'monitor trends in relation to the goals of reduction, reuse, selective collection and recycling of solid waste to be achieved by the logistics system and public selective collection services (MMA, 2016)'.

In addition to the public sector, SINIR has as a data source the industry and waste operators, but it does not involve CRMP, despite the various allusions to them, in different articles of the same Decree number 7404 (Brasil, 2010b). Data generation and process control are important tools for management and monitoring, and in the case of integrated management, they are crucial, as they involve different stakeholders. Even defining responsibilities, the actions implemented must be developed in a balanced way and, for that, monitoring / planning at all levels must be effective.



Buque & Ribeiro (2015) found that although the amount of waste is used as an indicator of the efficiency of the collection system and the quality of the separation at the generating source and at the sorting plant, the data collected in Maputo (Mozambique) indicated that most organizations it did not gather the information, making it difficult to estimate the generated waste. Another limitation found by Buque & Ribeiro (2015) concerning the management of the selective collection enterprises was the deficient financial analysis and lack of working capital, allied to the lack of remuneration for the collection and sorting, with the revenue coming only from the sale of recyclable materials.

Regarding the management of cooperatives in South Africa, Muswema et al. (2019) report that some of the challenges to be overcome are the reduced ability to manage enterprises due to the low qualification of the members of the cooperatives; low financial confidence among members, predominance of individual interests to the detriment of the collective and low self-sufficiency. The authors signalize that the survival rate of waste-related cooperatives in South Africa is low, around 8%.

Thus, in this study, a Matrix of Sustainability Indicators was suggested, according to different dimensions: economic, social, environmental and cultural, for Recyclable Material Pickers' Cooperatives using the Jardim Gramacho Neighborhood as a case study in the municipality of Duque de Caxias - RJ.

Based on the concept of 'Local Sustainable Development', the diagnosis of the local reality was carried out, where positive and negative components, internal and external, were analyzed in order to identify the current scenario and the desired future scenario. There is a strong relationship between the neighborhood and the issue of recycling because there is a contingent of more than 200 waste pickers organized in seventeen cooperatives that have a strong influence on local daily life. It is noted, therefore, that an action plan aimed at the development of CRMP tends to have a relevant social, economic and cultural impact. This can present itself as an example of thinking globally and acting locally, according to the precepts of 'Model management of the United Nations Global Compact' (United Nations, 2010).

In this sense, the development and validation of the Sustainability Indicator Matrix, has the general goal of promoting and monitoring the development of cooperatives, and the methodology can be used for other types of enterprises. Thus, the aim of this paper was to identify steps that could be followed so that small enterprises or organizations could make their management sustainable and participate in public policies.

## **MATERIALS AND METHODS**

The development of this work was done adapting the approach proposed by James (2014a) used in 'Circles of Social Life', which was based on the UN Global Compact Management Model. Thus, the paper was divided into the following steps:

- 1) The first stage - Commit: in this stage, the commitment regarding the proposal presented that promotes local development must be publicly stated, defining who will be responsible for managing the proposal, the question to be elucidated, and the general objective, as well as the necessary resources. This step was under the responsibility of one of the cooperatives whose president was involved in the project. The objectives of the work to be developed and how the matrix of indicators would be developed and

applied were presented in meetings at the cooperatives and the Community Forum of the neighborhood of Jardim Gramacho.

2) The second stage - Involve: in this stage, stakeholders are identified concerning the main issue of the project, which in this work is the promotion of waste recycling. The participation of those involved in the proposal is also sought. Thus, the cooperatives were informed about the project and its functions. Data were collected on the main local institutions and associations based on searches in the 'GoogleMaps' application and exploratory research following the concept of Gil (2008); at meetings of the Jardim Gramacho community forum and in the City Hall of Duque de Caxias (RJ).

3) The third step - Evaluate: in this step, the relevant information was determined, which data sources could be used. The cooperatives strengths and weaknesses were raised. The indicators usual collected were identified. It also identified what was the public and political involvement of the cooperatives, researching the social context in which they were involved, what would be the driving forces for local development, evaluating, therefore, the local reality and projecting future scenarios.

For the case of the community of Jardim Gramacho, there are no specific studies of the neighborhood, but through the census of the Brazilian Institute of Geography and Statistics (IBGE, 2010) it was possible to establish parameters considering data from the municipality of Duque de Caxias. It was also necessary to outline the profile of the institutions, with semi-structured interviews were conducted with each president of the cooperatives, according to the concept of Laville & Dionne (1999), to identify the different aspects that involve the full development of the Cooperatives, according to the sustainability dimensions addressed in 'Circles os Social Life' (James, 2014a).

Interviews were carried out containing 118 questions, the questions were divided into 8 sections, the different aspects of sustainability were questioned, and the strengths, weaknesses, threats, and opportunities of cooperatives were instigated as an institution and as part of a category (Networks / Federations).

The interview data were categorized into significant internal and external environmental factors for the CCMR, filling in the SWOT matrix (Fortaleza, Oportunidade, Weakness, and Threat). SWOT analysis was adopted because it is a tool generally used in the audit and analysis of the strategic position of a project or organization and its surroundings according to Osita, Idoko & Nzekwe (2014). To view the institutional network in the area surrounding the cooperatives to identify possible alliances and partnerships to promote local development, according to the concept of Buarque (2008), the 'Venn Diagram' was used. The Venn diagram is commonly used in participatory diagnostics because it graphically represents the relationships between groups in a community, facilitating the understanding of the role and importance of each and aiding decision making, having been applied according to Sarmento, Ferreira and Hurtado (2009). In the 'Venn Diagram', stakeholders were represented by circles arranged at different distances from the center of the diagram. This distance represented the institution's influence in the neighborhood, according to the frequency and intensity criteria of its performance. The interpretation of the 'Venn Diagram' allowed the projection of future scenarios.

4) The fourth stage - Define: in this stage the initial objective must be compared with the data collected in the previous stages, to assess the need for its alteration and to verify which indicators can be used to monitor the subsequent stages. The data from the interviews and the Venn diagram were evaluated. The indicators used in the Waste Pickers Project (CRS) were used as a basis.

The CRS project analyzed the socioeconomic and demographic profile of waste pickers in 41 municipalities in the state of Rio de Janeiro (PANGAEA/FGV, 2013) using 20 indicators, divided into three analytical dimensions. Consolidated works and research using indicators for waste picker organizations were also used, such as Besen (2011). Thus, the proposed matrix of indicators was weighed against the risks and challenges involved in achieving sustainability in cooperatives. The current legislation, which regulates the activity directly and / or indirectly, was also considered as the basis for defining the indicators, the main ones being: National Solid Waste Policy (Brasil, 2010a), Federal Decrees number 7404 (Brasil, 2010b) and number 7405 (Brasil, 2010c) and the Cooperativism Law (Brasil, 1971).

5) The fifth stage - Implement: this stage puts the project into action, defining responsibilities and revising the initial proposal whenever necessary. Thus, the indicators that would make up the sustainability matrix for cooperatives were defined. The indicators were grouped adapting to the different domains of sustainability according to the methodology of James' 'Circles of Sustainability' (2014b): economic (Production, Income, Commercialization, Institutional Support, and Control), ecological (Safety and Quality of Life at Work, Infrastructure and Final Destination of Waste), political (Formalization, Partnerships, Market Insertion) and cultural (Schooling, Training, Communication and Social and Environmental Responsibility). Qualitative data were converted into quantitative data by categorization, according to the Kronemberger methodology.

Data collections were made through interviews carried out between July and August 2016. The questions used were the cooperative's self-assessment so that they could be reassessed and compared whenever necessary. Gradation questions were also elaborated that allowed to verify what were the urgent demands and to compare them with the essential demands (which if solved would cause a greater impact), according to Kronemberger (2011).

The answers were translated into different indicators, each according to the different domains of sustainability, and the more affirmative answers, the closer to the ideal of sustainability the cooperative would be. The results of the characterization were organized in indices presented together with the weighting scale from 0 to 10 of the aspects raised: Cultural Index, Economic Index, Ecological Index, and Political Index; aiming at qualifying how they are affected and benefited. Thus, the CMRP Sustainability Circle was created, with the Sustainability Indicator Matrix, compiling data from all CMR cooperatives evaluated so that they could be used by development agencies and governments for actions to improve the recycling process, cooperatives as tools. The Economic, Ecological, Political and Cultural Sustainability Indexes were obtained according to the formulas shown in Table 1.

**Table 1.** Formulas used to obtain Economic, Ecological, Political and Cultural Sustainability Indexes

Indexes	Equations
Economic	$EDI = \frac{I(in) + I(comz) + I(is) + I(ct)}{\text{number of indicators considered}}$
Ecological	$ELDI = \frac{I(slq) + I(Inf) + I(dot)}{\text{number of indicators considered}}$
Political	$PDI = \frac{I(for) + I(art) + I(mi)}{\text{number of indicators considered}}$
Cultural	$CDI = \frac{I(scho) + I(tra) + I(comm) + I(sr)}{\text{number of indicators considered}}$

Where: *EDI* = Economic Dimension Index; *ELDI* = Ecological Dimension Index; *PDI* = Political Dimension Index; *CDI* = Cultural Dimension Index; (*in*) = income; (*comz*) = commercialization; (*is*) = institutional support; (*ct*) = control; (*slq*) = safety and life quality; (*Inf*) = infrastructure; (*dot*) = disposal of tailings; (*for*) = formalization; (*art*) = artnerships; (*mi*) = market insertion; (*scho*) = scholling; (*tra*) = training; (*comm*) = communication; (*sr*) = socioenviromental responsibility.











The indices were organized under the same scale (from 1 to 10) so that the comparison was possible. With the indices, the Matrix of Indicators represented in a Sustainability Cycle was created, considering the results of all the CMR cooperatives participating in the research.

The scale was made with different colors in which the evaluation varied from ideal to critical (Table 2). Thus, the circle was divided into four quadrants, and within each quadrant, the slices represent each indicator. The order of the indicators mentioned in each quadrant is the same as the respective slices, that is, always read by quadrant and from top to bottom, according to the exposed order of indicators underlying the name of the Sustainability Dimension. Each slice represents an indicator and the slice radius represents the weighted value of the indicator. The gradation of each indicator varied from 0 to 10, thus varying from critical to ideal.

6) Sixth stage - Monitor: In this stage, progress is verified concerning the achievement of objectives and goals, and indicators are monitored. The matrix created in the previous step was validated with its application in one of the cooperatives in the municipality of Duque de Caixas: Cooper Ecológica. The primary data available were used in the equations of the indicators, finding the sustainability indexes. Cooper Ecológica's Social Sustainability Circle was designed to facilitate the communication of results. In the Sustainability Circle, the 15 indicators were arranged according to the four aspects of Sustainability: Economic, Ecological, Political and Cultural.

7) The seventh stage - Communicate: this stage seeks to disseminate the results to the community in accessible language. Each cooperative received its responses to the

**Table 2.** Scale of Sustainability Indexes of Waste Pickers' Cooperatives

Scale	Representation	Rating
10		Ideal
9		Vibrant
8		Good
7		High satisfaction
6		Satisfactory +
5		Satisfactory
4		Satisfactory -
3		High dissatisfaction
2		Bad
1		Critical

applied questionnaire. The sustainability circle was explained so that the results were understood. Only the technical staff had access to the responses of all cooperatives.

## **RESULTS AND DISCUSSION**

In the first stage of the project, meetings were held with the cooperative managers, on-site visits and direct contact by the media, presenting the proposal and checking the interest in participating. Of the 17 cooperatives in the Jardim Gramacho neighborhood, only 12 accepted the invitation.

In the second stage, a survey was made of which people, institutions and organizations were linked to the recycling process in the region. In the district of Jardim Gramacho, there are other types of enterprises linked to recycling that work together with the 17 local CMR cooperatives.

The stakeholders of Neighborhood de Jardim Gramacho in the recycling area are associations, non-governmental organizations, city hall secretaries, schools, health units, companies and the cooperatives themselves.

In the third stage, the internal and external environments of the cooperatives were evaluated. Because it housed one of the largest dumps in Latin America for 34 years, the Jardim Gramacho neighborhood, Duque de Caxias, developed its territorialities, mainly focused on recycling.

When planning actions aimed at the balanced development of cooperatives, it is relevant to have knowledge of the internal scenario and of which it is inserted. The S.W.O.T. matrix was organized based on information obtained through a questionnaire applied to 12 cooperatives in the neighbourhood of Jardim Gramacho. The demands and potentialities that had the greatest recurrence in the results were highlighted (Table 2).

Among the strengths shown in Table 3, the privileged location of the cooperatives can be highlighted, close to important roads in the country such as BR-040 and the municipalities that make up the metropolitan region of the municipality of Rio de Janeiro, which facilitates both the entry of material recycled as for disposal for sale. In addition to this fortress, it is worth mentioning the experience and specialization in the field, since the cooperative members are in a neighborhood, which was influenced by the operation of one of the largest landfills in Latin America for more than three decades.

The main weaknesses are mainly related to the lack of control of the entry and exit of material, together with the lack of updating or the absence of a cash book, since these factors prevent the taking advantage of opportunities. It can also be highlighted the inadequate destination of the tailings generated after the material was sorted, which negatively impacts the environment and can also damage the image of the cooperatives vis-à-vis other sectors of the neighborhood and the population.

The opportunities (Table 3) are mainly linked to the technical and financial support of public and private institutions, and the payment for the service of collection, sorting and proper final disposal of recyclable waste, which can be considered an internalization of the waste disposal costs, which for some sectors it is still considered an externality.

The threats (Table 3) are mainly linked to municipal management, through public policies of mechanization of waste sorting and political discontinuity, when there is a change of government, without the inclusion of cooperatives in the process.

The articulation between the different stakeholders has a greater social, ecological, economic and cultural impact on the whole neighborhood. For this to happen, it is necessary to know what these institutions are, what situation they are experiencing, what they intend for the future, the degree of engagement with the community and their level of social and economic development.

**Table 3.** Strengths, Opportunities, Weaknesses and Threats in CRMP

INTERNAL FACTORS			
STRENGTHS		WEAKNESSES	
P	Womem empowerment;	Deficiencies in basic infrastructure:	N
O	Experience in the business;	water and sewage network; equipment	E
S	Privileged location for waste	High illiteracy rate	G
I	management logistics, as it is close to	Informalization of most cooperatives;	A
T	highways and economically important	Lack of internal and external process	T
I	cities;	control;	I
V	Supply of specialized labor;	Most of the updated cash-book	V
E	Fixed income guarantee	cooperatives are lacking;	E
F	Participation in networks	Inadequate waste disposal.	A
A	Accountability to participants	Most of the material sold to	C
C		intermediaries	T
T			O
O			R
R			S
S			
OPPORTUNITIES		THREATS	
C	Presence of commercial and industrial	Lack of basic infrastructure: public	
T	activities related to recycling close to the	lighting, pavement;	
O	cooperatives.	Insecurity: overt presence of violence;	
R	Reverse Logistics Sector Agreements	Economic crisis;	
S	Technical / financial support from public	Vulnerability to climatic conditions (rain	
	and private institutions;	/ heat);	
	Payment for collection service, sorting	Political and administrative	
	and proper final disposal of recyclable	discontinuity;	
	waste.	Lack of public policies to encourage the	
		recycling sector;	
		Mechanization of waste collection and	
		sorting;	
		Creation / Implementation of public	
		policies that encourage recycling through	
		large multinational companies.	
EXTERNAL FACTORS			

The Venn diagram was designed to illustrate the interactions between the institutions, to understand how each could act to promote sustainable local development in the neighborhood. It should be noted that the Diagram is the representation of interactions at a given moment. Kronemberger (2011) points out that ‘the closer the circle is to the center, the greater the institution's influence on development, meaning that it acts directly in the daily life of the community and with daily or weekly frequency’. According to author, the intersection between the circles shows that there is some form of relationship between the institutions. The institutional network in the area

surrounding the cooperatives is presented in Fig. 1, actual and ideal scenario, respectively.

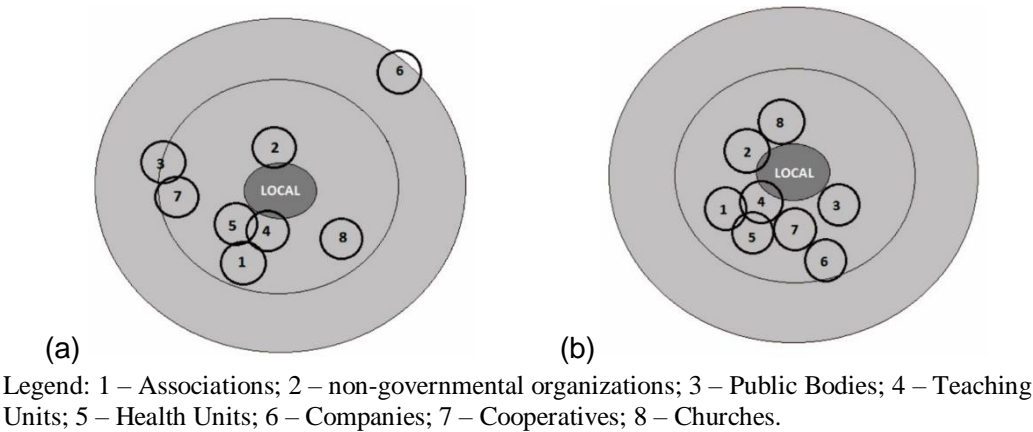


**Figure 1.** Venn Diagram Model – Current Scenario (a) and ideal scenario (b).

Through the interview conducted with the cooperative members, it was verified that public agencies do not seem to have the expected role, despite presenting themselves as supporting agents for projects in the community. Its close relationship with the cooperatives is due to a specific structuring project aimed at seven cooperatives in the neighborhood to meet the National Solid Waste Policy, implementing Solidary Selective Collection. It was also found that companies based in the neighborhood often do not employ local labor, and when they do, it is for positions that require little qualification. There is no consolidated employee training plan or career plan.

Cooperatives also do not operate in the community with the frequency and intensity that they should. Although cooperatives are the means of formalization and organization for waste pickers, it was found that this in practice does not work satisfactorily, since the cooperatives posture is not very proactive, not promoting good practices and entrepreneurship.

The major community service providers in the region, due to the degree of involvement with cooperative waste pickers, are the Teaching Units, Health Units, and Associations. These stakeholders are more influential in the neighborhood and show concern for the quality of life of the community, despite suffering from external threats to their management and other internal barriers to the institutions. And NGOs work in the community independently, without broad planning that seeks to share information and demands for the neighborhood.

In the ideal scenario (Fig. 1, b), there would be greater integration between all organizations and greater frequency and intensity of stakeholder actions in the neighborhood. Public agencies, although close, would not imply dependency. The cooperatives would form networks with the other institutions (Public and Private Schools) to use the potential of these institutions for the development of Environmental Awareness projects. Health units could relate to cooperatives by offering lectures to raise awareness of the use of Personal Protective Equipment (PPE) in the workplace in the prevention of accidents and occupational risks. And public institutions would act to

foster the creation of collaborative networks between companies, schools, health units and cooperatives, for the development of commercial partnerships (such as the donation of recyclable waste). Besides, public institutions could support the creation and implementation of waste management plans that can be converted into job and income generation to reduce the population's situation of social vulnerability and also qualify them for the job market.

In the fourth stage, the data obtained in the previous stage were evaluated considering the main issue to be solved and the general objective to achieve the solution. The motivating issue was the guarantee of CRMP's autonomy, competitiveness, and financial and administrative independence. The general objective to elucidate this issue was the creation of a tool that would allow cooperatives to evaluate their management, identifying their strengths and weaknesses, their opportunities and threats to set goals for their development.

The 'Matrix of Indicators' was created based on the results found in S.W.O.T. (Table 3).

The indicators were grouped into four different Dimensions of Sustainability: Cultural, Economic, Ecological and Political. Within the dimensions, key indicators were chosen to better diagnose the reality of CMR Cooperatives.

The starting point was primary data that could produce history to monitor the evolution of the performance of each cooperative and that the cooperatives themselves could collect autonomously and complete the spreadsheet created to generate the matrix, without the need for support specific technician. In the fifth stage, the 15 indicators were defined, organized in 'Sustainability Indexes'. In calculating the value of the indicator, a factor was used to maintain the final value on a scale of 1 to 10. The indices present the weighted sum of each set of indicators according to the dimension to which they refer (Table 1).

### **Cultural Dimension Index**

The Cultural Dimension Index (CDI) represents the degree of involvement of cooperatives with the recycling market and with the community, that is, how the cooperative relate socially. In this index, the indicators that indicate the level of education of the cooperative members were considered, also considering the different modalities of communication of the cooperatives with their customers, partners, and community.

The index also includes the development of public or private partnerships linked to environmental education or training for the population surrounding the cooperatives; and the development of training plans for cooperative members in the areas of management, processes, and efficiency. To maintain the Cultural Dimension Index in base 1 to 10 the equation was multiplied by the factor (0.25). The representation of this index is presented in Eq. 1 below:

$$CDI = (Education + Training + Communication + Responsibility) \times Factor \quad (1)$$

where CDI – Cultural Dimension Index; Responsibility – socioenvironmental responsibility; Factor – 0.25 (Base index: 1–10).

The indicators that make up the Cultural Index equation were obtained using the equations presented in Table 4 as a form of calculation. The factor that was used to standardize the scale is also presented.



**Table 4.** Index of cultural sustainability of recyclable material pickers' cooperatives according to the indicators that compose it

Indicators	Calculation form	Factor
Education	(Number of members with schooling equal to or higher than the complete average / Total number of members of the cooperative) *10	0.25
Training	(Gradation attributed to the participation of the members <sup>1</sup> + Number of Training Courses held in the last year <sup>2</sup> ) / 2	0.25
Communication	(Number of communication items present in the cooperative <sup>3</sup> + Gradation of the cooperative's relationship with other waste pickers' cooperatives <sup>1</sup> ) / 2	0.25
Socio-environmental responsibility	Action carried out to promote selective collection in the last year <sup>4</sup> / Interest in carrying out action to promote selective collection <sup>4</sup>	0.25

<sup>1</sup>Gradation: Poor = 1, Bad = 4, Good = 6, Very Good = 8 and Great = 10;

<sup>2</sup>Training courses: Administrative Management, Use of Computer and / or Computer Programs, Arrangement of production equipment – layout, Use of Collection Equipment, Sorting and Processing, Financial Management, Work Safety, Cooperatives, Marketing and others;

<sup>3</sup>Communication items present (if YES = 1 / NO = 0): Website, Blog, Folder or Institutional Brochure, Business Card, Facade Plaque (\* YES = 2 / NO = 0), Banners or Material for Events, Logo , Digital Presentation, Facebook;

<sup>4</sup>Action Done / Interest in: Schools = 3, Community = 3, Companies = 3, Not Done / Not interested = 1.

Based on Table 4 and using the data obtained in the interviews with the cooperative members, the values for the indicators were obtained, as well as the corresponding ‘Cultural Dimension Index’ for each of the evaluated cooperatives, presented in Table 5.

The names of the participating cooperatives of the work were replaced by numbers so as not to hurt the image right. Of the twelve cooperatives analyzed, 75% obtained an index lower or equal to 6, with values considered from bad to satisfactory. The highest index was 7 (High Satisfaction). Considering that all organizations are located in the same neighborhood, there was considerable scope between the cooperative with the the highest index (value 7) and the lowest(value 2).

These results point to the need for government action plans, as well as for the private sector, to improve education and training indicators, respectively. The Education Indicator is the worst among the indicators analyzed in this dimension. It appears that among the 12 cooperatives, the ones that most need action plans are cooperatives 5 and

**Table 5.** Results obtained in the analysis of cultural indicators of the cooperatives of Jardim Gramacho

CRMC	Education	Training	Communication	Socio-environmental responsibility	CDI
1	1	4	9	7	5
2	1	7	6	7	5
3	0	7	6	0	3
4	0	7	6	10	6
5	0	5	5	0	2
6	1	6	6	0	3
7	1	10	8	10	7
8	0	8	10	10	7
9	3	7	7	10	7
10	0	7	7	10	6
11	0	5	5	0	3
12	0	4	5	0	2

12 that obtained the worst result (2- Bad). However, cooperatives must act to improve communication and socio-environmental responsibility rates.

### Economic Dimension Index

The Economic Dimension Index (EDI) represents the degree of development of cooperatives taking into account the following indicators: production, income, commercialization, institutional support, and control. The representation of this index is presented in Eq. 2 below:

$$EDI = (Production + Income + Marketing + Control) \times Factor \quad (2)$$

where *EDI* – Economic Dimension Index, Factor – 0.2 (Base Index: 1–10).

The indicators serve to point out the efficiency and effectiveness of the collection, sorting, and marketing of recyclable waste through the income-generating capacity of the evaluated cooperatives.

In the marketing indicator, data on the consumer market and participation or organization in cooperative networks were considered. Institutional support was measured based on the grading attributed to technical or financial support from the public and private institutions. And for the control indicator, the existence of an updated Cash Book was considered, as well as the gradation concerning the control of the cooperative's waste flow (Input and output). The results obtained are shown in Table 6.

**Table 6.** Index and indicators of economic sustainability of recyclable material pickers' cooperatives

Indicators	Calculation Form	Factor
Production	(Quantity of material sold <sup>1</sup> / Quantity of material collected <sup>1</sup> ) multiply for 10	0.2
Income	Cash Fund <sup>2</sup> + Weighted Value (PV) of the Average Monthly Salary (MS) of the Cooperative in the last year <sup>3</sup>	0.2
Commercialization	To whom the cooperative sells sorted / processed waste <sup>4</sup> + Participation of cooperatives in Networks <sup>2</sup>	0.2
Institutional Support	Gradation attributed to financial / technical support from public institutions in the last year <sup>5</sup> + Gradation attributed to financial / technical support from the Private Sector in the last year <sup>5</sup>	0.2
Control	Gradation Control of input and output of material from the Cooperative <sup>5</sup> + UPDATED cash register of the cooperative <sup>2</sup>	0.2

<sup>1</sup>Average value month of last year (t);

<sup>2</sup>If you have: YES = 5, NO = 0;

<sup>3</sup>In view of the Minimum Salary (MS) based on IBGE: ≤ SM = 1, Up to 5% above MS = 2, Up to 25% above MS = 3, Up to 40% above MS = 4, > 40% above MS = 5;

<sup>4</sup>If sold: Most for Industry = 5, Smallest for Industry = 3, Exclusively for Intermediate = 1;

<sup>5</sup>Gradation: Bad = 1, Bad = 2, Good = 3, Very Good = 4 and Great = 5.

1 Average value month of last year (t) 2 If you have: YES = 5, NO = 0.3 In view of the minimum wage (SM) based on IBGE: ≤ SM = 1, Up to 5% above SM = 2, Up to 25% above SM = 3, Up to 40% above SM = 4, > 40% above SM = 5.4 If sold: Most for Industry = 5, Smallest for Industry = 3, Exclusively for Intermediate = 1.5 Gradation: Bad = 1, Bad = 2, Good = 3, Very Good = 4 and Great = 5.

The index of the economic dimension of the cooperatives in the neighborhood of Jardim Gramacho is shown in Table 7.

In Table 7 can be seen that all the analyzed cooperatives obtained an index equal to or greater than 5 (Satisfactory), standing out from the other indexes analyzed as the best as a set of cooperatives. It appears that 67% of the cooperatives obtained rates between 5 (Satisfactory) and 6 (Satisfactory +), representing that, despite the good performance, there is still a need for action plans for improvement. The Indicators that presented the worst result were Income and Institutional Support with an average of 4 (Satisfactory -), which may indicate a starting point for future action plans to improve the economic sustainability indexes of the group of cooperatives.

**Table 7.** Results obtained in the analysis of economic indicators of the cooperatives of Jardim Gramacho

CRMC	Production	Income	Commercialization	Institutional Support	Control	EDI
1	8	3	5	4	10	6
2	6	2	6	5	4	5
3	8	1	6	2	1	4
4	8	8	6	2	1	5
5	7	3	6	6	9	6
6	7	1	6	2	9	5
7	8	5	10	2	10	7
8	9	8	10	7	9	9
9	8	10	8	2	8	7
10	9	4	6	4	8	6
11	8	3	6	4	3	5
12	7	4	1	2	9	5

**Political Dimension Index**

The ‘Political Dimension Index’ represents the degree of development of the cooperatives taking into account the following indicators: formalization, partnerships, and insertion in the market. The representation of this index is presented in Eq. 3 below:

$$PDI = (Formalization + Partnerships + Market insertion) \times Factor \quad (3)$$

where PDI – Political Dimension Index; Factor – 0.20 (Base Index: 1–10).

How the indicators were considered, as well as the factor used is shown in Table 8.

**Table 8.** Indices and indicators of political sustainability of recyclable material pickers' cooperatives

Indicators	Calculation Form	Factor
Formalization	(Sum of the number of formalization documents that the cooperative has) <sup>1</sup> divided by eight	0.33
Partnerships	If the cooperative has a partnership (through Decree 5.940), with any company, agency, or federal government agency <sup>2</sup>	0.33
Market Insertion	Number of paid service contracts <sup>3</sup> divided by the number of unpaid service contracts <sup>4</sup>	0.33

<sup>1</sup>Formalization Documents (If YES = 10 / NO = 0): Updated Election Act, Updated Bylaws / Floor Plan and Land Status, Environmental License, Municipal Waste Transport Exemption, State Waste Transport Exemption, Exemption for Federal Waste transportation, Firefighters' Certificate, Municipal Permit;

<sup>2</sup>YES = 10 / NO = 0;

<sup>3</sup>Number of paid contracts: Up to 2 = 1, Up to 4 = 8, From 5 upwards = 10;

<sup>4</sup>Number of Unpaid Contracts: Up to 2 = 10, Up to 4 = 8, From 5 upwards = 1.

In the indicator of the degree of formalization presented in Table 8, it was considered whether all legal requirements related to documentation were met. In addition to the development of public and or private partnerships linked to physical and administrative infrastructure, the different types of service provision contracts and types of connection between cooperatives with the public and private sectors were also considered. A partnership is an indicator that promotes other indicators since, through partnerships, cooperatives improve their performance in income, control, among others.

The political index obtained with the indicators in Table 8 is shown in Table 9. It is possible to verify that 75% of the cooperatives obtained a political index equal to or less than 5 (Satisfactory). Among the four Dimensions of Sustainability, the Political index stood out as the worst, analyzing the set of cooperatives. Despite the cooperative identified by the number 8 having obtained a maximum index of 10 (Ideal), 42% of the cooperatives obtained the worst index 1 (Critical), which requires a deeper analysis. The data suggest the observation of the action plan of the cooperative number 8 to reach this index, checking the possibility of implementing it in the others or even using it as a goal for the other cooperatives to improve their indexes.

**Table 9.** Results obtained in the analysis of political indicators of the cooperatives of Jardim Gramacho

CRMC	Formalization	Partnerships	Market Insertion	PDI
1	8	10	0	6
2	3	0	0	1
3	3	0	0	1
4	3	0	1	1
5	4	10	0	5
6	4	10	0	5
7	8	10	1	6
8	9	10	10	10
9	5	10	1	5
10	4	10	1	5
11	4	0	0	1
12	3	0	0	1

### Ecological Dimension Index

The ‘Ecological Dimension Index (ELDI)’ represents the degree of development of the Cooperatives taking into account the following indicators: safety and, quality of life at work, infrastructure and disposal of waste. The representation of this index is presented in Eq. 4 below:

$$ELDI = (Safety\ and\ quality\ of\ life + Infrastructure + Tailings) \times Factor \quad (4)$$

where ELDI – Ecological Dimension Index, Safety and quality of life – Safety and quality of life at work, Tailings – Tailings destination, Factor = 0.25 (Base Index: 1–10).

The indicators were chosen to point out the efficiency and effectiveness of the actions and protocols implemented in the areas of safety and quality of life at work and infrastructure. The intention was also to point out how the waste generated in the evaluated cooperatives is destined.

The indicator of safety and quality of life at work, for example, was defined to indicate standards in the cooperative's working environment, through information on identification and organization of the work process, use of personal protective equipment and awareness of the importance of using these. The infrastructure is represented by physical aspects necessary or mandatory for the cooperative to function fully, such as:

paving and covering the waste sorting site, formal water and electricity services. And, finally, the disposal of tailings was also considered, which can represent an environmental problem after sorting, being one of the greatest difficulties encountered by cooperatives for environmental adequacy.

How the indicators were obtained, as well as the factor considered for the index, are shown in Table 10.

**Table 10.** Ecological sustainability indicators of recyclable material pickers' cooperatives

Indicators	Calculation Form	Factor
Safety and quality of life at work	(Physical organization of the cooperative <sup>1</sup> + Use of personal protective equipment <sup>2</sup> + Resistance to the use of personal protective equipment <sup>3</sup> ) divided by three	0.33
Infrastructure	(Workplace structure of the cooperative headquarters <sup>4</sup> + Public Services Regularized by Responsible Company <sup>5</sup> + Paving the workplace <sup>6</sup> + Receipt / Collection of Waste with motorized vehicles <sup>3</sup> + Average age of vehicles <sup>7</sup> ) divided by five	0.33
Tailings Destination	Proper destination of the waste generated in the cooperative is carried out <sup>3</sup>	0.33

<sup>1</sup>Sum Areas defined physically by means of marking / visual identification (YES = 10; NO = 0) divide by seven. The areas are Unloading / storage, Sorting, Storage, Bales Stock, Truck transit area, Cafeteria / Bathrooms, Office;

<sup>2</sup>Sum of the types of PPE's (Personal protective equipment) used by the members (YES = 10 / NO = 0) divided by nine. The PPE's are Uniforms, Gloves, Glasses, Boots, Ear protector, Mask, Helmet, Apron, Rain cap;

<sup>3</sup>If YES = 10 / NO = 0;

<sup>4</sup>If Adapted Land = 3, Adapted Construction = 6, Shed = 10;

<sup>5</sup>Sum of Regularized Public Services (YES = 10 / NO = 0) divided by seven because it are Electricity, Water, Sewage, Waste Collection, Fixed Telephony, Internet and if there is no regularized service;

<sup>6</sup>If YES = 10, NO = 0, PARTIALLY = 5;

<sup>7</sup>Vehicles with: more than 10 years = 10, less than 10 years = 0, do not have = 0.

Applying the calculation methods indicated in Table 10 to obtain the 'Ecological Indicators'. The indicators and Ecological Index presented in Table 11 were obtained.

Analyzing the Ecological Index, it appears that only 25% of the cooperatives reached an index equal to or greater than 6 (Satisfactory +).

The indicator 'Adequate destination of tailings' presented the worst performance among the other ecological indicators, pointing to an emergency demand for action plans that promote public or private partnerships to collect and dispose of this waste, or even impose the acceptance of contracts between cooperatives and companies collection

**Table 11.** Results obtained in the analysis of ecological indicators of the cooperatives of Jardim Gramacho

CRMC	Safety and quality of life at work	Infrastructure	Tailings destination	ELDI
1	8	6	0	5
2	4	1	10	5
3	3	1	0	2
4	3	1	0	1
5	9	5	0	4
6	6	8	0	4
7	8	9	10	9
8	7	8	10	8
9	7	2	10	6
10	8	6	0	5
11	2	4	0	2
12	7	5	0	4

or receipt of residues that enable the proper disposal of the waste, or even analysis for converting the waste into waste and reintroducing it into the production scale. The transformation of tailings into an energy source is also an interesting alternative, which is already being studied by some researchers, such as Mala'ák, Velebil, and Bradna (2018).

Action plans in this sense improve the 'Ecological Index', not only of the cooperative but also of the surrounding community, reducing the number of clandestine dumps in the Jardim Gramacho neighborhood. The 15 indicators distributed in the four proposed Indices are similar to the matrix of Sustainability Indicators of Waste Pickers Organizations proposed by Besen (2011). Despite making use of different construction and validation methodologies, the indicators, for the most part, address the same theme of self-management, formalization, quality of life at work and efficiency. However, the differential of the Matrix of sustainability indicators for recyclable materials Cooperatives proposed here is in the organization of the indexes of the different dimensions of sustainability that can be used and interpreted by the pickers themselves as a way of monitoring activities.

It is possible to analyze, jointly or individually, the results, allowing the assessment of which indicators need improvement. This does not occur in the work of Besen (2011) in which the matrix of indicators was made for public policies and thus the assessment is joint. Thus, the cooperatives do not have the autonomy to evaluate the results when using this matrix, depending on the opinion of those responsible.

This flexibility in the communication of indicators and indices enables and encourages the creation of Networks and Federations of Cooperatives and facilitates the macro analysis necessary for public administration. With the same matrix of indicators, it is possible to create different types of action plans with an internal origin, starting from the cooperatives themselves, and creating and monitoring municipal public policies.

The indicators organized in different dimensions of sustainability facilitate the understanding and analysis of positive and negative impacts of different types of projects since they indicate the good or bad performance of each indicator, that is, the project or action plan can emphasize only in the aspect to be improved. And with the sustainability circles, it is possible to compare different action plans that impact the same dimension of sustainability, or even create and monitor action plans that generate impacts in more than one aspect of the sustainability circle.

In the sixth stage were validate the sustainability indicators.

The data represented in the Cooperative Cooperative Ecological Sustainability Circle are presented in Fig. 2. When analyzing the results of the Cooperative Ecological Social Sustainability Circle, it is possible to verify that the aspect with the worst result is Ecological, where the set of indicators varied the gradation between 8 (good) in Safety and Quality of life at work and 1 (critical) in Waste disposal. In other aspects of sustainability, there was at least 1 indicator with a gradation better than 8 (good), as in the case of the Economic aspect, where the Control indicator had a maximum gradation of 10 (ideal).

The figure facilitates the visualization of the main demands of Cooper Ecológica. From this, it is possible to create 'Action Plans' according to the aspects of the worst performance or even the individual indicators. The ideal would be to create 'Action Plans' that generate positive impacts on different indicators simultaneously. A suggestion for an 'Action Plan' with separate indicators would be regular (supplementary) and

technical training courses for members, thus generating positive impacts on the Indicator of Education and Market Insertion, which are graded 1.0 (critical).

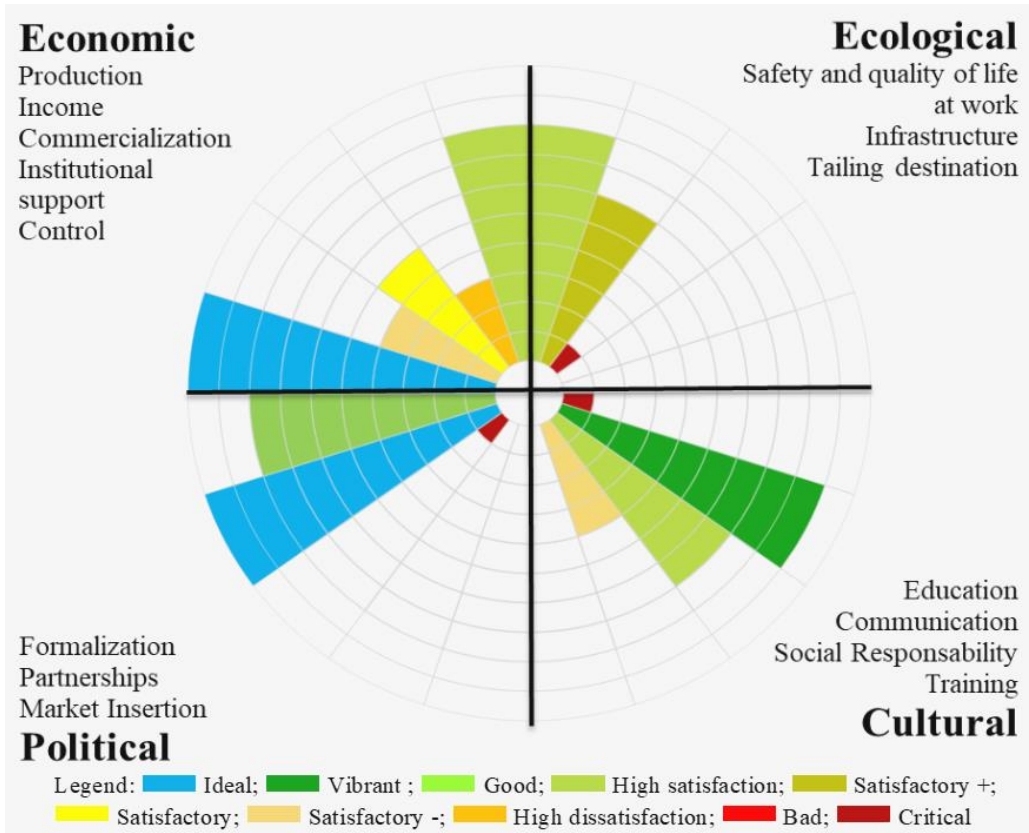


**Figure 2.** Cooperative Ecological Social Sustainability Circle.

In the case of the Public Power, be it municipal or state, it would be interesting to see the demands and strengths or potentialities of the ‘Circle of Social Sustainability of Cooperatives’, contemplating all that could be done, or by neighborhood, depending on the number of cooperatives in the region to be served. analyzed.

The ‘Sustainability Indexes’ of the 12 CMR Cooperatives interviewed were presented in Fig. 3. Like the individual Sustainability Circle, the indexes of the cooperative set were also divided into four quadrants, each representing an aspect of sustainability. Each quadrant is subdivided into 12 slices, each representing a cooperative. The slice radius represents the gradation of the sustainability index according to the legend in Fig. 3. The slices represent the sustainability indexes of each cooperative, therefore, each cooperative was represented by four slices, one per quadrant. The share of each cooperative is represented in the same order as the list of cooperatives arranged just below the quadrant title. Always read from top to bottom, according to the programmed order of the quadrant. It is worth mentioning that the number of slices per quadrant will always be proportional, with the cooperative always being represented by four indexes.

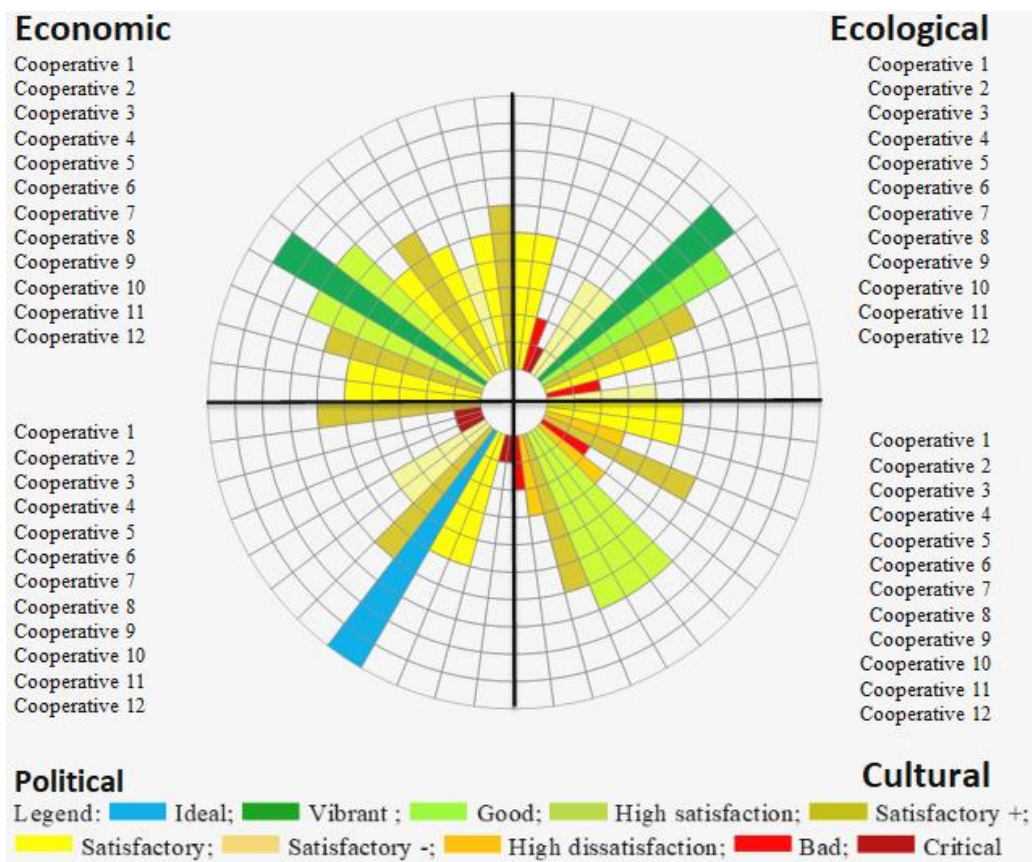


**Figure 3.** Sustainability indexes of the 12 cooperatives evaluated.

Also jointly analyzing the four aspects in Fig. 3 it is possible to verify that the political dimension has the worst result. Despite the cooperative 9 obtaining the maximum index 10 (ideal), the average among the 12 cooperatives is only 4 (satisfactory -), and five cooperatives obtained the worst gradation in this aspect: 1 (critical). The indices of ecological and cultural dimension have a graded average, with most of the values as satisfactory (value 5). The economic dimension indexes had the best average performance: 6 (satisfactory +). This joint analysis is of great value for the municipal government and the class movements, which can assess the main demands of the group of cooperatives in order to facilitate the understanding and analysis of stakeholders involved. In the case of the cooperatives in the Jardim Gramacho neighborhood, through the analysis of the indices, programs are recommended that encourage the formalization of cooperatives, facilitate the hiring of cooperatives in the Municipal Selective Collection program or even promote the creation of laws that encourage large generators to hire cooperatives in companies' waste management.

The 'Indicator Matrix' can function as a tool to assist in internal and external planning. The use of a tool that allows the analysis of the results and the creation of action plans by the entrepreneurs themselves is of vital importance, especially for such an informal sector and with organizational difficulties, such as recycling in Brazil. The



developed matrix presents several results in a simple and easy to understand way, being able to be replicated to other locations, as well as to other types of enterprises.

The presentation of the 'Circle of Sustainability of Recyclable Material Pickers' Cooperatives' demonstrated that it is an instrument of easy analysis and handling that can function as the institution's self-analysis tool and short, medium and long term planning, depending on the goals established in assembly. Besides, such a tool can also be used to provide data to the government, which needs information from the set of CMR Cooperatives to create public policies geared to the category. This tool presents in which dimension that group of cooperatives needs more attention, that is, dimensions of sustainability with a higher incidence of lower rated indexes.

In addition to the panorama by dimension, it is possible to verify the performance of the set of CMR Cooperatives considering the different aspects of sustainability, without having extensive tables, on the contrary, an interesting tool for decision making and of a transparent nature. At the same time that it presents the individual sustainability indices, it also provides information about the group. In addition to the practical nature, the 'Matrix of Indicators' presents itself as a suggestion of data standardization for the form of the Annual List of Information of Work Cooperatives (RAICT). The 'Matrix of Indicators', the 'Circle and Sustainability' and the 'Sustainability Indices' proposed would comply with the principles of Law number 12890 (Brasil, 2012).

## CONCLUSIONS

The 'Matrix of Sustainability Indicators' was composed for 15 indicators, being organized into indexes in different dimensions: cultural, political, ecological and economic. The indicators and indices created were organized in Sustainability Circles that allowed the correlation and easy visualization of data as a matrix of indicators. In the Sustainability Circle, the 15 indicators were presented with gradations ranging from 1.0 (critical) to 10 (ideal). When applying the matrix to all cooperatives in the Jardim Gramacho neighborhood, it was found that the political dimension had the worst result, the ecological and cultural dimension indexes presented most of the values as satisfactory (value 5) and the economic dimension indexes showed the best average performance presenting most of the values as 6, considered satisfactory (+).

The Sustainability Indicator Matrix was developed not only as a diagnostic tool, but also for monitoring, that is, using the same model and scale, it is possible to generate a history of indicators that measure the development of cooperatives in search of the ideal result, which is sustainability. It was found that the tool makes it possible to communicate the diagnosis of the collective of cooperatives in a simple way, where it is possible to verify the amplitude of performance among the cooperatives, and, at the same time, to identify in which aspect the collective of cooperatives has greater difficulty. The matrix demonstrates impartially and democratically in which aspects the collective of cooperatives needs greater investment, be it through Public Policies and Private Sector Projects.

**ACKNOWLEDGEMENTS.** We thank all the cooperatives that agreed to participate in the project.

## REFERENCES

- Besen, G.R. & Dias, S.M. 2011. Sustainable public management of solid waste? Use of official databases and sustainability indicators. *Revista Pegada Eletrônica* (Online), v. Especi, pp. 112–134 (in Portuguese).
- Brasil, Decree number 7404. Diário Oficial da União, Section 1, Extra Edition, p.1, December 23, 2010b. Accessed 2.2.2017 [http://www.planalto.gov.br/ccivil\\_03/\\_ato2007-2010/2010/decreto/d7404.htm](http://www.planalto.gov.br/ccivil_03/_ato2007-2010/2010/decreto/d7404.htm) (in Portuguese).
- Brasil, Federal Law number 12305. Diário Oficial da União, Section 1, p. 3, 03 august 2010a. Accessed 2.2.2017. [http://www.planalto.gov.br/ccivil\\_03/\\_ato2007-2010/2010/lei/l12305.htm](http://www.planalto.gov.br/ccivil_03/_ato2007-2010/2010/lei/l12305.htm) (in Portuguese).
- Brasil. Federal Law number 5764. Diário Oficial da União, Section 1, p. 10354, 16 december 1971. Available in: <[http://www.planalto.gov.br/ccivil\\_03/LEIS/L5764.htm](http://www.planalto.gov.br/ccivil_03/LEIS/L5764.htm)> Accessed January 12.2020. (in Portuguese).
- Brasil. Federal Law number 12690. Diário Oficial da União, Section 1, p. 2, 20 july 2012. Available in: <[http://www.planalto.gov.br/ccivil\\_03/\\_Ato2011-2014/2012/Lei/L12690.htm](http://www.planalto.gov.br/ccivil_03/_Ato2011-2014/2012/Lei/L12690.htm)>. Accessed January 12, 2020. (in Portuguese).
- Brasil. Ministry of Regional Development. National Secretaria of Sanitation - SNS. National Sanitation Information System: *Diagnosis of Urban Solid Waste Management* –2018. Brasília: SNS/MDR, 2019. 247 pp. (in Portuguese).
- Buque, L.I.B. & Ribeiro, H. 2015. Overview of the selective waste collection with pickers in Maputo municipality, Mozambique: challenges and perspectives. *Saúde Soc.* **24**(1), 298–307.
- Chotovinský, O. & Altmann, V. 2018. A comparative case study of the efficiency of collection systems for paper and biodegradable municipal solid waste. *Agronomy Research* **16**(S1), 997–1009.
- Chotovinský, O. & Altmann, V. 2017. Performance analysis of biodegradable municipal solid waste collection in the Czech Republic. *Agronomy Research* **15**(4), 1559–1570.
- Fiksel, J., Eason, E. & Frederickson, H. 2012. *A framework for sustainability Indicators at EPA*. United States Environmental Protection Agency, october 2012, 59 pp. Accessed 5.7.2020 <<https://www.epa.gov/sites/production/files/2014-10/documents/framework-for-sustainability-indicators-at-epa.pdf>>
- Garrett, R.D. & Latawiec, A.E. 2015. What are sustainability indicators for? In A. Latawiec & D. Agol (Eds.), *Sustainability indicators in practice* (p. 271). Warschau/Berlin: De Gruyter.
- Gil, AC. 2008. *Methods and techniques of social research*. 6. ed., São Paulo, *Atlas publisher*, 220 pp. (in Portuguese).
- IBGE - Brazilian Institute of Geography and Statistics. Duque de Caixas: panorama Accessed 1.2.2017 <https://cidades.ibge.gov.br/Brasil/rj/duque-de-caxias/panorama>
- James, P. Guideline 1.1.Circles of Social life: Process Pathway.v.3.2. Global Compact Cities Programme and metropolis, 2014. Accessed 1.2.2017 <http://www.circlesofsustainability.org/wp-content/uploads/2014/10/Tool-1.1-Overview-and-Process-Pathway.pdf>
- James, P. 2014b. *Urban Sustainability in Theory and Practice*: Circles of Sustainability. Advances in Urban Sustainability Series. Routledge, London & New York, 284 pp.
- Kronemberger, D. 2011. *Sustainable local development: a practical approach*. Publishing company Senac. São Paulo. Ed.1, 280 pp. (in Portuguese).

- Laville, C. & dionne, J. 1999. The construction of knowledge: manual of research methodology in human sciences. Translation Heloisa Monteiro & Francisco Settineri. Porto Alegre: Artmed; Belo Horizonte: Editora UFMG, 341 pp. (in Portuguese) Available in: [https://edisciplinas.usp.br/pluginfile.php/1048063/mod\\_resource/content/1/A%20construc%C3%A7%C3%A3o%20do%20saber%20-%20Laville%20e%20Dionne.pdf](https://edisciplinas.usp.br/pluginfile.php/1048063/mod_resource/content/1/A%20construc%C3%A7%C3%A3o%20do%20saber%20-%20Laville%20e%20Dionne.pdf) Accessed January 18, 2020.
- Malat'ák, J. Velebil, J. & Bradna, J. 2018. Specialty types of waste paper as an energetic commodity. *Agronomy Research* **16**(2), 534–542.
- Mimra, M., Kavka, M. & Renfus, R. 2016. Analysis and Evaluation of the Waste Management in the Municipality. *Agronomy Research* **14**(S1), 1180–1190.
- Muswema, A.P., Okem, A. Von Blottnitz, H. & Oelofse, S. 2018. Cooperatives in waste and recycling: a recipe for failed waste hierarchy implementation. Conference: The 24th WasteCon Conference and Exhibition, 15-19th October 2018, Emperors Palace, Johannesburg, Gauteng. 1–18. Available in: <http://researchspace.csisr.co.za/dspace/handle/10204/10508> . Accessed April 10, 2020.
- Osita, I.C.; Idoko, I.O. & Nzekwe, J. 2014. Organization's stability and productivity: the role of SWOT analysis an acronym for strength, weakness, opportunities and threat. *International Journal of Innovative and Applied Research* **2**(9), 23–32.
- PANGEA/FGV. *Project Waste pickers in Solidary Networks. Systematization of the experience and socioeconomic and demographic diagnosis*. v. **1**, 2013. Accessed 1.2.2017: [http://fgvprojetos.fgv.br/sites/fgvprojetos.fgv.br/files/publicacao\\_crs\\_volume1\\_site.pdf](http://fgvprojetos.fgv.br/sites/fgvprojetos.fgv.br/files/publicacao_crs_volume1_site.pdf) (in Portuguese).
- Sarmiento, F., Ferreira, J. & Hurtado, A. *Territorial diagnosis handbook*. Actionaid.org/FAO, 2009, 66 pp. Available in: [https://actionaid.org/sites/default/files/territorial\\_diagnosis\\_guidebook.pdf](https://actionaid.org/sites/default/files/territorial_diagnosis_guidebook.pdf). Accessed January 8, 2020.
- United Nations Global Compact. 2010. Un global compact management model: framework for implementation human rights, labour, environment, anti-corruption. Deloitte. Accessed 2.2.2017. [https://www.unglobalcompact.org/docs/news\\_events/9.1\\_news\\_archives/2010\\_06\\_17/UN\\_Global\\_Compact\\_Management\\_Model.pdf](https://www.unglobalcompact.org/docs/news_events/9.1_news_archives/2010_06_17/UN_Global_Compact_Management_Model.pdf)

## Study of transhydrogenase systems features in the mutants of the yeast *pachysolen tannophilus* for the production of ethanol and xylitol from agricultural wastes

O. Bolotnikova<sup>1,2</sup>, J. Bazarnova<sup>2</sup>, E. Aronova<sup>2</sup> and T. Bolotnikova<sup>2,\*</sup>

<sup>1</sup>Petrozavodsk State University, Institute of Medicine, Department of biomedical chemistry, immunology and laboratory diagnostics, Lenina Str., 33, RU 185910 Petrozavodsk, Republic of Karelia, Russia

<sup>2</sup>Peter the Great St. Petersburg Polytechnic University, Graduate school of biotechnology and food science, Polytechnicheskaya Str., 29, RU 195251 Saint Petersburg, Russia

\*Correspondence: bolotnikova@biocad.ru

**Abstract.** The key catabolic enzymes of D-xylose, an important structural component of different agricultural wastes, were studied in cells of mutant strains of the xylose-assimilating yeast *Pachysolen tannophilus*. The evaluation of catalytic activity and cofactor specificity of xylose reductase (EC 1.1.1.307) and xylitol dehydrogenase (EC 1.1.1.9) confirmed the dependence of intracellular catabolic pathway for D-xylose on the NAD<sup>+</sup>/NADP<sup>+</sup> ratio, formed under microaerobic conditions. The study of total activity of some NAD<sup>+</sup>/NADP<sup>+</sup>-dependent dehydrogenases revealed the metabolic characteristics of the yeast cells, which could ensure selective ethanol or xylitol production. Thus, the efficient involvement of D-xylose into the Embden–Meyerhof–Parnas pathway provided not only the high activities of xylose reductase and xylitol dehydrogenase, but also of 1-glycerophosphate dehydrogenase (EC 1.1.1.8) and lactate dehydrogenase (EC 1.1.1.27), respectively. The inhibition of activity of these enzymes led to selective production of xylitol from D-xylose. On the base of the experimental results, the principles of metabolic engineering of xylose-assimilating yeasts were formulated. The possibility of bioethanol and xylitol production from different agricultural wastes using xylose-assimilating yeasts are discussed.

**Key words:** agricultural wastes, D-xylose, mutants of the yeast *P. tannophilus*, xylose reductase, xylitol dehydrogenase, 1-glycerophosphate dehydrogenase, lactate dehydrogenase, ethanol, xylitol.

## INTRODUCTION

Development of the global food industry has close connections with an increasing the number of agro-industrial wastes, represented mostly by heteropolysaccharides (Sadh et al., 2018). Its hydrolysis leads to the formation of hexoses (D-glucose, D-mannose, D-galactose) and pentoses (D-xylose, L-arabinose) mixtures. Innovations in bioethanol production based on such substrates are the top-most priority in EU's environmental policies (Bedoić et al., 2019). However, microbial strains suitable for this technologies must actively utilize different hexoses and pentoses.

It is known that the yeast *Saccharomyces cerevisiae* is characterized by efficiently ethanol fermentation of hexoses, the principles underlying its regulation are well studied (Siti et al., 2017). The key enzymes, encoding NAD $\times$ H/NADP $\times$ H-dependent xylose reductase (XR, EC 1.1.1.21) and NAD $^{+}$ -dependent xylitol dehydrogenase (XD, EC 1.1.1.9), are necessary to utilize D-xylose, the main structural component of hemicellulose (Kwak & Jin, 2017). After phosphorylation, D-xylulose is involved in the non-oxidative phase of the pentose phosphate pathway and the Embden-Meyerhof-Parnas pathway. However, genetically modified strains of *S. cerevisiae* produce xylitol under microaerobic conditions, which activate the formation of ethanol from D-xylose (Kwak & Jin, 2017). This fact indicates the important role of transhydrogenase systems that regulate the ratio of NAD(P) $^{+}$ /NAD(P) $\times$ H during the catabolism of D-xylose, minor sugar for yeast cells. Its analysis will be an prerequisite, necessary for the construction of *S. cerevisiae* strains capable to efficient production of xylitol and ethanol from D-xylose.

The ‘respiratory’ type of D-xylose catabolism, characteristic of yeasts Kreger van Rij (1984), declares the paramount importance of mitochondria for regulating the ratio of NADP $^{+}$ /NAD $^{+}$ . However, the functions of 1-glycerophosphate dehydrogenase (GPD, EC 1.1.1.8) and NAD $^{+}$ -dependent malate dehydrogenase (MD, EC 1.1.1.37), which provide transport of reduced equivalents from cytosol to mitochondria, as well as cytochrome c oxidase (CO, EC 1.9.3.1), the main enzymatic complex of the electron transfer chain, has not yet been studied for xylose-assimilating yeast. Its adaptation to acidic media Kreger van Rij (1984) does not exclude the participation of lactate dehydrogenase (LD, EC 1.1.1.27) in the regulation of the ratio NAD $\times$ H /NAD $^{+}$ , when the oxygen concentration in the medium decreases significantly. The effect of this enzyme on the production of ethanol from D-xylose was also not detected. *Pachysolen tannophilus* has previously been shown to be a convenient experimental object for identifying factors that regulate the catabolism of D-xylose in yeast cells (Yablochkova et al., 2004). Therefore, the goal was to study the activity and specificity of XR and XD, as well as the general activities of GPD, total MD, CO and LD in *P. tannophilus* mutants producing xylitol or ethanol from D-xylose.

## MATERIALS AND METHODS

It has been experimentally proved that naturally occurring xylose-assimilating yeasts *P. tannophilus* have the unique ability to produce comparable amounts of xylitol and ethanol during microaerobic fermentation of D-xylose (Yablochkova et al., 2003). This practical result makes possible studying the conditions conducive to the formation of each target product on the example of the same model object. However, highly pronounced homotallism, population heterogeneity, instability of diplophase significantly complicate the using of genetic engineering techniques for constructing *P. tannophilus* strains, that can selectively produce xylitol or ethanol (Kreger van Rij, 1984). Nonetheless, methods for isolation of *P. tannophilus* mutants which are characterized by various defects of D-xylose catabolism, directly affected on ethanol and xylitol levels are well known (James et al., 1989). Therefore, based on the *P. tannophilus* strain -Y-1532 (Museum of Microorganisms, All-Russian Research Institute of Hydrolysis, St. Petersburg), the haploid *P. tannophilus* 22-Y-1532 was isolated (Bolotnikova et al., 2007). Two-day-old *P. tannophilus* 22-Y-1532 cells were exposed to 1-methyl-3-nitro-1'-nitrosoguanidine under experimental conditions (Bolotnikova et

al., 2007). Changes in the level of production of xylitol and ethanol were detected by analyzing the growth rate of mutants on selective media with D-glucose, D-xylose, xylitol or ethanol as the sole carbon source. In all cases, the growth of haploid *P. tannophilus* 22-Y-1532 served as a positive control. Thus, out of 51 mutants, only 3 strains were selected that produced xylitol (No. 664) or ethanol (No. 390, No. 442) from D-xylose. Evaluation of the morphological characteristics (diameter, color, shape and texture of the colonies, as well as the size, type of budding and the nature of sporulation of cells) in accordance with the criteria developed previously Bolotnikova et al. (2005), confirmed the haploidy of these mutants. These mutant strains of *P. tannophilus* were used for microaerobic fermentation of D-xylose.

The inoculum for fermentation was obtained by growing yeast in 500 mL round bottom flasks containing 100 mL of YEPD medium with 2% D-glucose, on a shaker (230 rpm) at  $30 \pm 20^\circ\text{C}$ . After 18–24 hours, 10 mL of yeast suspension from these the flasks were transferred to 500 mL flasks containing 100 mL YAPX medium with 2% D-xylose, which were incubated under similar conditions. The yeast biomass concentration for the fermentation of D-xylose was  $6.0 \pm 0.5 \text{ g d w L}^{-1}$ . All fermentations were conducted at 250 mL round-bottom flasks containing 100 mL of the medium with 2.0% D-xylose, 2.0% peptone and 0.5% yeast extract on a shaker (100 rpm) at  $+30 \pm 2^\circ\text{C}$  for 24 h. During this time, the parent haploid strain *P. tannophilus* 22-Y-1532 used 97% D-xylose and produced a maximum xylitol, although the ethanol yield did not reach its maximum (Bolotnikova et al., 2012; Bolotnikova et al., 2013). This allowed us to reduce the toxic effect of ethanol on the metabolic activity of mutant strains of *P. tannophilus*. The concentration of yeast biomass after fermentation was analyzed spectrophotometrically (Bazarnova et al., 2018). The concentration of reducing substances (RB) was determined with Fehling's reagent. Ethanol and xylitol were determined by gas chromatography (Vista 600, 'Varian', USA) according to the recommendations (Bolotnikova et al., 2019).

Cell-free yeast extracts were obtained in accordance with (Bolotnikova et al., 2015). The concentration of total protein was determined by the Lowry method using bovine serum albumin as a standard. The total and specific activities of XR and XD were evaluated by monitoring the concentrations of  $\text{NAD(P)}\times\text{H}/\text{NAD(P)}^+$  redox pairs at 340 nm under the conditions described in (Zverlov et al., 1990). The unit of enzymes' activity was defined as the amount of the enzyme that capable to oxidize mMol of  $\text{NAD(P)}\times\text{H}$  per min. A similar monitoring of the concentrations of the  $\text{NAD}\times\text{H}/\text{NAD}^+$  pair was used for spectrophotometric determination of LD activity, total MD, and GDP (Kochetov, 1980). The activity of CO was determined after its recovery with ascorbic acid according to the procedure (Smith, 1955). The statistical analysis of experimental results was carried out using Student's T-Test for a significance level of 0.05 with MS Excel computer program.

## RESULTS AND DISCUSSION

### Microaerobic fermentation of D-xylose by mutant strains of *P. tannophilus*

A comparative analysis of the yields of xylitol, ethanol, and biomass by mutant *P. tannophilus* strains during microaerobic fermentation of D-xylose is presented in Fig. 1. Experimental results indicate that mutant No. 664 selectively produced xylitol with an efficiency of 2.3 times exceeding a similar control characteristic. At the same

time, its biomass level was significantly lower than the value obtained for the original parent strain. Mutants No. 390 and No. 442 without xylitol accumulation produced ethanol 19.0% and 27.0% better than *P. tannophilus* 22-Y-1532. The biomass yield of these strains was also lower than that of *P. tannophilus* 22-Y-1532 (Fig. 1). After fermentation, yeast biomass was used to determine the activity of XR, XD, GPD, total MD, CO, and LD involved in various stages of D-xylose catabolism.

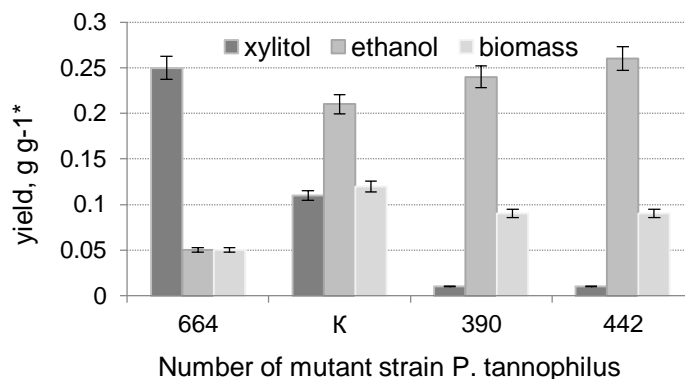


**Figure 1.** The yield of xylitol, ethanol and biomass by the mutants of the yeast *P. tannophilus* 22-Y-1532.

Notes: K – the parent strain of *P. tannophilus* 22-Y-1532; \* – Yield for per gram of D-xylose.

*Activity and coenzyme specificity of xylose reductase and xylitol dehydrogenase.* The enzymes of the initial steps of D-xylose catabolism, XR and XD, have a strong effect on the level of xylitol and ethanol in yeast cells (Kwak & Jin, 2017). The specific acceptors and donors of pairs of electrons and protons in such reactions are derivatives of the NAD(P)<sup>+</sup> and NAD(P)×H dinucleotides (Zverlov et al., 1990). Therefore, the rate of these coenzymes oxidation (reduction) was used to evaluate the activity of XR and XD in the mutants of *P. tannophilus* 22-Y-1532, producing xylitol and ethanol.

As expected, the activity of the both enzymes in mutant cells turned out to be lower than the control values (Fig. 2). The lowest XR and XD activity was observed in mutant No. 664, which showed a low degree (56.0%) and a rate of utilization of D-xylose (0.078 g g<sup>-1</sup> h<sup>-1</sup>) during microaerobic fermentation. The XR of xylitol producing mutant had a predominant affinity for NADP×H (Fig. 3). However, 95.0% of XD activity of that yeast strain was coupled with coenzyme NAD<sup>+</sup>.

The highest experimental values of XR and XD activity were found in ethanol-producing mutants that used 86.0% (strain No. 390) or 78.6% (strain No. 442). D-xylose. The rate of its consumption under microaerobic conditions increased to 0.119 g g<sup>-1</sup> h<sup>-1</sup> and 0.109 g g<sup>-1</sup> h<sup>-1</sup>, respectively. The pronounced double NAD×H/NADP×H specificity of XR was a common feature of these mutant strains. Moreover, the largest contribution of the NAD×H-dependent form to the total XR activity of was noted for mutant No. 390 (Fig. 3). The XD of the both yeast strains producing ethanol from D-xylose retained metabolic dependency from NAD<sup>+</sup> (Fig. 2).

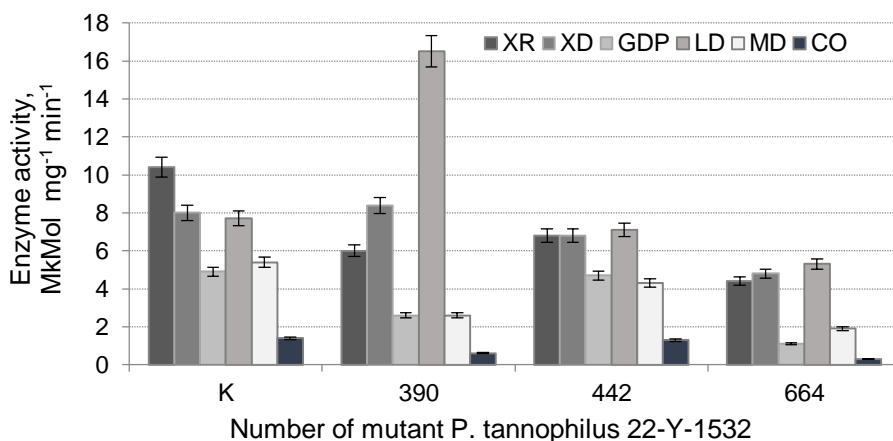


**Figure 2.** Activity of enzymes involved in the catabolism of D-xylose in mutants of the yeast *P. tannophilus* 22-Y-1532.

Notes: K – the parent strain of *P. tannophilus* 22-Y-1532; XR – xylose reductase; MD – malate dehydrogenase; XD – xylitol dehydrogenase; GDP – glycerol-3-phosphate dehydrogenase; LD – lactate dehydrogenase; CO – cytochrome *c* oxidase.

### The activity of $\text{NAD}^+/\text{NAD}\times\text{H}$ dehydrogenases of common catabolic pathways

It is known that transformation of D-xylulose-5-phosphate in the reactions of non oxidative phase of pentose phosphate pathway is necessary for the formation of fructose-6-phosphate and glyceraldehyde-3-phosphate, intermediates of the Embden-Meyerhof-Parnas pathway. The direction of their further metabolism in the yeast cell depends on the aeration degree in the fermentation medium (Liu et al., 2018). However, microaerobiosis favoring the production of ethanol from D-xylose also stimulate the use of pyruvate in Krebs cycle. Therefore, the  $\text{NAD}\times\text{H}$  regeneration points necessary for XD functioning can be located into the general sugar-catabolic pathways, which located in different cell compartments.

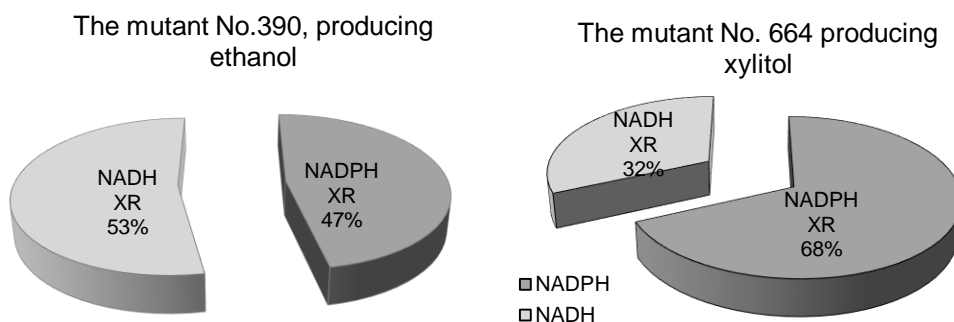


**Figure 3.** Contribution of various specific activities in total xylose reductase activity (XR) for mutants of *P. tannophilus*, producing ethanol and xylitol.

The activities of a number of  $\text{NAD}^+/\text{NAD}\times\text{H}$ -dependent dehydrogenases (GPD, total MD, CO and LD) of the mutants *P. tannophilus* 22-Y-1532 were studied. In most



cases, their values were lower than the control values (Fig. 2). The NAD<sup>+</sup>/NAD×H dehydrogenases activities of the ethanol-producing mutants *P. tannophilus* were significantly different. Thus, the mutant strain No. 390 was characterized by a more than two-fold increase of LD activity against the background of significant decrease of GPD, total MD and CO activities. On the other side, the mutant No. 442 had activities of all these enzymes, comparable with the dates for the parent strain *P. tannophilus* 22-Y-1532.

### **The correlation of various HAD /HAD×H-dehydrogenases activity in the biochemical mutants of the yeast *P. tannophilus***

To identify the features of NAD×H regeneration under microaerobic conditions favoring the selective production of xylitol and ethanol from D-xylose, the ratios of activity the enzymes capable to oxidizing NAD×H were calculated to the activity of NAD<sup>+</sup>- dependent xylitol dehydrogenase (Table 1).

**Table 1.** The ratio of the activity of different HAD<sup>+</sup>/ HADH-dehydrogenases to xylitol dehydrogenase activity in the mutant strains of *P. tannophilus* 22-Y-1532

Number of mutant strain	Main product	The ratio of enzymes activities				
		HAD×H XR / XD	GPG / XD	LDG / XD	MDG /XD	CO / XD
664	<i>xylitol</i>	0.29	0.2	1.11	0.38	0,06
390	<i>ethanol</i>	0.38	0.3	1.96	0.36	0.06
442		0.47	0.6	1.05	0.62	0.19

Notes: XR – xylose reductase; MD – malate dehydrogenase; XD – xylitol dehydrogenase; GPD – glycerol-3-phosphate dehydrogenase; LD – lactate dehydrogenase; CO – cytochrome *c* oxidase; Colors show characteristics, similar in different mutant strains. The maximum error in all cases did not exceed 5.0%.

An analysis of the results revealed some metabolic features that determine the effectiveness of xylitol incorporation to reactions of the common sugar-catabolic pathways. For the mutant No. 664 the lowest ratios of activity of NAD×H-dependent XR, GPD, total MD and CO were noted compared to XD activity. This indirectly indicates the insignificant role of Embden-Meyerhof-Parnas pathway and the mitochondrial respiratory chain in retention of NAD<sup>+</sup>/NAD×H balance, necessary for D-xylulose formation.

A common feature in the ethanol-producing mutant strains was the significant contribution of XR to the NAD×H oxidation. However, other metabolic characteristics of these strains of *P. tannophilus* varied. So, NAD×H regeneration was ensured by a rather high LD activity in the cells of the mutant No. 390. The oxidation of xylitol to D-xylulose was supported by the functioning of the respiratory chains of mitochondria (fairly high ratios of activity of total MD and CO to XD activity) in mutant No. 442.

At the same time, features of D-xylose metabolism, common to different type mutants of *P. tannophilus* 22-Y-1532 were marked. The ratios of total MD and CO activities to XD activity did not differ in principle for the strains No. 390 and No. 664. The mutant No. 664, producing xylitol, and mutant No. 442, which formed the highest amounts of ethanol, were characterized by a similar participation of LD activity in the regeneration of NAD<sup>+</sup> coenzyme. Thus, assessment of the metabolic characteristics of *P. tannophilus* mutant strains indirectly confirmed the functioning of various mechanisms for the NAD<sup>+</sup>/NAD×H balance regulation under microaerobic fermentation of D-xylose.

## CONCLUSION

The dynamic development of the world economy is impossible without the search for cheap renewable energy sources, alternative to oil and coal. Ethanol, in comparison with other forms of bioenergy, is favorably distinguished by low cost and environmental toxicity (Sadh et al., 2018; Bedoić et al., 2019). A promising stock for its production are different agricultural wastes, which, after hydrolysis, turn into multicomponent mixtures of hexoses and pentoses, consisting of 20–92% of D-xylose. Utilization of such substrates by yeast has a number of technological advantages (Spalvins et al., 2018). However, attempts at the genetic construction of industrial strains of *S. cerevisiae*, effectively producing bioethanol from D-xylose, has not yet been successful (Cristobal-Sarramian & Atzmüller, 2018).

The catabolism of D-xylose, functioning with the participation of the non-oxidizing phase of the pentose phosphate pathway, the Embden-Meyerhof-Parnassus pathway and the Krebs cycle, leads to the formation of intermediates similar to catabolism of hexoses (fructose-6-phosphate, glyceraldehyde-3-phosphate, pyruvate, ethanol). However, a living cell is a complexly organized whole system. Often, even its genetic and biochemical assessment *in vitro* ignores aspects that fundamentally affect the course of the entire process of bioconversion of an organic substrate. Thus, evidence of the key role of enzymes in the initial stages of D-xylose catabolism has not yet fully revealed the causes of xylitol formation in the aeration, favoring ethanol production. Xylitol is widely used as a substitute for sucrose in the food and medical industry (Ur-Rehman et al., 2015). The microbiological method for producing xylitol is characterized by environmental friendliness, as well as the ease of isolation and purification of this alcohol (Cristobal-Sarramian & Atzmüller, 2015). Given this, an analysis of the metabolic characteristics of yeast that contribute to the production of xylitol and ethanol have great importance.

An experimental analysis of the mutants of *P. tannophilus* showed that the production of xylitol and ethanol from D-xylose represents as the rearrangement of whole metabolism of carbohydrates in oxygen deficiency - the final electron and proton acceptor by  $\text{NAD}\times\text{H}$ . The increased ratio of  $\text{NADP}^+/\text{NAD}\times\text{H}$  in microaerobiosis is not only the difference in the coenzyme

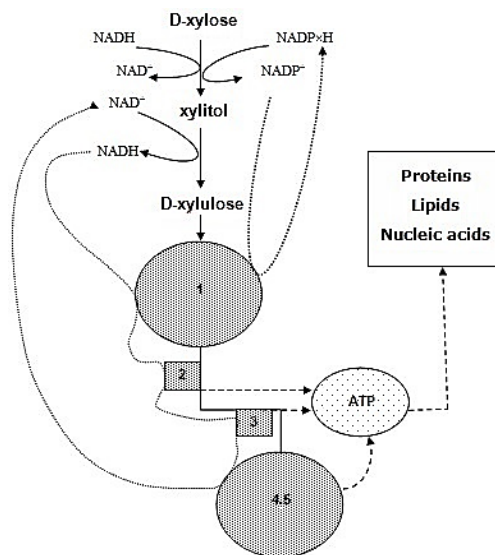


**Figure 4.** Regeneration of coenzymes  $\text{NAD(P)}\times\text{H}$  in yeast during microaerobic fermentation of D-xylose.

Notes: 1 – Warburg-Dickens pathway; 2 – Embden-Meyerhof-Parnas pathway; 3 – The oxidative decarboxylation of pyruvate; 4 – Krebs cycle; 5 – Biological oxidation and oxidative phosphorylation. Dotted lines indicate regeneration points for  $\text{NADP}\times\text{H}$  and  $\text{NAD}\times\text{H}$ .

specificity of XR and XD, but also the inhibition of NAD<sup>+</sup>/NADH dehydrogenases of common sugars catabolism pathways (Fig. 4). Therefore, high production of xylitol may be a manifestation of ‘the Pasteur effect’ for D-xylose, a reserved carbon source in yeast cells.

The production of ethanol from D-xylose is impossible without flexible regulation of NAD<sup>+</sup>/NADH balance in oxygen deficiency. In addition to the respiratory chains of mitochondria, the xylose-assimilating yeast has at least three to four NADH regeneration points. One of them is reduction of D-xylose to xylitol, although the degree of its influence on the balance of NAD<sup>+</sup>/NADH directly depends on the activity and specificity of XR (Yablochkova et al., 2004; Kwak & Jin, 2017; Siti et al., 2017; Cristobal-Sarramian & Atzmüller, 2018; Liu et al., 2018). The participation of pyruvate and dioxiacetonphosphate, as well as the mitochondrial respiratory chains in the regeneration of NAD<sup>+</sup>, clearly illustrates the close relationship of ethanol formation from D-xylose with yeast growth. A likely explanation for this phenomenon is the greater sensitivity of the xylose-assimilating yeast to ethanol in compared to *S. cerevisiae* (Bolotnikova et al., 2012; Siti et al., 2017). The prevalence of *P. tannophilus* growth over the ethanol-forming activity may be genetically determined. Therefore, studying the genetic system of this yeast becomes an important prerequisite for determining the biochemical steps that restrict the production of ethanol from D-xylose. It will help determine the strategy for genetic construction of *S. cerevisiae* strains with high yield of ethanol and xylitol on the base of variety agricultural wastes.

**ACKNOWLEDGMENTS.** This work was supported by the grant No 18-44-100001 from Russian Foundation for Basic Research (RFBR).

## REFERENCES

- Bazarnova, Y., Bolotnikova, O., Michailova, N. & Pu, J. 2018. Optimization of parameters of alcohol fermentation of xylose-containing inedible substrates using the yeast *Pachysolen tannophilus*. In: *International Scientific Conference on Energy, Environmental and Construction Engineering. MATEC Web of Conferences*, Saint-Petersburg, pp. 1–5 (in Russian)
- Bolotnikova, O.I., Mikhailova, N.P., Bodunova, E.N., Shabalina, M.V. & Ginak, A.I. 2005. Conditions favoring differentiation and stabilization of the life cycle of the yeast *Pachysolen tannophilus*. *Microbiology* **74**, 483–488.
- Bolotnikova, O.I., Mikhailova, N.P., Bodunova, E.N., Yablochkova, E.N., Trushnikova, E.P. & Ginak, A.I. 2007. Isolation and primary characterization of xylose-utilizing yeast *Pachysolen tannophilus* mutants. *Biotechnologiya* **1**, 35–40.
- Bolotnikova, O.I., Mikhailova, N.P., Meshcheryakova, O.V. & Ginak, A.I. 2015. Metabolic properties of *Pachysolen tannophilus* mutants producing xylitol and ethanol from D-xylose. *Microbiology* **84**, 485–490.
- Bolotnikova, O.I., Mihajlova, N.P. & Ginak, A.I. 2012. Physiological properties of the yeast *Pachysolen tannophilus* growth. *Mikologiya i fitopatologiya* **46**, 136–139.
- Bolotnikova, O., Bazarnova, J., Aronova, E., Mikhailova, N., Bolotnikova, T. & Pu, J. 2019. Spent sulphite liquor utilization by xylose-assimilating yeast *Pachysolen tannophilus*, capable of bioethanol producing. In: *International Scientific Conference on Energy, Environmental and Construction Engineering. MATEC Web of Conferences*, Saint-Petersburg, pp. 1–4 (in Russian).

- Bolotnikova, O.I., Mihajlova, N.P. & Ginak, A.I. 2013. Alcohol-forming activity of *Pachysolen tannophilus* yeast on xylose-containing substrates /Спиртообразующая активность дрожжей *Pachysolen tannophilus* на ксилозосодержащих субстратах/. Bulletin of the Saint Petersburg State Institute of Technology (Technical University) **20**, 1–16.
- Bedoić, R., Ćosić, B. & Duić N. 2019. Technical potential and geographic distribution of agricultural residues, co-products and by-products in the European Union. *Science of The Total Environment* **686**, 568–579.
- Cristobal-Sarramian, A. & Atzmüller, D. 2018. Yeast as a production platform in biorefineries: conversion of agricultural residues into value-added products. *Agronomy Research* **16**, 377–388.
- Dubrovskis, V., Plume, I. & Straume, I. 2019. Use of ethanol production and stillage processing residues for biogas production. *Agronomy Research* **17**, 1881–1890.
- James, A.P., Zahab, D.M., Mahmoudides, G., Maleszka, R. & Schneider H. 1989. Genetic and biochemical characterization of mutations affecting the ability of the yeast *Pachysolen tannophilus* to metabolize D-xylose. *Applied and Environmental Microbiology* **55**, 2871–2876.
- Kochetov, G.A. 1980. *Practical guide to Enzymology* /Практическое руководство по энзимологии/. High school, Moscow, 272 pp.
- Kreger van Rij, N.J.W. 1984. *The yeasts, a taxonomic study*. 3rd edition. Elsevier Science, Amsterdam, 1082 pp.
- Kwak, S. & Jin, Y.S. 2017. Production of fuels and chemicals from xylose by engineered *Saccharomyces cerevisiae*: a review and perspective. *Microbial Cell Factories* **16**, 82–97.
- Liu, J., Li, H., Zhao, G., Caiyin, Q. & Qiao, J. 2018. Redox cofactor engineering in industrial microorganisms: strategies, recent applications and future directions. *Journal of Industrial Microbiology & Biotechnology* **45**, 313–327.
- Sadh, P.K., Duhan, S. & Duhan, J.S. 2018. Agro-industrial wastes and their utilization using solid state fermentation: a review. *Bioresources and Bioprocessing* **5**, 1–15.
- Siti, A.H.M., Rahmath, A., Siti, A.J., Hartinie, M.J., Azlan, G.A., Azifa, M.F. & Kenneth, F.R. 2017. Yeasts in sustainable bioethanol production: A review. *Biochemistry and Biophysics Reports* **10**, 52–61.
- Smith, L. 1995. *Spectrophotometric assay of cytochrome c oxidase*. Methods of Biochemical Analysis, Glick, D., New York, pp. 427–434.
- Spalvins, K., Ivanovs, K. & Blumberga, D. 2018. Single cell protein production from waste biomass: review of various agricultural by-products. *Agronomy Research* **16**, 1493–1508.
- Ur-Rehman, S., Mushtaq, Z., Zahoor, T., Jamil, A. & Murtaza, M.A. 2015. Xylitol: a review on bioproduction, application, health benefits, and related safety issues. *Critical Reviews in Food Science and Nutrition* **55**, 1514–1528.
- Yablochkova, E.N., Bolotnikova, O.I., Mikhailova, N.P., Nemova, N.N. & Ginak, A.I. 2004. The activity of key enzymes in xylose-assimilating yeast at different rates of oxygen transfer to the fermentation medium. *Microbiology* **73**, 129–133.
- Yablochkova, E.N., Bolotnikova, O.I., Mikhailova, N.P., Nemova, N.N. & Ginak, A.I. 2003. Specific features of fermentation of D-xylose and D-glucose by xylose-assimilating yeast. *Applied Biochemistry and Microbiology* **39**, 265–269.
- Zverlov, V.V., Yur'ev, M.Z. & Mogutov, I.A. 1990. *The study of xylose conversion enzymes in yeast* /Изучение ферментов конверсии ксилозы у дрожжей/. *Biotechnology* **5**, 1–6.

## The advanced application of the wood-originated wastewater sludge

J. Brovkina<sup>1,\*</sup>, G. Shulga<sup>1</sup>, J. Ozolins<sup>2</sup>, B. Neiberte<sup>1</sup>, A. Verovkins<sup>1</sup> and V. Lakevics<sup>2</sup>

<sup>1</sup>Latvian State Institute of Wood Chemistry, Dzerbenes street 27, LV–1006 Riga, Latvia

<sup>2</sup>Riga Technical University, Faculty of Material Science and Applied Chemistry, Paula Valdena street 3/7, LV–1048 Riga, Latvia

\*Correspondence: yuli@inbox.lv

**Abstract.** The wood hydrothermal treatment is one of the plywood production's stages, which resulting in the production of wastewater containing such components as hemicelluloses, lignin and wood extractive substances (HLES). It is necessary to improve the wastewater treatment technology with the aim to enhance the yield of sludge from plywood wastewater for its effective and rational recycling. In the present study, the optimal coagulation conditions for the HLES removal have been found using the developed aluminium salt-based coagulant. The developed composite coagulant is characterized by lower doses, a wide range of the work pH values, the insensitivity against temperature changes and a higher coagulation efficacy compared with traditional aluminium salts. The proposed treatment technology generates many tons of wood-originated sludge – a biomass coagulate. It was found that the formed coagulate produced in the process of wastewater treatment can increase the sorption ability of clay. The optimal content of the dry coagulate in a clay sorbent does not exceed 0.11%. The sorption capacity of the developed sorbent for water, rapeseed and silicone oil increases by 35%, 31% and 21%, respectively, relative to the unmodified clay sorbent. The sorption efficiency of heavy metals from water solutions is also increased by 10–12%. The thermal treatment of the modified clay sorbent at the high temperature leads to an increase in its sorption capacity for oil products.

**Key words:** coagulation, composite coagulant, woodworking wastewater, sludge, clay sorbent.

## INTRODUCTION

The plywood industry is an industrial sector where a high amount of wood materials and water is used during the manufacturing process. One of the stages of raw material preparation is the hydrothermal treatment of wood. Wastewater of hydrothermal basins are characterized by the high degree of contamination. The presence of lignin and its derivatives, as well hemicelluloses and extractive substances (HLES) contribute to strong colour of wastewater, turbidity and high chemical oxygen demand (COD).

There are different treatment methods for removing organic and inorganic substances from wastewater. They include biological treatment (Viraraghan, 2004; Leiviska et al., 2008; Buyukkamaci & Koken, 2010), various membrane technologies (Chen et al., 2015; Doruk et al., 2016), electrochemical methods (Chanworrawoot &

Hunsom, 2012), chemical oxidation (Kishimoto et al., 2010), physicochemical methods (Ganjidoust et al., 1997; Ashrafi et al., 2015) or combination of them (Klauson et al., 2015; Hubbe et al., 2016; Brink et al., 2018).

One of the most used methods for wastewater treatment is a coagulation/flocculation process. The coagulation/flocculation method is not only an economic, but also an effective mode for removal of COD and colour from the wastewater. The chemical coagulants such as inorganic metal salts (aluminum and ferric salts) and polyelectrolytes (Sharma et al., 2006; Lee et al., 2014) are often used in the coagulation/flocculation process.

It is known that polyaluminium chloride (PAC) is a more effective coagulant than aluminium sulphate and aluminium chloride for paper and pulp mill wastewater treatment (Kumar et al., 2011; Aziz et al., 2017). PAC faster forms flocs due the high positive electrical charge that allows it easily reducing the electrical charge on the surface of colloidal particles. At the same time, PAC is a more expensive coagulant in comparison with the classic aluminium salts used for wastewater treatment.

To enhance the efficiency of the coagulation, PAC is used in compositions with different chemical reagents, for example, calcium oxide and chloride (Palone et al., 2011), iron oxides or halogenides (Lee et al., 2008), with a cationic flocculant, for example, polyacrylamide (Lukerchenko, 2008; Katrivesis et al., 2019). There are also known two-stage coagulation method, firstly with aluminium sulphate and then with polyaluminium chloride (Kevin et al., 2004). However, such the method is complicated from the technological point of view due to the multistageness of the coagulation process.

The main drawbacks of the coagulation method are its sensitivity to pH and low temperature (Toczyłowska-Mamińska, 2017), as well as high volumes of the formed sludge that is defined by a wastewater composition, a type and a dosage of the applied coagulant and process conditions.

Due to the increased requirements for water environmental, it is very important to regenerate industrial wastewater sludge for obtaining new products with added value. The effective usage of sludge is an actual challenge for each industry, where a wastewater treatment technology is applied. It is known that wastewater sludge can be used as a biofuel (Seiple, 2017), for soil recovery (Lakhdar et al., 2010) and agricultural needs (Mtshali, 2014), for bricks production (Lin & Weng, 2001), in road layers (Lucena et al., 2014), for cements and concretes manufacturing (Barrera-Díaza et al., 2011), as fertiliser (Lazdina et al., 2011) and as a sorbent (Rio et al., 2006; Smith et al., 2009).

Methods of combining wastewater sludge with other natural materials are already widely used. Manufacturing of such sorbents is traditionally based on the chemical activation of components and the further thermal treatment. There are methods for a recycling of wastewater sludge with wood chips, cement, lime, slag, mineralized refuse and construction waste (Kamon et al., 2002; Kim et al., 2005; Ma et al., 2007; Fang et al., 2010; Zhou et al., 2011). The obtained sorbents of these types are efficient and cheap. The clay based materials often correspond to the above mentioned requirements and are characterized by low cost and high specific surface (Lakevics et al., 2011).

The increasing interest towards modified clays is related to the necessity to create environmentally safe sorbents. Clay modification can be done by using of inorganic acids and metal salts (Ismadji et al., 2015), humic acid (Jemeljanova et al., 2019), aluminium and iron polyhydroxy complexes (Khankhasaeva et al., 2006), chitosan

(Unuabonah et al., 2017) and organic additives (Olalekan et al., 2010). Clay based sorbents can be used for discoloration of rapeseed oil (Frost Ray et al., 2007), sorption of dyes (Ho et al., 2001) and heavy metals (Carvalho et al., 2007).

The study aim was to show the effectiveness of usage of the developed inorganic composite coagulant based on PAC for plywood wastewater treatment procedure and to present a perspective trend in the possible application of the obtained wood-originated sludge.

## MATERIALS AND METHODS

### Model wastewater

The wastewater sample has been presented by a model solution obtained via the hydrothermal treatment of the birch wood sawdust (Brovkina et al., 2010). The main parameters of the model solution are listed in the Table 1.

### Coagulation process

For the treatment of the model solution, the new developed composite coagulant (KHPAC) based on PAC and aluminium chloride ( $\text{AlCl}_3$ ) was used (Shulga et al., 2014). The efficacy of the coagulation was compared with the parameters of the model solution obtained after treatment with PAC, aluminium chloride and composite coagulant, containing PAC and aluminium sulphate (KSPAC) (Shishkin, 2004).

The jar test procedures was carried out using 50 mL of the model wastewater and 50 mL of a coagulant solution. Sample was stirred at 200 rpm for 1 minute and then for 2 minutes at 40 rpm. The flocs formed during coagulation were allowed to settle for 120 minutes. Coagulation efficiency was evaluated by a residual concentration of HLES, which comprised hemicelluloses, lignin-containing substances (LCS) and extractives. For their determination, the analytical chemistry methods developed at the Latvian State Institute of Wood Chemistry (Zakis & Neiberte, 2003) were used. Each experiment was carried out three times. The results are presented as mean values.

### Characterisation of the wood-originated coagulate

Sizes of the air-dried coagulate granules were measured with the Laser Particle Sizer ANALYSETTE 22 NanoTec (Fritsch GmbH). The functional and structural composition of the coagulate was studied with Carbon Nuclear Magnetic Resonance ( $^{13}\text{C}$ -NMR) (Bruker 300MHz spectrometer) and Fourier Transform Infrared spectroscopy (FT-IR) (Perkin-Elmer Spectrum One). The elemental composition of the wood-originated coagulate was studied using catalytic combustion process (Elementar Analysensysteme GmbH, Germany).

**Table 1.** Model wastewater physico-chemical characteristics

Parameters	Value
Hemicelluloses, lignin and wood extractive substances (HLES)	1,400 mg L <sup>-1</sup>
Lignin containing substances (LCS)	280 mg L <sup>-1</sup>
Chemical Oxygen Demand (COD)	1,285 mg O L <sup>-1</sup>
Total Organic Compounds (TOC)	732 mg L <sup>-1</sup>
Colour	746 mg L <sup>-1</sup> Pt <sup>-1</sup>

### Clay modification with coagulate

The obtained wood-originated sludge in the form of a coagulate was used as an active additive to improve a Latvian Triassic clay (LTM) from the Vadakste deposit for obtaining a sorbent. The modification of clay granules with sizes between 0.25 mm and 3 mm was performed by spraying a coagulate solution with a concentration of 1.8–1.9% to the clay surface. The treated clay samples were dried at 105 °C for 24 hours. The dry coagulate content in the clay samples varied from 0.05 to 0.26%. The modified clay samples were labeled as: LTM 005 (0.05% coagulate content), LTM 011 (0.11% coagulate content), etc. Then, the modified samples were thermally treated at 800 °C in a high temperature furnace for 2 hours. After this procedure, the clay samples were labeled as: LTM–800 (unmodified thermally treated sample at 800 °C); LTM 011–800 (modified thermally treated sample at 800 °C with a 0.11% coagulate content).

### Determination of water carrying capacity by modified clay samples

To determine the water carrying capacity a glass tube with porous bottom was used. The tube filled with clay sample was kept in water for 15 minutes. The water level was 1 cm above the clay level in tube. After contact time the tube was removed and weighed. The water carrying capacity ( $W$ , mg H<sub>2</sub>O g<sup>-1</sup>) was calculated using follow equation (1):

$$W = \frac{m_3 - m_2}{m_2 - m_1} \cdot 1,000 \quad (1)$$

where  $m_1$  – tube mass, g;  $m_2$  – tube and clay mass, g;  $m_3$  – tube and treated clay mass, g.

Each experiment was carried out two times. The results are presented as mean values.

### Determination of water (oil) binding capacity by modified clay samples

A clay sample of  $5 \pm 0.05$  g was deposited on a metal sieve using filter paper. The sieve was submerged in water (or oil), so that the sample was held from 1 to 15 minutes. For studying oil binding, rapeseed and silicone oils were used. After this time, the sieve with the clay sample was removed from the water (or oil) and left to drain for 2 minutes. The water (oil) binding capacity ( $A$ , mg H<sub>2</sub>O (or oil) g<sup>-1</sup>) was calculated using follow Eq. (2):

$$W = \frac{m_3 - m_2 - m_1}{m_2} \cdot 1,000 \quad (2)$$

where  $m_1$  – control experiment with submersion without clay, g;  $m_2$  – dry clay sample mass, g;  $m_3$  – mass of the sieve, filter and clay after the saturation with water (oil), g.

Each experiment was carried out two times. The results are presented as mean values.

### Determination of heavy metal ion sorption

The adsorption experiments were carried out by adding the clay samples to water solutions, containing copper chloride and zinc chloride, for 24 hours. Residual zinc and copper concentrations in water solutions were determined by flame atom absorption spectrometry at the wavelengths of 324.8 nm and 213.9 nm, respectively, using the calibrated curves for copper and zinc chloride water solutions. A single measurement was performed.



The amount of metal adsorbed at equilibrium,  $q_e$  (mg g<sup>-1</sup>) was calculated by the following mass balance relationship:

$$q_e = \frac{(C_0 - C_e) \cdot V}{m} \quad (3)$$

where  $C_0$  and  $C_e$  – initial and equilibrium metal concentrations, mg L<sup>-1</sup>;  $V$  – volume of the solution, L<sup>-1</sup>;  $m$  – mass of the adsorbent, g.

To predict the adsorption, process the Freundlich isotherm model was applied to experimental data. The Freundlich isotherm model describes the reversible adsorption, which can be applied to multilayer adsorption, on the basis of surface heterogeneity. The linear form of the Freundlich isotherm equation can be expressed as follows:

$$\log q_e = \log K_F + \frac{1}{n} \log C_e \quad (4)$$

where  $q_e$  a – amount of metal adsorbed at equilibrium, mg g<sup>-1</sup>;  $C_e$  – equilibrium metal concentrations, mg L<sup>-1</sup>;  $n$  – constant which measure adsorption intensity;  $K_F$  – constant which is related to adsorption capacity.

## RESULTS AND DISCUSSION

### HLES removal by coagulation

Early, it was found that optimal pH value for the HLES removal by the aluminium salts was 5.0–6.0 (Brovkina et al., 2011). At pH 6.0, the critical coagulation concentration was 170 mg L<sup>-1</sup> for Al<sub>2</sub>(SO<sub>4</sub>)<sub>3</sub>, 65 mg L<sup>-1</sup> for AlCl<sub>3</sub> and 100 mg L<sup>-1</sup> for PAC at temperature 20°C. The residual concentration of aluminium system after treatment varied from 0.07 mg L<sup>-1</sup> to 0.45 mg L<sup>-1</sup>, depending on a type of aluminium salt. The settling time was 50–60 minutes for Al<sub>2</sub>(SO<sub>4</sub>)<sub>3</sub>, 30–40 minutes for AlCl<sub>3</sub> and 10–20 minutes for PAC. At a relatively lower temperature (13°C), the HLES removal was 60%, 62% and 80% in the present of Al<sub>2</sub>(SO<sub>4</sub>)<sub>3</sub>, AlCl<sub>3</sub> and PAC, respectively. The residual concentration of aluminium ions after the treatment with these salts was 0.62 mg L<sup>-1</sup>, 0.26 mg L<sup>-1</sup> and 0.09 mg L<sup>-1</sup>. A higher recovery of the HLES, a lower residual concentration of aluminium ions in water, a smaller settling time and a non-sensitivity to the temperature changes indicated that PAC was a more effective coagulant for the HLES than Al<sub>2</sub>(SO<sub>4</sub>)<sub>3</sub> and AlCl<sub>3</sub>.

In Table 2, the results of the usage of the new composite coagulant with a different mass ratio between PAC and AlCl<sub>3</sub> for removing the HLES and LCS from the model wastewater, depending on a temperature of the treatment, are shown.

According to the obtained results, an optimal composition of the new coagulant, characterised by the maximal efficiency of the HLES removal (92%) in the wide temperature interval, is a composition KHPAC<sub>50</sub>,

**Table 2.** HLES removal depend on KHPAC composition and temperature

Mass balance between PAC and AlCl <sub>3</sub>	Temperature, °C		
	13 °C	20 °C	40 °C
50% PAC+50% AlCl <sub>3</sub> (KHPAC <sub>50</sub> )	92	95	88
40% PAC+60% AlCl <sub>3</sub> (KHPAC <sub>40</sub> )	86	95	88
20% PAC+80% AlCl <sub>3</sub> (KHPAC <sub>20</sub> )	77	75	74
10% PAC+90% AlCl <sub>3</sub> (KHPAC <sub>10</sub> )	77	85	85
100% Al <sub>2</sub> (SO <sub>4</sub> ) <sub>3</sub>	60	81	81
100% AlCl <sub>3</sub>	62	81	80
100% PAC	80	80	82

in which 50% of the PAC content is replaced by  $\text{AlCl}_3$ . It is known that a low temperature has a negative effect on the efficacy of a coagulation process. The coagulation at lower temperatures requires a higher dosage and a bigger contact time for flocs sedimentation. However, from the data obtained,  $\text{KHPAC}_{50}$  is not particularly sensitive to temperature.

It is found that the removal efficiency of the HLES and LCS with the new coagulant depends on pH value, and the optimal pH range varies from 6.0 to 7.0 (Fig. 1).

In comparison with PAC, the new coagulant increases HLES and LCS removal on 12% and 14%, respectively, at pH 6.0. In the case of pH 7.0, the removal efficacy of these pollutants increases by 50% and 25%. Taking into account that the residual aluminium concentration has higher values in the wastewater at  $\text{pH} \geq 7$ , the optimal pH value for the usage of the new coagulant is 6.0.

The results of the model wastewater treatment with the new coagulant ( $\text{KHPAC}_{50}$ ) and the known KSPAC composite coagulant, composed from PAC and aluminium sulphate, at pH 6.0 and a temperature of  $14^\circ\text{C}$  are shown in Fig. 2.

According to the obtained results, the new coagulant demonstrates a higher degree of removal of the HLES and LCS from the model wastewater than the composite coagulant KSPAC. Besides, the treated wastewater after filtration is characterised by a lower concentration of the residual aluminium ions (Fig. 3).

The optimal KHPAC dosage varies from 75–125  $\text{mg L}^{-1}$ . The removal efficiency of the HLES, LCS, COD and colour is 91%, 65%, 47% and 90%, respectively.

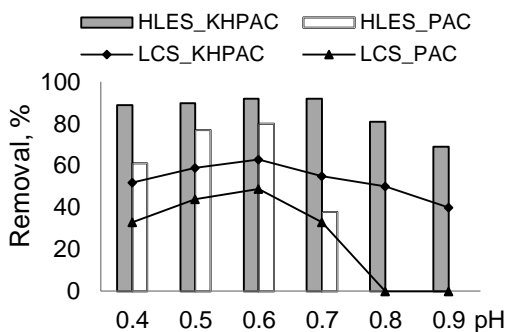


**Figure 1.** HLES and LCS removal with PAC and the new cogulant depending on pH.

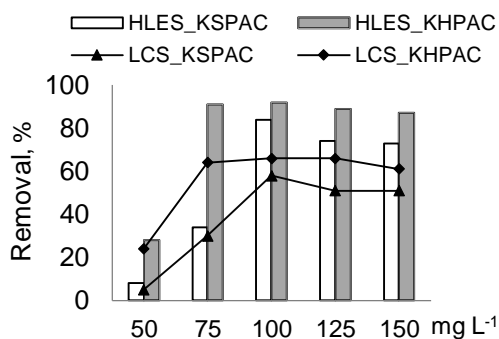


**Figure 2.** HLES and LSV removal in the model in the wastewater treated with the new and the known coagulant at temperature  $14^\circ\text{C}$  and pH 6.0.

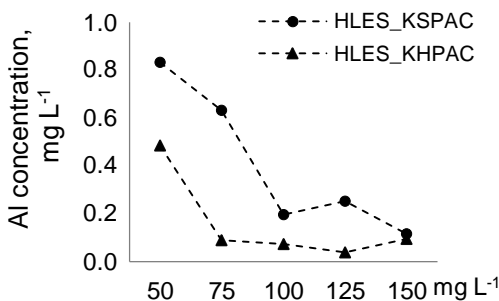


**Figure 3.** Residual aluminium concentration treated model wastewater at  $14^\circ\text{C}$  and pH 6.0.

The visual dynamic of the wood biomass settling during the coagulation/flocculation process can be seen in Fig. 4.

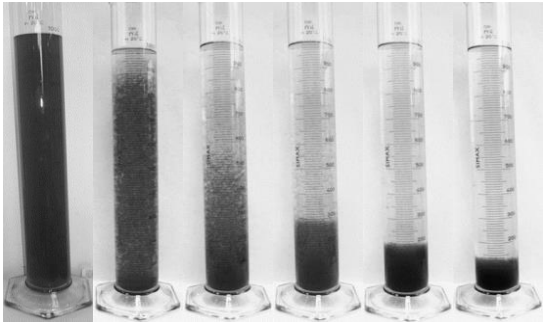


**Figure 4.** Formation of the wood-originated coagulate in the model wastewater treated with the new composite coagulant during 30 minutes.

### Characterisation of the wood-originated coagulate

According to the results obtained with the Laser Particle Sizer device, the air-dried coagulate sample was characterized by a size of particles between 2 to 246  $\mu\text{m}$ , but an average size was equal to 45.8  $\mu\text{m}$  (Fig. 5).

The precipitated coagulate was characterised by the elemental composition presented in Table 3. The obtained coagulate is composed primarily of carbon (27.9%) and oxygen (49.4%). The aluminum and sodium arising due to the presence of the composite coagulant in the flocs dominate among the inorganic elements in the elemental composition.

The chemical analysis of the coagulate, performed according to the developed procedures (Zakis & Neiberte, 2003). The coagulate contained 75% hemicelluloses, 14% lignin-containing substances and 11% extractives.

The previal content of hemicelluloses in the obtained coagulate are testified by FT-IR and  $^{13}\text{C}$ -NMR spectroscopy.

Following the FT-IR spectrum (Fig. 6, a), the presence of the intensive peak at  $1,567\text{ cm}^{-1}$  characterises  $\text{COO}^-$  skeletal vibrations in glucuronic acid. The characteristic wave number for typical xylan is  $1,046\text{ cm}^{-1}$ . The absorbance at  $849\text{ cm}^{-1}$  was attributed to  $\beta$ -glycosidic linkages between the sugars units. It can be assumed that the interaction between aluminum and HLES takes place via  $\text{HLES-OH}$  and  $\text{HLES-COOH}$  coordinate

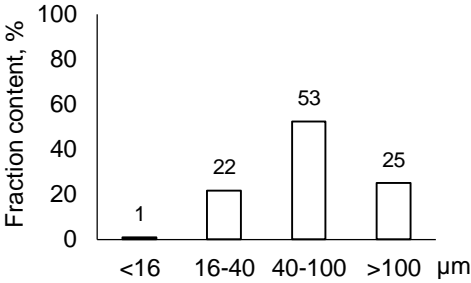


**Figure 5.** Wood-originated coagulate's granulometric composition.

**Table 3.** Wood-originated coagulate's elemental composition

C, %	O, %	H, %	N, %	Al, %	Na, %	Cl, %
27.9	49.4	4.3	0.3	10.9	4.1	3.1

bonds formation. This testifies the presence of the absorption band at  $619\text{ cm}^{-1}$  in the region, in which Al coordinate bonding appears.

The analysis of  $^{13}\text{C}$ -NMR spectrum (Fig. 6, b) of the coagulate shown that the main component of the sample was hemicelluloses (75–80%) in the form of O-acetyl-4-O-methyl-D-glucuron- $\beta$ -D-xylan with the presence of small amounts of  $\beta$ - (1-4) linked glucomannose.

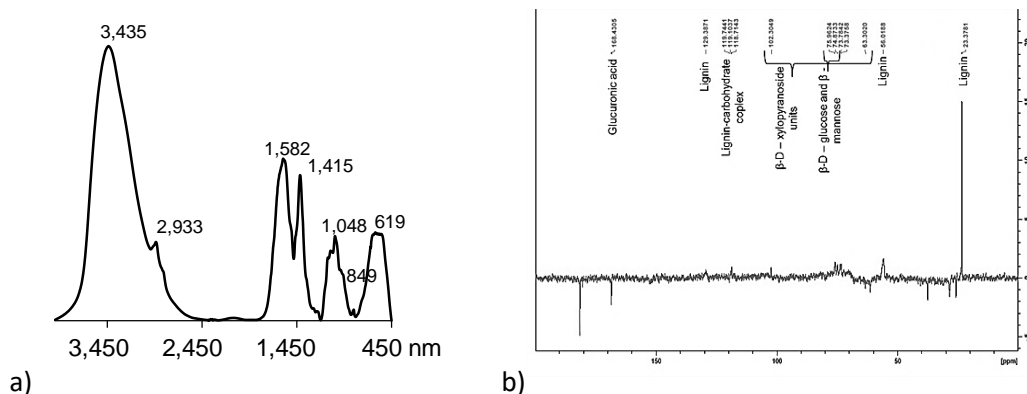


**Figure 6.** FT-IR (a) and  $^{13}\text{C}$ -NMR (b) spectra of the wood-originated coagulate's.

### Determination of water carrying capacity by modified clay samples

The clay modification leads to changing its fractional composition depending on the amount of the added coagulate. After adding 0.11% of the dry coagulate, the fraction content with grain diameter  $> 3\text{ mm}$  increased 6 times, but the fraction with grain size  $1.00 < d < 0.25\text{ mm}$  decreased by 5 times in comparison with control (the clay treated with pure water).

The further study was related to determination of water carrying capacity according to the methods described in the experimental part. The obtained results show (Fig. 7) that a better water carrying capacity of  $740\text{ mg H}_2\text{O per 1 g}$  of clay is found for the modified sample (LTM 011) granules with the sizes between 2.0 and 3.0 mm. This value is 35% higher than the capacity for the control LTM clay sample. The further increasing of the coagulate amount in the clay doesn't impact on water carrying capacity. This effect can be explained by the presence of the hydrophilic groups in the biomass coagulate.

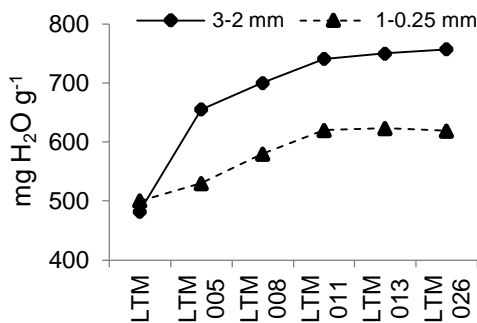


**Figure 7.** water carrying capacity of the control and modified clay samples depending on coagulate content.

### Determination of water (oil) binding capacity by modified clay samples

The LTM and LTM 011 samples were used for a study of their ability to adsorb water and oil depending on time. The obtained kinetic curves of water/oil sorption are presented in Fig. 8 and Fig. 9.

The water binding capacity of both the unmodified and the modified clay sample was conditioned by the presence of montmorillonite, characterised by the peculiar property of water molecule entry into crystal smectite lattice channels. It is seen (Fig. 8) that the water sorption is higher for the modified clay sample than for the control clay that could be explained by the presence of hydrophilic hemicelluloses fragments presented in the modified sample.

Based on the data obtained (Fig. 9, a, b), the oil binding capacity of the LTM control and LTM 011 sample is lower than their water sorption results. Evidently, both the hydrophilicity of clay and the enhanced oil viscosity could be a reason of the lower sorption values. At the same time, the rapeseed and silicone oil binding capacity of the modified sample is higher by 32% and 21%, respectively, compared to the LTM sample.

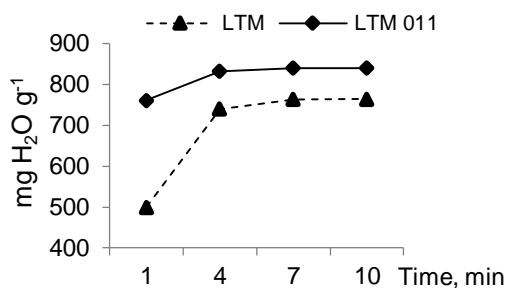


**Figure 8.** Water binding capacity of the control and modified clay samples depending on time.

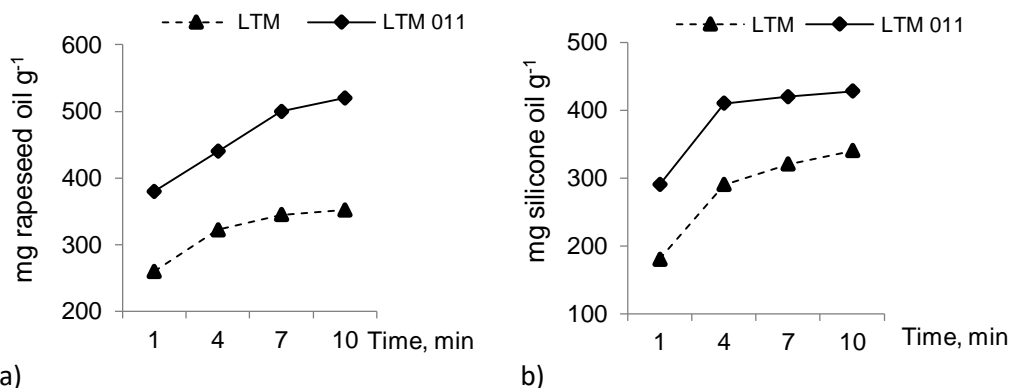


**Figure 9.** Rapeseed oil (a) and silicone oil (b) binding capacity of the control and modified clay samples depending on time.

To increase hydrophobicity of the clay samples, they were thermally treated at 800 °C. The oil binding capacity of the clay samples was studied for the LTM and the LTM 011 sample. It was found that 480 mg of silicone oil was absorbed by 1 gram of the LTM-800 sample, but for the sample LTM 011-800, this value was 640 mg per 1 gram. The sorption ability of rapeseed oil for the LTM and LTM 011-800 samples were 420 mg and 610 mg per 1 gram, respectively. The essential increase of the oil binding capacity for the LTM 011-800 sample was explained by its more hydrophobic

internal structure with higher pore sizes formed as a result of its thermal treatment compared with the structure of the thermally treated unmodified clay sample.

### Determination of heavy metal ion sorption

As the conducted experiment shown, the LTM 800 and LTM 011–800 clay samples have tendency for metal ions sorption. After a 24-hour study, the concentration of zinc ions from water solution was reduced from  $135 \text{ mg L}^{-1}$  to  $55 \text{ mg L}^{-1}$  and  $37 \text{ mg L}^{-1}$  in presence of the LTM–800 and LTM 011–800 samples, respectively. Thus, the sorption efficiency was 60% and 72% for the unmodified and modified clay samples, respectively. It was found that the LTM 011–800 sample was a more effective sorbent for zinc ions than the unmodified clay.

Fig. 10 shows Freundlich adsorption isotherms for zinc adsorption by LTM 800 and LTM 011–800 clay samples.

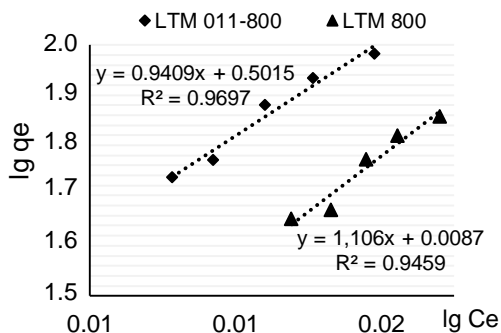


**Figure 10.** The Freundlich adsorption linear isotherm for  $\text{Zn}^{2+}$  ion adsorption by LTM 800 and LTM 011–800 clay samples.

Freundlich isotherm model parameters  $K_F$  and  $n$  for adsorbent LTM 011–800, calculated according to Eq. 4, are 3.17 for adsorption capacity and 1.06 for intensity of the adsorption. The correlation coefficient of Freundlich isotherm is 0.969 (Fig. 10). The present study results indicated that the Freundlich model fit the experimental data well. Freundlich isotherm model parameters  $K_F$  and  $n$  for adsorbent LTM 800 are 1.02 and 0.9 respectively. Larger value of  $n$  (smaller value of  $1/n$ ) implies a stronger interaction between the adsorbent and the adsorbate. If the value of  $n$  is between 1 and 10, it indicates a favorable adsorption. Therefore, it can be concluded that, for the adsorption of  $\text{Zn}^{2+}$ , the modified clay sample is more powerful.

The same tendency was observed for  $\text{Cu}^{2+}$ . In summary, the recovery of  $\text{Cu}^{2+}$  from water solution by LTM 011–800 was 10% higher in comparison with the LTM 800.

## CONCLUSIONS

The wood originated coagulate, obtained as a result of the treatment of the model solution with the new composite coagulant, was characterised by sizes of the particles and a chemical composition. The formed wood-originated coagulant was used as an additive for obtaining clay sorbents. The water carrying capacity of the modified clay increases by 35% in comparison with the unmodified sample. The sorption capacity of the modified clay for a rapeseed and silicone oil increases by 31% and 21%, respectively, relative to the unmodified clay. The heavy metals sorption capacity for the modified clay also increases by 10–12%. These results testified that the wood-originated sludge formed as a result of plywood wastewater treatment with the new developed coagulant can be used to obtain of environmentally friendly and inexpensive clay-based sorbents.

## REFERENCES

- Aziz, N., Effendy, N. & Basuki, K.T. 2017. Comparison of poly aluminium chloride (PAC) and aluminium sulphate coagulants efficiency in waste water treatment plant. *InovasiTeknik Kimia* **2**(1), 24–31.
- Ashrafi, O., Yerushalmi, L. & Haghighat, F. 2015. Wastewater treatment in the pulp-and-paper industry: A review of treatment processes and the associated greenhouse gas emission. *Journal of Environmental Management* **158**, 146–157.
- Barrera-Díaza, C., Martínez-Barrera, G., Gencel, O., Bernal-Martínez, L.A. & Brostow, W. 2011. Processed wastewater sludge for improvement of mechanical properties of concretes. *Journal of Hazardous Materials* **192**, 108–115.
- Brink, A., Sheridan, C. & Harding, K. 2018. Combined biological and advance oxidation processes for paper and pulp effluent treatment. *South African Journal of Chemical Engineering* **25**, 116–122.
- Brovkina, J., Shulga, G. & Ozolins, J. 2011. The Colloidal Stability of Wood Originated Pollutants in the Presence of Aluminium Salts. *Scientific Journal of Riga Technical University* **23**, 98–102.
- Brovkina, J., Skudra, S., Šakels, V., Shulga, G. & Ozolins, J. 2010. Choice of parameters for the model process simulating hydrothermal treatment of birch wood in veneer producing. *Scientific Journal of Riga Technical University Material Science and applied Chemistry* **22**, 140–143.
- Buyukkamaci, N. & Koken, E. 2010. Economic evaluation of alternative wastewater treatment plant options for pulp and paper industry. *Science of the Total Environment* **408**, 6070–6078.
- Carvalho, W.A., Vignado, C., Fontana, J. & Riboldi, M.B. 2007. The removal of heavy metal ions from aqueous effluents by modified clays: retention of Cd(II) and Ni(II) ions. *Adsorption Science & Technology* **25**(9), 673–692.
- Chanworrawoot, K. & Hunsom, M. 2012. Treatment of wastewater from pulp and paper mill industry by electrochemical methods in membrane reactor. *Journal of Environmental Management* **113**, 399–406.
- Chen, C., Mao, S., Wang, J., Bao, J., Xu, H., Su, W. & Dai, H. 2015. Application of ultrafiltration in a paper mill: Process water reuse and membrane fouling analysis. *Bioresources* **10**(2), 2376–2391.
- Doruk, N., CengizYatmaz, H. & Dizge, N. 2016. Degradation efficiency of textile and wood processing industry wastewater by photocatalytic process using in situ ultrafiltration membrane. *Clean soil air water* **44**(3), 219–324.
- Fang, P., Cen, C., Chen, D. & Tang, Z. 2010. Carbonaceous adsorbents prepared from sewage sludge and its application for HgO adsorption in simulated flue gas. *Chinese Journal of Chemical Engineering* **18**(2), 231–238.
- Frost Ray, C.O., Yunfei, X. & Kokot, S. 2007. Adsorption of hydrocarbons on organoclays – implications for oil spill remediation. *Journal of Colloid and Interface Science* **305**(1), 17–24.
- Ganjidoust, H., Tatsumi, K., Yamagishi, T. & Gholian, RN. 1997. Effect of synthetic and natural coagulant on lignin removal from pulp and paper wastewater. *Water Science and Technology* **35**, 291–296.
- Ho, Y.S., Chiang, C.C. & Hsu, Y.C. 2001. Sorption kinetics for dye removal from aqueous solution using activated clay. *Separation Science and Technology* **36**(11), 2473–2488.
- Hubbe, M.A., Metts, J.R., Hermosilla, D., Blanco, M.A., Yerushalmi, L., Haghighat, F., Lindholm-Lehto, P., Khodaparast, Z., Kamali, M. & Elliott, A. 2016. Wastewater Treatment and Reclamation: A Review of Pulp and Paper Industry Practices and Opportunities. *Bioresources* **11**(3), 7953–8091.

- Ismadji, S., Soetaredjo, F.E. & Ayucitra, A. 2015. Modification of Clay Minerals for Adsorption Purpose. *Clay Materials for Environmental Remediation*, pp. 39–56.
- Jemeljanova, M., Ozola, R. & Klavins, M. 2019. Physical-chemical properties and possible applications of clay minerals and humic acid composite materials. *Agronomy Research* **17**(S1), 1023–1032.
- Kamon, M., Inazumi, S. & Katsumi, T. 2002. Performance evaluations of landfill cover systems with sludge barriers. *Geotechnical Engineering* **33**(3), 113–132.
- Katrivesis, F.K., Karela, A.D., Papadakis, V.G. & Paraskeva, C.A. 2019. Revisiting of coagulation-flocculation processes in the production of potable water. *Journal of Water Process Engineering* **27**, 193–204.
- Kevin, M.C., Kenneth, C. & Dean, G. 2004. Floc morphology and cyclic shearing recovery: comparison of alum and polyaluminum chloride coagulant. *Water Research* **38**, 486–494.
- Khankhasaeva, S.T., Badmaeva, S.V., Dashinamzhilova, E.T., Bruzgalova L.V. & Ryazantsev A.A. 2006. Adsorption of Anionic Dyes on Montmorillonite Modified with Polyhydroxo Complexes of Aluminium and Iron. *Chemistry for Sustainable Development* **14**, 287–294.
- Kim, E.H., Cho, J.K. & Yim, S. 2005. Digested sewage sludge solidification by converter slag for landfill cover. *Chemosphere* **59**(3), 387–395.
- Kishimoto, N., Nakagawa, T., Okada, H. & Mizutani, H. 2010. Treatment of paper and pulp mill wastewater by ozonation combined with electrolysis. *Journal of Water and Environment Technology* **8**, 99–109.
- Klauson, D., Klein, K., Kivi, A., Kattel, E., Viisima, M., Dulova, N., Velling, S., Trapido, M. & Tenno, T. 2015. Combined methods for the treatment of a typical hardwood soaking basin wastewater from plywood industry. *International Journal of Environmental Science and Technology* **12**(11), 3575–3586.
- Kumar, P., Teng, T.T., Chand, S. & Wasewar, K.L. 2011. Treatment of paper and pulp mill effluent by coagulation. *International Journal of Chemical and Molecular Engineering* **3**(3), 222–227.
- Lakevics, V., Ruplis, A. & Berzina-Cimdina, L. 2011. Sorption Properties of Latvian Clays and Research of Innovative Applications of Clays. *Scientific Journal of Riga Technical University Material Science and Applied Chemistry* **24**, 20–25 (in Latvian).
- Lakhdar, A., Scelza, R., Scotti, R., Rao, M.A., Jedidi, N., Gianfreda, L. & Abdelly, C. 2010. The effect of compost and sewage sludge on soil biologic activities in salt affected soil. *Journal of Soil Science and Plant Nutrition* **10**(1), 40–47.
- Lazdina, D., Bardule, A., Lazdins, A. & Stola, J. 2011. Use of waste water sludge and wood ash as fertiliser for Salix cultivation in acid peat soils. *Agronomy Research* **9**(1–2), 305–314.
- Lee, C.S., Robinson, J. & Chong, M.F. 2014. A review on application of flocculants in wastewater treatment. *Process Safety and Environmental Protection* **92**(6), 489–508.
- Lee, S.J., Lee, Y.J. & Nam, S.H. 2008. Improvement in the coagulation performance by combining Al and Fe coagulants in water purification. *Korean Journal of Chemical Engineering* **25**(1), 505–512.
- Leiviska, T., Nurmesniemi, H., Poykio, R., Ramo, J., Kuokkanen, T. & Pellinen, J. 2008. Effect of biological wastewater treatment on the molecular weight distribution of soluble organic compounds and on the reduction of BOD, COD and P in pulp and paper mill effluent. *Water research* **42**, 3952–3960.
- Lin, D. & Weng, C. 2001. Use of sewage sludge ash as brick material. *Journal of Environmental Engineering* **127**(10), 922–928.
- Lucena, L.C.D.F.L., Juca, J.F., Soares, J.B. & Marinho, P.G.T. 2014. Use of wastewater sludge for base and sub-base of road pavements. *Transportation Research Part D: Transport and Environment* **33**, 210–219.
- Lukerchenko, V.N., Maslov, D.N., Shabalina, T.M. & Molchanov, V.A. 2008. Universal method for wastewater treatment. Patent RU 2007100306A (in Russian).



- Ma, P.D., Wang, L.A., Huang, C., Chen, M., Ren, Y.K. & Jiao, Y.J. 2007. Test on daily cover material of landfill site based on modified sludge from municipal sewage treatment plant. *China Water Wastewater* **23**, 38–41.
- Mtshali, J.S., Tiruneh, A.T. & Fadiran, A.O. 2014. Characterization of Sewage Sludge Generated from Wastewater Treatment Plants in Swaziland in Relation to Agricultural Uses. *Resources and Environment* **4**(4), 190–199.
- Olalekan, S.T., Qudsieh, I.Y. & Kabbashi, N.A. 2010. Effect of modification on the physicochemical and thermal properties of organophilic clay modified with octadecylamine. *International Journal of Engineering & Technology* **10**(1), 27–35.
- Omi, A., Laleh, Y. & Fariborz, H. 2015. Wastewater treatment in the pulp-and-paper industry: A review of treatment processes and the associated greenhouse gas emission. *Journal of Environmental Management* **158**, 146–157.
- Palone, H., Paloniemi, A., Taittonen, R. & Rousu, P. 2011. Method for the removal of lignin from water, Patent RU 2408543C2, (in Russian).
- Rio, S., Coq, L.L., Faur, C. & Cloirec, P.L. 2006. Production of porous carbonaceous adsorbent from physical activation of sewage sludge: application to wastewater treatment. *Water Science & Technology* **53**(3), 234–244.
- Seiple, T.E., Coleman, A.M. & Skaggs, R.L. 2017. Municipal wastewater sludge as a sustainable bioresource in the United States. *Journal of Environmental Management* **197**, 673–680.
- Sharma, B.R., Dhuldhoya, N.C. & Merchant, U.C. 2006. Flocculants – an ecofriendly approach. *Journal of Polymers and the Environment* **14**, 195–202.
- Shishkin, A.J. 2004. Method for purifying wastewaters from suspended substances. Patent RU 2234464C1, (in Russian).
- Shulga, G., Brovkina, J., Neiberte, B., Ozoliņš, J. & Neilands, R. 2014. A method for wastewater treating from lignin and hemicellulose substances at wood processing plants. Patent LV 14789 B, (in Latvian).
- Smith, K.M., Fowler, G.D., Pullket, S. & Graham, N.J. 2009. Sewage sludge-based adsorbents: A review of their production, properties and use in water treatment applications. *Water Research* **43**, 2569–2594.
- Toczyłowska-Mamińska, R. 2017. Limits and perspectives of pulp and paper industry wastewater treatment – A review. *Renewable and Sustainable Energy Reviews* **78**, 764–772.
- Unuabonah, E.I., Adewuyi, A., Kolawole, M.O., Omorogie, M.O., Olatunde, O.C., Fayemi, S.O., Günter, C., Okoli, C.P., Agunbiade, F.O. & Taubert, A. 2017. Disinfection of water with new chitosan-modified hybrid clay composite adsorbent. *Heliyon* **3**(8), e00379.
- Viraraghan, P.D. 2004. Treatment of pulp and paper mill wastewater – a review. *Science of the Total Environment* **333**, 37–58.
- Zāķis, G. & Neiberte, B. 2003. *Basic of wood chemistry*. Riga, 63 pp. (in Latvian).
- Zhou, L.Q., Wu, C.L. & Wu, J.J. 2011. Study of modified sludge as landfill cover soil. *Chinese Journal of Chemical Engineering* **5**(12), 2864–2868.

## **Theoretical study on motion of potato tuber on surface of separator**

V. Bulgakov<sup>1</sup>, S. Nikolaenko<sup>1</sup>, Z. Ruzhylo<sup>1</sup>, I. Fedosiy<sup>1</sup>, J. Nowak<sup>2</sup> and J. Olt<sup>3,\*</sup>

<sup>1</sup>National University of Life and Environmental Sciences of Ukraine, 15 Heroyiv Oborony Str., Kyiv, UA03041, Ukraine

<sup>2</sup>University of Life Sciences in Lublin, 13 Akademicka Str., 20-950 Lublin, Poland

<sup>3</sup>Estonian University of Life Sciences, Institute of Technology, 56 F.R. Kreutzwaldi Str., EE51006 Tartu, Estonia

\*Correspondence: [jyri.olt@emu.ee](mailto:jyri.olt@emu.ee)

**Abstract.** The aim of the study was to determine the optimal design and kinematic parameters of the separator that cleans potatoes from impurities and has a design of the spiral type. The authors have devised a highly efficient design of the spiral type potato heap separator, in which the motion of the potato tubers takes place in the channel formed by two spiral members made in the form of cylindrical spiral springs. In order to substantiate the optimal kinematic and design parameters of the new spiral type potato heap separator, the authors have generated a mathematical model of the motion of a single potato tuber on the cleaning surface formed by two spirals. As a result of solving the obtained analytical expressions, the graphical relations between the parameters of the investigated process of the motion of a single potato tuber body situated between two adjacent spirals have been plotted, which has enabled selecting the optimal design and kinematic parameters of the spiral separator. It has been established in the completed investigation that the angular velocity of rotation of the cleaning rolls has to be within the range of 27–40 rad s<sup>-1</sup> in order to ensure the efficient transportation and cleaning of the potato tuber with a diameter of 50 mm that moves on the surface of the spiral with a radius of 75 mm wound from the round bar with a diameter of 15 mm, in case the spirals are mounted with an eccentricity of 10 mm. By analysing the kinematics of motion of the potato tuber on the surface of the spiral type cleaning machine, in case the tuber contacts the spirals at two points, it has been established that the increase of the angular velocity of rotation of the spirals results in the respective growth of the transportation capacity of the cleaning tool, while the separating efficiency at the same time becomes reduced to some extent.

**Key words:** cleaning, impurity, potato, quality, separator efficiency, spiral, transportation.

### **INTRODUCTION**

In the process of harvesting potatoes, their cleaning from soil and plant impurities is a highly important problem, in view of the fact that the mechanical harvesting results in the removal of fertile soil from the fields together with the harvested potatoes.

This phenomenon is caused by the situation, where the harvesting of potatoes with the use of lifting tools involves undercutting and lifting tubers together with considerable volumes of soil bed, in which the potato tubers themselves can hold as little as 10%. As

the moisture content in the soil in the harvesting period reaches sometimes 20%, it becomes a great hindrance to the efficient separation of soil from the potato tubers. Hence, the search for new engineering solutions aimed at the improvement of the potato heap cleaning at the stage of harvesting is a topical research and technology task.

In order to improve substantially the performance indices of the lifting and separating tools of potato harvesters, in particular, to improve the efficiency of separating the potato heap lifted from soil, the authors have developed a new design of the spiral potato heap separator (Fig. 1).

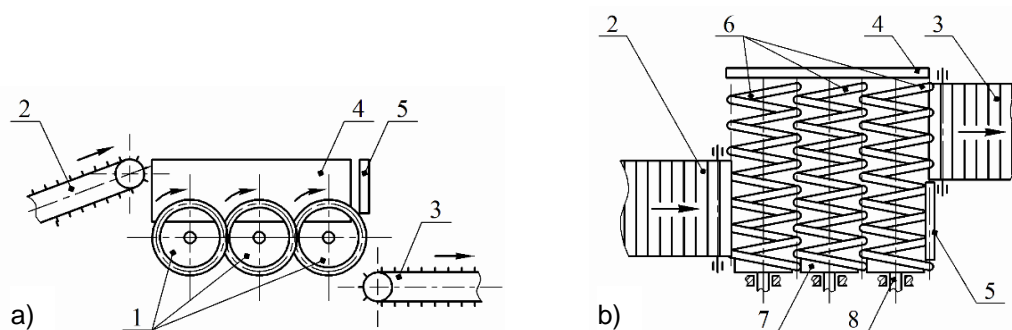


**Figure 1.** Structural layout of spiral potato heap separator: a – side view, b – top view; 1 – spirals; 2 – feeding conveyor; 3 – discharge conveyor; 4 – side protective apron; 5 – face protective apron; 7 – hub; 8 – drive shaft (Bulgakov et al., 2019).

The spiral potato heap separator comprises the three sequentially placed spirals 1, which form an even cleaning surface on top of them. The spirals 1 are installed as cantilevers in such a way that their first ends are fixed in the hubs 7 connected with the drive shafts 8, and their second ends overhang freely. At the same time, the spirals 1 are positioned with overlapping and the drive shafts 8 provide for their rotation at the same angular velocities and in the same sense. The feeding conveyor 2 leads to one of the sides of the above-mentioned cleaning surface, the discharge conveyor 3 starts at the opposite side. The side areas around the spirals 1 are covered with protective side apron 4 and face protective apron 5.

The spiral potato heap separator under consideration operates as follows. The feeding conveyor 4 continuously feeds the tuber-bearing bed lifted from the soil onto the cleaning surface formed by the three spirals 1. As a result of its fall from the small height, the soil bed with potato tubers disintegrates partially and spreads initially over the closest spiral 1, then proceeds to the other spirals 1. Since the spirals 1 are connected via the hubs 7 with the drive shafts 8, they rotate and entrain with their turns potato tuber bodies and soil clods and start transporting them both along the spirals' axes and along their radii. However, due to the large gaps (between the turns of each spiral 1 and spaces between the spirals 1), the smaller soil particles immediately sieve in considerable amounts down and outside of the separator.

The spiral potato heap separator comprises the several consecutively positioned power driven cleaning spiral rolls 1, which are designed as cantilever suspended spiral springs and form the cleaning surface, the feeding conveyor 2 positioned on the one side of it and the discharge conveyor 3 positioned on the other side. In order to prevent the

loss of potato tuber bodies, the flat guard shield 4 is installed on the side of the free ends of the cantilevered spiral rolls 1, the flat guard shield 5 is installed beside the discharge conveyor 3. Each cleaning roll 1, that is, each spiral spring 6 is installed on the hub 7 connected with the drive shaft 8. The rotation of all the three spiral cleaning springs 6 actuated by the drive shafts 8 has the same sense, that is, in the direction towards the discharge conveyor 3.

In the proposed potato heap cleaning machine with power-driven cantilever spiral springs, there are openings with a significant area formed by the spaces between the own turns of the spirals and the spaces between the windings of adjacent spirals (Bulgakov et al., 2018a, 2018b, 2018c; 2019; Nowak et al., 2019). Due to that, the effective separation area (that is, the total area of all separating openings), in comparison with the total surface area, is significantly increased. Consequently, the machine's throughput capacity in the sieving of soil and plant impurities downwards, i.e. outside the separator, is also increased, which results in the improved quality indices of its operation.

Moreover, the absence of any shaft inside each cleaning spiral spring facilitates the unobstructed passage of all impurities downwards and also allows to avoid the undesirable wrapping of plant debris. The hollowness of the internal space in each spiral spring provides for a significant increase in the capacity of positively transporting the whole mass of soil and plant impurities that has entered the spring towards the outlet (cantilever) end of each spiral spring and dropping it through the free end face onto the surface of the field.

In order to prevent the soil caking on each separating roll and avoid the complete choking of the gaps between the spiral windings with wet soil, the rolls are installed with certain overlapping, that is, the turns of each roll partially enter the spaces between the turns of the adjacent roll.

The systems of cleaning tools used in potato combines and harvesters not always provide for a high level of the soil impurity separation (Petrov, 1984). The reduced quality of cleaning results most frequently from the heavy caking of wet soil on the surfaces of the cleaning tools. The engineering solutions based on the more active handling of the potato heap in the soil separation process have the increased level of tuber damage, which is an undesirable factor in view of the deteriorated consumer and storage qualities of the produced potatoes.

Therefore, the potato heap cleaning units not only have to deliver the reliable and high quality performance of the work process, but they also must clean themselves in the process of their operation. Obviously, the potato tuber damage has to be at the minimum level, if possible.

The problem of developing efficient and reliable potato heap cleaning units for the lifting stage as well as potato cleaning and grading machines for stationary potato-grading plants has been discussed in many papers (Petrov, 1984; Feller et al., 1987; Misener & McLeod, 1989; Bishop et al., 2012; Ichiki et al., 2012; Guo & Campanella, 2017; Wang et al., 2017; Wei et al., 2017; Ye et al., 2017). However, despite the great variety of potato heap cleaning work processes used in the harvesting, the studies on the optimisation of the parameters and modes of operation of spiral separators that have been carried out by now are relatively few (Holland-Batt, 1989; Krause & Minkin, 2005).

The aim of the study was to determine the rational design and kinematic parameters for the spiral type unit that cleans potatoes from impurities.

## MATERIALS AND METHODS

The movement of a potato tuber on the surface of the cleaning spiral spring takes place due to the pressure of the mass behind it, which is continuously fed to the cleaning unit. In order to ensure the uninterrupted progress of the separation process and avoid jamming, the bed of potato tubers along the length of the spiral tool has to have a thickness of one tuber.

The background experimental and theoretical research into the motion of a body on the surface of the spiral potato heap cleaning unit carried out by the authors suggests that, in order to describe the interaction between the body and the working surface of the cleaning spiral, it is necessary to analyse the relative motion of the single potato tuber as a solid body, which is approximated by the body that has a shape close to spherical (Peters, 1997). The equivalent schematic model devised by the authors (Fig. 2) features the said body situated on the surface of the spiral cleaning spring with a radius of  $R$  and an angle of helix of  $\gamma$ . The body has its own radius of  $R_K$ . It is assumed that to a first approximation the initial velocity of the body under consideration, that is, the initial velocity of the potato tuber, when it arrives onto the surface of the spiral cleaning spring in the machine for cleaning the potato heap from impurities, is equal to zero.

At the same time, the body (potato tuber) is under the action of the following forces shown in the equivalent schematic model:

$G = mg$  – force of gravity of the potato tuber with a mass of  $m$ , which rotates together with the moving system of coordinates at an angular velocity of  $\omega$ ;

$\bar{N}$  – force of normal reaction of the surface of the spiral coil directed normally to the path of the spiral relative motion of the body;

$\bar{F} = fN$  – force of the sliding friction between the body and the surface of the spiral coil directed opposite to the direction of the relative motion of the body, where  $f$  – coefficient of sliding friction of the body on the material of the spiral coil. For potato tubers, it can be assumed (in case of metal spiral surface) that  $f = 0.2\text{--}0.3$  (Bulgakov et al., 2018a);

$\bar{P}_n^e$  – centrifugal force of inertia directed normally to the motion path, its magnitude being equal to

$$\bar{P}_n^e = m\omega^2\rho,$$

where  $\rho$  – radial parameter of the position of the centre of gravity of the body with respect to the spiral's longitudinal axis;  $\bar{P}_u^k$  – Coriolis force directed normally to the relative motion path, i.e. opposite to the direction of the Coriolis acceleration vector, its magnitude being equal to:

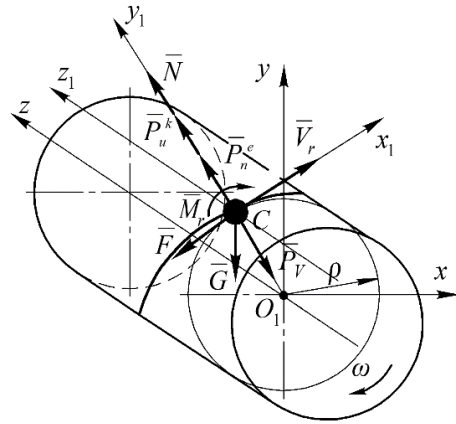


**Figure 2.** Equivalent schematic model of motion of potato tuber on surface of spiral cleaning spring.

$$P_u^k = 2m \cdot \omega \cdot V \sin\left(\omega, \hat{\bar{V}}\right);$$

$\bar{P}_V$  – force of pressure applied by the potato heap fed onto the spiral separator;  
 $\bar{M}_r$  – moment of rolling friction force, the magnitude of which is found with the use of the formula:

$$M_r = \delta N,$$

where  $\delta = R_K \cdot \tan \mu$  – coefficient of rolling friction,  $\mu$  – rolling friction angle.

## MATHEMATICAL MODELLING

The equivalent schematic model (Fig. 2) features two frames of reference. It is, first of all, the fixed system of coordinates  $xO_1yz$ , the  $O_1z$  axis of which coincides with the longitudinal axis of the spiral, while the  $O_1x$  axis is directed towards the adjacent spiral, the same as the motion of the potato tuber. Also, it includes the moving system of coordinates  $x_1Cy_1z_1$ , the origin of which (point  $C_1$ ) coincides with the centre of gravity of the potato tuber.

Using the above-said and basing on Newton's second law, the differential equation of motion of the body (potato tuber) on the surface of the cleaning spiral spring can be generated (Grote & Antonsson, 2008).

The equation of motion of the potato tuber on the surface of the spiral in the vector notation appears as follows:

$$m\bar{a} = \bar{G} + \bar{N} + \bar{F} + \bar{P}_n^e + \bar{P}_u^k + \bar{P}_v, \quad (1)$$

where  $\bar{a}$  – acceleration of the centre of the potato tuber moving on the surface of the cleaning spiral spring.

The motion of the centre of the potato tuber in the  $O_1xyz$  coordinate system can be represented by the projections of the vector equation (1) on the respective coordinate axes. They appear as follows:

$$\left. \begin{aligned} m\ddot{x} &= -\left(P_n^e + N + P_u^k - P_v\right) \cdot \cos\left(x, \hat{\bar{n}}\right) - F \cos\left(\dot{x}, \hat{\bar{V}}\right), \\ m\ddot{y} &= \left(P_n^e + N + P_u^k - P_v\right) \cdot \cos\left(y, \hat{\bar{n}}\right) - F \cos\left(\dot{y}, \hat{\bar{V}}\right) - G. \end{aligned} \right\} \quad (2)$$

Further, the differential equation of the potato tuber rotation about its centreline has to be written down:

$$I\ddot{\theta} = M_r - F \cdot R_K, \quad (3)$$

where  $I$  – moment of inertia of the potato tuber body with respect to the central axis.

For a spherical body:  $I = \frac{2}{5}m \cdot R_K^2$  (Grote & Antonsson, 2008);  $\ddot{\theta}$  – angular acceleration of the rotary motion of the potato tuber;  $\cos\left(x, \hat{\bar{n}}\right)$  and  $\cos\left(y, \hat{\bar{n}}\right)$  – direction cosines, which are defined in accordance with (Petrov, 1984) by the following expressions:

$$\cos\left(x, \hat{\bar{n}}\right) = \frac{\frac{\partial p}{\partial x}}{\Delta p}, \quad \cos\left(y, \hat{\bar{n}}\right) = \frac{\frac{\partial p}{\partial y}}{\Delta p}, \quad (4)$$

where  $\Delta p = \sqrt{\left(\frac{\partial p}{\partial x}\right)^2 + \left(\frac{\partial p}{\partial y}\right)^2 + \left(\frac{\partial p}{\partial z}\right)^2}$  – modulus of the gradient of the function  $p(x, y, z)$ ;

$p = p(x, y, z)$  – equation of constraint corresponding to the equation of the surface of the spiral winding. For a cylindrical spiral with an outside diameter of  $2R$  wound from a round bar with a radius of  $r$  with a winding pitch of  $S$ , the equation of the unit gradient function (accordingly, the equation of constraint) appears as follows (Vasilenko, 1996):

$$p = \frac{S^2}{4\pi^2} \cdot \left| \frac{x \cdot \sin \frac{2\pi \cdot z}{S} - y \cdot \cos \frac{2\pi \cdot z}{S}}{\sqrt{x^2 + y^2}} \right| \cdot \cos \left( \frac{S}{2\pi \sqrt{x^2 + y^2}} \right) + \left( \sqrt{x^2 + y^2} - R \right)^2 - r^2 = 0. \quad (5)$$

After differentiating the equation of constraint and substituting into it the respective expressions from the kinematic analysis, the following values of the direction cosines are obtained:

$$\cos \left( \hat{x}, \hat{n} \right) = \frac{\frac{1}{4} \cdot \frac{S^2}{\pi^2} \cdot \frac{\sin \psi}{R + \varepsilon} \cdot \cos \left[ \frac{1}{2} \cdot \frac{S}{\pi \cdot (R + \varepsilon)} \right] + 2\varepsilon \cdot \cos \psi}{\sqrt{\frac{1}{4} \cdot \frac{S^2}{\pi^2} \cos^2 \left( \frac{1}{2} \cdot \frac{S}{\pi (R + \varepsilon)} \right) \cdot \left[ \frac{S^2}{4\pi^2 (R + \varepsilon)^2} + 1 \right] + 4\varepsilon^2}}, \quad (6)$$

$$\cos \left( \hat{y}, \hat{n} \right) = - \frac{\frac{1}{4} \cdot \frac{S^2}{\pi^2} \cdot \frac{\cos \psi}{R + \varepsilon} \cdot \cos \left[ \frac{1}{2} \cdot \frac{S}{\pi \cdot (R + \varepsilon)} \right] + 2\varepsilon \cdot \sin \psi}{\sqrt{\frac{1}{4} \cdot \frac{S^2}{\pi^2} \cos^2 \left( \frac{1}{2} \cdot \frac{S}{\pi (R + \varepsilon)} \right) \cdot \left[ \frac{S^2}{4\pi^2 (R + \varepsilon)^2} + 1 \right] + 4\varepsilon^2}}.$$

Here, the angular parameter represented by an angle of  $\psi$ , which defines the position of the spherical potato tuber body on the two turns of the cleaning spiral, depends on the geometrical parameters of the said spiral and varies as a function of the radial parameter  $\rho$  that represents the position of the potato tuber with respect to its own centreline, the spiral radius  $R$  and the spiral winding parameter  $\gamma$ . However, this angular parameter is exactly the factor that determines the motion of the potato tuber entrained by the spiral turns over the surface of the cleaning unit.

The direction cosines  $\cos \left( \hat{x}, \hat{V} \right)$  and  $\cos \left( \hat{y}, \hat{V} \right)$  can be found with the use of the following expressions:

$$\cos \left( \hat{x}, \hat{V} \right) = \frac{\dot{x}}{V} = \frac{\dot{x}}{\sqrt{\dot{x}^2 + \dot{y}^2 + \dot{z}^2}}, \quad \cos \left( \hat{y}, \hat{V} \right) = \frac{\dot{y}}{V} = \frac{\dot{y}}{\sqrt{\dot{x}^2 + \dot{y}^2 + \dot{z}^2}}. \quad (7)$$

After substituting the obtained values of all the components (4)–(7) into the differential Eqs (2) and (3), the system of differential equations representing the motion of the potato tuber on the spiral spring of the potato heap cleaning unit is obtained. It appears as follows:

$$\left. \begin{aligned}
m\ddot{x} = & - \left( m \cdot \omega^2 \cdot \rho + N + 2m \cdot \omega \cdot V \sin \left( \omega, \bar{V} \right) - P_v \right) \times \\
& \times \frac{\frac{1}{4} \cdot \frac{S^2}{\pi^2} \cdot \frac{\sin \psi}{(R + \varepsilon)} \cdot \cos \left[ \frac{1}{2} \cdot \frac{S}{\pi \cdot (R + \varepsilon)} \right] + 2\varepsilon \cdot \cos \psi}{\sqrt{\frac{1}{4} \cdot \frac{S^2}{\pi^2} \cos^2 \left( \frac{1}{2} \cdot \frac{S}{\pi (R + \varepsilon)} \right) \cdot \left[ \frac{S^2}{4\pi^2 (R + \varepsilon)^2} + 1 \right] + 4\varepsilon^2}} - \\
& - fN \frac{\dot{x}}{\sqrt{\dot{x}^2 + \dot{y}^2 + \dot{z}^2}}, \\
m\ddot{y} = & - \left( m \cdot \omega^2 \cdot \rho + N + 2m \cdot \omega \cdot V \sin \left( \omega, \bar{V} \right) - P_v \right) \times \\
& \times \frac{\frac{1}{4} \cdot \frac{S^2}{\pi^2} \cdot \frac{\cos \psi}{(R + \varepsilon)} \cdot \cos \left[ \frac{1}{2} \cdot \frac{S}{\pi \cdot (R + \varepsilon)} \right] + 2\varepsilon \cdot \sin \psi}{\sqrt{\frac{1}{4} \cdot \frac{S^2}{\pi^2} \cos^2 \left( \frac{1}{2} \cdot \frac{S}{\pi (R + \varepsilon)} \right) \cdot \left[ \frac{S^2}{4\pi^2 (R + \varepsilon)^2} + 1 \right] + 4\varepsilon^2}} - \\
& - fN \frac{\dot{y}}{\sqrt{\dot{x}^2 + \dot{y}^2 + \dot{z}^2}} - G, \\
I \cdot \ddot{\theta} = & N \cdot R_K \cdot \tan \mu - fN \cdot R_K.
\end{aligned} \right\} \quad (8)$$

At the same time:

$$\sin \left( \omega, \bar{V} \right) = \sin(90^\circ - \gamma) = \cos \gamma, \quad (9)$$

When the motion state becomes steady, all points of the potato tuber (in particular, the points of contact between the tuber and the surface of the spiral spring) retain the constant value of their motion velocity. That means that it is reasonable to substitute  $\ddot{x} = 0$  and  $\ddot{y} = 0$  into the equations of the system (8).

After that, it is possible to derive from the first two equations of the system of Eqs (8) the normal reaction of the surface. Following the appropriate transformations, the result is:

$$N = - \frac{mg \sqrt{\dot{x}^2 + \dot{y}^2 + \dot{z}^2}}{f \cdot \dot{x}} \cdot \left[ \frac{\frac{1}{4} \cdot \frac{S^2}{\pi^2} \cdot \frac{\sin \psi}{(R + \varepsilon)} \cdot \cos \left[ \frac{1}{2} \cdot \frac{S}{\pi \cdot (R + \varepsilon)} \right] + 2\varepsilon \cdot \cos \psi}{\frac{1}{4} \cdot \frac{S^2}{\pi^2} \cdot \frac{\cos \psi}{(R + \varepsilon)} \cdot \cos \left[ \frac{1}{2} \cdot \frac{S}{\pi \cdot (R + \varepsilon)} \right] + 2\varepsilon \cdot \sin \psi} \right] \quad (10)$$

The obtained value of the normal reaction of the surface  $N$  has to be substituted into the third equation of the system (8), then, after certain mathematical transformations are carried out, the following formula is obtained for the angular acceleration of the potato tuber about its centreline:



$$\ddot{\theta} = \frac{2.5(R_K \cdot \tan \mu - f \cdot \rho) g \cdot \sqrt{(R + \varepsilon)^2 + \frac{S^2}{4\pi^2}}}{R_K^2(R + \varepsilon) \cdot f \left[ \frac{-\frac{1}{4} \cdot \frac{S^2}{\pi^2} \cdot \frac{\cos \psi}{(R + \varepsilon)} \cdot \cos \left[ \frac{1}{2} \cdot \frac{S}{\pi \cdot (R + \varepsilon)} \right] + 2\varepsilon \cdot \sin \psi}{\frac{1}{4} \cdot \frac{S^2}{\pi^2} \cdot \frac{\sin \psi}{(R + \varepsilon)} \cdot \cos \left[ \frac{1}{2} \cdot \frac{S}{\pi \cdot (R + \varepsilon)} \right] + 2\varepsilon \cdot \cos \psi} - \cos \psi \right]} \quad (11)$$

at  $\psi = \omega \cdot t$ .

After integrating the expression (11) on time, the angular velocity  $\dot{\theta}$  of the potato tuber's rotation about its centreline during its motion on the surface of the spiral spring in the potato heap cleaning unit is obtained and it appears as follows:

$$\dot{\theta} = \int \frac{2.5(R_K \cdot \tan \mu - f \cdot \rho) g \cdot \sqrt{(R + \varepsilon)^2 + \frac{S^2}{4\pi^2}}}{R_K^2(R + \varepsilon) \cdot f \left[ \frac{-\frac{1}{4} \cdot \frac{S^2}{\pi^2} \cdot \frac{\cos \psi}{(R + \varepsilon)} \cdot \cos \left[ \frac{1}{2} \cdot \frac{S}{\pi \cdot (R + \varepsilon)} \right] + 2\varepsilon \cdot \sin \psi}{\frac{1}{4} \cdot \frac{S^2}{\pi^2} \cdot \frac{\sin \psi}{(R + \varepsilon)} \cdot \cos \left[ \frac{1}{2} \cdot \frac{S}{\pi \cdot (R + \varepsilon)} \right] + 2\varepsilon \cdot \cos \psi} - \cos \psi \right]} dt \quad (12)$$

## RESULTS AND DISCUSSION

In view of the complexity of integrating the above expression, the integration has been done graphically with the use of the PC. In these calculations, the authors have used as the input data the dimensions of a single potato tuber (mean value of the radius) as well as the design parameters of the spiral cleaning unit designed by the authors and subjected to field testing and experimental investigations (Fig. 3). For example, the radius of the potato tuber is assumed to be equal to  $R_K = 25$  mm, the radius of the spiral –  $R = 75$  mm, the spiral winding pitch –  $S = 30$  mm, the spirals are mounted with an eccentricity of  $\varepsilon = 10$  mm, the radial parameter of the potato tuber's position relative to its centreline is assumed at  $\rho = 120$  mm, the coefficient of sliding friction –  $f = 0.55$ , rolling friction angle –  $\mu = 17$  deg (or 0.297 rad). Thus, in the PC-assisted numerical calculations the authors have used the parameters of the spiral-type potato cleaning unit for removal of impurities designed by the authors, which is shown in Fig. 3.

By carrying out PC-assisted calculations with the use of the specially developed programme as well as the assumed values, the diagrams have been plotted for the variation of the angular velocity of rotation  $\dot{\theta}$  of the potato tuber, when the angular coordinate  $\psi$  varies from 0 to 1 rad at the spirals' angular velocities of  $\omega = 10, 20, 30, 40, 50$  rad s<sup>-1</sup>. As is proved by the obtained graphs (Fig. 4), when the angular velocity  $\omega$  of the cleaning spiral increases, the angular velocity  $\dot{\theta}$  of the potato tuber's rotation about its centreline decreases, coming close to zero, that is, the motion of the body without rolling is observed.

It is quite evident that increasing the angular velocity  $\dot{\theta}$  of the potato tuber's rotation about its centreline provides the conditions for the improvement of the quality of cleaning its surface from the stuck soil.

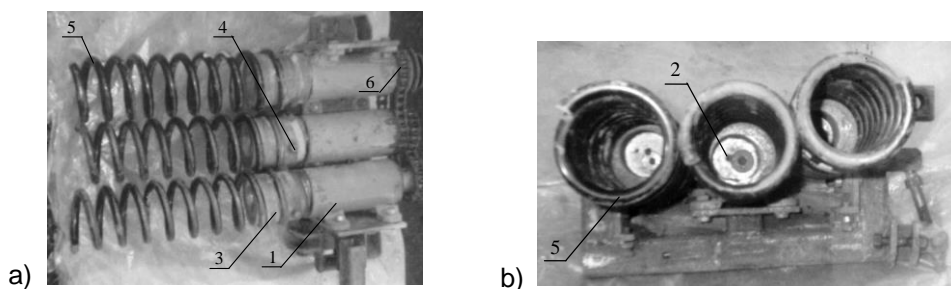


**Figure 3.** Spiral-type potato cleaning unit of authors' design (a – top view; b – side view): 1 – bearing assembly for mounting spirals; 2 – hub; 3 – holder; 4 – fastening bolt; 5 – spiral spring; 6 – chain drive.

The next step is to determine the effect that certain design parameters of the spiral separator have, by means of analysing the graphs of variation of the angular velocity of motion of the tuber, when the angular coordinate varies from 0 to 1 rad, the angular velocity of the spirals is equal to  $40 \text{ rad s}^{-1}$  and the parameters under consideration have the following different values (one parameter changes, all other remain constant, the same as in the previous case):

- 1)  $R = 75 \text{ mm}$ ,  $\varepsilon = 10 \text{ mm}$ ,  $S = 35 \text{ mm}$ ; 2)  $R = 100 \text{ mm}$ ,  $\varepsilon = 10 \text{ mm}$ ,  $S = 35 \text{ mm}$ ;
- 3)  $R = 75 \text{ mm}$ ,  $\varepsilon = 15 \text{ mm}$ ,  $S = 35 \text{ mm}$ ; 4)  $R = 75 \text{ mm}$ ,  $\varepsilon = 10 \text{ mm}$ ,  $S = 45 \text{ mm}$ .

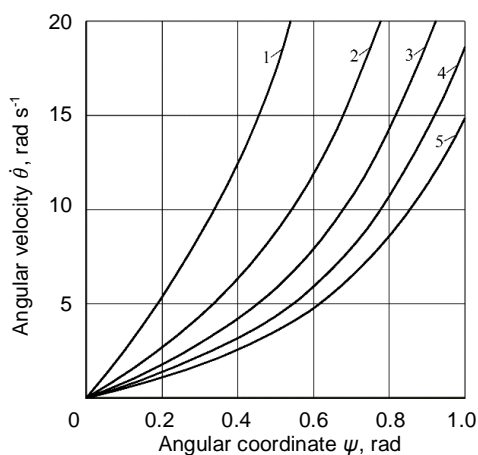


**Figure 4.** Relation between angular velocity  $\dot{\theta}$  of rotation of potato tuber and angular coordinate  $\psi$  at different angular velocities  $\omega$  of cleaning spiral spring:

- 1)  $\omega = 10 \text{ rad s}^{-1}$ ; 2)  $\omega = 20 \text{ rad s}^{-1}$ ;
- 3)  $\omega = 30 \text{ rad s}^{-1}$ ; 4)  $\omega = 40 \text{ rad s}^{-1}$ ;
- 5)  $\omega = 50 \text{ rad s}^{-1}$ .

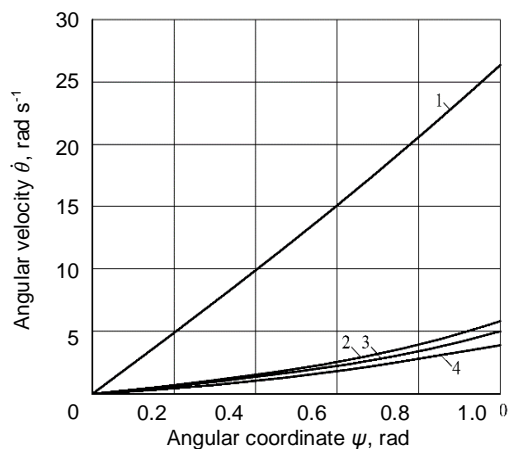


**Figure 5.** Relation between angular velocity  $\dot{\theta}$  of rotation of potato tuber and angular coordinate  $\psi$ , when angular velocity  $\omega$  of cleaning spiral spring is set at  $40 \text{ rad s}^{-1}$ :

- 1)  $R = 75 \text{ mm}$ ,  $\varepsilon = 10 \text{ mm}$ ,  $S = 35 \text{ mm}$ ;
- 2)  $R = 100 \text{ mm}$ ,  $\varepsilon = 10 \text{ mm}$ ,  $S = 35 \text{ mm}$ ;
- 3)  $R = 75 \text{ mm}$ ,  $\varepsilon = 15 \text{ mm}$ ,  $S = 35 \text{ mm}$ ;
- 4)  $R = 75 \text{ mm}$ ,  $\varepsilon = 10 \text{ mm}$ ,  $S = 45 \text{ mm}$ .

The obtained diagrams (Fig. 5) show the effect that the radius of the spiral (curve 2), the eccentricity in the mounting of the spirals (curve 3) and the winding pitch (curve 4) have on the angular velocity of the potato tuber's rotation about its centreline.

When the above-listed parameters increase, the angular velocity of rotation of the potato tuber decreases. The greatest effect on the tuber's angular velocity is observed in case of the variation of the winding pitch, the smallest – when the eccentricity changes. Consequently, it can be concluded from the above-said that these parameters have to be increased in order to achieve the minimum angular velocity of rotation of the potato tuber.

For the work process of cleaning the potato heap with the use of the potato heap cleaning unit under consideration to take place it is necessary to ensure that the centreline velocity of the potato tuber is below zero. Therefore, the minimum value of the angular velocity of the cleaning spiral spring's rotary motion has to be in accordance with the following relation:

$$\omega_{\min} = \dot{\theta} \left( 1 + \frac{2\pi \left( R_k + \frac{d_n}{2} \right)}{S} \cos \gamma \cdot \cos \theta \right). \quad (13)$$

For example, if the tuber has a radius of  $R_k = 25$  mm, the spiral has a radius of  $R = 75$  mm, the winding has a pitch of  $S = 35$  mm, the round bar, from which the spiral coil is made, has a radius of  $r = 7.5$  mm, the spiral is mounted with an eccentricity of  $\varepsilon = 10$  mm,  $\dot{\theta}$  can be found with the use of the graphic relation (Fig. 5) at a value of  $\psi = 0.8$  rad. After substituting the value of  $\dot{\theta}$  into the expression (13), it has been found that the magnitude of the angular velocity  $\omega_{\min}$  of the spiral's rotary motion has to be equal to at least  $27 \text{ rad s}^{-1}$ .

**Table 1.** Data on quality performance of spiral-type unit for cleaning potatoes from impurities obtained during field experiment investigations

Indicator	Spiral-type potato cleaning unit
Potato yield ( $\text{t ha}^{-1}$ )	10.0
Effective width of cleaning unit (1 row) (m)	0.7
Operating rate of travel of lifter equipped with cleaning unit under study ( $\text{km h}^{-1}$ )	2.41
Mass of cleaning unit (kg)	78.0
Entirety of potato tubers passing through cleaning unit (%)	100
Potato tubers damaged by cleaning unit (%)	1.8–3.2
Severely damaged potato tubers (%)	1.6–2.4
Potato tubers lost while passing through cleaning unit (%)	1.6–1.38
Contamination of potato tubers with soil impurities (%)	1.9–3.2
Contamination of potato tubers with plant impurities (%)	1.5–1.9

The authors have carried out field experiment investigations with the spiral-type potato cleaning unit of the design developed by them. Table 1 contains the data on the quality, with which the potato tubers lifted from the soil were cleaned from soil and plant impurities, as well as the conditions, in which the field experiment investigations were conducted. In the experiments, the cleaning unit of the design developed by the authors was installed in a single-row potato lifter attached to a Class 1.4 wheeled tractor. The general view of the single-row potato lifter (a share-type lifting implement and a raddle

chain conveyor, which feeds the heap to the cleaning unit) complete with the installed cleaning unit of the design developed by the authors is shown in Fig. 6.

The data in Table 1 prove that the spiral-type potato cleaning unit developed by the authors delivers the quality, the indices of which not only meet the agronomical requirements, but also exceed by far the similar indices of the other types of devices for cleaning potatoes from soil and plant impurities.

That is due to the fact that the cleaning spirals sieve with a high efficiency the soil and plant impurities through their own gaps and the clearances between the spirals. The new spiral cleaning unit completely rules out any positive entrainment of potato bodies as well as their strong compression, which virtually eliminates their damaging. The parameters obtained by the authors during the theoretical investigations with the use of PC-assisted calculations provide for the transportation of potato bodies by the spirals (especially their upper and side surfaces) at a high rate and that means the small duration of the contacts

between the potato tuber bodies and the spirals. It should be noted that, in case the turns of the cleaning spirals are coated with rubber or some other elastic material, the rate of potato tuber damage will be even lower. On the contrary, the soil and plant impurities, which virtually immediately fall into the space inside the turns, are transported by the spiral turns at a significantly lower rate. At the same time, the impurities, unlike the potato bodies, are actively entrained and compressed by the spiral turns. As a result of that, they are very efficiently positively carried down and outside the working space of the cleaning unit, which allows the potato bodies to move freely along the windings of the cleaning spirals and further onto the discharge conveyor. The contamination of the potato tubers with soil impurities also stays under 3.5% (and that contamination is caused not by free soil particles but by the soil caked on the tubers), while plant impurities are virtually absent in the cleaned potato heap.



**Figure 6.** General view of experimental unit with mounted spiral-type potato cleaning unit.

## CONCLUSIONS

1. The mathematical model of the motion of a single potato tuber on the cleaning spiral spring of the spiral potato heap cleaning unit has been generated. The model enabled obtaining the system of differential equations that describes the motion of the potato tuber on the cleaning unit's spiral spring.

2. As a result of the performed integration, the analytical expressions have been obtained for the angular velocity of rotation of the potato tuber about its centreline and the angular velocity of rotation of the cleaning spiral spring.

3. Using the specially developed computer programme and assuming the selected main values of the parameters of the work process under consideration, PC-assisted

numerical calculations have been carried out and the diagrams have been plotted for the variation of the angular velocity of rotation of the potato tuber in relation to the design and kinematic parameters of the spiral cleaning unit.

4. Basing on the completed analytical study, it has been established that, when a potato tuber (approximated by a spherical-shape body) with a diameter of 50 mm moves on the surface of the cleaning spiral with a radius of 75 mm wound from the round bar with a diameter of 15 mm, in case the spirals are mounted with an eccentricity of 10 mm, it is necessary to maintain the angular velocity of rotation of the spirals within the range of  $27\text{--}40\text{ rad s}^{-1}$  in order to ensure the efficiency of transporting and cleaning the tuber.

5. The results of the undertaken experimental investigations indicate the following indices of cleaning quality for the spiral-type cleaning unit of the design developed by the authors, the design and kinematic parameters of which have been determined theoretically: the damage rate does not exceed 3.5% (including severe damage – 2.4%), the loss rate is 1.5% or less, while the rate of contamination with impurities is not more than 3.3%, which is significantly lower, than the similar indices of other types of potato cleaning units, and does not exceed the agronomical requirements to the potato harvesting process.

## REFERENCES

- Bishop, C., Rees, D., Cheema, M.U.A., Harper, G. & Stroud, G. 2012. *Potatoes*. Crop Post-Harvest: Science and Technology: Perishables. Book Chapter, pp. 179–189.
- Bulgakov, V., Nikolaenko, S., Adamchuk, V., Ruzhylo, Z. & Olt, J. 2018a. Theory of retaining potato bodies during operation of spiral separator. *Agronomy Research* **16**(1), 41–51. doi: 10.15159/AR.18.036
- Bulgakov, V., Nikolaenko, S., Adamchuk, V., Ruzhylo, Z. & Olt, J. 2018b. Theory of impact interaction between potato bodies and rebounding conveyor. *Agronomy Research* **16**(1), 52–64. doi: 10.15159/AR.18.037
- Bulgakov, V., Nikolaenko, S., Adamchuk, V., Ruzhylo, Z. & Olt, J. 2018c. Mathematical model of cleaning potatoes on surface of spiral separator. *Agronomy Research* **16**(4), 1590–1606. doi: 10.15159/AR.18.173
- Bulgakov, V., Pascuzzi, S., Nikolaenko, S., Santoro, F., Anifantis, A.S., Olt, J. 2019. Theoretical study on sieving of potato heap elements in spiral separator. *Agronomy Research* **17**(1), 33–48. doi: 10.15159/AR.19.073
- Feller, R., Margolin, E., Hetzroni, A. & Galili, N. 1987. Impingement angle and product interference effects on clod separation. *Transactions of the American Society of Agricultural Engineers* **30**(2), 357–360.
- Grote, K.-H., Antonsson, E. 2008. Springer Handbook of Mechanical Engineering. 1580 p.
- Guo, W. & Campanella, O.H. 2017. A relaxation model based on the application of fractional calculus for describing the viscoelastic behavior of potato tubers. *Transactions of the ASABE* **60**(1), 259–264.
- Holland-Batt, A.B. 1989. Spiral separation: theory and simulation. *Transactions of the Institution of Mining and Metallurgy, Section C: Mineral Processing and Extractive Metallurgy* **98**, 46–60.
- Ichiki, H., Nguyen Van, N. & Yoshinaga, K. 2013. Stone-clod separation and its application to potato in Hokkaido. *Engineering in Agriculture Environment and Food* **6**(2), 77–85.
- Krause, F. & Minkin, A. 2005. Research on shaftless screw conveyors. *Bulk Solids Handling* **25**(2), 92–100.

- Misener, G.C. & McLeod, C.D. 1989. Resource efficient approach to potato-stone-clod separation. *AMA, Agricultural Mechanization in Asia, Africa and Latin America* **20**(2), 33–36.
- Nowak, J., Bulgakov, V., Holovach, I., Olt, J., Arak, M., Ruzhylo, Z., Nesvidomin, A. 2019. Oscillation theory of the free ends of the spiral separator for a potato heap. In: X International Scientific Symposium FMPMSA 2019: *Farm Machinery and Process Management in Sustainable Agriculture*, 157–162. doi: 10.24326/fmpmsa.2019.1
- Peters, R. 1997. Damage of potato tubers: A Review. *Potato Research* **39**(Spec. Issue), 479–484.
- Petrov, G. 1984. *Potato harvesting machines*. Mashinostroeniye (Mechanical Engineering), Moscow, 320 pp. (in Russian).
- Vasilenko, P.M. 1996. *Introduction to agricultural mechanics*. Kiev, Agricultural Education, 252 pp.
- Wang, X., Sun, J., Xu, Y., Li, X. & Cheng, P. 2017. Design and experiment of potato cleaning and sorting machine. *Nongye Jixie Xuebao/Transactions of the Chinese Society for Agricultural Machinery* **48**(10), 316–322 and 279.
- Wei, Z., Li, X., Sun, C. 2017. Analysis of potato mechanical damage in harvesting and cleaning and sorting storage. *Journal of Agricultural Science and Technology* **19**(8), 63–70. doi: 10.6041/j.issn.1000-1298.2019.01.014
- Ye, G., Ma, L., Huang, G., Yu, Y., Sun, X. & Wu, L. 2017. Dynamic and optimization analysis of spiral separator. *Meitan Xuebao/Journal of the China Coal Society* **42**, 479–485. doi: 10.13225/j.cnki.jccs.2017.0271

## Design and data comparison of the photovoltaic power plants in the southern and northern hemispheres

M. Daneček<sup>1</sup>, M. Havrlík<sup>1</sup>, V. Beránek<sup>2</sup>, J. Šafránková<sup>1,\*</sup>, M. Libra<sup>1</sup>,  
V. Poulek<sup>1</sup>, J. Sedláček<sup>1</sup> and R. Belza<sup>1</sup>

<sup>1</sup>Czech University of Life Sciences Prague, Kamýcká 129, CZ16500 Prague, Czech Republic

<sup>2</sup>Solarmonitoring, Ltd., Prague, Czech Republic

\*Correspondence: [janicka.safrankova@gmail.com](mailto:janicka.safrankova@gmail.com)

**Abstract.** We have recently developed a unique monitoring system for photovoltaic power plants and have gradually improved it in recent years. The system is installed at about 80 power plants in several European countries and at one power plant in Chile. We collect and evaluate all data in our laboratory. In this paper we describe the unique design of a photovoltaic power plant in the southern hemisphere in Chile with photovoltaic panels installed on tracking stands. We present the evaluated data and we discuss their comparison with photovoltaic power plants installed in Europe. We also discuss different solar conditions of these locations.

**Key words:** photovoltaics, PV power plant, data monitoring.

### INTRODUCTION

The amount of electricity generated is significantly influenced by the design of the photovoltaic (PV) power plant and its location. Monitoring data from PV systems is important for the operator. For example, the works (Ayompe et al., 2011, Madeti & Singh, 2017) talk about monitoring data from PV power plants. We have also developed our own monitoring system Solarmon-2.0 (Beránek et al., 2018), which is already installed on about 80 PV power plants in the Czech Republic and abroad (Romania, Slovakia, Hungary, Chile). Data are continuously collected and evaluated and some results have already been reported e.g. in previous works (Libra et al., 2016, Šafránková et al., 2019). We compare our data with predicted values according to the internationally used internet application Photovoltaic Geographical Information System ([https://re.jrc.ec.europa.eu/pvg\\_tools/en/tools.html](https://re.jrc.ec.europa.eu/pvg_tools/en/tools.html)). This application predicts the expected values of electricity generated according to the location and the basic design of the PV power plant.

Fig. 1 shows the world map with iso-areas of average solar energy incident per unit area and of the respective amount of produced electric energy (kWh m<sup>-2</sup> year<sup>-1</sup>). It is evident that the best areas for PV systems installation are in Tibet and in the half-desert mountains of Chile. There is enough of solar radiation, cold weather and high altitudes. Sahara is a good locality but not a top one. The climate is very hot and PV panels overheat so that the efficiency of PV energy conversion decreases.

If the electricity generated does not meet the expected values, this indicates a failure of the PV power plant and the most common failure is faulty PV panels. Our Solarmon-2.0 monitoring system is intelligent and can predict the location and type of failure. We have investigated methods of defects monitoring in PV panels, see for example works (Olšan et al., 2017, Libra et al., 2019). Similar investigation is also in works (Rösch et al., 2012, Spertino et al., 2015, Bilčík et al., 2019). It is sometimes advisable to store surplus electricity for later use. For example, works (Papež & Papežová, 2016, Papež & Papežová, 2019) deal with the accumulation of electric energy into electrochemical accumulators.

In this paper, we compare advanced PV system with tracking stands of PV panels installed in Chile in the southern hemisphere in a location with excellent solar conditions with two PV systems of conventional construction with fixed PV panels installed in Central Europe with temperate solar conditions (see below). We compare the amount of electricity produced.

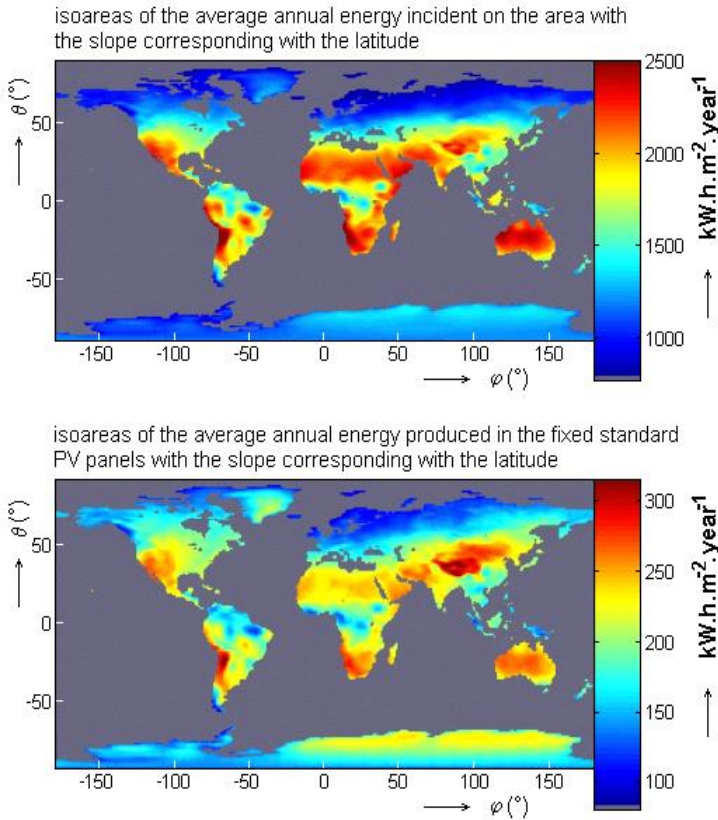


**Figure 1.** World map with iso-areas of the average solar energy incident per unit area and of the respective amount of produced electric energy.



## MATERIALS AND METHODS

The PV system in Cuz Cuz in Chile (see Fig. 2) is installed in a subtropical half-desert area in a location with excellent solar conditions (see Fig. 1). Its coordinates are  $31.665^{\circ}$  S,  $71.222^{\circ}$  W, altitude 275 m. Chinese BYD PV panels based on polycrystalline silicon with a nominal output power of  $305\text{ W}_p$ , type P6C-36, were used. The nominal output power of the whole PV system is about  $3000\text{ kW}_p$ . The tracking axes are oriented horizontally in the north-south direction.

Two comparative PV systems of different constructions are installed in Prague (Czech Republic) in a locality with solar conditions common in Central Europe. One comparative PV system in Prague-Suchdol (see Fig. 3) is installed on the roof of our Faculty of Engineering. Its coordinates are  $50,129^{\circ}$  N,  $14,374^{\circ}$  E, altitude 280 m. PV panels Renesola, GmbH of German production based on polycrystalline silicon with a nominal output of  $260\text{ W}_p$ , type JC 260M-24/Bb were used. The PV system has a standard construction with fixed PV panels inclined to the south at an angle of  $35^{\circ}$ . The nominal output power of the whole PV system is about  $10\text{ kW}_p$ .

The second comparative PV system in Prague-Vršovice (see Fig. 4) is located approximately 10 km from the first, so it is in a location with similar solar conditions. Flexible waterproof PV foils VAEPLAN V Solar 432 with a nominal power of  $432\text{ W}_p$  were used for the construction. They lie nearly horizontally on the roof of a football stadium without supporting stands. A total of 1,040 foils are connected to eight independent sections and these are connected to eight merge switchboards. 26 strings are connected into each switchboard and each string consists of 5 PV foils. The total nominal output power of the PV power plant is therefore approximately  $449\text{ kW}_p$ .



**Figure 2.** PV system in Cuz Cuz (Chile), advanced construction with tracking stands of PV panels with horizontal tracking axis.



**Figure 3.** PV system in Prague (Czech Republic) with standard construction with fixed stand of PV panels inclined to the south at an angle of  $35^{\circ}$ .



**Figure 4.** PV system in Prague (Czech Republic) with standard construction with PV panels laid horizontally without supporting stands.

All PV these systems are connected to the AC grid via DC/AC converters. PV systems are connected to our above-mentioned Solarmon-2.0 monitoring system. Data collection and evaluation takes place in our laboratory. For better comparison, the values of generated electricity are converted to 1 kW<sub>p</sub> of installed nominal power.

## RESULTS AND DISCUSSION

Fig. 5 shows the amount of electricity produced in said PV systems during one year. The values are given by months and for the whole year. In the southern hemisphere of Cuz Cuz, the seasons of the summer and winter are opposite to that of Europe, so there are the highest values of electricity produced in December and January and the lowest values are in May and June. It can be also seen that the total annual value of the generated electricity (2,043 kWh kW<sub>p</sub><sup>-1</sup> year<sup>-1</sup>) in Cuz Cuz is almost double compared to the PV system in Prague-Suchdol with fixed PV panels inclined to the south at an optimal angle. And the value is nearly triple compared to the PV system in Prague-Vršovice with fixed PV panels placed horizontally.

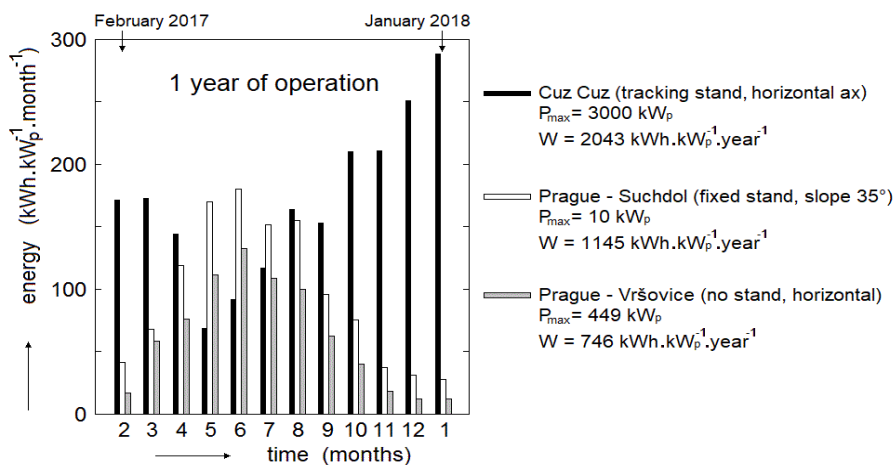


**Figure 5.** The amount of electricity produced in the said PV systems during one year.

The high value of electricity generated in Cuz Cuz is certainly related to the location with excellent solar conditions as well as to the advanced design of the PV system with tracking stands of PV panels. In the half-desert region, PV panels are often dusty with desert dust, but still the value of the electricity generated is high. It can also be seen that in subtropical locations the percentage differences between these values between summer and winter months are smaller than in Central Europe. Sun tracking racks of PV panels can increase the annual value of generated electricity by up to 30% (Poulek & Libra, 1998). Thus, in the case of fixed racks, an annual value of generated electricity of about 1,570 kWh.kW<sub>p</sub><sup>-1</sup> year<sup>-1</sup> could be expected at Cuz Cuz, which corresponds to the values in Fig. 1. 1 kW<sub>p</sub> of nominal output power corresponds approximately to the area of PV panels 5 m<sup>2</sup>.

In the case of PV systems installed in Prague, the values of electricity generated correspond to the values according to the above-mentioned and internationally used internet application Photovoltaic Geographical Information System ([https://re.jrc.ec.europa.eu/pvg\\_tools/en/tools.html](https://re.jrc.ec.europa.eu/pvg_tools/en/tools.html)). In the case of a PV system in Prague-Suchdol, the actual annual value is slightly higher than expected ( $1,145 \text{ kWh kWp}^{-1} \text{ year}^{-1}$  versus  $1,015 \text{ kWh kWp}^{-1} \text{ year}^{-1}$ ), which can be explained by high-quality PV panels with high efficiency of energy conversion. In the case of the PV system in Prague-Vršovice, the actual annual value is slightly lower than expected ( $746 \text{ kWh kWp}^{-1} \text{ year}^{-1}$  as opposed to  $850 \text{ kWh kWp}^{-1} \text{ year}^{-1}$ ). This we have seen in the previous work (Libra et al., 2016) and it was explained by the dusty environment near the railway track and by a slight rounding of the roof, where all PV panels are not completely horizontal.

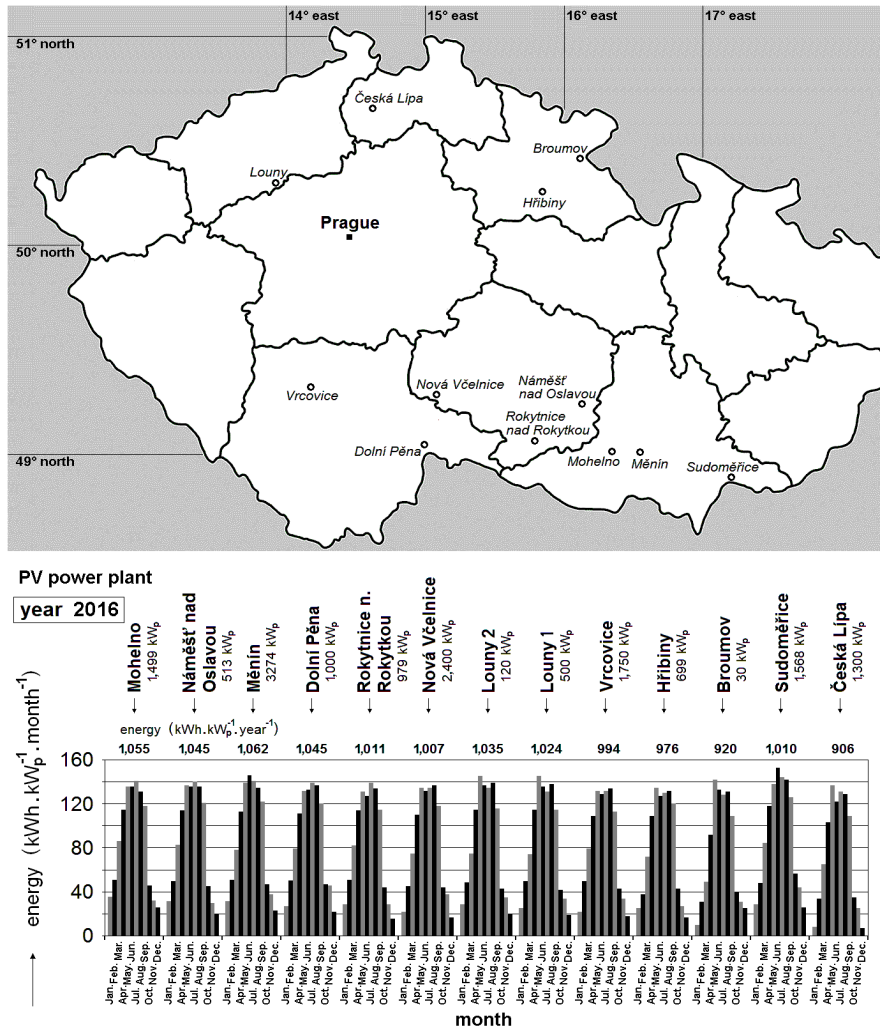


**Figure 6.** The amount of electricity produced in selected thirteen PV power plants located in the Czech Republic during one year.

We consider the roofs and facades of buildings to be suitable places for the installation of photovoltaic systems in high population density areas of Central Europe. We do not consider occupation of agricultural land a good solution here. On the other hand, in desert and half-desert areas the price of land is low and the population density is low as well. Therefore, we consider the installation of PV systems suitable also in open areas. Therefore, all three photovoltaic systems mentioned in this article were chosen in this way.

For a better comparison of the PV power plants located in Central Europe, Fig. 6 shows the amount of electricity generated during one year in the other selected thirteen PV power plants located in the Czech Republic. All these power plants are connected to our above mentioned monitoring system Solarmon-2.0 and the data are evaluated in our laboratory. The graph was created by evaluating a large data set. It can be seen that the annual values of electricity generated are around the expected values ( $1,000 \div 1,100 \text{ kWh kWp}^{-1} \text{ year}^{-1}$ ), only in the north of the Czech Republic the values are slightly lower. We have been evaluating this data for many years and the annual values of the electricity generated from individual years differ only slightly in terms of the year-on-year fluctuation in meteorological conditions.

## CONCLUSIONS

Our monitoring system Solarmon-2.0 monitors about 80 PV power plants in different parts of the world and works without significant defects. It is well proven and significantly helps operators of PV power plants with management and troubleshooting. In this paper, we compared and discussed the evaluated data from power plants in locations with very different solar conditions. The location in the half-desert area in northern Chile is, according to all forecasts, one of the places with excellent solar conditions, as confirmed by our data.

Sun tracking stands slightly increase the amount of electrical energy produced, but at higher latitudes they must have an inclined polar axis. The individual racks must be set apart from each other so that they do not shield each other. In this way, however, the use of the area of the PV power plant is reduced and the price of the area is high in Central Europe. Conversely, in subtropical half-desert regions, the rotational axis can be oriented horizontally, thereby minimizing shielding. In addition, the price of the power plant area is lower.

In densely populated areas of Central Europe, we recommend installing PV systems on roofs and facades of buildings and not on farmland. In the desert and half-desert areas, installation on open areas is also suitable with regard to the lower price of the PV power plant area.

**ACKNOWLEDGEMENTS.** The work was supported by the internal research project of the Faculty of Engineering IGA 2020:31120/1312/3106.

## REFERENCES

- Ayompe, L.M., Duffy, A., McCormack, S.J. & Conlon, M. 2011. Measured performance of a 1.72 kW rooftop grid connected photovoltaic system in Ireland. *Energy Conversion and Management* **52**, 816–825.
- Beránek, V., Olšan, T., Libra, M., Poulek, V., Sedláček, J., Dang, M.Q. & Tyukhov, I. 2018. New Monitoring System for Photovoltaic Power Plants' Management. *Energies* **11**, Article ID 2495, 1–13.
- Bilčík, M., Božiková, M. & Malínek, M. 2019. The Influence of Selected External Factors on Temperature of Photovoltaic Modules. *Acta Technologica Agriculturae* **22**, 4, 122–127.
- Libra, M., Beránek, V., Sedláček, J., Poulek, V. & Tyukhov, I.I. 2016. Roof photovoltaic power plant operation during the solar eclipse. *Solar Energy* **140**, 109–112.
- Libra, M., Daneček, M., Lešetický, J., Poulek, V., Sedláček, J. & Beránek, V. 2019. Monitoring of Defects of a Photovoltaic Power Plant Using a Drone. *Energies* **12**, 5, Article ID 795, 1–9.
- Madeti, S.R. & Singh, S.N. 2017. Monitoring system for photovoltaic plants: A review. *Renewable and Sustainable Energy Reviews* **67**, 1180–1207.
- Olšan, T., Libra, M., Poulek, V., Chalupa, B. & Sedláček, J. 2017. Combination of Three Methods of Photovoltaic Panels Damage Evaluation. *Scientia Agriculturae Bohemica* **48**(2), 98–101.
- Papež, V. & Papežová, S. 2016. Optimization of a solar power station by LiFePO<sub>4</sub> accumulators. *Agronomy Research* **14**(S1), 1200–1211.
- Papež, V. & Papežová, S. 2019. Effective control and battery charging system of an island PV power plant. *Agronomy Research* **17**, (S1), 1181–1190.
- Photovoltaic Geographical Information System [online], 2020. Available from: [https://re.jrc.ec.europa.eu/pvg\\_tools/en/tools.html](https://re.jrc.ec.europa.eu/pvg_tools/en/tools.html). Accessed 3<sup>rd</sup> January 2020.
- Poulek, V. & Libra, M. 1998. New solar tracker. *Solar Energy Materials and Solar Cells*, **51**, 113–120.
- Rösch, R., Krebs, F.C., Tanenbaum, D.M. & Hoppe, H. 2012. Quality control of roll-to-roll processed polymer solar modules by complementary imaging methods. *Solar Energy Materials & Solar Cells* **97**, 176–180.
- Spertino, F., Ciocia, A., Di Leo, P., Tommasini, R., Berardone, I., Corrado, M., Infuso, A. & Paggi, M. 2015. A power and energy procedure in operating photovoltaic systems to quantify the losses according to the cause. *Solar Energy* **118**, 313–326.
- Šafránková, J., Beránek, V., Libra, M., Poulek, V. & Sedláček, J. 2019. Construction and monitoring of the unique roof photovoltaic system in Prague. In: *Proc. 7<sup>th</sup> International Conference Trends in Agricultural Engineering*, Prague, 17<sup>th</sup>-20<sup>th</sup> September 2019, pp. 476–481.

## **Investigation of the anticorrosion performance of lignin coatings after crosslinking with triethyl phosphate and their adhesion to a polyurethane topcoat**

A. Dastpak, B.P. Wilson\* and M. Lundström

Aalto University, School of Chemical Technology, Department of Chemical and Metallurgical Engineering (CMET), Hydrometallurgy and Corrosion, Vuorimiehentie 2, P.O. Box 16200, Espoo, Finland

\*Correspondence: [ben.wilson@aalto.fi](mailto:ben.wilson@aalto.fi)

**Abstract.** This study investigates the anticorrosion properties of sustainable organic coatings, which were prepared by dissolution of two different types of technical lignins - organosolv lignin (OL) and kraft lignin (KL) - in an organic solvent and applied onto iron-phosphated steel by air-assisted spray coating. Influence of triethyl phosphate (TEP) as a crosslinking agent for lignin and its effect on the anticorrosion properties of coatings during 24 h of immersion in 3.5% NaCl were investigated. Results obtained from electrochemical impedance spectroscopy (EIS) of coated steels suggest that the initial protection performance (1 h immersion) of non-crosslinked OL is higher than that of KL. Nevertheless, KL coatings that contained TEP and were heat-treated at elevated temperature (180 °C) demonstrated the best overall anticorrosion performance. In contrast, a similar trend was not observed for OL coatings, which indicates that the structural properties of lignin may be a crucial factor in applicability of TEP as a crosslinking agent. In addition, a layer of polyurethane was applied on all the different types of lignin coatings prepared and their adhesion characteristics were studied by crosscut adhesion measurements (ISO 2409). These adhesion results revealed that neither KL-TEP nor OL-TEP coatings demonstrate proper adhesive characteristics with a polyurethane (PU) topcoat and consequently these coatings are not suitable for utilization as a primer coating for the PU topcoat studied.

**Key words:** corrosion protection, kraft lignin, organosolv lignin, triethyl phosphate crosslinker, sustainable coatings.

## **INTRODUCTION**

Organic coatings are one of the most common methods for the protection of metallic surfaces against corrosion (Lyon et al., 2017). Generally, most organic coating systems contain multiple layers for enhanced functionalities, for example, a layer adjacent to the surface of metal – also known as primer – is usually utilized to not only protect the surface of metal from oxidation, but also to enhance the adhesion of the subsequent layers (Hinder et al., 2005). Nevertheless, as the production of most organic coatings is dependent on finite and depleting petroleum resources, there is an increasing shift in industrial and scientific communities to replace petroleum-based materials with alternatives sourced from sustainable and renewable feedstocks (Deka & Karak, 2009).

Amongst these materials, lignin – the second most abundant biopolymer on earth – is a promising candidate, due to its chemically-rich structure, low price and high production rate as a by-product of pulp, paper and biorefinery industries (Holladay et al., 2007; Upton & Kasko, 2016; Brzonova et al., 2017).

Lignin is one of the main constituents of wood biomass (Kriauciuniene et al., 2008; Vitáček et al., 2019), and is hydrophobic in nature (Kunecová & Hlaváč, 2019). The potential of lignin as the main ingredient of anticorrosion coatings has been recently recognized (Dastpak et al., 2018; Haro et al., 2019), although the corrosion inhibition capability of lignin is well-understood (Ren et al., 2008; Hazwan Hussin et al., 2015). In a recent work (Dastpak et al., submitted), it was demonstrated that coatings prepared from kraft lignin have a high degree of protection in the early stages of immersion within an aggressive electrolyte, but prolonged exposure negatively affects the protection performance of the coating. In a study by Basso et al. (2017), the authors have demonstrated an easy route for enhancing the functionality of lignin coatings (resistance to water uptake and adhesion) by crosslinking the materials with triethyl phosphate (TEP). However, the anticorrosion properties of TEP-crosslinked lignin for metallic surfaces was not addressed in that study. Consequently, this study aims to investigate the anticorrosion properties of lignin coatings that are crosslinked with TEP, using electrochemical impedance spectroscopy (EIS). Furthermore, this study investigates the adhesion of the TEP-crosslinked coatings to a commonly used topcoat chemistry (polyurethane) to determine the applicability of crosslinked lignin as a primer coating.

## MATERIALS AND METHODS

### Materials and sample preparations

Two different grades of lignin were used for coatings preparation, namely a commercial grade softwood kraft lignin (KL), BioPiva™ 190 (UPM, Finland) and a pilot-scale hardwood organosolv lignin (OL) (Fraunhofer Centre for Chemical-Biotechnological Processes (CBP), Germany). Two lignin dissolutions were prepared by mixing each type of lignin (9 g) with an organic solvent (30 mL), i.e. diethylene glycol monobutyl ether (Butyl Carbitol™, ≥ 98%; Sigma-Aldrich, Germany), in order to form dissolutions with comparable lignin concentrations of 300 g L<sup>-1</sup>. Furthermore, in some samples Triethyl phosphate (TEP) (≥ 99%, Merck, Germany) was added with a 1:1 weight ratio of TEP:lignin. Solutions were magnetically stirred for (24 h) at room temperature and were subsequently applied by spray coating using a conventional cup gun equipment (Satajet 20 B, Germany) onto commercial grade iron-phosphated steel panels (R-46-ICF, Q-lab, USA). The elemental composition of the utilized steel is outlined in Table 1.

**Table 1.** Elemental composition of the utilized iron-phosphated steel panel (Q-lab, <https://www.q-lab.com/q-panel-selector/>)

Element	C	P	S	Mn	Fe
Wt. %	< 0.15	< 0.03	< 0.035	< 0.6	balance

Prior to application of coatings, surfaces were cleaned with a low lint tissue paper (VWR, USA) and ethanol (94.2%, Altia Oyj, Finland). Following coating, panels were placed in a pre-heated oven and dried at different temperatures and durations (Table 2).

In the final stage, for specific samples (#3 and #6 in Table 2) a layer of a commercial grade polyurethane (PU) topcoat (TEKNODUR 0290, Teknos, Finland)

sprayed onto the lignin-coated samples, which were then left to cure at ambient temperature for 7 days. As a reference, a PU layer with the same thickness was applied directly on the iron-phosphated steel panel. Measurements of the dry thickness values for these coatings were conducted using a thickness gauge (Elcometer 456, UK) for sample #3 and #6 (Table 2) before and after application of the PU topcoat.

**Table 2.** The parameters used for preparation of samples. In the sample designations, OL stands for organosolv lignin, KL for kraft lignin, TEP for triethyl phosphate, and numbers for the heat-treatment temperatures

No.	Sample Designation	TEP:lignin weight ratio	Heat-treatment temperature (°C)	Heat-treatment duration (min)
#1	OL	-	90	60
#2	OL-TEP-90	1:1	90	60
#3	OL-TEP-180	1:1	180	20
#4	KL	-	90	60
#5	KL-TEP-90	1:1	90	60
#6	KL-TEP-180	1:1	180	20

### Characterization of coated surfaces

The lignin coated surfaces were primarily characterized with electrochemical impedance spectroscopy (EIS) in order to evaluate their anticorrosion properties. Measurements were carried out using an Iviumstat XRe (Ivium Technologies, Netherlands) after exposure of a fixed surface area (0.785 cm<sup>2</sup>) to 5 wt.% sodium chloride (NaCl) solution at room temperature. The set-up comprised of a conventional three-electrode cell with a Ag/AgCl (saturated KCl) as the reference electrode (RE), a platinum (Pt) wire as the counter electrode (CE) and the coated/uncoated steel surfaces as the working electrode (WE). Prior to commencement of measurements, coatings were immersed and left to stabilise in the electrolyte for 1 h. EIS measurements were performed at open circuit potential (OCP) and over a frequency range of 100 kHz to 0.01 Hz, with logarithmically spaced frequency values (10 steps per decade) and a voltage amplitude of 10 mV<sub>rms</sub> (root mean square). The EIS data were obtained after 1 h and 24 h immersion in the NaCl electrolyte.

For adhesion studies, a crosshatch cutter (Paint Test Equipment, UK) was utilized and measurements were performed using the EN ISO 2409 (2013) standard procedure. Firstly, all lignin-coated surfaces were cut using a multiple blade cutter and an adhesive tape was applied to the incised area, which was subsequently removed after 5 minutes at a fixed angle (~60°). Result of these adhesion tests were evaluated by optical microscopy imaging (OM, Motic BA310Met-T, China). Similar measurements were also conducted for the double layer coating systems, which contained a lignin layer (sample #3 and #6 in Table 2) and an additional PU topcoat as well as the iron-phosphated steel-PU top-coated reference for comparison.

## RESULTS AND DISCUSSION

Electrochemical properties of the prepared surfaces were investigated by electrochemical impedance spectroscopy (EIS) and during 24 h immersion in 5% NaCl. Fig. 1 represents the Bode representations of EIS data, in the form of impedance modulus



vs. frequency, for coatings based on organosolv lignin (OL, Fig. 1, a) and kraft lignin (KL, Fig. 1, b). A straightforward method for evaluation of Bode impedance modulus plot, is the comparison of impedance values within the low frequency region, which for coated metals means that higher impedance values demonstrate a higher degree of a protection due to the coating (Kumar & Buchheit, 2006). By comparing the total impedance values of OL samples at low frequencies (Fig. 1, a) after 1 h immersion, it can be seen that OL coatings provide the highest impedance values when compared to either bare steel or TEP containing samples. Moreover, neither the addition of TEP nor the curing temperature appears to have an impact on the anticorrosion capability of the coatings. Consequently, among the three different OL samples investigated the non-treated sample (OL) demonstrates the best anticorrosion capabilities. Nevertheless after 24 h immersion, the total impedance of coatings (OL, OL-TEP-90 and OL-TEP-180) dropped dramatically, which suggests that the degree of protection against corrosion is severely decreased during the immersion period and the trend in the Bode impedance modulus (Fig. 1, a) of all three OL coatings are comparable with those of the bare steel. On the other hand, for coatings that were made from kraft lignin (Fig. 1, b), the best anticorrosion performance for both 1 h and 24 h immersion durations were obtained from the KL-TEP-180 coatings, followed by KL and KL-TEP-90, respectively. Furthermore, it can be noticed that KL-TEP-180 coatings that were immersed for 24 h outperformed the other two KL coatings (KL and KL-TEP-90) already after 1 h immersion, which suggests that the addition of TEP and subsequent heat-treatment at 180 °C enhanced the performance of kraft lignin coatings. Consequently, it is clear that the addition of TEP alone is not enough to enhance the anticorrosion capability of kraft lignin and heat-treatment is a necessary step in the coating preparation. Moreover, amongst the three different KL coatings tested, the KL-TEP-180 is least affected by the electrolyte (5% NaCl) over the 24 h immersion, which suggests the coating protection is maintained.

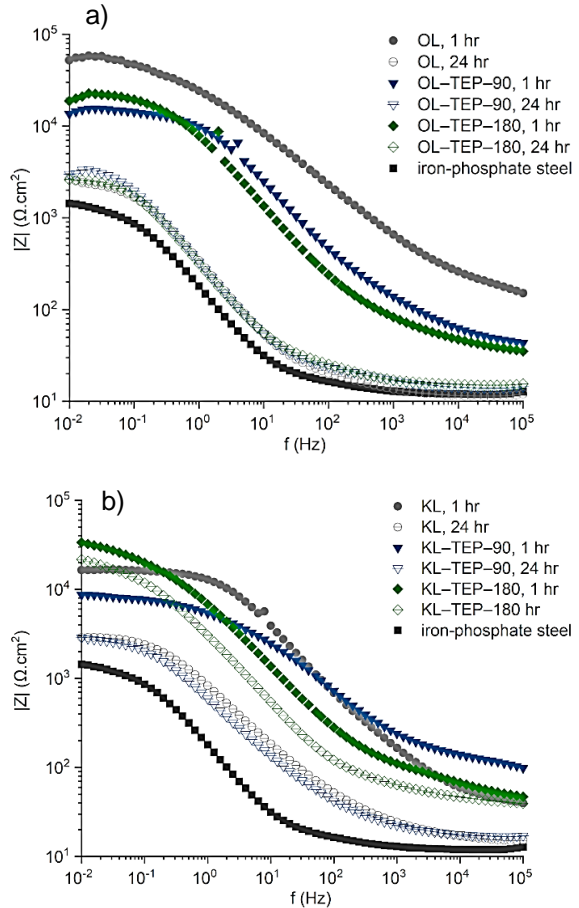


**Figure 1.** EIS Bode plots of impedance modulus vs. frequency for coatings prepared based on a) organosolv lignin (OL) and b) kraft lignin (KL).

Basso et al. (2017), have previously obtained a TEP-crosslinked kraft lignin and their results highlighted that there is a temperature-dependent reaction of TEP with both the phenolic and aliphatic hydroxyl groups within lignin. In relation to the EIS studies detailed here, it can be hypothesised that the crosslinking reactions were successful with KL, but was essentially absent with OL coatings as the anticorrosion performance of the TEP-free sample (OL) was better than the TEP containing coatings (OL-TEP-90 and OL-TEP-180). In our recent work (Dastpak et al., submitted), the  $^{31}\text{P}$  NMR studies of OL and KL lignin samples demonstrated that the content of both phenolic and aliphatic hydroxyl groups in KL was higher than OL, highlighting the idea that a higher number of reaction sites between KL and TEP facilitated a greater extent of crosslinking, which resulted in the better anticorrosion capabilities of KL-TEP-180 coatings.

In order to study the adhesion performance of lignin coatings to iron-phosphated steel surfaces, crosscut measurements were conducted. As illustrated in Fig. 2, the adhesion of the organosolv lignin coating (OL, Fig. 2, a) is slightly weaker than that of the kraft lignin (KL, Fig. 2, b) and addition of TEP to both coatings results in a decrease of the coating adhesion strengths (Fig. 2, c–f). However, the difference between detached area from the non-crosslinked samples and TEP containing samples is negligible (especially for coatings based on OL) and all samples can be similarly categorized according to the ISO 2409 standard as shown in Table 3.

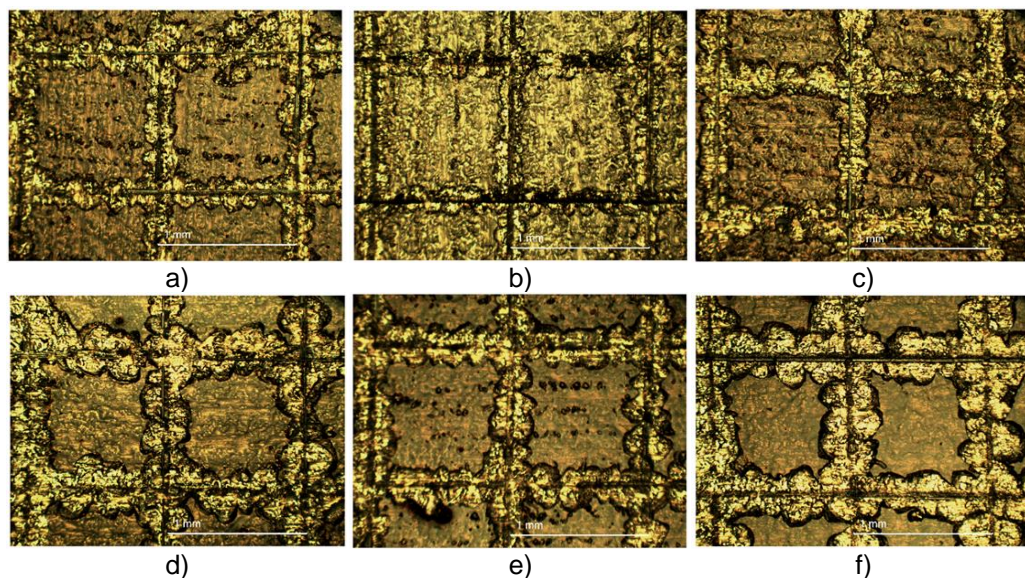


**Figure 2.** Optical microscopy (OM) images of lignin coatings after crosscut adhesion measurements, for a) OL, b) KL, c) OL-TEP-90, d) KL-TEP-90, e) OL-TEP-180 and f) KL-TEP-180. (scale bar: 1 mm).

In order to study the adhesion of a polyurethane topcoat with lignin coatings of OL-TEP-180 and KL-TEP-180, the crosscut adhesion measurements were also conducted on the lignin coatings that also contained a layer of PU coating with comparable thicknesses of 30  $\mu\text{m}$ . Furthermore, a PU coating that was directly applied onto iron-phosphated steel surface with a similar thickness value was used as reference.

Digital images of the surfaces after the measurements are displayed in Fig. 3. As can be observed, the PU sample that was directly applied to surface demonstrates the best adhesion, unlike samples that contain lignin coatings of OL–TEP–180 (Fig. 3, a) and KL–TEP–180 (Fig. 3, b) that completely peel-off from the surface, to leave behind two different regions that either contain a layer of lignin coating (red circles, Fig. 3) or regions where the lignin coating is partially detached from the surface along with the PU top-coat (black circles, Fig. 3). Magnified OM images of these regions can be seen in Fig. 4 and the related adhesion results are detailed in Table 4.

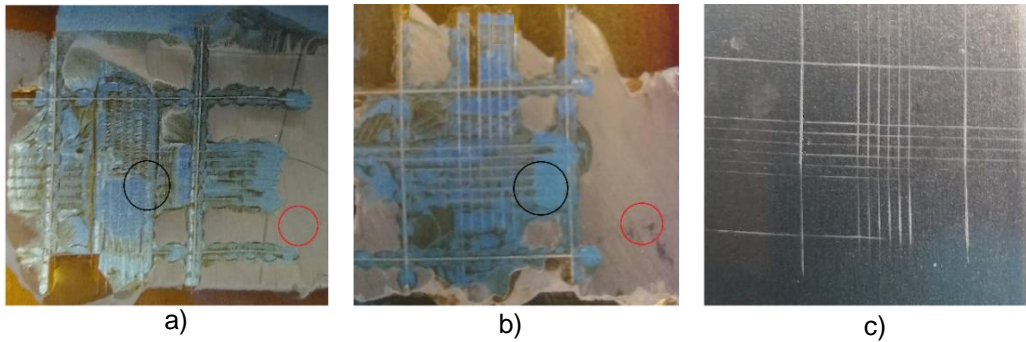


**Figure 3.** Digital images of double layer coatings after adhesion crosscut measurements. (a) PU on OL–TEP–180, (b) PU on KL–TEP–180 and (c) PU coating on iron-phosphated steel.

In order to study the adhesion of a polyurethane topcoat with lignin coatings of OL–TEP–180 and KL–TEP–180, the crosscut adhesion measurements were also conducted on the lignin coatings that also contained a layer of PU coating with comparable thicknesses of 30  $\mu\text{m}$ . Furthermore, a PU coating that was directly applied onto iron-phosphated steel surface with a similar thickness value was used as reference. Digital images of the surfaces after the measurements are displayed in Fig. 3. As can be observed, the PU sample that was directly applied to surface demonstrates the best adhesion, unlike samples that contain lignin coatings of OL–TEP–180 (Fig. 3, a) and KL–TEP–180 (Fig. 3, b) that completely peel-off from the surface, to leave behind two different regions that either contain a layer of lignin coating (red circles, Fig. 3) or regions where the lignin coating is partially detached from the surface along with the PU top-coat (black circles,

**Table 3.** Results obtained from crosscut adhesion measurements of lignin coatings. Based on ISO 2409, best adhesion performance is represented as 0 and adhesion failure as 5 (EN ISO 2409, 2013)

No.	Sample designation	Adhesion results (scale: 0–5)
#1	OL	2
#2	OL–TEP–90	2
#3	OL–TEP–180	2
#4	KL	1
#5	KL–TEP–90	2
#6	KL–TEP–180	2

**Table 4.** Results obtained from crosscut adhesion measurements with double layer coatings of lignin-PU topcoat and steel-PU topcoat reference

Samples' code	Adhesion results (scale: 0–5)
PU on steel	0
PU on OL–TEP–180	5
PU on KL–TEP–180	5



Fig. 3). Magnified OM images of these regions can be seen in Fig. 4 and the related adhesion results are detailed in Table 4.

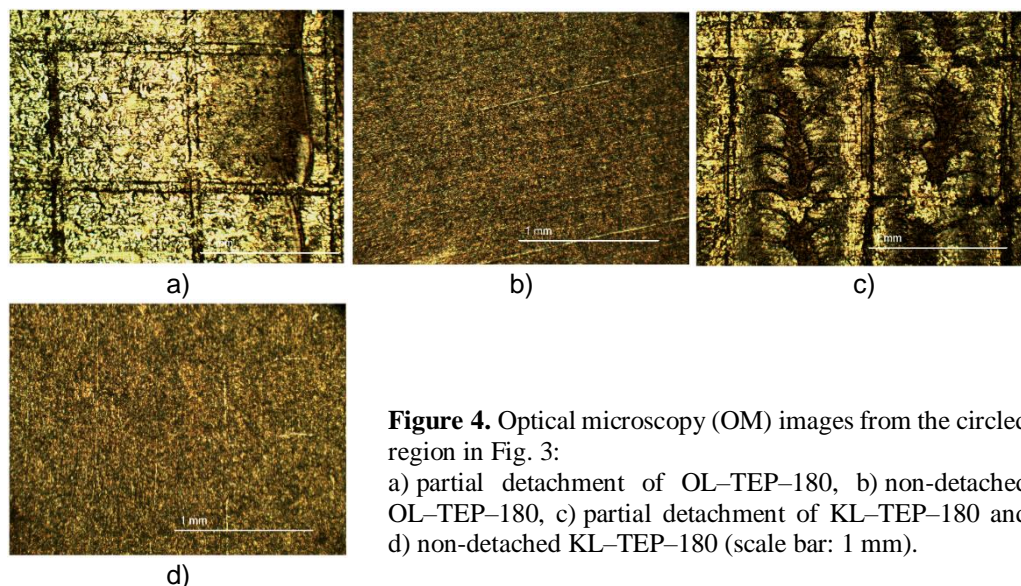


**Figure 4.** Optical microscopy (OM) images from the circled region in Fig. 3:

a) partial detachment of OL-TEP-180, b) non-detached OL-TEP-180, c) partial detachment of KL-TEP-180 and d) non-detached KL-TEP-180 (scale bar: 1 mm).

The difference in adhesion behaviour between the two layers suggests that when the underlying lignin coatings are not mechanically stressed, the adhesion between the steel and lignin is higher than that of lignin with PU topcoats, therefore separation occurs at the interface between lignin and PU. However, when the surface is damaged (by the cutting tool in this case) the underlying lignin coating loses the adhesion to the steel substrate and detaches along with the PU topcoat. This adhesion loss of lignin coatings from the substrate might be related to the brittle nature of lignin (Kai et al., 2012), which results in the cracking of coatings after the application of an external stress.

Based on these findings, neither kraft lignin nor organosolv lignin coatings that are crosslinked with TEP provide a reliable adhesion to the PU topcoat and therefore are not suitable for use as a primer coating in the investigated system. Nevertheless, the enhanced performance of KL-TEP-180 as a single layer protective coating or a primer for other organic coatings types, e.g. epoxies, could be a subject for further investigation.

## CONCLUSIONS

In this study, a high-performance anticorrosion coating was obtained from the crosslinking of triethyl phosphate (TEP) with kraft lignin (KL) after heat-treatment of samples at 180 °C. Although an aggressive electrolyte (5% NaCl) was used for long-term corrosion tests, the KL-TEP coatings maintained the anticorrosion capabilities. Although satisfactory adhesion performance of this coating with a polyurethane topcoat was not obtained, this investigation demonstrates the possibility to further enhance the corrosion protection of sustainable coatings by use of 100% kraft lignin as a component.

ACKNOWLEDGEMENTS. The funding of this research was provided by Technology Industries of Finland/Jane and Aatos Erkko Foundations ‘*Future Makers: Biorefinery Side Stream Materials for Advanced Biopolymer Materials (BioPolyMet)*’ and Academy of Finland (NoWASTE, No. 297962). The necessary facilities for conducting this research was provided by the RawMatTERS Finland Infrastructure (RAMI) at Aalto University, supported by the Academy of Finland. Additionally, we express our gratitude to Antti Karkola and Mikael Rähkä (Teknos Ltd.) for sharing expertise, services and for providing metallic panels. Furthermore, Dr. Moritz Leschinsky (Fraunhofer Center for Chemical-Biotechnological Processes (CBP)) is acknowledged for providing the organosolv lignin.

## REFERENCES

- Basso, M.C., Pizzi, A., Delmotte, L. & Abdalla, S. 2017. Analysis of the Cross-Linking Reaction of Lignin with Triethyl Phosphate by MALDI-TOF and  $^{13}\text{C}$  NMR. *Polymers* **9**(6), 206. <https://doi.org/10.3390/polym9060206>
- Brzonova, I., Kozliak, E.I., Andrianova, A.A., LaVallie, A., Kubátová, A. & Ji, Y. 2017. Production of lignin based insoluble polymers (anionic hydrogels) by C. Versicolor. *Scientific Reports* **7**, No. 17507. <https://doi.org/10.1038/s41598-017-17696-1>
- Dastpak, A., Lourençon, T.V., Balakshin, M., Hashmi, S.F., Lundström, M. & Wilson, B. (in press). Solubility study of lignin in industrial organic solvents and investigation of electrochemical properties of spray-coated solutions. *Industrial Crops and Products*, submitted.
- Dastpak, A., Yliniemi, K., de Oliveira Monteiro, M., Höhn, S., Virtanen, S., Lundström, M. & Wilson, B. 2018. From Waste to Valuable Resource: Lignin as a Sustainable Anti-Corrosion Coating. *Coatings* **8**(12), 454. <https://doi.org/10.3390/coatings8120454>
- Deka, H. & Karak, N. 2009. Bio-based hyperbranched polyurethanes for surface coating applications. *Progress in Organic Coatings* **66**(3), 192–198. <https://doi.org/10.1016/j.porgcoat.2009.07.005>
- EN ISO 2409. 2013. Paints and Varnishes – Cross-cut test. International Organization for Standardization, Geneva, Switzerland.
- Haro, J.C., Magagnin, L., Turri, S. & Griffini, G. 2019. Lignin-Based Anticorrosion Coatings for the Protection of Aluminum Surfaces. *ACS Sustainable Chemistry & Engineering* **7**(6), 6213–6222. <https://doi.org/10.1021/acssuschemeng.8b06568>
- Hazwan Hussin, M., Mohd Shah, A., Abdul Rahim, A., Mohamad Ibrahim, M., Perrin, D. & Brosse, N. 2015. Antioxidant and anticorrosive properties of oil palm frond lignins extracted with different techniques. *Annals of Forest Science* **72**(1), 17–26. <https://doi.org/10.1007/s13595-014-0405-1>
- Hinder, S.J., Lowe, C., Maxted, J.T., Perruchot, C. & Watts, J.F. 2005. Intercoat adhesion failure in a multilayer coating system: An X-ray photoelectron spectroscopy study. *Progress in Organic Coatings* **54**(1), 20–27. <https://doi.org/10.1016/j.porgcoat.2005.03.012>
- Holladay, J.E., White, J.F., Bozell, J.J. & Johnson, D. 2007. *Top Value-Added Chemicals from Biomass, Volume II—Results from Screening for Potential Candidates from Biorefinery Lignin*. Technical Report No 16983, Pacific Northwest National Laboratory (PNNL). Available at [https://www.pnnl.gov/main/publications/external/technical\\_reports/PNNL-16983.pdf](https://www.pnnl.gov/main/publications/external/technical_reports/PNNL-16983.pdf)
- Kai, D., Tan, M.J., Chee, P.L., Chua, Y.K., Yap, Y.L. & Loh, X.J. 2016. Towards lignin-based functional materials in sustainable world. *Green Chemistry* **18**, 1175–1200. <https://doi.org/10.1039/c5gc02616d>
- Kumar, G. & Buchheit, R. G. 2006. Development and Characterization of Corrosion Resistant Coatings Using the Natural Biopolymer Chitosan. *ECS Transactions* **1**(9), 101–117. <https://doi.org/10.1149/1.2215582>

- Kunecová, D. & Hlaváč, P. 2019. Determination of activation energy of the pellets and sawdust using thermal analysis. *Agronomy Research* **17**(6), 2306–2316. <https://doi.org/10.15159/AR.19.211>
- Kriauciuniene, Z., Velicka, R., Raudonius, S. & Rimkeviciene, M. 2008. Changes of lignin concentration and C:N in oilseed rape, wheat and clover residues during their decomposition in the soil. *Agronomy Research* **6**(2), 489–498.
- Lyon, S.B., Bingham, R. & Mils, D.J. 2017. Advances in corrosion protection by organic coatings: What we know and we would like to know. *Progress in Organic Coatings* **102**(A), 2–7. <https://doi.org/10.1016/j.porgcoat.2016.04.030>
- Q-lab, iron-phosphated steel (type R-XX-ICF). Available at <https://www.q-lab.com/products/q-panel-standard-substrates/q-panel-selector> (accessed on 23 January 2020).
- Ren, Y., Luo, Y., Zhang, K., Zhu, G. & Tan, X. 2008. Lignin terpolymer for corrosion inhibition of mild steel in 10% hydrochloric acid medium. *Corrosion Science* **50**(11), 3147–3153. <https://doi.org/10.1016/j.corsci.2008.08.019>
- Upton, B.M. & Kasko, A.M. 2016. Strategies for Conversion of Lignin to High-Value Polymeric Materials: Review and Perspective. *Chemical Reviews* **116**(4), 2275–2306. <https://doi.org/10.1021/acs.chemrev.5b00345>
- Vitázek, I., Ondro, T., Sunitrová, I., Majdan, R. & Šotnar, M. 2019. Thermoanalytical investigations of selected fuel during isothermal heating. *Agronomy Research* **17**(6), 2455–2459. <https://doi.org/10.15159/AR.19.216>

## **Comparison of phosphorus removal efficiency of conventional activated sludge system and sequencing batch reactors in a wastewater treatment plant**

V. Denisova\*, K. Tihomirova, J. Neilands, K. Gruskevica, L. Mezule and T. Juhna

Riga Technical University, Research Centre for Civil Engineering, Water Research Laboratory, P. Valdena 1-204, LV-1048 Riga, Latvia

\*Correspondence: viktorija.denisova@rtu.lv

**Abstract.** The aim of this study was to evaluate the effectiveness application of sequencing batch reactors (SBRs) for phosphorus removal compared to the conventional activated sludge (CAS) treatment system. The results showed that the removal efficiency of phosphorus reached about 99% at wastewater treatment plant with CAS system. At the same time, the maximum phosphorus removal efficiency can be achieved to 88% if the SBRs system operating parameters are optimized. Finally, this study demonstrated that even if granules are not fully developed, the SBR system is working with a good efficiency.

**Key words:** phosphorus removal, activated sludge process, SBR, aerobic granules, wastewater treatment plant.

### **INTRODUCTION**

Phosphorus (P) and nitrogen (N) are important nutrients known for stimulation of excess growth of plants, algae and some bacteria such as cyanobacteria in surface waters, thus, being responsible for the intensity of eutrophication (Gorham et al., 2017; Yan et al., 2017; Bhagowati & Ahamad, 2018). P is the critical element which affects eutrophication in most fresh waters. Most of the P load comes from large animal farms, fish farming, waste disposal sites and municipal wastewater treatment plants (WWTP) (Tihomirova et al., 2019). As a result, the demand for P removal from wastewater is increasing nowadays (Qiu & Ting, 2014). Therefore, the need for efficient removal of P from wastewaters and regulation of P limit in final effluent before the discharge into watercourses will help to prevent eutrophication of receiving surface water bodies. As a result, to avoid the potential hazard of P pollution to surface waters, the European Economic Community (EEC) has created an urban wastewater treatment directive 91/271/EEC as a framework to specify the minimum wastewater treatment requirements for the discharge of P-containing compounds into receiving waters depending on the size of WWTPs (EEC, 1991). Usually, the measurement of the total phosphorus (TP) concentration is used for discharge criteria. It includes soluble phosphorus (SP) and particulate phosphorus (PP) (Ge et al., 2018). According to the size of the sewage treatment plant, TP values are 2 mg L<sup>-1</sup> for 10,000–100,000 population equivalents (PE)

and 1 mg L<sup>-1</sup> TP for > 100,000 PE. At the same time, the effluent limit values for WWTPs with pollution load less than 2,000 PE are not regulated by these requirements (ECC, 1991). As a result of a formation of disperse agglomerations, there are a lot of small-size WWTPs without any legal requirements for P removal. Therefore, biological removal of P from the wastewater is still the challenge in small and local WWTPs within Europe. Implementation of new methods to reduce nutrient loadings are necessary, especially for the treatment of runoff waters from agriculture. Sand filters and nutrient binding compounds are not efficient at the moment. Currently, numerous research groups are focusing on combined processes that can be effective for the removal and recovery of P from wastewaters (Bassin et al., 2012; Lochmatter et al., 2013; Yan et al., 2015). As shown, biological P removal methods are more affordable and environmentally friendly than the chemical ones (Manas et al., 2011; Pronk et al., 2015).

Conventional activated sludge (CAS) systems are the most widely applied technologies for biological nutrient (P and N) and organic matter removal from municipal wastewaters worldwide (Meerburg et al., 2015). However, this technology requires high energy consumption and produces huge amount of excessive activated sludge (Gu et al., 2017). The current practice shows that 45–75% of the total plant operation costs are used for intensive aeration (Capodici et al., 2019; Wu et al., 2019), since dissolved oxygen (DO) represents an essential factor for biological processes in WWTPs (Tang et al., 2015). At the same time, the treatment of the excess activated sludge may account for 25–65% of the total plant operation costs (Gu et al., 2017). Therefore, the demand for more cost-efficient and less-occupied technologies is critically important to improve wastewater treatment process sustainability.

Recently aerobic granular sludge (AGS) has been investigated as an alternative to traditional CAS process (De Kreuk, 2006; Nancharaiah & Kiran Kumar Reddy, 2018). AGS technology has been developed to improve the settling properties of the activated sludge and mainly has been applied in the sequencing batch reactor (SBR) systems which have been incorporated into several full-scale domestic WWTPs within Europe (Pronk et al., 2015; Barrios-Hernandez et al., 2020). The operation of an SBR is based on fill-and-draw principles, which typically consist of four steps—fill, aeration, settling and drawing within the same reactor. When compared to traditional activated sludge systems, AGS technology has many advantages, such as excellent settleability, resulting in a short settling time for good liquid-solid separation, stronger granule structure, good biomass retention, high resistance to toxicity and simultaneous P and N removal (Adav et al., 2008; Li et al., 2014). Additionally, AGS technology has smaller space requirements, lower energy consumption and lower overall operational costs. Due to these advantages, it is regarded that AGS technology has a great potential to become one of the most prospective biological wastewater treatment approaches in the future (Zhang et al., 2016).

The objective of this study was to evaluate the effectiveness of the application of SBRs for P removal. Studies were performed at a full scale municipal WWTP in Latvia. Both processes were operated in parallel from August 2017 to April 2018.

## MATERIALS AND METHODS

### Study site

A pilot-scale SBRs were located in the municipal WWTP in Adazi, Latvia. The influent wastewater was directly introduced into the SBRs from the grit chamber in the



Adazi WWTP. The composition of the influent was within the required ranges (Table 1). The SBRs were directly inoculated with 120 L of activated sludge at the beginning of the experiment and 40 L twice a month taken from an aeration tank at the Adazi WWTP. The seeding sludge had a mixed liquor suspended solids (MLSS) concentration of  $3.5\text{--}6.1\text{ g L}^{-1}$ , a sludge volume index (SVI) of  $136\text{--}187\text{ mL g}^{-1}$  and the sludge volume was  $520\text{--}920\text{ mL L}^{-1}$  after 30 min settling. Monitoring of both processes (AGS at WWTP and SBR in pilot-system) was performed in parallel over a 9 month period with receiving the same influent wastewater.

### Pilot-scale SBR set-up and operation

The two identical parallel column reactors with internal diameters of 0.6 m and working volumes of  $0.33\text{ m}^3$  were used in this study. The operating flow rate was  $5\text{ L min}^{-1}$ . The reactors were aerated by using fine bubble aerators. The dissolved oxygen (DO) concentration was  $60\text{ L sec}^{-1}$ . The pilot-scale SBRs with a volumetric exchange ratio of 8% were operated in a fill-draw mode, in successive cycles of 4 h each. One cycle consisted of 5 min feeding, 210 min aeration, 25 min settling and 5 min effluent discharge. Feeding and discharge of wastewater was conducted at one time. The procedures of the reactors operation, including feeding, aeration, setting and discharging, were controlled automatically by a digital process controller (Controller, Adrona). The wastewater was introduced in the top part of the reactors. The effluent was at the height of 1.18 m from the bottom of the reactors.

### Sample collection

Wastewater (influent and effluent) samples were collected from a pilot and full-scale systems in plastic carboys (2 L) and stored in a refrigerator ( $2\text{ }^{\circ}\text{C}$  to  $5\text{ }^{\circ}\text{C}$ ) after transport. All analysis were performed within 24 h after collection. All wastewater and sludge samples analyses were conducted according to the standard methods (Table 2).

**Table 1.** Composition of the municipal wastewater

Parameter, $\text{mg L}^{-1}$	Mean $\pm$ 1 S.D.	Range (min – max)
COD	$691 \pm 410$	260–1,920
BOD <sub>5</sub>	$446 \pm 275$	150–1,300
SS	$293 \pm 222$	82–1,000
TN	$78 \pm 26$	33–137
TP	$9.2 \pm 2.9$	4.2–15.2
pH	$7.8 \pm 0.6$	6.5–8.6

**Table 2.** Wastewater quality analytical methods

Parameter	Reference
Chemical Oxygen Demand (COD)	LVS ISO 6060:1989
Biochemical Oxygen Demand (BOD <sub>5</sub> )	LVS EN 1899–2:1998
Total Nitrogen (TN)	LVS EN ISO 11905–1:1998
Total Phosphorus (TP)	LVS EN ISO 6878:2005 (part 7)
Suspended solids (SS)	LVS EN 872:2007
Mixed liquor suspended solids (MLSS)	LVS EN 872:2007
pH	LVS EN ISO 10523:2012
Sludge volume index (SVI)	APHA, 2005

Determination of the concentration of Total Nitrogen (TN) and Total Phosphorus (TP) were performed with UV–Vis spectrophotometer M501 (Camspec, UK) after sample mineralisation. Multiple repetitions of each sample ( $n = 3$ ) and control solutions were analysed to obtain the reproducibility of each method.

## RESULTS AND DISCUSSION

### TP removal

A long-term study was performed in order to evaluate the effectiveness of two technologies in achieving high phosphorus removal efficiency for municipal wastewater, after which the performances of SBR and CAS systems for TP removal were compared (Fig. 1). The results showed that the removal efficiency of TP was higher in CAS process than in SBR. The values of average influent TP of  $4.2\text{--}9.2\text{ mg L}^{-1}$  decreased in the effluent to  $1.2\text{ mg L}^{-1}$  and  $3.5\text{ mg L}^{-1}$  in CAS and SBR, respectively.

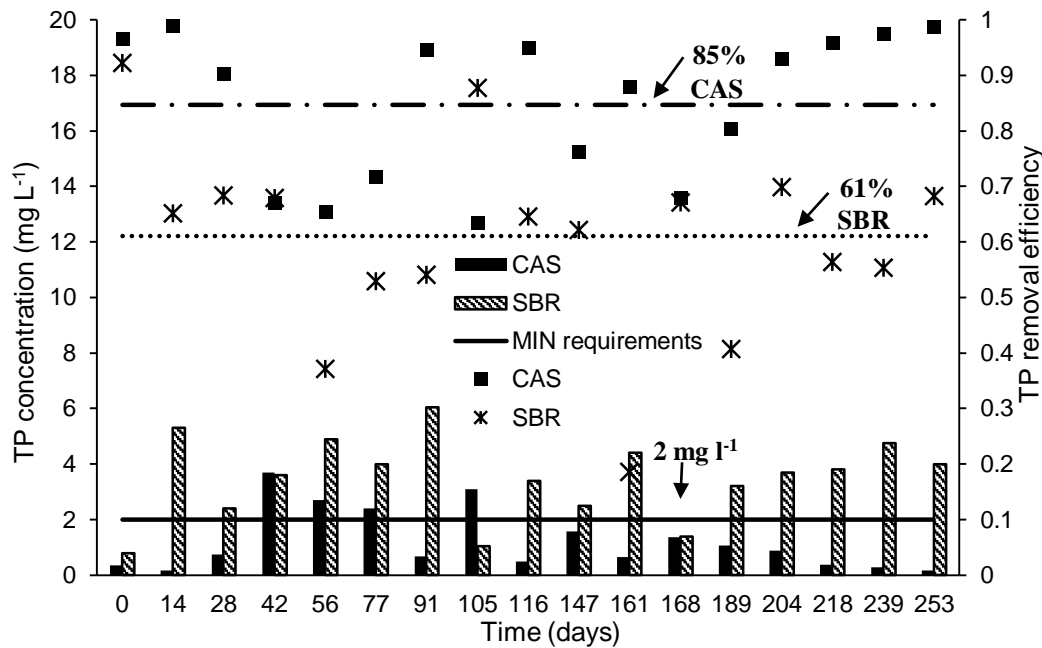


**Figure 1.** Long-term total phosphorus (TP) effluent concentrations, and its removal efficiencies in CAS and SBR systems. The average TP removal efficiency (— · —) in CAS and (·····) SBR.

Thus, demonstrating the average removal efficiency of TP in CAS - 85% and 61% in SBR. At the same time, it should be noted that the TP removal efficiency in SBR reached the maximum value of 88% on day 105, and the discharge requirements were achieved. In contrast to the SBR results on 105 day, the TP of the CAS system was higher than is allowed (Fig. 1).

The physical characteristics such as MLSS and SVI of the sludge in both systems were monitored (Table 3). During the study operation, the average SVI of sludge in CAS system ( $147 \pm 15 \text{ mL g}^{-1} \text{ SS}$ ) was two times higher than in SBR ( $73 \pm 26 \text{ mL g}^{-1} \text{ SS}$ ). Interestingly, the highest reduction of TP in SBR (on day 105) was achieved when the minimum value of SVI ( $33 \text{ mL g}^{-1} \text{ SS}$ ) and the maximum value of MLSS ( $1.2 \text{ g L}^{-1}$ ) was observed.

### COD and BOD<sub>5</sub> removal

Fig. 2. shows the values of effluent COD concentrations, and its removal efficiency in CAS and SBR systems during 253 days of operation. The results showed that the average removal efficiency of COD was 94% in CAS and 80% in SBR.

**Table 3.** Physical characteristics of sludge in the CAS and the SBR during 9 month operation

Operation duration (day)	MLSS ( $\text{g L}^{-1}$ )		SVI <sub>30</sub> ( $\text{mL g}^{-1}$ )	
	CAS	SBR	CAS	SBR
0	5.3	0.6	155	86
14	5.5	0.4	158	71
28	6.0	0.4	142	91
42	5.1	0.8	137	93
56	4.9	0.7	155	43
77	5.0	0.8	168	125
91	5.2	1.1	154	73
105	4.9	1.2	147	33
116	6.1	0.9	138	56
147	5.4	1.1	141	100
168	5.3	0.7	136	86
189	4.5	1.7	164	59
204	5.5	0.8	160	25
218	5.7	1.1	154	55
239	8.5	1.1	108	73
253	7.3	1.1	129	91
Average values	$5.6 \pm 1$	$0.9 \pm 0.3$	$147 \pm 15$	$73 \pm 26$

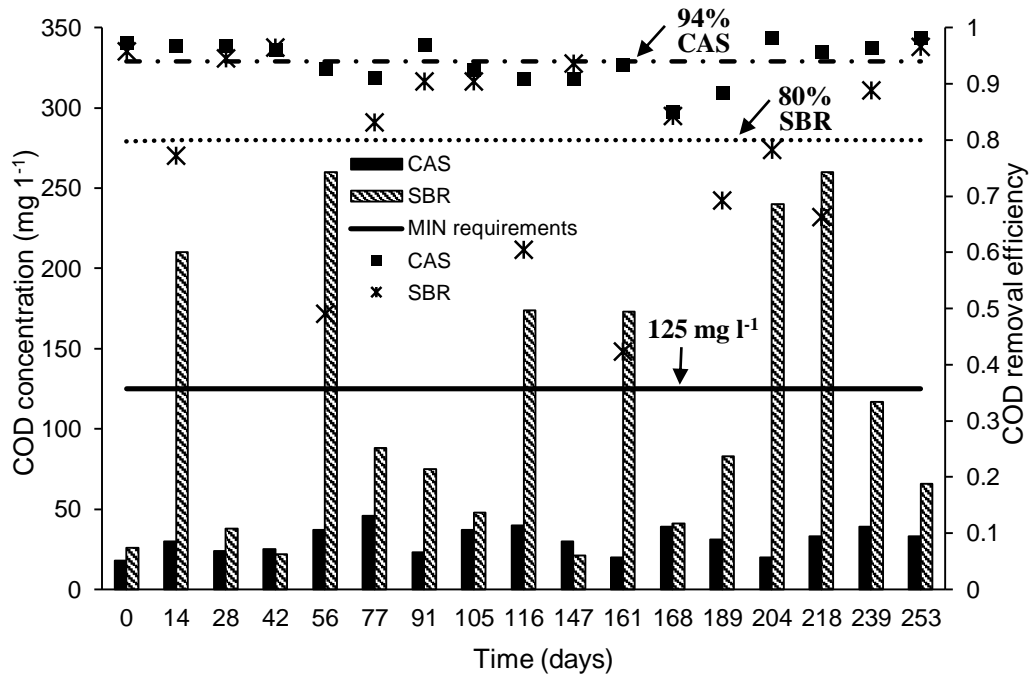


**Figure 2.** Long-term total Chemical Oxygen Demand (COD) effluent concentrations, and its removal efficiencies in CAS and SBR systems. The average COD removal efficiency (— · —) in CAS and (·····) SBR.

Fig. 3. shows the values of effluent BOD<sub>5</sub> concentrations, and its removal efficiency in CAS and SBR systems during 253 days of operation. The results showed that the average removal efficiency of BOD<sub>5</sub> was 99% in CAS and 90% in SBR.

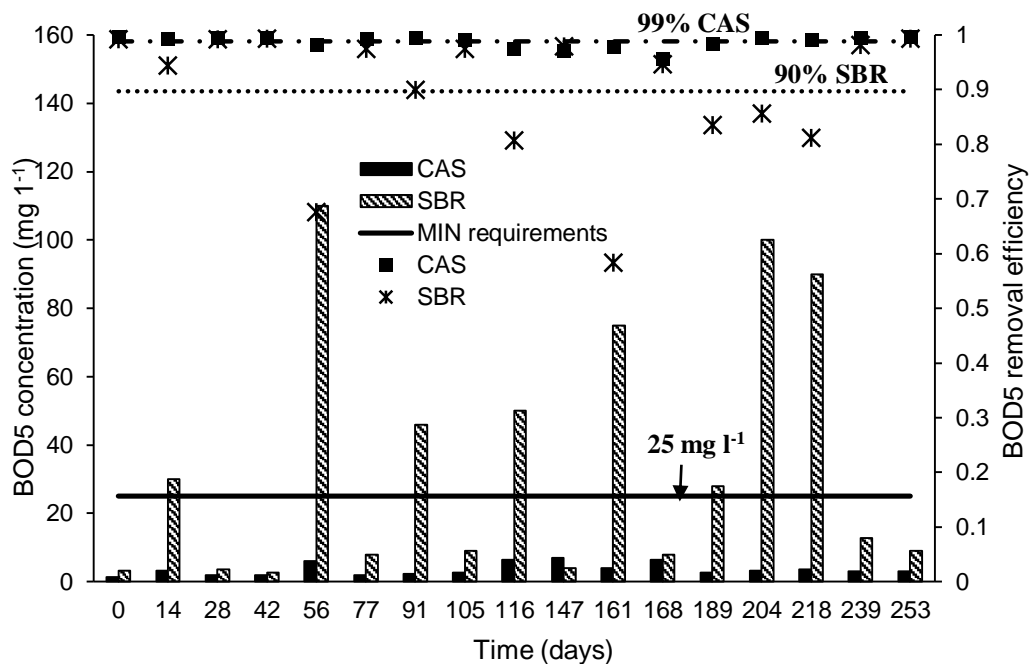


**Figure 3.** Long-term total Biochemical Oxygen Demand (BOD<sub>5</sub>) effluent concentrations, and its removal efficiencies in CAS and SBR systems. The average BOD<sub>5</sub> removal efficiency (— · —) in CAS and (·····) SBR.

The COD and BOD<sub>5</sub> removal efficiency were high in SBR at 105 day of the system operation. At the same day, the minimum value of SVI (33 mL g<sup>-1</sup> SS) and the maximum value of MLSS (1.2 g L<sup>-1</sup>) in the SBR was observed, the COD removal rate was 90% (at effluent - 48 mg L<sup>-1</sup>) and the COD removal rate was 97% (at effluent - 9 mg L<sup>-1</sup>). According to these results, the high COD and BOD<sub>5</sub> removal efficiency presented good performance in both systems. However, this parameter can be optimized for SBR in future investigations, aiming not only high TP, COD, BOD<sub>5</sub> removals, but also energy saving.

### Calculations of aeration costs

Modernization of the classic active sludge technology can be connected with reactor system rebuilding or building of new additional reactors in case of increasing wastewater load. Aeration is the main energy consumption stage (Drewnowski et al., 2019). To evaluate the efficiency of the possible technology, aeration costs were calculated. Usually, aeration operates 24 h per day in the classic CAS system, in SBR

the system is operated in a periodic cycle regime and aeration is necessary only for 21 h daily (210 min aeration on experimental system, 6 full cycles per day). Main equipment and its technological parameters in the full-scale station Adazi that were used for the calculations are summarised in Table 4. The calculations were based only on the changes of aeration regime.

Electricity consumption (E) per day for full scale aeration system with CAS process can be calculated by the following Eq. (1):

$$E(\text{CAS}) = (3 \cdot 37.0 \text{ kW} \cdot 24 \text{ h}) + (6 \cdot 2.75 \text{ kW} \cdot 24 \text{ h}) + (3 \cdot 2.5 \text{ kW} \cdot 24 \text{ h}) + (2.6 \text{ kW} \cdot 8 \text{ h}) = 3260.8 \text{ kWh} \quad (1)$$

Electricity consumption (E) per day for full scale aeration system with SBR can be calculated by the following Eq. (2):

$$E(\text{SBR}) = (3 \cdot 37.0 \text{ kW} \cdot 21 \text{ h}) + (6 \cdot 2.75 \text{ kW} \cdot 21 \text{ h}) + (3 \cdot 2.5 \text{ kW} \cdot 21 \text{ h}) + (2.6 \text{ kW} \cdot 8 \text{ h}) = 2855.8 \text{ kWh} \quad (2)$$

CAS ekspluatation costs per day (EURd (CAS)) can be calculated by Eq. (3):

$$\text{EURd (CAS)} = 3260.8 \text{ kWh} \cdot 0.12 \text{ kWh EUR}^{-1} = 391.3 \text{ EUR} \quad (3)$$

SBR ekspluatation costs per day (EURd (SBR)) can be calculated by Eq. (4):

$$\text{EURd (CAS)} = 2855.8 \text{ kWh} \cdot 0.12 \text{ kWh EUR}^{-1} = 342.7 \text{ EUR} \quad (4)$$

CAS ekspluatation costs per year (EURy (CAS)) can be calculated by Eq. (5):

$$\text{EURy (CAS)} = 391.3 \text{ EUR} \cdot 365 \text{ dn} = 142823.0 \text{ EUR} \quad (5)$$

SBR ekspluatation costs per year (EURy (SBR)) can be calculated by Eq. (6):

$$\text{EURy (SBR)} = 342.7 \text{ EUR} \cdot 365 \text{ dn} = 125084.0 \text{ EUR} \quad (6)$$

Calculation of economy (E) can be calculated by Eq. (7):

$$E = (142823.0 \text{ EUR} - 125084.0 \text{ EUR}) / (142823.0 \text{ EUR}) \cdot 100\% = 12\% \quad (7)$$

Each of the CAS reactors at full scale WWTP is equipped 3 compressors and one mixer. The exploitations costs per year are calculated by Eq. (8). Taking into account the fact, that SBR type reactors take up less space (up to 75% smaller area), it can be predicted that only one compressor will be necessary for the aeration. Thus, the predicted economy can be calculated by following Eqs (9–12).

**Table 4.** The main equipment and its technological paratemers of the Adazi full scale station

Equipment	Piece (n)	Technological paratemers
Aerotank	n = 3	1,500 m <sup>3</sup>
Compresors	n = 3 (type 1)	n = 6 (type 2)
	1,400 m <sup>3</sup> h <sup>-1</sup>	
	37.0 kW/ 28.3 kW	4.0 kW / 2.75 kW
	24 h / 7 d	24 h / 7 d
Mixers	n = 3	
	3.5 kW/ 2.5 kW	
	24 h / 7 d	
Sludge dewatering equipment	n = 1	
	140 kg h <sup>-1</sup> ; 2.6 kW	
	8 h / 7d	

Predicted CAS exploitations costs per year for full scale aeration system with CAS process (EURy (CAS1)p) can be calculated by the Eq. (8):

$$\text{EURy (CAS1)p} = \text{EURy (CAS)}/3 = 47607.7 \text{ EUR} \quad (8)$$

Predicted electricity consumption (Ep) per day for full scale aeration system with SBR can be calculated by the following Eq. (9):

$$\text{E(SBR)p} = (1 \cdot 37.0 \text{ kW} \cdot 21\text{h}) + (12.5 \text{ kW} \cdot 21 \text{ h}) + \frac{(2.6 \text{ kW} \cdot 8 \text{ h})}{3} = 836.4 \text{ kW} \quad (9)$$

Predicted SBR exploitations costs per day (EURd (SBR)p) can be calculated by the Eq. (10):

$$\text{EURd (CAS)p} = 836.4 \text{ kWh} \cdot 0.12 \text{ kWh EUR}^{-1} = 100.4 \text{ EUR} \quad (10)$$

Predicted SBR exploitation costs per year (EURy (SBR)p) can be calculated by the Eq. (11):

$$\text{EURy (SBR1)p} = 100.4 \text{ EUR} \cdot 365 \text{ dn} = 36634.3 \text{ EUR} \quad (11)$$

Calculation of economy due to the equipment amount (Eep.) (12):

$$\text{Eeq.} = (47607.7 \text{ EUR} - 36634.3 \text{ EUR})/(47607.7 \text{ EUR}) \cdot 100\% = 23\% \quad (12)$$

Full market search on appropriate equipment was not performed within this study. To calculate the exploitation costs and economy, the technological parameters of existing equipment were taken into account. Therefore, the estimations can be regarded as approximate and minimal. In case of full scale-larger size equipment, the economy is expected to be higher.

## CONCLUSIONS

This study demonstrated that the removal efficiency of phosphorus reached about 99% at wastewater treatment plant with CAS system. At the same time, the maximum removal efficiency was 88% using SBRs, when the operating parameters were optimized (MLSS - 1.2 g L<sup>-1</sup> and SVI - 33 mL g<sup>-1</sup> SS). But, the SBR system has a flexibility to modify the process control conditions during the operational phases that allows SBR facilities to adapt to changing influent conditions and achieve effluent water quality parameters. The obtained results showed that AGS treatment is effective in biological phosphorus removal and has a good application potential in treatment of municipal wastewater even if stable aerobic activated granules have not developed. To conclude, the proposed SBRs system with the operation of the aeration system allows to reduce about 23% of the operating costs at WWTP.

**ACKNOWLEDGEMENTS.** This work has been supported by the Central Baltic INTERREG Programme within the project CB50 'Pilot watersheds as a practical tool to reduce the harmful inflows into the Baltic Sea – WATERCHAIN'. We thank Kaspars Neilands for technical assistance and Ltd. Adazu water for support during this research.

## REFERENCES

- Adav, S.S., Lee, D.J., Show, K.Y. & Tay, J.H. 2008. Aerobic granular sludge: recent advances. *Biotechnology Advances* **26**(5), 411–423.
- APHA. 2015. Standard Methods for the Examination of Water and Wastewater, 23<sup>rd</sup> edition. *American Public Health Association*, Washington DC.
- Barrios-Hernandez, M.L., Pronk, M., Garcia, H., Boersma, A., Brdjanovic, D., van Loosdrecht, M.C.M & Hooijmans, C.M. 2020. Removal of bacterial and viral indicator organisms in full-scale aerobic granular sludge and conventional activated sludge systems. *Water Research X* **6**, 100040.
- Bassin, J.P., Kleerebezem, R., Dezotti, M. & van Loosdrecht, M.C.M. 2012. Simultaneous nitrogen and phosphorus removal in aerobic granular sludge reactors operated at different temperatures. *Water Research* **46**, 3805–3816.
- Bhagowati, B. & Ahamad, K.U. 2018. A review on lake eutrophication dynamics and recent developments in lake modelling. *Ecohydrology & Hydrobiology* **1**, 155–166.
- Capodici, M., Corsino, S.F., Di Trapani, D., Torregrossa, M. & Viviani, G. 2019. Effect of biomass features on oxygen transferrin conventional activated sludge and membrane bioreactor systems. *Journal of Cleaner Production* **240**, 1118071.
- De Kreuk, M.K. 2006. *Aerobic granular sludge scaling up a new technology*. PhD thesis, Delft University of Technology, Delft, The Netherland, 199 pp.
- Drewnowski, J., Remiszewska-Skwarek, A., Duda, S. & Lagod, G. 2019. Aeration process in bioreactors as the main energy consumer in a wastewater treatment plant. Review of solutions and methods of process optimization. *Processes* **7**, 311. doi:10.3390/pr7050311
- European Economic Community (ECC). 1991. Council Directive 91/271/EEC of 21 May 1991 concerning Urban Waste Water Treatment. <https://eur-lex.europa.eu/legal-content/EN/TXT/?uri=CELEX:01991L0271-20140101>. Accessed 22.01.2020.
- Ge, J., Meng, X., Song, Y. & Terracciano, A. 2018. Effect of phosphate releasing in activated sludge on phosphorus removal from municipal wastewater. *Journal of Environmental science* **67**, 216–223.
- Gorham, T., Jia, Y., Shum, C.K. & Lee, J. 2017. Ten-year survey of cyanobacterial blooms in Ohio's waterbodies using satellite remote sensing. *Harmful Algae* **66**, 13–19.
- Gu., J., Xu, G. & Liu, Y. 2017. An integrated AMBBR and IFAS-SBR process for municipal wastewater treatment towards enhanced energy recovery, reduced energy consumption and sludge production. *Water Research* **110**, 262–269.
- Li, Y., Ding, L.B., Cai, A., Huang, G.H. & Horn, H. 2014. Aerobic sludge granulation in a full-scale sequencing batch reactor. *BioMed Research International* **2014**, 268789.
- Lochmatter, S., Gonzalez-Gil, G. & Holliger, C. 2013. Optimized aeration strategies for nitrogen and phosphorus removal with aerobic granular sludge. *Water Research* **47**, 6187–6197.
- LVS EN ISO 6060:1989. Water quality. Determination of the chemical oxygen demand.
- LVS EN ISO 11905–1:1998. Water quality. Determination of nitrogen. Method using oxidative digestion with peroxodisulfate.
- LVS EN 1899–2:1998. Water quality. Determination of biochemical oxygen demand after n days (BOD<sub>n</sub>). Part 2: Method for undiluted samples (modified ISO 5815:1989).
- LVS EN ISO 6878:2005 (part 7). Water quality. Determination of phosphorus. Ammonium molybdate spectrometric method.
- LVS EN 872:2007. Water quality – Determination of suspended solids. Method by filtration through glass filters.
- LVS EN ISO 10523:2012. Water quality. Determination of pH.
- Manas, A., Biscans, B. & Sperandino, M. 2011. Biologically induced phosphorus precipitation in aerobic granular sludge process. *Water Research* **45**, 3776–3786.

- Meerburg, F.A., Boon, N., Van Winckel, T., Vercamer, J.A.R., Nopens, I. & Vlaeminck, S.E. 2015. Toward energy-neutral wastewater treatment: A high-rate contact stabilization process to maximally recover sewage organics. *Bioresource Technology* **179**, 373–381.
- Nancharaiyah, Y.V. & Kiran Kumar Reddy, G. 2018. Aerobic granular sludge technology: mechanisms of granulation and biotechnological applications. *Bioresource Technology* **247**, 1128–1143.
- Pronk, M., de Kreuk, M.K., de Bruin, B., Kamminga, P., Kleerebezem, R. & van Loosdrecht, M.C.M. 2015. Full scale performance of the aerobic granular sludge process for sewage treatment. *Water Research* **84**, 207–214.
- Qui, G. & Ting, Y.P. 2014. Direct phosphorus recovery from municipal wastewater via osmotic membrane bioreactor (OMBR) for wastewater treatment. *Bioresource Technology* **170**, 221–229.
- Tang, B., Qui, B., Huang, S., Yang, K., Bin, L., Fu, F. & Yang, H. 2015. Distribution and mass transfer of dissolved oxygen in a multi-habitat membrane bioreactor. *Bioresource Technology* **182**, 323–328.
- Tihomirova, K., Denisova, V., Golovko, K., Kirilina-Gutmane, O., Mezule, L. & Juhna, T. 2019. Management of wastewater from landfill of inorganic fiberglass. *Agronomy Research* **17**(S1), 1216–1226.
- Wu, X., Huang, J., Lu, Z., Chen, G., Wang, J. & Liu, G. 2019. *Thiothrix eikelboomii* interferes oxygen transfer in activated sludge. *Water Research* **151**, 134–143.
- Yan, P., Guo, J.S., Wang, J., Chen, Y.P., Ji, F.Y., Dong, Y., Zhang, H. & Ouyang, W.J. 2015. Enhanced nitrogen and phosphorus removal by an advanced simultaneous sludge reduction, inorganic solids separation, phosphorus recovery, and enhanced nutrient removal wastewater treatment process. *Bioresource Technology* **183**, 181–187.
- Yan, X., Xu, X., Wang, M., Wang, G., Wu, S., Li, Z., Sun, H., Shi, A. & Yang, Y. 2017. Climate warming and cyanobacterial blooms: looks at their relationships from a new perspective. *Water Research* **125**, 449–457.
- Zhang, Q., Hu, J. & Lee, D.J. 2016. Aerobic granular processes: current research trends. *Bioresource Technology* **210**, 74–80.



## **Thermal decontamination of sewage sludge**

L. Dubova<sup>1,\*</sup>, N. Strunnikova<sup>2</sup>, N. Cielava<sup>3</sup>, I. Alsina<sup>1</sup>, O. Kassien<sup>4</sup> and  
A. Bekker<sup>2</sup>

<sup>1</sup>Latvia University of Life Sciences and Technologies, Faculty of Agriculture, Institute of Soil and Plant Sciences, 2 Liela street, LV-3001 Jelgava, Latvia

<sup>2</sup>Ekosoil Ltd, 26 Academy street, UA65009 Odessa, Ukraine

<sup>3</sup>Latvia University of Life Sciences and Technologies, Laboratory of Biotechnologies, 1 Strazdu street, LV-3004 Jelgava, Latvia

<sup>4</sup>Earth Revival, Ltd, Maskavas street 57-3, LV-1003 Riga, Latvia

\*Correspondence: Laila.Dubova@llu.lv

**Abstract.** Every year a huge amount of sewage sludge is formed at municipal wastewater treatment plants. Sewage sludge contains a sufficient amount of biogenic elements and organic components, which characterizes them as possible raw materials for the production of organic fertilizers. However, direct incorporation of these sediments into the soil is impossible due to the fact that, in addition to useful organic and mineral components, they contain pathogens, viruses and helminth eggs. The aim of the study was to optimise thermal disinfection conditions for preparing of safety sewage sludge fertilizer. Laboratory studies were carried out using sediments from wastewater treatment plants of some cities. During laboratory experiments, the conditions for thermal disinfection of sediments – the thickness of the sediment layer, the air temperature in the disinfection furnace, and the treatment time of the sediment – were determined. When conducting industrial tests of a conveyor-type sediment decontamination furnace, the operating conditions of the furnace were determined, i.e., the temperature regimes of the sludge heating zone, the decontamination zone and the cooling zone, and the optimum parameters of the sludge layer thickness on the conveyor and the conveyor speed were determined.

**Key words:** layer thickness, movement speed, organic fertilizers, sewage sludge, thermal disinfection, residence time.

## **INTRODUCTION**

Every year, a huge amount of sewage sludge is formed at municipal wastewater treatment plants, which are aqueous suspensions or sludges with a high content of organic substances of different composition (Lukasevich & Barskaja, 2007). Significant health hazard for sewage sludge relates to the wide range of pathogenic microorganisms which could present in sludge from municipal or industrial wastewater. Therefore, hygienic principles must be followed in processing, storage or agricultural use of sewage sludge (Romdhana et al., 2009). The situation is exacerbated by the constant increase in the population of the Earth and followed increased amounts of municipal sewage sludge.

On the other hand, population growth requires a significant increase in the production of food products, including agricultural products, which is impossible

without increasing soil fertility. It is possible to increase soil fertility and reduce its degradation by use of organic fertilizers. The main source of organic fertilizers is livestock enterprises and poultry farms. However, these enterprises are not able to fully provide agriculture with high-quality organic fertilizers. The deficit can be compensated by fertilizers obtained from municipal sewage sludge (MSS) (Alaru et al., 2009, Raheem et al., 2018).

The content of biogenic elements in sewage sludge is comparable to their content in manure, commonly used as organic fertilizer. Municipal sewage sludge also contains valuable inorganic ingredients such as N, P, K, Ca, S and Mg. Bacterial constituents (proteins, lipids etc.) and their decay products coupled with inorganic matter and cellulose form the chemical structure of sewage sludge. In addition, the use of sludge as a fertilizer allows largely recoup the costs associated with wastewater treatment (Charnok, 1983, Raheem et al., 2018).

However, direct incorporation of these sediments into the soil is impossible due to the fact that, in addition to useful organic and mineral components, they contain pathogens, viruses and helminth eggs. Sludge is unstable and after its application into the soil, the biochemical processes continue, leading to the release of harmful odorous substances to the environment.

To use sewage sludge as fertilizer, it is necessary to solve the following tasks:

- to decontaminate sediments, i.e., to reduce the content of pathogenic microorganisms to the required standards;
- to neutralize sediments, i.e., detoxify sediments and reduce the content of harmful substances in them to the permitted limits;
- to eliminate the unpleasant smell of sludge, i.e., to ensure the complete flow of biochemical processes, accompanied by release of foul-smelling substances into the atmosphere;
- to achieve maturation of fertilizer, i.e. to transfer organic matter in the sediment into forms that are easily absorbed by plants (Romdhana et al., 2009, Kelessidis & Stasinakis, 2012, Lombardi et al., 2017, Raheem et al., 2018).

These tasks can be solved by subjecting sediments to a standard composting scheme, for example, having sustained sludge in piles for a long time (up to several months and even years). This solution of the tasks has a number of drawbacks, of which the most significant is environmental pollution (soil, atmosphere and groundwater) with harmful substances and pathogenic microorganisms, as well as the need for specially prepared areas for the composting (Alvarenga et al., 2015; Ciešlik et al., 2015; Raheem et al., 2018). According to Heiba et al. (2016) more efficient and safer use of sewage sludge could be achieved through development of novel and more efficient composting technologies to solve environmental problems related to sludge use in agriculture.

The aim of this study was to improve the treatment conditions of municipal sewage sludge as the first stage in the production of organic fertilizers.

## MATERIALS AND METHODS

**Laboratory experiments** were conducted at the Laboratory of company ‘Ecosoil’ (1<sup>st</sup> set of experiments) and Latvia University of Life Sciences and Technologies (2<sup>nd</sup> set of experiments).

1<sup>st</sup> set of experiments at the Laboratory of company 'Ecosoil' were conducted to determine the optimal regime of heat treatment in the experimental heating chamber for determining the conditions for effective decontamination of sediments. Heating chamber was equipped with electric heaters, a thermocouple and a temperature controller.

The experimental procedure was as follows: sediments of 500–1,000 g were placed in a special basket; the basket was placed in a heating chamber. The temperature in the chamber and inside the sludge was recorded. Two treatment regimes, differed in temperature mode and the duration of heating after reaching the specified temperature, were tested:

1. Sewage sludge was preheated to a temperature of 70–80 °C, the sediment was kept 180 minutes;
2. Sludge was preheated to a temperature of 140–150 °C, the sediment was kept 15 minutes.

The efficiency of decontamination was controlled according to the results of the determination of *Escherichia coli* (expressed as colony-forming unit (CFU) per 1 g of dry matter of the treated sludge. Bacteriological studies were carried out in a specialized laboratory 'Bactochem' of Israel.

2<sup>nd</sup> set of experiments were carried out at Latvia University of Life Sciences and Technologies. Dehydrated sewage sludge (dry matter 15–17%) was obtained from two waste water treatment plants in Zemgale region, Latvia. Sewage sludge was placed on polypropylene trays (l : w : h = 40.0 : 29.0 : 3.0 cm). The sludge layer was  $3 \pm 0.5$  cm thick. The trays were placed in a heating chamber with a temperature of 150 °C. Pasteurization was carried out for 15 minutes from the time when the layer temperature reached 70 °C. After pasteurization samples were placed in test tubes. Total amount of microorganisms (MAFAM) was tested according LVS EN ISO 6222:1999, CFU of *E. coli* according LVS ISO 16649-2, and *Salmonella* spp. according LVS EN ISO 6579-1 was determined at Laboratory of Biotechnologies Latvia University of Life Sciences and Technologies.

### **Industrial Testing**

Industrial tests of thermal disinfection technology were carried out at the wastewater treatment plant of Odessa Vodokanal. For this, a conveyor oven with a total length of the heat-affected zone of 6 meters was designed and built. The furnace is designed to handle 25 tons of sediment with a humidity of 80% per day. The furnace has 3 zones (heating, disinfection, cooling zone), each of which has a length of 2 meters. The first and second zones of the furnace are equipped with electric heaters, each of the zones is equipped with temperature sensors allowing to control the temperature in this zone. Sediment enters the furnace through a special loading device, before entering the heating zone, it is distributed along the conveyor with a layer of thickness specified by adjusting the volume of the material supply and its distribution over the width of the conveyor. The rate of passage of sludge through the furnace is regulated by a special device and adapted to the thickness of sludge layer so that the residence time of the sludge in the zone of disinfection is 15 minutes.

## RESULTS AND DISCUSSION

The 1<sup>st</sup> set of experiments showed that sediment in the basket (layer thickness was 1–5 cm), and the air temperature in the chamber 70–80 °C, even with a significant warm-up time up to 3 hours, the sediments were not disinfected (Table 1). The number of CFU reached an extremely high value, i.e., 1,100,000 CFU g<sub>dw</sub><sup>-1</sup> in 5 cm sewage sludge layer. Decrease of layers thickness reduced CFU of *E. coli* (coefficient of correlation  $r = 0.995$ ) (Table 1).

The results showed that holding the sediment at a temperature of 70–80 °C in a heating chamber even in a thin layer for 180 minutes does not provide disinfection, since the sediment does not warm up in its entirety. The heat consumption for heating the sediment, heating the water and its evaporation is determined by the heat capacity of the sediment and water, as well as the heat of evaporation of the water. The energy calculations showed that the greatest amount of heat is spent on heating the water and its evaporation from the sludge, it is obvious that the

heat energy input to the sludge material under these conditions is not sufficient to ensure its heating to the temperature necessary for disinfection. Only after enough energy is supplied to the system for these processes, heating of the sediment begins, the effectiveness of which depends on the thermo–physical characteristics of the sediment – thermal diffusivity ( $a$ ), heat capacity ( $c_p$ ) and thermal conductivity of the sediment ( $\lambda$ ).

In accordance with the Fourier law (Antipov et al., 2001), the heat flux ( $Q$ ) passing through the material is directly proportional to the temperature gradient ( $\Delta T$ ), the area  $S$  through which the heat flux passes, and the thermal conductivity coefficient  $\lambda$ .

$$Q = -\lambda \cdot \Delta T \cdot S \quad (1)$$

On the other hand, the thermal diffusivity of the sediment depends on its thermal conductivity, heat capacity and density, as well as on the thickness of the sediment layer and the time of exposure of thermal energy to the sediment and can be described by the equations:

$$a = \frac{\lambda}{c_p \cdot \rho} \quad (2)$$

$$a = \frac{R^2}{4 \cdot Z^2 \cdot \tau} \quad (3)$$

where  $a$  – thermal diffusivity;  $\lambda$  – coefficient of thermal conductivity;  $c_p$  – heat capacity;  $\rho$  – sludge density;  $R$  – sludge layer thickness;  $\tau$  – time of thermal energy impact on the sludge;  $Z$  – coefficient determined experimentally.

**Table 1.** Sediment disinfection results with adjustable layer thickness at air temperature in the heating chamber 70–80 °C

Nr.	Time of exposition, min	Thickness of layer, cm	Temperature in heating chamber, °C	Temperature in sludge, °C	<i>E.coli</i> , CFU
1	180	5	70–80	40–45	1,100,000
2	180	4	70–80	45–50	123,000
3	180	3	70–80	45–50	24,000
			70–80	45–50	,
			70–80	50–55	

From Eqs (2) and (3) it follows that the greater the thermal conductivity of the sediment, the greater the thickness of the layer can be heated to achieve the required temperature for a certain time.

According to Antipov et al. (2001), the coefficient of thermal conductivity of precipitation depends on its water content. Considering that the water content of the sediments was reduced by centrifugation to 80%, the temperature range was experimentally found to provide a heat flux sufficient to reach a temperature in the sediment layer of 70–80 °C and decontaminate the sediment for 15–20 minutes.

The 2<sup>nd</sup> set of experiments was carried out in the chamber where air temperature was maintained in the range of 140–150 °C. Other temperature ranges were also tested, but at lower temperatures, the results of disinfection were unstable, and the use of higher temperatures is impractical, as it will significantly affect the cost of fertilizer due to high energy costs. The indicators of bacterial contamination of the treated sludge fluctuated dramatically, i.e., *E.coli* appeared from  $\leq 3$  (no bacterial contamination) up to 11,000 CFU g<sub>dw</sub><sup>-1</sup>. This effect was caused by uneven heating of the sludge due to different thickness of the sludge layer, which did not provide the conditions for disinfection. Therefore, in further experiments, the sediment was leveled in thickness with a special roller. The layer thickness was varied within 1–5 cm. The air temperature inside the chamber was maintained within 140–150 °C. After installing the basket with sediment in the chamber, a sharp drop in temperature to 90–100 °C was observed, since intensive evaporation of water from the sediment began, but after 15–20 minutes the temperature again reached 140–150 °C, while temperature control in the sediment showed that after the temperature in the chamber had risen to 140–150 °C, it was 70–80 °C in the sediment. The sediment was kept under these conditions for 15 minutes (Table 2).

Results showed that the selected temperature range in the heating chamber provides stable disinfection performance even at a layer thickness

of 5 cm in 15 minutes. Increasing the thickness of the sludge layer to 7 or more centimeters led to unstable results. Therefore, it was recommended to vary the design of an experimental industrial disinfection furnace with a sediment layer 2–5 cm. A smaller layer thickness is impractical because it reduces the productivity of the heating chamber.

Experiments done at Latvia University of Life Sciences and Technologies approved final experiments done in Ukraine. Thermal treatment for 15 minutes killed *E. coli* and *Salmonella enterica*, but CFU of MAFAM decreased 5.3 times (waste water treatment plant 1) and 12.1 times (waste water treatment plant 2) (Table 3).

During pasteurization the content of dry matter in the sludge from the 1<sup>st</sup> Waste water treatment plant increased by 4.8% (from 144.4 g kg<sup>-1</sup> to 151.3 4 g kg<sup>-1</sup>), whereas from Waste water treatment plant 2 – by 8.9% (from 158.0 g kg<sup>-1</sup> till 172.1 g kg<sup>-1</sup>), respectively.

**Table 2.** Results of sediment disinfection with adjustable layer thickness at air temperature in the heating chamber 140–150 °C

Nr.	Time of exposition, min	Thickness of layer, cm	Temperature in heating chamber, °C	Temperature in sludge, °C.	<i>E.coli</i> , CFU
1	15	5	140–150	70–80	< 3
2	15	4	140–150	70–80	< 3
3	15	3	140–150	75–85	< 3
4	15	2	140–150	85–90	< 3
5	15	1	140–150	85–90	

**Table 3.** Sediment disinfection results of two waste water treatment plants in Zemgale region, Latvia

Microorganisms, CFU g <sub>dw</sub> <sup>-1</sup>	Sewage sludge 1		Sewage sludge 2	
	Before treatment	After treatment	Before treatment	After treatment
<i>E.coli</i>	1.4×10 <sup>5</sup>	0	2.8×10 <sup>4</sup>	0
<i>Salmonella</i> spp	<i>Salmonella enterica</i>	0	0	0
MAFAM	4.1×10 <sup>6</sup>	7.8×10 <sup>5</sup>	3.4×10 <sup>6</sup>	2.8×10 <sup>5</sup>

### Industrial Testing

Results of industrial testing at the wastewater treatment plant of Odessa Vodokanal showed that in the heating zone, the sludge is heated from ambient temperature to 70 °C, in the disinfection zone, the sludge continues to warm to 80–90 °C and its disinfection, in the cooling zone, the sediment cools to 60–70 °C. The disinfected sediment from the furnace is fed into a special bunker, in which it is cooled to a temperature of 40–50 °C and transferred to further processing (Table 4).

**Table 4.** Performance indicators of industrial decontamination in pasteurization chamber

Thick-ness of layer, cm	Move-ment rate, cm min <sup>-1</sup>	1 <sup>st</sup> zone		2 <sup>nd</sup> zone		3 <sup>rd</sup> zone		Conta- mination <i>E.</i> <i>coli</i> CFU
		t entrance	t exit	t entrance	t exit	t entrance	t exit	
2	5	20	110	120	160	150	80	0
2	10	20	110	120	160	150	80	0
3	5	20	110	120	160	150	90	0
3	10	20	110	120	160	150	80	0
4	5	20	110	120	160	150	85	0
4	10	20	110	120	160	150	90	300
5	5	20	110	120	160	150	85	1,500
5	10	20	110	120	160	150	80	3,000

As can be seen from the presented data, stable indicators of sediment disinfection are achieved with a layer thickness of not more than 3 cm and a movement rate up to 10 cm min<sup>-1</sup>. With a layer thickness of 4 cm and a rate of 10 cm min<sup>-1</sup> disinfection does not occur completely, and with a thickness of 5 cm disinfection is not achieved even at a speed of 5 cm min<sup>-1</sup>.

Thus, based on the required performance of the decontamination in pasteurization chamber, a layer thickness of no more than 3 cm can be recommended with a conveyor speed of 10 cm min<sup>-1</sup>.

## CONCLUSIONS

1. To ensure disinfection of the whole volume of sludge, it is necessary to maintain a temperature of 140–150 °C in the heating chamber, while the temperature reaches 70–80 °C in the entire volume of sediment, which ensures reliable performance in 15 minutes disinfection.

2. Complete disinfection of sediment occurs at a layer thickness of no more than 5 cm. Reduction of the thickness of the sludge layer increases microbiological quality of material.

3. An increase in the duration of temperature exposure without an increase in its intensity seems to be irrational, since a further increase in the thickness of the layer unnecessarily slows down the process of disinfection of large amounts of sludge.

4. Based on laboratory studies, a conveyor thermal disinfection furnace was constructed at the municipal waste water treatment facilities in Odessa, including a heating zone, a disinfection zone and a cooling zone with established optimum temperature conditions 20–110 °C, 120–160 °C and 150–80 °C respectively and with an optimum sediment layer thickness of 3 cm and conveyor speed of 10 cm min<sup>-1</sup>, providing complete disinfection of the sediment.

ACKNOWLEDGEMENTS. This research is being conducted based on agreement signed between SIA 'Earth Revival' and SIA 'ETKC' (Centre of Competence for Energy and Transportation) within the framework of project Nr. 1.2.1.1/18/A/001 co-funded by the European Regional Development Fund.

## REFERENCES

- Alaru, M., Noormets, M., Raave, H., Lauk, R., Selge, A. & Viiralt, R. 2009. Farming systems and environmental impacts. *Agronomy Research* **7**(1), 3–10.
- Alvarenga, P., Mourinha, C., Farto, M., Santos, T., Palma, P., Sengo, J., Morais, M-C. & Cunha-Queda, C. 2015. Sewage sludge, compost and other representative organic wastes as agricultural soil amendments: Benefits versus limiting factors. *Waste Management* **40**, 44–52.
- Antipov, S.T., Kretov, I.T. & Ostrikov, A.N. 2001. *Machines and equipment for food production*. Vishaja shola, 703 pp.(in Russian).
- Charnok, G. 1983. Euro code seeks safer sludge. *New Civ. Eng. Int.* **146**, 146–147.
- Ciešlik, B.M., Namieśnik, J. & Konieczka, P. 2015. Review of sewage sludge management: standards, regulations and analytical methods. *Journal of Cleaner Production* **90**, 1–15.
- Haiba, E., Nei, L., Ivask, M., Peda, J., Järvis, J., Lillenberg, M., Kipper, K. & Herodes, K. 2016. Sewage sludge composting and fate of pharmaceutical residues – recent studies in Estonia. *Agronomy Research* **14**(5), 1583–1600.
- Kelessidis, A. & Stasinakis, A.S. 2012. Comparative study of the methods used for treatment and final disposal of sewage sludge in European countries. *Waste Manag.* **32**(6), 1186–1195.
- Lombardi, L., Nocita, C., Bettazzi, E., Fibbi, D. & Carnevale, E. 2017. Environmental comparison of alternative treatments for sewage sludge: An Italian case study, *Waste Management* **69**, 65–376. <https://doi.org/10.1016/j.wasman.2017.08.040>
- Lukasevich, O.D. & Barskaja, I.V. 2007. Environmental problems of treatment and disposal of sewage sludge. *Ekologija promishlenovo proizvodstva* **3**, 68–75 (in Russian).
- Raheem, A., Sikarwar, V.S., He, J., Dastyar, W., Dionysiou, D., Wang, W. & Zhao, M. 2018. Opportunities and Challenges in Sustainable Treatment and Resource Reuse of Sewage Sludge: A Review. *The Chemical Engineering Journal* **337**, 616–641
- Romdhana, M.H., Lecomte, D., Ladevie, B. & Sablayrolles, C. 2009. Monitoring of pathogenic microorganisms contamination during heat drying process of sewage sludge. *Process Safety and Environmental Protection* **87**, 377–386.

## **Comparison of airflow homogeneity in Compost Dairy Barns with different ventilation systems using the CFD model**

B. Fagundes<sup>1</sup>, F.A. Damasceno<sup>2,\*</sup>, R.R. Andrade<sup>3</sup>, J.A.O. Saraz<sup>4</sup>, M. Barbari<sup>5</sup>,  
F.A.O. Vega<sup>4</sup> and J.AC. Nascimento<sup>2</sup>

<sup>1</sup>Professional Faculty, Department of Climatization Engineering, Porto Alegre, Tocantins Street, 937, n. 8, BR91.540.420 Porto Alegre, Brazil

<sup>2</sup>Federal University of Lavras, Department of Engineering, BR37200-000 Lavras, Minas Gerais, Brazil

<sup>3</sup>Federal University of Viçosa, Department of Agricultural Engineering, Av. Peter Henry Rolfs, s/n Campus University of Viçosa, BR36570-900, Viçosa, Minas Gerais, Brazil

<sup>4</sup>Univeridad Nacional de Colombia, Agrarian Faculty, Department of Agricultural and Food Engineering, Carrera 65 n. 59A – 110, Bloque 14 - Oficina 430, Medellin, Colombia

<sup>5</sup>University of Florence, Department of Agriculture, Food, Environment and Forestry, Via San Bonaventura, 13, IT50145 Firenze, Italy

\*Correspondence: [flavio.damasceno@ufla.br](mailto:flavio.damasceno@ufla.br)

**Abstract.** In the pursuit of high milk productivity, producers are using confinement systems in order to improve performance and animal welfare. Among the housing systems, the Compost bedded-pack barns (CBP) stand out. In these barns a bedding area is provided inside, where cows move freely. Generally this area is covered with carbon source material (such as sawdust or fine dry wood shavings) which together with manure, thanks a regular mechanically stirring, ensures the aerobic composting process. The ventilation in these facilities has the function of dehumidifying the air, improving the air quality, drying the bedding, improving the thermal comfort conditions of the confined animals. This work aimed at validating a computational model using Computational Fluid Dynamics (CFD) to determine the best homogeneity of airflows generated by different forced ventilation systems used in CBP barns. Two CBP barns were compared with different ventilation systems: high volume low speed (HVLS) and low volume high-speed (LVHS) fans. The results showed that the proposed model was satisfactory to predict the flows generated by both types of fans. It was concluded that the use of HVLS fans produced a more homogeneous airflow when compared to LVHS fans. The use of mechanical ventilation in tropical conditions is necessary for the proper functioning of the system. In this study, the systems used promoted the increase in air speed to levels close to adequate.

**Key words:** airflow, animal housing, compost-bedded pack barn, dairy cows, simulation.

## **INTRODUCTION**

In dairy cattle farming, one of the major concerns of producers is the effect that the breeding environment can have on animals during lactation, especially in summer. High air temperature values are included among the main stressors that negatively affect the performance of lactating cows, especially in temperate climates.



The housing system can affect dairy cow's welfare and performance and have a major influence on the ecological footprint and the consumers' perception of dairy farming. Since shifting from tie-stall to loose housing, many different systems have been developed (Leso et al., 2020). Among the housing systems, the Compost bedded-pack barns (CBP) stand out.

The CBP are a relatively new loose housing system for dairy cows that seem to offer improved cow comfort (Leso et al., 2013; Leso et al., 2019). In compost barns the cows are free to move in a bedding area used for resting and exercise. Usually a feeding alley is present in the barn, with concrete floor. There are no obstacles to the movement of the animals like individual stalls of freestall housing (Oliveira et al., 2019b).

The main characteristic of the CBP system is to have a compost bedded pack resting area, consisting of carbon source material, which together with the animal excreta, thanks to the regular turning of this material, guarantees the main feature of the system, the degradation of organic material through microbiological decomposition (Janni et al., 2007).

The choice of the proper ventilation system is very important for its correct functioning in the CBP system, as it allows creating a comfortable thermal environment for the cows and the elimination of gases, dust and other pollutants, the maintenance of the air temperature and relative humidity of the bedding at levels suitable for composting (Damasceno, 2012). The main types of fans found in the CBP are: high volume and low speed (HVLS), and low volume and high speed (LVHS).

The evaluation of different ventilation systems in dairy cattle facilities, whether naturally or mechanically, were carried out through field studies by some authors (Endres et al., 2011; Lobeck et al., 2012; Oliveira et al., 2019a). However, there are limitations to carry out these studies, such as the difficulty in finding similar facilities in the same location and the high costs that must be paid for the experiments, among other factors. So, validated computer simulations can be carried out in the first phase of the study. Field tests of variables of interest are performed in a second phase.

The application of Computational Fluid Dynamics (CFD) in animal production is becoming increasingly important. The versatility, precision and ease of use offered by CFD makes it suitable to solve problems related to thermal environment in animal production facilities (Norton et al., 2007). Spatial and temporal solutions for air speed, air temperature, relative humidity and air pressure can be easily reproduced through the use of CFD simulations, reducing the number of field experiments.

The aim of this study was to evaluate and validate a computational model, using CFD, to determine the best homogeneity of air flows generated by different forced ventilation systems used in CBP.

## **MATERIALS AND METHODS**

### **Characterization of the evaluated CBP barns**

The experimental study was carried out in two CBP systems during the months of September and October 2018. One of the dairy farm was located in the Sete Lagoas, Minas Gerais, Brazil (CBP<sub>LVHS</sub>). The other animal facility was located in the Piracicaba, São Paulo, Brazil (CBP<sub>HVLS</sub>).

The evaluated CBP barns had dimensions of 20.0 m wide × 80.0 m long × 5.0 m side height. Both CBP barns had different ventilation systems and open sides. One CBP

barn had six High Volume Low Speed (HVLS) fans, placed horizontally, with a diameter of 7.3 m, speed of 50 rpm, power of 2.0 hp and a flow rate of  $478,500 \text{ m}^3 \text{ h}^{-1}$  each. The HVLS fans were distributed along the length of the CBP barn at a distance of 12.0 m at a height of 3.0 m.

The other CBP barn had twenty Low Volume High Speed (LVHS) fans, with a diameter of 2.0 m, rotation of 360 rpm, a power of 3.0 hp and a flow rate of  $120,000 \text{ m}^3 \text{ h}^{-1}$  each. The LVHS fans were distributed, in pairs, along the length of the CBP barn at a distance of 8.0 m at a height of 3.0 m.

The stirring of the bedding in the two CBP barns occurred twice a day, during the milking periods (5:00 am and 4:00 pm), with a modified cultivator on small tractor.

Holstein cows were housed in both CBP barns with an average production of 32 kg of milk per day. The stocky densities were  $12 \text{ m}^2 \text{ head}^{-1}$  in CBP<sub>LVHS</sub> and  $15 \text{ m}^2 \text{ head}^{-1}$  in CBP<sub>HVLS</sub>. Sawdust was used in the bedding area of the CBP<sub>HVLS</sub> and peanut shell in CBP<sub>LVHS</sub>.

### Field data collection

For the test and validation of the computational model, dry bulb temperature ( $T_{db}$ ), relative humidity (RH), air speed and direction ( $V_{air}$ ) and bed surface temperature ( $T_{bed}$ ) data at two-second intervals, for two days consecutive at each CBP barn, were collected. The data were collected at 27 distributed points, in a  $3 \times 9$  equidistant grid along the compost pack resting area at 0.50 m high (Fig. 1). For this, a portable digital thermo-hygrometer (Instrutherm®, mod. TI-400, with accuracy of  $\pm 1.0\%$ ) was used. In the case of  $V_{air}$ , a hot wire anemometer was used (Highmed®, mod. HM-385 with an accuracy of  $\pm 5.0\%$ ). The wind direction was checked with a windsock. An infrared thermometer (Highmed®, mod. HM-88C with  $\pm 2.0\%$  accuracy) was used to measure  $T_{bed}$ .

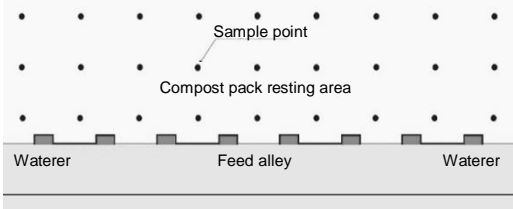


**Figure 1.** Spatial layout used for data collection.

### Geometry

The definition of the domain geometry represents the first stage of the simulation in CFD.

Domain geometry for this study was generated with the software SolidWorks® (Fig. 2). The simulations were carried out by means of software ANSYS® version 17 (available at the Federal University of Rio Grande do Sul, Mechanical Engineering).

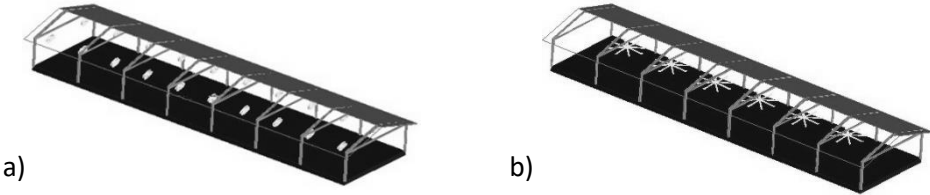


**Figure 2.** Geometries of CBP barns with different domains: a) LVHS and b) HVLS.

### Computational mesh

Due to the complexity of the geometry and the dimensions of the fans, we chose to use the software ANSYS ICEM CFD® for designing a computational mesh with tetrahedral cells.

Tests with different mesh sizes were conducted until there were no significant differences between measured and simulated data ( $p < 0.05$ ). As a result, a mesh of 3,805,719 tetrahedral elements (Fig. 3) was designed and used as the computational domain, which consisted of a system with 696,322 nodes. The Reynolds number for the proposed problem was  $2.0917 \times 10^7$ , which indicated a turbulent flow inside the CBP barns.

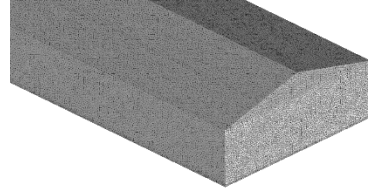


**Figure 3.** Mesh generated for implementation of the CFD model.

### Numeric modelling

In this study the solution of the Reynolds number average system extracted from the Navier – Stokes equations allowed to define the CFD technique.

The model concerning the non-isothermal fluid flow is defined by equations of continuity, momentum and energy. The equations are simplified as suggested by Fluent (2004) and Ahmadi & Hashemabadi (2008):

$$\nabla \cdot (\rho U) = 0 \quad (1)$$

$$\nabla \cdot (\rho U U) = \nabla p + [\mu_t (\nabla U + \nabla U^T)] \quad (2)$$

$$\nabla \cdot (-k \nabla T + \rho C_p T U) = Q \quad (3)$$

$\rho$  – density,  $\text{kg m}^{-3}$ ;  $U$  – velocity vector;  $p$  – static pressure,  $\text{N m}^{-2}$ ;  $T$  – tensor transposition;  $\mu_t$  – fluid dynamic viscosity,  $\text{kg m}^{-1} \text{s}^{-1}$ ;  $\kappa$  – turbulent kinetic energy,  $\text{m}^2 \text{s}^{-2}$ ;  $C_p$  – specific heat,  $\text{W kg}^{-1} \text{K}^{-1}$ ;  $Q$  – term related to source,  $\text{W m}^{-3}$ .

The k- $\epsilon$  standard model was used to model the turbulent flow. The viscosity ( $\mu_t$ ) is calculated as relationship between turbulent kinetic energy ( $\kappa$ ) and dissipation of turbulent kinetic energy  $\epsilon$ .

$$\mu_t = C_\mu \rho \frac{\kappa^2}{\epsilon} \quad (4)$$

Eqs 5 and 6 allow to calculate k- $\epsilon$  values:

$$-\nabla \cdot \left[ \left( \eta + \rho \frac{C_\mu k^2}{\sigma_k \epsilon} \right) \nabla_k \right] + \rho U \cdot \nabla_k = \rho C_\mu \frac{k^2}{\epsilon} + (\nabla U + \nabla U^T)^2 - \rho \epsilon \quad (5)$$

$$-\nabla \cdot \left[ \left( \eta + \rho \frac{C_\mu k^2}{\sigma_\epsilon \epsilon} \right) \nabla_\epsilon \right] + \rho U \cdot \nabla_\epsilon = \rho C_{\epsilon 1} C_{\mu k} (\nabla U + \nabla U^T)^2 - \rho C_{\epsilon 2} \frac{\epsilon^2}{k} \quad (6)$$

$\epsilon$  – dissipation of turbulent kinetic energy,  $\text{m}^2 \text{s}^{-3}$ ;  $\eta$  – ratio between mean flow and temporal scale;  $C_\mu = 0.09$ ;  $C_{\epsilon 1} = 1.44$ ;  $C_{\epsilon 2} = 1.92$ ;  $\sigma_k = 1.3$ ;  $\sigma_\epsilon = 1.0$ .

### Boundary conditions

The purpose of the CFD simulations was to carry out an evaluation of the flow homogeneity, that is, to verify the flow behaviour and its distribution in the compost pack resting area.

In simulations ANSYS CFX software was used assuming four conditions (a: steady state; b: single-phase flow; c: thermal energy condition; d: incompressible and turbulent flow).

The simulated solution was validated using experimental data. The mean residue for linear systems technique (RMS, Root Mean Square) was considered with a tolerance of  $10^{-4}$  as convergence criterion and a limit of 100 interactions.

Additionally, to create the CFD model, dimensions and operating conditions of the air velocity distribution in CBP barns model were used. Then, the measured values coming from the experimental CBP barn for boundary conditions were averaged out and implemented to the computational model as presented in Table 1.

**Table 1.** Average of input values used as the boundary conditions

Fan speed (LVHS)	360 rpm
Fan speed (HVLS)	50 rpm
Air dry bulb temperature	25.0 °C
Bed surface temperature	25.0 °C
Atmospheric pressure	0 Pa

The geometry of the fans was suppressed, due to the high computational cost that would be involved in the complete modelling of the fans. To represent the fans, the condition (Momentum Source) was applied to the cylinders representative of the fans. This condition is an adequate approach for the evaluation in question, since it correctly represents the flow and velocities obtained experimentally.

The condition of source of moment makes use a determined force per unit of volume. The force in Newtons generated by the fan in the volume that it occupies was estimated. In addition, the rotation speed of each fan was properly used for the cylinders.

A comparison of data coming from CFD model and data obtained in experimental trials was carried out. As recommended by ASTM (2002) (Eq. 7 and 8), the normalized mean square error (NMSE) was used to verify the agreement between experimental and model data. The same procedure and has been followed to validate the computational model in several studies with CFD (Zhao et al., 2007; Saraz et al., 2012). In this study a sample size of 160 data points was considered to calculate the NMSE. A high degree of agreement between measured and predicted values yields in an NMSE that is equal to 0. However, NMSE values lower than 0.25 are considered good indicators of agreement.

$$NMSE = \frac{(\overline{C_p} - C_o)^2}{(C_{pm} \cdot C_{om})} \quad (7)$$

$$(\overline{C_p} - C_o)^2 = \frac{\sum (C_{pi} - C_{oi})^2}{n} \quad (8)$$

$C_{pi}$  – predicted value;  $C_{oi}$  – observed value;  $C_{pm}$  – average predicted value;  $C_{om}$  – observed value;  $n$  – number of measurements.

# RESULTS AND DISCUSSION

For validation, a comparison between  $CBP_{LVHS}$  and  $CBP_{HVLS}$  of the data found by the CFD model and by experimental trials points out that the mean values of air velocity coming from the experiments show NMSE values of 0.12 and 0.10, respectively. Therefore, a good agreement between the results is reached. As conclusion, the average behaviour of air velocity inside the CBP barns with different ventilation systems can be predicted by means of the developed CFD model (Table 2).

**Table 2.** Comparison between model and experimental data for air velocity ( $m s^{-1}$ )

Data	$CBP_{LVHS}$	$CBP_{HVLS}$	
	Experiment	CFD Model	CFD Model
Mean	3.98	4.11	2.07
NMSE	0.12		0.10

The relationship between air velocity data coming from experimental tests and from the model is illustrated in Fig. 4. Results of the application of a simple t-test for the null hypothesis ( $H_0$ ) that the difference between model and experimental values of air velocity inside the  $CBP_{LVHS}$  is equal to 0, were in favour of  $H_0$  ( $p = 0.877$ ). When fit to a linear model the correlation coefficient between experimental and model data is 0.949. So, the regressed model gives a good explanation of the change in this variable (F test,  $P < 0.0001$ ), with  $2.5 m s^{-1}$  average error (Fig. 4, a).

The mean air velocity at the  $CBP_{HVLS}$  calculated with the CFD model was  $1.97 \pm 0.9 m s^{-1}$ . The difference with the experimental mean air speed ( $2.07 \pm 0.83 m s^{-1}$ ) is not significant (simple t-test,  $p = 0.718$ ). The linear model allowed explaining the variability of air velocity between model and experiment data (F test,  $P < 0.0001$ ;  $R^2$ : 0.937) (Fig. 4b).

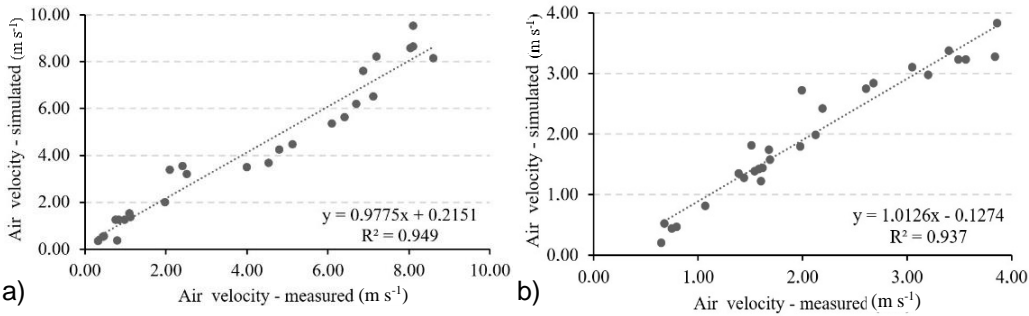


**Figure 4.** Relationship between model and experiment data for air velocity in CB barns with different ventilation systems: a) LVHS and b) HVLS.

The airflow lines and velocity distribution on the surface of compost pack resting area in the modelled  $CBP_{LVHS}$  barn can see in Fig. 5. The results demonstrate the current air flow lines for the HVLS fan (Fig. 5, a) that may undergo small variations. These variations are of small magnitude and do not significantly affect the results. The current air flow lines, through an HVLS fan, coming from the fan, close to the bed surface, is oriented in all directions. Below each fan, specifically in the centre, is a region of lower

speeds (Fig. 5, b). Higher speeds are developed around this centre of the barn (ranging from 2.5 to 3.8 m s<sup>-1</sup>).

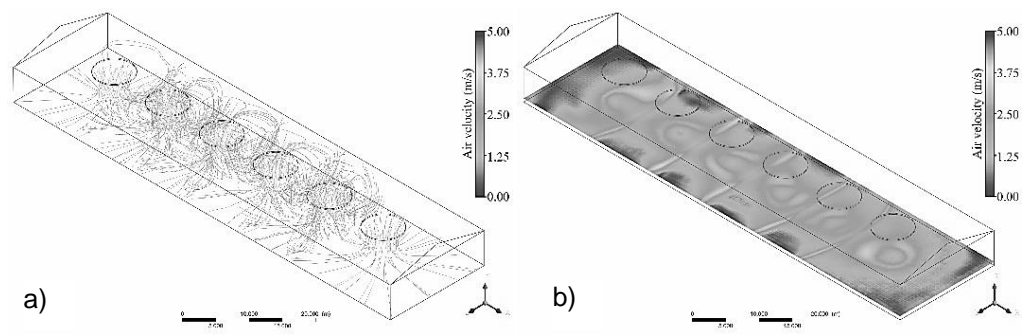


**Figure 5.** Results of CFD simulation of CBP barns with HVLS ventilation system: a) air flow lines and b) air velocity distribution on the surface of compost pack resting area.

According to Black et al. (2013), in CBP facilities, the ventilation should be provided such that the  $V_{\text{air}}$  is close to 1.8 m s<sup>-1</sup> throughout the entire CBP, so that it can dry the bed, remove gases and favour the heat exchanges between the animal and the environment. Oliveira et al. (2019a), evaluating the spatial distribution of thermal conditions in CBP barns with different ventilation systems in Brazil, observed that in all facilities examined the  $V_{\text{air}}$  was lower (1.0 m s<sup>-1</sup>) than the recommended. In this study, the systems used promoted the increase of such an attribute to levels close to adequate in most of the facilities. In addition, the results also show that the use of mechanical ventilation in tropical conditions is necessary for the proper functioning of the system, since only the natural ventilation was not sufficient to promote  $V_{\text{air}}$  values according to the recommendation for CBP barns.

The result of the CFD simulation in the CBP barn with the LVHS ventilation system is shown in Fig. 6. The air flow created by LVHS fans is distributed close to the surface of the compost bed, following the longitudinal direction of the barn (Fig. 6, a).

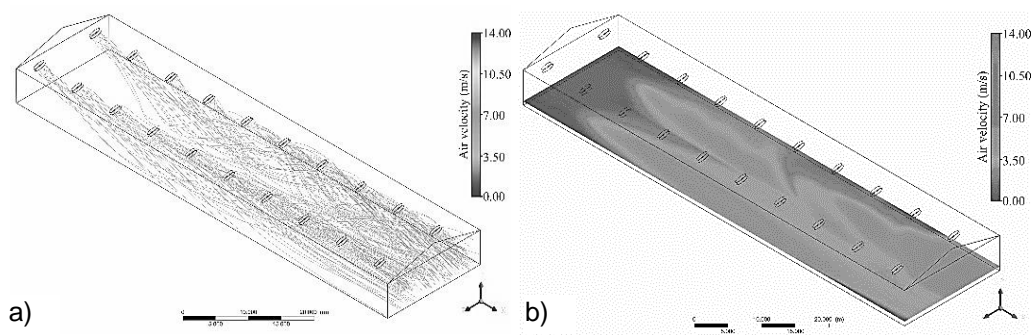


**Figure 6.** Results of CFD simulation of CBP barns with LVHS system: a) air flow lines and b) air velocity distribution on the surface of compost pack resting area.

Fig. 6, b shows the distribution of air velocity on the bed surface. At one end of the bedding area the air velocity values are very low. Two regions are observed at the opposite end of the CBP facility with higher speeds in the centre (around  $4.0 \text{ m s}^{-1}$ ) and lower ones on the sides (around  $2.5 \text{ m s}^{-1}$ ) of the compost bedding area. Air velocity values close to  $5 \text{ m s}^{-1}$  can be observed in the region of the right end of the compost bedding area due to the position of the LVHS fans and instability of air flow. The average air velocities caused an acceleration of the flow of air in this region.

Oliveira et al. (2019b) evaluating several CBP facilities in Brazil found that an artificial ventilation system was used by the compost barns in most cases (94.1%). They detected an air velocity at 0.05 and 1.50 m height of  $1.3 \pm 0.7$  and  $1.7 \pm 0.8 \text{ m s}^{-1}$ , respectively. The mechanical ventilation system in 76.4% of barns was realized by LVHS. Low Volume High Speed fans are spread in several parts of the world. In Kentucky 48.0% of CBP barns has LVHS fans as ventilation system (Damasceno, 2012).

## CONCLUSIONS

The model was validated and could be used to predict the behavior in real time of air velocity distribution inside the CBP barns with different ventilations systems.

The comparative analysis of the air flows generated by the HVLS and LVHS fans showed visual information that allows the evaluation to determine the best air flow homogeneity. The results indicate a better homogeneity in the CBP barn with HVLS fans with a smaller area with speed close to zero.

In all CBP barns evaluated, the air velocity ( $V_{\text{air}}$ ) was higher than the recommended ( $1.8 \text{ m s}^{-1}$ ) in most of the bedding area, so that it can dry the bed, remove gases and favour the heat exchanges between the animal and the environment.

Nevertheless, in future studies, CFD models could be used to predict the distribution of heat within the CBP barns at different air speed and types of ventilations systems.

**ACKNOWLEDGEMENTS.** The authors thank the following groups for financial support: Brazilian State Government Agency, FAPEMIG; National Counsel of Technological and Scientific Development (CNPq - Brazil); Federal agency, CAPES.

## REFERENCES

- Ahmadi, A.H. & Hashemabadi, S.H. 2008. 3D CFD simulation and experimental validation of particle-to-fluid heat transfer in a randomly packed bed of cylindrical particles. *International Communications in Heat and Mass Transfer* **35**, 1183–1189.
- Ansys. 2016. Ansys Fluent 17.0 - Theory Guide - Ansys, INC. Canonsburg, PA, USA, 1236 pp.
- ASTM. 2002. Guide for statistical evaluation of indoor air quality models (D5157-97). In: *American Society for Testing Materials. ASTM Standards on Indoor Air quality, 2nd edition*. West Conshohocken, pp. 68–71.
- Black, R.A., Taraba, J.L., Day, G.B., Damasceno, F.A. & Bewley, J.M. 2013. Compost bedded pack dairy barn management, performance, and producer satisfaction. *J. Dairy Sci.* **96**, 8060–8074.
- Damasceno, F.A. 2012. *Compost bedded pack barns system and computational simulation of airflow through naturally ventilated reduced model*. Thesis, Universidade Federal de Viçosa, Brazil, 404 pp.

- Endres, M.I., Lobeck, K., Janni, K., Godden, S. & Fetrow, J. 2011. Barn Environment Study. *Minnesota Dairy Health Conference*. St. Paul. Minnesota, pp. 47–56.
- Fluent. 2004 The manual of computational fluid dynamics (CFD), version 5.5. New Hampshire, USA, 625 pp.
- Janni, K.A., Endres, M.I., Reneau, J.K. & Schoper, W.W. 2007. Compost dairy barn layout and management recommendations. *Appl. Eng. Agr.* **23**, 97–102.
- Leso, L., Uberti, M., Morshed, W. & Barbari, M. 2013. A survey of Italian compost dairy barns. *J. Agr. Eng.* **44**(3), 120–124.
- Leso, L., Pellegrini, P. & Barbari, M. 2019. Effect of two housing systems on performance and longevity of dairy cows in Northern Italy. *Agronomy Research* **17**(2), 574–581. <https://doi.org/10.15159/AR.19.107>
- Leso, L., Barbari, M., Lopes, M. A., Damasceno, F.A., Galama, P., Taraba, J.L. & Kuipers, A. 2020. Invited review: Compost-bedded pack barns for dairy cows. *J. Dairy Sci.* **103**(2), 1072–1099.
- Lobeck, K.M., Endres, M.I., Janni, K.A., Godden, S.M. & Fetrow, J. 2012. Environmental characteristics and bacterial counts in bedding and milk bulk tank of low profile cross-ventilated, naturally ventilated, and compost bedded pack dairy barns. *Appl. Eng. Agr.* **28**, 117–128.
- Norton, T., Sun, D.W., Grant, J., Fallon, R. & Dodd, V. 2007. Applications of computational fluid dynamics (CFD) in the modelling and design of ventilation systems in the agricultural industry: a review. *Bioresource technology* **98**, 2386–2414.
- Oliveira, C.E.A., Damasceno, F.A., Ferraz, P.F.P., Nascimento, J.A.C., Ferraz, G.A.S. & Barbari, M. 2019a. Geostatistics applied to evaluation of thermal conditions and noise in compost dairy barns with different ventilation systems. *Agronomy Research* **17**(3), 783–796. <https://doi.org/10.15159/AR.19.116>
- Oliveira, V.C., Damasceno, F.A., Oliveira, C.E.A., Ferraz, P.F.P., Ferraz, G.A.S. & Saraz, J.A.O. 2019b. Compost-bedded pack barns in the state of Minas Gerais: architectural and technological characterization. *Agronomy Research* **17**(5), 2016–2028. <https://doi.org/10.15159/AR.19.179>
- Saraz, J.A.O., Tinôco, I.F.F., Rocha, K.S.O., Martins, M.A. & Damasceno, F.A. 2012. Validation of a CFD model for prediction of the efficiency of evaporative cooling in porous panels. *Revista U.D.C.A Actualidad & Divulgación Científica* **15**, 209–217.
- Zhao, J., Manbeck, H.B. & Murphy, D.J. 2007. Computational fluid dynamics simulation and validation of H<sub>2</sub>S removal from fan-ventilated confined-space manure storages. *Trans. ASABE* **50**(6), 2231–2246.



## **Thermal analysis of cement panels with lignocellulosic materials for building**

P.F.P. Ferraz<sup>1,\*</sup>, R.F. Mendes<sup>2</sup>, G.A.S. Ferraz<sup>1</sup>, V.R. Carvalho<sup>2</sup>,  
M.R.C. Avelino<sup>2</sup>, C.R.P. Narciso<sup>3</sup>, T.M.C. Eugênio<sup>3</sup>, V.C. Gonzalez<sup>4</sup> and  
G. Bambi<sup>5</sup>

<sup>1</sup>Federal University of Lavras, Department of Agricultural Engineering, Campus Universitário, PO Box 3037, Lavras, Minas Gerais, Brazil

<sup>2</sup>Federal University of Lavras, Department of Engineering, Campus Universitário, PO Box 3037, Lavras, Minas Gerais, Brazil

<sup>3</sup>Federal University of Lavras, Department of Forest Sciences, Campus Universitário, PO Box 3037, Lavras, Minas Gerais, Brazil

<sup>4</sup>Grupo de Investigación en Biodiversidad y Genética Molecular (BIOGEM), Departamento de Producción Animal, Universidad Nacional de Colombia, Sede Medellín, Carrera 65 No. 59 A-110, Código, 050034, Colombia

<sup>5</sup>University of Firenze, Department of Agriculture, Food, Environment and Forestry (DAGRI), Via San Bonaventura 13, IT50145 Firenze, Italy

\*Correspondence: [patricia.ponciano@ufla.br](mailto:patricia.ponciano@ufla.br)

**Abstract.** The use of lignocellulosic material residue in cement composites can be considered as a good option because they allow good thermal behaviour. This paper aimed to compare three kinds of cement panels reinforced with different lignocellulosic materials (Coffee husk, Coconut shell, and Banana pseudostem) based on their thermal properties. To produce each panel, the methodology suggested by Souza (1994) was used. Six replicates of each lignocellulosic panel with dimensions of 7.0×7.5 were evaluated. The thermal analysis was performed in a chamber composed of MDP (medium density particleboard). The chamber contained the heat source (incandescent lamp) connected to a thermostat that maintained the temperature at 48.0 °C. The porosity and thickness of the panels and the thermal behaviour of each sample panel (thermal conductivity, resistivity, resistance, and transmittance) and the difference in temperature of both sides of the panel were evaluated. The temperature difference to stabilization was obtained after a sampling time of 200 minutes, with 1,000 readings of 12 s each. Although all the panels were submitted under the same temperature, the inner and external superficial temperatures of the coffee husk panels reached smaller values. Besides, coconut and banana pseudostem panels presented the best results of thermal transmittance and thermal resistance. Thus, coconut shell panels present the best thermal performance, which means that this panel might be an attractive alternative building material, in terms of heat insulation for indoor applications.

**Key words:** conductivity, thermal cameras, thermal transmittance, alternative building material, coffee husk, coconut shell, and banana pseudostem.

## INTRODUCTION

Many studies have focused on the use of natural materials in buildings since these materials present high sustainability (Conti et al., 2017), they are relatively abundant and inexpensive (Castro et al., 2019). The engineering design of rural and civil buildings must take the availability of the local materials into account, encouraging wherever possible the use of natural materials that can be regenerated (Bambi et al., 2019). Nowadays, industries are focusing more and more attention on lignocellulosic based natural fibres as reinforcement for composites (Das & Chakraborty, 2006). The use of lignocellulosic material residues to produce cement composites used in building constructions is considered as a good option for new lignocellulosic cement formulations. Agricultural lignocellulosic material cement-based panels can be considered as alternative building materials because they allow a better thermal behaviour of the composite since they offer more significant potential for insulation (Teixeira et al., 2018).

Cement-bonded particleboards/panels are products manufactured from a mixture of Portland cement, chemical additives, and particles generated from lignocellulosic materials (Mendes et al., 2017). Increasing research are ongoing to develop environmentally friendly, sustainable and reusable composite materials (Alao et al., 2019). According to César et al. (2017), the basic principle of panel production is that most of the lignocellulosic materials may be used for panel production. Besides, these panels produced with raw materials present the following advantages: good fire resistance, good thermal and acoustic insulation, good resistance to fungus and insects attack, and they can be considered as good materials to work (Iwariki & Prata, 2007).

According to Barbari et al. (2014a) in less economically developed countries, it is challenging to access data on building materials to design the buildings properly. The outcome is the abandonment of natural materials in favour of more expensive materials but with inferior thermal characteristics and higher environmental impact (Barbari et al., 2014b). The concern with the energetic efficiency of the constructions has considerably increased in the last years considering that the majority of energy consumed comes from the residential buildings, with a predominance of heating and cooling systems. It culminated with an effective increase in the adoption of air conditioners (Doukas et al., 2006; Castro et al., 2019). Therefore, it is mandatory to look for solutions for alternative natural materials that can reduce the thermal conductivity of the building and improve thermal comfort. According to Topol et al. (2019), thermal comfort can be defined as the state of mind, which expresses satisfaction with the thermal environment, and it is an important aspect of the building design process.

This paper aimed to compare three kinds of cement composites panels reinforced with the following residues agricultural lignocellulosic materials: Coffee husk, Coconut shell, and Banana pseudostem based on their thermal properties.

## MATERIAL AND METHODS

The experiment was carried out on the Federal University of Lavras (UFLA), Lavras, Brazil. Three different kinds of lignocellulosic composites were produced using: coconut shell (*Cocos nucifera*), coffee husk (*Coffea arabica*), banana pseudostem (*Musa acuminata*). Lignocellulosic materials were processed in a hammer-mill. The material

particles were selected through a sieve and the fraction retained between 20 (0.841 mm) and 40 (0.420 mm) mesh was used to produce the composites.

For the calculations of the components of each panel (lignocellulosic material, cement, water, and  $\text{CaCl}_2$ , as an accelerator), the methodology suggested by Souza (1994) was used to determine the equivalent mass of components. In the production of panels, the following parameters were applied: material and cement ratio, 1:2.75; water and cement ratio, 1:2.5; hydration water rate of 0.25; additive, 4% (based on cement mass); the percentage of losses, 6%. The calculations were performed for a nominal panel density of  $1.2 \text{ g cm}^{-3}$ .

The mixture of the components was produced in a mixer, and the particulate materials were gradually added in order to obtain a homogeneous mixture. After mixing, the mass of each panel was properly separated, weighed, and randomly distributed in aluminum moulds of  $480 \times 480 \times 150 \text{ mm}$ . The moulding and stapling was carried out in a cold process for 24 hours, and then the panels were kept in a climatic room at a temperature of  $20 \pm 2 \text{ }^\circ\text{C}$  and  $65 \pm 3\%$  relative humidity to ensure uniform drying for 28 days.

The determination of the density of the composites was performed according to NBR 11936 (NBR 1977). The density was calculated by dividing the mass (measured in analytical balance) by the volume calculated (base area multiplied by height, measured by calliper ruler). Porosity was determined following procedures described in the ASTM C 948 standard.

To determine the thermal properties of the lignocellulosic panels, a thermal chamber composed of MDP (medium density particleboard) of sugar cane bagasse (Fig. 1, A) was used. The chamber has two layers of coatings, styrofoam, and a thermal blanket, to isolate the external medium (Fig. 1, B). The lower part contains the heat source (incandescent lamp) connected to a thermostat that maintained the temperature at  $48.0 \text{ }^\circ\text{C}$ . The system had four thermocouples: the lamp temperature controller, the ambient temperature, the temperature

before entering the sample, and the temperature after exiting the sample, according to the methodology proposed by Gandia et al. (2019). The system was connected to an Arduino microcontroller that was programmed to collect and storage the collected data at every 5 seconds. To validate the system, the heat output was verified with an infrared sensor camera, Fluke TI55FT20/54/7.5, with an accuracy of  $\pm 0.05 \text{ }^\circ\text{C}$ .

The thermal properties of the lignocellulosic panels were evaluated in six replicates of each lignocellulosic panel with dimensions of  $7.0 \times 7.5 \text{ cm}$  at the 28 days age. The samples were assayed alone, and the material was exposed at temperature, around  $48 \text{ }^\circ\text{C}$ . The heating rate was  $1 \text{ }^\circ\text{C min}^{-1}$ . and the test cycle for each treatment was approximately 3.33 hours (200 minutes) with 1,000 readings of 12 seconds each.

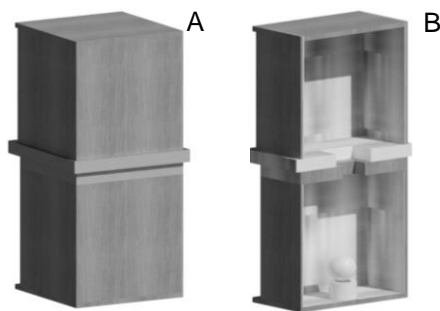


**Figure 1.** Schematic draw of the external side of the thermal chamber (A) and the internal side of the thermal chamber (B).

The ISO 6946 (2017) and Evangelisti et al. (2015) describe a method for calculating the thermal resistance and thermal transmittance of building elements based on the electrical analogy. The equations below were used to calculate the thermal conductivity (Eq. 1), thermal resistance (Eq. 2), thermal transmittance (Eq. 3).

Thermal conductivity is the heat flow that passes through a unit area of a 1 m thick homogeneous material due to a temperature gradient equal to 1 K (Schiavoni et al., 2016). The thermal conductivity was calculated using the following equation:

$$\lambda = \frac{P \cdot t}{\Delta T} \quad (1)$$

where  $\lambda$  – thermal conductivity in  $\text{W m}^{-1}\text{K}^{-1}$ ;  $P$  – radiation of the heat source;  $t$  is the thickness of the sample panel in m;  $\Delta T$  – difference between internal and external panels temperature (K).

The radiation of the heat source was determined by a solar radiation meter, Instrutherm model MES-100. Five samples were measured, and the mean value was  $843.15 \text{ Wm}^{-2}$ .

Thermal properties are expressed by thermal transmittance (ISO 6946, 2017), or U-value, which is the heat flow that passes through a unit area of a complex component or in homogeneous material due to a temperature gradient equal to 1 K (Schiavoni et al., 2016). The inverse of thermal transmittance is the thermal resistance, or R-value (Schiavoni et al., 2016).

According to Evangelisti et al. (2015), the thermal resistance is accordingly calculated using the following equations:

$$R = \frac{t}{\lambda} \quad (2)$$

$$U = \frac{1}{R} \quad (3)$$

where  $R$  – thermal resistance ( $\text{m}^2 \text{K W}^{-1}$ );  $t$  – thickness of the panel (m);  $\lambda$  – thermal conductivity ( $\text{W m}^{-1}\text{K}^{-1}$ );  $U$  – thermal transmittance value evaluated by the calculation method ( $\text{W m}^{-2}\text{K}^{-1}$ ).

The data analysis of this study was evaluated in a randomized design. The results were submitted to analysis of variance (ANOVA) and Tukey test, both at a 5% significance level.

## RESULTS AND DISCUSSION

According to Guillou et al. (2018), thermophysical properties are not as often reported, although they are essential for thermal applications of the composite and for modelling thermal behaviour. In this study, the thermophysical properties were calculated, and the results are shown in Table 1.

Thermal conductivity is the intrinsic property of a material that relates its ability to conduct heat and an indicator for determining if the sample can be used as a heat insulator (Vidil et al., 2016). This property is a function of several internal and external variables such as e.g. moisture, temperature, density, porosity, chemical and mineralogical composition and phase composition etc. (Muizniece et al., 2015; Têbl & Kic, 2016; Sair et al., 2019). The panel which presented the smallest thermal conductivity in this study was the coconut shell panel ( $0.0321 \text{ W m}^{-1} \text{K}^{-1}$ ). For thermal comfort, this low value is even more favourable, considering that buildings constructed with materials with lower

thermal conductivity values imply milder temperatures inside the environments (Castro et al., 2019). Samples with lower thermal conductivity have better thermo-barrier properties (Hakkarainen et al., 2005). This low conductivity value can be explained by the lower density of the sample ( $0.984 \text{ g cm}^{-3}$ ). Usually, the lower the density is, the lower thermal conductivity is. Indeed, the lighter the boards, the more voids and the porous they contain, and the lower their thermal conductivity (Vidil et al., 2016).

**Table 1.** Thermophysical properties of the evaluated lignocellulosic panels

Material	t (mm)	Porosity (%)	Density ( $\text{g cm}^{-3}$ )	$\lambda$ ( $\text{W m}^{-1}\text{K}^{-1}$ )	$U$ ( $\text{W m}^{-2}\text{K}^{-1}$ )	$R$ ( $\text{m}^2 \text{K W}^{-1}$ )
Coffee husk	16 <sup>b</sup>	52.5 <sup>b</sup>	1.267 <sup>a</sup>	0.0325 <sup>b</sup>	2.027 <sup>a</sup>	0.493 <sup>b</sup>
	$\pm 0.6$	$\pm 9.7$	$\pm 79.757$	$\pm 0.000$	$\pm 0.017$	$\pm 0.004$
Coconut shell	16 <sup>b</sup>	62.8 <sup>b</sup>	0.984 <sup>c</sup>	0.0321 <sup>c</sup>	2.005 <sup>b</sup>	0.499 <sup>a</sup>
	$\pm 0.3$	$\pm 2.7$	$\pm 82.010$	$\pm 0.000$	$\pm 0.010$	$\pm 0.002$
Banana pseudostem	17 <sup>a</sup>	87.5 <sup>a</sup>	1.003 <sup>b</sup>	0.0340 <sup>a</sup>	1.988 <sup>b</sup>	0.503 <sup>a</sup>
	$\pm 0.8$	$\pm 2.7$	$\pm 22.055$	$\pm 0.000$	$\pm 0.007$	$\pm 0.002$
P value	0.000	0.0015	0.0024	0.0000	0.0002	0.0002
CV (%)	0.000	9.53	6.31	0.59	0.60	0.6

t – thickness of the panel (mm);  $\lambda$  – thermal conductivity ( $\text{W m}^{-1}\text{K}^{-1}$ );  $U$  – thermal transmittance value evaluated by the calculation method ( $\text{W m}^{-2}\text{K}^{-1}$ );  $R$  – thermal resistance ( $\text{m}^2 \text{K W}^{-1}$ ).

Averages followed by the same letter in the line present statistical equality by the Tukey test at 5% significance. \*The values in parentheses are standard deviation.

According to Wang (1988), a particleboard can be used as insulating components of building materials since its thermal conductivity is lower than  $0.25 \text{ W m}^{-1}\text{K}^{-1}$ . BS EN 13986 recommends thermal conductivities of 0.07 and  $0.12 \text{ W m}^{-1}\text{K}^{-1}$  for panels with apparent densities of 0.300 and  $0.500 \text{ g cm}^{-3}$ , respectively. So, the panels presented in this study do not meet the thermal conductivity requirement. Nevertheless, on the other hand, the produced coconut shell panel that presented the best conductivity value showed better values than the coconut husk panel described by Panyakaew & Fotios, (2011), who found values of 0.046 and  $0.068 \text{ W m}^{-1} \text{K}^{-1}$ .

Thermal transmittance ( $U$ ) is an essential measure of heat loss through the material (Damdelen, 2019). According to Sánchez-Palencia et al. (2019), the thermal transmittance denotes how effective a building element is at preventing heat from transmitting through it. The  $U$ -value of the building material is the major factor in the determination of the steady-state heat losses and gains (UNI EN ISO 6946, 2008). It is also important to state that the thickness of the lignocellulosic panels is also a significant concept in  $U$ -value. There is a relationship between density, thickness, thermal conductivity, and  $U$ -value. When the density and thickness get more significant, the thermal conductivity and  $U$ -value increase (Demirboğa, 2003; Damdelen, 2019). However, all of the evaluated panels have similar thicknesses in this research, around 16 mm. Based on the evaluated panels, coconut shell and banana pseudostem presented similar  $U$ .

To evaluate a building's thermal comfort for occupants, the thermal resistance ( $R$ ) is an important factor in defining the total energy consumption of heating and cooling systems (Desogus et al., 2011). With higher  $R$ -values, insulating effectiveness is more significant. The  $R$ -value depends on the type of insulation, including the material, thickness, and density (Peng & Wu, 2008). According to Table 1, coconut shell and

banana pseudostem presented the highest R-values, which indicates that those materials present higher resistance to the heat-flux.

After analyzing the thermophysical properties of the evaluated lignocellulosic panels, an additional study has been carried out to analyze the heat flows exchanged between the internal (on contact with the heat source) and external (without contact with the heat source) panels surface. Surface temperatures and heat-flux rate through the test panels are shown in Fig. 2 and Table 2.

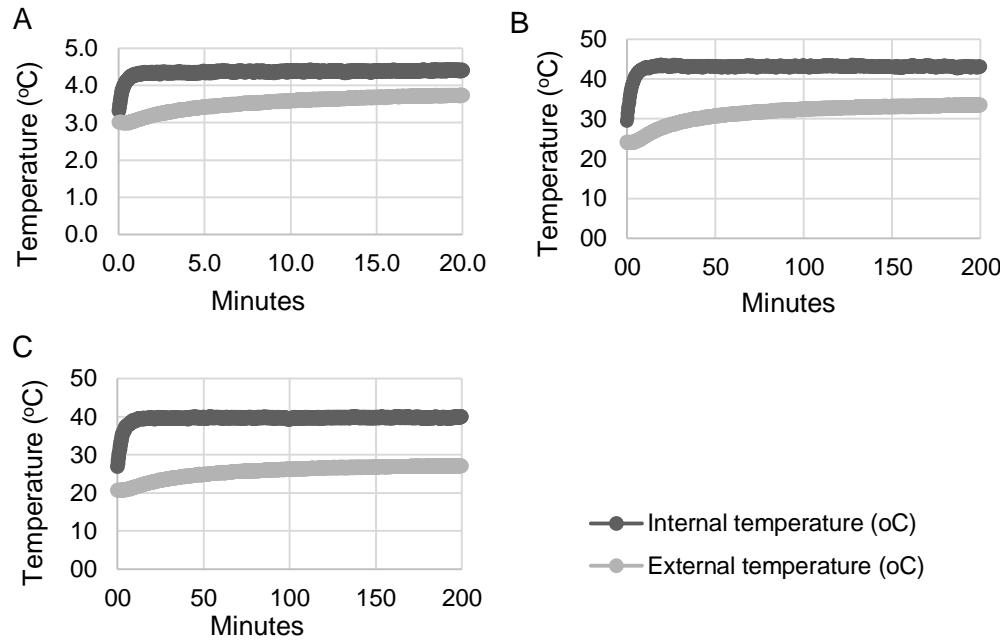


**Figure 2.** Internal and external temperature surface of the lignocellulosic panels (A) Coffee husk, (B) coconut shell, (C) banana pseudostem during 200 minutes of heat.

It is possible to observe that despite all the lignocellulosic materials being subjected to the same heat-flux, there was a difference in the internal and external temperature surface of the evaluated panels. Coffee husk presented the smallest difference between the external and internal temperature surfaces. According to Table 1, R-value of coffee husk was the smallest, which means the coffee husk panel presented a smaller resistance to the heat-flux.

On the other hand, Fig. 2 and Table 2 indicate that coconut shell and banana pseudostem presented no

**Table 2.** Difference between the internal and external temperature surface of the lignocellulosic panels (A) Coffee husk, (B) coconut shell, (C) banana pseudostem during 200 minutes of heat

Material	$T_{\text{int}} - T_{\text{ext}} (^{\circ}\text{C})$	$T_{\text{int}} - T_{\text{ext}} (\text{K})$
Coffee husk	8.09 <sup>b</sup> ± 2.36	281.24 <sup>b</sup> ± 2.360
Coconut shell	11.14 <sup>a</sup> ± 1.37	284.29 <sup>a</sup> ± 1.367
Banana pseudostem	13.59 <sup>a</sup> ± 1.08	286.74 <sup>a</sup> ± 1.076
P value	0.0002	0.0002
CV (%)	15.47	0.6

T<sub>int</sub> – panel internal surface temperature. Text – panel external surface temperature. Averages followed by the same letter in the line present statistical equality by the Tukey test at a 5% significance.

\*The values in parentheses are standard deviation.

statistical difference, and they presented the highest difference surface temperature and highest R-value (Table 2). The R-value is a measure of how well an envelope resists the heat-flow (Desogus et al., 2011). Based on these results, it is possible to affirm that Table 2 and Fig. 2 confirm the results of Table 1.

Fig. 3 allows us to compare the results presented by the difference between the internal and external superficial temperature of the panels. It is possible to notice that the surface temperature difference, in the three evaluated panels, becomes stable after a period. It is known that only some of the heat on the one side surface of building envelopes can be transferred into the building and arrive on the inside surface because of the thermal resistance of the building materials. The heat of one surface of building envelopes is not immediately transferred to the inside due to the thermal storage capacity of the building material (Peng & Wu, 2008). The results prove that all evaluated lignocellulosic composites can become an alternative biological building material because they offer significant potential thermal property (Teixeira et al., 2018). It is possible to conclude that it is very important to study the thermal dynamic properties of the lignocellulosic panels in order to optimize the choice of the envelope materials for maximizing the thermal comfort and energy performance leading to energy consumption.

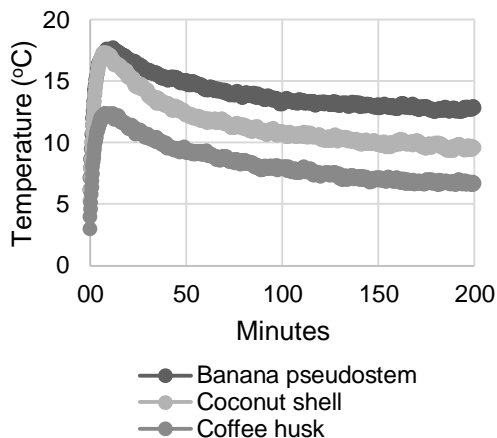


**Figure 3.** Difference of internal (in contact with the heat source) and external (without contact with the heat source) temperature surface of the evaluated lignocellulosic panels.

## CONCLUSION

It was possible to investigate the thermal performance of the three cement-based composites properly reinforced with lignocellulosic materials (coffee husk, coconut shell, banana pseudostem) with satisfactory results.

According to the results of the current work, the coconut shell panel presented the best thermal conductivity ( $0.0321 \text{ W m}^{-1} \text{ K}^{-1}$ ).

Besides, coconut and banana pseudostem panels presented the best results of thermal transmittance and thermal resistance. It indicates that coconut panel can be considered an alternative biological building material because they offer significant thermal properties.

The thermophysical properties evaluated can be considered useful tools for the study of the thermal behaviour of the lignocellulosic panels to be used in building constructions.

**ACKNOWLEDGEMENTS.** The authors would like to thank the Minas Gerais State Agency for Research and Development (FAPEMIG Grant n. CAG-APQ-01100-15).

## REFERENCES

- Alao, P.F., Kallakas, H., Poltimäe, T. & Kers, J. 2019. Effect of hemp fibre length on the properties of polypropylene composites. *Agronomy Research* **17**(4), 1517–1531.
- Bambi, G., Ferraz, P.F.P., Ferraz, G.A.S., Pellegrini, P. & Di Giovannantonio, H. 2019. Measure of thermal transmittance of two different infill wall built with bamboo cultivated in Tuscany. *Agronomy Research* **17**(S1), 923–934.
- Barbari, M., Monti, M., Rossi, G., Simonini, S. & Sorbetti Guerri, F. 2014a. Simple methods and tools to determine the mechanical strength of adobe in rural areas. *Journal of Food, Agriculture & Environment* **12**(2), 904–909.
- Barbari, M., Monti, M., Rossi, G., Simonini, S. & Sorbetti-Guerri, F. 2014b. Proposal for a simple method of structural calculation for ordinary earthen buildings in rural areas. *Journal of food, Agriculture & Environment* **12**(2), 897–903.
- Castro, E.D.D., Villela, L.S., Mendes, L.M., Mendes, R.F., Ribeiro, A.G.C., Guimarães Junior, J.B. & Rabelo, G.F. 2019. Analysis of the coffee peel application over the soil-cement bricks properties. *Coffee Science* **14**(1), 12–23.
- César, A.A.D.S., Bufalino, L., Mendes, L.M., Mesquita, R.G.D.A., Protásio, T.D.P., Mendes, R.F. & Andrade, L.M.F. 2017. Transforming rice husk into a high-added value product: potential for particleboard production. *Ciência Florestal* **27**(1), 303–313.
- Conti, L., Goli, G., Monti, M., Pellegrini, P., Rossi, G. & Barbari, M. 2017. Simplified Method for the Characterization of Rectangular Straw Bales (RSB) Thermal Conductivity. In *IOP Conference Series: Materials Science and Engineering*. IOP Publishing. **245**(5). p. 052035.
- Damdelen, O. 2019. Influences of construction material type and water-cement ratio reduction on thermal transmittance of sustainable concrete mixes. *Construction and Building Materials* **196**, 345–353.
- Das, M. & Chakraborty, D. 2006. Influence of mercerization on the dynamic mechanical properties of bamboo, a natural lignocellulosic composite. *Industrial & engineering chemistry research* **45**(19), 6489–6492.
- Demirboğa, R. 2003. Influence of mineral admixtures on thermal conductivity and compressive strength of mortar. *Energy and buildings* **35**(2), 189–192.
- Desogus, G., Mura, S. & Ricciu, R. 2011. Comparing different approaches to in situ measurement of building components thermal resistance. *Energy and Buildings* **43**(10), 2613–2620.
- Doukas, H., Patlitizianas, K. D., Kagiannas, A. G. & Psarras, J. 2006. Renewable energy sources and rationale use of energy development in the countries of GCC: Myth or reality?. *Renewable Energy* **31**(6), 755–770.
- Evangelisti, L., Guattari, C., Gori, P. & Vollaro, R. 2015. In situ thermal transmittance measurements for investigating differences between wall models and actual building performance. *Sustainability* **7**(8), 10388–10398.
- Gandia, R.M., Gomes, F.C., Corrêa, A.A.R., Rodrigues, M.C. & Mendes, R.F. 2019. Physical, mechanical and thermal behavior of adobe stabilized with glass fiber reinforced polymer waste. *Construction and Building Materials* **222**, 168–182.
- Guillou, J., Lavadiya, D. N., Munro, T., Fronk, T. & Ban, H. 2018. From lignocellulose to biocomposite: Multi-level modelling and experimental investigation of the thermal properties of kenaf fiber reinforced composites based on constituent materials. *Applied Thermal Engineering* **128**, 1372–1381.
- Hakkarainen, T., Mikkola, E., Östman, B., Tsantaridis, L., Brumer, H. & Piispanen, P. 2005. Innovative ecoefficient high fire performance wood products for demanding applications. *InnoFireWood*: 11, 12, 17–21 pp.
- International Organization for Standardization, ISO 6946: 2017 Building Components and Building Elements—Thermal Resistance and Thermal Transmittance - Calculation Methods. *International Organization for Standardization: Geneva, Switzerland*.



- Iwariki, S. & Prata, J. G. 2008. Utilização da madeira de *Eucalyptus grandis* e *Eucalyptus dunnii* na produção de painéis cimento-madeira. *Cerne* **14**(1), 68–74.
- Mendes, R.F., Vilela, A.P., Farrapo, C.L., Mendes, J.F., Tonoli, G.H.D. & Mendes, L.M. 2017. Lignocellulosic residues in cement-bonded panels. In: *Sustainable and Nonconventional Construction Materials using Inorganic Bonded Fibre Composites*. Woodhead Publishing. pp. 3–16.
- Muizniece, I, Vilcane, L. & Blumberga, D. 2015. Laboratory research of granulated heat insulation material from coniferous forestry residue. *Agronomy Research* **13**, 690–699.
- NBR 11936. 1977. *Brazilian Association of Technical Standards – ABNT*. Determination of the Specific Weight of Plastics Using a Pycnometer. (in Portuguese).
- Panyakaew, S. & Fotios, S. 2011. New thermal insulationboards made from coconut husk and bagasse. *Energy and Buildings* **43**(7), 1732–1739.
- Peng, C. & Wu, Z. 2008. In situ measuring and evaluating the thermal resistance of building construction. *Energy and Buildings* **40**(11), 2076–2082.
- Sair, S., Mandili, B., Taqi, M. & El Bouari, A. 2019. Development of a new eco-friendly composite material based on gypsum reinforced with a mixture of cork fibre and cardboard waste for building thermal insulation. *Composites Communications* **16**, 20–24.
- Sánchez-Palencia, P., Martín-Chivelet, N. & Chenlo, F. 2019. Modeling temperature and thermal transmittance of building integrated photovoltaic modules. *Solar Energy* **184**, 153–161.
- Schiavoni, S., Bianchi, F. & Asdrubali, F. 2016. Insulation materials for the building sector: A review and comparative analysis. *Renewable and Sustainable Energy Reviews* **62**, 988–1011.
- Souza, M.R. 1994. *Durability of cement-bonded particle board made conventionally and carbon dioxide injection*. These (Doctor of Philosophy)–University of Idaho, Idaho, 123 pp.
- Têbl, J. & Kic, P. 2016. Thermal properties and reduction of energy consumption of buildings. *Agronomy Research* **14**, 1222–1231.
- Teixeira, J.N., Silva, D.W., Vilela, A.P., Junior, H.S., Brandão, L.E.V.S. & Mendes, R.F. 2018. Lignocellulosic Materials for Fiber Cement Production. *Waste and Biomass Valorization*, 1–8.
- Topol, M., Kic, P. & Neuberger, P. 2019. Reduction of moisture and thermal conductivity of wet walls by special plaster. *Agronomy Research* **17**(S1), 1235–1245.
- UNI EN ISO 6946:2008, Building components and building elements – thermal resistance and thermal transmittance – calculation method.
- Vidil, L., Fiorelli, J., Bilba, K., Onésippe, C., Arsène, M. A. & Savastano Junior, H. 2016. Thermal insulating particleboards reinforced with coconut leaf sheaths. *Green Materials* **4**(1), 31–40.
- Wang, S.H. 1988. *Construction Materials Science*. Construction Industry Publisher, Beijing, China.

## Comparison between the thermal properties of cement composites using infrared thermal images

P.F.P. Ferraz<sup>1,\*</sup>, R.F. Mendes<sup>2</sup>, G.A.S. Ferraz<sup>1</sup>, F.A. Damasceno<sup>2</sup>, I.M.A. Silva<sup>2</sup>,  
L.E.V.S.B. Vaz<sup>2</sup>, L.M. Mendes<sup>3</sup>, D. Cecchin<sup>4</sup> and J.O. Castro<sup>2</sup>

<sup>1</sup>Federal University of Lavras, Department of Agricultural Engineering, Campus Universitário, PO Box 3037, Lavras, Minas Gerais, Brazil

<sup>2</sup>Federal University of Lavras, Department of Engineering, Campus Universitário, PO Box 3037, Lavras, Minas Gerais, Brazil

<sup>3</sup>Federal University of Lavras, Department of Forest Sciences, Campus Universitário, PO Box 3037, Lavras, Minas Gerais, Brazil

<sup>4</sup>Federal University Fluminense, Department of Agricultural Engineering and Environment, Campus Praia Vermelha, São Domingos, Niterói, Rio de Janeiro, Brazil

\*Correspondence: [patricia.ponciano@ufla.br](mailto:patricia.ponciano@ufla.br)

**Abstract.** The use of agribusiness residual lignocellulosic fibres can be a good alternative in the development of lignocellulosic composites. The current work aimed to investigate the thermal performance of cement-based composites with lignocellulosic materials: Eucalyptus, sugarcane bagasse, coconut fibre in comparison with commercial gypsum board to be used as internal partitions of the building using infrared thermal images. Three repetitions for each kind of lignocellulosic material were made, and three commercial gypsum boards were used. In the production of the panels, the following parameters were applied: material and cement ratio, 1:2.75; water and cement ratio, 1:2.5; hydration water rate of 0.25; additive, 4% (based on cement mass). The calculations were performed for a nominal panel density of 1,200 kg m<sup>-3</sup>. The thermal analysis was performed in a chamber composed of MDP (Medium-Density Particleboard) and with an internal layer of rock wool and the heat source (thermal resistance). For the superficial temperature measurement, a FLIR E75 camera was used to capture the infrared images. When the internal temperature of the chamber stabilized at 50 °C, an infrared thermal image was collected from each side of the composite. Thermal properties were analysed: thermal conductivity, resistivity, resistance, and transmittance. Based on the results, sugar cane cement composites were characterized by higher values of thermal conductivity. Related to thermal resistivity, thermal resistance, and thermal transmittance, only the coconut panel presented similar behaviour to the commercial gypsum board. Thus, cement composite using coconut can be a potential alternative that might solve energy and environmental concerns simultaneously.

**Key words:** conductivity; thermal cameras; thermal transmittance, thermal analyses, alternative building material.

## INTRODUCTION

According to Rheinheimer et al. (2017), heating and cooling system of U.S. buildings are responsible for 37% of the country's energy consumption. Similarly, in the

European Union (E.U.) buildings, 43% of the E.U.'s energy is used for air heating or cooling. According to the same authors in tropical and subtropical countries, the energy used only for air conditioning in buildings is approximately 50% of the country's energy consumption, and another 20% is consumed for ventilation. Bambi et al. (2019b) stated that rural areas are facing different challenges, and according to Barbari et al. (2014a), in these areas, especially in less economically developed countries, it is complicated to access to data on building materials, to design the buildings properly. The outcome is the realization of structures wrongly dimensioned or, in some cases, the abandonment of natural materials in favour of more expensive materials but with inferior thermal characteristics and higher environmental impact (Barbari et al., 2014b). Therefore, it is mandatory to look for solutions for alternative natural materials that can reduce the thermal conductivity of the building envelope.

Agricultural lignocellulosic materials on cement-based panels can be considered as alternatives building materials because they allow a better thermal behaviour of the composite since they offer more significant potential for insulation (Teixeira et al., 2018). The materials used for the build construction may allow good thermal insulation, so climatic variations less influence their internal environment. The use of lignocellulosic material residue in cement composites is seen as a good option for new fibre cement formulations (Cevallos & Olivito et al., 2015). Besides, according to Conti et al. (2017), many studies have been focused on the use of natural materials in buildings, since these materials present high sustainability. Fibre-cements manufactured with lignocellulose fibres have been commercially obtained thanks to technological advances in the raw materials, in the optimization of the production processes with rationalized energy consumption, and lower investment costs (Ardanuy et al., 2015, Wei & Meyer, 2015; Fonseca et al., 2019).

Residuals lignocellulose fibres occupy a special place in the development of fibre-reinforced cement and concrete, because of the abundance and availability of natural and waste fibres in many parts of the world. Besides, these materials can also lead directly to energy savings, conservation of a country's scarce resources, and reduction in environmental pollution (Sudin & Swamy, 2006). These natural fibres have already been considered as potential alternatives, given their ecological friendliness and ready availability in fibrous form and also, since they can be extracted from plant leaves at low cost, in the most of cases (Silva et al., 2008). Currently, cement panels with lignocellulosic fibres are applied in the manufacturing of roofing tiles, corrugated and flat sheets, sealing panels (walls) and other construction materials, mainly nonstructural thin boards (Fonseca et al., 2019). Although several works have been done on the mechanical properties of the composite containing lignocellulosic materials, few papers have been previously reported on the thermal analyzes. Therefore, the development of composite building materials with low thermal conductivity will be an interesting alternative that might solve energy and environmental concerns simultaneously (Benazzouk et al., 2008).

Infrared cameras can be used to evaluate the thermal properties of the lignocellulosic cement composites. The thermal cameras measure the amount of invisible heat energy emitted by surfaces and convert them into surface temperature, producing thermal images (Nascimento et al., 2011). This methodology had already been used in different scientific areas such as medicine (Raja et al., 2017), animal welfare (Castro et al., 2019), building materials analyses (Meola et al., 2015; Gholizadeh, 2016;

Zhang et al., 2016; Bambi et al., 2019a) and others. Infrared thermography is a safe, nondestructive, and low-cost technique that allows analyzing the thermal information obtained from a sample.

The current work aimed to investigate the thermal performance of three cement-based composites properly reinforced with lignocellulosic materials (Eucalyptus, sugar cane and coconut fibre) and commercial gypsum board to be used as in internal partitions of the building using infrared thermal images.

## MATERIALS AND METHODS

The experiment was carried out at the Federal University of Lavras (UFLA), Lavras, Brazil. For the production of panels, the following lignocellulosic materials were used: Eucalyptus (*Eucalyptus grandis*), sugarcane bagasse (*Saccharum officinarum*), coconut fibre (*Cocos nucifera*) and commercial gypsum board.

A *Eucalyptus grandis* wood tree was obtained from local experimental cultivation at Federal University of Lavras – UFLA. Sugar cane (*Saccharum officinarum*) was obtained in a commercial cachaça distillery in Lavras – Minas Gerais state, Brazil. The coconut fibre (*Cocos nucifera*) is derived from local floriculture in Lavras – Minas Gerais state, Brazil. Moreover, three commercial gypsum boards were bought at specialized stores in the city.

Initially, the Eucalyptus wood was cut into short logs and passed through a laminator for delaminating. Sugar cane and coconut fibres were processed in a hammer-mill. The materials were dried in stoves until 12% of humidity. The particulate materials were sieved through a set of two superposed sieves with 0.50 mm (top) and 0.42 mm (bottom) particle sizes for fine contents (lower than 0.42 mm) removal.

Lignocellulosic cement panels were produced using the Eucalyptus, sugar cane and coconut. Three repetitions for each kind of lignocellulosic material were made. Furthermore, three commercial gypsum board ( $\text{CaSO}_4 \cdot 2\text{H}_2\text{O}$ ) which satisfies the criteria of ASTM Methods C-36 (2004) with 15 mm of thickness were bought. Totalizing four treatments and three repetitions.

For the calculations of the components of each panel (lignocellulosic material, cement, water, and  $\text{CaCl}_2$ ), the methodology suggested by Souza (1994) was used to determine the equivalent mass of components. In the production of panels, the following parameters were applied: material and cement ratio, 1:2.75; water and cement ratio, 1:2.5; hydration water rate of 0.25; additive, 4% (based on cement mass); the percentage of losses, 6%. The calculations were performed for a nominal panel density of  $1,200 \text{ kg m}^{-3}$ .

In order to produce each panel, components were weighed and then mixed in a concrete mixer for eight minutes. The total mass of components for three panels equivalent to each treatment (at the same time) was mixed. After mixing, the mass of each panel was separated, weighed, and randomly distributed in aluminum moulds of  $480 \times 480 \times 150 \text{ mm}$ . The moulding and stapling were carried out in a cold process for 24 hours, and then panels were kept in a climatic room at a temperature of  $20 \pm 2^\circ\text{C}$  and  $65 \pm 3\%$  relative humidity to ensure uniform drying for 21 days.

To measurement of the thickness (mm) of each panel, it was used a calliper in 4 points in each sample. The dimensional size and weight measured were used to calculate the thickness and density of the composites. Density ( $\text{kg m}^{-3}$ ) was calculated by the

relationship between the panel mass (Kg) and the panel size (m<sup>3</sup>). All of these analyses were developed based on the ASTM standard method (ASTM D1037, 2016) and Deutsches Institut für Normung – DIN (1982) standards.

The thermal analysis was performed in a chamber composed of MDP (Medium-Density Particleboard) and with an internal layer of rock wool. The lower part of the chamber contains the heat source (thermal resistance) connected to a thermostat that maintained the temperature at 50.0 °C. The system had two thermocouples: the resistance temperature controller and the ambient temperature. The thermocouple signals were digitized in real-time with a data acquisition board (cDAQ-9174, National Instruments, Austin, TX, USA) equipped with an analogue input module (NI 9211, National Instruments).

For the temperature measurement, a FLIR E75 camera, with 320 × 240 resolution and 0.03 °C thermal sensitivity, emissivity factor,  $\varepsilon = 0.95$  was used to capture the infrared images. The measurements were done with a distance of 1.50 m between the sample and the camera.

When the internal temperature of the chamber stabilized at 50 °C (Bambi et al., 2019), an infrared thermal image was collected from each side of the panel. Initially, it was collected an image of the external side of the panel and then an image of the inner side of the panel that is the side in contact with the heat source. Three replicates were made per treatment (Eucalyptus, sugar cane, coconut, and gypsum board). The infrared thermography was used to measure the temperature of the panels using the FLIR Researcher IR software to obtain the mean temperature of the area.

### Theory and modeling

Thermal conductivity is the heat flow that passes through a unit area of a 1 m thick homogeneous material due to a temperature gradient equal to 1 K (Schiavoni et al., 2016). The thermal conductivity was calculated using the following equation (Gandia et al., 2019):

$$\lambda = \frac{P d}{\Delta T} \quad (1)$$

where  $\lambda$  – thermal conductivity in W m<sup>-1</sup> K<sup>-1</sup>;  $P$  – radiation of the resistance (836.45 W m<sup>-2</sup>);  $d$  is the thickness of the sample panel in m;  $\Delta T$  – difference between internal and external panels temperature (K).

Thermal properties are expressed by thermal transmittance (ISO 6946, 2017), or U-value, which is the heat flow that passes through a unit area of a complex component or inhomogeneous material due to a temperature gradient equal to 1 K (Schiavoni et al., 2016). The inverse of thermal transmittance is the thermal resistance, or R-value (Schiavoni et al., 2016). The ISO 6946 (2017) describes a method for calculating the thermal resistance and thermal transmittance of building elements based on the electrical analogy. According to Evangelisti et al. (2015), the thermal resistance is accordingly calculated using the following equations:

$$R = \frac{d}{\lambda} \quad (2)$$

$$U = \frac{1}{R} \quad (3)$$

where  $R$  – thermal resistance ( $\text{m}^2 \text{K W}^{-1}$ );  $d$  – thickness of the panel (m);  $\lambda$  – thermal conductivity ( $\text{W m}^{-1} \text{K}^{-1}$ );  $U$  – thermal transmittance value evaluated by the calculation method ( $\text{W m}^{-2} \text{K}^{-1}$ ).

The data analysis of this study was evaluated in a randomized design. The results were submitted to analysis of variance (ANOVA) and Tukey test, both at a 5% significance level.

## RESULTS AND DISCUSSION

In order to evaluate the measurements of the thermal properties of the cement composites with lignocellulosic materials, the results were compared with the commercial gypsum board. Gypsum board is a widely used building material that can be used for indoor applications (Butakova & Gorbunov, 2016). Gypsum boards are considered a material with good properties in terms of heat insulation, comply with the standards for fire safety and provide a pleasant room climate (De Korte, 2015; Butakova & Gorbunov, 2016; Schug et al., 2017).

During the thermal analysis, the ambient temperature was kept in  $22\text{ }^{\circ}\text{C}$  ( $\pm 1.2$ ).

Fig. 1 shows the surface temperature distribution of the cement composites with lignocellulosic materials from external size measured by infrared thermography. Also, it shows the temperature distribution from the internal side (in contact with the heat resource). The colour scale is based on the variation of the surface temperature.

The thermal performance results of the evaluated panels are shown in Table 1. Thermal properties were analyzed, evaluating thermal conductivity, thermal resistivity, thermal resistance, and thermal transmittance. Overall performance depends on material type, thickness, and mass density of the material (Gandia et al., 2019).

The commercial gypsum board presented lower values of thickness and density in comparison with the other composites evaluated. According to Costes et al. (2017), the highest thermal performances are obtained with the lowest densities' materials. Moreover, the same occurred in this study, the gypsum board and the coconut cement composite presented the lower values of thickness and density. Consequently, they showed better thermal performance.

**Table 1.** Thermal properties of the evaluated panels

Material	Thickness (mm)	Density ( $\text{kg m}^{-3}$ )	Thermal conductivity ( $\text{W m}^{-1}\text{K}^{-1}$ )	Thermal Resistivity ( $\text{K W}^{-1}$ )	Thermal Resistance ( $\text{m}^2 \text{K W}^{-1}$ )	Thermal Transmittance ( $\text{W m}^{-2}\text{K}^{-1}$ )
Eucalyptus	17 <sup>b</sup> $\pm 0.667$	1,182.1 <sup>c</sup> $\pm 68.471$	0.050 <sup>a</sup> $\pm 0.002$	20.103 <sup>b</sup> $\pm 0.624$	0.344 <sup>b</sup> $\pm 0.003$	2.903 <sup>a</sup> $\pm 0.024$
Sugar cane	17 <sup>b</sup> $\pm 0.845$	1,172.1 <sup>c</sup> $\pm 82.297$	0.058 <sup>b</sup> $\pm 0.003$	17.295 <sup>a</sup> $\pm 0.899$	0.345 <sup>b</sup> $\pm 0.003$	2.900 <sup>a</sup> $\pm 0.027$
Coconut	16 <sup>ab</sup> $\pm 0.269$	984.3 <sup>b</sup> $\pm 82.010$	0.047 <sup>a</sup> $\pm 0.001$	20.028 <sup>bc</sup> $\pm 1.672$	0.333 <sup>a</sup> $\pm 0.000$	3.007 <sup>b</sup> $\pm 0.002$
Commercial gypsum board	15 <sup>a</sup> $\pm 0.030$	1,608.0 <sup>a</sup> $\pm 30.000$	0.045 <sup>a</sup> $\pm 0.000$	21.991 <sup>c</sup> $\pm 0.096$	0.330 <sup>a</sup> $\pm 0.001$	3.032 <sup>b</sup> $\pm 0.013$

Average followed by the same lowercase letter in the columns did not differ statistically by the Tukey test at 5% significance; \*Values in parentheses are standard deviation.

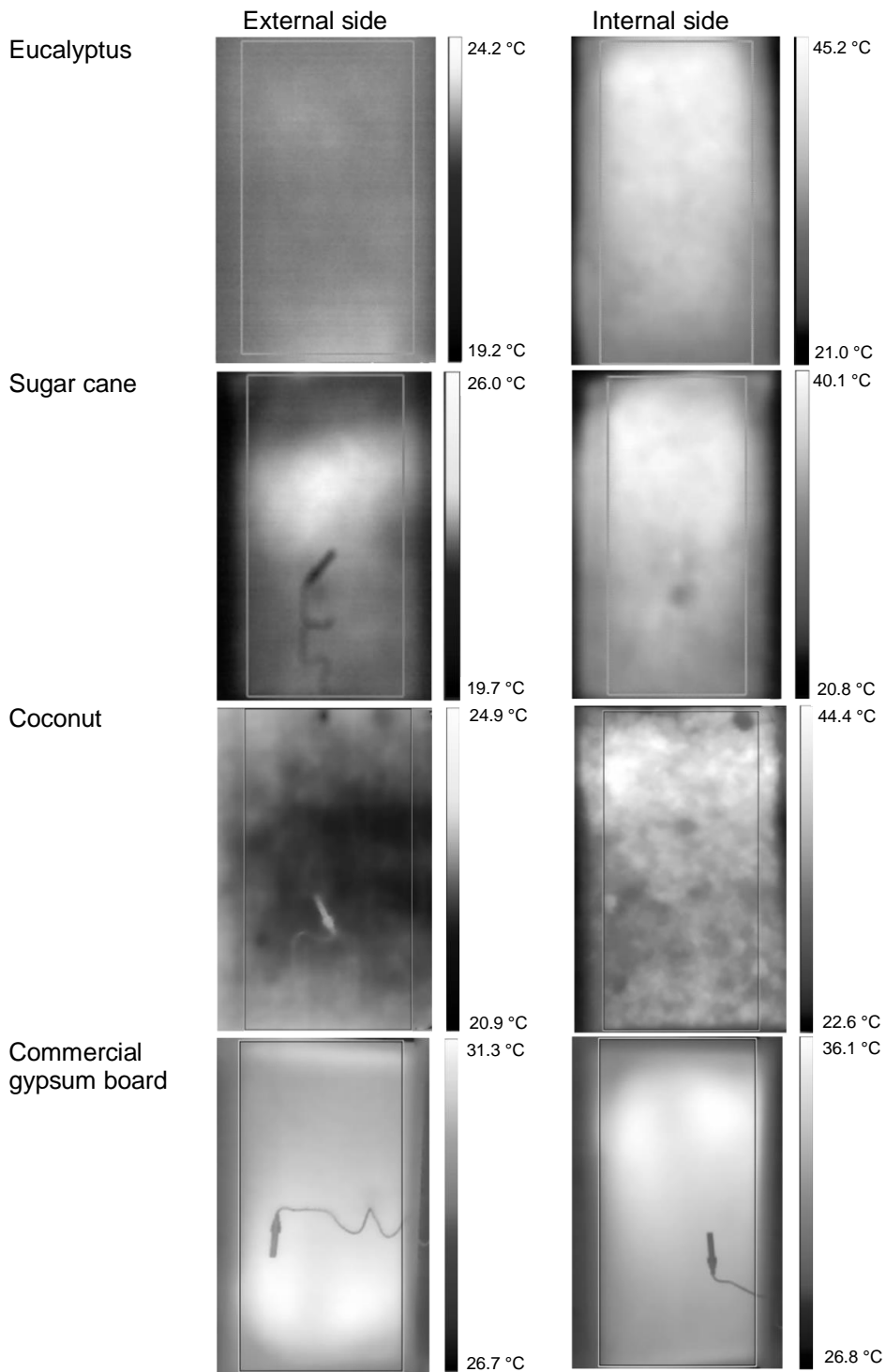


**Figure 1.** Infrared thermal images form external and internal sides of the panels based on the colour scale.

The highest density values of the composites were obtained for cement panels reinforced with Eucalyptus and sugar cane. It can be associated with the cement penetration into the permeable pores from the gaps and lumens found in the particles (Savastano et al., 2009).

Thermal conductivity is one of the most influencing factors on the performance of a building element (Schiavoni et al., 2016). It is evidenced in Table 1 that sugar cane cement composites panels were characterized by higher values of thermal conductivity. The commercial gypsum board, coconut, and Eucalyptus cement composite had similar thermal conductivity. Nevertheless, related to thermal resistivity, thermal resistance, and thermal transmittance, only the coconut panel presented the same behaviour to the commercial gypsum board. Higher thermal resistance values are obtained with lower thermal conductivity values.

According to Korjenic et al. (2011), the new approaches to energy efficient design are not only moving in the direction of lower thermal transmittance value to achieve lower energy consumption, but also the development and use of natural and local building materials.

Based on the thermal properties of the cement composites with lignocellulosic materials is possible to associate energy and environmental issues. The energy consumption required to heat or cool an environment is relatively higher in buildings with fewer insulation materials (Gandia et al., 2019). Therefore, based on the thermal analyses, a building constructed with coconut fibre might present energy expenditure to maintain thermal comfort similar to the commercial material widely used in the market (gypsum board). Besides, other advantage of the use of coconut fibre is that it is an extremely natural and ecological product (Bambi et al., 2018).

## CONCLUSIONS

It was possible to investigate the thermal performance of the three cement-based composites properly reinforced with lignocellulosic materials (Eucalyptus, sugar cane and coconut fibre) and a commercial gypsum board using infrared thermal images.

According to the results of the current work, coconut presented the best thermal performance of the three cement-based composites properly reinforced with lignocellulosic materials evaluated (Eucalyptus, sugar cane and coconut fibre).

ACKNOWLEDGEMENTS. The authors would like to thank the Minas Gerais State Agency for Research and Development (FAPEMIG Grant n. CAG-APQ-01100-15).

## REFERENCES

- American Society for Testing and Material. ASTM D-1037-12 (2016): Standard Test Methods for Evaluating Properties of Wood-Base Fiber and Particle Panel Materials, ASTM International, West Conshohocken, PA.
- Ardanuy, M., Claramunt, J. & Toledo Filho, R.D. 2015. Cellulosic fiber reinforced cement-based composites: A review of recent research. *Construction and building materials* **79**, 115–128.
- ASTM 2004. Standard Specification for Gypsum Wallboard, C 36/C 36M – 03, ASTM International, West Conshohocken, PA, USA.



- Bambi, G., Ferraz, P.F.P., Ferraz, G.A.S., Pellegrini, P. & Di Giovannantonio, H. 2019a. Measure of thermal transmittance of two different infill wall built with bamboo cultivated in Tuscany. *Agronomy Research* **17**(S1), 923–934.
- Bambi, G., Iacobelli, S., Rossi, G., Pellegrini, P. & Barbari, M. 2019b. Rural tourism to promote territories along the ancient roads of communication: case study of the rediscovery of the St. Francis's ways between Florence and La Verna. *European Countryside* **11**(3), 462–474.
- Bambi, G., Rossi, G. & Barbari, M. 2018. Comparison between different types of bedding materials for horses. *Agronomy Research* **16**(3), 646–655.
- Barbari, M., Monti, M., Rossi, G., Simonini, S. & Sorbetti Guerri, F. 2014a. Simple methods and tools to determine the mechanical strength of adobe in rural areas. *Journal of Food, Agriculture & Environment* **12**(2), 904–909.
- Barbari, M., Monti, M., Rossi, G., Simonini, S. & Sorbetti-Guerri, F. 2014b. Proposal for a simple method of structural calculation for ordinary earthen buildings in rural areas. *Journal of food, agriculture & environment* **12**(2), 897–903.
- Benazzouk, A., Douzane, O., Mezreb, K., Laidoudi, B. & Quéneudec, M. 2008. Thermal conductivity of cement composites containing rubber waste particles: Experimental study and modelling. *Construction and Building Materials* **22**(4), 573–579.
- Butakova, M.D. & Gorbunov, S.P. 2016. Study of the Influence of Complex Additives on Properties of the Gypsum-Cement-Puzzolan Binder and Concretes on its Basis. *Procedia Engineering* **150**, 1461–1467.
- Castro, J.O., Abreu, A.L., Conti, L., Moura, G.B., Cecchin, D., Yanagi Junior, T. & Ferraz, P.F.P. 2019. Use of thermography for the evaluation of the surface temperature of Japanese Quail submitted at different temperatures. *Agronomy Research* **17**(4), 1560–1567.
- Cevallos, O.A. & Olivito, R.S. 2015. Effects of fabric parameters on the tensile behaviour of sustainable cementitious composites. *Composites Part B: Engineering* **69**, 256–266.
- Conti, L., Goli, G., Monti, M., Pellegrini, P., Rossi, G. & Barbari, M. 2017. Simplified Method for the Characterization of Rectangular Straw Bales (RSB) Thermal Conductivity. In *IOP Conference Series: Materials Science and Engineering* (Vol. **245**, No. 5, p. 052035). IOP Publishing.
- Costes, J.P., Evrard, A., Biot, B., Keutgen, G., Daras, A., Dubois, S., Lebeau, F. & Courard, L. 2017. Thermal conductivity of straw bales: Full-size measurements considering the direction of the heat flow. *Buildings* **7**(1), 11.
- De Korte, A.C.J. 2015. *Hydration and thermal decomposition of cement/calcium-sulphate based materials* (Doctoral dissertation, Ph. D. Thesis, Eindhoven University of Technology. <https://research.tue.nl/en/publications/hydration-and-thermal-decomposition-of-cementcalcium-sulphate-bas>).
- Deutsches Institut für Normung. 1982. Testing of wood chipboards, bending test, determination of bending strength: *DIN*, **52362**. Berlin, 40, pp.
- Evangelisti, L., Guattari, C., Gori, P. & Vollarò, R. 2015. In situ thermal transmittance measurements for investigating differences between wall models and actual building performance. *Sustainability* **7**(8), 10388–10398.
- Fonseca, C.S., Silva, M.F., Mendes, R.F., Hein, P.R.G., Zangiacomo, A.L., Savastano, Jr.H. & Tonoli, G.H.D. 2019. Jute fibers and micro/nanofibrils as reinforcement in extruded fiber-cement composites. *Construction and Building Materials* **211**, 517–527.
- Gandia, R.M., Gomes, F.C., Corrêa, A.A.R., Rodrigues, M.C. & Mendes, R.F. 2019. Physical, mechanical and thermal behavior of adobe stabilized with glass fiber reinforced polymer waste. *Construction and Building Materials* **222**, 168–182.
- Gholizadeh, S. 2016. A review of non-destructive testing methods of composite materials. *Procedia Structural Integrity* **1**, 50–57.

- International Organization for Standardization, ISO 6946: 2017 Building Components and Building Elements—Thermal Resistance and Thermal Transmittance—Calculation Methods. *International Organization for Standardization: Geneva, Switzerland*.
- Korjenic, A., Petráněk, V., Zach, J. & Hroudová, J. 2011. Development and performance evaluation of natural thermal-insulation materials composed of renewable resources. *Energy and Buildings* **43**(9), 2518–2523.
- Meola, C., Boccardi, S., Carlomagno, G.M., Boffa, N.D., Monaco, E. & Ricci, F. 2015. Nondestructive evaluation of carbon fibre reinforced composites with infrared thermography and ultrasonics. *Composite Structures* **134**, 845–853.
- Nascimento, G.R., Nääs, I.A., Pereira, D.F., Baracho, M.S. & Garcia, R. 2011. Assessment of broiler surface temperature variation when exposed to different air temperatures. *Brazilian Journal of Poultry Science* **13**(4), 259–263.
- Raja, N., Rajinikanth, V., Fernandes, S.L. & Satapathy, S.C. 2017. Segmentation of breast thermal images using Kapur's entropy and hidden Markov random field. *Journal of Medical Imaging and Health Informatics* **7**(8), 1825–1829.
- Rheinheimer, V., Wu, Y., Wu, T., Celik, K., Wang, J., De Lorenzis, L. & Monteiro, P.J. 2017. Multi-scale study of high-strength low-thermal-conductivity cement composites containing cenospheres. *Cement and Concrete Composites* **80**, 91–103.
- Savastano, H.Jr., Santos, S.F. & Agopyan, V. 2009. *Sustainability of Construction Materials*. Elsevier, Amsterdam. pp. 55–81.
- Schiavoni, S., Bianchi, F. & Asdrubali, F. 2016. Insulation materials for the building sector: A review and comparative analysis. *Renewable and Sustainable Energy Reviews* **62**, 988–1011.
- Schug, B., Mandel, K., Schottner, G., Shmeliov, A., Nicolosi, V., Baese, R., Bernd Pietschmann, B., Biebl, M. & SEXTL, G. 2017. A mechanism to explain the creep behavior of gypsum plaster. *Cement and Concrete Research* **98**, 122–129.
- Silva, F.A, Chawla, N. & Toledo Filho, R.D. 2008. Tensile behavior of high performance natural (sisal) fibers. *Composites Science and Technology* **68**(15–16), 3438–3443.
- Souza, M.R. 1994. *Durability of cement-bonded particle board made conventionally and carbon dioxide injection*. Thesis (Doctor of Philosophy) – University of Idaho, Idaho, 123 pp.
- Sudin, R. & Swamy, N. 2006. Bamboo and wood fibre cement composites for sustainable infrastructure regeneration. *Journal of materials science* **41**(21), 6917–6924.
- Teixeira, J.N., Silva, D.W., Vilela, A.P., Junior, H.S., Brandão, L.E.V.S. & Mendes, R.F. 2018. Lignocellulosic Materials for Fiber Cement Production. *Waste and Biomass Valorization*, 1–8.
- Wei, J. & Meyer, C. 2015. Degradation mechanisms of natural fiber in the matrix of cement composites. *Cement and Concrete Research* **73**, 1–16.
- Zhang, H., Xing, F., Cui, H.Z., Chen, D.Z., Ouyang, X., Xu, S.Z., Wang, J.X., Huang, Y.T., Zuo, J. D. & Tang, J.N. 2016. A novel phase-change cement composite for thermal energy storage: Fabrication, thermal and mechanical properties. *Applied energy* **170**, 130–139.

## **Chemical analyses of lignocellulosic materials residue for cement panels reinforcement**

P.F.P. Ferraz<sup>1,\*</sup>, R.F. Mendes<sup>2</sup>, G.A.S. Ferraz<sup>1</sup>, G. Rossi<sup>3</sup>, L. Conti<sup>3</sup> and M. Barbari<sup>3</sup>

<sup>1</sup>Federal University of Lavras, Department of Agricultural Engineering, Campus Universitário, PO Box 3037, Lavras, Minas Gerais, Brazil

<sup>2</sup>Federal University of Lavras, Department of Engineering, Campus Universitário, PO Box 3037, Lavras, Minas Gerais, Brazil

<sup>3</sup>University of Firenze, Department of Agriculture, Food, Environment and Forestry (DAGRI), Via San Bonaventura 13, IT50145 Firenze, Italy

\*Correspondence: [patricia.ponciano@ufla.br](mailto:patricia.ponciano@ufla.br)

**Abstract.** The use of lignocellulosic material residue in cement composites is on the rise as sustainable building materials in most developing countries. Besides, this alternative is seen as a good option for new cement panels formulations for indoor applications. Thus, the current paper aims to evaluate the chemical properties of five potential lignocellulosic materials residues to be used for cement panels reinforcement: Eucalyptus, sugarcane bagasse, coconut fibre, coffee rusk, and banana pseudostem. The following physical properties of the lignocellulosic materials were evaluated: lignin, extractives, ash, and holocellulose. To evaluate the similarity of the chemical composition of the lignocellulosic materials, Hierarchical Cluster Analysis (HCA) was used identified by using Ward's method of cluster analysis. These compositions were grouped by dendrograms in which the similarity of these data was qualified. It was observed that there were statistical differences among all types of lignocellulosic materials related to the chemical composition. Coconut showed the smallest amount of extractives, and sugar cane the most significant amount. Eucalyptus and coffee husk presented the most similar chemical composition. All of the evaluated materials could be used in fibre cement production for indoor applications.

**Key words:** cementitious composites, chemical properties, dendrograms, hierarchical cluster analysis.

## **INTRODUCTION**

The use of residues lignocellulosic materials as cement-based reinforcement is on the rise as sustainable building materials in most developing countries (Sudin & Swamy, 2006; Teixeira et al., 2018). Many studies have been focused on the use of natural materials in buildings materials since these materials present high sustainability (Conti et al., 2017). Besides, the residues lignocellulosic materials can be abundant in the environment in many parts of the world and relatively inexpensive (Castro et al., 2019).

The lignocellulosic residues can be considered as potential alternatives for rural and civil buildings, given their ecological friendliness and ready availability in fibrous form

and also, since they can be extracted from plant leaves at low cost, in the most of cases (Silva et al., 2008). The engineering design of rural and civil buildings must take the availability of the local materials into account, encouraging wherever possible the use of natural materials that can be regenerated (Bambi et al., 2019).

The use of lignocellulosic material residues to produce cement composites to be used in building constructions is considered as a good option for new lignocellulosic cement formulations. However, one of the challenges for the production of cementitious composites reinforced with lignocellulosic materials is reinforcement/matrix interaction (Teixeira et al., 2018). Thus, to use adequately, the lignocellulosic materials is mandatory to know the chemical composition of these materials. The chemical concentrations may influence the cement composites' mechanical properties, the bond behaviour, and degradation of natural fibres in composites components (Onuaguluchi & Banthia, 2016).

To compare the difference of chemical composition of the lignocellulosic residues, techniques of Hierarchical cluster analysis (HCA) can be used. HCA, also known as hierarchical clustering, is a popular method for cluster analysis in big data research and data mining, aiming to establish a hierarchy of clusters (Muntaner et al., 2012). HCA attempts to group subjects with similar features into clusters (Ferraz et al., 2019).

Thus, this paper aimed to evaluate the chemical properties of lignocellulosic materials residue to produce cement panels using agglomerative hierarchical clustering.

## MATERIAL AND METHODS

The experiment was developed at the Federal University of Lavras (UFLA), Lavras, Brazil. To evaluate the chemical properties of five potential lignocellulosic materials residues to be used for cement panels reinforcement a sample of the following materials were collected: sugarcane bagasse (*Saccharum officinarum*), eucalyptus (*Eucalyptus grandis*), banana pseudostem (*Musa acuminata*), coconut shell (*Cocos nucifera*) and coffee husk (*Coffea arabica* L.).

Eucalyptus wood tree and banana pseudostem were obtained from local experimental cultivations at Federal University of Lavras - UFLA. Sugar cane was obtained in a commercial cachaça distillery for the production of sugar-cane liquor (cachaça) in Lavras - Minas Gerais state (MG), Brazil. The coconut shell was taken from local floriculture in Lavras - MG, Brazil. Coffee husk was obtained from a farm in the municipality of Santo Antônio do Amparo - MG, Brazil.

Eucalyptus and sugar cane passed through a laminator for delaminating. Coconut shell, coffee husk, and banana pseudostem were processed in a hammer-mill. The material particles were selected through a sieve, and the fraction retained between 20 (0.841 mm) and 40 (0.420 mm) mesh was used to the experimental chemical analyses as established in the NBR 14853 (2010) Standards.

Panels were produced following the methodology suggested by Latorraca (2000), and Lopes (2004), and described by Mendes et al. (2017).

To evaluate the chemical properties of the lignocellulosic materials to produce cement panels, the following analyses were carried out: lignin, total extractives, ash, and holocellulose.

Holocellulose content was calculated by extracting lignin with sodium chlorite and acetic acid, according to the procedure reported in Browning (1963). Total extractive content was measured as established in the NBR 14853 (2010) Standards.

The insoluble lignin content was measured according to the NBR 7989 (2010) Standards. An oven was used to obtain the mineral content of ashes, according to the NBR 13999 (2017) Standards.

The data of chemical properties lignocellulosic materials analysis was performed using Hierarchical cluster analysis (HCA). The basic idea of this technique is to put in the same group objects that are similar according to some predetermined criterion (Linden, 2009). Within each cluster, the objects are similar to each other, while objects located in other clusters are different from one another (Dominick et al., 2012). The results of the HCA method were described using a dendrogram, which is a similarity diagram, quantified using Ward's method and Euclidean distance, described by Ferraz et al., (2014).

According to Dominick et al. (2012), the Euclidean distance (DE) is described by Eq. 1:

$$DE = \left[ \left( \frac{Dlink}{Dmax} \times 100 \right) \right] \quad (1)$$

where *Dlink* is the connection or linkage distance, and *Dmax* is the maximum distance. To standardize the bond distance represented by the y-axis, the ratio is usually multiplied by 100.

As the initial cluster, the Ward method considers individuals who provide the lowest sum of squares of deviations (Melo Júnior et al., 2006).

The HAC analysis and the dendrograms of the chemical properties were performed using the statistical computer system R (R Development Core Team, 2019), and the cophenetic correlation coefficient fit was also estimated using the same software.

Internal bonding (IB) analyzes were performed according to the American Society for Testing and Material - ASTM D1037 (2016).

## RESULTS AND DISCUSSION

Fig. 1 indicates the chemical composition of the lignocellulosic materials evaluated. It is possible to observe that there is a big variation in the chemical composition of the lignocellulosic materials. According to Onuaguluchi & Banthia (2016), the concentrations of the chemical components in a raw material depend on factors such as fibre type, growth condition, dimension, age, cultivation site, extraction, and processing method. Besides, the amount of these components (lignin, total extractives, ash, and holocellulose) can affect the properties of the cement composite reinforced with these materials. Chemical composition of lignocellulosic materials can affect the mechanical properties of the panels (Onuaguluchi & Banthia, 2016).

To evaluate the chemical properties of the lignocellulosic materials, the agglomerative hierarchical clustering (HCA) was used. HCA separates the lignocellulosic materials into groups, based on the characteristics of their chemical composition. These materials are separated using classification criteria in such a way that there is homogeneity within the group and heterogeneity between the groups. The results of the HCA method were described using dendrograms (Fig. 2, a, b, c, and d), which is a similarity diagram, quantified using Ward's method and Euclidean distance. Fig. 2 shows the chemical composition of every evaluated lignocellulosic residue

materials hierarchically clustered separated a) lignin (%), b) total extractives (%), c) ash (%), d) holocellulose (%). In the dendrogram, the level of similarity is indicated on the horizontal scale, and the evaluated lignocellulosic materials are represented on the vertical axis in convenient order for grouping. The horizontal axis displays the distance between observations and/or clusters. The horizontal bars indicate the point at which two clusters/observations are merged. It means that smaller values of the horizontal axis indicate more similarity between the groups.

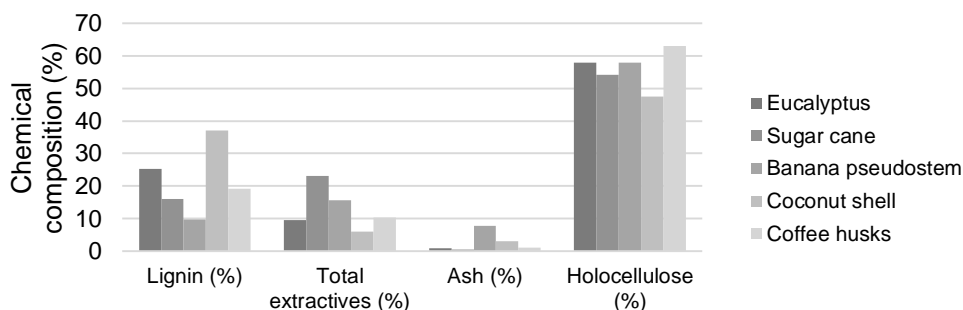


**Figure 1.** Chemical composition of the lignocellulosic materials: a) lignin (%), b) total extractives (%), c) ash (%), d) holocellulose (%) of eucalyptus, sugar cane, banana pseudostem, coconut shell and coffee husk.

In Fig. 2, a is evident that sugar cane and coffee husks presented a similar amount of lignin. It is indicated because the distance scale (horizontal axis) is closer to 0. Sugar cane and coffee husk presented a similar amount of lignin, 16.0%, and 19.2%, respectively. The distance scale of the other materials presented bigger values, which indicates that they are not similar. It means that coconut shell, sugar cane, and eucalyptus presented statistical differences related to the amount of lignin in their composition. Eucalyptus presented a smaller amount of lignin (9.7%).

Fig. 2, b shows the groups formed based on the total extractives composition. This Figure indicates that eucalyptus and coffee husk are in the same group of similarity, with a scale distance of 0.1. Both materials presented an intermediate amount of total extractives (9.5 and 10.3% for eucalyptus and coffee husk, respectively). Coconut shell is the material with the smaller amount of total extractives (5.9%). Sugar cane and banana pseudostem presented the bigger dissimilarity, and they presented the bigger values of the scale distance in comparison with the other materials (> 1.8).

According to Angles et al. (1997) the ash fraction is formed by most of the inorganic substances present in the native substrate. All the materials presented a similar amount of ash, around (1%, Fig. 1, c), except banana pseudostem that presented 7.8%. In Fig. 2, c, it is possible to observe that banana pseudostem presented the bigger dissimilarity in comparison with the other materials. Banana pseudostem showed a scale distance of the other materials bigger than 2.0, while the other materials presented the distance scale smaller than 0.5. It indicates that coffee husk, eucalyptus, and sugar cane can be part of the same group because they have a similar amount of ash, with a distance scale smaller than 0.2. While coconut shell is alone in a different group (distance scale of 0.5) and banana pseudostem is the lignocellulosic material most different than the others with a distance scale bigger than 2.0.

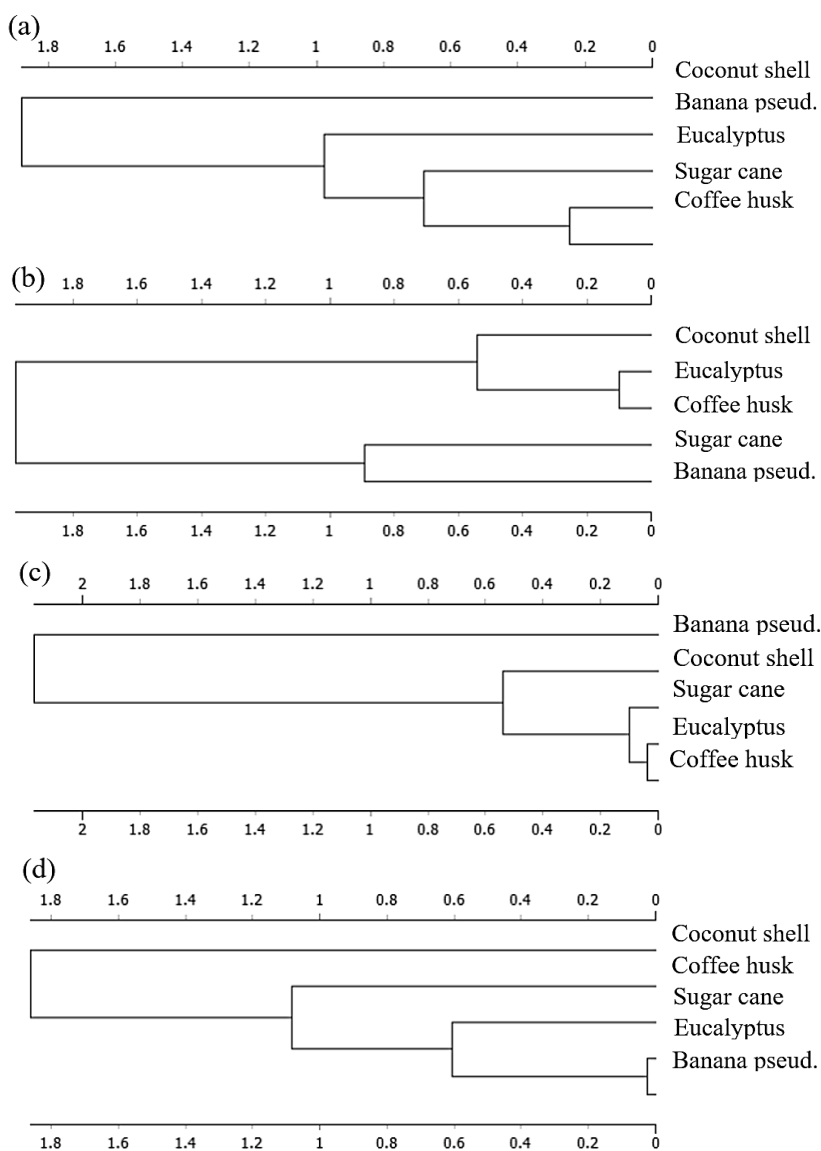


**Figure 2.** Dendrograms of the chemical properties of lignocellulosic materials: a) Lignin (%), b) total extractives (%), c) ash (%), d) holocellulose (%) of eucalyptus, sugar cane, banana pseudostem, coconut shell and coffee husk.

Based on the amount of holocellulose (Fig. 2, d) eucalyptus and banana pseudostem presented a similar amount of this element, around 58%, which means that they are in the same group. The other materials presented dissimilarities concerning the amount of holocellulose. It means that there is a significant variation in the composition of holocellulose of these materials. According to Fig. 1, coffee husk presented the biggest amount of holocellulose of the evaluated materials. Holocellulose has a significant influence on the cement composite properties. This chemical component can be one of the responsible for the mechanical resistance of the composites (Teixeira et al. (2018).

While in Fig. 2 is possible to see the lignocellulosic materials grouped based on each chemical component separately, In Fig. 3, the lignocellulosic materials are grouped based on all chemical components at the same time. Based on Fig. 3, it is possible to observe that none of the evaluated material presented a similar chemical composition. The materials that presented the most similar chemical composition were eucalyptus and coffee husk. These materials presented the smaller values of the distance scale. Eucalyptus and coffee husk presented intermediate values of lignin, total extractives, and ash. However, on the other hand, coconut shell was the material that presented the most different composition concerning the other evaluated materials. It can be explained because the coconut shell showed the biggest amount of lignin and the smaller values of total extractives and holocellulose.

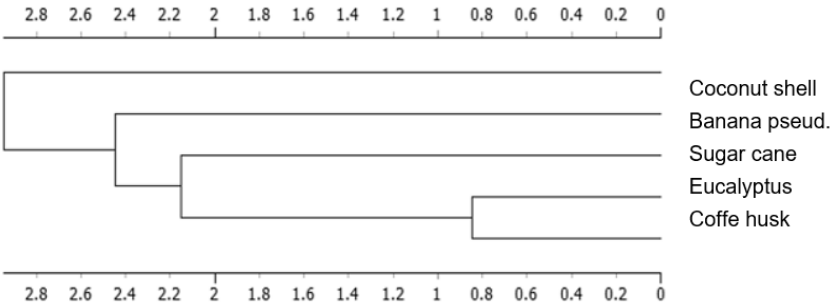


**Figure 3.** Dendrograms of the chemical properties of lignocellulosic materials.

Internal bonding (IB) is related to the transmission of the stress that occurs between lignocellulosic and cement particles, which is affected by factors such as the content of extractives, interaction between particle and cement matrix, and cement matrix and particle dimensions (Mendes et al., 2017).

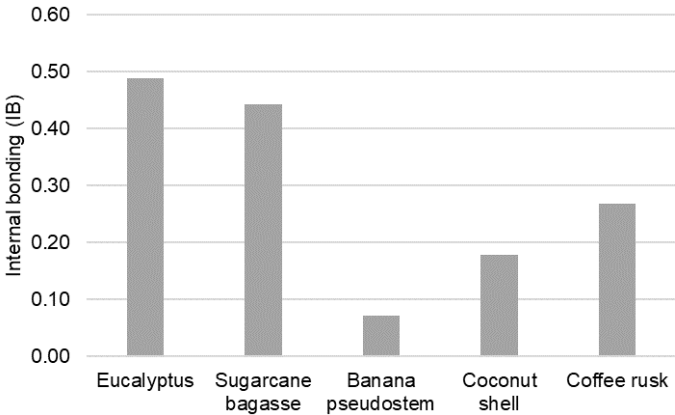


**Figure 4.** Internal bonding (IB) of the lignocellulosic composites.

Fig. 4 shows that the chemical content of the lignocellulosic materials affected the mechanical properties of composites. The Eucalyptus composites can be highlighted because they presented the best results of internal bonding (IB). This higher IB may be



related to the lower extractives content (Fig. 1), which may affect the cement cure and to prejudice the interaction of the lignocellulosic particles with the cement matrix (Mendes et al., 2017).

Panels with banana pseudostem presented the lower values of IB. Despite not having the highest amount of extracts, banana pseudostem presented low values of lignin, which affects the fiber union and, consequently, the mechanical resistance of the material used in the production of cement-based panels (Asasutjarit et al., 2009). In general, the lower values of resistance to the IB are related to the small adhesion of matrix fiber in the composite (Kochova et al., 2020).

## CONCLUSION

It was possible to investigate the chemical properties of the five potential lignocellulosic materials residues to be used for cement panels reinforcement using Hierarchical Cluster Analysis.

According to the results of the current work, eucalyptus and coffee husk presented the most similar chemical composition. These materials presented the smaller values of the distance scale. Eucalyptus and coffee husk presented intermediate values of lignin, total extractives, and ash.

The coconut shell was the material that presented the most different composition concerning the other evaluated materials. It can be explained because the coconut shell showed the biggest amount of lignin and the smaller values of total extractives and holocellulose.

**ACKNOWLEDGEMENTS.** The authors would like to thank the Minas Gerais State Agency for Research and Development (FAPEMIG Grant n. CAG-APQ-01100-15).

## REFERENCES

- Angles, M.N., Reguant, J., Martinez, J.M., Farriol, X., Montane, D. & Salvado, J. 1997. Influence of the ash fraction on the mass balance during the summative analysis of high-ash content lignocellulosic. *Bioresource Technology* **59**(2–3), 185–193.
- Asasutjarit, C., Charoenvai, S., Hirunlabh, J. & Khedari, J. (2009). Materials and mechanical properties of pretreated coir-based green composites. *Composites Part B: Engineering*, **40**(7), 633–637.
- American Society for Testing and Materials - ASTM: Standard test methods for evaluating properties of wood-based fiber and particle panel materials: ASTM D 1037 - 96a. Philadelphia: ASTM, 1998. v. 04.09: (Annual Book of ASTM Standards).
- Bambi, G., Ferraz, P.F.P., Ferraz, G.A.S., Pellegrini, P. & Di Giovannantonio, H. 2019. Measure of thermal transmittance of two different infill wall built with bamboo cultivated in Tuscany. *Agronomy Research* **17**(S1), 923–934.
- Brazilian Association of Technical Standards. NBR 13999: Paper, paperboard, cellulosic pulp and wood: determination of the residue (ash) after incineration at 525 °C. Rio de Janeiro, Brazil; 2017 (in Portuguese).
- Brazilian Association of Technical Standards. NBR 14853: Wood - determination of ethane-toluene-soluble material and dichloromethane and acetone. Rio de Janeiro, Brazil; 2010 (in Portuguese).

- Brazilian Association of Technical Standards. NBR 7989: Cellulosic Pulp and Wood – Determination of Acid-Insoluble Lignin, Rio de Janeiro, Brazil; 2010 (in Portuguese).
- Browning, B.L. 1963. The Chemistry of Wood. *Interscience*, Warrenville, 689 pp.
- Castro, E.D.D., Villela, L.S., Mendes, L.M., Mendes, R.F., Ribeiro, A.G.C., Guimarães Junior, J.B. & Rabelo, G.F. 2019. Analysis of the coffee peel application over the soil-cement bricks properties. *Coffee Science* **14**(1), 12–23.
- Conti, L., Goli, G., Monti, M., Pellegrini, P., Rossi, G. & Barbari, M. 2017. Simplified Method for the Characterization of Rectangular Straw Bales (RSB) Thermal Conductivity. In *IOP Conference Series: Materials Science and Engineering* (Vol. **245**, No. 5, p. 052035). IOP Publishing.
- Dominick, D., Juahir, H., Latif, M.T., Zain, S.M. & Aris, A.Z. 2012. Spatial assessment of air quality patterns in Malaysia using multivariate analysis. *Atmospheric Environment* **60**, 172–181. Oxford.
- Ferraz, P.F.P., Ferraz, G.A.S., Barbari, M., Silva, M.A.J.G., Damasceno, F.A., Cecchin, D. & Castro, J.O. 2019. Behavioural and physiological responses of rabbits. *Agronomy Research* **17**, 704–710.
- Ferraz, P.F.P., Yanagi Junior, T., Alvarenga, T.A.C., Reis, G.M., Campos, A.T. 2014. Behavior of chicks to thermal challenge. *Engenharia Agrícola*, Jaboticabal, **34**(6), 1039–1049.
- Kochova, K., Gauvin, F., Schollbach, K. & Brouwers, H.J.H. 2020. Using alternative waste coir fibres as a reinforcement in cement-fibre composites. *Construction and Building Materials* **231**, 117121.
- Latorraca, J.V.F. 2000. *Eucalyptus spp.* in the production of cement-wood panels. Thesis (D.Sc.), Federal University of Paraná, 191 pp. (in Portuguese).
- Lopes, Y.L.V. 2004. Use of *Eucalyptus grandis* wood and bark Hill ex Maiden in the production of cement-wood panels. Thesis (M. Sc.), Federal University of Lavras, 60 pp. (in Portuguese).
- Linden, R. 2009. Grouping Techniques. *Revista de Sistema de Informação da FSMA*, Macaé, **4**, 18–36 (in Portuguese).
- Melo Júnior, J.C.F. de, Sediya, G.C., Ferreira, P.A. & Leal, B.G. 2006. Determination of homogeneous regions as to the distribution of rain frequency in the east of the State of Minas Gerais. *Revista Brasileira de Engenharia Agrícola e Ambiental* **10**(2), 408–416.
- Mendes, R.F., Vilela, A.P., Farrapo, C.L., Mendes, J.F., Tonoli, G.H.D. & Mendes, L.M. 2017. Lignocellulosic residues in cement-bonded panels. In *Sustainable and nonconventional construction materials using inorganic bonded fiber composites* (pp. 3–16). Woodhead Publishing.
- Muntaner, C., Chung, H., Benach, J. & Ng, E. 2012. Hierarchical cluster analysis of labour market regulations and population health: a taxonomy of low-and middle-income countries. *BMC Public Health* **12**(1), 286.
- Onuaguluchi, O. & Banthia, N. 2016. Plant-based natural fibre reinforced cement composites: A review. *Cement and Concrete Composites* **68**, 96–108.
- R Development Core Team. R: A language and environment for statistical computing. R Foundation for Statistical Computing, Vienna, 2019.
- Silva, F.A., Chawla, N. & Toledo Filho, R.D. 2008. Tensile behavior of high performance natural (sisal) fibers. *Composites Science and Technology* **68**(15–16), 3438–3443.
- Sudin, R. & Swamy, N. 2006. Bamboo and wood fibre cement composites for sustainable infrastructure regeneration. *Journal of Materials Science* **41**(21), 6917–6924., R.F. 2018. Lignocellulosic Materials for Fiber Cement Production. *Waste and Biomass Valorization*, 1–8.

## **Research on energy efficiency of pneumatic cylinder for pneumatic vehicle motor**

M. Gailis<sup>1,2,\*</sup>, J. Rudzitis<sup>1</sup>, M. Madissoo<sup>3</sup> and J. Kreicbergs<sup>1</sup>

<sup>1</sup>Riga Technical University, Faculty of Mechanical Engineering, Transport and Aeronautics, Institute of Transport, Kalku 1, LV 1658 Riga, Latvia

<sup>2</sup>University of Life Sciences and Technologies, Faculty of Engineering, Institute of Mechanics, Liela 2, LV 3001 Jelgava, Latvia

<sup>3</sup>Estonian University of Life Sciences, Institute of Technology, Fr. R. Kreutzwaldi 56/1, EE51014 Tartu, Estonia

\*Correspondence: maris.gailis@rtu.lv

**Abstract.** Compressed gas is relatively expensive source of energy. When compressed gas is used for propelling of pneumatically driven vehicle, efficient gas utilization is favoured. Design and control strategy of pneumatic cylinder, with the emphasis on effective energy conversion is being discussed in this paper. Mathematical model, results of computer simulation and experimental work are provided and discussed. Experimental research is performed on the competition vehicle, equipped with pneumatically driven piston motor and instrumented. Relative significance of various geometric and control parameters of pneumatic cylinder on efficiency of energy conversion is presented.

**Key words:** gas consumption, compressed air vehicle, pneumobile, gas expansion, efficacy.

### **INTRODUCTION**

Pneumatic actuators are important part of industrial machinery. Pneumatic cylinders are typically used to move or hold tools or products. Pneumatic cylinders include wide variety of linear actuators, such as spring load single acting, double acting and rodless cylinders (Cambell, 2018).

This research is focused on the improvement of the efficiency of pneumatic motor for pneumatic vehicle, built for participation in International AVENTICS Pneumobile Competition. The competition is organised by company AVENTICS Hungary Ltd since 2008 (Aventics Hungary Kft, 2019). Pneumatic vehicle used in this research is shown on Fig. 1. Recent results of this competition shows large variation of the results of different teams (Emerson Electric Co, 2019). Energy source and design rules are similar to all teams. Efficiency of mechanical and pneumatic systems, correct operation of control system along with level of team training and some luck makes the difference.

For typical industrial application one chamber of double acting pneumatic cylinder is continuously supplied with air at certain pressure until the piston reaches the end position. At the end of piston's course air in the chamber is at high pressure and it is then released to the surroundings. To control piston and rod speed, air flow from the chamber

on the other side of the piston can be throttled to maintain certain pressure. Such control strategy provide relatively even motion profile (Barber, 1997).

In the industrial applications actuators usually are the last elements in the large and complex system that also contains air filters, compressors, dehumidifiers, distribution pipes and control valves. Air compressor efficiency and losses in the pipelines are discussed in technical information sources (Barber, 1997; SMC Pneumatics, 1997). The efficiency of pneumatic actuators is usually left out of the technical documentation. Energy efficiency of pneumatic actuators is approximately 20–30%, thus affecting overall energy efficiency of compressed air systems (Cai et al., 2001; Wang & Gordon, 2011; Luo et al., 2013; Du et al., 2018). Energy efficiency of the pneumatic cylinders and its improvement is analysed in the previous work by research community.

Fleischer developed concept of dual pressurisation that is based on supplying dual action cylinder working side chambers with different pressure during expansion and retraction. In case, when equal force during expansion and retraction is needed, pressure is adjusted to compensate difference in piston surface area. In case when opposite piston movement is needed for positioning only, little force is required and pressure can be significantly reduced. Dual pressurisation can considerably reduce air consumption (Fleischer, 1995; Harris et al., 2012).

Reutilisation of air which otherwise would be released to surroundings at the end of working cycle is proposed by several researchers. Luo developed energy recovery system that utilises scroll expander that converts mechanical energy to electrical, increasing efficiency by 18.1% (Luo et al., 2013). Li et al. proposed use of recovery tank to collect air from cylinder exhaust. The boost valve then is used to increase air pressure and resupply high pressure supply circuit. They reported recovery of up to 40% of air amount (Li et al., 2006). Shen and Goldfarb presented energy saving approach which is based on additional control valve to enable air flow between cylinder chambers or so called crossflow. They reached energy savings up to 25–52% (Shen & Goldfarb, 2007). Létai et al. (2017) presented a design of pneumatic vehicle with four cylinder pneumatic motor. The engine uses sequentially working paired cylinders, where smaller cylinder works in constant gas supply mode at 10 bar pressure, and the gas then is transferred to a larger cylinder where it expands. Proposal of Létai et al. combines gas reutilization and expansion. The authors claim that in this way the energy is reused. Theoretical analysis is not fully developed and presented (Létai et al., 2017).

Doll et al. proposed and discussed pneumatic cylinder control system, in which air supply is cut at certain point of piston travel and expanded until the end of the stroke. They achieved up to 85% savings in air consumption, comparing to regular pneumatic cylinder control system (Doll et al., 2011). Du et al. proposed and experimentally validated bridge-type control system of pneumatic cylinder, in which gas expansion is used and piston motion is controlled. Improvement in energy efficiency by 50–70% where achieved (Du et al., 2018). Harris et al. explored energy efficiency of pneumatic cylinder for vertical load lifting application, using computer model and experimental



**Figure 1.** Pneumatic vehicle during the competition, Eger, Hungary.

setup. They compared traditional, dual pressurising and gas expansion control circuits. With dual pressurising they achieved 27% and with gas expansion 29% in savings of compressed air consumption (Harris et al., 2014).

Analysis of previous work has shown, that gas expansion can provide greater efficiency increase, comparing to other known control strategies.

Use of pneumatic cylinder as part of pneumatic vehicle motor has some differences comparing to industrial application. For instance, other gas type can be used, instead of air, and at higher pressure. Furthermore, gas temperature can be increased, using heat exchanger. Equalized motion profile and piston speed limits are non-essential.

The subject of this research is an efficiency of double acting pneumatic cylinder, used in the gas expansion mode, in the conditions that are specific to pneumatic vehicle. The novelty of the research consists of finding relative significance of gas type and temperature, geometric and control parameters on the efficiency of energy to work conversion. Another novelty of this paper is use of normalised parameters, which are not dependent on cylinder size, absolute amount of work done or quantity of gas used. Such parameters are well known in another fields of research, but rarely used in relation with pneumatic actuators. Results of mathematical modelling, computer simulation and experimental research are presented and discussed.

## MATERIALS AND METHODS

### Theory and modelling

To develop relations between control parameters and efficiency of energy conversion in the pneumatic cylinder, a simplified theoretical model is developed. Graphical representation of the modelled pneumatic cylinder is shown in the Fig. 2. The numbers in the diagram correspond to index used for parameters in the equations.

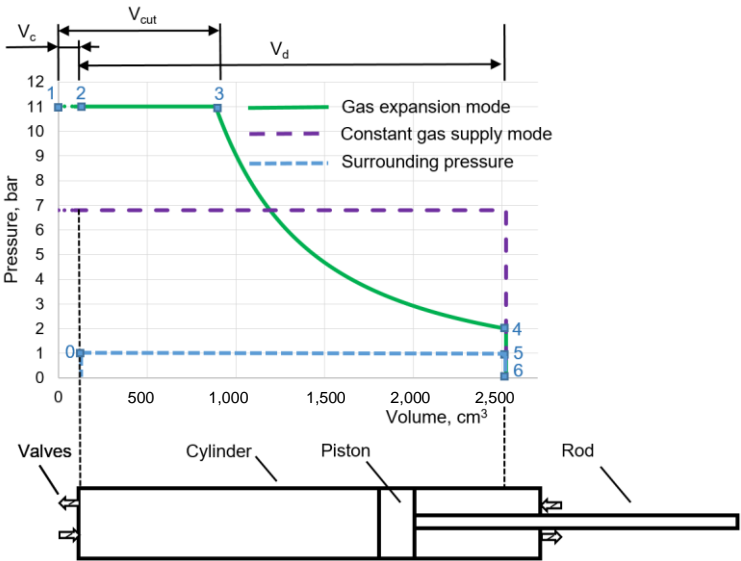


**Figure 2.** Pneumatic cylinder and pressure-volume diagram.  $V_c$  – volume of supply pipe and control valve;  $V_d$  – displacement volume;  $V_{cut}$  – volume at which gas supply is stopped.

Heat exchange, turbulence effects and friction are not included. Effect of temperature on heat capacity is not accounted.

### Energy conversion efficacy

Energy conversion efficacy is the ratio of work done and energy supplied:

$$\eta_{th} = \frac{W}{E} = \frac{U_{1,2} + H_{2,3} - U_{4,6}}{U_{1,2} + H_{2,3}} = 1 - \frac{U_{4,6}}{U_{1,2} + H_{2,3}} \quad (1)$$

where  $W$  – work, J;  $E$  – energy, J;  $U$  – internal energy, J;  $H$  – enthalpy, J.

Internal energy can be expressed (Serway & Kirkpatrick, 2014):

$$U = c_v \cdot n \cdot T \quad (2)$$

where  $c_v$  – specific molar heat capacity at constant volume, J mol<sup>-1</sup> K<sup>-1</sup>;  $n$  – amount of gas, mol;  $T$  – temperature, K.

Enthalpy can be expressed (Serway & Kirkpatrick, 2014):

$$H = c_p \cdot n \cdot T \quad (3)$$

where  $c_p$  – specific molar heat capacity at constant pressure, J mol<sup>-1</sup> K<sup>-1</sup>.

Expression 1 can be rewritten:

$$\eta_{th} = 1 - \frac{c_v \cdot T_4 \cdot (n_{1,2} + n_{2,3})}{c_v \cdot T_1 \cdot n_{1,2} + c_p \cdot T_1 \cdot n_{2,3}} \quad (4)$$

where  $W$  – work, J;  $E$  – energy, J;  $U$  – internal energy, J;  $H$  – enthalpy, J.

Ratio of heat capacities (Caton, 2016):

$$\gamma = \frac{c_p}{c_v} \quad (5)$$

Ratio of expansion is defined:

$$r_e = \frac{V_c + V_d}{V_{cut}} \quad (6)$$

where  $V_c$  – total volume of supply pipe and control valve, m<sup>3</sup>;  $V_d$  – displacement volume, m<sup>3</sup>;  $V_{cut}$  – volume at which the gas supply is stopped, m<sup>3</sup>.

If initial pressure  $P_1$  and desirable final pressure  $P_4$  is known,  $V_{cut}$  can be found, basing on pressure and volume relations during isoentropic and adiabatic process, where from point 3 to 4 in the Fig. 2,  $PV^\gamma = const$ :

$$V_{cut} = \left( \frac{P_4(V_c + V_d)^\gamma}{P_1} \right)^{\frac{1}{\gamma}} \quad (7)$$

where  $P$  – pressure, Pa.

Using isentropic relations, stating that from point 3 to 4 in the Fig. 2,  $TV^{\gamma-1} = const$  temperature at the end of expansion can be calculated (Heywood, 2018):

$$T_4 = T_1 \cdot r_e^{1-\gamma} \quad (8)$$

Expression (4) now can be rewritten with temperature  $T_l$  cancelled out:

$$\eta_{th} = 1 - \frac{c_v \cdot r_e^{1-\gamma} \cdot (n_{1,2} + n_{2,3})}{c_v \cdot n_{1,2} + c_p \cdot n_{2,3}} \quad (9)$$

Heat capacities can be replaced by ratio of heat capacities according to the Eq. 5:

$$\eta_{th} = 1 - \frac{r_e^{1-\gamma} \cdot (n_{1,2} + n_{2,3})}{n_{1,2} + \gamma \cdot n_{2,3}} \quad (10)$$

According to ideal gas law, molar quantity of gas can be expressed:

$$n = \frac{P \cdot V}{R \cdot T} \quad (11)$$

where  $R$  – universal gas constant,  $8.314 \text{ J mol}^{-1} \text{ K}^{-1}$ .

As the gas is supplied at constant temperature  $T_l$  and constant pressure  $P_l$  and  $R$  is a constant, they cancel out when Eq. 11 is used to replace molar quantity  $n$  in the Eq 10:

$$\eta_{th} = 1 - \frac{r_e^{1-\gamma} \cdot (V_c + V_{cut} - V_c)}{V_c + \gamma \cdot (V_{cut} - V_c)} = 1 - \frac{r_e^{1-\gamma} \cdot V_{cut}}{V_c + \gamma \cdot (V_{cut} - V_c)} \quad (12)$$

In case of practical application of pneumatic cylinder as energy conversion device for pneumatic vehicle, consumption (which corresponds to work done by certain amount of gas) and efficiency using specific type of gas might be subjects of interest. Also additional work to expel gas from the cylinder or perform work on surrounding should be accounted for. Specific work can be used for that purpose and it is expressed as ratio of effective work done to molar quantity of gas:

$$W_m = \frac{W_g - W_s}{n} = \frac{U_{1,2} + H_{2,3} - U_{4,6} - W_s}{n_{1,2} + n_{2,3}} \quad (13)$$

where  $W_m$  – specific work,  $\text{J mol}^{-1}$ ;  $W_g$  – work done by gas, J;  $W_s$  – work done on surroundings, J.

Combining Eq. 13 with Eqs 2 and 3:

$$W_m = \frac{n_{1,2} \cdot T_1 \cdot c_v + n_{2,3} \cdot T_1 \cdot c_p - c_v \cdot T_4 \cdot (n_{1,2} + n_{2,3}) - W_s}{n_{1,2} + n_{2,3}} \quad (14)$$

Stating  $T_4$  according to the Eq. 8:

$$W_m = \frac{n_{1,2} \cdot T_1 \cdot c_v + n_{2,3} \cdot T_1 \cdot c_p - c_v \cdot T_1 \cdot r_e^{1-\gamma} \cdot (n_{1,2} + n_{2,3}) - W_s}{n_{1,2} + n_{2,3}} \quad (15)$$

Expressing  $n$  according to the Eq. 11 and separating work on surroundings:

$$W_m = \frac{\frac{P_1 \cdot V_c}{R \cdot T_1} \cdot T_1 \cdot c_v + \frac{P_1 \cdot (V_{cut} - V_c)}{R \cdot T_1} \cdot T_1 \cdot c_p - c_v \cdot T_1 \cdot r_e^{1-\gamma} \cdot \frac{P_1 (V_c + V_{cut} - V_c)}{R \cdot T_1}}{\frac{P_1 (V_c + V_{cut} - V_c)}{R \cdot T_1}} - \frac{W_s}{\frac{P_1 (V_c + V_{cut} - V_c)}{R \cdot T_1}} \quad (16)$$

Cancelling out  $P$ ,  $T$  and  $R$  and rearranging work on surroundings:

$$W_m = \frac{V_c \cdot c_v + (V_{cut} - V_c) \cdot c_p - c_v \cdot r_e^{1-\gamma} \cdot V_{cut}}{\frac{V_{cut}}{T_1}} - \frac{W_s \cdot R \cdot T_1}{P_1 \cdot V_{cut}} \quad (17)$$

Multiplying and dividing the numerator of the first member of equation by  $c_v$ :

$$W_m = \frac{c_v \cdot (V_c \cdot c_v + (V_{cut} - V_c) \cdot c_p - c_v \cdot r_e^{1-\gamma} \cdot V_{cut})}{\frac{c_v}{\frac{V_{cut}}{T_1}}} - \frac{W_s \cdot R \cdot T_1}{P_1 \cdot V_{cut}} \quad (18)$$

Applying Eq. 5 and rearranging:

$$W_m = \frac{T_1 \cdot c_v \cdot ((V_c + \gamma \cdot (V_{cut} - V_c)) - r_e^{1-\gamma} \cdot V_{cut})}{V_{cut}} - \frac{W_s \cdot R \cdot T_1}{P_1 \cdot V_{cut}} \quad (19)$$

Specific molar heat capacity at constant pressure can be expressed (Caton, 2016):

$$c_p = R + c_v \quad (20)$$

Inserting Eq. 20 in the Eq. 5 and simplifying:

$$c_v = \frac{R}{\gamma - 1} \quad (21)$$

Replacing  $c_v$  in Eq. 19 by Eq. 21 and expressing work on surroundings according to the Eq. 25:

$$W_m = \frac{T_1 \cdot R \cdot ((V_c + \gamma \cdot (V_{cut} - V_c)) - r_e^{1-\gamma} \cdot V_{cut})}{V_{cut} \cdot (\gamma - 1)} - \frac{p_0 \cdot V_d \cdot R \cdot T_1}{P_1 \cdot V_{cut}} \quad (22)$$

where  $p_0$  – surrounding pressure, bar.

### Computer modelling of energy efficacy and specific work

A computer model was developed in software environment *MATLAB*. It is based on the equations that are presented in previous sub-chapter. The purpose of this computer simulation is to simplify and automatize input parameter sweep, speed-up calculation and present numerical and graphical results. The main script sets initial parameters:

- Gas type;
- Initial temperature;
- Initial pressure;
- Final pressure;
- Geometric parameters of the pneumatic cylinder and supply pipe;
- Number of simulations and variable parameter.

Any initial parameter can be set as variable, and its value then is gradually changed during selected number of simulations.

Separate scripts contains code to calculate changes in cylinder volume, gas pressure, temperature, heat capacity and internal energy during one the course of piston movement from minimal to maximal cylinder volume. Calculation is performed at the resolution of 1,000 points per cycle. As the heat capacity of the gas changes with the temperature, an external database is called at each calculation step to get thermodynamic parameters of the gas (Lemmon et al., 2018). Changes in gas pressure inside the cylinder during expansion are calculated using following equation:

$$dP_{i+1} = \frac{\gamma_{i+1} \cdot P_i \cdot dV_{i+1}}{V_i} \quad (23)$$

where  $i$  – calculation step.



Temperature change:

$$dT_{i+1} = \frac{T \cdot dV_{i+1}}{V_i} + \frac{T \cdot dP_{i+1}}{P_i} \quad (24)$$

Changes in pressure and temperature are then numerically integrated. Volume, at which the gas supply is cut, to satisfy the requirement of initial and final pressure, is calculated, using Eq. 7. Energy conversion efficiency and specific work are calculated using correspondingly Eqs 1 and 13. For the control of the results, work is also calculated using Eq. 25 (Caton, 2016).

$$W = \int_{V_{min}}^{V_{max}} P \cdot dV \quad (25)$$

Mean effective pressure is used to measure work output of pneumatic cylinder, regardless of its size (Stone, 1999):

$$MEP = \frac{W}{V_d} \quad (26)$$

Geometric parameters of the simulated pneumatic cylinder are following:

- Bore 80 mm;
- Stroke 500 mm;
- Volume of supply pipe  $V_c = 20 \text{ cm}^3$ .

Initial temperature of the gas was 20 °C, initial pressure 11 bar and minimal pressure after expansion 2 bar. Three sweeps were simulated:

- Gradual change of final pressure from 2 bar to 11 bar;
- Gradual change of initial temperature from 20 °C to -30 °C;
- Five-fold increase of supply valve and pipe volume  $V_c$  from 20 cm<sup>3</sup> to 100 cm<sup>3</sup> and gradual change of final pressure from 2 bar to 11 bar.

Each sweep was simulated using Nitrogen and then repeated using Argon.

### Experimental setup

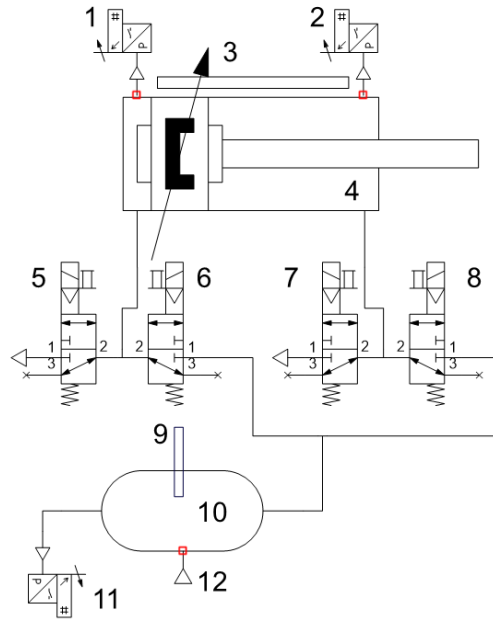
The experimental work was performed on the instrumented pneumatic vehicle, designed according to the rules of International AVENTICS Pneumobile Competition (Aventics Hungary Kft, 2019). In this research vehicle served as realistic load for pneumatic cylinder and the parameters of vehicle movement like acceleration and velocity were not analysed. Pressure in the both chambers of the pneumatic cylinder and also temperature and pressure in the buffer tank was measured synchronously with piston position. The aim of experimental research was to validate findings of mathematical modelling, particularly effect of gas expansion on efficiency in real-world conditions. Other reason for the experiments was to identify other significant factors, which affect efficiency of pneumatic cylinder and can be addressed in the future work. For this purpose mathematical modelling was performed assuming ideal gas behaviour, without heat exchange, turbulence and friction, and results compared with experimental ones. Analysis of the differences between modelling and experiment results were used to identify next research area.

Diagram of the experimental pneumatic circuit is shown in Fig. 3. Relative pressure sensors *Aventics PE5* were installed in the buffer and connected to the cylinder heads by specially made holes. Absolute pressure sensor *AC Delco 213-3205* was used to measure ambient air pressure, which was added to relative pressure. *Aventics SM6-AL* piston position sensor was used. *Aventics PRA* double acting cylinder with bore 80 mm, stroke 500 mm and diameter of rod 25 mm was used. Separate valves of type *Aventics CD12 3/2* were used for inlet and exhaust gas supply control. Only Nitrogen was used as the working gas for experimental research. Use of Argon was dismissed, as the results of computer simulation showed, that work done by specific amount of gas will be smaller, comparing Argon to Nitrogen. The control and data acquisition system is shown on Fig. 4. It is based on National Instruments modular hardware, and programmed in *LabVIEW*. The experiments were performed on the test track, at ambient temperature around 22 °C. Gas temperature in the buffer was approximately 18 – 21 °C.

Experimental data were acquired in piston movement domain, with resolution approximately 1 mm. As analogue piston position sensor was used, it led to some uncertainty. Cylinder volume and its differential at each data point were calculated. Work in the instroke and outstroke sides of the cylinder was calculated, using Eq. 25. Force was calculated by taking into account difference in piston areas on both sides. Instroke side work was subtracted from outstroke side work to find effective work. The same principle was used for calculating effective force. Molar quantity of the supplied gas was calculated using Eq. 11 at each data point and then numerically integrated. Mean piston speed was calculated using time data, which were recorded for each data point with resolution 1 μs. Specific work was calculated by applying Eq. 13. All the calculations were performed in *MATLAB*. Force on the rod was calculated according to following equation:

$$F_k = A_o \cdot P_{ok} - A_n \cdot P_{nk} \quad (27)$$

where  $A_o$  – piston area at outstroke side, m<sup>2</sup>;  $P_o$  – pressure at outstroke side, Pa;  $A_n$  – piston area at instroke side, m<sup>2</sup>;  $P_n$  – pressure at instroke side, Pa;  $k$  – data point.



**Figure 3.** Pneumatic circuit diagram. 1, 2, 11 – pressure sensors; 3 – piston position sensor; 4 – pneumatic cylinder; 5, 7 – exhaust valves; 6, 8 – inlet valves; 9 – temperature sensor; 10 – gas buffer tank; 12 – gas inlet.

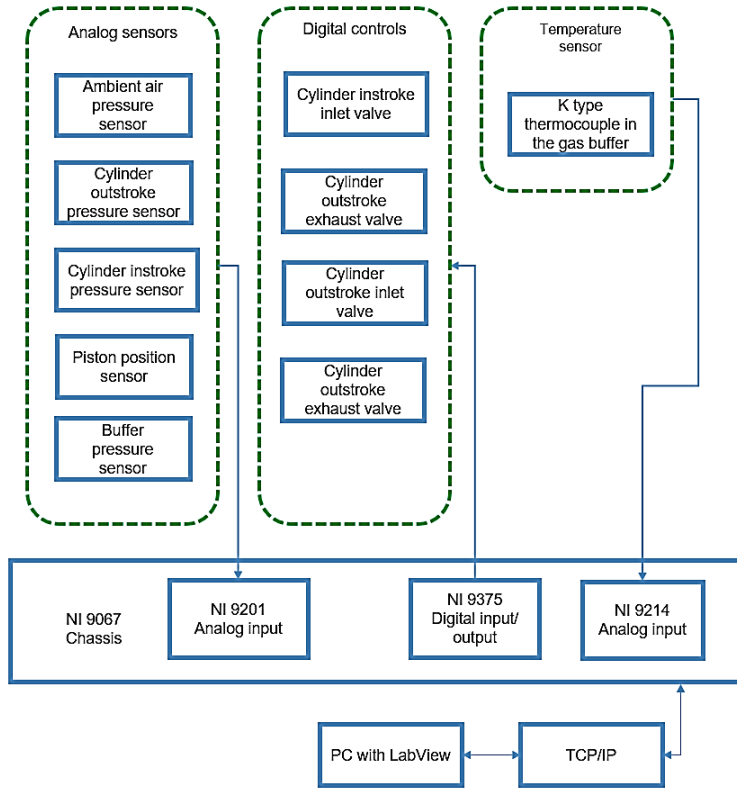


**Figure 4.** Layout of control and data acquisition system.

## RESULTS AND DISCUSSION

### Mathematical and computer modelling

Energy conversion efficacy  $\eta_{th}$ , calculated according to Eq. 12, increases when ratio of expansion  $r_e$  and ratio of heat capacities  $\gamma$  increase. Increase in additional volume  $V_c$  which includes supply pipe volume and control valve volume, decreases  $\eta_{th}$ . Those findings might be useful for efficacy considerations for general use of pneumatic cylinders. One may assume that use of gas which has higher  $\gamma$ , for instance, Argon instead of Nitrogen, can give an advantage and lead to higher work output per gas amount used in the cycle. This might not be true, as shown in Fig. 7.

In specific case of competition pneumatic vehicle the gas (Nitrogen  $N_2$ ) is supplied in metal bottles which have a internal volume of 10 l and pressure of 200 bar at a temperature of 20 °C. According to ideal gas law, show in Eq. 11, independently to the gas type, molar quantity in equal thermodynamic conditions will be the same.

Specific work  $W_m$ , calculated according to Eq. 22, follows the same tendency which applies to energy conversion efficiency  $\eta_{th}$ , except the ratio of heat capacities,  $\gamma$ . Ratio of heat capacities increases with decrease of heat capacity of the gas, as shown in Eq. 20. Specific work will increase with increase of initial gas temperature and heat capacity of the gas. Use of gas with diatomic molecules instead of monatomic gas, for instance, Nitrogen instead of Argon, will increase specific work and therefore the driving range

of the pneumatic vehicle, assuming that gas bottle of similar volume and pressure is used. Use of heat exchanger and increase of inlet gas temperature will also increase specific work. Relative significance of the work on surrounding reduces by increase of initial gas pressure.

The pneumatic cylinder can be operated by continuously supplying it with gas at constant pressure, or by cutting the gas supply at some point of piston travel and letting the gas to expand. In practical application of pneumatic cylinder as part of pneumatic vehicle motor, maximal pressure at the beginning of the cycle is limited for safety reasons. The minimal pressure at the end of the cycle should be:

- Above atmospheric pressure of the surroundings;
- Sufficient to create force to overcome mechanical resistance.

Those two conditions ensure that the piston of the pneumatic cylinder finishes its course.

Effects of gas type and operational mode on gas amount per work done are shown in Fig. 5.

In the operating mode with gas expansion, certain pressure at the end of expansion is reached by cutting gas supply upon reaching certain cylinder volume, calculated by Eq. 7. Mean effective pressure (*MEP*) and gas amount per cycle depends from gas type. Using gas with higher ratio of heat capacities ( $\gamma$ ), Argon instead of Nitrogen, *MEP* is larger and amount of gas per cycle greater.

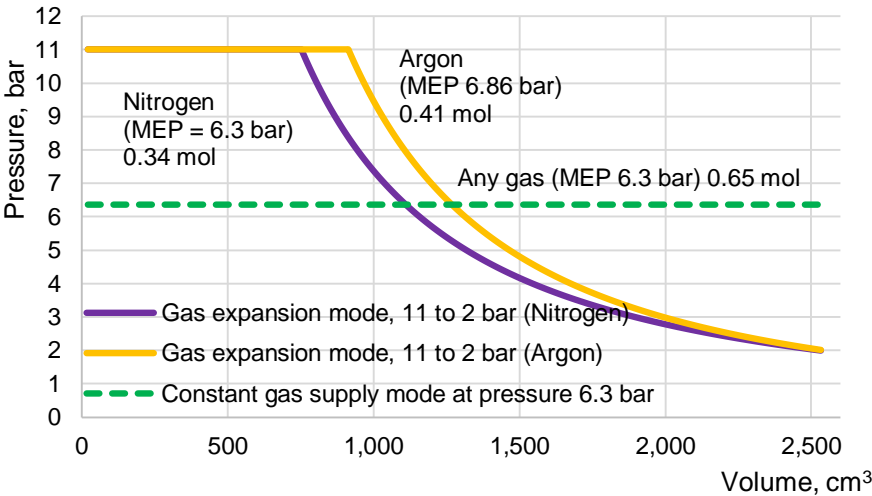


**Figure 5.** Effect of gas type and operational mode on gas amount per cycle.

In the operating mode with constant gas supply in the cylinder, shown for comparison at the same *MEP* as for Nitrogen in expansion mode, gas amount per cycle is almost two times larger, comparing to Nitrogen in expansion mode, and does not depend on gas type.

Drop of gas temperature during expansion is shown in Fig. 6, which explains higher energy conversion efficiency using expansion process instead of constant pressure process. Gas with lower heat capacity, Argon exhibits larger temperature reduction during expansion.

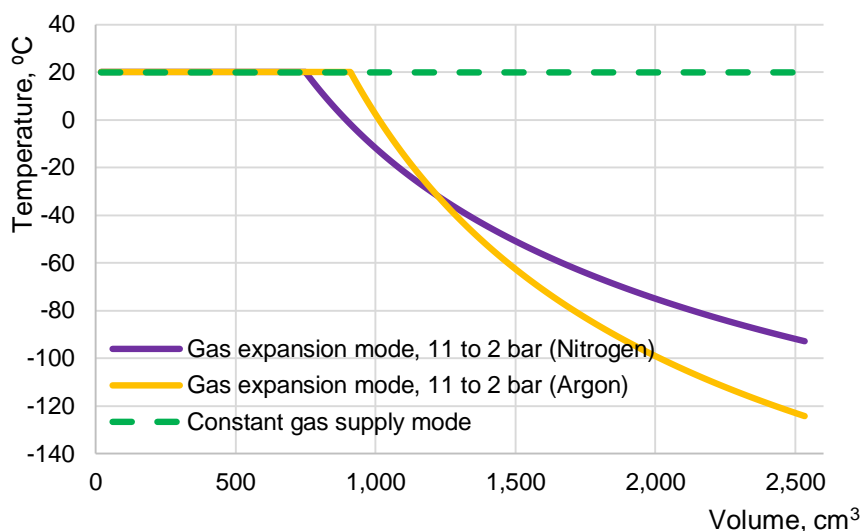


**Figure 6.** Effect of gas type and operational mode on gas temperature.

Effects of gas type and expansion ratio on energy conversion efficiency and specific work are shown in Fig. 7. A practical parameter – difference of gas pressure in the beginning and end of the piston travel is used in the diagram instead of more theoretical parameter - ratio of expansion ( $r_e$ ). Simulation was performed at constant initial pressure  $P_1 = 11$  bar, in 90 steps with gradual increase of cycle final pressure  $P_4$  from 2 bar to 11 bar.

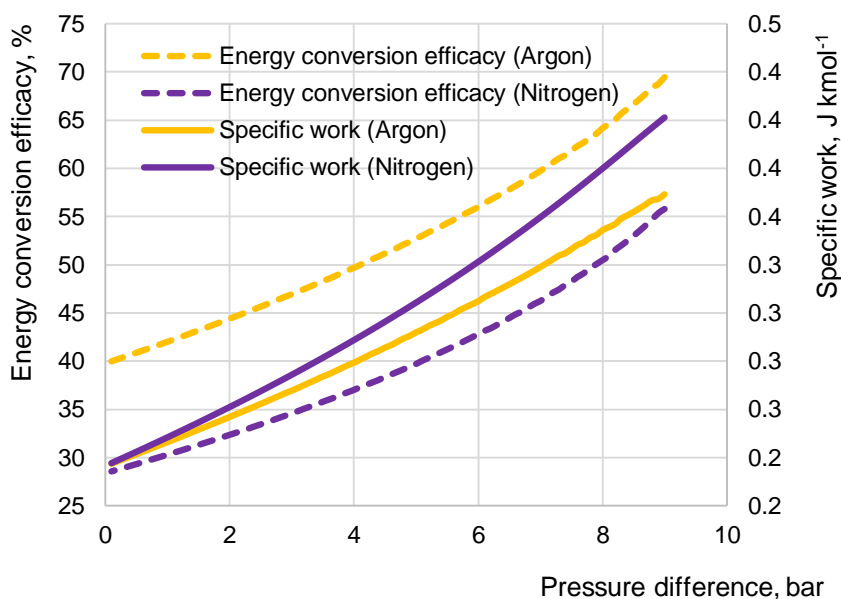


**Figure 7.** Effect of gas type and expansion on energy conversion efficacy and specific work, initial pressure 11 bar.

As the ratio of expansion or pressure difference increases, energy conversion efficacy and specific work increases. Differences in specific work between gases of different heat capacity increases with increase of ratio of expansion and therefore result in pressure difference. Technical information on pneumatic systems suggest reduction of air pressure to reduce consumption, which is opposite to findings of this research (Li et al., 2006; SMC Pneumatics, 2019). Reduction of pressure for pneumatics might reduce energy consumption of industrial plant, where pneumatic cylinders are operated in constant air supply mode. When gas is stored in the bottle at relatively high pressure (for instance, 200 bar), reduced to safe level for pneumatic components (6 – 11 bar) and cylinder operated in expansion mode, maximising pressure difference between beginning and end expansion will increase efficacy which will also lead to reduce of gas consumption.

Gas temperature is discussed in technical literature concerning water condensation and permissible conditions for polymeric materials (Barber, 1997). Saidur et al. shows that air temperature in the compressor inlet should be reduced to increase its volumetric efficiency (Saidur et al., 2010). To the author’s knowledge, there is a little or no discussion in research community on the subject of gas temperature impact on efficiency of pneumatic cylinder. Gas temperature at the high-pressure bottle reducer’s output usually is lower than ambient temperature. Heat exchangers can be used to warm up the gas. As the maximal pressure in the pneumatic motor feed circuit is limited at certain value, increase of temperature will lead to reduction of gas density. Effect of temperature increase by one degree on relative changes in specific work is shown in Fig. 8. The effect does not depend on type of gas, ratio of expansion or initial and final pressure difference. The effect depends on initial gas temperature, which can be explained by reduction of gas density.

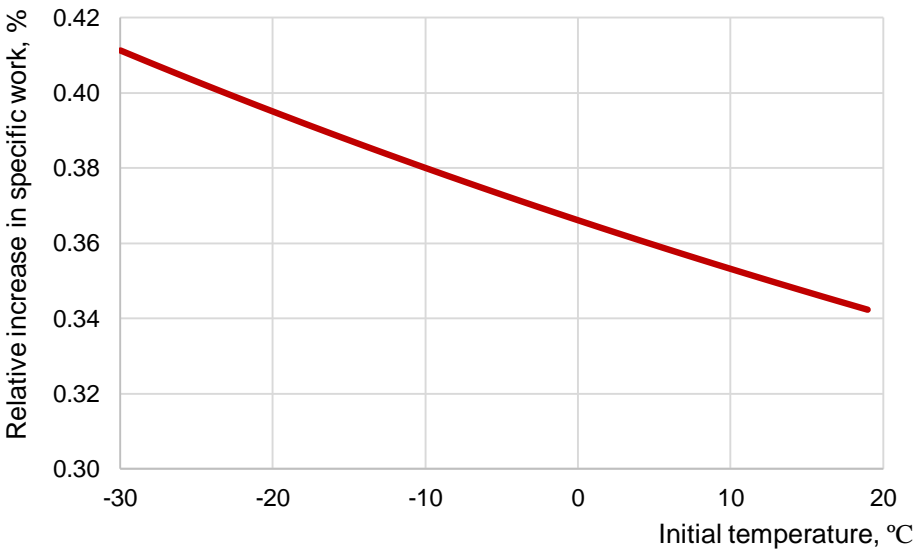


**Figure 8.** Effect of gas temperature increase by one degree on specific work depending on initial gas temperature.

Increase of  $V_c$  reduces specific work and this effect depends mainly on ratio of  $V_c$  to  $V_d$ . The reduction in specific work is more pronounced when ratio of expansion or initial and final pressure difference increases, as shown in Fig. 9.

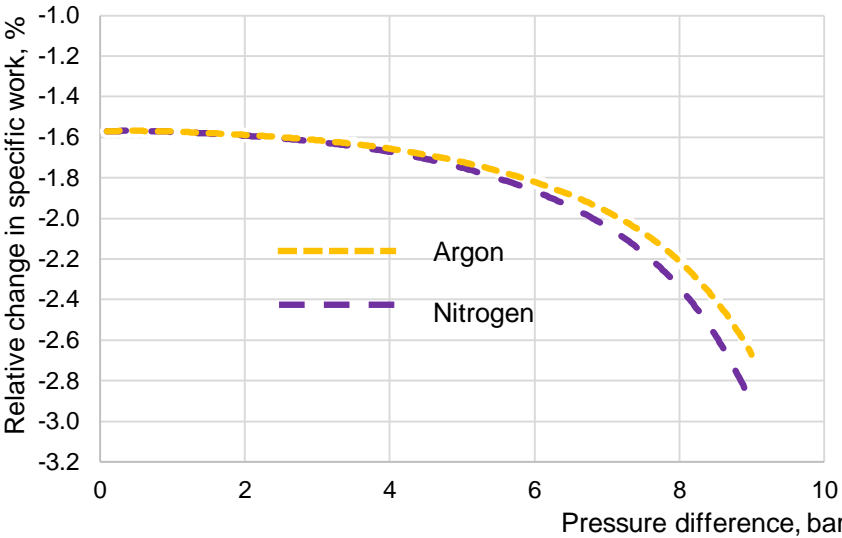


**Figure 9.** Effect of fivefold increase of volume  $V_c$  on specific work.

### Experimental results

Experimentally obtained results show effects of different gas supply strategies on the efficiency of energy conversion into work. Only one extension cycle for each case was selected, as the data were acquired during the test drive, and each repeated cycle had slightly different piston speed and gas temperature. Pressure - volume diagrams of the extending stroke (outstroke) are shown in Figs 10–12.

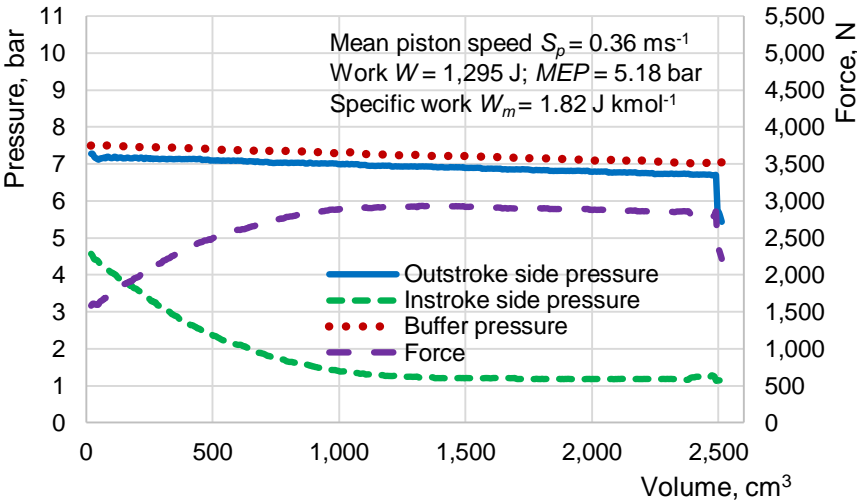


**Figure 10.** Pressure–volume diagram at uninterrupted gas supply mode, piston speed 0.36 m s<sup>-1</sup>.

By supplying the gas during all the course of piston movement, in a traditional control mode, cylinder operation resembles the one modelled in the scenario of constant pressure, shown in Fig. 2. Pressure changes in both sides of the piston and the buffer during relatively slow piston speed,  $S_p = 0.36 \text{ m s}^{-1}$ , are shown in Fig. 10. Restriction to the gas flow by control valves and pipes creates pressure difference of approximately 0.2 bar between buffer and pneumatic cylinder, which is relatively stable within the course of piston travel. In the chamber on the other side of the piston, gas flow restriction by exhaust valve creates gradual pressure drop until the pressure drops close to ambient pressure. Specific work during constant pressure operation, predicted by mathematical model according to Eq. 22 and the computer model, shown in Fig. 7, should be  $2.21 \text{ J kmol}^{-1}$ . Experimentally obtained result for specific work is  $1.82 \text{ J kmol}^{-1}$ , which is smaller than predicted. That can be explained by the increased pressure on the other side of the piston during initial part of the piston travel. Force on the rod increases gradually, then stabilises for the rest of the piston travel. Experimental results published by Harris et al. using traditional control mode (continuous air supply) for extend stroke show similar outstroke and instroke side pressure curves, although mean piston speed in their case was approximately two times higher. (Harris et al., 2014). From the pressure – time graphs it appears, that they continued to supply the cylinder with air even after the piston has finished its course, increasing pressure in the working chamber and in that way increasing air consumption.

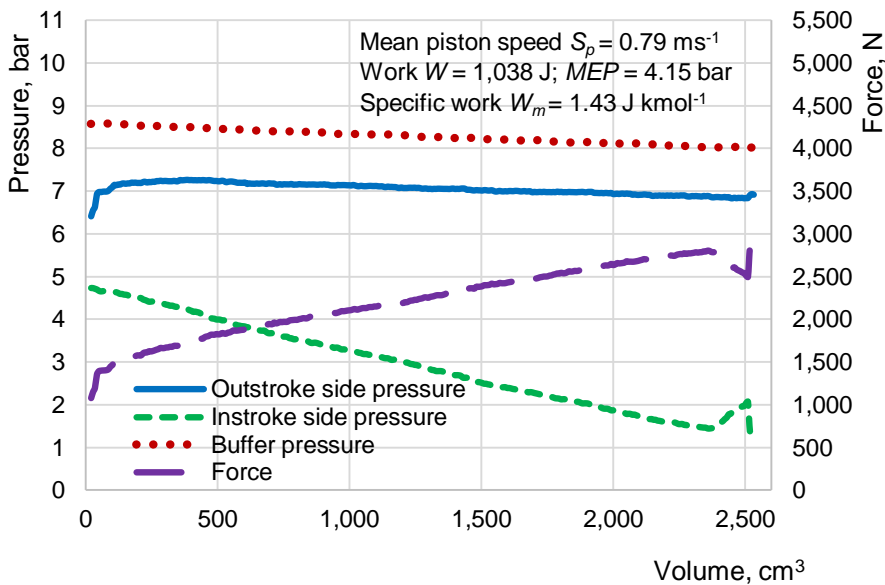


**Figure 11.** Pressure–volume diagram at uninterrupted gas supply mode, piston speed  $0.79 \text{ m s}^{-1}$ .

Pressure changes during similar operation mode, with uninterrupted gas supply, are shown in Fig. 11. Mean piston speed was almost two time larger,  $S_p = 0.79 \text{ m s}^{-1}$ , comparing to case with the slower piston speed. The difference in cylinder outstroke side pressure and buffer pressure is approximately 1.2 bar, which is significant increase comparing to case of the lower piston speed. Restriction, created by exhaust valve or



pipe on the instroke side, leads to slow, almost linear drop of the gas pressure on instroke side during whole cycle. Instroke side pressure reaches ambient pressure only at the very end of cycle, when piston has stopped. Outstroke side pressure diagram is similar to the one in case of slower piston speed, showed in Fig. 10. Considering this, gas amount per cycle in both cases is similar too. Force diagram is in significantly different shape.

Indicated (calculated from pressure and volume changes) and specific work are reduced approximately by 20%, comparing to slower piston speed case. Sudden increase of instroke side pressure at the end of the cycle probably is caused by pneumatic piston cushioning. Comparing the pressure diagrams in Figs 9 – 11 to the results obtained by other researchers, significant difference in pressure curve in the chamber on the instroke side is noticeable. In the work of Doll et al., Du et al. and Harris et al. initial pressure in the non-working side is close to surrounding pressure (1 absolute or 0 bar relative). It probably means that they present and analyse data of first cycle or there is sufficiently long pause between the cycles for pressure drop to ambient level. Pressure at the end of the piston travel in the non-working side is increased for speed control purposes (Doll et al., 2011; Du et al., 2018; Harris et al., 2014). Optimisation of pneumatic cylinder operation for industrial purposes significantly differs from objectives set for pneumatic cylinder as the part of pneumatic competition vehicle motor. It appears that in trade-off between linearity of motion and pneumatic cylinder efficiency. Linearity of piston movement and longitude stiffness of pneumatic cylinder plays more significant role in industrial applications comparing to competition vehicle.

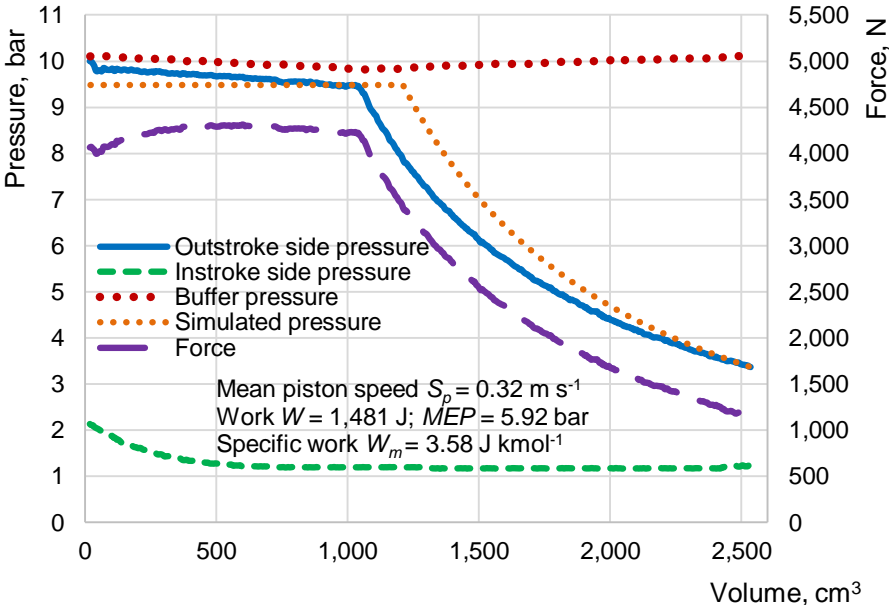


**Figure 12.** Pressure–volume diagram at gas expansion mode.

Pressure in the buffer, cylinder and force on the piston during gas expansion mode are presented in Fig. 12. In this operating mode gas supply is cut at certain point of piston travel, and pressure in the buffer is returning to the initial value, as gas is resupplied to

the buffer from the pressure bottle. Pressure on the instroke side is 2 bar at the beginning of the cycle and quickly stabilises at the value which close to ambient pressure. Force diagram thus mostly follows the value of outstroke pressure. Specific work is  $3.58 \text{ J kmol}^{-1}$ , which shows a more efficient operation when, compared to the previous cases of interrupted gas supply without expansion. This finding is in agreement with other researchers, who proposed operational mode with gas expansion (Doll et al., 2011; Harris et al., 2014; Du et al., 2018). Direct comparison of the results is complicated, as most other authors do not use normalised efficiency parameters.

The value of specific work, predicted by theoretical model for such geometry, initial pressure, pressure difference and gas type is  $3.38 \text{ J kmol}^{-1}$ . It is unusual to have theoretical efficiency smaller then experimentally obtained, but this effect will be explained. Computer simulation of gas pressure with similar pressure at the beginning and end of the gas expansion process shows different  $V_{cut}$  value and path of pressure changes. Pressure – volume diagram of gas expansion part in logarithmic scale ( $\log P$   $\log V$ ) is shown in Fig. 13. The term of the slope in the equation of linear regression corresponds to apparent ratio of heat capacities. In case of simulated data ratio of heat capacities is as expected for the gas type (Nitrogen) in the given temperature range,  $\gamma = 1.403$ . For experimental data its value is  $\gamma = 1.158$ . As the gas type in both cases is the same, difference in the pressure changes can be explained by effect of heat transfer, which is not included in computer simulation. As the gas temperature decreases during the expansion, difference in temperature and heat transfer intensity between cylinder wall and gas increases. Relative significance of heat transfer increases by increase of ratio of expansion.

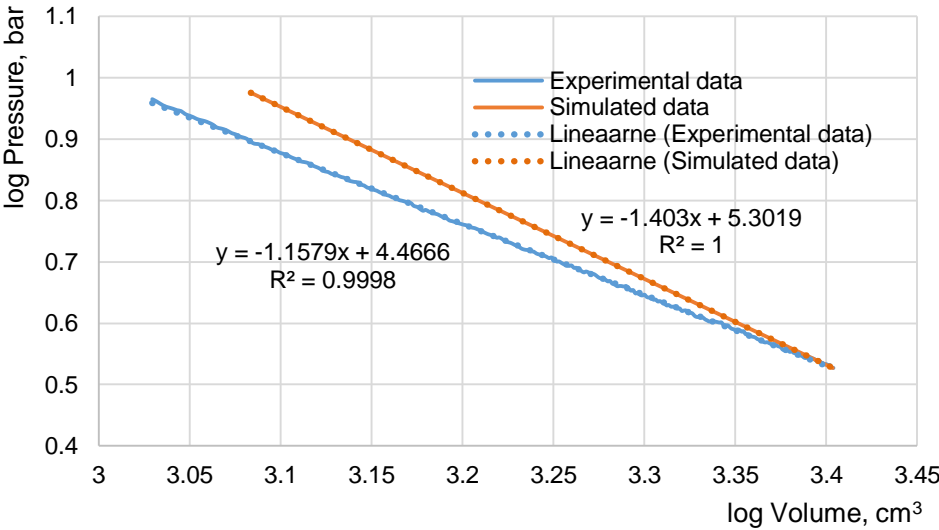


**Figure 13.** Pressure–volume diagram in logarithmic scale.

For practical calculations of pneumatic cylinder control parameters, such as  $V_{cut}$  value, apparent ratio of heat capacities can be calculated from pressure and volume relations on the previous cycle.

## CONCLUSIONS

1. Mathematical model was developed for assessment of effect of gas type, geometric and control parameters on energy conversion efficacy of pneumatic motor. Energy conversion efficacy increases when:

- Ratio of expansion  $r_e$  increases;
- Ratio of gas heat capacities  $\gamma$  increases.

2. Another mathematical model was developed to evaluate effect of pneumatic motor control parameters on specific work, which is the work that can be done by certain amount of gas.

- Specific work can be increased by using gas of larger heat capacity. In practical terms it means that Nitrogen is a suitable choice.
- Increase of gas temperature by 10 °C at the same supply pressure will increase specific work by approximately 3.8%.
- Geometric parameters of the pneumatic cylinder, such as bore and stroke do not have direct effect on specific work of pneumatic cylinder.
- Relative size of additional volume  $V_c$ , connected to pneumatic cylinder inlet, such as volume of gas supply pipe and inlet control valve have mild effect on specific work. For practical pneumatic motor fivefold increase of additional volume can decrease specific work by approximately 2.9%.
- Specific work will increase by approximately 80% by increasing the rate of expansion  $r_e$  from 1 to 3.38 at initial pressure  $P_1 = 11$  bar, which corresponds to range of pressure at the end of the cycle  $P_4$  from 11 to 2 bar.

3. In continuous gas supply mode experimentally obtained specific work is lower than predicted by computer simulation using ideal gas model. Specific work is reduced by additional work to expel gas from cylinder on the other side of the piston. This additional work depends on final gas pressure of previous cycle, piston speed and gas flow restriction by output hole, pipe and valve.

- In case of relatively slow piston speed,  $S_p = 0.36 \text{ m s}^{-1}$ , experimentally obtained specific work is by 17.6% lower than predicted.
- In case piston speed  $S_p = 0.79 \text{ m s}^{-1}$ , relative difference between measured and predicted specific work is 35.3%.
- The differences in modelled and experimental results demonstrate strong effect of restrictions to the gas flow on the efficiency of a pneumatic motor.

4. In gas expanding mode experimentally obtained specific work is by 5.9% higher than predicted by computer simulation of ideal gas model. It can be explained by cooling of the gas during expansion, which leads to increased intensity and significance of heat transfer between cylinder walls and gas.

5. Low gas pressure at the end of cycle as the result of gas expansion leads to reduced work to expel gas from the cylinder on the other side of the piston.

## Future work

Prediction and evaluation of heat transfer between components of the pneumatic system, gas and surroundings can lead to deeper understanding and improvement of efficiency of pneumatic motor.

ACKNOWLEDGEMENTS. The authors thank Emerson Electric Co and National Instruments for the inspiration and provided hardware.

## REFERENCES

- Aventics Hungary Kft. 2019. *Pneumobil 2019 Competition rules*, Eger, 67 pp.
- Barber, A. 1997. *Pneumatic Handbook, 8th edition*, Elsevier Science, Oxford, 659 pp.
- Cai, M., Fujita, T. & Kagawa, T. 2001. Energy Consumption and Assessment of Pneumatic Actuating Systems. *Transactions of The Japan Hydraulics & Pneumatics Society* **32**(5), 118–123. doi: 10.14888/jfps1998.32.118
- Cambell, S. 2018. Guidelines for Selecting Pneumatic Cylinders. <https://www.machinedesign.com/mechanical-motion-systems/pneumatics/article/21831605/guidelines-for-selecting-pneumatic-cylinders>. Accessed 04.02.2020.
- Caton, J.A. 2016. *An Introduction to Thermodynamic Cycle Simulations for Internal Combustion Engines*, John Wiley & Sons, West Sussex, 367 pp.
- Doll, M., Neumann, R. & Sawodny, O. 2011. Energy efficient use of compressed air in pneumatic drive systems for motion tasks. In: *Proceedings of 2011 International Conference on Fluid Power and Mechatronics*, IEEE, Beijing, pp. 340–345.
- Du, H., Xiong, W., Jiang, Z., Li, Q. & Wang, L. 2018. Energy efficiency control of pneumatic actuator systems through nonlinear dynamic optimization. *Journal of Cleaner Production* **184**, 511–519. doi: 10.1016/j.jclepro.2018.02.117
- Emerson Electric Co. 2019. Results of Pneumobile competition. <https://en.pneumobil.hu/results>. Accessed 05.02.2020.
- Fleischer, H. 1995. *Manual of Pneumatic Systems Optimization*. McGraw-Hill, New York, 364 pp.
- Harris, P., Nolan, S. & O'Donnell, G.E. 2014. Energy optimisation of pneumatic actuator systems in manufacturing. *Journal of Cleaner Production* **72**, 35–45. doi: 10.1016/j.jclepro.2014.03.011
- Harris, P., O'Donnell, G.E. & Whelan, T. 2012. Energy Efficiency in Pneumatic Production Systems: State of the Art and Future Directions. In: *Leveraging Technology for a Sustainable World*. Heidelberg, Berlin, pp. 363–368.
- Heywood, J.B. 2018. *Internal Combustion Engine Fundamentals*. McGraw-Hill, New York, 1028 pp.
- Lemmon, E.W., Bell, I.H., Huber, M.L. & McLinden, M.O. 2018. *NIST Standard Reference Database 23: Reference Fluid Thermodynamic and Transport Properties-REFPROP, Version 10.0*. National Institute of Standards and Technology. <https://dx.doi.org/10.18434/T4JS3C>
- Létai, L.S., Pop, O., Buzguta, P. & Canlas, F. 2017. PLC controlled racing vehicle with pneumatic engine. In: *Proceedings of 1st Agria Conference on Innovative Pneumatic Vehicles – ACIPV 2017*. Óbuda University, Institute of Mechatronics and Vehicle Engineering, Eger, pp. 1–8.

- Li, T.C., Wu, H.W. & Kuo, M.J. 2006. A Study of Gas Economizing Pneumatic Cylinder. *Journal of Physics: Conference Series* **48**(1), 1227–1232. doi: 10.1088/1742-6596/48/1/228
- Luo, X., Wang, J., Sun, H., Derby, J.W. & Mangan, S.J. 2013. Study of a New Strategy for Pneumatic Actuator System Energy Efficiency Improvement via the Scroll Expander Technology. *IEEE/ASME Transactions on Mechatronics* **18**(5), 1508–1518. doi: 10.1109/TMECH.2012.2203920
- Saidur, R., Rahim, N.A. & Hasanuzzaman, M. 2010. A review on compressed-air energy use and energy savings. *Renewable and Sustainable Energy Reviews* **14**(4), 1135–1153. doi: 10.1016/j.rser.2009.11.013
- Serway, R.A. & Kirkpatrick, L.D. 2014. *Physics for Scientists and Engineers with Modern Physics. The Physics Teacher (9th ed.)*. Brooks Cole, Boston, 1622 pp.
- Shen, X. & Goldfarb, M. 2007. Energy Saving in Pneumatic Servo Control Utilizing Interchamber Cross-Flow. *Journal of Dynamic Systems, Measurement, and Control*, **129**(3), 303–310. doi: 10.1115/1.2718244
- SMC Pneumatics. 1997. Basic pneumatics. [http://www.smcpneumatics.com/pdfs/smc/basic\\_pneumatics.pdf](http://www.smcpneumatics.com/pdfs/smc/basic_pneumatics.pdf). Accessed 04.02.2020.
- SMC Pneumatics. 2019. Energise your efficiency. [https://www.smc.eu/portal\\_ssl/webpages/02\\_solutions/energy\\_efficiency/pdf/ENERGY-EFFICIENCY\\_leaflet\\_en.pdf](https://www.smc.eu/portal_ssl/webpages/02_solutions/energy_efficiency/pdf/ENERGY-EFFICIENCY_leaflet_en.pdf). Accessed 04.02.2020.
- Stone, R. 1999. *Introduction to Internal Combustion Engines (Third edition)*. Palgrave Macmillian, New York, 641 pp.
- Wang, J. & Gordon, T. 2011. Energy-efficient tracking control of pneumatic cylinders. In: *IEEE Conference on Decision and Control and European Control Conference*. IEEE, Orlando, pp. 7956–7961.

## **Utilization of fused deposition method 3D printing for evaluation of discrete element method simulations**

P. Hnízdl<sup>1</sup>, R. Chotěborský<sup>1,\*</sup> and J. Kuře<sup>2</sup>

<sup>1</sup>Czech University of Life Science Prague, Faculty of Engineering, Department of Material Science and Manufacturing Technology, Kamycka 129, CZ165 00 Prague – Suchdol, Czech Republic

<sup>2</sup>University of Life Sciences Prague, Faculty of Engineering, Department of Electrical Engineering and Automation, Czech Kamycka 129, CZ165 21 Prague – Suchdol, Czech Republic

\*Correspondence: [choteborsky@tf.czu.cz](mailto:choteborsky@tf.czu.cz)

**Abstract.** FDM 3D printing is used for designing prototype assessment in engineering production. It is usually used to verify the functionality of kinematics mechanisms. It can also be used for innovation in agricultural production, eg. the development of new mechanisms for agriculture tools. Such a mechanism as well as the entire components is printed using FDM and they are made of plastics. This whole can be experimentally verified in a laboratory trough. The article deals with the verification of the possibilities of using FDM technology for the design of agricultural tools. The material properties, namely stress-strain, of the plastics after printing are entered into the Ansys mechanical library, and the DEM results are also imported into Ansys mechanical. Material properties of plastics for FDM technology such as PLA, PETG show that its mechanical properties limited their using for validation.

**Key words:** FEM, DEM, design of tools, mechanical, manufacturing, industry 4.0.

### **INTRODUCTION**

The development of manufacturing sectoral lines is increasingly showing its latest innovations with each line by continuous improvement, taking various best steps. All improvements in existing processes are according to the kaizen principle has already been made by previous founder and researcher in Mechanical Engineering (Shahrubudin et al., 2019). An industry concept 4.0 is synonymous with the transformation of manufacturing activities into smart manufacturing, designed to meet and exceed current challenges (Cahyati, 2019). The application is carried out with a shorter product manufacturing cycle, an adjustment to the manufacturing of the product through competitive measures, one of the applications being to eliminate borderless and boundaries.

Fused Deposition Modelling (FDM) is currently become a popular fabrication process and commonly used for modelling, prototyping, and production application. This process favour the ease of fabricating three-dimensional objects of almost any form and less waste than traditional subtractive production method. As one of methods

in additive manufacturing process, fused deposition modelling utilizes extrusion of material formed in filament to build structural 3D model by layering from bottom to the top. The filament is melted according to the melting temperature of certain material and extrusion occurs through the nozzle, subsequently. Materials are subjected to phase changes under relatively high temperature. The material is soon after being deposited and it cools down and solidifies right after deposition. The movement of the nozzle is based on the process parameters resulting the path generation. A desired structure, such as accurate dimension and splendid mechanical performance, may be achieved accurately and precisely by configuring each component of parameters. Wide range materials, from polymers, ceramics, to metals, has been developed into 3D printing filaments. These materials have two main roles, which could be as the build material and support material. The common material combination is Polylactic Acid (PLA) and Polyvinyl Alcohol (PVA) (Yang et al., 2015; Ziemian et al., 2015; Wulle et al., 2017; Alief et al., 2019).

Present research are focused on material innovation, inside structure printed geometry and mechanical properties (Hao et al., 2011; Alief et al., 2019), commonly using of 3D printing for geometry and kinematic testing of design (Guerrero-Villar et al., 2015) or how to influence the mechanical properties with changing technological parameters by printing (Hossain et al., 2014; Lanzotti et al., 2015; Ning, Cong, Hu, & Wang, 2017; Khan et al., 2018; Poudel et al., 2018). In the existing literature, many studies were reported on the strength of the FDM 3D printed parts and their anisotropic behaviour using the traditional layer-based 3D printing (Poudel et al., 2018).

These technologies and with the use of various printing materials are also suitable for designing and testing parts of agricultural machines or testing a new shape of agricultural tools such as chisels, discs, etc. or full frames with them. It is necessary to verify the computational tasks, either in a field test or as in the case of tool shape innovation, first is under laboratory conditions using 3D printing technologies. Due to the load and shape of the agricultural tools, it is possible that the 3D printing technology used using conventional printing materials may cause deformations in the test that affect, for example, the drought force and thus it is not possible to correctly evaluate the simulation results (Fig. 1).



**Figure 1.** Detail of model soil trough.

The aim of this work is determined condition for testing of chisel with using DEM and FEM analysis for 3D printed prototypes.

## MATERIALS AND METHODS

The BCN 3D printer was used to print samples to determine mechanical properties. The setting of the printing properties is shown in Table 1, 3D printer type is BCN3D sigma R19.

The mechanical properties of the printed sample (Fig. 3) were determined by a tensile test on a Labortech MPtest 5.050 universal tester (Fig. 2) with a maximum load of 5 kN.

The dependencies of force and elongation was measured. These dependencies were recalculated to stress-strain diagram (Fig. 2, b). Young modulus was determined from stress-strain diagram, and relationship between stress and strain was given to Ansys material library like multilinear.

**Table 1.** Table of parameters settings 3D printer, print layer 0.3 mm, perimeters 0.4 mm, print speed 50 mm s<sup>-1</sup>, object infill 100%, orientation 45° and 90°

Print parameters	Place	Nozzle temperature (°C)	Bed temperature (°C)
PETG	close	225	70
PLA	open	215	60
ABS (90°)	close	245	90
ABS (45°)	close	250	100

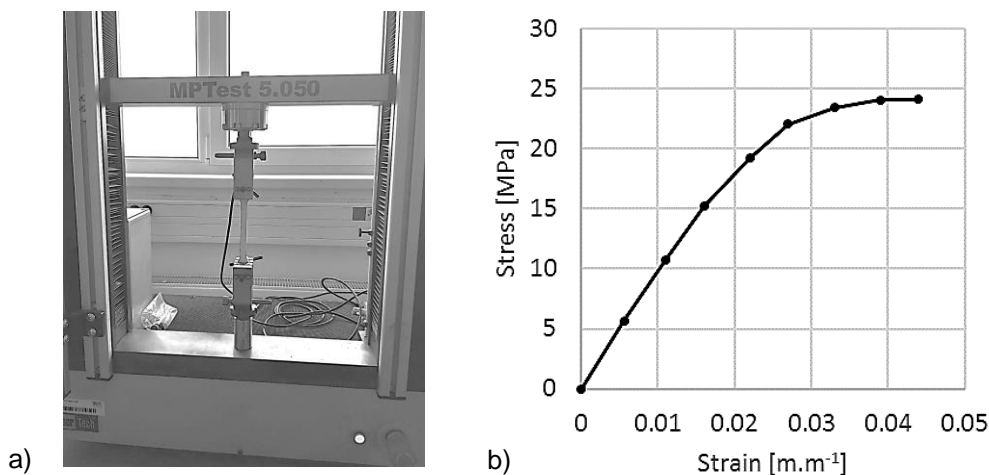


**Figure 2.** Sample testing in universal testing machine and data for plastic model in ANSYS.

SpaceClaim software was used for drawing of small agriculture tools. For the deformation analysis and future use in the laboratory soil trough, the tools were created in 1 : 2 scale. Specifically, it was a chisel with a chisel and wings, it is used in agriculture for loosening with no-tillage technology. RockyDEM software was used to simulate chisels in a bulk matter environment. Material properties of bulk matter were determined by shear test, pressing test and angle of repose. These tests are described in (Kadau et al., 2006; Sadek et al., 2011; Kotrocz et al., 2016).



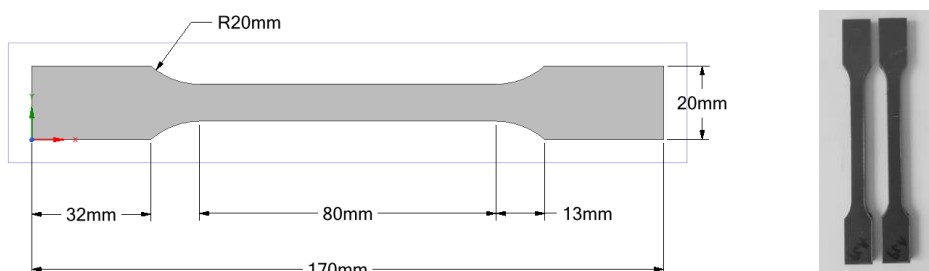


**Figure 3.** Test sample, Samples from PLA material, 3D printing technology and laser cutting.

The material model settings are shown in Table 2. The chisel body was simulated at a constant speed of  $1 \text{ m s}^{-1}$  and a depth of 100, 150 and 200 mm, which would correspond to twice the depth under field conditions.

**Table 2.** Table of parameters ANSYS settings, Poisson's Ratio 0.35 (-)

Materials	Young modulus (MPa)	Maximal Stress (MPa)	Stress 0.02 (MPa)	Elongation (-)
PETG	$1,048 \pm 23.8$	$32.0 \pm 1.4$	$20.0 \pm 0.4$	$4.66 \pm 1.2$
PLA	$1,313 \pm 19.2$	$42.7 \pm 1.3$	$25.2 \pm 3.1$	$5.05 \pm 1.0$
ABS (45°)	$914 \pm 10.5$	$23.6 \pm 0.7$	$17.4 \pm 0.3$	$5.92 \pm 0.4$

The chisel body pressure results were exported for each node, averaged, and imported into Ansys mechanical. The mesh deformation shape result was exported from Ansys mechanical as a \*.stl file and then inserted into the RockyDEM simulation using the same material model (Table 3). The maximum stress, and strain at points of interest were also analysed. These points of interest on the geometry mesh can represent the deformation state of the tool for easy understanding of the process. The procedure is shown schematically in Fig. 4. The result of the tensile force of the simulation was compared for the deformed and deformed part. Only simulations results give us information about invisible processes into laboratory trough during experiment.

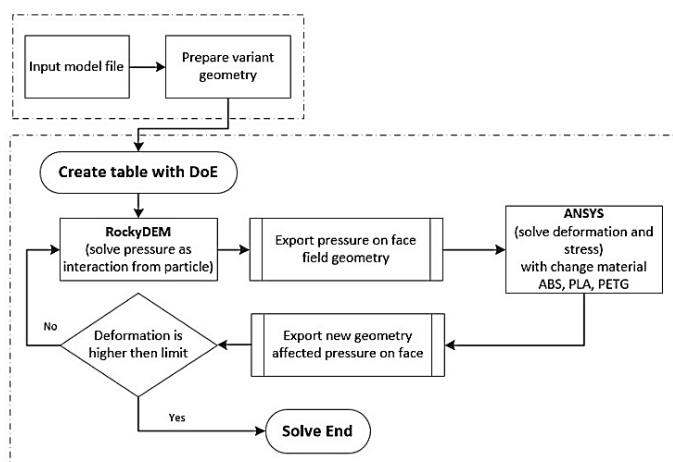


**Figure 4.** System analyses diagram.

**Table 3.** Table of parameters for RockyDEM

Parameters	Detail of Parameters	Data Source	
Normal force	Hysteretic linear spring	(ESSS Rocky, 2018)	
Adhesive force	Linear	(ESSS Rocky, 2018)	
Tangential force	Linear spring coulomb limit	(ESSS Rocky, 2018)	
Numerical softening factor	1	Selected	
Gravity	$9.81 \text{ m s}^{-2}$	Selected	
Material properties	Dry sand /dry dredged sand/wet dredged sand	Material of Chisel	–
Bulk density (density), $\text{kg}\cdot\text{m}^{-3}$	1560/1533/1620	7850	(Ucgul et al., 2015)
Young's modulus, MPa	40/35/32	Table 5	(Budynas & Nisbett, 2015; Ucgul et al., 2015)
Poisson's ratio	0.3	0.3	Selected
Particle size, mm	10	–	Selected
Number of particles	0.383 million	–	Selected
Material interaction properties	Particle–particle	Particle–tine	–
Static friction	0.6/0.33/0.33	0.5	Selected
Dynamic friction	0.3/0.83/0.83	0.5	Selected
Tangential stiffness ratio	1/1/1	1	Selected
Adhesive distance, m	0/0/0.0001	0.0001	Selected
Stiffness fractiona	0/0/0.05	0	Selected
Restitution coefficient	0.2/0.3/0.3	0.3	Selected

## RESULTS AND DISCUSSION

The results of the tensile tests show that the highest Young's modulus has PLA and subsequently PETG. The same order is for maximum strength and deformation strength of 0.2%. At the same time, the stress specified for the deformation of 0.2% is the maximum design stress that must not be overcome. Otherwise, the printed sample will be permanently deformed and degraded for further use in the experimental laboratory soil trough. The values of deformations at the points of interest of the mesh and the maximum stress of the chisel model are given in Table 4 and Fig. 5 (schematically indicates A, B, C spot).

The results of deformations and stresses show that materials usable for prototype production and their use for experiments in the laboratory soil trough will be problematic in the case of high area loads due to the interaction of the particulate matter and the tool body. While it is possible to replace 3D printing with the production of prototypes made of metals on CNC machines or conventional technologies, we clearly lose simplicity, speed and cheapness.

The load simulation results imported as a result of the RockyDEM simulation show that the ABS material, which is toughness, has very large deformations and it been only applicable to dry sand experiments conditions at shallow depths. This is due to his small Young modulus. PLA and PETG may be more suitable, but these are more brittle materials. According to the analyses, they are also suitable for dredged sand and wet dredged sand up to 150 mm depth. At a greater depth, the tool is deformed completely.

**Table 4.** Data of sand materials – ABS/PLA/PETG (Stress limit is 20 MPa/38MPa/28 MPa – bold highlight)

Stress (MPa)				
ABS/PLA/PETG Type 5		type 10	type 15	type 20
Dry sand				
A		3.31/3.25/3.28	6.83/6.53/6.68	14.16/12.55/13.48
B		12.63/12.43/15.53	14.56/14.60/14.67	<b>35.40/35.90/35.29</b>
C		4.72/3.20/3.22	7.60/4.83/4.86	12.54/8.61/9.13
Dry dredged sand				
A		1.17/1.15/1.16	11.46/10.44/11.04	4.78/4.60/4.71
B		8.49/8.49/8.49	17.40/17.32/17.38	<b>23.43/22.81/23.20</b>
C		3.35/2.40/2.41	10.63/6.29/6.58	9.27/6.41/6.71
Wet dredged sand				
A		8.88/8.50/8.72	13.71/12.84/13.35	<b>32.72/25.45/29.73</b>
B		13.23/12.85/13.13	<b>32.12/32.27/32.21</b>	<b>32.27/32.51/32.42</b>
C		3.41/3.38/3.40	16.59/14.68/15.84	<b>73.96/81.82/77.18</b>
			16.13/14.68/15.60	<b>32.79/30.24/31.86</b>

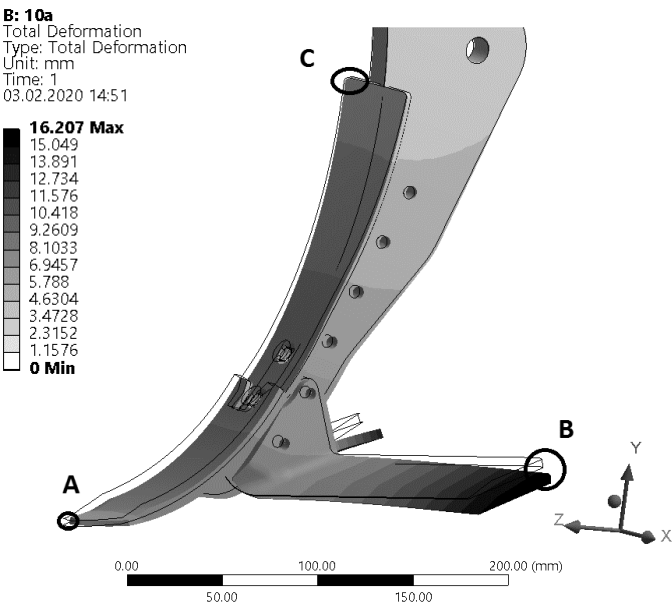


**Figure 5.** Total deformation agricultural tool in ANSYS, load is from RockyDEM.

The results of the deformed meshes, which were imported into RockyDEM from Ansys mechanical, show that PLA and PETG material in the prototype tool construction has enough stiffness to avoid affecting the draught forces that can be measured in the experimental soil trough. The Fig. 6 shows an example of vertical export ( $F_y$  – original shape and  $F_{y\_A}$  – deformed as a result of Ansys mechanical simulation) and tensile force ( $F_z$  – original shape and  $F_{z\_A}$  – deformed as a result of Ansys mechanical simulation) acting on chisel body, lateral force  $F_x$  is neglected because of the symmetry of the body. This result is valid for dry sand and a depth of 150 mm. The results of the mean values of the individual forces are given for comparison in Table 5.

The results of the draught force that was simulated on the deformed chisel body with the deformed wings as a result of the simulation in Ansys mechanical are shown in Fig. 6 for dry dredged sand.

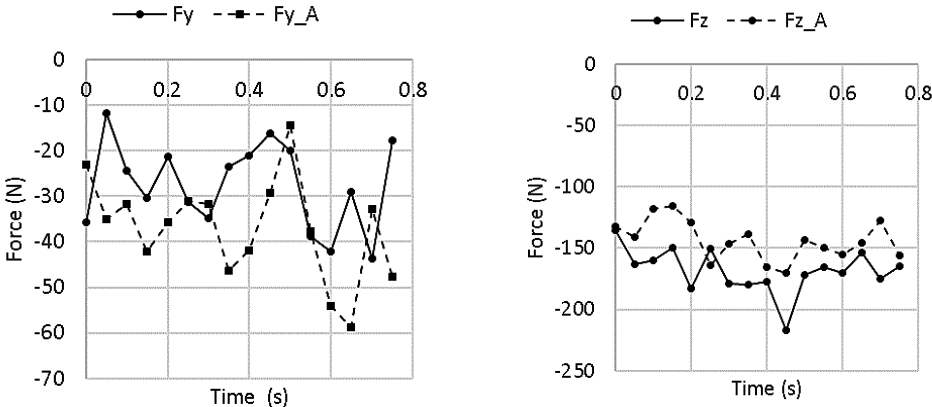


**Figure 6.** Results of simulation – vertical force  $F_y$  (A is deformed) and draught force  $F_z$  (A is deformed), ex. For dry sand at 150 mm depth.

**Table 5.** Sand,  $F_{xA}$  (ansys deformed mesh),  $F_{xO}$  – original shape

Dry sand	$F_{x\_A}$ (N)	$F_{y\_A}$ (N)	$F_{z\_A}$ (N)	$F_{x\_O}$ (N)	$F_{y\_O}$ (N)	$F_{z\_O}$ (N)
10 cm depth	5.07	-6.5	-94.3	6.76	-14.1	-90.2
15 cm depth	-3.32	-31.5	-165.9	-2.11	-37.0	-158.7
20 cm depth	-0.81	-60.0	-248.1	-0.41	-66.9	-245.0
Dry dredged sand	$F_{x\_A}$ (N)	$F_{y\_A}$ (N)	$F_{z\_A}$ (N)	$F_{x\_O}$ (N)	$F_{y\_O}$ (N)	$F_{z\_O}$ (N)
10 cm depth	-1.24	-12.9	-82.4	-1.44	-12.3	-84.6
15 cm depth	-0.05	-27.7	-177.1	-1.16	-35.8	-151.4
20 cm depth	-4.42	-48.9	-249.1	-7.30	-67.4	-240.5
Wet dredged sand	$F_{x\_A}$ (N)	$F_{y\_A}$ (N)	$F_{z\_A}$ (N)	$F_{x\_O}$ (N)	$F_{y\_O}$ (N)	$F_{z\_O}$ (N)
5 cm depth	-5.40	36.4	-151.3	-1.31	16.7	-149

Although it may appear that the deformation error is small to determine the draught and vertical forces, it appears to be a combination of deformations of the individual parts of the chisel body prototype with wings that deform due to the load so that the total force error is small. However, if we compare the individual body parts, i.e. the chisel, the wings, the mouldboard at points of interest that represent the deformation A, B and C of Fig. 7, we find that due to the deformation the chisel resistance increases, and the wing resistance decreases. The total force therefore appears to be like the undeformed body. ABS as a material is also not suitable from this point of view, since the total deformations at points of interest A and B are greater than 20 mm already at a depth of 150 mm in dry dredged sand. On the contrary, it seems to be a suitable material to produce the prototype PETG or PLA, which have a maximum deformation of about 20 mm, but at a depth of 200 mm or in shallow processing in wet dredged sand.

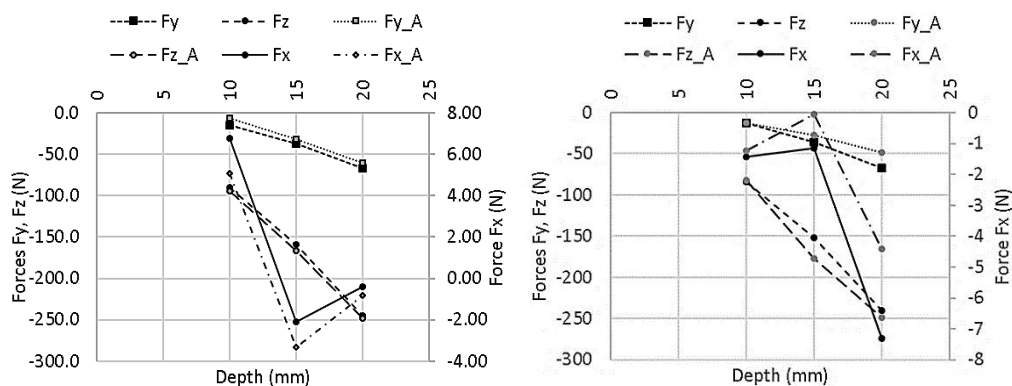


**Figure 7.** Left is original shape and right is shape after RockyDEM analyses.

At smaller depths, the deformations are smaller and do not affect the vertical or draught forces overall. Therefore, to set up the prototype of an agricultural tool, this material is used in less stressed prototype structures. For example, a mouldboard. For other parts, special consideration should be given to the deformation of the parts or the use of a metal part. This, however, completely loses the effect of flexibility, low time and low cost. Another possibility would be to create these stressed parts of composite material or metals (Kešner et al., 2019; Ucgul & Saunders, 2020), which we can expect longer time and higher price, but not in the complexity of the metal prototype. Therefore, although 3D printing of prototypes is widely used (Guerrero-Villar et al., 2015; Wulle et al., 2017; Alief et al., 2019), it will have limitations for model validation in agricultural tool experiments. Several publications (Lanzotti et al., 2015; Yang et al., 2015; Ziemian et al., 2015; Cahyati, 2019) mention usability for prototype production but are usually aimed at manufacturing mechanical systems to verify kinematics, stability, or deformation. Our results show that it is possible to use 3D printing from these materials to decrease the time of innovation in the field of agricultural machines, but with limitations, especially in experimental validation of simulation results.

## CONCLUSIONS

Using 3D printing technology to produce prototype models of agricultural tools and structural parts is possible. However, it has the limitations of the relatively low Young modulus of elasticity and hence the stiffness of the printed models. The results of the simulations have shown that it will be possible to use this technology for validation in a laboratory soil trough, but in an environment that produces a relatively low draught resistance.

3D printing technology for the production of agricultural tool prototypes will be applicable, for example, to dry sand up to 150 mm deep or wet dredged sand up to 100 mm deep. Greater depths for validation of simulations in the laboratory soil trough lead to a large deformation of parts of the agricultural tool and hence to draught force. For this purpose, it will be necessary to use either material like metals or composite materials. However, it will decrease the advantage of using 3D printing technology for its variability, production speed and cost of prototype.

ACKNOWLEDGEMENTS. Supported by Internal grant 31200/1312/3102 agency of Faculty of Engineering, Czech University of Life Sciences in Prague.

## REFERENCES

- Alief, N.A., Utomo, M.S., Kartika, I. & Whulanza, Y. 2019. Geometrical and mechanical performance of multi-material fused deposition modelling. *IOP Conf. Series: Materials Science and Engineering* **557**. doi:10.1088/1757-899X/557/1/012022
- Budynas, R. & Nisbett, K. 2015. *Shigley's mechanical engineering design (10th ed.)*.
- Cahyati, S. 2019. Integrated CAD customization system for fused deposition models in additive manufacture with 3D printing machine. *IOP Conference Series Materials Science and Engineering* (**694**). doi:10.1088/1757-899X/694/1/012008
- ESSS Rocky. 2018 *Rocky DEM technical manual*.
- Guerrero-Villar, F., Torres-Jimenez, E., Dorado-Vicente, R. & Jiménez-González, J.I. 2015. Development of Vertical Wind Turbines via FDM Prototypes. In *Procedia Engineering*, Vol. **132**, pp. 78–85. Elsevier Ltd. doi:10.1016/j.proeng.2015.12.482
- Hao, L., Raymont, D., Yan, C., Hussein, A. & Young, P. (2011). Design and additive manufacturing of cellular lattice structures. In *Innovative Developments in Virtual and Physical Prototyping* (pp. 249–254). CRC Press. doi:10.1201/b11341-40
- Hossain, M.S., Espalin, D., Ramos, J., Perez, M. & Wicker, R. 2014. Improved Mechanical Properties of Fused Deposition Modeling-Manufactured Parts Through Build Parameter Modifications. *Journal of Manufacturing Science and Engineering, Transactions of the ASME* **136**(6). doi:10.1115/1.4028538
- Kadau, D., Schwesig, D., Theuerkauf, J. & Wolf, D.E. 2006. Influence of particle elasticity in shear testers. *Granular Matter* **8**(1), 35–40. doi:10.1007/s10035-005-0217-y
- Kešner, A., Chotěborský, R., Linda, M. & Hromasová, M. 2019. Methodology of the stress determination in the tool module during the work of the agriculture machine. *Agronomy Research* **17**(2), 481–490. doi:10.15159/AR.19.103
- Khan, S., Fayazbakhsh, K., Fawaz, Z. & Arian Nik, M. 2018. Curvilinear variable stiffness 3D printing technology for improved open-hole tensile strength. *Additive Manufacturing* **24**, 378–385. doi:10.1016/j.addma.2018.10.013
- Kotrocz, K., Mouazen, A.M. & Kerényi, G. 2016. Numerical simulation of soil-cone penetrometer interaction using discrete element method. *Computers and Electronics in Agriculture* **125**, 63–73. doi:10.1016/j.compag.2016.04.023
- Lanzotti, A., Grasso, M., Staiano, G. & Martorelli, M. 2015. The impact of process parameters on mechanical properties of parts fabricated in PLA with an open-source 3-D printer. *Rapid Prototyping Journal* **21**(5), 604–617. doi:10.1108/RPJ-09-2014-0135
- Ning, F., Cong, W., Hu, Y. & Wang, H. 2017. Additive manufacturing of carbon fiber-reinforced plastic composites using fused deposition modeling: Effects of process parameters on tensile properties. *Journal of Composite Materials* **51**(4), 451–462. <https://doi.org/10.1177/0021998316646169>
- Poudel, L., Sha, Z. & Zhou, W. 2018. Mechanical strength of chunk-based printed parts for cooperative 3D printing. In *Procedia Manufacturing*, Vol. **26**, pp. 962–972. Elsevier B.V. doi:10.1016/j.promfg.2018.07.123
- Sadek, M.A., Chen, Y. & Liu, J. 2011. Simulating shear behavior of a sandy soil under different soil conditions. *Journal of Terramechanics* **48**(6), 451–458. doi:10.1016/j.jterra.2011.09.006
- Shahrubudin, N., Lee, T.C. & Ramlan, R. 2019. An overview on 3D printing technology: Technological, materials, and applications. In *Procedia Manufacturing*, Vol. **35**, pp. 1286–1296. Elsevier B.V. doi:10.1016/j.promfg.2019.06.089

- Ucgul, M., Fielke, J.M. & Saunders, C. 2015. Three-dimensional discrete element modelling (DEM) of tillage: Accounting for soil cohesion and adhesion. *Biosystems Engineering* **129**, 298–306. doi:10.1016/j.biosystemseng.2014.11.006
- Ucgul, M. & Saunders, C. 2020. Simulation of tillage forces and furrow profile during soil-mouldboard plough interaction using discrete element modelling. *Biosystems Engineering* **190**, 58–70. doi:10.1016/j.biosystemseng.2019.11.022
- Wulle, F., Coupek, D., Schäffner, F., Verl, A., Oberhofer, F. & Maier, T. 2017. Workpiece and Machine Design in Additive Manufacturing for Multi-Axis Fused Deposition Modeling. In *Procedia CIRP*, Vol. **60**, pp. 229–234. Elsevier B.V. doi:10.1016/j.procir.2017.01.046
- Yang, S., Tang, Y. & Zhao, Y. F. 2015. A new part consolidation method to embrace the design freedom of additive manufacturing. *Journal of Manufacturing Processes* **20**, 444–449. doi:10.1016/j.jmapro.2015.06.024
- Ziemian, S., Okwara, M. & Ziemian, C.W. 2015. Tensile and fatigue behavior of layered acrylonitrile butadiene styrene. *Rapid Prototyping Journal* **21**(3), 270–278. doi:10.1108/RPJ-09-2013-0086

## **Physico-mechanical properties of modified antifriction coatings based on babbitt B83**

A.G. Ipatov<sup>1</sup>, A.B. Spiridonov<sup>2</sup>, R.R. Shakirov<sup>3</sup>, A.V. Kostin<sup>3</sup>, S.N. Shmykov<sup>1</sup>  
and V.S. Kukhar<sup>4,\*</sup>

<sup>1</sup>Operation and repair of machines, Izhevsk State Agricultural Academy, Studencheskaya street 9, RU426069 Izhevsk, Russia

<sup>2</sup>Technologies and equipment for food and processing industries, Izhevsk State Agricultural Academy, Studencheskaya street 9, RU426069 Izhevsk, Russia

<sup>3</sup>Theoretical mechanics and materials resistance, Izhevsk State Agricultural Academy, Studencheskaya street 9, RU426069 Izhevsk, Russia

<sup>4</sup>Ural State Agrarian University, Street Karla Libknekhta, 42, RU620075 Ekaterinburg, Russia

\*Correspondence: viktorurgau@mail.ru

**Abstract.** The introduction presents the primary reasons for the decrease in the working efficiency of plain bearing assemblies and suggests key areas for the formation of a stable working capacity of these assemblies.

In addition, the introduction discusses preexisting methods for improving the working efficiency of plain bearings. These methods are based on the use of antifriction coatings and have the drawbacks which are considered in the text. The authors proposed a technology for producing an antifriction coating based on a metal composition. This antifriction coating is produced by high-speed laser processing of powder materials. The technology allows to create antifriction coatings, which have significant wear resistance and the effect of self-lubrication while also provide a minimum run-in time of the bearing assembly.

The methodology validates the choice of materials for the formation of an antifriction coating. An alloy with significant tribotechnical properties based on babbitt B83 was chosen as the basis (matrix). To improve the bearing capacity of the coating, the babbitt base was transformed with MoS<sub>2</sub> molybdenum disulfide. The laser radiation usage in the formation of an antifriction coating based on babbitt B83 synthesizes finely dispersed intermetallide phases and forms a porous coating structure due to incomplete melting of the powder material. Molybdenum disulfide is released mainly through the porous structure, which leads to self-lubrication of the bearing assembly during oil starvation.

The results of microstructural and X-ray diffraction analysis are presented to display the structure of the obtained coatings based on antifriction materials. Research value is characterized by the presence of the following intermetallide phases in the structure of the formed coating: Fe<sub>2</sub>Sn, SnSb, Cu<sub>3</sub>Sn. The dispersivity of the formed phases is much greater than that of standard babbitt coatings, which is determined by higher crystallization rates under conditions of laser radiation processing. The analysis of diffractograms makes it possible to conclude that the distribution of intermetallide phases along the coating depth is uneven. The underlying layers close to the basis (matrix) are more soft and supple due to the presence of  $\alpha$  - solid solution. The surface layers are solid and saturated with the finely crystalline Cu<sub>3</sub>Sn phase. The research undertaken on formed



coating under conditions of dry friction allows to conclude that the antifriction coating can work without supplying lubricant to the bearing assembly.

**Key words:** laser radiation, babbitt B83, antifriction coating, plain bearing, working efficiency, wear, intermetallide phases, molybdenum disulfide.

## INTRODUCTION

Modern agronomic science is continuously related to the development of innovative machines and mechanisms used in the agricultural production. In order to ensure the reliability and working efficiency of machine components and assemblies, it is necessary to increase the wear resistance of contacting surfaces under severe operating conditions, which include frequent oil starvation, high dynamic and kinematic loads.

Plain bearings are an essential part of modern mechanical engineering. They are used not only at the assemblies where high speeds of linear and rotational motion are needed, but also at the ones the transmission of large dynamic and alternating loads is required.

Wear of friction surfaces in a plain bearing significantly increases the gap clearance between the shaft and the inner surface of the sleeve, which in turn leads to a decrease in the bearing capacity of the oil wedge and causes strong shaft vibration relative to the sleeve. These vibrations provoke uneven wear of the shaft surface and the sleeve inner surface (elliptical shape), which as a result negatively affects the condition of the oil wedge and its bearing capacity. Subsequently, this leads to an acceleration of surfaces wear processes, which results in a bearing assembly failure.

Currently, there is a huge variety of manufacturing processes and restoring methods to prevent the occurrence of the above phenomena. Most of these methods are based on modern technologies for sputtering and surfacing of antifriction coatings with attraction of complex powder compositions on friction working surfaces. Presently known application and restoring methods consider only providing the necessary linear dimensions of the friction surfaces and providing the necessary clearance in the bearing assembly. To extend the working efficiency of bearing assemblies, it is necessary to provide not only coatings with antifriction properties, but also an uninterrupted supply of lubricant or self-lubrication of the coating. An important feature of the created coatings is the fast and high-quality running-in ability of friction surfaces.

In this regard, it is necessary to solve a whole range of problems in the restoration of plain bearing assemblies:

1. Selection and research of efficient materials for shafts; development of technology for creating coatings on the journals of the shafts from the analyzed materials with using the most effective methods (according to the criteria of manufacturability and economy).
2. Development of a balanced composition of materials and optimal technology for their use in the restoration of plain bearings sleeves (providing the best tribological performance).
3. Ensuring high efficiency of plain bearings assemblies due to the quality of the surfaces running-in ability and their increased wear resistance.

The approach to ensuring surface quality should also be changed. The roughness of the restored or created surfaces should correspond to the roughness of the joints that have

worked for a long time, and not be limited to the correspondence of the roughness to the allowable accuracy of the part manufacture. When restoring surfaces, it is necessary to make allowance the possibility of ensuring the optimum coating thickness on the surfaces of the joint parts, taking into account the compatibility of the coating materials in accordance with the requirement of tribology.

It should be noted that modern antifriction coatings should have good bearing capacity by virtue of the base material's high strength, a minimum running-in time (due to the protective, supple layer), and also have a greater shear strength due to high adhesive strength (Fig. 1). Usually the transition layer is a nickel or titanium sublayer, which provides high adhesive strength of the main bearing coating with the substrate. This transition layer is also a barrier to prevent the main layer components diffusion deep into the product. Running-in coating is applied by chemical deposition or galvanic synthesis from pure tin.

Creating an antifriction coating with these characteristics is fraught with great difficulties. They arise mainly

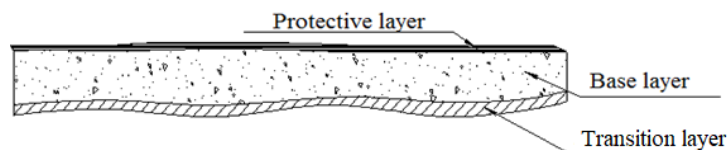


**Figure 1.** The structure of the modern antifriction coatings.

when it is needed to provide an ultra-small coating thickness (up to 1 mm), the compatibility of the used materials and the complexity of the coating formation technology itself.

This problem is solved by using composite materials made of metals and polymers. The development of this method is carried out in both domestic and foreign mechanical engineering. Bearings made of antifriction materials are based on metals or alloys containing polymer components (Panova, 2014). Lead, stannum, iron, copper and alloys of these metals are used. Polymers (mainly phenoplasts and fluoropolymers) act as alloying components; there are also used some thermosetting resins, which are mostly applied by two methods: impregnation method or rubbing method, both of which are low-tech and ineffective. Tribological properties of these coatings are different, which allows their use in a wide range. A signature feature of the used materials is a rather low coefficient of friction, a minimum running-in time and high anticorrosion properties that determine small amounts of wear. It should not be forgotten that the polymer component has low heat resistance, which leads to the friction coefficient instability, as well as to a decrease in the strength of the base material, which is a serious drawback. To stabilize the temperature within the established limits in the friction zone, it is required to provide an intensive supply of coolant, which in most assemblies is structurally difficult to implement.

It is a difficult task to increase shear strength and in most cases this problem is solved by creating a special layer made of a nickel or copper base, which greatly increases the technology complexity and the cost of manufacturing a plain bearing (Tarelnik et al., 2010).

To simplify the technology of creating coatings based on antifriction materials, you need to strive for the idea of using simple standard and cheap materials with minimal exposure to an energy source, which implies the formation of an antifriction layer in one pass, with ensuring the required coating thickness, properties and roughness (Ločs & Boiko, 2018; Ipatov et al., 2019a; Ipatov et al., 2019b). The use of such technology for coating significantly reduced the cost of plain bearings and as a result improved their quality.

The creation of these coatings is possible while providing ‘strict’ processing modes. The traditionally used methods of applying many antifriction coatings are based on powder metallurgy technologies (sintering) or casting methods (babbitt coatings). The above methods for creating antifriction coatings have significant drawbacks based on inadequate control of processing parameters and the inability to control them during application, which leads to uncontrolled phase transformations with the formation of unintended phases. These drawbacks result in the limited properties of the created coatings, as well as to a decrease in mechanical properties.

Therefore, in this work, we propose to use laser radiation as an energy source for obtaining antifriction coatings. Local laser action allows supplying energy to the fusion zone in a graduated way, which make it possible to control the processes of structure formation. High crystallization and recrystallization rates allow to obtain a wide range of intermetallide phases different from the traditional ones (Ipatov et al., 2019a; Ipatov et al., 2019b).

A signature feature of creating a coating technology is not only structural and phase transformations with the formation of intermetallide phases, but also the dendritic structure formation. The dendritic structure is determined by the feature of crystallization and directed growth of dendrites mainly from the substrate surface to the antifriction coating outer surface. Existing methods for applying babbitt coatings provide the chaotic formation of dendrites. The resulting structure is not homogeneous, but heterogeneous with dendritic segregations. To reduce the structure inhomogeneity effect, subsequent heating or pressure shaping of the created coating is used (Potekhin et al., 2006; Potekhin et al., 2010). Other significant drawbacks of babbitt coatings (B83) are intermetallide compounds of the Sn-Sb system -  $\beta$ -phases and acicular particles of the  $\gamma$ -phase ( $\text{Cu}_3\text{Sn}$ ) (Table 1).

**Table 1.** Characteristics of babbitt B83 intermetallide compounds

Intermetallide compound	HB phases hardness, $\text{kgf mm}^{-2}$
$\beta$ -phase ( $\text{SnSb}$ )	54
$\gamma$ -phase ( $\text{Cu}_3\text{Sn}$ )	383

The presence of these phases significantly reduces the wear resistance and fatigue strength of babbitt coatings. The striving to quantitatively reduce these phases will obviously lead to an increase in the friction coefficient and a decrease in the hardness and bearing capacity of the coating. The negative influence of these phases is caused by their uneven distribution in the applied coating volume and low dispersion of crystals, which results in the development of microcracks and the formation of dislocations along the boundaries. Some works cite the fact that a decrease in the dimension of these phases (Barykin et al., 2006; Barykin et al., 2000) with a more uniform distribution in the coating volume allows to increase the mechanical properties of babbitt coatings. Moreover, all operations to improve the structure and properties are performed on

standard finished babbitt coatings, which increases the final cost of production and does not fully provide the intended effect.

At high friction speeds the friction coefficient instability is demonstrated for babbitt coatings. To solve this problem lubricant is intensively supplied to the bearing assembly, but in many of them there is usually no possibility to provide the supply of lubricant due to certain design features. Therefore, self-lubrication is the most relevant issue. Self-lubrication of the antifriction coating is formed in the presence of a lubricant in the porous coating structure (the lubricant fills the pores). The porous coatings creation is impossible when babbiting, therefore, methods for sintering powder materials in the liquid phase are necessary.

To increase the technological effectiveness of creating an antifriction babbitt coating and to lower the product cost while maintaining the necessary tribotechnical and strength properties, we propose the coating formation based on B83 babbitt modified with MoS<sub>2</sub> molybdenum disulfide by using laser processing of powder material. This results in the formation of a structure with a finely crystalline intermetallide phase, which is uniformly distributed throughout the entire coating volume; this is facilitated by high crystallization rates, as well as the diffusion kinetics.

The formation of dendritic structures is uniform and contributes to the production of highly dispersed structures, usually formed from the substrate surface to the coating upper layers. However, it should be noted that the coating structure is porous, which is provided by incomplete fusion of powder particles. The molybdenum disulfide powder (modifier) is added into the powder composition. And it is mainly released through the porous structure of the formed coating during its processing.

### **Methodology for creating coatings**

This paper presents a technique for producing modern antifriction coatings by using highly concentrated laser radiation. We use babbitt B83 as an antifriction coating matrix because it has low and stable friction coefficient and relatively high bearing capacity. To maintain the stability of the tribotechnical parameters at high speeds (more than 50 m s<sup>-1</sup>) and high running-in ability of the coating, as well as to increase the bearing capacity, it is proposed to use the antifriction material molybdenum disulfide MoS<sub>2</sub>.

Laser processing was carried out in a special chamber made of organic glass in laboratory conditions (in accordance with the technology presented in the paper (Ipatov et al., 2015) (Fig. 2).

The pulsed laser radiation was generated by a fiber-optic laser machine LRS AUTOMATIC manufactured by OKB 'Bulat'. To protect the coating from oxidation, fusion was carried out in a medium of chemically pure argon. The processing modes were specially selected to ensure the fact that the structure remelting occurred over the



**Figure 2.** Application of an antifriction coating in a shielded chamber.

entire thickness of the antifriction coating. Scanning speed  $v_{sc}$  ( $\text{mm s}^{-1}$ ), pulse energy  $\varepsilon$  (W), and pulse frequency  $\lambda$  (kHz) were taken as main processing parameters. The processing conditions values were adopted on the basis of exploratory researches (presented in the paper (Ipatov et al., 2019)) and had the following indicators:  $v_{sc}$  -  $25 \text{ mm s}^{-1}$ ,  $\varepsilon$  -  $60 \text{ W}$ ,  $\lambda$  -  $50 \text{ Hz}$ .

X-ray diffraction studies were conducted on the DRON-6 automated diffractometer to determine the coating phase composition. The survey was performed by using the constant time method in monochromatic  $\text{Co-K}\alpha$  radiation with a wavelength of  $\lambda = 1.7902 \text{ \AA}$ , with the angle step of  $0.05^\circ$  and an exposure time of  $5 \text{ s}$  at each point. To research the structural and phase composition of the resulting coating as well as to determine the porosity and dimensionality of the structural components metallographic studies were conducted by using a Neophot-32 microscope. Micrographs in the cross section of coating were prepared in order to conduct a metallographic analysis. The micrographs were preliminarily pickled in the conditions of nitric acid. The dimensionality of the structural components was determined by the micrometer scale installed in the microscope eyepiece. Wear tests were carried out under dry and liquid friction conditions on an SMT-2070 friction machine. The following values were taken as the modes of tribo-loading: the friction speed was  $2 \text{ m / s}$ ; the loading mode was varied in the range from  $5$  to  $20 \text{ mPa}$ . The cycle time under one load was  $5$  minutes.

## RESULTS AND DISCUSSION

In the process of producing antifriction coatings, priority was assigned to the appearance of the resulting coating; also such parameters as the absence of delamination from the substrate, the presence of incomplete fusions and flaws, as well as the uniformity of the applied coating over the thickness were controlled (Fig. 3). The resulting coatings have a uniform structure. There are no visible defects. The uniform coating thickness is on average  $0.45\text{--}0.5 \text{ mm}$ .

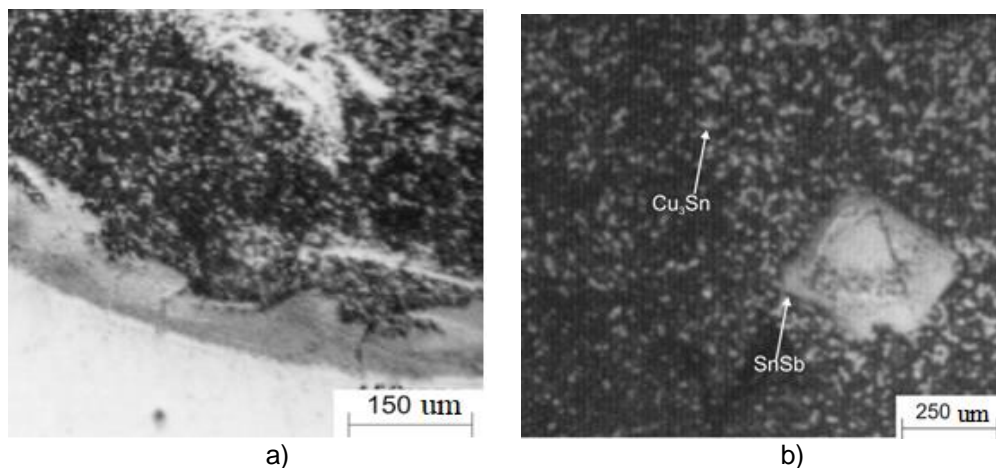


**Figure 3.** The microstructure of the cross section of the analyzed coating.

The coating top layer is dark in color, with the presence of subtle pores filled with molybdenum disulfide. The surface is oily and layered to the touch.

The main tasks of the analysis were to determine the phase composition and phase dispersion, as well as to reveal the adhesion pattern of the coating to the substrate. The microstructures research showed the presence of a coating soft matrix ( $\alpha$  is a solid solution), solid inclusions consisting of Sn-Sb intermetallide compounds of  $\beta$ -phase and acicular inclusions of  $\gamma$ -phase -  $\text{Cu}_3\text{Sn}$ .

As expected, the size of the obtained phases is smaller than that of the babbitt coatings obtained by the traditional method, which is explained by high crystallization rates, especially in the  $\gamma$  phase. Micrometric analysis showed a decrease in the size of intermetallide compounds by 65%. The dimensionality of the obtained phases was determined by using a micrometer scale applied on the microscope eyepiece.

Adhesion zone with the substrate is characterized by a lighter shade, which indicates the presence of additional phases. The fusion zone has no pores or incomplete fusions, which proves that the optimal processing conditions were selected and the necessary joint strength was attained. In this work there were no researches devoted to the adhesion strength determination, but it is worth mentioning that the impact force did not lead to the coating delamination from the substrate.

X-ray diffraction researches were carried out to determine the phase distribution uniformity in the coating volume (Fig. 4). To provide a more detailed analysis of the phase distribution in the cross section, the coating was divided into three layers by diamond grinding method at every 20  $\mu\text{m}$  interval: 1<sup>st</sup> layer characterizes the adhesion zone of the coating with the substrate, 2<sup>nd</sup> layer characterizes the phase state of the coating at a distance of 20  $\mu\text{m}$  from the adhesion zone, 3<sup>d</sup> layer characterizes the surface condition.

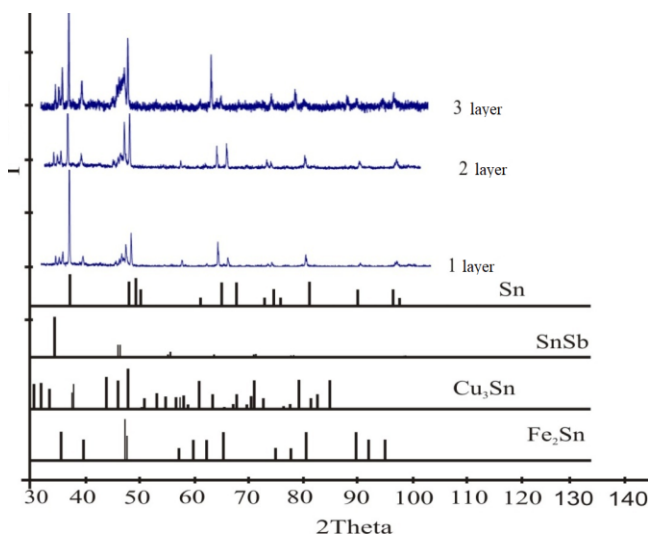


**Figure 4.** Diffractograms of the coatings with increasing thickness of the applied babbitt coating.

According to the results of the experiment, the formation of the 'standard' intermetallide compounds mentioned above and  $\text{Fe}_2\text{Sn}$  compounds was revealed. The

producing of this compound mainly occurs in the underlying layers close to the substrate, which characterizes the processes of mixing the metals volumes of the substrate and the applied composite during laser processing. The presence of this phase in the microstructural analysis is no indicated, which characterizes its fine-crystalline structure. Intermetallides have a relatively high strength, which in return provides high adhesion strength of the created coating to the substrate. In order to determine the thickness of the phases quantitative composition, an X-ray diffraction analysis was carried out, in which the conditionally formed coating was divided into three layers. The main data of quantitative analysis are presented in Table 2. The table shows the intermetallide compounds formed under equilibrium crystallization conditions.

**Table 2.** Phase and quantitative composition of the coating

Phase	The amount of phase in layer 1, %	The amount of phase in layer 2, %	The amount of phase in layer 3, %
Sn	6.29	19.74	0.25
SnSb	44.48	6.04	14.14
Cu <sub>3</sub> Sn	43.91	68.24	84.94
Fe <sub>2</sub> Sn	5.32	5.98	0.67

The quantitative phase composition of the formed coating (Table 2) shows that when the thickness of the applied layer is increasing, the amount of the Sn phase tends to zero, and the amount of the Cu<sub>3</sub>Sn intermetallide phase significantly increases, which is attributed to the increase in laser processing time. The decrease in the amount of the Fe<sub>2</sub>Sn phase close to the surface layer is associated with an increase in the coating thickness and the absence of iron in the upper layers. Thus, the features of phase transformations during laser processing have resulted in a quantitative change in the phase composition over the thickness. Based on the data in Table 1, it can be concluded that the coating has optimal mechanical properties: in particular, the underlying layers are softer and more flexible due to the presence of the  $\alpha$  – solid solution and  $\beta$  – phase (SnSb), and the upper layers are harder due to the increase in the amount of  $\gamma$  – phase (Cu<sub>3</sub>Sn), which has a higher solidness. Under operating conditions high surface hardness resists intense wear, and a soft, flexible base resists dynamic, alternate loads, increasing the fatigue and cyclic strengths of the coating. Thus, the presented results fully meet the requirements of modern antifriction coatings.

The main tribotechnical indicators of coatings were presented in the work (Ipatov et al., 2015), which examined the effect which the structure of the created coating has on its wear under dry friction conditions (Fig. 5).

During wear tests the operation of plain bearing was simulated under dry friction conditions as the most aggressive operating conditions possible. The following parameters were accepted as the research modes: friction speed of 2 m s<sup>-1</sup>, specific load of 20 mPa in dry lubrication conditions

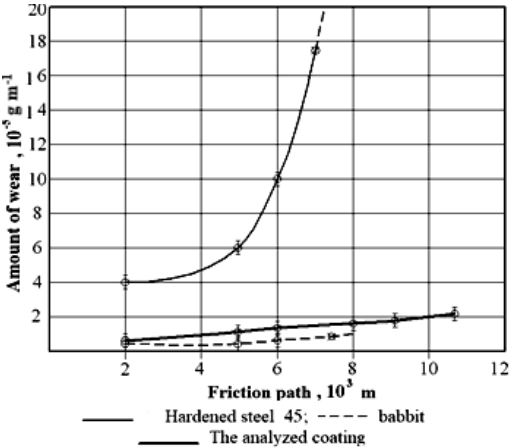


**Figure 5.** Dry friction wear characteristics (Ipatov et al., 2015).

(the modes were determined on the basis of averaged empirical parameters of internal combustion engines operation under medium load). To compare the amount of wear, we considered the wear of standard materials in the following joints: 'hardened steel - hardened steel 45', 'hardened steel - babbitt B83 coating obtained by casting method', 'hardened steel - analyzed coating'. Test modes for all coatings were the same. All surfaces were running-in under conditions of hydrodynamic friction, after which the surfaces of the samples were wiped dry.

The research showed the smallest wear for a standard babbitt coating. The porosity lack of the molded babbitt coating gives it a high cohesive strength, which reflects in a decrease in the surface damage probability. The high density of the coating material gives good thermal conductivity, which reduces the setting process of micro unevenness of friction surfaces. This affects the coating wear rate reduction. However, the work duration of the babbitt coating in conditions of dry friction is limited and the setting process of friction surfaces occurs when the path length is 7,500 m. Setting moment for hardened steel 45 occurs even earlier, but significant wear is observed over the entire range of the friction path. During the research, the process of setting surfaces has never been seen in the coating forming, which shows the effective coating ability of self-lubrication. The formed surface has porosity filled with molybdenum disulfide, which results in friction surfaces separation and ensuring uninterrupted operation of the assembly under dry friction conditions.

Therefore, the presented results of comparative wear tests clearly illustrate the following idea: in the conditions of emergency wear (lack of intensive lubrication) the analyzed coating has a higher resistance to wear and to seizing of friction surfaces.

## CONCLUSIONS

The developed technology for producing antifriction coatings is feasible. The structure formation of the created coatings differs from the standard ones and is characterized by the presence of finely dispersed intermetallide phases. The research devoted to the distribution of these phases over the thickness indicates the optimality of the mechanical properties the coating has, which confirmed the expected results.

The results of wear tests make it possible to conclude that the proposed antifriction coating is functional even in dry friction conditions, which corresponds to the research objectives.

## REFERENCES

- Barykin, N.P., Fazlyakhmetov, R.F. & Valeev, A.H. 2006. The influence of the babbitt B83 structure on the wear rate of tribological conjunctions. *Metallurgy and heat treatment* 2(608). 44–46 (in Russian).
- Barykin, N.P., Sadykov, F.A. & Aslanyan, I.R. 2000. Surface treatment of a plain bearing shell. *Friction and wear*. T.21, 6, 634–639 (in Russian).
- Ipatov, A.G., Kharanzhevsky, E.V., Strelkov, S.M. & Shmykov, S.N. 2015. Research on the tribological properties of metal-polymer coatings in the B83-MoS<sub>2</sub>-F4 system. *Herald of Izhevsk Agricultural Academy* 3(44), 7–20 (in Russian).



- Ipatov, A.G., Ostaev, G.Ya., Shmykov, S.N., Novikova, L.Ya. & Deryushev, I.A. 2019a. An analysis of the functional properties of super hard coatings on boron carbide synthesized by short-pulse laser processing. *International Journal of Mechanical and Production Engineering Research and Development* T. 9. **2**. pp. 921–928.
- Ipatov, A.G., Shmykov, S.N., Deryushev, I.A., Novikova, L.Ya. & Sokolov, V.A. 2019b. Analysis and synthesis offunctional coatings by high-speedlaser processing of ultrafine powder compositions. *International Journal of Mechanical and Production Engineering Research and Development* T. **9(3)**, pp. 421–430.
- Ločs, S. & Boiko, I. 2018. Quality assessment of laser clad HSS coatings with deep penetration into base material to obtain a smooth gradient of properties in coating-substrate interface. *Agronomy Research* **18**(Special Issue 1), 1095–1109.
- Potekhin, B.A., Glushchenko, A.N. & Ilyushin, V.V. 2006. Properties of babbitt B83. *Technology of metals* **3**, 17–23 (in Russian).
- Potekhin, B.A., Ilyushin, V.V. & Khristolyubov, A.S. 2010. Special properties of B83 babbit obtained by turbulent casting method. *Casting and Metallurgy* **3(57)**, 79–81 (in Russian).
- Panova, I.M. Wear of triboplasts in plain bearings. 2014. *"Naukovedenie" online magazine*, Issue **2** (in Russian).
- Tarelnik, V.B., Martsinkovsky, V.S. & Belous, A.V. 2010. Study of the cohesion strength between babbitt layer in plain bearings with a substrate. *Herald of the Kharkiv National Technical University named after Peter Vasylenko*. Issue **94**, pp. 102–108 (in Russian).

## **Study on performance of compression engine operated by biodiesel fuel**

H. Kaletnik<sup>1</sup>, V. Mazur<sup>1</sup>, I. Gunko<sup>1</sup>, V. Ryaboshapka<sup>1</sup>, V. Bulgakov<sup>2</sup>, V. Raide<sup>3</sup>,  
R. Ilves<sup>3</sup> and J. Olt<sup>3,\*</sup>

<sup>1</sup>Vinnytsia National Agrarian University of Ukraine, 3 Soniachna Str., UA21008 Vinnytsia, Ukraine

<sup>2</sup>National University of Life and Environmental Sciences of Ukraine, Ukraine, 15 Heroyiv Oborony Str., UA 03041 Kyiv, Ukraine

<sup>3</sup>Estonian University of Life Sciences, Institute of Technology, 56 Kreutzwaldi Str., EE 51006 Tartu, Estonia

\*Correspondence: jyri.olt@emu.ee

**Abstract.** The analysis of the performance of biofuel is aimed at evaluating the energy efficiency of operating the engine with the use of biodiesel fuel as function of the fuel's composition and other physical-and-chemical parameters. The mathematical models and analysis techniques known to the authors do not take into account the effect that the use of different bio-diesel fuels has on the operation of the engine and, therefore, need refinement in terms of the mathematical expressions and empirical formulae that describe the physical processes taking place in the engine's cylinders. The aim of the study is to improve the mathematical relations taking into consideration the physical-and-chemical parameters of different types of fuel. The research methods proposed in the article are based on step-by-step consideration of the mathematical models of processes that follow each other, with due account for their possible overlapping, which jointly have an effect on the engine's output indices. The boundary conditions and parameter increments are pre-set in electronic work sheets. Thus, it becomes possible, using the refined mathematical model, to calculate the main performance indices of the diesel engine with due account for the changes in the physical-and-chemical parameters of the fuel. The novelty of the described approach is in the possibility, through the use of the refined model and taking into account the data on the composition of the fuel and the design and operation parameters of the engine, to calculate the indices that allow evaluating the efficiency of use of specific fuels in the internal combustion engine under consideration. In results, formulas for the calculation of the effective power of the engine, fresh air charge density, excess air factor, effective specific fuel consumption and combustion pressure have been developed. Combustion pressure modelling and experimental data is presented.

**Key words:** biofuel, efficiency, composition, physical-and-chemical parameters of the fuel, internal combustion engine.

## **INTRODUCTION**

In the process of analysing the efficiency of use of a biofuel, the determining factor is the operating efficiency of the engine running on that fuel and many researches are

made on this topic (Raheman et al., 2004; Ulusoy et al., 2004; Choi et al., 2006; Kaplan et al., 2006; Reyes et al., 2006; Özgünay et al., 2007; Utlu, 2008; Hazar, 2009; Ozsezen et al., 2009; Xue et al., 2011). Thus, the consideration is given to the main factors that have effect on the energy performance of the engine (Apostolakou et al., 2009; Baranauskas et al., 2015). The other important issue is the fuel consumption rate per unit of energy output.

Hence, the output parameters of the problem under study are the external characteristics of the engine running on different types of fuel. There is a great number of models describing the work processes that take place in the engine cylinder (Naitoh et al., 1992; Mikita et al., 2012; Shabir et al., 2014; Olt et al., 2015; Zhou et al., 2015). However, such models not always take into account the effect that the fuel has on the performance indices of the engine, while those taking this effect into consideration are complicated and require carrying out a number of additional experimental studies in order to determine the coefficients and characteristics of the related processes used as input data (Osetrov, 2005).

Accordingly, it is a task of current concern to develop a mathematical model capable of describing with the use of semi-empirical relations the work processes in the diesel engine cylinder and, on the basis of their analysis, modelling the engine's external characteristics with due account for the physical-and-chemical properties of different types of fuel.

The mathematical models used for the calculation of external characteristics of engine performance can be divided into two types. The models of the first type are based on the heat calculation of the engine (Merker et al., 2012a). They are rather complicated, since they include quite a number of various parameters specifying the involved processes: gas exchange (intake-scavenging-exhaust), air and fuel mixing and combustion in the engine cylinder, heat transfer, internal energy losses and other. While such a mathematical model is suitable for calculating the engine operation at its rated duty, it cannot be used in case of the maximum torque duty in view of the absent coefficients that can be determined only experimentally. The second type of models is used more extensively for practical calculations and is based on the use of semi-empirical equations of the external characteristics with experimentally obtained coefficients (Osetrov, 2005; Ghobadian et al., 2013), and it is represented by the cubic trinomial formula:

$$\bar{N} = A \cdot \bar{n} + B \cdot \bar{n}^2 - C \cdot \bar{n}^3, \quad (1)$$

where  $\bar{N} = N/N_{max}$  – relative (normed) power equal to the ratio between the current power  $N$  and the maximum (rated) power  $N_{max}$ ;  $A$ ,  $B$  and  $C$  – coefficients depending on the type of engine;  $\bar{n} = n/n_{max}$  – relative rate of rotation equal to the ratio between the current rate of rotation  $n$  and the maximum rate of rotation  $n_{max}$  of the engine's crankshaft.

In the simplified case, the formula, in which only the relation with the torque is taken into account, can be used. The empirical model (1) for the calculation of the engine's external characteristic based on the statistical generalization of the external characteristics of engines of the same type.

The task of investigating the engine performance is important in case of changing the fuel type. When the engine is operated with the use of an alternative fuel, a need arises to adjust the control parameters (Osetrov, 2005; Küüt et al., 2015, Ilves et al.,

2019) in view of the fact that the fuel of another type has different physical-and-chemical parameters and, in order to optimise the operation of the engine with another type of fuel, it is necessary to take into account the changed parameters of the work process.

To make allowance for the effect of the fuel's physical-and-chemical parameters on the engine's performance indices, it will not suffice just to make use of one empirical relation, because the above-mentioned properties of the fuel can have a considerable impact on the working conditions of the engine.

For that reason, it is suggested to use in the formula (1) not the engine's rated power specified in the engine's specification, but rather the power rating obtained by calculation or experimentally at a rated duty under the pre-set operating conditions, taking into account the type of fuel, ambient conditions etc. In recent years, a number of scientific studies have mainly focused on the kinetics of the combustion of biofuels, including biodiesel (Ra & Reitz, 2011; Ismail et al., 2013; Maawa et al., 2020; Lejre et al., 2020). In addition, models for calculating engine torque have been developed (Alcan et al., 2020). All research deals with models one by one. For example, reactions of sulfur compounds, optimization of torque models, etc. are discussed. However, a model system that takes into account the characteristics of the engine being developed and the fuels used in it is important for engine development.

In that case, one more mathematical model is required, which would provide for carrying out the calculation on the basis of the physical-and-chemical properties of the bio-diesel fuel. In other words, it is necessary to find relations determining the engine's power at its rated duty.

The aim of the study is the development of a mathematical model for the practical analysis of the efficiency of use of biofuel in diesel engines, which would take into account the fuel's composition. The developed model in the article is designed to develop the 4Q11.0 / 12.5 diesel engine.

## **MATERIAL AND METHODS**

### **Mathematical model**

The methods of research are based on mathematical modelling of the physical and physical-and-mechanical processes taking place in the engine cylinder, which are taken into consideration one after another and related with each other in a cause-effect relationship. Microsoft Excel electronic work sheets have been used for the mathematical modelling of the processes that take place in the diesel engine cylinder, when bio-diesel fuels of different compositions are used. Developed model and non-referred equations based on the theory of the internal combustion engine of the Heywood (1988).

The analysis and calculation of the effective power of the engine can be carried out with the use of the following known analytical dependence (Heywood, 1988):

$$N_e = \frac{p_e \cdot V_h \cdot n \cdot i}{30 \cdot \tau_{en}}, \quad (2)$$

where  $p_e$  – mean effective pressure in the cylinder [MPa];  $V_h$  – cylinder displacement;  $n$  – rate of rotation of the crankshaft [ $\text{min}^{-1}$ ];  $i$  – number of cylinders;  $\tau_{en}$  – number of strokes in the cycle of the engine.

Pressure  $p_e$  can be expressed as the following difference:

$$p_e = p_i - p_m, \quad (3)$$

where  $p_i$  – actual mean indicated pressure, with due account for the smoothing out of the indicator diagram [MPa];  $p_m$  – mean pressure of the mechanical losses [MPa].

Pressure  $p_i$  is determined by the formula:

$$p_i = p'_i \cdot v, \quad (4)$$

where  $p'_i$  – theoretical mean indicated pressure [MPa];  $v$  – coefficient of smoothing of the indicator diagram.

The theoretical mean indicated pressure can be found using the Grinevetsky – Mazing formula for the composite Diesel cycle (Merker et al., 2012a, 2012b):

$$p'_i = \frac{p_c}{\varepsilon - 1} \cdot \left[ r_p \cdot (\rho - 1) + \frac{r_p \cdot \rho}{n_2 - 1} \cdot \left( 1 - \frac{1}{\delta^{n_2 - 1}} \right) - \frac{1}{n_1 - 1} \cdot \left( 1 - \frac{1}{\varepsilon^{n_1 - 1}} \right) \right], \quad (5)$$

where  $p_c$  – pressure at the end of the compression stroke [MPa];  $\varepsilon$  – compression ratio;  $r_p$  – pressure ratio;  $\rho$  – preliminary expansion ratio;  $n_1$  – polytropic index of compression;  $n_2$  – polytropic index of expansion;  $\delta$  – subsequent expansion ratio.

The  $r_p$  index is determined as follows:

$$r_p = \frac{p_z}{p_c}, \quad (6)$$

where  $p_z$  – maximum pressure of the engine operating cycle [MPa].

Preliminary expansion ratio:

$$\rho = \frac{V_z}{V_c}, \quad (7)$$

where  $V_z$  and  $V_c$  – volumes of the cylinder at the piston's position that corresponds to the maximum pressure in the cylinder during the cycle (point  $z$  on the indicator diagram) and the combustion chamber, respectively by Mikita et al. (2012).

The established formula of the total cylinder volume can be used to determine the volume  $V_z$  (Merker et al., 2012a, 2012b):

$$V_a = V_h + V_c. \quad (8)$$

The next step is to use the cylinder displacement formula with due account for the number of dimensions:

$$V_h = \frac{\pi \cdot D^2}{4} \cdot S \cdot 10^3, \quad (9)$$

where  $D$  – cylinder diameter [m];  $S$  – piston stroke [m].

The formulae (8, 9) can be used to find the current volume, when the piston is at a random point (for example, at the point  $z$  of the indicator diagram):

$$V_x = \frac{\pi \cdot D^2}{4} \cdot S_x \cdot 10^3 + V_c \quad (10)$$

where  $S_x$  – current stroke position of the piston [m], which depends on the angular displacement of the crankshaft and is determined by the formula (Merker et al., 2012a):

$$S_x = r + L_{cr} - r \cdot \cos \varphi - L_{cr} \cdot \cos \beta, \quad (11)$$

where  $r$  – crank throw [m];  $L_{cr}$  – connecting rod length [m];  $\varphi$  and  $\beta$  – angles of the position of the crank and the deflection of the connecting rod from the vertical axis, respectively.

The variable  $L_{cr}$  can be eliminated with the use of the parameter  $\alpha$  – crank-and-rod mechanism constant (ratio between the crank throw and the connecting rod length):

$$\alpha = \frac{r}{L_{cr}} \quad (12)$$

hence,

$$L_{cr} = \frac{r}{\alpha}. \quad (13)$$

Taking into account the centred type of the crank-and-rod mechanism (for example, in case of the 4Ч11,0 / 12,5 diesel engine), the piston stroke is equal to two throws of the crank:

$$S = 2 \cdot r \quad (14)$$

hence,

$$r = \frac{S}{2}. \quad (15)$$

After substituting the relations (11, 13, 15) and the values of the angles  $\varphi$  and  $\beta$  corresponding to the position of the crank at the point  $z$  of the indicator diagram with the respective index into the Eq. (10), the following formula for the volume  $V_z$  is obtained:

$$V_z = \frac{\pi \cdot D^2 \cdot S}{8} \cdot \left[ 1 + \frac{1}{\alpha} \cdot (1 - \cos \beta_z) - \cos \varphi_z \right] \cdot 10^3 + V_c \quad (16)$$

Subsequent expansion ratio:

$$\delta = \frac{\varepsilon}{\rho}. \quad (17)$$

Mean pressure of the mechanical losses (Merker et al., 2012a):

$$p_m = a + b \cdot W_{p.av}, \quad (18)$$

where  $a$  and  $b$  – empirical coefficients [MPa and MPa s m<sup>-1</sup> respectively];  $W_{p.av}$  – mean piston speed [m s<sup>-1</sup>], which for practical calculations can be found from the formula:

$$W_{p.av} = \frac{S \cdot n}{30}. \quad (19)$$

### Calculations principles

In order to verify the adequacy of the obtained mathematical model of the work processes in the engine cylinder, it is necessary to set the initial data. The 4Ч11,0/12,5 diesel engine has been chosen by the authors as the subject of research. The initial data are represented in the Table 1.

After substituting the initial data into the developed mathematical model represented by the formulae (31–35), (42), (43), (47–50), (53–55), it is possible to calculate the part of the indicator diagram that includes the compression polytropy curve and the combustion curve of the 4Ч11,0/12,5 engine.

In order to obtain the value  $T$  of the gas temperature in the cylinder, it is necessary to carry out experimental research. The main point of such research is in the indication of the engine's performance.

**Table 1.** Initial data for modelling work processes in 4U11,0/12,5 engine at its rated duty

Pos.	Description	Designation [unit]	Numerical value		
			At rated duty	At experimental duty with diesel fuel	At experimental duty with biofuel
1	2	3	4	5	6
1	Rotation rate of crankshaft	$n$ [rpm]	2,200	2,200	2,200
2	Compression ratio	$\varepsilon$	16	16	16
3	Atmospheric pressure	$p_0$ [MPa]	0.101325	0.09799167	0.09799167
4	Combined effect of air intake system coefficients on fresh air charge parameters	$\beta_{in}^2 + \xi_{in}$	2.5	2.5	2.5
5	Piston stroke	$S$ [m]	0.125	0.125	0.125
6	Cylinder diameter	$D$ [m]	0.11	0.11	0.11
7	Crank-and-rod mechanism constant	$\alpha$	0.272	0.272	0.272
8	Ambient air temperature	$T_0$ [K]	293.15	303.15	303.15
10	Angle of bevel of valve couple (seat angle) in gas distribution mechanism	$\alpha_v$ [deg]	45	45	45
11	Stroke of intake valve in:	first cylinder $h_{v1}$ [m]	0.01215	0.01215	0.01215
12		second cylinder $h_{v2}$ [m]	0.01215	0.01215	0.01215
13		third cylinder $h_{v3}$ [m]	0.0122	0.0122	0.0122
14		fourth cylinder $h_{v4}$ [m]	0.0124	0.0124	0.0124
15	Valve throat diameter on machined face in intake port	$d_n$ [m]	0.0462	0.0462	0.0462
16	Cyclic fuel injection rate	$V_{fc}$ [mm <sup>3</sup> cycle <sup>-1</sup> ]	62.7365	56.5148	56.5148
17	Density of fuel:	diesel $\rho_{df}$ (at $T = 323$ °K) [kg m <sup>-3</sup> ]	825	-	-
18		bio-diesel $\rho_{bf}$ (at $T = 323$ °K) [kg m <sup>-3</sup> ]	856	-	-
19		Molar mass of air $\mu_a$ [kg kmol <sup>-1</sup> ]	28.96	28.96	28.96
20	Cylinder purging coefficient	$\varphi_c$	1	1	1
21	Additional cylinder charging coefficient	$\varphi_{c.ad}$	1.0996	1.022	1.022
22	Residual gas temperature	$T_r$ , K	825	825	825

Table 1 (continued)

1		2	3	4	5	6
23	Mass fractions of main elements in composition of diesel fuel:	carbon	$C_{df}$	0.85665	0.85665	-
24		hydrogen	$H_{df}$	0.133	0.133	-
25		sulphur	$S_{df}$	0.005	0.005	-
26		oxygen	$O_{df}$	0.01	0.01	-
27	Mass fractions of main elements in composition of bio-diesel fuel:	carbon	$C_{bf}$	0.772	-	-
28		hydrogen	$H_{bf}$	0.119	-	-
29		sulphur	$S_{bf}$	0	-	-
30		oxygen	$O_{bf}$	0.109	-	-
31	Fresh air charge preheating temperature	$\Delta T$ , [K]		20–40	20	22

Brief technical description of subject of research. The engine under research is a naturally aspirated four-cylinder four-stroke Diesel engine with an open combustion chamber and a liquid cooling system. The model is D-240, produced by the Minsk Engine Works. The fuel system is of a closed type. The split-type fuel-feed equipment comprises the UTN-5 inline fuel-injection pump with an inbuilt all-speed governor and closed-type FD-22 fuel nozzles with 5-orifice spray atomizers as well as thick-walled steel high pressure fuel lines. The diameter of an injection orifice in the spray atomizer is 0.32 mm. The pear-shaped combustion chamber in the piston has been developed by the Central Research and Development Diesel Institute (TsNIDI). The engine power rating is 58.8 kW.

The following grades of fuel have been used, when carrying out the experimental studies: mineral diesel fuel EN 950 grade C and biofuel RSOME (methyl ethers of rapeseed and sunflower oils).

In the next paragraphs, the engine indication procedure is described.

The indication of the engine's performance implies plotting its indicator diagram that shows the relation between the pressure  $p$  in the cylinder and the crankshaft angular displacement  $\varphi$ , i.e. finding the function  $p = f(\varphi)$ .

The the following equipment is required to indicate an engine: an indicator instrument, the tested engine, a braking device, instruments for measuring the fuel and air consumption and other metering equipment.

## Experimental tests

### Equipment for experiment

The indicator instruments used for tests can be of different types. In the study under consideration an electronic indicator has been used, as that is the most accurate and compact type of design. The principle of operation of the electronic indicator is in the conversion of the gas pressure into an electronic signal. The conversion is performed by the piezoelectric transducer 1 (Fig. 1, a), screwed into the cylinder head 2 of the engine in the area of the fourth cylinder.



However, the installation of the pressure transducer alone will result in obtaining only the ordinates for the indicator diagram. In order to find the abscissae, an engine crankshaft position sensor (CSPS), i.e. the induction pick-up (Fig. 1, b) has to be installed.

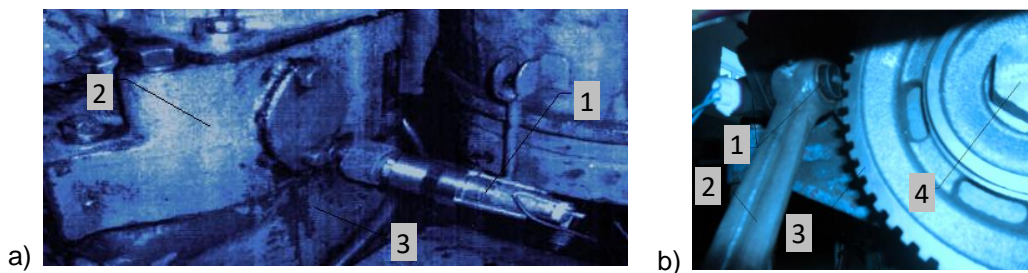


**Figure 1.** Placement of transducers in engine: a) 1 – piezoelectric gas pressure transducer DW-150, 2 – engine cylinder head, 3 – engine crankcase; b) 1 – induction pick-up 191.38472Д, 2 – sensor mounting bracket, 3 – crankshaft balancer pulley 21214-1005060-4, 4 – pulley hold-down bolt.

The reception and processing of the signals sent by the pressure transducer and the CSPS have been performed by the measurement module ZET 210, an analogue-to-digital and digital-to-analogue converter (ADC DAC), connected with the personal computer (PC) via a USB cable (Fig. 2, a). The special ZETLab interface included in the measurement module supply package has been used for displaying the signals on the PC monitor. In essence, the measurement module is an electronic oscillograph capable of simultaneously receiving and processing up to 16 signals.

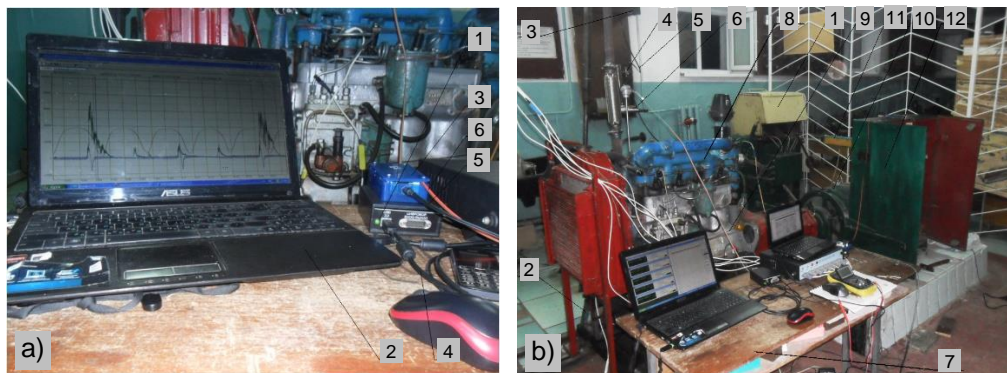


**Figure 2.** Equipment for laboratory experiments: a) ZETLab measurement module connected to 4Ч11,0/12,5 diesel engine: 1 – ADC DAC; 2 – PC; 3 – switching unit (SB); 4 – cable HS USB 2.0; 5 – power cable of SB (12 V); 6 – cable of input signals from transducers. b) KИ-5542 run-in check-out test bed for internal combustion engines: 1 – rheostat; 2 – stand; 3 – fuel tank; 4 – three-way valve; 5 – fuel supply line; 6 – weighing unit; 7 – measuring and recording equipment; 8 – diesel engine; 9 – linkage (cable) for driving governor lever of fuel injection pump; 10 – balancing electric machine; 11 – control panel; 12 – weighing system.

In order to support the supply of power and reception of signals to/from the transducers, the special switching unit 3 (Fig. 2, a) has been developed. Power is supplied to the switchboard (SB) from the standard accumulator battery of the engine, the unit, in its turn, transforms the voltage as necessary to supply power to each of the sensors (if needed) and receives from the latter their respective signals. Further, the signals are transmitted to the ADC DAC and displayed on the PC monitor in the form of oscillograms. In the study under consideration, two oscillograms are enough to generate the indicator diagram – the oscillograms of the signals from the pressure transducer and the CSPS with the same axis of abscissae (shows the duration of the experiment in time). The data from the oscillograph can be recorded both in the graphical and tabular formats, which is convenient for their further processing.

In the capacity of the braking unit, the KH-5542 commercial run-in check-out test bed for internal combustion engines (Fig. 2, b) has been used. The test bed comprises the balancing asynchronous electric machine 10 with a phase-wound rotor, model 4AHK, coupled with the diesel engine 8 via a universal joint. The electric machine is used for starting the diesel engine, when it acts as an electric motor and rotates the engine at the starting frequency, and for putting load on the diesel engine during the test, when it acts as an electric brake and imparts to the diesel engine the loading magnetic moment that arises due to the rotating magnetic field. The stator of the electric machine is mounted so as to allow it to rotate about its axis and is balanced via a system of cable and lever linkages by the pendulum of the weighing system 12, which, in its turn, is attached to the gauging pointer that swings on the dial gauged in kg. Thus, when the electric machine switches to the electric brake mode of operation putting load on the engine, a rotational torque arises, which turns the stator through some angle until it is balanced by the weight of the weighing system's pendulum. The amount of deflection of the pendulum is what identifies the rotational torque delivered by the engine.

The load on the diesel engine is changed by changing the strength of current on the rotor windings of the electric machine with the use of the liquid rheostat 1, which is a 300 L tank with electrolyte (water solution of caustic soda) and three steel electrodes immersed in the electrolyte. The area of contact between the electrodes and electrolyte changes together with the electrode immersion depth, which implies varying the resistance on the rotor windings and that results in the alteration of the electromagnetic braking torque that loads the diesel engine 8.

During the operation of the test bed, when the electric machine rotor windings are energized, the electrolyte is continuously mixed by the agitator, which is switched on from the push-button station on the control panel 11. The other push-button station also installed in the control panel is for switching on the motor reducer that sinks or hoists the electrodes. Apart from them, the control panel features the standard engine metering equipment, in particular, the engine tachometer, which has been used for measuring the crankshaft rotation frequency in order to control the speed condition of the engine.

The values of the gas temperature  $T$  in the cylinder for the formula (43) are taken from the experimental indicator diagram of the 4Ч11,0/12,5 engine presented in the paper by Romanov (2010).

In order to supply the engine with fuel and measure its consumption rate, the test bed is equipped with the tank 3, the three-way valve 4 connected with the tank via the low pressure fuel supply line 5 and the electronic weighing unit 6 for measuring the mass

consumption, on which a graduated cylinder is placed for measuring the volume consumption of fuel.

Thus, the КИ-5542 test bed provides for establishing various load and speed duties of the tested engine as well as measuring its effective parameters under these duties.

Besides, the following sensors have been used for measuring auxiliary parameters in the process of engine indicator diagram plotting: a mass air flow (MAF) sensor BOSCH 0280218116, two thermoelectric couples ТЭРА TXA 1-24 К-2-И 500Ф10 (0...+ 1,060 °C) 10/2008 and TXA – 2088 XA(K)/21 (– 40...+ 600 °C) 90.06.04600 placed in the exhaust manifold for measuring the exhaust gas temperature in the middle of the flow, VIKA sensors for recording the fuel-feed equipment operation parameters and a pressure transducer from the Delfin-1M test bench. The VIKA pressure transducer is installed in the fuel injection line for measuring the pressure of fuel before the fuel nozzle, while the Delfin-1M pressure transducer is put as a clip on the fuel supply line after the pump outlet for measuring the deformation of the fuel supply line. These sensors have also been connected to the ZETLab measurement module by means of the SB.

Also, the ambient air temperature and pressure have been measured with the use of mercury-filled thermometer and barometer gauge as well as the relative air humidity with the use of an aspirated psychrometer.

### **Preparation of experiment**

The laboratory experiment was carried out in the laboratory of internal combustion engines. In order to install the DW-150 gas pressure transducer, it was necessary to prepare the engine cylinder head. For that purpose, the engine was partially disassembled, the engine head was dismantled. After a thorough examination of the head, two canals were bored – one horizontal and one vertical – for connecting the transducer with the internal chamber of the cylinder. In the horizontal bore, thread was tapped for screwing the transducer into the cylinder head. Before mounting the cylinder head back into its position, the valve system was checked with regard to the tightness and seating of the valve disks, also the seating of the injector nozzle needles in the wells of spray tips as well as the evenness of the sealing surfaces on the cylinder head and the cylinder block were checked.

The design of this model of engine did not provide for the installation of a CSPS sensor, therefore, a 191.38472Д sensor and a 21214-1005060-40 crankshaft balancer pulley supplied for standard VAZ-2105 motor cars were used. In order to equip the diesel engine with the sensor, the bracket 2 (see Fig. 2, b) and the pulley hold-down bolt 4 were used. As the 21214-1005060-40 pulley and the tested engine's standard crankshaft pulley were of different sizes, two pulleys had to be used together, which implied manufacturing an increased length bolt. Copper washers were foreseen for the adjustment of the clearance between the sensor 1 and the teeth of the balancer pulley 3.

In order to connect the sensor to the oscillograph, the switching circuit connecting the sensor and the ZETLab measurement module was designed and assembled by soldering in the SB. To ensure a reliable signal, the maximum possible clearance between the sensor and the teeth of the balancer pulley that provided a dependable signal was established experimentally.

Prior to fixing the balancer pulley, it was necessary to ensure that its missing tooth was against the sensor at the moment, when the pistons of the first and fourth cylinders were at their top dead centres (TDC). The TDC was determined with the use of a dial

indicator with the cylinder head removed from the engine, while the correct position of the balancer pulley with its missing tooth against the CSPA was found by simultaneously rotating the crankshaft and watching the oscillogram on the PC. As soon as the signal oscillogram crossed the X-axis in the area of the missing tooth in correspondence with the TDC mark, the balancer pulley 3 was fixed with the hold-down bolt 4 (see Fig. 2, b).

In order to ensure the correct operation of the weighing system of the КИ-5542 test bed, it was necessary to carry out its calibration. For the calibration of the weighing system, a gauging arm and a set of standard scale weights were used. A scale weight was put on the free end of the gauging arm and the deflection of the weighing system's pointer by one scale division value was fixed. Then greater scale weights were put on and the further pointer deflections were fixed. The scale weight that weighed 1 kg had to deflect the system's pointer through the one kilogramme mark on the dial. If the pointer deflections did not coincide with the marks corresponding to the weights put on the end of the gauging arm, the system's dial had to be re-graduated. After gauging the dial clockwise, it was gauged counter-clockwise as well.

After calibrating the measuring mechanisms, the standard tachometer and the electronic scales, the installed transducers were calibrated.

The gas pressure transducer was gauged with the use of a compressor with a pressure gauge. As a result of the gauging, the relation between the measured voltage and the gas pressure had been established.

The signal received from the CSPA could be converted into the crankshaft revolutions. For that purpose, it was sufficient to start the command 'Tachometer' under the tab 'Measurement' of the ZETLab interface, then, in the opened dialog box 'Revolutions', select the channel that corresponded to the CSPA signal. After that, the rpm values obtained by the electronic means were verified with the use of a hand tachometer. In case the readings disagreed, correction factors had to be input into the electronic tachometer settings.

The calibration of the MAF sensor was carried out in the heat engineering laboratory in the ICE and AFR department of the VNAU with the use of the unit for measurement of the isochoric heat capacity of air that comprised a differential pressure gauge and a fan. After connecting the MAF sensor with the fan in sequence, so as to make the whole flow of the air taken into the unit to pass through the sensor, the sensor could be gauged. As a result of the calibration of the sensor, a gauging characteristic of the relation between the measured voltage and the mass of air passing through the sensor in a unit time was obtained.

The calibration of the thermoelectric couples was done by immersing them into a container with vegetable oil. The oil temperature was changed with the use of a heat source. A mercury-filled thermometer with a dial that had its upper limit at a level of at least 300 °C was used for measuring the oil temperature variation. As a result, a gauging characteristic of the measured voltage variation as a function of the temperature was obtained.

The transducers for recording the operation parameters of the fuel supply system were calibrated with the use of the КИ-3333 fuel nozzle check-out test bed. In order to place the VIKA transducer on the centre line of the fuel flow, a T-joint was manufactured, which connected the fuel injection line, the nozzle and the sensor. As a result, a gauging characteristic of the relation between the measured voltage and the fuel

pressure was obtained. The pressure transducer from the Delfin-1M was not calibrated. It was used for correlation of the signal from the VIKA sensor.

In the process of calibration, all the sensors were connected to the ZETLab measurement module and their signals were displayed on the electronic oscillograph. For that purpose, a circuit was developed for connecting the sensors with due consideration of the need to supply power to them. All the transducer power supply and switching circuits were soldered together on one motherboard installed in the SB.

Prior to starting the engine indication, it was also necessary to synchronize the signals received from the gas pressure transducers and the CSPS. For the synchronization of the mentioned signals, the 'Multichannel Oscillograph' tab was selected in the ZETLab interface, then the respective channels were selected, the required adjustments were made and the oscillograms of the said signals were started. In order to generate the signals, the crankshaft was rotated by the electric machine, while the supply of fuel to the diesel engine was stopped. The maximum value of the signal from the gas pressure transducer had to coincide with the moment, when the signal from the CSPS sensor crossed the X-axis in the area of the missing tooth, which corresponded to the TDC. In case the maximum pressure did not coincide with TDC, it was necessary to loosen the bolt 4 (Fig. 1, b)) and adjust the position of the balancer pulley 3 with regard to the position of the crankshaft, then tighten the bolt.

### **Procedure of experiment**

For obtaining the indicator diagram, the electronic oscillograph is set to operate with seven measurement channels in order to be able to receive signals from all the above-mentioned sensors. The engine is started and warmed up until the temperature of the cooling fluid in the cooling system reaches 50 °C, then it is set to its rated operating duty. For that purpose, the fuel injection pump governor control arm is brought to the position of the maximum fuel supply rate. After the engine crankshaft reaches the maximum revolution rate, the electric machine 10 (Fig. 2, b) is switched on and the electrodes of the rheostat 1 are immersed into the electrolyte, thus increasing the load on the diesel engine. Under these conditions, the rotation frequency of the crankshaft will go down. After reaching a revolution rate of  $n = 2,200 \text{ min}^{-1}$  and the maximum possible load for that frequency, the immersion of the electrodes is stopped. At this stage, the engine is under its rated duty. After reaching the rated duty, it is necessary to check whether the operating conditions have stabilised. The conclusion about the stabilization of the reached conditions can be made on the basis of the indications of the thermoelectric couples. The stabilised indications of the thermocouples represent the stabilised exhaust gas temperature, which implies the stabilised engine load conditions. In case the load conditions change during the stabilization of the thermal conditions, that can be adjusted by manually turning the electrode immersion motor reducer with the use of the special hand wheel. The stable rated operating duty is considered to be established, when the load and speed and thermal parameters become constant.

After the engine has reached its rated operating duty, the fuel consumption rate is to be measured. For that purpose, the time, in which the mass of the fuel is reduced by 100 g according to the readings of the electronic scales, is measured with the use of a stop watch. Also, the readings of the weighing system pointer in kg are registered. When the fuel consumption rate is measured, the start and the end of the experiment are recorded from the time scale of the oscillograph.

After the experiment is completed, the marked interval of the oscillogram is saved in the memory.

## RESULTS AND DISCUSSION

### Mathematical model

Substituting the formulae (3–7, 16–19) into the expression (2), the following equation is obtained:

$$\begin{aligned}
 N_e = & \frac{\pi \cdot D^2 \cdot S \cdot n \cdot i}{120 \cdot \tau_{en}} \times \left( \frac{p_c \cdot v}{\varepsilon - 1} \cdot \left\langle \frac{p_z}{p_c} \cdot \left\{ \frac{\varepsilon - 1}{2} \cdot \left[ 1 - \cos \varphi_z + \frac{1}{\alpha} \cdot (1 - \cos \beta_z) \right] + \right. \right. \right. \\
 & \left. \left. \left. + \frac{1 + \frac{\varepsilon - 1}{2} \cdot \left[ 1 - \cos \varphi_z + \frac{1}{\alpha} \cdot (1 - \cos \beta_z) \right]}{n_2 - 1} \right] \right\rangle \times \right. \\
 & \left. \times \left[ 1 - 1 \cdot \left( \varepsilon \cdot \left( 1 + \frac{\varepsilon - 1}{2} \cdot \left[ 1 - \cos \varphi_z + \frac{1}{\alpha} \cdot (1 - \cos \beta_z) \right] \right)^{-1} \right)^{n_2 - 1} \right] \right\} - \\
 & \left. - \frac{1}{n_1 - 1} \cdot \left( 1 - \frac{1}{\varepsilon^{n_1}} \right) \right\rangle - \left[ a + \frac{b \cdot n \cdot S}{30} \right].
 \end{aligned} \tag{20}$$

In order to simplify the notation, the following coefficients are introduced in the formula (20):

$$k_1 = \frac{\varepsilon - 1}{2} \cdot \left[ 1 - \cos \varphi_z + \frac{1}{\alpha} \cdot (1 - \cos \beta_z) \right], \tag{21}$$

$$k_2 = n_2 - 1. \tag{22}$$

Thereby, the following is obtained:

$$\begin{aligned}
 N_e = & \frac{\pi \cdot D^2 \cdot S \cdot n \cdot i}{120 \cdot \tau_{en}} \cdot \left[ \frac{p_c \cdot v}{\varepsilon - 1} \cdot \left\langle \frac{p_z}{p_c} \cdot \left\{ k_1 + \frac{1 + k_1}{k_2} \cdot \left[ 1 - \left( \frac{\varepsilon}{1 + k_1} \right)^{-k_2} \right] \right\} - \frac{1 - \varepsilon^{-n_1}}{n_1 - 1} \right\rangle - \right. \\
 & \left. - \left( a + \frac{b \cdot n \cdot S}{30} \right) \right],
 \end{aligned} \tag{23}$$

where  $k_1$ ,  $k_2$  – simplification coefficients representing the position of the piston at the point  $z$  of the indicator diagram and the polytropic index of expansion less unity respectively.

With the use of the formula (23), the rated power can be determined for the two typical duties of the engine – the rated duty and the maximum torque duty. As regards the other duties of the engine, they require applying the method of calculation, in which the empirical cubic trinomial equation (1) is used. The equation can be written out in the following form (Komakha & Ryaboshapka, 2016):

$$N_{ex} = N_{enom} \cdot \frac{n_x}{n_{nom}} \cdot \left[ A + B \cdot \frac{n_x}{n_{nom}} - C \cdot \left( \frac{n_x}{n_{nom}} \right)^2 \right] \tag{24}$$

where  $A, B, C$  – empirical coefficients depending on the types of engine and fuel;  $N_{enom}$  – engine power rating [kW];  $n_x$  – current value of the rate of revolution of the engine crankshaft [ $\text{min}^{-1}$ ];  $n_{nom}$  – rated revolutions of the crankshaft [ $\text{min}^{-1}$ ].

The relation between the engine's torque and effective power output is determined by the known expression:

$$M_e = \frac{9,550 \cdot N_e}{n} \quad (25)$$

the effective specific fuel consumption is determined by the formula:

$$g_e = \frac{120 \cdot G_{fc} \cdot n \cdot i}{N_e \cdot \tau_{en}}, \quad (26)$$

where  $G_{fc}$  – cyclic fuel injection rate [ $\text{g cycle}^{-1}$ ].

The following relation exists between the volume and mass rates of the cyclic injection:

$$G_{fc} = V_{fc} \cdot \rho_f \cdot 10^{-9}, \quad (27)$$

where  $V_{fc}$  – cyclic fuel injection rate [ $\text{mm}^3 \text{cycle}^{-1}$ ];  $\rho_f$  – density of the fuel [ $\text{kg m}^{-3}$ ].

Thus, the relation (27) defines the cyclic fuel injection rate depending on the fuel density. The relation can be used in practical calculations in case of switching to another biofuel with a different density as compared to the standard diesel fuel (Osetrov, 2005).

After substituting the formula (23) into the equation (26), while taking into account (27), the following equation for determining the specific fuel consumption is obtained:

$$g_e = \frac{1,44 \cdot 10^{-5} \cdot V_{fc} \cdot \rho_f \cdot D^{-2} \cdot (S \cdot \pi)^{-1}}{\left[ \frac{p_c \cdot \nu}{\varepsilon - 1} \cdot \left\langle \frac{p_z}{p_c} \cdot \left\{ k_1 + \frac{1+k_1}{k_2} \cdot \left[ 1 - \left( \frac{\varepsilon}{1+k_1} \right)^{-k_2} \right] \right\} - \frac{1-\varepsilon^{-n_1}}{n_1-1} \right\rangle - \left( a + \frac{b \cdot n \cdot S}{30} \right) \right]}, \quad (28)$$

The formula (28) allows determining the specific fuel consumption at the two typical engine duties – the rated duty and the maximum torque duty. For calculating the specific fuel consumption at other load and revolution duties of the engine, the method of calculation based on the empirical equation can be used:

$$g_{ex} = g_{enom} \left[ D - E \frac{n_x}{n_{nom}} + G \left( \frac{n_x}{n_{nom}} \right)^2 \right], \quad (29)$$

where  $D, E, G$  – empirical coefficients that depend on the type of engine and the fuel type.

The hourly fuel flow rate (Heywood, 1988; Merker et al., 2012a,b):

$$G_f = g_e \cdot N_e \cdot 10^{-3} \quad (30)$$

Thereby, the equations (21–25, 28–30) represent a mathematical model for the calculation of the external control characteristic, the analysis of which allows evaluating the operating efficiency of the engine, while the indices  $\rho_f, p_c, p_z, \varphi_z, \beta_z$ , and the coefficients  $A, B, C, D, E, G$  vary depending on the type of fuel and have an effect on the performance parameters  $N_e, M_e, g_e, G_f$ .

In order to determine the parameters  $p_c, p_z, \varphi_z, \beta_z$ , it is necessary to take under consideration the work processes in the engine cylinder, in particular, the combustion process.

The pressure in the engine cylinder during the compression process changes according to the polytropy relation:

$$p = p_a \cdot \left( \frac{V_a}{V_x} \right)^{n_1}, \quad (31)$$

where  $p_a$  – pressure at the end of the intake [MPa], which in case of the 4Ч11,0/12,5 engine, i.e. a naturally aspirated engine, is determined as the following difference:

$$p_a = p_0 - \Delta p_a, \quad (32)$$

where  $p_0$  – atmosphere pressure [MPa];  $\Delta p_a$  – loss of pressure at intake due to intake system resistance and decrease of the charge velocity in the cylinder [MPa], which with some allowance can be determined from the Bernoulli equation:

$$\Delta p_a = (\beta_{in}^2 + \xi_{in}) \cdot \left( \frac{\omega_{in}^2}{2} \right) \cdot \rho_0 \cdot 10^{-6} \quad (33)$$

where  $\beta_{in}$  – coefficient of charge velocity decrease in the cylinder cross-section under consideration;  $\xi_{in}$  – coefficient of the intake system's resistance referred to its narrowest cross-section;  $\omega_{in}$  – mean charge velocity at the smallest cross-section of the intake system [ $\text{m s}^{-1}$ ];  $p_0$  – density of the charge at the inlet (in case of a naturally aspirated engine – density of the atmospheric air) [ $\text{kg m}^{-3}$ ].

The  $\omega_{in}$  velocity can be found using the formula:

$$\omega_{in} = n \cdot \frac{r \cdot \pi^2 \cdot D^2}{120 \cdot f_{in}} \cdot \sqrt{1 + \alpha^2}. \quad (34)$$

where  $f_{in}$  – area of the smallest cross-section in the intake system, which corresponds to the area of the passage section between the valve's head and seat and is determined with the use of the formula:

$$f_{in} = \pi \cdot h_v \cdot (d_n \cdot \cos \alpha_v + h_v \cdot \alpha_v \cdot \cos^2 \alpha_v), \quad (35)$$

where  $h_v$  – intake valve stroke [m];  $d_n$  – intake port throat diameter [m];  $\alpha_v$  – valve seat angle [rad].

The density of the atmospheric air depends on the absolute temperature  $T_0$  [K] and pressure  $p_0$  [MPa] of the ambient air and is found from the known formula (Heywood, 1988):

$$\rho_0 = p_0 \cdot 10^6 / (R_a \cdot T_0) \quad (36)$$

where  $R_a$  – specific gas constant of air [ $\text{J (kg} \cdot \text{K)}^{-1}$ ].

On the other hand, there is a formula for the density of the air charge fed into the cylinder obtained in the technique by Pyadichev (1989):

$$\rho_a = \frac{1.29}{1 + 3.665 \cdot 10^{-3} \cdot (T_a - 273)} \quad (37)$$

where  $\rho_a$  – air density [ $\text{kg m}^{-3}$ ] and  $T_a$  – air temperature [K] at the end of the intake stroke (point  $a$  of the indicator diagram of the engine).

The formula (37) is of practical interest, since it requires changing only one parameter, i.e. the temperature  $T_a$ , to determine the density of the charge.



In the authors' opinion, the formula (37) can be used for determining the charge density at the beginning of the intake, i.e. the atmospheric air density, if the temperature  $T_a$  is replaced with the temperature  $T_0$ . In order to verify the suggested replacement, it is necessary to check the relation between the formulae (36) and (37).

First, the temperature  $T_0$  in the formula (36) is substituted by the following expression:

$$T_0 = 273.15 + \Delta T_0, \quad (38)$$

where 273.15 – Kelvin scale temperature equal to 0 centigrade;  $\Delta T_0$  – difference between the ambient temperature and zero centigrade [ $^{\circ}\text{C}$ ].

After the values of the pressure and the gas constant of the air corresponding to normal atmospheric conditions, i.e.  $p_0 = 0.101325$  MPa,  $R_a = 287$  J (kg·K) $^{-1}$ , are substituted into the formula (36) and the expression (38) is taken into account, the following is obtained:

$$\rho_0 = \frac{p_0 \cdot 10^6}{R_a \cdot T_0} = \frac{0.101325 \cdot 10^6}{287 \cdot (273.15 + \Delta T_0)} = \frac{353.05}{273.15 + \Delta T_0}. \quad (39)$$

After factoring the coefficient 273.15 out from the denominator of the formula (39), the following expression is arrived at:

$$\rho_0 = \frac{p_0 \cdot 10^6}{R_a \cdot T_0} = \frac{1.2925}{1 + \frac{\Delta T_0}{273.15}} = \frac{1.2925}{1 + 3.661 \cdot 10^{-3} \cdot \Delta T_0}. \quad (40)$$

In the formula (40), the coefficient 1.2925 represents the density value  $\rho_0$  [kg m $^{-3}$ ] at 0  $^{\circ}\text{C}$ , the coefficient  $3.661 \cdot 10^{-3}$  K $^{-1}$  is a quantity per degree of absolute temperature (the difference that takes account of the effect the temperature variation by one degree has on the air density).

Hence, the known formula (36) and the formula (37) proposed by Pyadichev (1989) can be equated and written in the following form:

$$\rho_0 = \frac{p_0 \cdot 10^6}{R_a \cdot T_0} = \frac{1.2925}{1 + 3.661 \cdot 10^{-3} \cdot (T_0 - 273.15)}. \quad (41)$$

The obtained formula takes into account the effect of the ambient temperature on the air density, but it leaves out of account the effect of the atmospheric air pressure on it. For that reason, the authors suggest improving the formula (41) by means of introducing the coefficients that take into consideration the deviation of the atmospheric pressure from its value (101,325 Pa) that corresponds to the normal (standard) atmospheric conditions:

$$\rho_0 = \frac{1.2925 \cdot [1 + 9.869233 \cdot (p_0 - 1.01325 \cdot 10^{-1})]}{1 + 3.661 \cdot 10^{-3} \cdot (T_0 - 273.15)}, \quad (42)$$

where 9.869233 MPa $^{-1}$  – quantity per MPa of the atmospheric pressure at normal conditions;  $p_0 - 1.01325 \cdot 10^{-1} = \Delta p$  (the pressure difference that takes account of the effect the deviation of the pressure from its normal value has on the air density).

Thus, the formula (42) can be used for the practical calculation of the intake charge density for a naturally aspirated diesel engine taking into account the effect of the ambient air pressure and temperature on it, which in its turn has effect on the performance parameters of the engine.

Hence, through the use of the formulae (31–35), (42), it becomes possible to model the polytropic curve of compression of the engine, which allows analysing the quality of the work process in the engine cylinder. Also, that enables assessing the adequacy of the mathematical model by comparing the modelled and experimental polytropic curves of compression.

The next important process, the parameters of which have effect on the performance indices of the engine, is the combustion process.

The authors suggest modelling the variation of the pressure during the working medium expansion as a result of combustion with the use of the relation proposed by Pyadichev (1989):

$$p = \frac{V_{\beta} \cdot R \cdot T \cdot 10^{-3}}{V_x}, \quad (43)$$

where  $V_{\beta}$  – current volume of the working medium [mol];  $R$  – absolute gas constant,  $R = 8.314 \text{ kJ (kmol} \cdot \text{K)}^{-1}$ ;  $T$  – temperature of the gases in the cylinder [K].

The current volume of the working medium has to be determined taking into account the quantity of moles of the intake charge and the molecular change of the working medium (Merker et al., 2012b):

$$V_{\beta} = M_a \cdot \left( 1 + \frac{m_H \cdot x}{19.04 \cdot \lambda \cdot \left( n_C + \frac{m_H}{4} \right)} \right) \quad (44)$$

where  $M_a$  – quantity of air charge [mol] at the end of the intake stroke;  $m_H$ ,  $n_C$  – quantities of the hydrogen and carbon molecules in the fuel, respectively;  $x$  – fraction of the fuel burnt out in the combustion process;  $\lambda$  – excess air factor.

The quantity of air charge  $M_a$  is determined with the use of the formula:

$$M_a = M_1 \cdot (1 + \gamma_r) \quad (45)$$

where  $M_1$  – quantity of intake air charge [mol] fed into the cylinder;  $\gamma_r$  – coefficient of residual gas.

The quantity of air intake charge fed into the cylinder can be found with the use of the formula:

$$M_1 = \frac{V_h \cdot \eta_v \cdot \rho_o}{\mu_{mix}}, \quad (46)$$

where  $V_h$  – cylinder displacement;  $\eta_v$  – volumetric efficiency factor;  $\mu_{mix}$  – current molecular mass of the gas mixture, which changes as a result of combustion of the fuel.

The formulae (44–46) can be used to refine the formula by Pyadichev (1989) for determining the current volume of the working medium used in the operating duty cycle:

$$V_{\beta} = \frac{V_h \cdot \eta_v \cdot \rho_o}{\mu_{mix}} \cdot (1 + \gamma_r) \cdot \left( 1 + \frac{m_H \cdot x}{19.04 \cdot \lambda \cdot \left( n_C + \frac{m_H}{4} \right)} \right) \quad (47)$$

The volumetric efficiency factor is found with the use of the formula (Merker et al., 2012b):

$$\eta_v = \varphi_{c.ad} \cdot \frac{\varepsilon}{\varepsilon - 1} \cdot \frac{p_a}{p_0} \cdot \left( 1 - \frac{\varphi_c}{\varepsilon \cdot \varphi_{c.ad}} \cdot \frac{p_r}{p_a} \right) \cdot \frac{T_0}{T_0 + \Delta T} \quad (48)$$

where  $\varphi_{c.ad}$  – coefficient of the additional charging of the cylinder due to the valve overlapping;  $\varphi_c$  – coefficient of cylinder purging;  $p_r$  – residual gas pressure [MPa];  $\Delta T$  – temperature of air charge preheating at the intake [K].

Coefficient of residual gas (Merker et al., 2012a):

$$\gamma_r = \frac{\varphi_c}{\eta_v \cdot (\varepsilon - 1)} \cdot \frac{p_r}{p_0} \cdot \frac{T_0}{T_r} \quad (49)$$

The current molecular mass of the gas mixture (working medium) in the cylinder can be found using the formula (Pyadichev, 1989):

$$\mu_{cm} = \left[ 44.01 \cdot n_c \cdot x + 9.01 \cdot x \cdot m_H + 32 \cdot \left( n_c + \frac{m_H}{4} \right) \cdot (\lambda - x) + \right. \\ \left. + 105.844 \cdot \lambda \cdot \left( n_c + \frac{m_H}{4} \right) \right] \cdot \left[ 4.76 \cdot \lambda \cdot \left( n_c + \frac{m_H}{4} \right) + \frac{m_H \cdot x}{4} \right]^{-1} \quad (50)$$

The excess air factor is determined with the use of the formula:

$$\lambda = \frac{M_1}{G_{jc} \cdot L_0}, \quad (51)$$

where  $L_0$  – theoretical air quantity needed for the combustion of one kilogramme of fuel.

The quantity of moles of intake air charge can be determined using the following formula:

$$M_1 = \frac{p_0 \cdot \eta_v \cdot V_h \cdot 10^{-3}}{8.314 \cdot T_0}. \quad (52)$$

The next step is to substitute formulae (9, 27, 52,) into (51) with due account for the known stoichiometric relations (Deviatin et al., 2007). Then, introducing the simplification coefficients, the following refined formula for determining the excess air factor is obtained:

$$\lambda = \frac{\pi \cdot D^2 \cdot S \cdot k_3 \cdot (1 - k_4) \cdot \left( 1 - \frac{\varphi_c}{k_3} \cdot \frac{p_r}{p_0 - k_4} \right) \cdot \frac{p_0}{T_0 + \Delta T}}{6.315 \cdot 10^{-9} \cdot V_{jc} \cdot \rho_f \cdot \left( \frac{C}{12} + \frac{H}{4} + \frac{S}{32} - \frac{O}{32} \right) \cdot (\varepsilon - 1)} \quad (53)$$

where  $k_3$ ,  $k_4$  – simplification coefficients representing the product of the coefficient of additional charging by the compression ratio and the effect of the main parameters of the crank-and-rod mechanism, gas distribution mechanism and the ambient air parameters on the process of the cylinder filling, respectively; C, H, S, O – composition of the fuel in unit fractions representing carbon, hydrogen, sulphur and oxygen, respectively.

The coefficients  $k_3$  and  $k_4$  can be determined using the formulae:

$$k_3 = \varphi_{c.ad} \cdot \varepsilon, \quad (54)$$

$$k_4 = \frac{(\beta_{in}^2 + \xi_{in}) \cdot n^2 \cdot S^2 \cdot \pi^2 \cdot D^4 \cdot (1 + \lambda_{cr}^2) \cdot (12,755982 \cdot p_0 + 2,925 \cdot 10^{-1})}{2,4 \cdot 10^5 \cdot h_v^2 \cdot (d_n \cdot \cos \alpha_v + h_v \cdot \alpha_v \cdot \cos^2 \alpha_v)^2 \cdot (7,33 \cdot p_0 \cdot T_0 - 2,19)} \quad (55)$$

Thus, the formulae (43), (47–50), (53–55) make it possible to model the part of the indicator diagram that represents the process of combustion in the engine cylinder.

### Results of experimental and mathematical simulation study

The duration of the laboratory experiment, in which the fuel consumption rate under the rated duty is measured, is usually equal to  $t = 20$  s and can be expressed in cycles with the use of the following formula:

$$n_c = \frac{n}{120} \cdot t \quad (56)$$

After the values at a revolution rate of  $n = 2,200 \text{ min}^{-1}$  are substituted into the formula (56), the following is obtained:

$$n_c = \frac{2,000}{120} \cdot 20 = 366.7 \text{ cycles.}$$

Within that time, the oscillograph records 366 full cycles, i.e. the data for 366 indicator diagrams.

Further, the data obtained from the gas pressure gauge and the CSPS are saved for the consequent processing in the tabular format. The data are processed in the Microsoft Excel electronic spreadsheet environment.

First, the values on the  $x$  scale are converted from the time  $\tau$  into the degrees of turn of the crankshaft  $\varphi$  with the use of the formula:

$$\varphi = 6 \cdot n \cdot \tau. \quad (57)$$

It should be noted that  $\varphi$  varies from 0 to  $720^\circ$ , starting from the zero mark of the crankshaft (the piston of the fourth cylinder is at its TDC, at the end of the exhaust stroke). The zero mark corresponds to the moment when the signal of the CSPS sensor crosses the X-axis in the area of the missing tooth on the balancer pulley. Hence, the variation of the indicator on the axis of abscissae is of the cyclic type.

Thereafter, the signal received from the gas pressure gauge is converted from mV into MPa, using for that purpose the gauging characteristic that was obtained earlier.

The further processing of the experimental data is carried out in accordance with the procedure described in the paper (Johnson & Leone, 1977; Slavinskas et al., 2018). For all the 366 cycles the arithmetical mean values are found and, consequently, a single indicator diagram is obtained, which is cropped leaving only the  $300^\circ$ – $430^\circ$  range, because only the processes of compression and expansion as well as the combustion process are of greater importance for the analysis of the operating duty cycle efficiency.

The next step is to estimate the random error value using for that purpose the root-mean-square deviation  $\sigma_i$ , the variance  $\sigma_i^2$ . Further, the gross errors are excluded from the experimental data by using the method of the maximum and minimum possible measurement values in the sequence under consideration. In case two or more blunders are revealed, the experiment has to be repeated.

As a result, the following indicator diagram for diesel fuel has been obtained (Fig. 3, the solid line).

A similar indicator diagram is presented for the type of engine under consideration in the paper (Johnson & Leone, 1977) which confirms the validity of the authors' experimental study.

After the experiment with diesel fuel is completed, the fuel in the test bed tank is replaced by biodiesel fuel, then the engine is run idle for some time in order to consume the diesel fuel remaining in the fuel supply system and switch to the operation of the engine completely on R SOME. The signs of the complete transition are a certain reduction of the engine operation loudness and the emergence of the specific aroma of the exhaust gas. It has been experimentally established that the time for the complete changeover to the operation with biofuel for the 4Ч11,0/12,5 engine idling at a crankshaft revolution rate of  $n = 1,500 \text{ min}^{-1}$  is equal to 20 min (Ilves et al., 2017).

Then the similar experiment is carried out with the use of R SOME biofuel.

The results of the experiment with the use of biofuel have been processed following the procedure described earlier in the paper.

Having completed the processing procedure, the indicator diagram for biofuel operation has been obtained (Fig. 3, dot line).

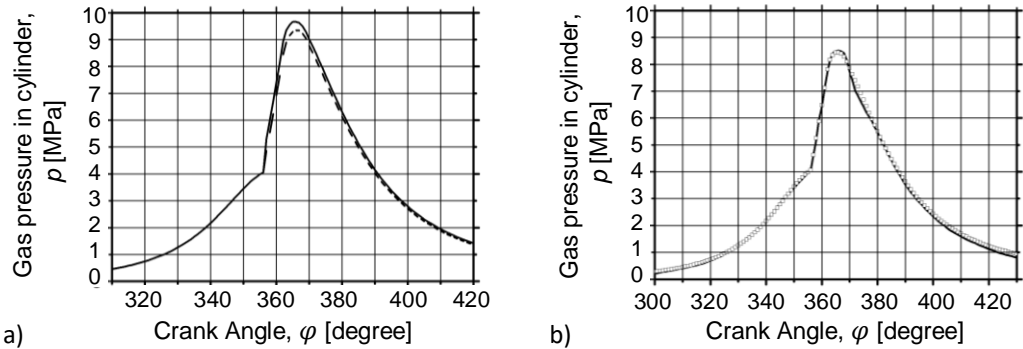


**Figure 3.** Relation between gas pressure in cylinder  $p$  and angular displacement of engine crankshaft  $\varphi$ : a) experimental data for operation with: ———— – diesel fuel; - - - - - biodiesel fuel; b) for operation with diesel fuel: ———— – experimental □□□□ – analytical.

Engine performance parameters are present in Table 2. Differences between the biodiesel power data of model and experimental test is approximately 2.7%. The accuracy is a similar for the all calculated data in Table 2.

**Table 2.** Analysis results of the engine Ч11.0/12.5 pressure diagrams

Indicator	Diesel fuel, model	Diesel fuel, experiment		Biodiesel fuel, model	Biodiesel fuel, experiment
		Special condition ( $p_0 = 0.098 \text{ MPa}$ , $T_0 = 273 \text{ K}$ )	Standard condition ( $p_0 = 0.101 \text{ MPa}$ , $T_0 = 273 \text{ K}$ )		
$N_e$ , kW	49.62	50.61	55.61	50.60	52.01
$p_e$ , MPa	0.57	0.581	0.639	0.581	0.597
$M_e$ , Nm	215.4	219.7	241.4	219.6	225.8
$g_e$ , g (kWh) <sup>-1</sup>	248.0	243.1	245.6	253.3	245.4
$\lambda$	1.61	1.61	1.67	1.79	1.79

The value of the gas temperature in the cylinder is found on the basis of the formula (43):

$$T = \frac{p \cdot V_x \cdot 10^3}{V_\beta \cdot R}. \quad (58)$$

The values of the gas temperature in the cylinder  $T$  obtained by analysing the indicator diagram are substituted into the formula (43) of the mathematical model.

In Fig. 4, the temperature change with diesel and biodiesel fuel is calculated. The temperature of the biodiesel combustion in cylinder is higher as it is with diesel fuel. The results are realistic because the biodiesel combustion is carry out on leaner mixture (relative air/fuel ratio is 1.79).

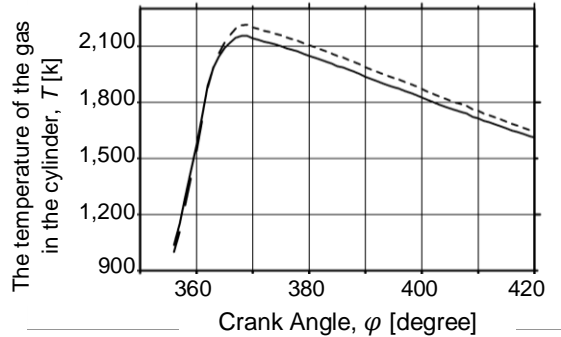


**Figure 4.** Temperature change in engine cylinder depending on crankshaft rotation angle.

Temperatuuri  $T$  muutumise dünaamika mootori silindris olenevalt väntvõlli pöördenurgast  $\varphi$ : ——— – diesel fuel; ■ ■ ■ – biodiesel fuel.

### Opportunities for synthesis of indicator diagram.

In order to determine the amount of the burnt out fuel  $x$ , it is necessary to synthesise the indicator diagram. After synthesising the indicator diagram, the combustion curve  $x = f(\varphi)$  can be obtained.

For synthesising the indicator diagram, the equation (Merker et al., 2012a) can be used:

$$dQ = G_{fc} \cdot Q_H \cdot \frac{dx}{d\varphi} d\varphi - \delta Q_w \quad (59)$$

where  $dQ$  – elementary quantity of heat supplied to the working medium in the cylinder [J];  $Q_H$  – lower calorific value [ $\text{J kg}^{-1}$ ];  $\frac{dx}{d\varphi}$  – combustion rate [ $\text{deg}^{-1}$ ];  $d\varphi = 6 \cdot n \cdot d\tau$  – increment of the angular displacement of the crankshaft in a time of  $d\tau$ ;  $\delta Q_w$  – elementary quantity of heat transferred from the working medium into the cylinder wall [J]:

$$\delta Q_w = \alpha_T \cdot F \cdot (T - T_{cm}) \cdot d\tau, \quad (60)$$

where  $\alpha_T$  – heat-transfer coefficient;  $F$  – cylinder bore area;  $T_{cm}$  – cylinder wall temperature.

The obtained equation represents the differential of the quantity of heat removed into the cylinder wall with respect to time, i.e. the rate of the energy loss due to the transfer of heat from the gas to the wall.

The energy loss rate can be transformed into the function of the crankshaft rotation angle (Heywood, 1988):

$$dQ_w = \frac{\alpha_T \cdot F \cdot (T - T_{cm})}{6 \cdot n} \cdot d\varphi, \quad (61)$$

Taking into account the (61), the equation (59) can be written in the differential form:

$$dQ = G_{fc} \cdot Q_H \cdot dx - dQ_w, \quad (62)$$

On the basis of the obtained equation (62), the burnt out fuel amount differential  $dx$  can be expressed as follows:

$$dx = \frac{dQ + dQ_w}{G_{fc} \cdot Q_H}. \quad (63)$$

$dQ$  can be found using the first law of thermodynamics (Merker et al., 2012a):

$$dQ = p \cdot dV + dU, \quad (64)$$

where  $p \cdot dV$  – work for changing the volume [J];  $c$  [J].

In order to determine the elementary volume  $dV$  in the formula (64), the following property of differentials in approximate analysis can be applied:

$$dV = \Delta V = V - V_0, \quad (65)$$

where  $V - V_0$  – increment of the cylinder volume function, which is determined by the formula (16) for an arbitrary point on the indicator diagram in relation to the crankshaft's angular displacement  $\varphi$ .

The change of internal energy  $dU$  can be determined by the formula (Romanov, 2010; Semyonov & Ryaboshapka, 2013):

$$dU = \frac{d(mC_{vm} \cdot p \cdot V)}{8314}, \quad (66)$$

where  $mC_{vm}$  – average heat capacity of the working medium at a constant volume [ $\text{kJ kg}^{-1} \cdot \text{K}^{-1}$ ], which is represented by the following linear function in the paper (Romanov, 2010):

$$(mC_{vm})_{t_0}^t = a_1'' + b'' \cdot (t - t_1), \quad (67)$$

where  $t$  and  $t_1$  – current and minimum values of the final temperature °C of the combustion gases in the work process under consideration; the coefficients  $a_1''$  and  $b''$  for an interval of the final temperatures  $(t_1 - t_2)$  of the combustion gases in the internal combustion engine are determined with the use of the following expressions for  $\lambda \geq 1$ :

$$\begin{cases} a_1'' = (mC_{vm})_{t_0, (\lambda=1)}^t - \left[ \frac{(mC_{vm})_{t_0, (\lambda=1)}^{t_1} - (mC_{vm})_{t_0, (\lambda_{\max})}^{t_1}}{\lambda_{\max} - 1} \right] \cdot (\lambda - 1); \\ a_2'' = (mC_{vm})_{t_0, (\lambda=1)}^t - \left[ \frac{(mC_{vm})_{t_0, (\lambda=1)}^{t_2} - (mC_{vm})_{t_0, (\lambda_{\max})}^{t_2}}{\lambda_{\max} - 1} \right] \cdot (\lambda - 1); \end{cases} \quad (68)$$

The values for the fraction of burnt out fuel  $x$  in the formulae (47), (50) for the engine under consideration have been determined with the use of the formulae (59)–(68)

and are presented in the papers (Romanov, 2010; Semyonov & Ryaboshapka, 2013) in the form of fuel combustion (heat generation) characteristic curves.

In Fig. 3, two indicator diagrams are shown: 1) experimentally obtained indicator diagram of the 4Q11,0/12,5 engine presented in the paper (Romanov, 2010) (solid line) and 2) indicator diagram calculated with the use of the mathematical model under consideration (marker line).

As is seen from the figure, the mathematical model provides a close approximation of the experimental indicator diagram by the calculated one. Therefore, the described model can be considered adequate and used for modelling the work process in the 4Q11,0 / 12,5 engine cylinder.

By analysing the indicator diagram (Fig. 3), it is possible to obtain the parameters  $p_c$ ,  $p_z$ ,  $\varphi_z$ ,  $\beta_z$ , which specify the course of the work process in the engine cylinder and determine the work of the working medium done in one cycle. Hence, these parameters have effect also on the operating efficiency of the engine. As the operating efficiency of the engine is laid down already at the stage of its design calculation and engineering, all the parameters involved in the discussed mathematical model (parameters of design, duty etc.) can be assumed as not depending on the technical condition of the engine, but corresponding to the performance data specified by the manufacturer. Subsequently, it would be reasonable to suggest that in case of using bio-diesel fuel, the parameters that depend on the fuel properties change and, accordingly, the operating efficiency of the engine also changes.

In view of the aforesaid, it is reasonable to consider the problem of determining the efficiency of the engine from the point of view of determining the efficiency of the fuel utilisation, that is, the statement of problem becomes as follows: how does the operating efficiency of the engine change, when the type of fuel changes?

The formula (28) of the mathematical model refers to the efficient performance indices, the formula (53) refers to the performance of the engine's operating duty cycle, while the parameters  $C$ ,  $H$ ,  $S$ ,  $O$  and  $\rho_f$  vary depending on the type of fuel.

## CONCLUSIONS

1. A mathematical model that allows to determine the engine's efficient performance indices and operating duty cycle performance and to estimate the efficiency of its operation and the efficiency of fuel utilisation, including the use of bio-diesel fuel, has been developed.

2. The formula for the calculation of fresh air charge density introduced by Pyadichev (1989) has been refined and applied for determining the density of the atmospheric air fed into the engine cylinder. The refined formula (42) is suitable for practical calculations, since it takes into account the temperature and pressure of the ambient air and their effect on the air density and, consequently, on the engine's power output in case of deviation from standard conditions.

3. The formula for the calculation of the excess air factor has been refined. The refined formula (53) takes into account the design parameters of the crank-and-rod mechanism and the gas distribution mechanism, the ambient air parameters etc., which have effect on the process of the cylinder filling, the composition of the fuel and its density and cyclic injection rate.



4. The formula for the calculation of the effective power of the engine at its rated duty based on the well-known Grinevetsky – Mazing equation for determining the work in the composite Diesel cycle has been refined. The refined formula (23) takes into account the kinematic parameters of the crank-and-rod mechanism as well as the parameters of the diesel engine operating duty cycle.

5. The formula for the calculation of the effective specific fuel consumption, which allows to evaluate the operating efficiency of the engine taking into account the type of the fuel, has been refined. The refined formula (28) takes into account the density and cyclic injection rate of the fuel, which provides for estimating the efficiency of operating the engine on biomass fuel.

6. The analysis of the indicator diagrams (Fig. 3) has proved that the mathematical model provides close agreement between the calculated data and the results of the experiments. The difference between the experimentally obtained and calculated values of the parameters is equal to: for  $p_c - 0.1\%$ , for  $p_z - 0.77\%$ , which makes reasonable using the mathematical model under consideration for the comparative calculation of the operating duty cycle parameters of the engine run on diesel and bio-diesel fuels.

7. Thus, the obtained mathematical model allows obtaining the values of the effective parameters of operation of the engine with a sufficient degree of accuracy and evaluating the efficiency of use of bio-diesel fuel by means of calculation and analysis.

## REFERENCES

- Alcan, G., Aran, V., Unel, M., Yilmaz, M., Gurel, C. & Koprubasi, K. 2020. Optimization-Oriented High Fidelity NFIR Models for Estimating Indicated Torque in Diesel Engines. *International Journal of Automotive Technology* **21**(3), 729–737.
- Apostolakou, A.A., Kookos, I.K., Marazioti, C. & Anglopoulos, K.C. 2009. Techno-economic analysis of a biodiesel production process from vegetable oils. *Fuel Processing Technology* **90**(7–8), 1023–1031. doi: 10.1016/j.fuproc.2009.04.017
- Baranauskas, R., Ilves, R., Küüt, A. & Olt, J. 2015. Influence of the biodiesel fuels with multifunctional additives on the diesel engine efficiency. *7th International Scientific Conference Rural Development 2015: Towards the Transfer of Knowledge, Innovations and Social Progress. Rural Development*, 6 pp. doi: 10.15544/RD.2015.018
- Choi S-H, Oh Y. 2006. The emission effects by the use of biodiesel fuel. *Int. J. Mod. Phys. B*, **20**, 4481–4486.
- Deviatin, S.N., Markov, V.A. & Semenov, V.G. 2007. *Vegetable oils and biofuels for diesel engines*. Novoe Selo, Harkov, 452 pp. (in Ukrainian).
- Ghobadian, B., Najafi, G. & Nayeibi, M. 2013. A semi-empirical model to predict diesel engine combustion parameter. *Journal of Mechanical Engineering and Sciences (JMES)* **4**, 373–382.
- Ilves, R., Küüt, A., Küüt, K. & Olt, J. 2017. Impact of multifunctional biodiesel fuel additive on diesel engine combustion process. *Engineering for Rural Development*, 369–377.
- Ilves, R., Küüt, A. & Olt, J. 2019. Ethanol as Internal Combustion Engine Fuel. In: Angelo Basile Adolfo Iulianelli Francesco Dalena T. Nejat Veziroglu (Editors/Abbr). *Ethanol*, 1st Edition. *Science and Engineering*. Elsevier, 215–229.
- Ismail, H.M., Ng. H.K., Gan S., Lucchini, T. & Onorati, A. 2013. Development of a reduced biodiesel combustion kinetics mechanism for CFD modelling of a light-duty diesel engine, *Fuel* **106**, 388–400.
- Johnson, N.L. & Leone, F.C. 1977. *Statistics and experimental design in engineering and sciences*. II ed., John Wiley & Sons, New York, London, Sydney, Toronto, 520 pp.

- Heywood, J.B. 1988. *Internal combustion engine fundamentals*. New York: McGraw-Hill, 930 pp.
- Hazar, H. 2009. Effects of biodiesel on a low heat loss diesel engine. *Renewable Energy* **34**(6), 1533–1537. doi: 10.1016/j.renene.2008.11.008
- Kaplan, C, Arslan, R. & Sürmen, A. 2006. Performance characteristics of sunflower methyl esters as biodiesel. *Energ Source Part A* **28**, 751–5.
- Komakha, V.P. & Ryaboshapka, V.B. 2016. Study on relation between effective engine indices and traction performance of tractor using bio-diesel fuel based on consideration of traction-and-power balance. *Technology, Energy Performance, Transport in Industrial Agriculture* **3**(95), Vinnitsa, 193–198.
- Küüt, A., Ilves, R., Hönig, V., Vlasov, A. & Olt, J. 2015. The impact of bioethanol on two-stroke engine work details and exhaust emission. *Agronomy Research* **13**(5), 1241–1252.
- Lejre, K.H.L., Glarborg, P., Christensen, H., Mayer, S. & Kiil, S. 2020. Experimental investigation and mathematical modeling of the reaction between SO<sub>2</sub>(g) and CaCO<sub>3</sub>(s)-containing micelles in lube oil for large two-stroke marine diesel engines. *Chemical Engineering Journal* **388**, art. no. 124188.
- Maawa, W.N., Mamat, R., Najafi G. & Goey L.P.H. De. 2020. Performance, combustion, and emission characteristics of a CI engine fueled with emulsified diesel-biodiesel blends at different water contents. *Fuel* **267**, 117265.
- Merker, G.P., Schwarz, C. & Teichmann, R. 2012a. *Grundlagen Verbrennungsmotoren. Funktionsweise, Simulation, Messtechnik*. (ATZ/MTZ-Fachbuch) 6., ergänzte Ausgabe. Wieweg + Teubner Verlag / Springer, 796 pp.
- Merker, G.P., Schwarz, C. & Teichmann, R. 2012b. *Combustion Engines Development. Mixture Formation, Combustion, Emissions and Simulation*. Springer-Verlag Berlin Heidelberg, 642 pp. doi:10.1007/978-3-642-14094-5
- Mikita, V., Roots, J. & Olt, J. 2012. Simulation model of the combustion processes of a diesel engine. *Agronomy Research* **10**(1), 157–166.
- Naitoh, K., Kuwahara, K., Jeschke, M. & Krause, E., 1992. Numerical simulation of the small vortices in the intake and compression processes of an engine. *JSME International Journal, Series 2: Fluids Engineering, Heat Transfer, Power, Combustion; Thermophysical Properties*, **35**(4), 549–558. doi: 10.1299/jsmeb1988.35.4\_549
- Olt, J., Mikita, V., Roots, J. & Jasinskas, A. 2015. Cylinder pressure characteristics of turbocharged and naturally aspirated diesel engines. *Procedia Engineering* **100**, 350–359. doi: 10.1016/j.proeng.2015.01.378
- Osetrov, A.A. 2005. *Improvement of technical and economic indices of 4 CH 12/14 diesel engine run on biofuels*. Thesis for the degree of Candidate of Technical Sciences, Kharkov: NTU ‘KhPI’, 190 pp.
- Ozsezen, A.N., Canakci, M., Turkcan, A. & Sayin, C. 2009. Performance and combustion characteristics of a DI diesel engine fueled with waste palm oil and canola oil methyl esters. *Fuel* **88**(4), 629–36. doi: 10.1016/j.fuel.2008.09.023
- Özgünay, H.C., Olak, S., Zengin, G., Sari, Ö., Sarikahya, H. & Yüceer, L. 2007. Performance and emission study of biodiesel from leather industry pre-fleshings. *Waste Management* **27**, 1897–1901. doi: 10.1016/j.wasman.2006.08.014
- Pyadichev, E.V. 1989. Methods of calculation of theoretical cycles and processing of indicator diagrams. *Engine Engineering* **7**, Leningrad: TADI, pp. 19–25.
- Ra, Y. & Reitz, R.D. 2011. A combustion model for IC engine combustion simulations with multi-component fuels. *Combustion and Flame* **158**(1), 69–90.
- Raheman, H. & Phadatare, A.G. 2004. Diesel engine emissions and performance from blends of karanja methyl ester and diesel. *Biomass and Bioenergy* **27**, 393–397. doi: 10.1016/j.biombioe.2004.03.002

- Reyes, J.F. & Sepúlveda, M.A. 2006. PM-10 emissions and power of a diesel engine fueled with crude and refined biodiesel from salmon oil. *Fuel* **85**, 1714–1719.
- Romanov, S.A. 2010. Study on work process of 4Ч11,0/12,5 diesel engine run on methanol-fuel emulsion: *Abstract of Thesis for the degree of Candidate of Technical Sciences*. St.-Petersburg, 19 pp.
- Semyonov, V.G. & Ryaboshapka, V.B. 2013. Application of I.I. Vibe model for modelling and approximation of combustion process in 4Ч11,0/12,5 diesel engine. *Collection of scientific papers for XVII<sup>th</sup> International Conference “Raising the resource utilization efficiency in the production of agricultural goods – new technologies and new generation equipment for crop and animal production industries”*. Tambov: GNU VNIITiN of Russian Academy of Agricultural Sciences, 175–180.
- Shabir, M.F., Prasath, B.R. & Tamilporai, P. 2014. Analysis of combustion performance and emission of extended expansion cycle and iegr for low heat rejection turbocharged direct injection diesel engines. *Thermal Science* **18**(1), 129–142. doi: 10.2298/TSCI130707012S
- Slavinskas, S., Labeckas, G. & Mickevicius, T. 2018. Experimental study on injection characteristics of diesel and biodiesel fuel blends with common rail injection system. *17th International Scientific Conference for Rural Development*. Jelgava, 2134–2140. doi: 10.22616/ERDev2018.17.N504
- Xue, J., Grift, T.E. & Hansen, A.C. 2011. Effect of biodiesel on engine performances and emissions. *Renewable and Sustainable Energy Reviews* **15**(2), 1098–1116.
- Zhou, R.-P., Wang, M.-S., Zhu, J.-F. & Gong, J. 2015. Optimization method for dynamic matching of diesel engine silicone oil damper based on genetic algorithm. *Neiranji Gongcheng/Chinese Internal Combustion Engine Engineering* **36**(2), 68–74. doi: 10.13949/j.cnki.nrjgc.2015.02.012
- Ulusoy, Y., Tekin, Y., Çetinkaya, M. & Kapaosmanoğlu, F. 2004. The engine tests of biodiesel from used frying oil. *Energy Sources* **26**(10), 927–932. doi: 10.1080/00908310490473219
- Utlü, Z. & Koçak, M.S. 2008. The effect of biodiesel fuel obtained from waste frying oil on direct injection diesel engine performance and exhaust emissions. *Renewable Energy* **33**(8), 1936–1941. doi: 10.1016/j.renene.2007.10.006

## Recognition of retroreflective traffic signs by a vehicle camera system

M. Khrapova<sup>1,\*</sup>, M. Ružička<sup>1</sup> and V. Trnka<sup>2</sup>

<sup>1</sup>Czech University of Life Sciences Prague (CULS), Faculty of Engineering, Department of Vehicles and Ground Transport, Kamýcká 129, CZ165 00 Prague, Czech Republic

<sup>2</sup>ŠKODA AUTO a.s., tř. Václava Klementa 869, Mladá Boleslav II, CZ293 01 Mladá Boleslav, Czech Republic

\*Correspondence: khrapova@tf.czu.cz

**Abstract.** The systems of traffic sign recognition are based on the evaluation of three components of every sign: shape, colour and pictogram. There are different factors that can have an influence on the efficiency of detection and recognition of these components. One of the most important factors is the quality of the retroreflective sign surface. Retroreflective sheeting improves the readability of colour and pictogram of traffic sign by increasing brightness of its background and/or legend elements. The aim of the paper is to provide a comprehensive survey of the efficiency of sign's recognition by a modern vehicle camera system. The traffic sign sheeting was measured by the handled retroreflectometer. Then this measurement was repeated by the modern camera system used for recognition of traffic signs in the vehicle. The results of this paper present the analysis of the recognition efficiency of traffic signs and the overview of other factors that can have a significant impact on sign detection and recognition distance. The results can be used for creation a traffic sign database for learning-based recognition techniques to vehicle camera systems.

**Key words:** ADTF, recognition distance, attributes of the sign, TSDR.

### List of abbreviations:

ADTF	The Automotive Data and Time triggered Framework	$d$	Cohen's $d$
ANOVA	Analysis of variance	$df$	Degree of freedom
C	Internal retroreflective contrast	$N$	Number of samples
$R_A$	Coefficient of retroreflection	$R^2$	Coefficient of determination
RD	Recognition distance	$SD$	Standard deviation
TAS	Travel Assist System	$\mu$	Mean
TSDR	Traffic sign detection and recognition	$\eta_p^2$	Eta squared partial

## INTRODUCTION

### Background and the importance of the study

A fully autonomous vehicle requires determining exact position of the car throughout the whole trip. The GPS navigation system allows car to define its position in the tree-dimension system relative to other road users and elements of infrastructure.

However, it has two main drawbacks – the inaccuracy of determining the location (European GNSS Agency, 2020) and the use of off-line maps. Therefore, any temporary change (such as repair works on the road) is not considered by this system.

TSDR system is one of TAS that allows increasing the safety of driving by using the vehicle camera system in conjunction with navigation systems. Heavy traffic and a large number of signs increase the likelihood that the driver may not notice some important sign. TSDR eliminates this issue by showing important traffic information on the panel desk in the car and it can provide sound signal warning.

Nevertheless, TSDR system has its own limitation based on difficulties of signs recognition. The main problems of identification of traffic signs can be divided into three main groups: outdoor condition (i.e. weather and lighting conditions, presence of obstacles in front of the sign, scene complexity), vehicle camera system (i.e. quality of video source, vibration by a moving vehicle), properties of traffic sign (i.e. location of the sign, damage of sign surface, size, shape and colour) (Ritter et al., 1995; Paclík et al., 2000; Hsu & Huang, 2001; de la Escalera et al., 2003; Fang et al., 2004; Toth, 2012; Wali, 2015).

In terms of research, there is a growing interest in developing efficient and reliable TSDR system (Wali et al., 2019) that allows to increase the accuracy of detection and recognition sign by developing new algorithms and methods to minimize the effect of factors influencing on traffic signs. However, it is worth mentioning, that many researchers tested their algorithms using existing traffic sign databases (i.e. German TSDR Benchmark (Zaklouta & Stanciulescu, 2014; Yin et al., 2015; Zhu et al., 2016; Lim et al., 2017; Khan et al., 2018), Sweden Traffic Signs Dataset (Yin et al., 2015), Chinese Traffic Sign Detection Benchmark (Zhu et al., 2016) Korean Traffic Sign Dataset (Lim et al., 2017; Khan et al., 2018 etc.). These databases of traffic signs scene and images representing them is an essential requirement for improving the TSDR system (Wali, 2015; Wali et al., 2019) because it is used for self-adaptive systems that ‘are able to adapt their behavior at runtime without human intervention’ (Dajsuren & van den Brand, 2019). Nevertheless, the use of such database in research has one significant drawback - they become obsolete. New technologies allow creating pictures of road scenes in better quality and with better expansion than for example in 2013, when the German TSDR Benchmark was created (German Traffic Sign Benchmarks, 2013). In addition, regulations of use of traffic signs were changed. For example, in the Czech Republic during 2015–2016 (The Decree No 294/2015 Coll., 2015, The Decree No 84/2016 Coll., 2016), 15 new signs’ classes were introduced, so a large number of new traffic signs have been installed.

Accordingly, the authors are convinced that the precise knowledge of the sign’s properties and their technical standards and requirements is more useful for training TSDR systems than a prepared large database (Ministry of Transport of the Czech Republic, 2017). Using programmes that simulate traffic signs under various conditions for training TSDR system may become a more effective tool for a future. Moreover, the self-adaptive system needs a huge number of images of real traffic scenes (signing) under various light and weather conditions for teaching of this system. This is a big disadvantage because creating database like this (real road or traffic) scenes is resource intensive.

In a large number of studies the evaluation of the accuracy of the new methods or algorithms was based on determining the percentage of correctly defined signs to the

total number of signs (Vitabile et al., 2001; Fatmehsari et al., 2010; Hechri & Mtibaa, 2012; Laguna et al., 2014; Islam & Raj, 2017; Zhu et al., 2017; Khan et al., 2018). And only a few researchers for an assessment TSDR system used also the recognition speed (Yin et al., 2015), average time needed for recognition (Zaklouta & Stanciulescu, 2014; Gomes et al., 2017). Gao et al. (2006) simulated traffic signs on different distances for testing their method for recognition traffic signs. In this study, the author proposes to use the recognition distance (hereinafter ‘RD’) as a measure of evaluating the effectiveness and performance of the TSDR system. RD – is the distance in which the TSDR system correctly recognises the traffic sign. The longer the distance, the more time has the driver to react, the safer driving. This parameter becomes useful in evaluating the recognition efficiency of warning signs, for which it is especially important to warn the driver as soon as possible of potential danger, obstacle or hazardous conditions.

### Attributes of a traffic sign – a glossary of terms

The main attributes of traffic signs that are discussed and examined in the study are presented in Fig. 1. Traffic signs consist of two basic components:

1. Sign panel (or sign surface) – ‘a separate panel or piece of material containing a word, symbol, and/or arrow legend that is affixed to the face of a sign’ (MUTCD, 2012).
2. Sign post – a post bearing a sign.

The Czech Republic standards (e.g. ČSN EN 12899-1 (2007), TP 65 (2013)) prescribe specific limit values for the following attributes:

1. Position of the sign:
  - Lateral offset – is a distance from the edge of the shoulder of the road to the nearest edge of that sign (Traffic signs, 2008).
  - Vertical clearance – is the height from the lowest edge of the sign plate to the road surface (Traffic signs, 2008).
  - Siting – traffic signs are sited on the right-hand or left-hand sides of the road.

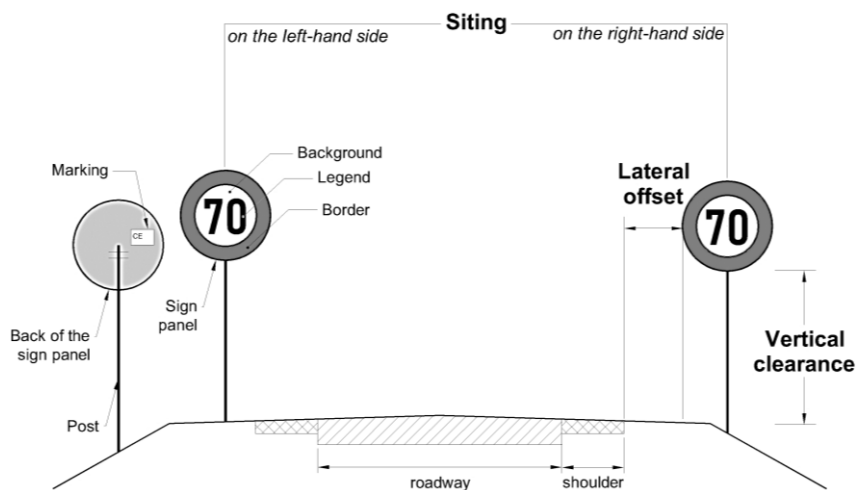


**Figure 1.** The main sign attributes that are discussed in the study. Source: Adopted from TP 65 (2013).

2. Elements of sign surface (MUTCD, 2012):

- Legend – the message on the face of a sign panel (including text, arrows, route markers and special symbols) (Traffic signs, 2008).
- Background – the element of the sign with the largest surface area of the sign.
- Border – the element that is different in colour (material) from the background.

3. Properties of surface elements:

- Coefficient of retroreflection ( $R_A$ ) – is the ratio of light returned versus the light striking a define section of sign surface area (Ré et al., 2010b). The coefficient is expressed in candelas per lux per square meter ( $\text{cd} \cdot \text{lx}^{-1} \cdot \text{m}^{-2}$ ).

The properties of surface elements that has been introduced by authors:

- Area of colour – the proportion of the area occupied by one colour to the total area of the sign, expressed as a percentage.
- Retroreflective contrast between background and border or retroreflective internal contrast (hereinafter ‘Contrast’) was derived using Michelson equation of luminance contrast (1) and definition of  $R_A$  (2).

$$C_M = \frac{L_{\max} - L_{\min}}{L_{\max} + L_{\min}} \quad (1)$$

where  $C_M$  – Michelson luminance contrast (-),  $L_{\min}$  and  $L_{\max}$  – the minimum and maximum luminance of two colours ( $\text{cd} \cdot \text{m}^{-2}$ ).

$$R_A = R_L \cdot \cos\beta = \frac{L \cdot \cos\beta}{E} \quad (2)$$

where  $R_A$  – coefficient of retroreflection of one colour ( $\text{cd} \cdot \text{lx}^{-1} \cdot \text{m}^{-2}$ ),  $R_L$  – coefficient of retroreflected luminance ( $\text{cd} \cdot \text{lx}^{-1} \cdot \text{m}^{-2}$ ),  $\beta$  – is the entrance angle of the light incident on the road sign ( $^\circ$ ),  $L$  – luminance of one colour ( $\text{cd} \cdot \text{m}^{-2}$ ),  $E$  – is the illuminance at the sign plate created by the light source, perpendicular to the direction of illumination ( $\text{lx}$ ).

The retroreflective contrast equation (3) is obtained by substituting Eq. 3 into Eq. 2.

$$\begin{aligned} C &= \frac{\frac{R_{A(B)} \cdot \cos\beta}{E} - \frac{R_{A(BO)} \cdot \cos\beta}{E}}{\frac{R_{A(B)} \cdot \cos\beta}{E} + \frac{R_{A(BO)} \cdot \cos\beta}{E}}; \\ C &= \frac{\frac{\cos\beta}{E} (R_{A(B)} - R_{A(BO)})}{\frac{\cos\beta}{E} (R_{A(B)} + R_{A(BO)})}; \\ C &= \frac{R_{A(B)} - R_{A(BO)^1}}{R_{A(B)} + R_{A(BO)^1}} \end{aligned} \quad (3)$$

where  $C$  – internal retroreflective contrast (-);  $R_{A(B)}$  – coefficient of retroreflection for background ( $\text{cd} \cdot \text{lx}^{-1} \cdot \text{m}^{-2}$ );  $R_{A(BO)}$  – coefficient of retroreflection for border ( $\text{cd} \cdot \text{lx}^{-1} \cdot \text{m}^{-2}$ );  $\beta$  – is the entrance angle of the light incident on the road sign ( $^\circ$ );  $E$  – is the illuminance at the sign plate created by the light source, perpendicular to the direction of illumination ( $\text{lx}$ ); <sup>1</sup> – for the retroreflective sign with legend only  $R_A$  of legend is used.

## Purpose of the Study

The main aim of the study is to assess effectiveness of TSDR and its ability to recognise traffic signs. The effectiveness is evaluated by new parameter suggested by authors - the measure of recognition influenced by of above-mention sign characteristics on distance in which the traffic sign was correctly recognised.

## MATERIALS AND METHODS

The current study is divided into five parts: a selection of the study location, creation a database with the basic signs' characteristics,  $R_A$  measurement of traffic signs, video recording of selected traffic signs by the vehicle camera system and statistical analysis of data.

### Study location

The retroreflective traffic signs alongside of roads in the Czech Republic were chosen for this study. The selected sections of the major arterials ('*silnice I. třídy*') number I/11 and I/35 are represented in Fig. 2. These arterials were deliberately selected because of their recent reconstruction of pavement (the period from 2017 and 2019) which entailed replacement of vertical road traffic signs.

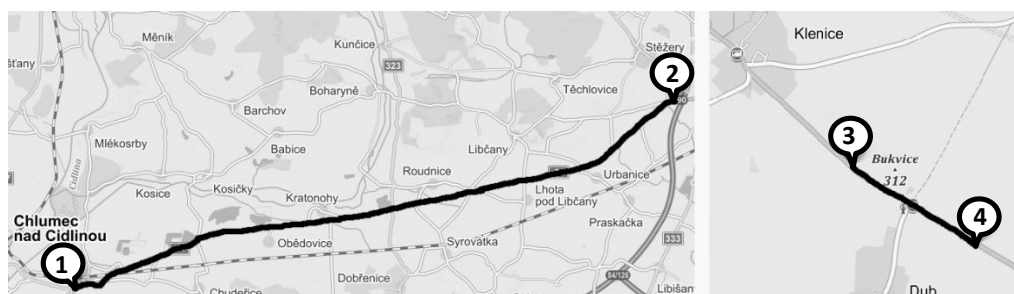


**Figure 2.** The representation of selected road sections of the Czech Republic. (Left) Section of the major arterials number I/11 from Nové Dvory, in the direction of Hradec Králové. (Right) Section of the major arterials number I/35 from Hradec Králové, in the direction of Klenice. Source: (Mapy.cz, 2020).

According to the Czech regulations (TP 65, 2013), the class of retroreflection for all signs should not lower than RA2. It is expected that more than 90% will correspond with TP 65 (2013). All general conditions and requirements of traffic signs' positioning and used materials are described the in part 'INTRODUCTION', subsection 'Attributes of a traffic signs'.

### Creation of an information database

There is not a unified information system for traffic signs in the Czech Republic. A large number of suppliers of reflective films and signs' manufacturers make it impossible to collect information remotely. Consequently, information about each of the signs was collected manually on the site.



The Czech standard ČSN EN 12899-1 (2007) obliges manufacturers to affix a marking containing important information about the road sign on its backside (Fig. 1). This marking provides information about the date when the marking was affixed, visibility properties (class of retroreflective sheeting), durability, the resistance of weathering and etc. Nevertheless, this marking does not contain information about the type of used reflective film that may have a different level of retroreflection within the same class.

Under these circumstances, three photos were taken for each traffic sign: general photo (to determine the category of a sign), photo of marking and a photo of the structure of the reflective film (to determine the type of film). Based on these three photos, an information card was created for each sign, that also includes GPS coordinates, the orientation of the sign, lateral and vertical positioning, the area of colour (Fig. 3). In total 100 such cards were created (Table 1).

The number of all assessed retroreflective traffic signs is represented in Table 1. Traffic signs were divided according to their categories, technology and class of the retroreflective sheeting.

Six main categories of traffic signs have been tested: mandatory; prohibitory; priority; direction, position, or indication signs; information, facilities, or service signs and additional panels (classification according to the Czech law (The Decree No 10/2019 Coll., 2015). The glass bead technology was provided by retroreflective class RA1, the microprismatic technology – by retroreflective classes RA2 and RA3 (Table 1). The classification depends on the mandated minimum  $R_A$  values which increase with the class number (ČSN EN 12899-1, 2007).

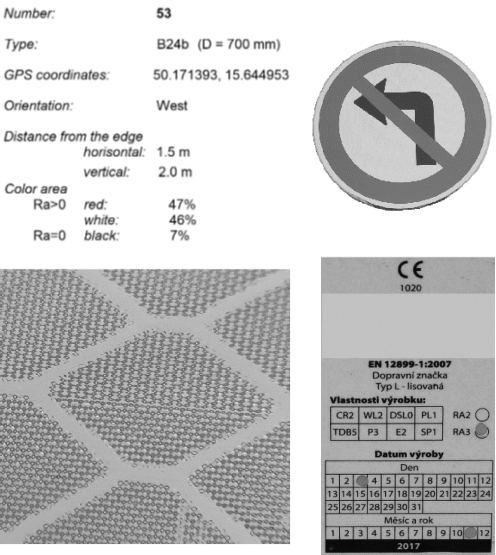


**Figure 3.** An example of an informational card from the created database of a traffic sign. Source: Authors' work.

**Table 1.** Summary of surveyed retroreflective traffic signs according to their category and the class of sheeting

Technology <sup>1</sup>	Class <sup>1</sup>	Number of traffic sign					
		warning	priority	prohib.	inform.	direct.	addit.
Glass Bead	RA1	1	3	9	3	1	3
Microprismatic	RA2	5	11	37	2	3	7
	RA3		4	6			5
Total number of signs		100					

<sup>1</sup> – according to ČSN EN 12899-1 (2007).

As can be seen in Table 1, the majority of traffic signs (80 signs) have retroreflective properties with classes  $R_{A2}$  and  $R_{A3}$ , that means 80% of all signs correspond to the national standard TP 65 (2013) but it is less than it was expected.

### **Measurement of the $R_A$**

The retroreflective level of traffic signs was measured by handled retroreflectometer Zehntner ZRS 6060. The retroreflectometer allows determining  $R_A$  in accordance with the Czech standard ČSN EN 12899-1 (2007), for illumination angle  $5^\circ$  and three observation angles –  $0.2^\circ$ ,  $0.33^\circ$ ,  $2^\circ$ .

The measuring principle with the retroreflectometer to get  $R_A$  value was the same for all measurements. The calibration of the device is necessary condition before the equipment use; then the retroreflectometer is planted on the surface of the traffic sign and the trigger is pulled. The measurement values of  $R_A$  are shown beside each observation on the display. Each measurement also contains information about the colour of the sample, ambient temperature, relative humidity and GPS coordinates. Using the retroreflectometer, three readings of each sign colour were collected.

The data analysis software 'MappingTools' was used to export data from the retroreflectometer and generate measuring reports.

The measurement of the  $R_A$  was done under the same conditions as a video recording by the vehicle camera system. It means they were not cleaned or dried as in the requirements for manufacturers in the Czech standard ČSN EN 12899-1 (2007). This was done specifically in order to get results close to reality.

### **Video recording by the vehicle camera system**

In order to eliminate the influence of ambient temperature and relative humidity (Khrapova, 2019), the recording of traffic signs by TSDR system was made under the same weather conditions and with the same temperature range.

The passenger car equipped with a TSDR system was selected for purpose of this research. The name of the car brand, as the type of installed camera systems, is not provided in this study since this car and research made is topic a commercial product development.

The selected TSDR system uses the monochromatic fixed focus multi-function camera that is mounted on the windscreen in front of the rear-view mirror. The camera scan and detect the traffic signs on the current section of the road. A picture processing module searches the scanned pictures for known traffic signs and compares the results with the Columbus or Amundsen navigation data.

An image processing module inspects the images captured for the speed limit and no-passing signs, some prohibitory signs as well as the signs announcing the end of the respective restriction. The traffic signs are shown as pictograms in the multi-functional display and/or the navigation system display since the validity of the sign. That is mean, the picture of the traffic sign is displayed after the car has passed the install location of the traffic sign.

The current TAS system is aimed at recognizing certain classes and types of traffic signs. The accuracy of recognition is more important than the RD for this system. Nevertheless, the picture processing module allows to detect and recognize a large number of types of road signs. For example, the ADTF development environment enables playback of stored data from camera memory, data processing and visualization.

The accuracy of recognition and RD of traffic signs were determined using the ADTF environment and visualization filters (Fig. 4).



**Figure 4.** The screen view of two visualization filters of ADTF. (Left) Video widget with the filter of recognition all traffic signs. (Right) Coordinate graph for determining RD of the signs. Source: ADTF development environment.

### Data analysis

Given a large number of identified values and traffic sign's characteristics, a summary and grouping of statistical data were carried out. Grouped data allowed to apply descriptive statistics and to test the normality of data. *Kolmogorov–Smirnov* and *Shapiro–Wilk* *W* tests were used to control normality of datasets. The 'STATISTICA' software was used for all kind of statistical tests.

The dispersion analysis was used to present and interpret the variation of the numerical range of RDs. Range, mean, standard deviation, coefficient of variation were calculated.

*T*-test for independent samples was used in order to determine whether there is a statistically significant difference between the means in two unrelated groups of one independent, categorical variable. Using this test was controlled if the positioning of the sign (vertical and lateral) and the number of signs on the post have an influence on the RD.

Main effect *ANOVA* and factorial *ANOVA* were used in the case of two independent variables and one dependent variable (RD). The datasets were controlled for normality and homogeneity of variance (*Levene's* test). Factorial *ANOVA* was used in cases where the interaction between variables was supposed to be high.

For all tests, the null and alternative hypotheses were defined as follows:

$H_0$ : no difference in means of RD between two or more (in the case of *ANOVA*) data sets.

$H_1$ : the average values of RD between two or more (in the case of *ANOVA*) data sets is significantly different.

The null hypothesis for the performed tests can be rejected if the obtained *P*-value is lower than 0.05. In order to control the family-wise error rate and to figure out which impact has considerable influence on the RD, the *Tukey's* honestly significant difference post hoc test was carried out at the significance level of 0.05.

## RESULTS AND DISCUSSION

As part of the establishment of an informational database, it was found 3 signs were recognized, but the RD was not determined by ADRF. These signs were direction road signs and additional panels. The level of retroreflection in 2 cases was significantly higher than the established minimum, 1 sign did not meet the requirements for reflective properties of signs. The above-mentioned signs were removed from subsequent statistical analysis.

There were also 4 road signs were not detected and 3 signs, whose  $R_A$  was below the mandatory minimum retroreflection level. These signs were excluded from the dispersion analysis and  $t$ -tests for independent samples.

### The dispersion analysis

The RD is a dependent variable for all subsequent statistical tests; therefore, it is necessary to understand the variation of the measurements among themselves and around the average value. The main measures of dispersion for 89 variables were found and presented in Table 2.

**Table 2.** The main measures of dispersion analysis for the variable of RD

$N$	$\mu$	Minimum	Maximum	Variance	$SD$	Coefficient of variation
[-]	[m]	[m]	[m]	[m <sup>2</sup> ]	[-]	[%]
89	41.7	13,0	63.0	133.7	11.5	27.6

Table 2 shows that the average RD was  $41.7 \pm 11.5$  m and data extremely varied (coefficient of variation is more than 20%). The high value of the coefficient of variation proves the existence of factors affecting this variable.

### $T$ -test for independent samples

All studied factors can be divided into two groups: properties of the sign's surface and other characteristics of the sign (e.g. the position of the sign in space and the number of signs on the post). In order to determine the influence of factors from the first group, it is necessary to exclude the influence of factors from the second group, i.e. check whether they have a statistically significant effect on the results of recognition of road signs.

The distance from the roadside edge (lateral positioning) to the sign post, location relative to the road (on the left or right side) and the number of signs on the post have been tested using three different  $t$ -test. Different separate tests were carried out because of a different number of samples that were tested. Before carrying out the tests, all variables conformed to the assumptions of normality (*Shapiro–Wilk test*  $W$  test,  $P > 0.05$ ; *Kolmogorov–Smirnov test*,  $P > 0.2$ ).

All signs were divided into two groups according to their lateral positioning (Table 3). According to the Czech standard (TP 65 Principles for traffic signs on communications, 2013), the sign should be located no further than 2 meters from the roadside edge. Thus, all signs were divided into two groups by lateral positioning: signs that correspond to TP 65 and signs that do not correspond to standard.  $T$ -test for independent samples was used to compare RD for signs that correspond or do not correspond with the Czech standard (TP 65, 2013).

**Table 3.** Grouping parameters by three factors that are not characteristics of the sign surface

Distance from roadside edge to post		Location relative to the road		Number of signs on a post	
[m]	group number	[-]	group number	[-]	group number
≤ 2	1	left	1	1	1
>2	2	right	2	2	2

From the results presented in Table 4, it can be concluded that there is no significant difference in RDs, since  $P > 0.05$ .

**Table 4.** The results of T-test for independent samples that are represented the main statistical parameters for three factors

Parameter	<i>p-value</i>	<i>d</i>	<i>t-value</i>	<i>df</i>	Group number 1			Group number 2		
					$\mu$	<i>N</i>	<i>SD</i>	$\mu$	<i>N</i>	<i>SD</i>
Lateral offset	0.06	0.5	1.9	87	45.5	41	4.1	41.3	46	12.3
Siting	0.14	0.6	-1.5	23	50.7	13	8.1	46.2	12	6.6
Number of signs	0.003	0.8	3.1	65	44.7	38	9.8	35.6	28	11.9

The results of the first test are unexpected since presumably the accuracy of detection and recognition traffic signs located far enough from the road might be low. The medians of these two groups do not statistically different from each other but the range of RDs is not similar (Fig. 5). The box plot of Fig. 5 more clearly demonstrates the range of values in two groups.

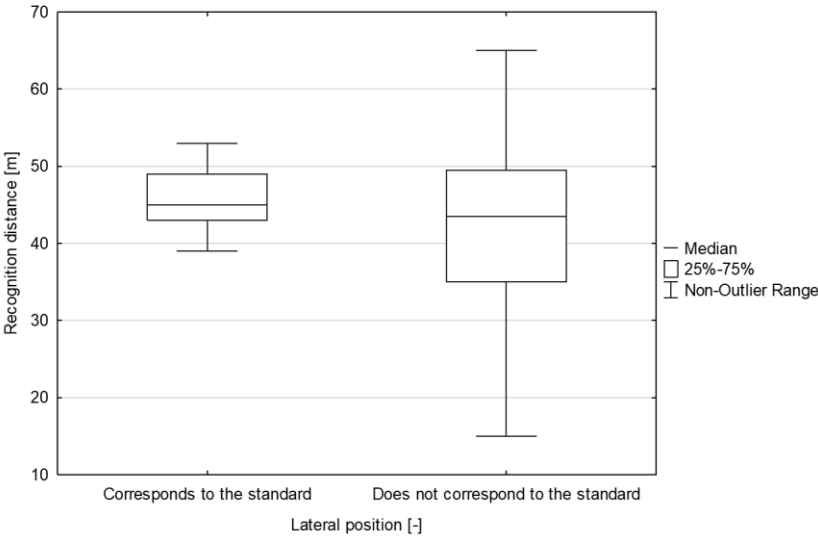


**Figure 5.** The box plot of RDs grouped by lateral position.

The duplication of road signs on the left-hand side of the road is not typical for all categories of signs. In the framework of this work, only the ‘no overtaking’ sign was located both on the right-hand and the left-hand of the road. Therefore, the influence of the location relative to the side of the road was tested only for this type of road sign. The T-test of two independent groups was used in order to determine whether there is a

statistical difference in the RDs between signs on the right-hand and the left-hand of the road. The most important results are shown in Table 4. As can be seen from the table, the  $p$ -value is much higher than the significance level of 0.05 that means there is no difference in means between two examined groups.

The third  $t$ -test was conducted to analyse the influence of the number of signs on their RD. The number of signs on the single support varied on the selected road sections. One, two or three signs were installed on the one post. The number of posts with three of signs was not large enough, that it is why only posts with one sign, or two signs were analysed. The results are also presented in Table 4. Contrary to previous results, the null hypothesis for the performed tests can be rejected because the obtained  $P$ -value is lower than 0.05.

Another additional  $t$ -test was carried out to determine if there is a difference in the level of retroreflection of two road signs located on the same post. The means of  $R_A$  values between two signs were statistical equal ( $367 \pm 110$  m,  $N = 14$  vs,  $317 \pm 70$  m,  $N = 14$ ;  $P = 0.34$ ,  $df = 25$ ,  $d = 0.6$ ).

The decrease in the RDs can be explained by the non-standard reflective area, which is formed due to traffic signs that are closely adjacent to each other and have almost the same retroreflective level. The example of this problem is demonstrated in Fig. 6. A conditional division of the recognition process into 3 stages shows that during the first stage the shape of the sign was determined incorrectly, the same as the code of the sign. In the second stage, the determining area was divided into two and in the third stage, the traffic signs were correctly recognized (correct codes were attached).



**Figure 6.** The problem in recognition of two traffic signs on a post is demonstrated in three steps. Source: Adopted from the ADTF development environment<sup>1</sup>.

Two tests are demonstrated there is no correlation between the RD and the position of the sign relative to a road. The third test revealed a significant impact of the number of traffic signs (on a single post) on the RD.

The effect sizes of all four tests were medium (for first, second and additional tests) and high (for the third test), which gives an indication of sufficiently high reliability of the results.

## ANOVA

The main effect ANOVA was used to determine the influence of properties of sign surface on its RD. The highest  $R_A$  value (in most cases white background sheeting), the

<sup>1</sup> Remark: text edited by authors of paper

area of colour with the highest  $R_A$  and the contrast of the sign have been selected for the analysis.

The signs that were not detected were included in the analysis ( $RD = 0$ ) since their retroreflective level was higher than 0. Also, the signs with the  $R_A$  below maintained retroreflectivity level were taken into account. Despite the discrepancy with Czech standards, these signs (2 directional and 1 prohibitory) were recognized from more than 30 meters.

Only signs that are alone on the post are analysed since the variable of RD is sensitive on the number on the signs on the post and because of the inability to evaluate the individual parameters of the sign when two signs are so close to themselves.

The area of colour was divided into two groups: the value of the area of colour is less or equal to 50% and the value of the area is higher than 50%. The values of contrast were also divided into two groups:  $C \leq 1.0$  and  $C > 1.0$ . The  $R_A$  values were separated into four ranges: 0–150, 151–300, 301–450, 451–600  $\text{cd lx}^{-1} \text{m}^{-2}$ . This grouping allowed to normalize datasets.

All variables conformed to the assumptions of normality (*Shapiro–Wilk test*  $W$  test,  $P > 0.05$ ) and homoscedasticity (*Levene's test*,  $P > 0.05$ ).

The results of multifactorial ANOVA are presented in Table 5.

The test indicated that the variables with the significant effects on the RD were the  $R_A$  and contrast. The size of the area with the highest  $R_A$  of the sign was not found to be statistically significant in the case of the one sign on the post.

The interaction of contrast and  $R_A$  values were controlled by the factorial ANOVA that indicated the considerable effect of this pair of variables on RD (Table 6).

The graphic result of General linear model is shown in Fig. 7. On the plot, there are two non-parallel lines that prove the statistically significant interaction between  $R_A$  and contrast. For the range of  $R_A$  from 0 to 150  $\text{cd lx}^{-1} \text{m}^{-2}$  and  $C \leq 1$  the RD is the lowest and the values are dramatically different from another.

*Tukey's* post hoc test was carried out to understand what combination of factors has considerable influence on the RD. Only above mention, a combination of  $R_A$  values and contrast has a significant effect on the RD.

As can be seen from Fig. 7, the RD increases with the increasing the  $R_A$  values. It was expected that brighter traffic signs (means with high  $R_A$ ) are recognized faster than signs with low  $R_A$  values (less than 150  $\text{cd lx}^{-1} \text{m}^{-2}$ ). An unanticipated development was

**Table 5.** The results of multifactorial main effect ANOVA that are presented as main statistical parameters for such factors of sign surface as area, contrast and coefficient of retroreflection

Factor	<i>Df</i>	<i>F-value</i>	<i>P-value</i>	$\eta_p^2$
Area of colour	1	0.41	0.53	0.01
Contrast	1	15.49	0.00 <sup>1</sup>	0.28
$R_A$	3	7.29	0.00 <sup>1</sup>	0.35
Error	40			

<sup>1</sup> – values lesser than three decimal places after the decimal point was neglected.

**Table 6.** The results of factorial ANOVA that are presented as the main statistical parameters of interaction between contrast and coefficient of retroreflection of sign surface

Factor	<i>Df</i>	<i>F-value</i>	<i>P-value</i>	$\eta_p^2$
Contrast	1	18.57	0.00 <sup>1</sup>	0.33
$R_A$	3	17.89	0.00 <sup>1</sup>	0.459
Contrast x $R_A$	3	5.16	0.00 <sup>1</sup>	0.249
Error	38			

<sup>1</sup> – values lesser than three decimal places after the decimal point was neglected.

that for the traffic signs with the contrast lower than or equal to one with  $R_A$  above  $450 \text{ cd lx}^{-1} \text{ m}^{-2}$  RD decreases. This can be explained by ‘overglow’ effect that was discussed by Schnell et al. (2004) and Batchelor & Sauter (2013).

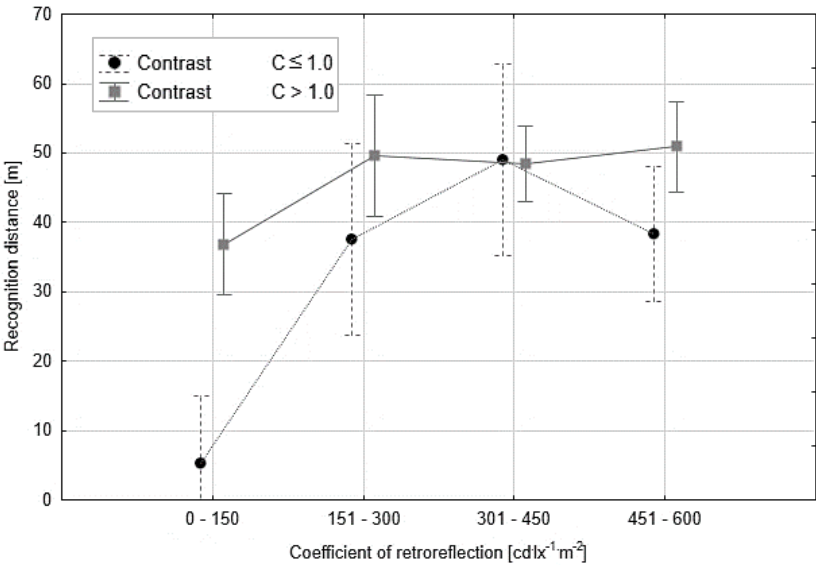


**Figure 7.** The combined effects of contrast and coefficient of retroreflection for the case of one sign on a slope.

In both analysis the highest  $\eta_p^2$  values (35% and 59%) were for  $R_A$  that means the highest retroreflective level is the most important main effect. However, the combination of  $R_A$  and contrast has also significant effect in the RD, since the  $\eta_p^2$  is higher much higher than 14%.

To determine how the coefficient of determination was found.  $R^2$  for main effect ANOVA was 0.75 and for factorial ANOVA is 0.82. That means that the second model better explained the variation of data.

### CONCLUSIONS

The traffic sign database is one of the key points necessary for the training of modern TSDR systems. The lack of public and well-structured databases is a significant obstacle in this area of research. One of the solutions is creating models of sign scenes that are close to real conditions based on knowledge of the laws and characteristics of the traffic signs. Technical regulations determine the limits for the use of road traffic signs that have certain characteristics on a certain type of roads. Knowledge of the influence of sign parameters on RD will predict the effectiveness of the whole TSDR system.

The main goal of this study was to determine which of the parameters or traffic sign characteristics ha a significant impact on the performance of the TSDR system, especially at night, when the number of accidents doubles (National Safety Council, 2018). In this paper, RD was chosen as a parameter for evaluating the effectiveness of



the TSDR system, since it is important not only whether the sign was recognized, but also how long does it take to this system to recognize traffic sign.

Number of exposure years, location relative to the road, orientation, class of retroreflective sheeting and the  $R_A$  were determined for 100 signs. For most of these signs (65%), the average exposure was 3 years, the level of retroreflection was equal to class  $R_{A2}$ , the orientation of the signs was to the West.

During data processing, it was noted that for some signs lateral offset does not correspond to the Czech standards. Unexpectedly, the statistical analysis did not reveal a statistical difference between the signs that do and do not correspond to the standard. There was no statistical difference between the signs on the left-hand side and right-hand side of the road.

On contrary, the number of signs on the post (one or two) has an effect on the RD. Especially if the signs have the same level of retroreflection, thereby forming an atypical area for determination. Based on this, a recommendation for local road agencies can be made: 'For two or more signs on the same post the  $R_A$  of each sign should be different in the way that the value of retroreflective contrast should be more than 1'.

In view of the foregoing, the influence of the coefficient of retroreflection was assessed only for signs located singly on a post. A significant difference was found in the RDs for a group of signs with the highest value of  $R_A$  below  $150 \text{ cd lx}^{-1} \text{ m}^{-2}$  and the internal contrast lower or equal to 1. However, these values indicate that such signs do not meet Czech standards and should be removed by the relevant road authorities.

It is necessary to remark that all unrecognized signs (only 4) were information road signs; their number of exposure years was not determined since there was no corresponding marking on the signs. The retroreflective surface was damaged, presumably from corrosion, and the  $R_A$  was much lower than the minimum level. It can be assumed that these signs were posted before 2004 when the Czech Republic adopted a standard obliging signs' manufacturer to place markings on the sign.

In conclusion, the efficiency of recognition of approved traffic signs (declared by the car manufacturer) was 100%.

The results and conclusion of the paper support the necessity of the further research. The property influence of traffic signs on the efficiency of recognition by TSDR system will play very important role in traffic control and road safety in a future.

**ACKNOWLEDGEMENTS.** The author gratefully acknowledges that the present research was supported by the Internal Grant of Faculty of Engineering, CULS Prague (grant number IGA 2019:31170/1312/3113).

## REFERENCES

- Batchelor, P. & Sauter, G. 2013. Are Traffic Signs too Bright? *Australas. Coll. Road Saf. Conf.* – "A Safe Syst. Road Saf. Discuss. pp. 1–12.
- ČSN EN 12899-1. 2007. 'Fixed, vertical road traffic signs'. (in Czech).
- Dajsuren, Y. & van den Brand, M. 2019. *Automotive Systems and Software Engineering*. Cham: Springer International Publishing. doi:10.1007/978-3-030-12157-0
- De la Escalera, A., Armingol, J.M. & Mata, M. 2003. Traffic sign recognition and analysis for intelligent vehicles. *Image Vis. Comput.* **21**(3), 247–258.
- European GNSS Agency. 2020. <https://www.gsa.europa.eu/>. Accessed 29.12.2019.

- Fang, C.Y., Fuh, C.S., Yen, P.S., Cherng, S. & Chen, S.W. 2004. An automatic road sign recognition system based on a computational model of human recognition processing. *Comput. Vis. Image Underst.*, Libk. **96**, 237–268. doi: 10.1016/j.cviu.2004.02.007
- Fatmehsari, Y.R., Ghahari, A. & Zoroofi, R.A. 2010. Gabor wavelet for road sign detection and recognition using a hybrid classifier. *2010 Int. Conf. Multimed. Comput. Inf. Technol.* pp. 25–28. doi:10.1109/MCIT.2010.5444860
- Gao, X.W., Podladchikova, L., Shaposhnikov, D., Hong, K. & Shevtsova, N. 2006. Recognition of traffic signs based on their colour and shape features extracted using human vision models. *J. Vis. Commun. Image Represent* **17**(4), 675–685.
- German Traffic Sign Benchmarks. 2013. <http://benchmark.ini.rub.de>. Accessed 26.03.2020.
- Gomes, S.L., Rebouças, E. de S., Neto, E.C., Papa, J.P., Albuquerque, V.H.C. d., Rebouças Filho, P.P. & Tavares, J.M.R.S. 2017. Embedded real-time speed limit sign recognition using image processing and machine learning techniques. *Neural Comput. Appl.* **28**(1), 573–584. doi:10.1007/s00521-016-2388-3
- Hechri, A. & Mtibaa, A. 2012. Automatic detection and recognition of road sign for driver assistance system. *2012 16th IEEE Mediterr. Electrotech. Conf.* pp. 888–891.
- Hsu, S.H. & Huang, C.L. 2001. Road sign detection and recognition using matching pursuit method. *Image Vis. Comput.* **19**(3), 119–129. doi:10.1016/S0262-8856(00)00050-0
- Islam, K. & Raj, R. 2017. Real-Time (Vision-Based) Road Sign Recognition Using an Artificial Neural Network. *Sensors* **17**(4), 853. doi:10.3390/s17040853
- Khan, J., Yeo, D. & Shin, H. 2018. New Dark Area Sensitive Tone Mapping for Deep Learning Based Traffic Sign Recognition. *Sensors* **18**(11), 3776. doi:10.3390/s18113776
- Khrapova, M. 2019. Determining the influence of factors on retroreflective properties of traffic signs. *Agron. Res.* **17**(S1), 1041–1052. doi:10.15159/AR.19.082
- Laguna, R., Barrientos, R., Felipe Blázquez, L. & Miguel, L.J. 2014. Traffic sign recognition application based on image processing techniques. *IFAC Proc. Vol.* **47**(3), 104–109.
- Lim, K., Hong, Y., Choi, Y. & Byun, H. 2017. Real-time traffic sign recognition based on a general purpose GPU and deep-learning. *PLoS One* **12**(3). Public Library of Science. doi:10.1371/journal.pone.0173317
- Mapy.cz. 2020. <https://mapy.cz>. Accessed 17.10.2019.
- Ministry of Transport of the Czech Republic. 2017. Action plan for autonomous driving. 51 pp. Available at [http://amsp.cz/wp-content/uploads/2019/02/Akční-plán-autonomního-řízení-ma\\_KORNB8UGXNR8.pdf](http://amsp.cz/wp-content/uploads/2019/02/Akční-plán-autonomního-řízení-ma_KORNB8UGXNR8.pdf) (in Czech).
- MUTCD. 2012. ‘Manual on Uniform Traffic Control Devices’. U.S. Department of Transportation, Federal Highway Administration, Washington, D.C.
- National Safety Council. 2018. <https://www.nsc.org/>. Accessed 29.08.2019.
- Paclík, P., Novovičová, J., Pudil, P. & Somol, P. 2000. Road sign classification using Laplace kernel classifier. *Pattern Recognit. Lett.* **21**(13–14), 1165–1173. Elsevier Science Publishers B.V. doi:10.1016/S0167-8655(00)00078-7
- Ré, J.M., Miles, J.D. & Carlson, P.J. 2011b. Analysis of In-Service Traffic Sign Retroreflectivity and Deterioration Rates in Texas. *Transportation Research Record: Journal of the Transportation Research Board* **2258**(1), 88–94.
- Ritter, W., Stein, F. & Janssen, R. 1995. Traffic sign recognition using colour information. *Math. Comput. Model.* **22**(4–7). doi:10.1016/0895-7177(95)00131-K
- Schnell, T., Aktan, F. & Li, C. 2004. Traffic Sign Luminance Requirements of Nighttime Drivers for Symbolic Signs. *Transp. Res. Rec. J. Transp. Res. Board* **1862**(1), 24–35.
- The Decree No 10/2019 Coll. 2015. ‘Decree implementing the road traffic rules’. (in Czech).
- The Decree No 294/2015 Coll. 2015. ‘Decree implementing the road traffic rules’. (in Czech).
- The Decree No 84/2016 Coll. 2016. ‘Decree implementing the road traffic rules’. (in Czech).
- Toth, Š. 2012. Difficulties of Traffic Sign Recognition. *7-th winter Sch. Math. Appl. to ICT.* Sachtický, pp. 7–10.

- TP 65. 2013. 'Principles for traffic signs on roads'. (in Czech).
- Traffic signs. 2008. In: *TRAFFIC ENGINEERING MANUAL*. Ohio Department of Transportation Office of Traffic Engineering. 164 pp.
- Vitabile, S., Pollaccia, G., Pilato, G. & Sorbello, F. 2001. Road signs recognition using a dynamic pixel aggregation technique in the HSV color space. *Proc. 11th Int. Conf. Image Anal. Process.*, pp. 572–577.
- Wali, S. 2015. Comparative survey on traffic sign detection and recognition: a review. *Przegląd Elektrotechniczny* **1**(12), 40–44. doi:10.15199/48.2015.12.08
- Wali, S.B., Abdullah, M.A., Hannan, M.A., Hussain, A., Samad, S.A., Ker, P.J. & Mansor, M. Bin. 2019. Vision-Based Traffic Sign Detection and Recognition Systems: Current Trends and Challenges. *Sensors (Basel)* **19**(9). Multidisciplinary Digital Publishing Institute (MDPI). doi:10.3390/s19092093
- Yin, S., Ouyang, P., Liu, L., Guo, Y. & Wei, S. 2015. Fast Traffic Sign Recognition with a Rotation Invariant Binary Pattern Based Feature. *Sensors* **15**, 2161–2180.
- Zaklouta, F. & Stanciulescu, B. 2014. Real-time traffic sign recognition in three stages. *Rob. Auton. Syst.* **62**(1), 16–24. doi:10.1016/j.robot.2012.07.019
- Zhu, Y., Zhang, C., Zhou, D., Wang, X., Bai, X. & Liu, W. 2016. Traffic sign detection and recognition using fully convolutional network guided proposals. *Neurocomputing* **214**, 758–766. doi:10.1016/j.neucom.2016.07.009
- Zhu, Z., Lu, J., Martin, R.R. & Hu, S. 2017. An Optimization Approach for Localization Refinement of Candidate Traffic Signs. *IEEE Trans. Intell. Transp. Syst.* **18**(11), 3006–3016. doi:10.1109/TITS.2017.2665647

## **Characterization of materials used in the manufacture of ceramic tile with incorporation of ornamental rock waste**

N.F. Luiz<sup>1</sup>, D. Cecchin<sup>1,\*</sup>, A.R.G. Azevedo<sup>1</sup>, J. Alexandre<sup>2</sup>, M.T. Marvila<sup>2</sup>,  
F.C. Da Silva<sup>1</sup>, A.L.C. Paes<sup>2</sup>, V.D. Pinheiro<sup>2</sup>, D.F. Do Carmo<sup>1</sup>, P.F.P. Ferraz<sup>3</sup>,  
C.M. Hüther<sup>1</sup>, V.M.F. Da Cruz<sup>4</sup> and M. Barbari<sup>5</sup>

<sup>1</sup>Federal Fluminense University (UFF), Engineering school, Department of Agricultural Engineering and Environment, Street Passo da Pátria, n.156, postal code: BR24210-240, Niterói, Rio de Janeiro, Brazil

<sup>2</sup>North Fluminense State University (UENF), Civil Engineering Department, Campos dos Goytacazes, Rio de Janeiro, Brazil

<sup>3</sup>Federal University of Lavras (UFLA), Department of Agricultural Engineering, Campus Universitário, PO Box 3037, Lavras, Minas Gerais, Brazil

<sup>4</sup>University of Évora, Polo da Mitra - Department of Rural Engineering - Évora/Portugal

<sup>5</sup>University of Firenze, Department of Agriculture, Food, Environment and Forestry (DAGRI), Via San Bonaventura 13, IT50145 Firenze, Italy

\*Correspondence: daianececchin@yahoo.com.br

**Abstract.** The production of ceramic tiles, such as tiles, has a great environmental impact, either in the extraction of natural raw materials or gas emissions in the burning stages. The use of industrial solid waste in ceramic materials can contribute to the reduction of these impacts, according to the characteristics of solid waste and its interaction with ceramic materials in the processing steps. Thus, this study aimed to characterize the materials needed to make a ceramic tile with incorporation of ornamental rock waste (ORW), thus evaluating its main characteristics regarding the feasibility of this incorporation. The physical characterization of the clays used in the production of ceramic artifacts was performed, and for the waste the mineralogical analyzes were performed, through x-ray diffraction (XRD), microstructure analysis from confocal optical microscopy, after sintering the prototypes and chemical analysis by X-ray spectroscopy (EDX). Soon after the raw materials went through the step of conformation and preparation of the prismatic specimens by the process of extrusion of the ceramic mass, with an incorporation of the ORW in 0% and 15% of the ceramic mass, for its subsequent The prototypes were sintered at three different temperatures (850 °C, 950 °C and 1,050 °C). The specimens were submitted to technological tests of mechanical resistance, water absorption, firing shrinkage and porosity to evaluate the incorporation viability. The results indicated the presence of quartz particles in all raw materials, and also that the clays of the study region are predominantly kaolinitic. The presence of these materials in the ceramic masses directly influences the micrographs, because they result in the formation of liquid phase, inert particles that can turn the site into a stress concentration point and when incorporated in the ORW the specimens met the technical specifications of the Brazilian standard for application on ceramic tiles. The results found in the technological tests carried out, that the incorporation of 15% of ornamental rock waste in both clays did not affect the tile properties, indicating the feasibility of incorporating this waste in civil construction, minimizing the impacts generated.

**Key words:** waste, reuse, rural constructions, sustainability.

## INTRODUCTION

One of the major problems of industrial activity worldwide is the generation of solid industrial waste, which has been growing at significant rates in several countries. The problem of the generation of industrial solid waste is related to environmental issues, linked to the disposal of these materials in the environment, such as in landfills and the pollution of soil and groundwater, due to incorrect packaging. Another eminent factor is the economic issue, since the disposal and proper transportation of this waste involves great costs for the producing companies (Azevedo et al., 2018).

Thus, the potential of using industrial solid waste in various ways has been discussed on several fronts, the most promising being its incorporation in civil construction materials, such as cement and ceramics, which are widely used worldwide (Marvila et al., 2019; Areias et al., 2020). The incorporation of waste in construction materials, in addition to providing a more noble destination for the material, than its simple disposal in landfills, can lead to an improvement in technological properties that enhance its use and increase its added value, in addition to allowing in some reduction in consumption of other raw materials (Azevedo et al., 2020a).

The ceramic industry is known for its high potential for damage to the environment, due to the use of a large amount of natural raw material, such as natural clay, which is extracted from deposits and causes impacts before and after extraction, due to the high energy consumption in the stage of burning the parts, which leads to increased financial costs and in cases where it is poorly executed in defects that may make the use of parts by civil construction unfeasible and the direct impacts such as the generation of solid waste, called the chamotte, increased emission polluting gases in the atmosphere and others (Coutinho & Vieira, 2016). All of these factors contribute to this type of industrial activity being the result of scientific research to improve its products and the production process, in order to reduce environmental impacts (Mendoza-Cuenca et al., 2015).

The minimization of the use of natural resources for the manufacture of ceramic products has been made from the incorporation of wastes from other productive chains in the manufacture of ceramic products, as in the study of Vieira et al. (2016), in which ornamental stone wastes were incorporated in ceramics in order to obtain contribution in the properties of the materials, as well as improvements in the final technological properties.

The incorporation of rock waste in clays allows the adjustment of plasticity in the ceramic mass, due to the coarse granulometry of the residue and an increase in dry density, in addition, in the study of Amaral et al. (2019), the increase in the waste content resulted in less linear shrinkage, decreased water absorption, which improves some properties of the ceramic mass.

The chemical and mineralogical composition of the clays depends on the formation deposits where they are located, and these compositions and the amounts of quartz, calcite, dolomite, feldspar and other organic compounds, can vary according to the level of these deposits. The composition can directly interfere in the properties of the materials to be manufactured, also influencing its final production cost (Tretjakova et al., 2018).

Brazil produces a significant amount of ornamental rocks, such as marble and granite, which together generate large amounts of solid waste in the stages of processing the blocks after their extraction from nature, this waste, called ornamental rock waste, is in general transported to landfills, which raises its production costs (Areias et al., 2020).

The state of Espírito Santo - ES is one of the largest producers of ornamental stones in Brazil and close to it is the municipality of Campos dos Goytacazes - RJ, which has one of the largest production centers for ceramic artefacts in the country (Azevedo et al., 2019). Thus, there is a potential for the use of ornamental rock waste in red ceramic pieces, such as blocks and floors, however its application in tiles is still little explored in the scientific literature, limited to small percentages and limited firing temperatures (Marvila et al., 2018; Azevedo et al., 2020b). Thus, this study aimed to characterize the materials needed to make a ceramic tile with incorporation of ornamental rock waste (ORW), thus evaluating its main characteristics regarding the feasibility of this incorporation.

## MATERIALS AND METHODS

The clays used in the present work come from the municipality of Campos dos Goytacazes, State of Rio de Janeiro, and were extracted from a local ceramic industry, called Arte Cerâmica Sardinha. The ornamental stone waste was collected in the municipality of Cachoeiro do Itapemirim, in Espírito Santo, from the company Decolores Marmores e Granitos do Brasil, in the form of mud, with natural humidity (in the range of 12 to 26%).

The industrial mass was made using clays locally called ‘strong’ (AF) clay, that is, a more plastic clay and a mixed clay (AM), containing ‘strong’ and ‘weak’ clay. Both the mass, the clays and the rock waste were previously subjected to drying.

For the preparation of the ceramic mass, 15% of ornamental rock waste was added for the weight of each clay. The amount of 15% is already known in other studies in the literature that evaluated the use of this waste for the production of other ceramic artefacts, such as tiles and blocks, which is different from this work, but we opted to start from this percentage called ‘excellent’ and to evaluate the influence of sintering temperatures for economic reasons (the cost of the sintering step is high) and environmental (maximal waste and reduction of gas emissions in the atmosphere with sintering).

The chemical characterizations of the clay and the waste were determined by X-ray fluorescence spectroscopy, with the SHIMADZU EDX-700 equipment, performed at the Civil Engineering Laboratory - LECIV at UENF.

X-ray diffraction determines the atomic and molecular structure of a crystal, it was performed using Rigaki MiniFlex 60 equipment at the Civil Engineering Laboratory - LECIV at UENF.

The prototypes were made using an extruder of the Verdés brand, model BR-051. After extrusion, the prototypes went through a natural and artificial drying process. The prototypes were sintered at three different temperatures (850 °C, 950 °C and 1,050 °C). The heating rate was 2 °C min<sup>-1</sup> with 120 minutes of stay at the threshold temperature. The cooling carried out natural convection until room temperature, when the oven was turned off. These sintering temperatures (850 °C, 950 °C and 1,050 °C) are the ones commonly used in the ceramic industry for this type of piece, very low temperatures compromise the transformation of mineral phases that exist in the clays and negatively influence the final properties of the tiles, since too high temperatures incur high costs and possibility of increased defects in parts, such as high linear shrinkage, so the

evaluation of temperature ranges becomes important, and the choice of these in a specific way was given by the literature.

Water absorption was analyzed. The water absorption test was carried out according to ASTM C373 (1972), in which the specimens were dried in an oven at  $\pm 110\text{ }^{\circ}\text{C}$  for 24 hours, and their masses were measured. Afterwards, they were placed in a container containing water for 24 hours and the excess surface water was removed for the new mass weighing.

The analysis of the linear shrinkage of the prototypes was carried out after sintering, being carried out according to ABNT-MB-305, using a 0.01 mm resolution pachymeter.

The three point flexural strength of the prototypes was analyzed. The flexural strength was determined according to ASTM C674 (1977) with the aid of an EMIC hydraulic press, model CL 3000. The load application speed was  $0.1\text{mm min}^{-1}$  and the distance between the cleavers was of 8.0 cm.

The confocal micrograph was performed in order to obtain enlarged images of the specimens and to distinguish details of the surface, using an Olymplus microscope and LAMAV / UENF CGA model.

## RESULTS AND DISCUSSION

The chemical compositions of the raw materials used were determined (Table 1).

**Table 1.** Chemical composition of the raw materials used to make the prototypes.

Raw material	$\text{SiO}_2$	$\text{Al}_2\text{O}_3$	$\text{Fe}_2\text{O}_3$	$\text{K}_2\text{O}$	$\text{TiO}_2$	$\text{SO}_3$	$\text{CaO}$
AF	60.35	31.33	2.88	2.20	1.17	1.35	0.57
AM	56.46	34.01	3.31	2.26	1.42	1.78	0.66
ORW	86.22	7.15	0.26	2.15	0.10	1.59	2.34

It was possible to observe that both clays are predominantly made up of  $\text{SiO}_2$  and  $\text{Al}_2\text{O}_3$  (91.68% for AF and 90.47% for AM), and according to Coutinho & Vieira (2016) these form the clay silicates like mica and kaolinite, also indicate high percentage of clay minerals. Also according to these authors, the high percentage of  $\text{Fe}_2\text{O}_3$ , between 1 and 5%, gives the beige-rosacea color after the burning of the clays.

However, the ornamental rock waste showed a high percentage of alkaline oxides ( $\text{K}_2\text{O} + \text{Na}_2\text{O}$ ), and according to Vieira et al. (2004) this indicates that these oxides form eutectic with silica at sintering temperatures above  $700\text{ }^{\circ}\text{C}$ .

With the x-ray diffractograms of the clays (Figs 1 and 2) it was possible to observe that both have higher diffraction peaks corresponding to kaolinite, and according to Babisk et al. (2019), this mineral clay is responsible for the plasticity of the clays. In addition, the presence of kaolinite proves that the clays are typically from the Campos region (Areias et al., 2017; Vieira et al., 2000).

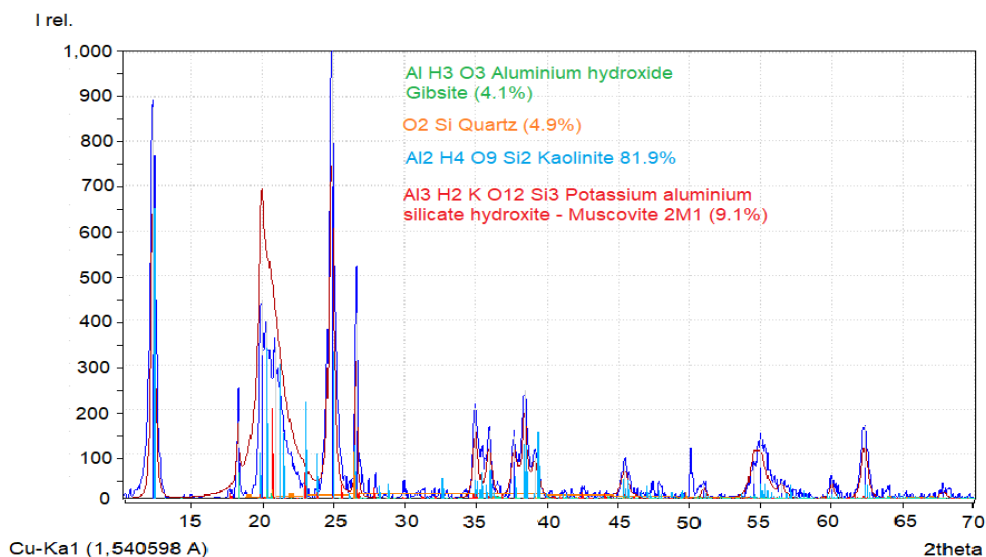


**Figure 1.** X-ray diffractogram - mixed clay (AM).

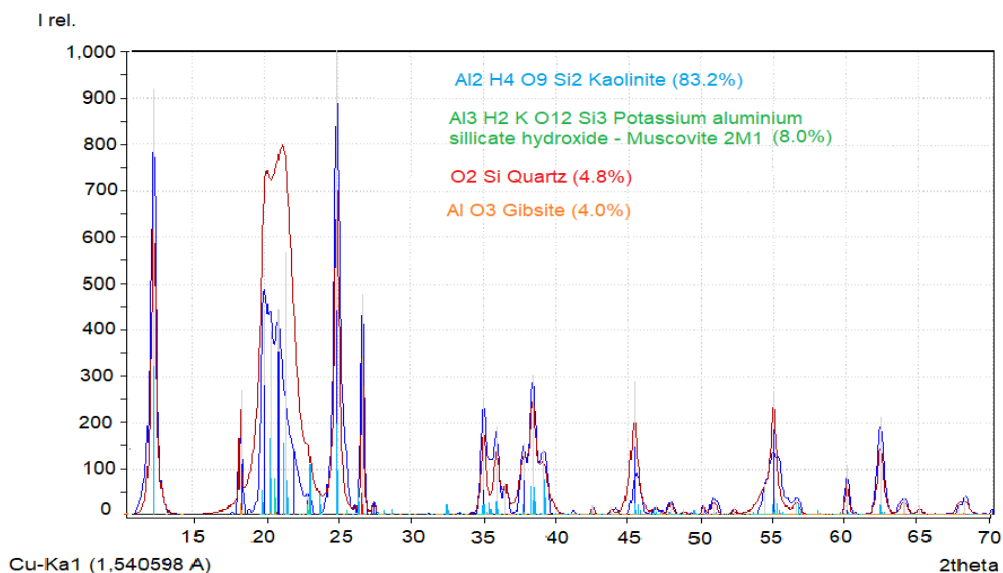


**Figure 2.** X-ray diffractogram - strong clay (AF).

The analysis performed by DRX for ORW (Fig. 3) indicates that the waste is rich in Ca due to the presence of this substrate in the form of dolomite, according to Neves et al. (2019), due to the sawing of blocks and also by the presence of marble waste in the composition of the ORW. The presence of quartz in the ORW indicates, according to Coutinho & Vieira (2016) impurities that act as non-plastic raw material inert substances during the sintering process.



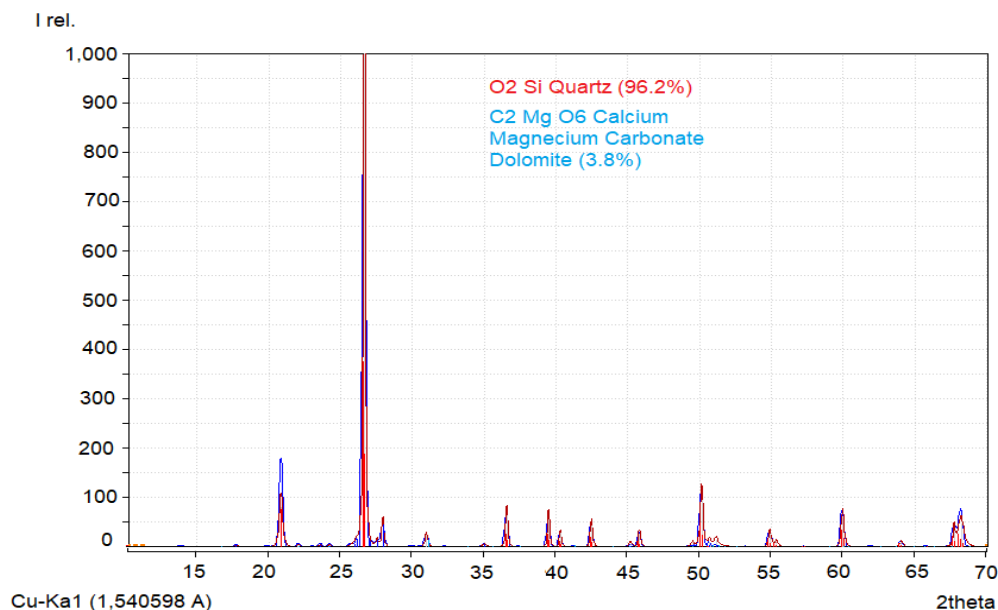


**Figure 3.** X-ray diffractograms - ornamental rock waste (ORW).

The average water absorption values after the sintering process are shown in Table 2. The sintered prototypes 1,050 °C showed lower water absorption values in all ceramic mass compositions. According to Vieira et al. (2016), this decrease is associated with the presence of fluxing oxides that contribute to the formation of a liquid phase and closing porosity. This change in behavior between temperatures of 850 to 1,050 °C is associated with the refractory behavior of a kaolinitic clay body that has low amounts of fluxing oxides and a high amount of alumina in its chemical composition (Vieira et al., 2016).

The reduction in the absorption value at a temperature of 1,050 °C, is associated with the mechanisms of sintering, diffusion in the solid state and formation of the liquid phase that act effectively in the clays of Campos dos Goytacazes, so the temperatures of 850 and 950 °C were also selected, due to the fact that they are not among some critical temperature ranges (Azevedo et al., 2018; Amaral et al., 2019).

According to the ABNT 15270-2 standard (ABNT, 2017) the maximum water absorption index indicated for ceramic blocks is 22%, which indicates that in this study all the ceramic masses tested fall within the standard's determination. The NBR 13582 (ABNT, 2005) for Roman ceramic tiles mentions that the ideal and maximum

**Table 2.** Average water absorption values observed in each ceramic mass composition

Temperature (°C)	Water absorption (%)			
	AM0	AM15	AF0	AF15
850	15.4	15.8	20.3	18.1
950	20.4	19.4	18.4	14.9
1,050	11.3	11.4	14.3	13.3

AM0: Ceramic clay made with mixed clay and 0% addition of ornamental rock waste; AM15: Ceramic clay made with mixed clay and 15% addition of ornamental rock waste; AF0: Ceramic clay made with strong clay and 0% addition of ornamental rock waste; AF15: Ceramic clay made with strong clay and 15% addition of ornamental rock waste.

value for water absorption must not exceed 18%, which was not met by all ceramic masses, at all temperatures. However, the ceramic masses sintered at 1,050 °C showed values that meet the standard for ceramic tiles. At 950 °C, only the AF15 mass met the requirements of the standard for tiles (Fig. 4).

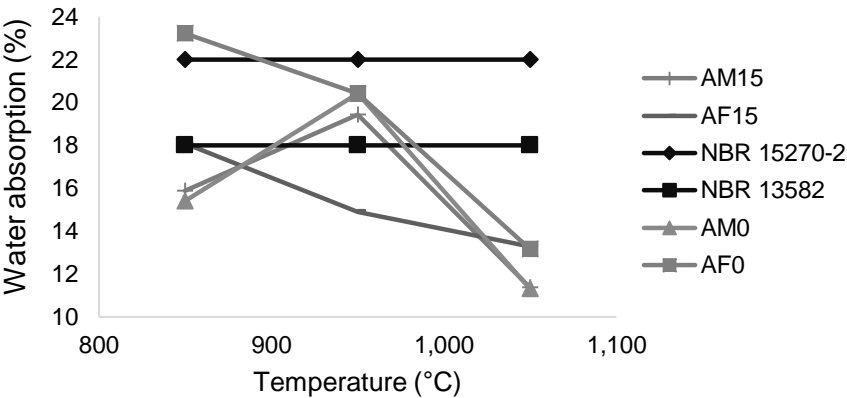


**Figure 4.** Average water absorption values for ceramic masses compared to standards.  
AM0: Ceramic clay made with mixed clay and 0% addition of ornamental rock waste; AM15: Ceramic clay made with mixed clay and 15% addition of ornamental rock waste; AF0: Ceramic clay made with strong clay and 0% addition of ornamental rock waste; AF15: Ceramic clay made with strong clay and 15% addition of ornamental rock waste; NBR 15270-2: Standard NBR 15270-2; NBR: 13582: Standard NBR: 13582.

The values regarding the linear shrinkage observed for each ceramic mass composition, at each sintering temperature can be seen in Table 3.

The increase in linear shrinkage is associated with the formation of a liquid phase, as well as the recrystallization of the ceramic phases at high temperatures, greater densification which is caused by physical changes and a reduction in the volume of the specimens, moreover, this increase may also be related the higher content of fluxing oxides which justifies the higher values in the ceramic mass with incorporation of 15% ORW (Vieira et al., 2015; Gaspareto & Teixeira, 2017; Silva et al., 2018).

Table 4 shows the flexural strength values at three points for each of the ceramic masses.

The mean of the rupture module increased as the sintering temperature increased, with the AM15 mass sintered at 1050 showing the highest mean value of resistance to rupture. According to Brito et al. (2015), this occurs due to the presence of the lowest

**Table 3.** Average values of linear shrinkage observed at home ceramic mass composition

Temperature (°C)	Linear shrinkage			
	AM0	AM15	AF0	AF15
850	1.39	1.02	1.42	1.54
950	2.11	2.01	2.36	2.52
1,050	3.50	3.17	3.99	4.17

AM0: Ceramic clay made with mixed clay and 0% addition of ornamental rock waste; AM15: Ceramic clay made with mixed clay and 15% addition of ornamental rock waste; AF0: Ceramic clay made with strong clay and 0% addition of ornamental rock waste; AF15: Ceramic clay made with strong clay and 15% addition of ornamental rock waste

silica content between clays and the highest ratio  $\text{Al}_2\text{O}_3/\text{SiO}_2$ , these are important characteristics for the compaction and densification of the masses, which favor the physical-mechanical properties.

In general, most of the evaluated ceramic masses presented values greater than or equal to 6.5 Mpa, established by the standard ABNT NBR 15310 (ABNT, 2005) for ceramic tiles. The prototypes sintered at 1050 °C showed higher values compared to the other temperatures for all tested compositions. The decrease in flexural strength may be related to the presence of quartz in the structure of the ceramic masses, which acts as fracture initiation sites.

According Viera & Pinheiro (2013) the microstructures of the ceramic masses showed different colors due to the dehydration of the iron hydroxide and hematite that are present in the clays, that can be seen in the present study, whereas the black particles indicate the presence of the iron compounds (Figs 5, 6, 7 and 8 (arrows 1)), the red ones are those of hematite and the white circle indicates muscovite mica (Figs 5 and 7 (arrows 2)), which it is present in the composition of the rock waste.

**Table 4.** Average flexural strength values found in each ceramic mass composition

Temperature (°C)	flexural strength (Mpa)			
	AM0	AM15	AF0	AF15
850	5.21	7.14	6.73	9.35
950	5.19	7.16	6.04	5.87
1,050	8.35	12.5	8.58	9.40

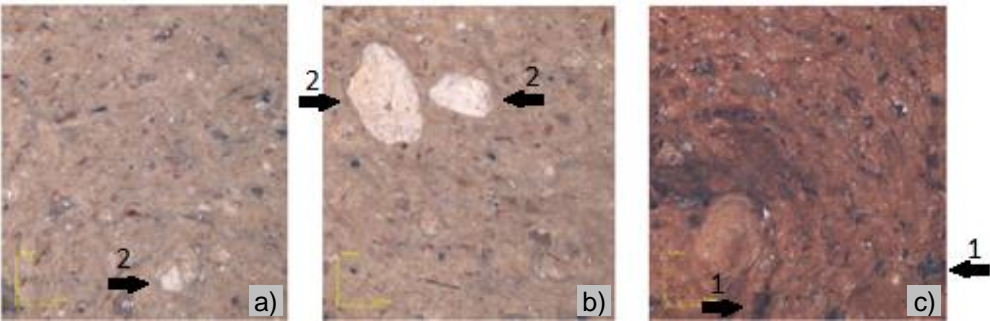


**Figure 5.** Confocal optical microscopy of ceramic masses with 0% incorporation of ORW in mixed clay (AM0) sintered at 850 °C (a), 950 °C (b) e 1,050 °C(c).

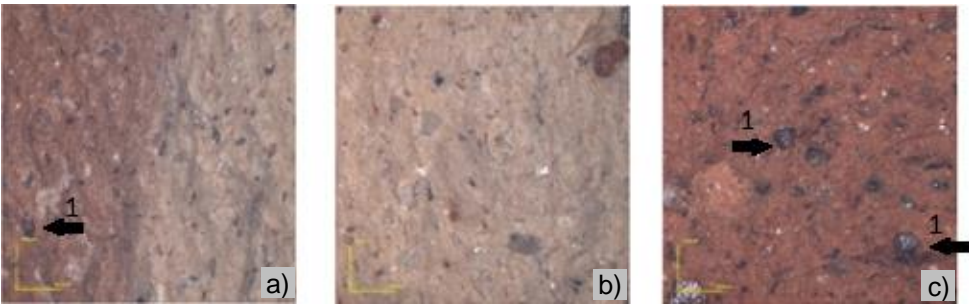


**Figure 6.** Confocal optical microscopy of ceramic masses with 15% incorporation of ORW in mixed clay (AM15) sintered at 850 °C (a), 950 °C (b) e 1,050 °C(c).

The micrographs of the ceramic masses with 15% ORW burned at 1,050 °C when enlarged in 108x have free quartz grains and some cracks around the quartz grain. It is also possible to observe in Fig. 7, c, according to the analysis of the Campos dos Goytacazes clays, that the presence of quartz grains separated from the matrix occurs only in the porous microstructure at temperatures above 1,050 °C due to the composition of the raw materials, in agreement with Vieira et al. (2000).

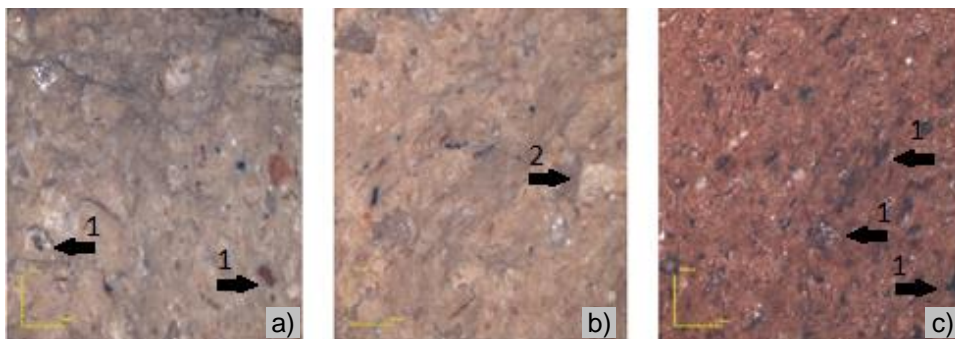


**Figure 7.** Confocal optical microscopy of the ceramic masses with 0% ORW incorporation in strong clay (AF0) sintered at 850 °C (a), 950 °C (b) e 1,050 °C(c).

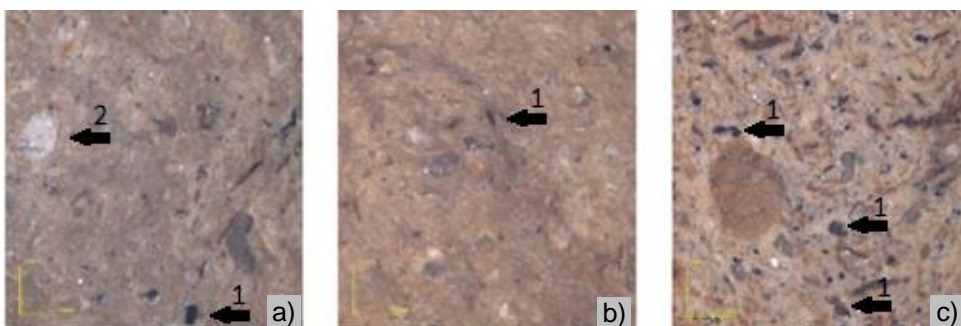


**Figure 8.** Confocal optical microscopy of the ceramic masses with 15% ORW incorporation in strong clay (AF15) sintered at 850 °C (a), 950 °C (b) e 1,050 °C(c).

## CONCLUSIONS

The ceramic mass composed of the clays and the waste present after the sintering properties expected from the raw materials due to the chemical composition and the x-ray analyzes, which indicated the reddish color, the presence of free quartz inert to sintering and the increased formation liquid phase which contributes to the densification of prototypes.

The sintering temperature that resulted in the best results was 1,050 °C.

It is possible to conclude from the results found in the technological tests carried out, that the incorporation of 15% of ornamental rock waste in both clays did not affect the tile properties, indicating the feasibility of incorporating this waste in civil construction, minimizing the impacts generated.

## REFERENCES

- Amaral, L.F., Carvalho, J.P.R.G., SILVA, B.M., Delaqua, G.C.G., Monteiro, S.N., Vieira, C.M.F. 2019. Development of ceramic paver with ornamental rock waste. *Journal of Materials Research and Technology* **8**(1), 599–608.
- American Society for Testing and Materials. 1972) ASTM C373. Water absorption, bulk density, apparent porosity and apparent specific gravity of fired whiteware products, USA.
- American Society for Testing and Materials. 1977. ASTM C674. Flexural properties of ceramic whiteware Materials.
- Areias, I.O.R., Vieira, C.M.F., Colorado, H.A., Delaqua, G.C.G., Monteiro, S.N. & Azevedo, A.R.G. 2020. Could city sewage sludge be directly used into clay bricks for building construction? A comprehensive case study from Brazil. *Journal of Building Engineering* **31**. doi: 10.1016/j.jobe.2020.101374
- Areias, I.O.R., Vieira, C.M.F., Manhães, R.S.T. & Intorne, A.C. 2017. Incorporation of sludge of the sewage treatment station (STS) into red ceramic. *Cerâmica* **63**(367), 343–349 (in Portuguese).
- Azevedo, A.R.G., Alexandre, J., Marvila, M.T., Xavier, G.D.C., Monteiro, S.N. & Pedroti, L.G. (2020a). Technological and environmental comparative of the processing of primary sludge waste from paper industry for mortar. *Journal of Cleaner Production* **249**. doi: 10.1016/j.jclepro.2019.119336
- Azevedo, A.R.G., Alexandre, J., Xavier, G.D.C. & Pedroti, L.G. 2018a. Recycling paper industry effluent sludge for use in mortars: A sustainability perspective. *Journal of Cleaner Production* **192**, 335–346. doi: 10.1016/j.jclepro.2018.05.011
- Azevedo, A.R.G., Cecchin, D., Luiz, N.F., Cruz, V.F., Marvila, M.T., Zanelato, E.B., Moraes, G., Alexandre, J. 2020b. Characterization of clay mix with incorporation of granite waste for the production of ceramic tiles. In: Li, J. et al. (eds) *Characterization of Minerals, Metals, and Materials. The Minerals, Metals & Materials Series*. Springer, Cham. doi: 10.1007/978-3-030-36628-5\_46
- Azevedo, A.R.G., Marvila, M.T., Barroso, L.S., Zanelato, E.B., Alexandre, J., Xavier, G.C. & Monteiro, S.N. 2019. Effect of granite residue incorporation on the behavior of mortars. *Materials* **12**(9). doi: 10.3390/ma12091449
- Azevedo, A.R.G., Franca, B.R., Alexandre, J., Marvila, M.T., Zanelato, E.B., Xavier, G.C. (2018b). Influence of sintering temperature of a ceramic substrate in mortar adhesion for civil construction. *Journal of Building Engineering* **19**, 342–348.
- Babisk, M.P., Amaral, L.F., Ribeiro, L.S., Vieira, C.M.F., Prado, U.S., Gadioli, M.C.B., Oliveira, M.S., Luz, F.S., Monteiro, S.N., Fiho, F.C.G. 2019. Evaluation and application of sintered red mud and its incorporated clay ceramics as materials for building construction. In: *Journal of Material Research and Technology* **9**(2), 2186–2195.
- Brazilian Association for Technical Norms. Ceramic components - Ceramic roof tiles – Terminology requirements and testing methods. Rio de Janeiro: ABNT 2009. (NBR 15310). (in Portuguese).
- Brazilian Association for Technical Norms. Ceramic components Part 2: Structural ceramic block, perforated block, load-bearing masonry -Terminology and requirements. Rio de Janeiro. ABNT 2005. (NBR 15270–2). (in Portuguese).
- Brazilian Association for Technical Norms. Ceramic tile - Roman type – Specification Descriptor: Ceramic tile. Rio de Janeiro. ABNT 2005. (NBR 13582). (in Portuguese).
- Brito, I.P., Almeida, E.P., Neves, G.A., Menezes, R.R., Silva, V.J., Santana, L.N.L. 2015. Assessment of new clay deposits of Paraíba State for application as ceramic raw materials. *Cerâmica* **61**(360), 391–398 (in Portuguese).
- Coutinho, N.C. & Vieira, C.M.F. 2016. Characterization and incorporation of MSWI ash in red ceramic. *Cerâmica* **62**(363), 249–255 (in Portuguese).

- Gaspareto, M.G. & Teixeira, S.R. Use of Civil Construction and Demolition Waste (RCD) as a Non-Plastic Material for the Production of Ceramic Bricks. *Ceramica Industrial* **22**(2), 40–46.
- Marvila, M.T., Alexandre, J., Azevedo, A.R.G., Zanelato, E.B., Monteiro, S.N., Xavier, G.C., Mendes, B. (2018). Study of the incorporation of residue of ornamental rocks in ceramic tiles. In: Li B. et al. (eds) *Characterization of Minerals, Metals, and Materials 2018*. TMS 2018. The Minerals, Metals & Materials Series. Springer, Cham., pp. 677–682. doi: 10.1007/978-3-319-72484-3\_72
- Marvila, M.T., Alexandre, J., de Azevedo, A.R.G. & Zanelato, E.B. 2019. Evaluation of the use of marble waste in hydrated lime cement mortar based. *Journal of Material Cycles and Waste Management* **21**(5), 1250–1261. doi: 10.1007/s10163-019-00878-6
- Mendoza-Cuenca, J.L., Mayorga, M., Romero-Salazar, L., Yee-Madeira, H.T., Jimenez-Gallegos, J., Arteaga-Arcos, J.C. 2015. Advances in the use of the steel industry by-products when manufacturing traditional ceramics for sustainable purposes. *Procedia Engineering* **118**, 1202–1207.
- Neves, M.A., Santos, M.A.A., Taguchi, S.P., Rangel, C.V.G.T., Raymundo, V. 2019. Environmental interactions and physical resistance of fine waste deposit from dimension stone industry. *Engenharia Sanitaria e Ambiental* **24**(4), 725–797 (in Portuguese).
- Silva, A.L., Luna, C.B.B., Chaves, A.C., Neves, G.A. 2018. Evaluation of new deposits of clays from the southern region of Amapa for application in the ceramic industry. *Cerâmica* **64**, 69–78 (in Portuguese).
- Tretjakova, R., Martinovs, A., Avisane, M., Kolcs, G. 2018. Lake blue clay – sapropel – flax shive briquettes for water absorption and desorption. *agronomy Research* **16**, 1266–1277.
- Vieira, C.M.F., Sales, H.F., Monteiro, S.N. 2004. Effect of illitic fluz clay addition in red ceramic of kaolinitic clays. *Ceramica*, **50**, 239–246.
- Vieira, C.M.F., Samarão Motta, T., Scarpini Candido, V., Monteiro, S.N. 2015. Addition of Ornamental Stone Waste to Improve Distinct Formulation of Clayey Ceramics. *Materials Science Forum* **820**, 419–424.
- Vieira, C.M.F., Silva, B.M., Carvalho, J.P.R.G. 2016a. Recycling of granite waste from sawing operation in clay brick for civil construction. *Modern Environmental Science and Engineering* **2**(6), 389–395.
- Vieira, C.M.F., Soares, T.M., Monteiro, S.N. 2016b. Use of mass granite ceramics for tiles. *Ceramica* **9**(1), 28–32 (in Portuguese).
- Vieira, C.M.F., Holanda, J.N.F., Pinatti, D.G. 2000. Characterization of red ceramic body used in the production of bricks in the region of Campos dos Goytacazes – RJ. *Cerâmica* **46**(297), 14–17.

## Qualimetry as productivity criteria in metal-cutting operations

D. Maksimov<sup>1,\*</sup>, H. Kalkis<sup>2</sup>, Y. Perevoschikov<sup>1</sup> and Z. Roja<sup>3</sup>

<sup>1</sup>Udmurt State University, Institute of Economics and Management, 1, Universitetskaya street, bld. 4, RU426034 Izhevsk, Russia

<sup>2</sup>Riga Stradins University, Faculty of European Studies, 16 Dzirciema street, LV-1007 Riga, Latvia

<sup>3</sup>University of Latvia, 19 Raina blv., LV-1586 Riga, Latvia

\*Correspondence: maksim.dan.gen@gmail.com

**Abstract.** The qualimetry method will allow an objective assessment of the performance of metal-cutting machines and the production capacity of machinery, as well as an objective assessment of their use in multi-product manufacturing, applying the qualimetry approach and qualimetry indicators, which are based on the concept of qualification of metal removing during machine operations. The aim of the study is to develop methods for measuring the performance of metal-cutting machines and open the way to create a regulatory framework based on quantitative indicators of the equipment quality. Qualimetry measured volume of metal removing allows setting the maximum possible productivity (quali-power) of metal cutting machinery, based on a small number of basic quality indicators contained in the machinery data sheets. It is essential that the quali-power of the machinery is an objective indicator of its quality, independent of the specific conditions of its operation at any given time. Hence the productivity criteria in metalworking cutting operations can be measured.

**Key words:** qualimetry, ergonomics, quantitative, manufacturing, equipment.

### INTRODUCTION

The results of scientific and practical activities of the American engineer F.W. Taylor are classical in enterprise management and organization. His methods constituted an essential scientific and practical part of the global system of economic measurements (Taylor, 1923). More than 120 years have passed since Taylor presented his conclusions on the theory of metal-cutting. Since then it has remained basically unchanged, and we cannot imagine the management of industry around the world without it.

It is worth noting that from the standpoint of the modern development of economy, the experiments conducted by Taylor on metal-cutting are the beginning of a qualitative modeling of the production of machine parts called ‘qualimetry’ (Azgaldov et al., 1968). It is important since one of the main components of the production potential in mechanical engineering is the technological machinery, a significant part of which falls on the share of metal-cutting machinery (Smailovskaya et al., 2011; Gardner Intelligence, 2018).



Labour productivity (Thomson & Webster, 2013; Yi & Chan, 2014) has been studied sufficiently in many industries both from the perspective of ergonomics (Orefkov & Perevoschikov, 2007; Maksimov & Kalkis, 2018), microelement rationing (Maynard et al., 1948; Golabchi et al., 2016; Koptak et al., 2017), and a subjective assessment of the time for completion of the work (Chan et al., 2017). However, the productivity of machines, in particular, metal-cutting equipment, from the qualitative side has been poorly studied.

Currently, the overage machine shift is the indicator that determines the use of equipment. This term refers to the average operating time of an equipment element at a site or enterprise (Podzorov, 2018). However, it does not fully characterize the equipment used, since it does not consider the technological capabilities of metal-cutting machines. In other words, qualitative characteristics are not considered in accordance with the purpose of the machines.

The purpose of the qualimetry analysis of the machine parts production is to develop methods for measuring the performance of metal-cutting machines and the production capacity of machine shops, as well as to create a regulatory framework for such a measurement based on quantitative indicators of equipment quality and processing technology conditions.

This work is part of a study conducted in the framework of economic metrology (Pevoshchikov et al., 2005; Perevoshchikov, 2015) using qualimetry methods. The first part is dedicated to creating an ergonomic workplace passport (Maksimov & Kalkis, 2018). The second one deals with the complexity of product manufacturing (Ermilov & Perevoshchikov, 2018; Maksimov et al., 2019). The aim of study is to develop methods for measuring the performance of metal-cutting machines, and, in the future, to create a regulatory framework based on quantitative indicators of the equipment quality. The beginning of the study is presented in the work of Perevoshchikov (Per, 2019).

## **MATERIALS AND METHODS**

The application of the concept of 'productivity' in relation to machine tools, used in the production of different types of products, is impossible since it is different for different types of products and operations. This value is inversely proportional to time per a piece, and therefore cannot serve as objective characteristics of the capability of metal-cutting machinery.

The methods currently used for calculating production capacities do not consider the capabilities of technological machinery determined by its qualitative composition, but consider the amount of equipment only (Liang & Shin, 2016).

In metal-cutting machinery, it is necessary to introduce a new, universal, concept of 'machine production capacity', which is not related to the manufacture of one particular product and is determined by the maximum productivity of the equipment. The production capacity of the site in which this equipment is used is defined as the sum of the production capacities of all metal-cutting machinery used.

The production capacity of the machine should be determined based on the indicators given in the equipment certificate, since they characterize maximum possibilities and do not depend on the characteristics of the workpiece. It should also be noted that metal-cutting machines are subdivided according to the degree of accuracy and the type of surface treatment performed – finishing and roughing. The maximum



productivity of the machine during the initial roughing should be measured by the maximum possible amount of metal that can be 'removed' in a certain unit of time under the established reference conditions for this type of equipment.

As the basic unit of measurement of the machine's operating time, the operating time for one minute will be used.

Production capacity per minute of the studied metal cutting section can be determined using the formula (Per, 2019)

$$Q_{max} = \sum_{i=1}^n q_{max_i} \quad (1)$$

where  $i$  – the serial number of the machine;  $n$  – number of machines;  $q_{max}$  – maximum amount of chips to be removed in one minute on a metal cutting machine.

The power utilization factor can be represented in the form of the following formulas:

– for one machine

$$\eta_{M_i} = \frac{q_{M_i}}{q_{max_i}} \quad (2)$$

where  $\eta_{M_i}$  – capacity factor by one machine;  $q_{M_i}$  – the amount of metal to be removed per one machine in 1 minute

– for the workshop (site)

$$\eta_M = \frac{Q_M}{Q_{max}} \quad (3)$$

where  $\eta_M$  – capacity factor by all machines;  $Q_M$  – the amount of metal, removed by all machines of the workshop or site in 1 min.

$$Q_M = \sum_{i=1}^n q_{M_i} \quad (4)$$

$$Q_M = nq_{M_{avr}} \quad (5)$$

where  $q_{M_{avr}}$  – the amount of metal removed per 1 minute per one machine on average.

However, the use of the above formulas (formula 1–5) is difficult, since for their application it is necessary to take into account a large number of processing conditions, which are determined by the quality of the tool, the material being processed and the quality of the internal mechanisms of the machine.

The quality of the material to be treated is characterized by hardness, strength, chemical composition, surface condition and ductility. During final processing, it is also necessary to take into account surface roughness and dimensional accuracy of the part. The quality of the tool used in the treatment is characterized by its material and geometry. The environmental quality of the machine, that is, the lubricating and cooling agents, is characterized by their composition and quantity.

Record of the variety of processing conditions presented above is possible based on the qualimetry assessment of productivity of the machine. For the qualimetry analysis of the production capacity of the machine it is necessary to establish its maximum qualimetry productivity (qualimetry production capacity – quali-power), determined by

the maximum possible amount of metal that can be removed by this machine under reference conditions in 1 minute of the cutting process. This value should not depend on the conditions of the product treatment, but is determined by the limiting parameters of the machine only which are constant.

The main task in this case is the development of methods for determining the maximum productivity of machines. To solve this problem, it is necessary to determine the maximum parameters of the removed chip volume for a certain period of time. The following conditions are set as limitations (Per, 2019):

- the power of the cutting process  $N_p$  should not exceed the power of the drive of the main movement  $N_{np}$ , taking into account the efficiency of the machine;
- the forces  $P$  and the rotational force  $M_{rf}$  arising during the cutting process should not exceed the forces  $P_c$  and the rotational force  $M_c$  allowed by the machine;
- the dimensions of the processed products  $G$  should not exceed those allowed by the machine  $G_k$ ;
- speeds of displacements (feeds)  $S$  and speeds of rotation  $n$  of the working parts of the machine must not be less than the minimum speeds allowed by the machine  $S_{min}$  and speeds  $n_{min}$ , and not greater than the maximum allowed by the machine  $S_{max}$ ,  $n_{max}$ ;
- the dimensions of the cutting tool  $L_i$  must be neither smaller nor bigger than the sizes allowed by the machine  $L_{min}$  and  $L_{max}$ . Symbolic record of the task in the general statement is:

$$V_M = f(v, s, t) \rightarrow (efficiency\ function) \quad (6)$$

$$\left\{ \begin{array}{l} N_p = \varphi_N(v, s, t, r^{st}) \leq N_{np} \\ P = \varphi_P(v, s, t, r^{st}) \leq P_c \\ M_{rf} = \varphi_M(v, s, t, r^{st}) \leq M_c \\ G \leq G_c \\ S_{min} \leq S \leq S_{max} \\ n_{min} \leq n \leq n_{max} \\ L_{min} \leq L \leq L_{max} \end{array} \right. \quad (7)$$

where  $v$  – cutting speed;  $t$  – cutting depth;  $r^{st}$  – factors taking into account standard conditions.

Using this method for specific machines and the necessary types of processing, it should be noted that the desired maximum quali-power of the machine will be obtained with certain combinations of cutting conditions. But it should be kept in mind that parameters that are not acceptable in practice from an economic and operational point of view may be calculated.

Based on the analysis of the machines, the following types of machine qualifications were identified:

- theoretical quali-power of the machine tool;
- real quali-power of the machine tool;
- actual quali-power of the machine tool;
- minute quali-power.

By theoretical power (quali-power) of a machine is meant its maximum productivity (quali-production) in one minute. In this work it is denoted by the symbol  $V_m$ .

The actual quali-power of the machine tool differs from the theoretical one in the fact that it takes into account the limited maximum treatment length on each particular machine and the corresponding additional costs of time during which the treatment process does not occur.

The actual quali-power is determined with the formula

$$V_a = \frac{V_M \cdot t_{o \max}}{t_{o \max} + t'_a} \quad (8)$$

where  $t'_a$  is conditional auxiliary time, taking into account the change of products with the maximum possible processing length;  $t_o$  – direct manufacturing time.

At present, the determination of the conditional auxiliary time ( $t'_a$ ) is a problem, since it should not depend on the specific products processed on this machine. To solve this issue, further theoretical research is needed.

By minute quali-power of a machine we mean a qualitatively measured volume of metal (metal quali-volume) removed in 1 minute of the treatment process.

The actual qualification productivity of the machine takes into account the necessary costs of auxiliary time and is determined with the formula

$$V_a = \frac{V_k \cdot t_o}{t_b} \quad (9)$$

where  $t_b$  – basic cycle time.

The utilization rate of the theoretical quali-power of the machine is determined by the ratio of actual productivity to the quali-power of the machine in the reference conditions:

$$\eta_t = \frac{V_k}{V_m} \quad (10)$$

The amount of metal being removed is measured by its corresponding volume of metal removed under reference processing conditions. The transformation of the real volume of metal removed under certain specific conditions into the quali-volume is a problem and the solution for practical application will be the next stage of this research in future.

## RESULTS AND DISCUSSION

As an example of the application of this methodology, we will consider the processing of a product on a 16K25 lathe (SCL, 1975).

Workpiece material – steel 20XM, rolled steel.

The diameter of the workpiece is 100 mm. The workpiece is fixed in the chuck, the part is treated from the loose side, the diameter after the workpiece is 92 mm, and treatment is performed with one tool. As a tool, a straight cutter with a hard alloy plate is used, and the main angle in the bar is 75°.

To calculate the data, we accept the following parameters (HME, 1985; Liang & Shin, 2016):

- feed (s) 1 mm rev<sup>-1</sup>
- cutting depth (t) 3 mm
- cutting speed.

$$v = \frac{C_v}{T^m \cdot t^x \cdot s^y} \cdot k_v \quad (11)$$

where  $C_v = 338$ ;  $x = 0.15$ ;  $y = 0.45$ ;  $m = 0.20$ .

Tool life (T) is set to 60 minutes

$$k_v = k_{mv} \cdot k_{nb} \cdot k_{ub} \cdot k_\varphi \quad (12)$$

where  $k_{mv} = 0.87$ ;  $k_{nb} = 0.86$ ;  $k_{ub} = 1$ ;  $k_\varphi = 0.8$ ;  $k_v = 0.599$ ;  $v = 75.7 \text{ m minute}^{-1}$ .

$$t_o = \frac{l}{s \cdot n} = \frac{150}{1 \cdot 276} = 0.54 \text{ minute}$$

where  $t_o$  – direct manufacturing time.

For reference conditions  $k_v = 1$ ;  $t_{st} = 3$ ;  $s_{st} = 1$ ;  $v_{st} = 122 \text{ m minute}^{-1}$ .

$$n_3 = \frac{1,000 \cdot 122}{3.14 \cdot 100} = 388 \text{ rpm}$$

$$V_t = V_k \cdot t_o = \pi \cdot d \cdot t \cdot s \cdot n \cdot t_o (\text{mm}^3)$$

where  $V_t$  – quali-volume of the removed metal in time  $t_o$ ;

$$V_k = 3.14 \cdot 100 \cdot 3 \cdot 1 \cdot 388 = 365,496 \text{ mm}^3 \text{ minute}^{-1}.$$

$$V_t = 365,496 \cdot 0.54 = 197,368 \text{ mm}^3 = 197,4 \text{ cm}^3.$$

Machine quali-power 16K25 is  $V_m = 668 \text{ cm}^3 \text{ minute}^{-1}$ .

The utilization factor of the theoretical power in this case will be:

$$\eta_t = \frac{365.6}{668} = 0.55$$

The described method shows the possibility of applying the qualimetry analysis for an objective assessment of the use of metal-cutting equipment.

Improvement of machine productivity is discussed also in other findings and some of them are ‘based on registering the moment when the cutting tool touches the workpiece during a machining operation’ (Nenov et al., 2002). The performance of machines to a large extent depends on their mechatronic behavior (Frieß et al., 2014), but does not provide information on the maximum of the equipment capacity. At the same time it is noted by other authors that the need for accessing the machine tool performance and not rely solely only on the specifications was considered by Deshpande (2012).

Considering the research results, the most common indicators of social labour costs per a production unit are the cost price and reduced costs. But to obtain accurate workpieces, expensive technological equipment is needed, which, with production of small-scale and single-type workpieces, increases their cost so much that often this increase is not covered by a reduction of expenses for metal cutting and economy of metal. And since in the near foreseeable future, it is likely that these types of production will remain rather common in mechanical engineering, in many relevant cases the most representative and logically justified will be the determination of the productivity of metal cutting machines by the amount of metal chips cut per unit of time.

This article presents part of the study, which describes only the preliminary treatment of products, but at the same time, it would be the final treatment, if it is consistent with the process. Here we need to once again return to the issue measuring

productivity, because, in the area of treatment technology, such directions as application of precision blanks and low-waste technologies can lead to the fact that the problem of the objective use of the production capacity of metal-cutting sections in preliminary procession is outdated and does not require attention.

## CONCLUSIONS

In conclusion it should be noted that qualimetry, used for measuring the amount of chips removed, allows setting the maximum productivity of metal-cutting equipment basing on the quantitative indicators given in the machine passport. The energy power of the main movement drive appears to be the main indicator. It should be noted that the quali-power of the machine is an objective indicator of its quality, which does not depend on specific working conditions at any given time.

For the practical application of the theoretical foundations given in this study, further development of the appropriate methodology for the application of qualimetry analysis of the production capacity of metal-cutting equipment is required.

## REFERENCES

- Azgaldov, G.G., Glichev, A.V. & Panov, V.P. 1968. What is quality? *Ekonomika*, Moscow, 135 pp. (In Russia).
- Chan, A.H.S., Hoffmann, E.R. & Chung, C.M.W. 2017. Subjective estimates of times for assembly work. *International Journal of Industrial Ergonomics* **61**, 149–155. doi: 10.1016/j.ergon.2017.05.017
- Deshpande, A. 2012. An empirical study to evaluate machine tool production readiness and performance. *The International Journal of Advanced Manufacturing Technology* **64**(9-12), 1285–1296. doi: 10.1007/s00170-012-4086-3
- Ermilov, V.V. & Perevoshchikov, Yu.S. 2018. *Economic metrology and qualimetry of labor: Automated system for calculating the qualimetric characteristics of machine parts based on CAD Compass 3D (Part 1 and 2 of the topic 1.4.10. Development of the concept of qualimetry analysis for areas of economic activity)*. Udmurt University Publishing Center, Izhevsk, 194 pp. (in Russia)
- Frieß, U, Hellmich, A., Hipp, K, Rentzsch, H. & Wabner, M. 2014. Machine-tool Productivity and Resource-efficiency through Mechatronic Simulation. In Neugebauer, R. & Drossel, W.-G.; (eds): *proceedings of the 3rd International Colloquium of the Cluster of Excellence eniPROD*. Technische Universität Chemnitz, Chemnitz, Germany, pp 325–347.
- Gardner Intelligence. 2018. World machine tool survey, Inc Gardner Business Media. Licence: <https://www.gardnerintelligence.com/>
- Golabchi, A., Han, S.U., AbouRizk, S. & Kanerva, J. 2016. Micro-motion level simulation for efficiency analysis and duration estimation of manual operations. *Automation in Construction* **71**, 443–452. doi: 10.1016/j.autcon.2016.08.028
- HME. 1985. *Handbook of a mechanical engineer*. Mashinostroenie, Moscow, 496 pp. (In Russia).
- Koptak, M., Džubáková, M., Vasilienė-Vasiliauskienė, V. & Vasiliauskas, A.V. 2017. Work standards in selected third partylogistics operations: MTM-LOGISTICS Case Study. *Procedia Engineering* **187**, 160–166.

- Liang, S.Y. & Shin, A.J. 2016. *Analysis of machining and machine tools*. Springer, Boston, MA, 230 pp.
- Maksimov, D.G. & Kalkis, H. 2018. Ergonomic modelling parameters and the influence of ergonomics on planning workplaces. *Agronomy Research* **16**(4), 1762–1770. doi: 10.15159/AR.18.169
- Maksimov, D., Kalkis, H., Perevoschikov, Y. & Roja, Z. 2019. Use of qualimetry method in production labour estimation. *Agronomy Research* **17**(S1), 1123–1131. doi: 10.15159/AR.19.127
- Maynard, H.B., Stegmen, G.J. & Schwab, J.L. 1948. *Methods-time measurement*. McGraw-Hill Book Co., New York, 252 pp.
- Nenov, G.V. & Szécsi, T. 2002. Increasing CNC machine tool productivity by using tool-part touch control. *Robotics and Computer-Integrated Manufacturing* **18**(3-4), 291–296. doi: 10.1016/s0736-5845(02)00020-0
- Orefkov, V.V. & Perevoschikov, Y.S. 2007. *Ergonomics rate fixing of labor*. Publishing House VCUZh, Moscow, 934 pp. (In Russian).
- Per, Yu.S. 2019. *Economic metrology. Qualimetry in project management*. Udmurt University Publishing Center, Izhevsk, 448 pp. (In Russian).
- Perevoschikov, Yu.S., Bobkov, V.N. & Nemirovchenko, N.M. 2005. *Qualimetry economics of an enterprise (clothing industry)*. VZUZH, Moscow, 570 pp. (in Russian).
- Perevoschikov, Yu.S. 2015. *Economic metrology. Labor qualimetry*. VZUZH, Moscow, 504 pp. (in Russian).
- Podzorov, A.V. 2018. Formation of technical and operational indicators of the department park of special equipment. *Quality and Life* **3**, 79–81.
- Smailovskaya, M.S., Boim, A.G., Gonyalin, S.I. & Grishin, V.M. 2011. Global developments in machine-tool production in 2010. *Russian Engineering Research* **31**(11), 1124–1132. doi: 10.3103/s1068798x11110244
- SCL. 1975. *Screw-cutting lathe. Model 16K20, 16K20P, 16K20G, 16K25. Manual*. Moscow, 68 pp.
- Taylor, F.W. 1923. *The principles of scientific management*. Harper, New York, 145 pp.
- Thomson, R. & Webster, E. 2013. Innovation and Productivity. *Australian Economic Review*, **46**(4), 483–488. doi: 10.1111/1467-8462.12046
- Yi, W. & Chan, A.P.C. 2014. Critical Review of Labor Productivity Research in Construction Journals. *Journal of Management in Engineering* **30**(2), 214–225. doi: 10.1061/(ASCE)ME.1943-5479.0000194

## **New approach for recycling spare parts, components and assemblies**

V. Mitrofanovs\*, I. Boiko and Ē. Geriņš

Riga Technical University, Institute of Mechanics and Mechanical Engineering,  
Kipsalas 6B, LV-1048 Riga, Latvia

\*Correspondence: v.mitrofanovs@meistars.lv

**Abstract.** Recycling and disposal are one of the most complicated topics in the lifecycle of a mechanism, especially in case of previous generations of machines that were designed without taking any care of post exploitation period. In the current work, the ‘feasibility points’ of recycling units, methods of recycling as well as pricing formation for recycling materials, reviewed and proposed by several world universities and scientific bureaus and applied by major world brands have been analysed. The general principles that should be rated as a basis when designing and creating new mechanisms, as well as the actions which we consider as a necessary supplement to the existing rules of the lifecycle of assemblies and which should be applied in practice, were introduced by authors in the ‘Management of parts and components for units and assemblies in mechanical engineering industry and its impact on the environment’. It was discovered that even modern assemblies, not to mention previous generations, are being designed without taking into consideration any possibilities of easy recycling the used materials. The number of components of mechanisms, which are being repaired as assemblies, is continuously increasing, while maintainability and repairability of separate parts is decreasing. Taking into account the state of the art in the field, the new approach for promoting the reusing natural resources and decreasing the harmful effects of obsolete components of mechanisms on the environment is proposed.

Thus, using the fast-moving parts that in post operational period can be easily detailed by type of a material will ensure more efficient consumption of natural resources. Our research and developments significantly reduce the costs of recycling and these materials become competitive comparing to the new ones.

Taking into account the state of the art in the field, the new approach for promoting the reusing natural resources and decreasing the harmful effects of obsolete components of mechanisms on the environment is proposed.

**Key words:** management of parts and components, impact on the environment, parts recycling.

### **INTRODUCTION**

Any modern manufacturer of mechanisms and components has the only goal – making profit. All designs and technological processes are subjected to the cost reduction of producing finished products.

Attention should be drawn to the fact that today none of the component manufacturers include into their technological process or take into consideration

recycling and disposal methodologies of their own products. Well-known methods for the development, production, operation and disposal of machine components are presented in the considerable amount of the scientific papers as well as in educational literature with the references to the current legislation, particularly in the European Union, for instance in (Duales System Holding, 2012; Driessen et al., 2015; Sanden et al., 2016; Schweitzer et al., 2017).

According to the traditional approach, the main accent is on the green manufacturing and maintenance of the products. Herewith, the utilization and reusing of the scrap are stated as a separate block of the Product life-cycle management (PLM) and considered only after a product is presented to the market. For instance, one of the well-known 3Rs ('reduce, reuse, recycle') – reuse – promoted by environmental agencies in many countries, covers a range of activities from informal product exchanges between acquaintances to industrial reuse of products and components (Cooper & Gutowski, 2015). However despite of efforts there is still minimal effect of the declared strategy to the reality. For example, European Commission statistics claim that currently in Europe 16 tonnes of materials per person per year are used and 6 tonnes of that becomes waste. Due to faulty waste management a significant amount of secondary raw materials, like metals, glass and plastics still get lost from the material stream (Karavida & Nommik, 2015).

On the other hand, in (Cooper & Gutowski, 2015) it is pointed out, that researches determine the theoretical maximum steel reuse rates for different product categories, none of which are above 30%. Moreover, the underlying assumption that reused products perfectly displace new items may often be incorrect. Threerby in the previous works of the authors, in particular, 'Management of parts and components for units and assemblies in mechanical engineering industry and its impact on the environment', the discussion about the necessity to introduce changes to the regulations and legislation that would force manufacturers to develop methods of recycling the used materials already during the design phase of the product was initiated.

A key thesis of the previous work (Mitrofanovs et al., 2019) was to introduce changes into the product life cycle by taking into account the influence of all factors on setting up the technical specifications for product design and implementing the ECO solutions being developed by authors (Fig. 1). On the Figure 1 the bright fields indicate the changes we bring into the already known pattern of the Product life-cycle. According to the proposed new approach, designers should include the reusing technology of the materials/components used in the project during the initial stages of the design. Implementation of the new model of the PLM (together with the actualization of the EU legislation), which provides the synergy between design and regeneration of the machine components, will reduce the utilization of the materials and increase it reusing.

Thus, the main point which could be changed is the 'Technical specification with new ECO solutions' (Fig. 1) contains the following elements (supported and regulated by the legislative framework, i.e. Ecological law):

- Technical requirement;
- Design and engineering;
- Economic evaluation;
- Production technology;
- Production engineering;
- Maintenance and repair equipment;



- Technology of recycling;
- Economic feasibility.

Each of the new points proposed, requires new methods of preliminary analysis and modelling, which are undoubtedly should be based on the practices of the available studies and researches in the world.

It is crucially important that the legislation (Ecological law) would indicate to the product manufacturers the processes which can reduce the negative impact of the Product life-cycle on the environment in general (Sanden et al., 2016).

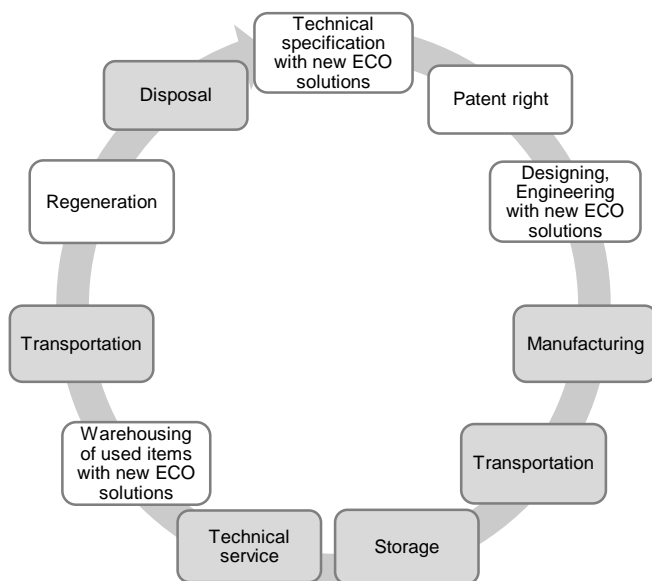


**Figure 1.** New vision of Product life-cycle.

Within further research authors consider possible scenarios for solving the tasks described above and possibilities of introducing these solutions into production, which would save logistics time, reduce inventory, deadstock, disposal of used and obsolete assembly units and components. The solution of each task will significantly reduce the consumption of natural resources, energy and negative impact of disposal on the environment.

However, our latest studies have shown that there are some more factors having influence on the result of the regeneration of the used materials and using recycled materials. As can be seen on the diagram of the production cost (Fig. 2), the basis is technological cost, which consists of raw materials, fuel and energy. All these components are independent of the manufacturer and their price is defined by exchange quotations and conditionally can be considered as Germanized for the region.

Unfortunately, it was revealed that manufacturers do not take into account the costs of recycling materials (see on the Fig. 3), so the manufacturer is not interested in the processes of sorting and regenerating used products. Currently, sorting and disposal of the components which life-cycle has been finished is carried out by specialized companies focused on this or that type of processing materials (Grafov, 2011). The full cost of the secondary raw materials is shown on the Fig. 3.

The more complex and accordingly more expensive way of used materials till processable secondary raw materials we have, the less expedient is the detailed processing of the used materials (Fig. 2). The feasibility of the entire technological process of material regeneration is in the interval between the sorting of the recycling materials and the exchange prices of the secondary raw materials.

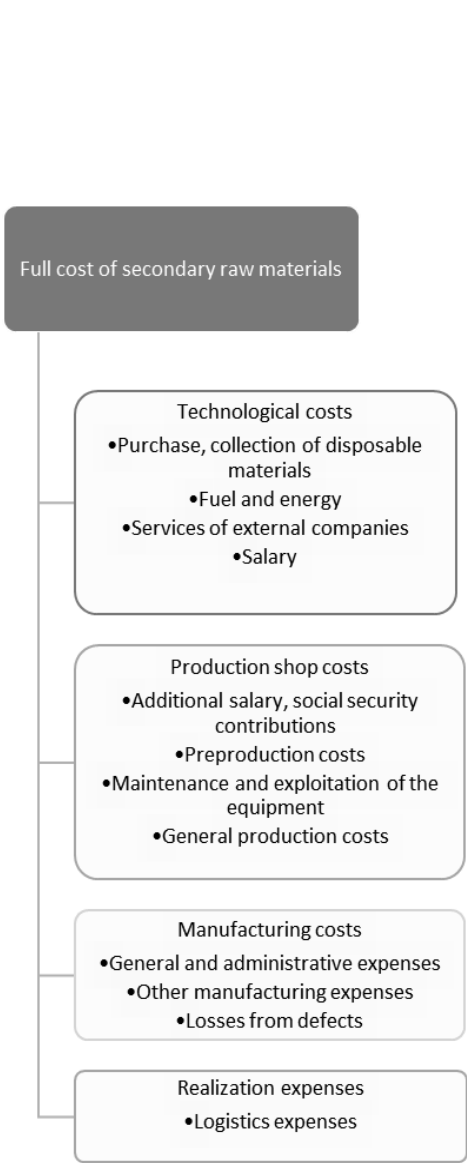


**Figure 2.** Diagram of the production cost.

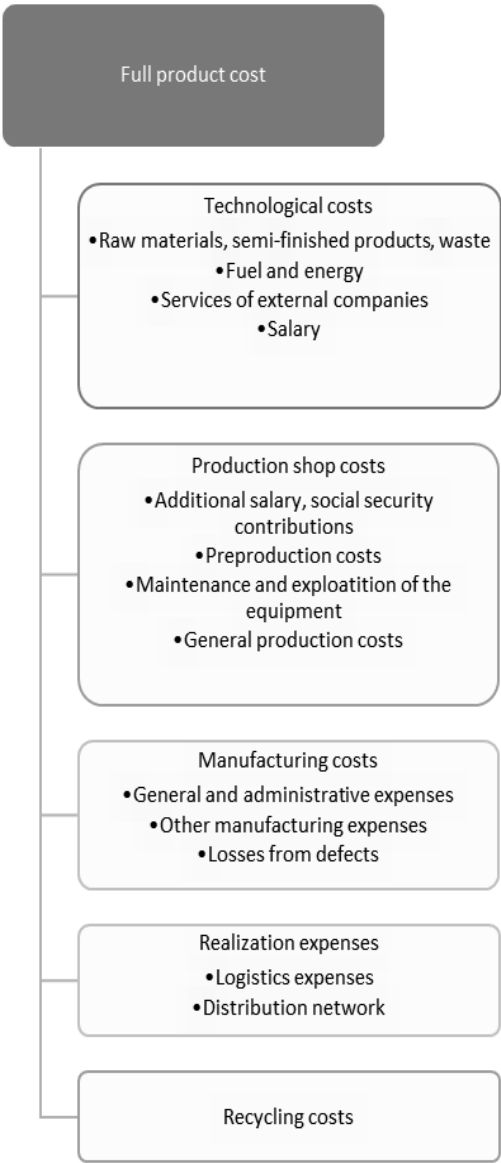


**Figure 3.** Diagram of full cost of the secondary raw materials.

In mass production, recyclers of the secondary raw materials cannot be 100% sure of the chemical composition of the materials, which implies a wider range of chemical composition tolerance, so as a result these products made of these materials can be only used for less critical structures.

Studies done by M. Orzolek (Orzolek, 2019), as well as studies of Recycling Research Institute (Recycling Research Institute, 2019) and others (Watkins & McAleer, 2004), show that the more complex the combination of composite materials, the less economic feasibility of recycling them (Fig. 4).

As a rule, complex materials are being cut into pieces and disposed in the ground or burned in furnaces. It might sound shocking, but in some countries, where environmental law does not apply, the burning of waste materials occurs in an open way (Fig. 5). According to the research of Recycling Research Institute only 7% of tires are being recycled and new products are being produced from the obtained materials.

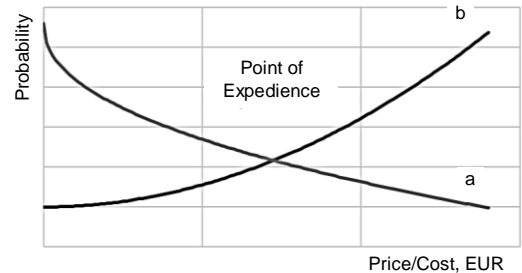


**Figure 4.** Probability of recycling: (a) price of recycled material and (b) cost of recycling the complexity of the material.

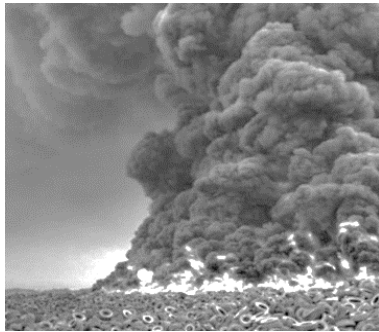


**Figure 5.** Burning tires.



**Figure 6.** Cars rest is grinding without dismantling.

In authors' opinion it is extremely important that the materials of quick wear assemblies, within reasonable limits, would be regulated by the legislative framework, and the manufacturer, already at the time of construction, would develop and provide the public with methods of maintainability, dismantling and recycling. The aim of this work is to develop a new approach for promoting the reusing natural resources and decreasing the harmful effects of obsolete components of mechanisms on the environment.

According to the Grüne Punkt the actual amount of recyclable materials from automotive industry is only 10%, while the rest is grinding without dismantling and disposal (Squintani, 2013). Avrashkov L.Y. also points out this problem in his works (Fig. 6) (Avrashkov, 2015).

## NEW APPROACH

In fact, manufacturers of assemblies can regulate several factors that make their recycling cheaper:

Ease of the dismantling of the assembly.

2. Standardization of the used materials.

3. Standardization of the collection of the used assemblies.

Acceptable correction in the country of the cost of raw materials, fuel and energy is possible only on the part of the government, which is able to provide subsidies for production, introduce tax preferences, introduce or cancel excise taxes (Fig. 7).

In countries with high labour costs and high excise taxes on energy, materials processing is extremely expensive. Therefore, in most cases, the entire technological cycle of processing is limited to the collection and optimization of the volume of worn assemblies. 'Raw materials' are sold, or sometimes delivered to countries with costs for low energy-intensive production, or to countries with 'sparing' environmental laws that allow waste to be disposed without separation and without environmental standards.

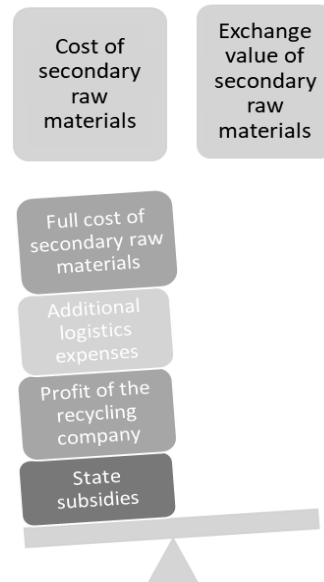


**Figure 7.** Prices model of secondary materials.

## RESULTS AND DISCUSSION

Taking into account the state of the art in the field, the new approach for promoting the reusing natural resources and decreasing the harmful effects of obsolete components of mechanisms on the environment is proposed. Thus, using the fast-moving parts, that in post operational period can be easily detailed by type of a material, will ensure more efficient consumption of natural resources. Research and developments done significantly reduce the costs of recycling and these materials become competitive comparing to the new ones.

It is necessary to change environmental legislation and, as we consider, to supplement the previously proposed Technical specification with new ECO solutions with the new points:

1. At the phase of product design, the manufacturer must propose a regeneration methodology.

2. The manufacturer must agree with the regenerating organizations on the labelling of the assemblies in order to ensure easy sorting of the used materials.

3. The manufacturer must agree on the methodology for collecting waste materials and assemblies with utilizing organizations.

4. In the development of new assemblies, the manufacturer is obliged to develop a methodology for producing easily dismantlable assemblies, while ensuring the ability to sort materials by their type.

5. The manufacturer is obliged to use environmental standards for fast moving parts.

Including of the mentioned points will significantly reduce production costs for storage, disassembly and sorting. This will increase the level of identification of recycled material.

As a result, it will significantly reduce the cost of secondary raw materials and increase its quality (Fig. 8), which in turn will become attractive from an economic point of view for use in new products, reduce the burden on the use of new materials and will significantly affect the environmental situation in general.

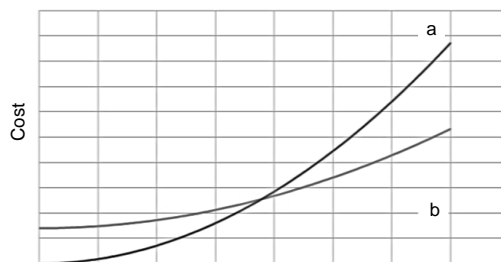


**Figure 8.** The complexity of the material: a) cost of new material; b) cost of recycled material.

## CONCLUSIONS

The new approach for recycling spare parts, components, and assemblies, which is a substantial part of a new vision for Product Life-Cycle management (PLM) is proposed. The necessity to promote the new vision for PLM is the fact, that the number of components of mechanisms, which are being repaired as assemblies, is continuously increasing, while maintainability and repairability of separate parts is decreasing.

According to the proposed new approach, designers should include the reusing technology of the materials/components used in the project during the initial stages of the design. Thus, using the fast-moving parts, that in post operational period can be easily detailed by type of a material, will ensure more efficient consumption of natural resources. Implementation of the new model of the PLM (together with the actualization of the EU legislation) significantly reduce the costs of recycling and these materials become competitive comparing to the new ones.

## REFERENCES

- Avrashkov, L.Y. Utilizacija starih avyomobilei: problemi i persepektivi. 2015. (in Russian).
- Cooper, D.R. & Gutowski, T.G. 2015. The Environmental Impacts of Reuse, A Review. *Journal of Industrial Ecology* **00**, 1–19.
- Driessen, M.A., Arts, J.J., van Houtum, G.J., Rustenberg, W.D. & Huisman, B. 2015. Maintenance Spare Parts Planning and Control: A framework for control and agenda for future research. *Production Planning & Control* **26**(5), 407–426.
- Duales System Holding GmbH & Co. KG. (2012): DSD continues to expand its processing business. Press release of 06.06.2012 (in German).

- Grafov, A.V. Pricing and competitiveness of secondary ferrous metals. 2011. *Vestnik Saratovskogo gosudarstvennogo socialno-ekonomicheskogo universiteta* **2**, 9–12. (in Russian).
- Karavida, S. & Nommik, R. 2015. *Waste Management of End-of-Service Wind Turbines*, Aalborg University Aalborg, Denmark, 63 pp.
- Mitrofanovs, V., Boiko, I. & Gerins, E. 2019. Management of parts and components for units and assemblies in mechanical engineering industry and its impact on the environment, *Agronomy Research* **17**(S1), 1138–1145.
- Orzolek, M. 2019. *A Guide to the Manufacture, Performance, and Potential of Plastics in Agriculture*. Elsevier, UK, 224 pp.
- Sanden, J., Lüneburg, Wilts, H. & von Gries, N. 2016. *Development of instruments and measures to increase the use of secondary raw materials – with a focus on secondary plastics*. Wuppertal Institute, Wuppertal, Germany, 346 pp. (in German).
- Schweitzer, J.-P. Eliaerts, S., Gionfra, S., Jones, H., Nanni, S. & Solovieva, A. 2017. *Supporting the Market for Secondary Raw Materials in a Circular Economy*, IP/A/ENVI/2016-17, The Institute for European Environmental Policy (IEEP), European Parliament, Brussels, Belgium, 42 pp.
- Scrap Tire & Rubber Users Directory. 2019. Recycling Research Institute, Leesburg, USA, 28<sup>th</sup> Edition, 44–73.
- Squintani, G.O. 2013. PTC presentation at Spare Parts. Available at <https://www.slideshare.net/Copperberg/giacomo-quintani>
- Watkins, C. & McAleer, M. 2004. Econometric modelling of non-ferrous metal prices. *Journal of Economic Surveys* **18**(5), 651–701.

## **Airflow profile study of a compost dairy barn using a low-cost 3D-printed anemometer network**

F.A. Obando Vega<sup>1,\*</sup>, A.P. Montoya Rios<sup>1</sup>, F.A. Damasceno<sup>2</sup>,  
J.A. Osorio Saraz<sup>1</sup> and J.A. Costa Do Nascimento<sup>2</sup>

<sup>1</sup>Universidad Nacional de Colombia sede Medellín, Facultad de Ciencias Agrarias, Departamento de Ingeniería Agrícola y Alimentos, CO050034 Medellín, Colombia

<sup>2</sup>Federal University of Lavras, Department of Engineering, BR37200-000 Lavras, Minas Gerais, Brazil

\*Correspondence: faobando@unal.edu.co

**Abstract.** Mechanical ventilation is commonly used for environmental thermal regulation inside closed-field agricultural production systems. Analyzing the air distribution inside these facilities and the correct operation of the fans can be a challenging. This could be determined using cost prohibitive techniques as particle image velocimetry or deploying large wind sensors networks on-site. To avoid this limitation without a lack of measurement accuracy, this research was focused on developing and test a low-cost anemometer network based in low cost propeller's anemometers, built using fused 3D-printed and open-hardware platforms. Four propeller anemometers with three to six blades were simulated using the 6-DOF method of ANSYS computer fluid dynamics software. Similar results were obtained for all the simulated models with minor differences. Anemometers were tested in an open circuit wind tunnel before to be evaluated in two open compost dairy barn building using high-volume low-speed and low-volume high-speed fans. Data were analyzed by employing contour maps, descriptive statistics and correlation. The results show that the anemometer network determines the fan's wind profile for wind speeds over  $0.7 \text{ m s}^{-1}$  and it was possible to determine the facilities spots with ventilation problems. The proposed anemometer network and methodology are a good alternative to analyze the operating conditions of the tested agricultural facilities and optimize its performance.

**Key words:** ventilation optimization; CFD; wind tunnel; Arduino; sensor network; directional anemometer; compost barn.

## **INTRODUCTION**

The air quality and homogeneity inside closed-field agricultural production systems such as greenhouses and plant factories (R.R. Shamshiri et al., 2018) depends on a good natural and mechanical ventilation. In order to have a suitable environment for the development of agricultural practices, adequate ventilation rates and air distribution are needed (Samer et al., 2011). The behavior of the airflow inside those facilities have been evaluated employing different techniques: Computer Fluid Dynamics (CFD) simulations, tracer gas and anemometer networks, among others. Being the last ones cost prohibitive (Fiedler et al., 2013; van Dooren & Sapounas, 2013; Bustamante et al., 2015). The characterization of airflow distribution in mechanical ventilated installations,

employing these techniques, allows to evaluate the performance of the ventilation system (R. Shamshiri & Ismail, 2012).

In particular, compost dairy barns are facilities that require an adequate control of the ventilation rates and air distribution in order to guarantee the compost drying homogeneity, the livestock bioclimatic comfort and proper management of gas emissions. The number of fans and its location in these facilities depend of the livestock density (Black et al., 2013) regardless the compost ventilation requirements. This kind of installations would benefit of the inside air distribution analysis near to the floor surface. No scientific publication related with the evaluation of the ventilation rate over the compost drying process was found. Air distribution analysis are also an important tool in modern greenhouses to characterize its ventilation and its relation with the microclimatic variables, several references in this matter can be found in literature (R. Shamshiri, 2017).

The low ventilation rates in closed-field agricultural facilities limits a uniform microclimate (R.R. Shamshiri et al., 2017), hence different types of anemometers are used for measuring air velocity. The most used types are the hot wire and the ultrasonic ones, which are some of the most expensive ones (Gao et al., 2016). Therefore, its implementation in sensor networks, composed by several anemometers, is limited. Hence, the rate and air profiles in these type of installations have been done mostly with CFD simulation (Zajicek & Kic, 2012; van Dooren & Sapounas, 2013; Vilela et al., 2019) and/or employing the tracer gas technique. In this matter, the tracer gas technique was used to compute the ventilation rate in two naturally ventilated dairy barns (Kiwani et al., 2012) with good results. While Calvet et al. (2010) found that the tracer gas technique underestimated the measurement when comparing with the direct measurement of the ventilation rate. However, van Dooren & Sapounas (2013) developed CFD simulations models to improve tracer gas techniques to measure the ventilation rate and pattern flow of from naturally ventilated livestock buildings with good agreement between measured data and computational results.

Mechanical anemometers are the most commonly used sensor for wind velocity measurement in climatic applications (Pindado et al., 2012). Among them, the low friction propeller anemometers are the most suitable for measuring low wind velocities, because their low starting speed and being less prone to overspending (Camuffo, 2019). Due to the elevated cost and measurement complexity of the air velocity implementation in real scale facilities (Luck et al., 2014; Bustamante et al., 2017), it is imperative to have low cost anemometer sensor networks that allows the study of air distribution in agricultural facilities. Particularly in the case of compost dairy barns facilities, it is necessary to study the behavior of the air near the floor to ensure an efficient drying rate of the compost.

Using 3-D printing it is possible to develop anemometers with specific characteristics for wind speed measurement in closed-field agricultural production systems. In this issue Leoni et al. (2018) developed a spherical anemometer, with 0 to 20 m s<sup>-1</sup> range of measurement using a 3D-printed with good results. Employing low-cost development platforms, it is possible to implement measurement systems for acquiring data from multiple sensors simultaneously, as it did (Obando Vega et al., 2020). In this area, (Gao et al., 2016) developed a low cost omnidirectional anemometer, based on Arduino platform, with measurement range of 0 to 6 m s<sup>-1</sup> for multipoint measurement applications. The developed anemometer sensor network could



be used to characterize wind behavior in agricultural facilities or ventilation systems, as was proposed by (Samer et al., 2011).

The developed anemometers can be calibrated in wind tunnels, as proposed by (Pindado et al., 2012), who studied the calibration of several mechanical anemometers, employing this technique. The aerodynamic behavior of the low-cost sensors could be studied using CFD simulation employing models with 6 degrees of freedom (CFD/6-DOF). This technique has been used by several authors to study the dynamics of the movement of a solid body against a fluid or vice versa. This novel technique has been applied to evaluations of wind turbines by several authors (Dunbar et al., 2015).

In the present work is proposed: (1) to develop four types of low-cost propeller's anemometers, using a 3D-printed and open-source development platform ([www.arduino.cc](http://www.arduino.cc)); (2) to study the dynamic behavior of the anemometers using CFD/6-DOF simulation, in order to evaluate their performance and select the most suitable instrument for measuring low wind speeds, by comparing its Root Mean Square Errors (RMSE) and settling times; (3) to calibrate the anemometers in an open circuit wind tunnel; (4) to implement a network of 10 sensors for the measurement of airflow velocity speed profiles using the anemometer model with the best performance; and (5) to study the air distribution in two compost dairy barns with mechanical ventilation, establishing the speed profiles near the ground surface and the air homogeneity distribution at compost surface.

## MATERIALS AND METHODS

### CFD analysis

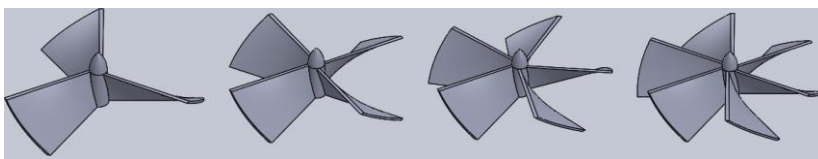


**Figure 1.** Propeller design with CAD software using different number of blades.

Four propeller anemometers of 150 mm of diameter and different number of blades (3 to 6) were designed employing SOLIDWORKS® CAD software (Fig. 1). The rotation speed of each propeller for specific airflow velocities were determined by mean of the ANSYS® R17.0 computer fluid dynamics (CFD) software using the dynamic mesh method and the 6-DOF solver (Ansys Inc., 2016) through simulations in transient state. ANSYS Fluent software was employed to solve the CFD model with convergence criteria of  $1 \times 10^{-3}$ . In order to determine differences between the propellers and to select the best suitable configuration, an airflow velocity of  $1 \text{ m s}^{-1}$  was established for the CFD simulations. A cylindrical shape around the propeller was considered as control volume of the CFD simulation, with 300 mm of diameter, 300 mm upstream and 500 mm downstream. In order to improve the CFD meshing process, the control volume were divided in four parts (Fig. 2), the first one enclosure the propeller surface, the second included the air flow around the propeller, finally the third and fourth ones include the upstream and downstream flow from the propeller. For the purpose to capture the

dynamics of the flow in the propeller surface, an inflation layer with a distance of  $1 \times 10^{-4}$  m from the surface, a growth rate of 1.2 and 5 layers maximum were implemented. A proximity and curvature mesh size function with a growth rate of 1.8 was used. To select the appropriate mesh size that gives a good balance between accuracy, computational time, and propeller rotation speed, a mesh sensibility analysis for the four-blade propeller was performed, for an airflow velocity of  $1.5 \text{ m s}^{-1}$  and three mesh sizes characterized by coarse, medium and fine relevant center sizes (Table 1). The orthogonal quality ( $> 1.0$ ) and the skewness statistics ( $< 0.9$ ) were used to quantify the goodness of the meshing process and the differences between the CFD results and the running computational time help to select the best mesh sizes.

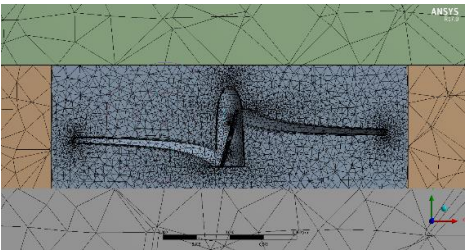


**Figure 2.** Four-blade propeller ANSYS mesh.

**Table 1.** Number of nodes, elements and statistics for the three mesh sizes used for the mesh sensibility analysis performed to the four-blade propeller

Mesh size		Coarse	Medium	Fine
Number of nodes		66767	70910	90379
Number of elements		212114	234177	325779
Orthogonal quality	Min	0.12543	0.11164	0.11161
	Max	0.99806	0.99664	0.99749
	Avg	0.7619	0.7663	0.79042
	SD	0.14297	0.1408	0.13299
Skewness	Min	$5.604 \times 10^{-6}$	$1.2217 \times 10^{-6}$	$2.9459 \times 10^{-6}$
	Max	0.86132	0.88939	0.86896
	Avg	0.38199	0.37329	0.33801
	SD	0.16854	0.16931	0.16907

The  $k-\varepsilon$  RNG turbulence model and near-wall treatment were used to capture the dynamics of airflow near to the propeller surface. A first order implicit model for transient formulation and a SIMPLE scheme for pressure-velocity coupled were used as solutions methods. For the transient simulations, a small fixed step of 0.001 s was used for the entire simulation, starting with a time step of 0.0001 s for the first 20 iterations and then increasing the step size to 0.00015 s for the next 20 iterations, due to convergence issues. A Hewlett-Packard Z44 workstation desktop computer with four processors in parallel and one GPU was used to solve the CFD simulations.

The Normalized Mean Square Error (NMSE), as recommended by (ASTM, 2019) was employed to quantify the agreement between the CFD results and the experimental data. NMSE values less than 0.25 are accepted as good indicators of agreement.

### Wind tunnel calibration test

ABS fused (Acrylonitrile Butadiene Styrene) 3D-printed models of the four propeller anemometers (Fig. 3, a), obtained with a height layer of 0.2 mm, were tested in an open circuit wind tunnel (Fig. 3, b). The propeller's axis rest on one ball bearing

(608ZZ) housed in an ABS 3D-printed support. The rotational speed of the propeller was measured using an encoder coupled to the propeller's axis (Fig. 3, c). The encoder was conformed by a perforated ABS 3D-printed wheel and a VISAY TCST2103 optical sensor ([www.vishay.com](http://www.vishay.com)), giving 15 pulses per propeller revolution. The number of pulses were determined with the low-cost open-source Arduino Nano microcontroller ([www.arduino.cc](http://www.arduino.cc)). For this, a general purpose input and a timer interrupts were configured to count the number of pulses per second (*pps*) and converted it to revolution per minutes (RPM). The Arduino Nano can monitor two encoder simultaneously. Data was send every 10 s to a master station for recording in a micro-SD memory. This master station was conformed by an Arduino Mega 2560 with the capacity to receive data in real time from several anemometers employing the  $I^2C$  protocol ([www.i2c-bus.org](http://www.i2c-bus.org)). The master station has a real time clock module (RTC DS3231-[www.adafruit.com](http://www.adafruit.com)) for keeping track of time and an  $I^2C$  LCD for displaying purposes (Fig. 3, d). The open-circuit wind tunnel has a test area of 0.5 m width  $\times$  0.5 height m  $\times$  1 m large. It was composed by a *SIEMENS*® three-phase exhaust fan (2CC2-634-5YB6T), controlled with a 2 hp *SIEMENS SINAMICS V20*® variable frequency drive. A Gill WindSonic® ultrasonic anemometer ([www.gillinstruments.com](http://www.gillinstruments.com),  $\pm 2\%$  accuracy, 0 to 60 m s<sup>-1</sup> range of measurement) was used as reference airflow velocity sensor. The airflow velocity was varied from 0 to 4.25 m s<sup>-1</sup>. The experimental results were compared with the CFD simulations results.

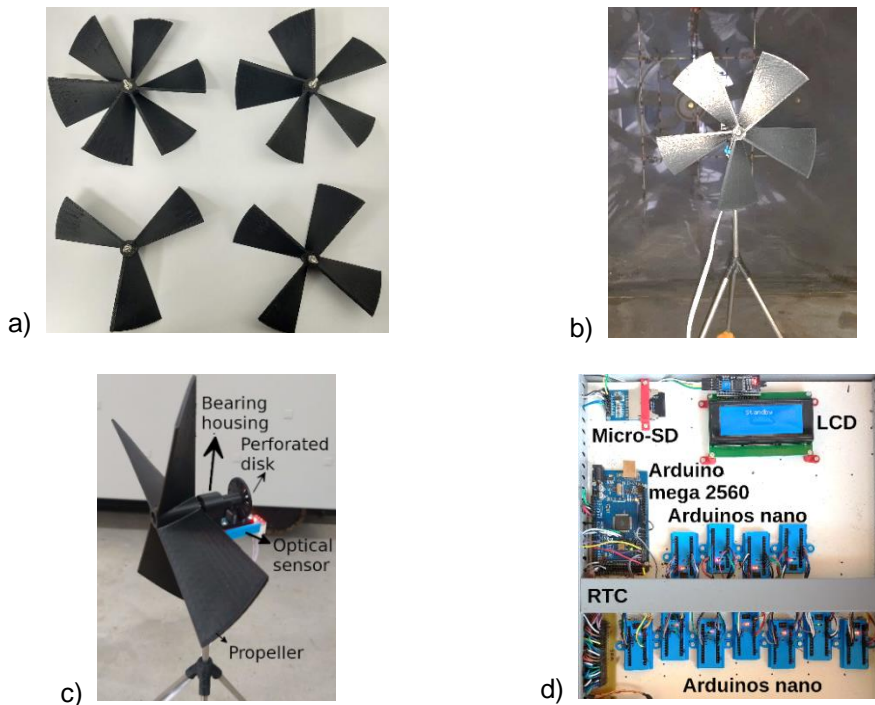


**Figure 3.** ABS 3D-printed propeller anemometers and datalogger system: a) Propeller with different number of blades tested; b) Five-blade propeller anemometer inside the open circuit wind tunnel; c) Propeller anemometer assembly; d) Master station components.

### Compost dairy barn tests

An anemometer network composed by ten four-blade anemometers was implemented and installed in two cattle dairy buildings with compost barn bedded and mechanical ventilation. The network was used for determine the airflow velocity distribution at 0.3 m above the compost surface. The cattle dairy buildings were located in Brazil, in the state of Minas Gerais in the cities of Cláudio (Fig. 4, a, 20°24'38.8"S 44°36'51.4"W, dimensions of 19×49×4 m) and Perdões (Fig. 4, b, 21°06'28.5"S 45°02'09.8"W, dimensions of 20×40×4 m), employing high-volume low-speed (HVLS) fans (7.5 m diameter, 2 hp, operating at 70% of its rotation speed by means of a SIEMENS SYNAMICS V20® variable frequency driver) and low-volume high-speed (LVHS) fans (1.6 m of diameter, 1.5 hp), respectively. Both ventilation systems were installed in the ceiling of the facilities. For one HVLS fan, a measurement area of 13.8×10 m was defined and the network of anemometers was distributed in a row along the 13.8 m axis. For one LVHS fan, a measurement area of 10.8×10 m was defined in front of the fan and the network of anemometers was distributed in a row along the 10.8 m axis. For both fans, six tests locations along the 10 m axis were performed, where the anemometers are moved after two minutes of data recorder after its settling time. The propellers were oriented to the predominant wind direction on each location.



**Figure 4.** Distribution of the anemometer network in the cattle dairy buildings with compost barn: a) High-volume low-speed fans; b) Low-volume high-speed fans.

## RESULTS AND DISCUSSION

### Mesh sensibility analysis

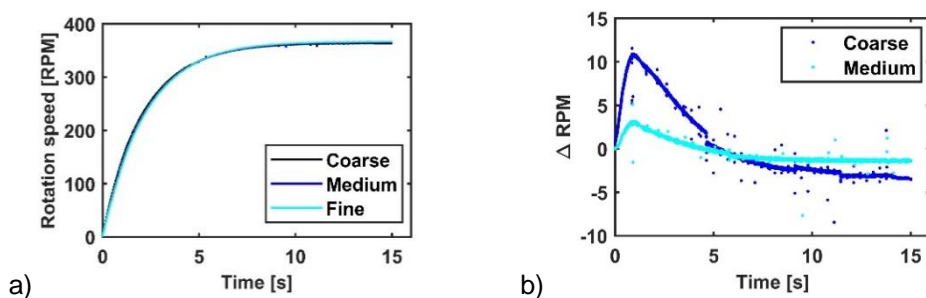


**Figure 5.** CFD simulation result using three mesh sizes: coarse, medium and fine, for the four-blade propeller with an air velocity of  $1.5 \text{ m s}^{-1}$ : a) Comparison of the transient response of the four-blade propeller for each mesh size; b) Difference between the rotation speed of the propeller for the fine mesh size with respect to the coarse and medium mesh size.

CFD results of the transient simulation of the four-blade propeller with a simulation time of 15 s are shown in Fig. 5, a. The dynamic behavior of the propellers was similar for all the employed meshes, with final rotation speeds of 363.1, 365.2 and 366.5 RPM, for the coarse, medium and fine mesh sizes, respectively. Assuming as the fine mesh approximate to the real value, the other values present a relative error below 1%, 0.94% and 0.36% for the coarse and medium mesh, respectively. Additionally, according to the computational time required for each mesh size (Table 2), the CFD simulation with coarse mesh require 40% less computational time than the fine mesh and 26.6% less that the medium one. According to this tendency, increasing the mesh size above the fine mesh size has not a significative effect over the final rotational speed but an exponential increasing in the computational time and in the number of the mesh elements. The differences between the rotation speeds of the propeller for the different meshes for 15 s of simulation time are shown in Fig. 5, b. The medium mesh presented the minor difference for all the simulation. Due this, the medium mesh size was selected as the optimal mesh size for the CFD simulations.

**Table 2.** Number of iterations, computational time and rotation speed of the four-blade propeller for 15 s

	Mesh size		
	Coarse	Medium	Fine
Number of iterations	120,337	109,221	112,780
Computational time	1,789 min	2,440 min	2,979 min
RPM at 15 s	363.1	365.2	366.5

### CFD results and wind tunnel tests

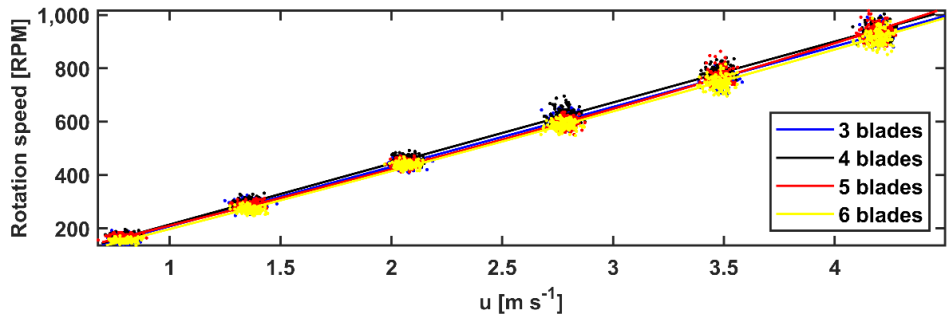


**Figure 6.** Experimental comparison of the propellers rotation speed.

The comparison between the rotational speeds of the propellers tested in the wind tunnel is shown in Fig. 6. All the anemometers have similar behaviors: a linear relation between the wind speed and the rotation speed as was found early by (Pindado et al., 2012). The four-blade propeller presents the higher rotation speed followed by the three-blade propeller, while the six-blade propeller presented the lower rotation speed. Although the three-blade propeller has the lowest mass, the four-blade propeller take advantage of the aerodynamic torque more efficiently in comparison with the other



propellers. At increasing the number of blades, an increase in the surface area of the propeller is achieved, but at the costs of increase the mass of the propeller, decreasing the final rotation speed. All propellers studied start to rotate with an airflow velocity above  $0.7 \text{ m s}^{-1}$  (threshold speed). In the Table 3, the parameters of the linear fitted equations of the propellers rotation speed with the airflow velocity ( $u = a \cdot pps + b$ ) are presented; where  $u$  is the airflow velocity [ $\text{m s}^{-1}$ ],  $pps$  is the number of pulses per seconds given by the encoder sensor and  $b$  is the fitted curve intercept. All the Pearson's correlation coefficient were above 0.99 and the standard deviation of the revolution speed measure were around 16 RPM for all the anemometers.

**Table 3.** Coefficient of the fitted linear equation ( $u = a \cdot pps + b$ ) of the propeller rotation speed with the air speed; where  $u$  is the air speed [ $\text{m s}^{-1}$ ],  $pps$  is the number of pulses per seconds given by the encoder sensor.  $r^2$  is the Pearson correlation coefficient  $s$  is the standard deviation of the rotational speed of each propeller in RPM

	Number of blades			
	3	4	5	6
a	0.0177	0.01745	0.01751	0.01788
b	0.08942	0.07018	0.1169	0.1294
$r^2$	0.9946	0.9951	0.9937	0.9946
$s$	16.6	16.0	16.6	15.2

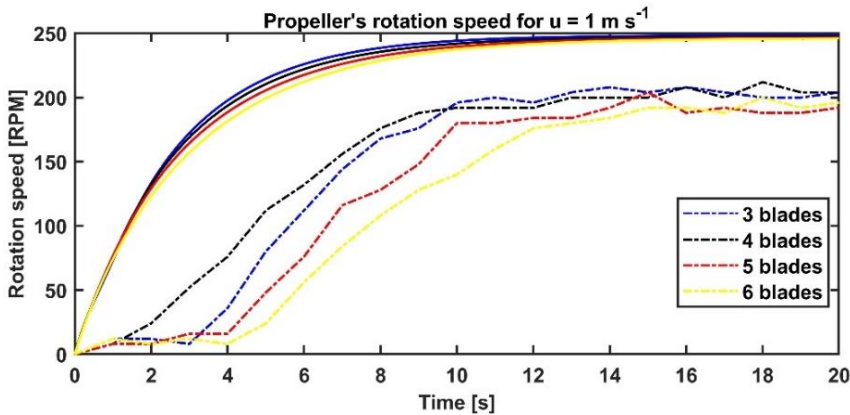


**Figure 7.** Comparison between the CFD results (solid line) and experimental data (dashed line) for the four propellers studied.

The final rotation speed of the propellers for an airflow velocity of  $1 \text{ m s}^{-1}$  was compared in the Fig. 7. All the propellers show a similar settling time (around 12 s) for the CFD results, while for the experimental data, the four-blade propeller present the lower settling time among them (around 18 s) and over the CFD results. The final rotation speed for the experimental test was very similar between propellers. The experimental results are up to 37% lower than the results obtained in CFD and the Normalized Mean Square Error (NMSE) computed were 0.31, 0.21, 0.43 and 0.54, for the three to six blade propeller, respectively. This difference could be attributed to the bearing friction torque as was studied by (Pindado et al., 2014), because the CFD model employed do not consider it. The same bearing was used in all experimental tests, just the propellers were interchanged. The four-blade propeller starts to rotate first, with the higher steady-state rotation speed, which leads it to have a lower rising time, as can be seen in Fig. 7. This is an indicative that this propeller is able to generate the higher

aerodynamic torque among the all. The steady-state rotation speed for the CFD results and the experimental data, and the Root Mean Square Error (RMSE) computed for all the experimental measurements are presented in the Table 4. The average of the last ten seconds of the steady-state condition was considered as experimental values. The four-blade propeller presents the lower RMSE value among the all.

A comparison between CFD simulation and experimental tests for different airflow velocities is showed in the Fig. 8, a for the four-blade propeller. The relative error (Fig. 8, b) increase exponentially with the air velocity, but tend to stabilized around 12.25%. This value can be explain again, by the lack of the bearing friction torque in the CFD model and because the effect of the rugosity of the material was not consider either. Both effects decrease the aerodynamic torque generate by the propeller and consequently the rotation speed in steady state.

**Table 4.** Steady-state rotation speed in RPM for the CFD results and experimental data in RPM and the Root Mean Square Error (RMSE) computed for all the experimental measurements

	Number of blades			
	3	4	5	6
CFD [RPM]	248.5	247.4	246.6	246
Experimental [RPM]	203.64	206.18	205.82	198.55
RMSE [RPM]	129.9	107.4	139.9	147.4

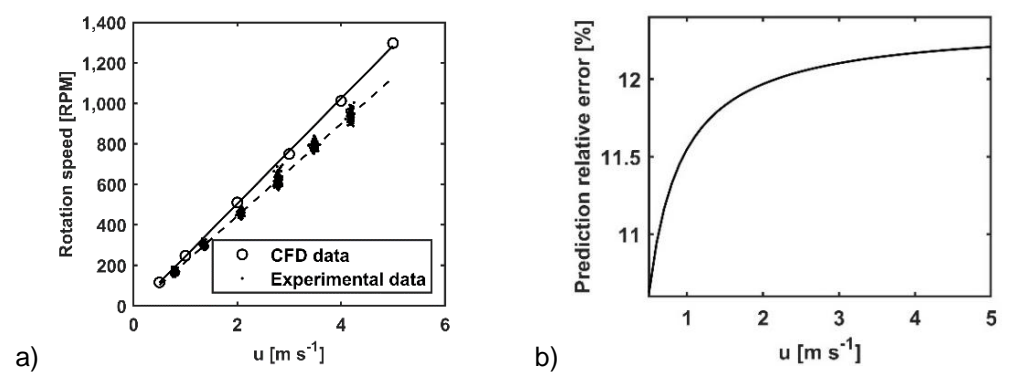


**Figure 8.** a) Comparison between the CFD results and experimental data for the four-blade anemometer. The solid and dashed lines corresponds to the linear fit to the CFD and experimental results, respectively; b) Prediction relative error between the CFD and experimental results.

### Cattle dairy compost barn building tests

A grid of 10 x 6 averaged air velocity measurements was obtained from an area of 126 m<sup>2</sup> below the HVLS fan and from an area of 108 m<sup>2</sup> below and in front of the LVHS fan. Surface functions were fitted to the measurements employing a thin plate spline interpolation (Keller & Borkowski, 2019) by mean of MATLAB® software. A grid of 100x100 points were evaluated for each surface to obtain a detailed behavior of the airflow velocity distribution in the area of study.

The averaged air velocity distribution due to the HVLS fan operation is shown in Fig. 9. The air flow was distributed around the fan with a low airflow velocity zone of approximately 2.5 m of diameter locate right below the fan, as was also found by (Perez Fagundes, 2016). It is also noticed a zone at the right side of the fan with a low airflow velocity, relate to an adjacent hill near to the right side of the facility, which affect the airflow distribution pattern. The minimum and maximum average airflow velocities were 0.48 and 3.48  $\text{m s}^{-1}$ , respectively.

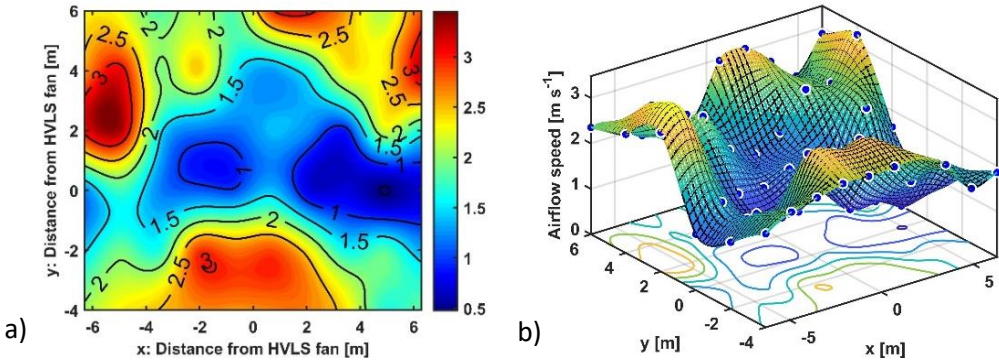


**Figure 9.** Contour map and surface map of the averaged airflow velocity distribution measured at 0.5 m above the dairy compost bed for a HLVS fan.

The averaged air velocity distribution due to the LVHS fan operation is shown in Fig. 10. The maximum airflow velocity was presented at 2 meters in front of it and the airflow velocity decrements to the sides, covering the entire width. The airflow velocity decreased to 1.4  $\text{m s}^{-1}$  at 8 m from the fan. The LVHS presented a low airflow velocity zones below of the fan and to the sides, spreading up to 4 meters. The airflow distribution has a cone shape, which is characteristic of high-speed fans. The minimum and maximum average airflow velocities obtained were 0.22 and 3.39  $\text{m s}^{-1}$ , respectively.

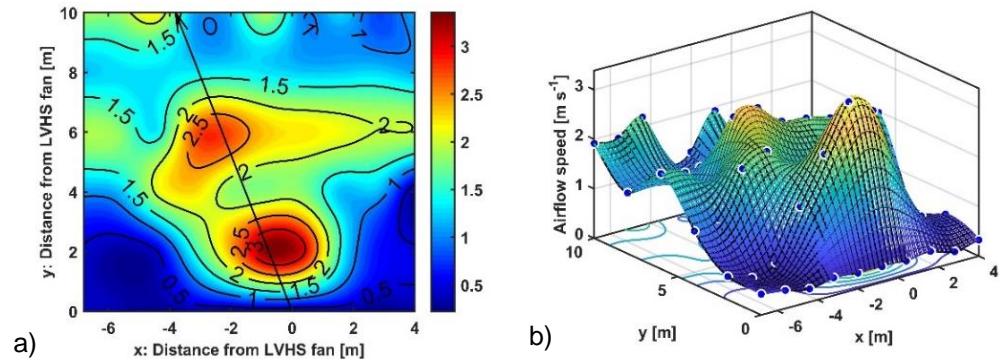


**Figure 10.** Contour map (a) and surface map (b) of the average airflow velocity distribution measured at 0.5 m above the dairy compost bed for a LVHS fan. The arrow in the contour map indicates the direction in which the fan is oriented.



Eqs (1) and (2) were developed to compute the fans ventilation area coverage (VAC) for a minimum airflow velocity and for an interval airflow velocity inside the compost dairy barns. Where  $n$  and  $m$  are the number of elements of the grid for each spatial dimension ( $x$  and  $y$ );  $u_{min}$  is the minimum airflow velocity for which the VAC is computed;  $u_{ij}$  is the airflow velocity in the coordinate  $(i, j)$  inside the grid;  $\Delta u$  is the amplitude of the airflow velocity interval around a specific airflow velocity for which the VAC is computed;  $\Delta A$  is the area of each element of the grid and  $A$  is the area of the grid.

$$VAC_k = \frac{\Delta A}{A} \sum_{i=1}^n \sum_{j=1}^m f(u_{ij}, U_k) \text{ where } f(u_{ij}, u_{min}) = \begin{cases} 1 & \text{if } u_{ij} \geq u_{min_k} \\ 0 & \text{otherwise} \end{cases} \quad (1)$$

$$VAC_k = \frac{\Delta A}{A} \sum_{i=1}^n \sum_{j=1}^m g(u_{ij}, U_k) \text{ where } g(u_{ij}, U_k) = \begin{cases} 1 & \text{if } |u_{ij} - U_k| \leq \Delta u \\ 0 & \text{otherwise} \end{cases} \quad (2)$$

The average area coverage relate to a specific minimum airflow velocity is shown in the Fig. 11. This is which ventilation area percentage present an airflow velocity above an specific value ( $u_{min}$ ); i.e. a ventilation area coverage of 89.62% and 77.05% have an airflow velocity above  $1 \text{ m s}^{-1}$  for the HVLS and LVHS fans, respectively. Between the two fans, exist a difference up to 20% in the ventilation area coverage, being the HVLS fan the one with the greater ventilation area coverage for a particular minimum airflow velocity.

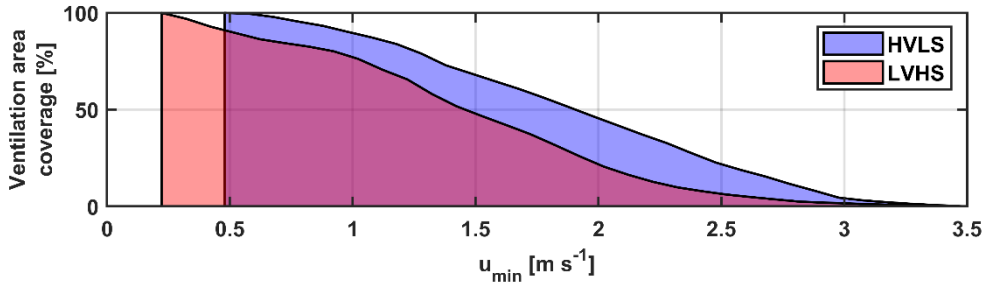


**Figure 11.** Ventilation area coverage that present airflow velocities above a specific value ( $u_{min}$ ).

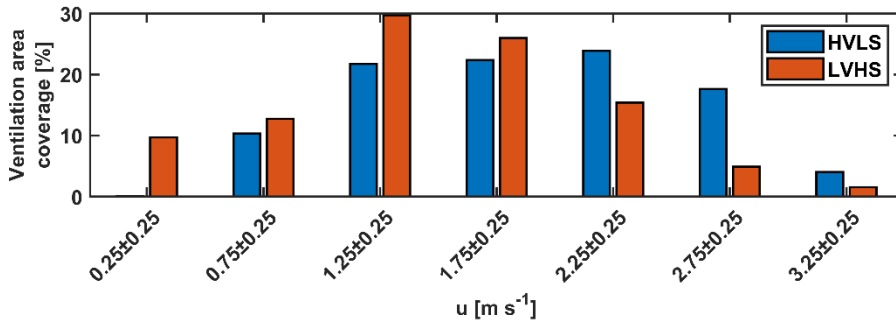


**Figure 12.** Ventilation area coverage with respect to specific ranges of airflow velocities.

The ventilation area coverage with respect to specific ranges of airflow velocities is shown in Fig. 12. An average airflow velocity between 0 and 0.5 m s<sup>-1</sup> for the LVHS fan covers 10% of the studied area. Meanwhile an airflow velocity between 0.5 and 1 m s<sup>-1</sup> for the HVLS fan covers 12.5% of the studied area; this fan not present lower airflow velocities values. The HVLS present a uniform ventilation area coverage between 22% and 24% for airflow velocities between 1 and 2.5 m s<sup>-1</sup>. However, for the LVHS fan, the ventilation area coverage change considerably for the same airflow velocity range, from 30% to 15%, being the 1 to 1.5 m s<sup>-1</sup> range the one that cover the greatest area. The total ventilation area coverage in the range of 1 to 2.5 m s<sup>-1</sup> were 68.01% and 77.55% for the HVLS and LVHS fans, respectively. However, for the airflow velocities above this range, the ventilation area coverage descent markedly to 6.43% and 21.61% for the LVHS and the HVLS system, respectively.

Those results suggest that the HVLS fan present the best airflow distribution at the measured airflow velocity level, covering all the studied area with airflow velocities above 0.5 m s<sup>-1</sup> while the LVHS fan cover 90.29% of the studied area for the same airflow velocities. The 9.71% missing area is located mainly below and to the sides of the LVHS fan. Damasceno et al. (2019) suggested that an airflow velocity above 1.8 m s<sup>-1</sup> could guarantee the proper drying of the compost bed. With this study, was possible to determine that the HVLS and LVHS fans present a ventilation area coverage of 55.2% and 33.1%, respectively, for airflow velocities above this value. This must be consider when selecting the ventilation system of the compost dairy barns, because this lack of air distribution homogeneity not only could lead to poor drying of the compost in certain location of the compost barn as was discussed by (Black et al., 2013), but also affect the bioclimatic condition of livestock.

## CONCLUSIONS

This paper proposed a feasible low-cost 3D printed anemometer network to characterize the airflow distribution inside closed-field agricultural production systems. The developed anemometers were simulated using the innovative CFD/6-DOF models allowing to determine their dynamic response to specific air conditions. Using the proposed anemometer network it was possible to compare the air flow distribution pattern of two compost stables with different fan configurations. Being the high-volume low-speed fan configuration which presented the best airflow distribution homogeneity.

To select the most suitable sensor for the measurement, comparison with a theoretical value was employed. For this purpose a model was simulated. The developed model can be improved, to give more realistic values, if the friction torque and inertia forces are considered in the equation. Even though, the low-cost anemometer network can be consider as a useful tool to determine airflow distribution in agricultural facilities with air velocities over 0.7 m s<sup>-1</sup>. In the case of compost dairy facilities with mechanical ventilations, it can be used as a diagnostic tool to study the heterogeneity of the air distribution near the compost surface in real time, providing important scientific and industrial information.

The developed tool and proposed methodology allow highlighting the zones with low airflow velocity, making possible to determine if the capacity, location or orientation of the fan are in agreement with the requirements of the facility. At compare the airflow

distribution measured with a previously airflow distribution is possible to detect fails in the ventilation system, as a decrement in the ventilation efficiency of the fans.

## REFERENCES

- Ansys Inc. 2016. *ANSYS Fluent User's Guide, Release 17.2*.
- ASTM. 2019. *ASTM D5157-19, Standard Guide for Statistical Evaluation of Indoor Air Quality Models*.
- Black, R.A., Taraba, J.L., Day, G.B., Damasceno, F.A. & Bewley, J.M. 2013. Compost bedded pack dairy barn management, performance, and producer satisfaction. *Journal of Dairy Science* **96**(12), 8060–8074. <https://doi.org/10.3168/jds.2013-6778>
- Bustamante, E., Calvet, S., Estellés, F., Torres, A.G. & Hospitaler, A. 2017. Measurement and numerical simulation of single-sided mechanical ventilation in broiler houses. *Biosystems Engineering* **160**, 55–68. <https://doi.org/10.1016/j.biosystemseng.2017.05.009>
- Bustamante, E., García-Diego, F.J., Calvet, S., Torres, A.G. & Hospitaler, A. 2015. Measurement and numerical simulation of air velocity in a tunnel-ventilated broiler house. *Sustainability (Switzerland)* **7**(2), 2066–2085. <https://doi.org/10.3390/su7022066>
- Calvet, S., Cambra-López, M., Blanes-Vidal, V., Estellés, F. & Torres, A. G. 2010. Ventilation rates in mechanically-ventilated commercial poultry buildings in Southern Europe: Measurement system development and uncertainty analysis. *Biosystems Engineering* **106**(4), 423–432. <https://doi.org/10.1016/j.biosystemseng.2010.05.006>
- Camuffo, D. 2019. Measuring Wind and Indoor Air Motions. In *Microclimate for Cultural Heritage* (Third Edit, pp. 483–511). Elsevier. <https://doi.org/10.1016/b978-0-444-64106-9.00020-1>
- Damasceno, F.A., Oliveira, C.E.A., Ferraz, G.A.S., Nascimento, J.A.C., Barbari, M. & Ferraz, P.F.P. 2019. Spatial distribution of thermal variables, acoustics and lighting in compost dairy barn with climate control system. *Agronomy Research* **17**(2), 385–395. <https://doi.org/10.15159/AR.19.115>
- Dunbar, A.J., Craven, B.A. & Paterson, E.G. 2015. Development and validation of a tightly coupled CFD/6-DOF solver for simulating floating offshore wind turbine platforms. *Ocean Engineering* **110**, 98–105. <https://doi.org/10.1016/j.oceaneng.2015.08.066>
- Fiedler, M., Berg, W., Ammon, C., Loebstin, C., Sanftleben, P., Samer, M., von Bobrutzki, K., Kiwan, A. & Saha, C.K. 2013. Air velocity measurements using ultrasonic anemometers in the animal zone of a naturally ventilated dairy barn. *Biosystems Engineering* **116**(3), 276–285. <https://doi.org/10.1016/j.biosystemseng.2012.10.006>
- Gao, Y., Ramirez, B.C. & Hoff, S.J. 2016. Omnidirectional thermal anemometer for low airspeed and multi-point measurement applications. *Computers and Electronics in Agriculture* **127**, 439–450. <https://doi.org/10.1016/j.compag.2016.06.011>
- Keller, W. & Borkowski, A. 2019. Thin plate spline interpolation. *Journal of Geodesy* **93**(9), 1251–1269. <https://doi.org/10.1007/s00190-019-01240-2>
- Kiwan, A., Berg, W., Brunsch, R., Özcan, S., Müller, H.J., Gläser, M., Fiedler, M., Ammon, C. & Berckmans, D. 2012. Tracer gas technique, air velocity measurement and natural ventilation method for estimating ventilation rates through naturally ventilated barns. *Agricultural Engineering International: CIGR Journal* **14**(4), 22–36.
- Leoni, A., Stornelli, V. & Pantoli, L. 2018. A low-cost portable spherical directional anemometer for fixed points measurement. *Sensors and Actuators, A: Physical* **280**, 543–551. <https://doi.org/10.1016/j.sna.2018.08.025>
- Luck, B.D., Davis, J.D., Purswell, J.L., Kiess, A.S., Hoff, S.J. & Olsen, J.W.W. 2014. Effect of measurement density on characterizing air velocity distribution in commercial broiler houses. *Transactions of the ASABE* **57**(5), 1443–1454. <https://doi.org/10.13031/trans.57.10409>

- Obando Vega, F.A., Montoya Ríos, A.P., Osorio Saraz, J.A., Vargas Quiroz, L.G. & Alves Damasceno, F. 2020. Assessment of black globe thermometers employing various sensors and alternative materials. *Agricultural and Forest Meteorology* **284**(August 2019), 107891. <https://doi.org/10.1016/j.agrformet.2019.107891>
- Perez Fagundes, B. 2016. *Determinação do fluxo de ar mais homogêneo, comparativo a dois sistemas de ventilação forçada por ventiladores, aplicados em galpões de confinamento de vacas leiteiras em sistemas de camas de compostagem (compost barn)*. Faculdade Profissional - Curitiba.
- Pindado, S., Cubas, J. & Sorribes-Palmer, F. 2014. The cup anemometer, A fundamental meteorological instrument for the wind energy industry. Research at the IDR/UPM institute. In *Sensors (Switzerland)* (Vol. **14**, Issue 11). <https://doi.org/10.3390/s141121418>
- Pindado, S., Sanz, A. & Wery, A. 2012. Deviation of cup and propeller anemometer calibration results with air density. *Energies* **5**(3), 683–701. <https://doi.org/10.3390/en5030683>
- Samer, M., Loebstin, C., von Bobrutzki, K., Fiedler, M., Ammon, C., Berg, W., Sanftleben, P. & Brunsch, R. 2011. A computer program for monitoring and controlling ultrasonic anemometers for aerodynamic measurements in animal buildings. *Computers and Electronics in Agriculture* **79**(1), 1–12. <https://doi.org/10.1016/j.compag.2011.08.006>
- Shamshiri, R. 2017. Measuring optimality degrees of microclimate parameters in protected cultivation of tomato under tropical climate condition. *Measurement* **106**, 236–244. <https://doi.org/10.1016/j.measurement.2017.02.028>
- Shamshiri, R. & Ismail, W.I.W. 2012. Performance Evaluation of Ventilation and Pad-and-Fan Systems for Greenhouse Production of Tomato in Lowland Malaysia. *World Research Journal of Agricultural & Biosystems Engineering* **1**(1), 1–5. <http://www.bioinfo.in/contents.php?id=250>
- Shamshiri, R.R., Kalantari, F., Ting, K.C., Thorp, K.R., Hameed, I.A., Weltzien, C., Ahmad, D. & Shad, Z. 2018. Advances in greenhouse automation and controlled environment agriculture: A transition to plant factories and urban agriculture. *International Journal of Agricultural and Biological Engineering* **11**(1), 1–22. <https://doi.org/10.25165/j.ijabe.20181101.3210>
- Shamshiri, R.R., Mahadi, M.R., Thorp, K.R., Ismail, W.I.W., Ahmad, D. & Man, H.C. 2017. Adaptive Management Framework for Evaluating and Adjusting Microclimate Parameters in Tropical Greenhouse Crop Production Systems. In *Plant Engineering*. INTECH. <https://doi.org/10.5772/intechopen.69972>
- van Dooren, H.J.C. & Sapounas, A. 2013. *Use of computational fluid dynamics (CFD) modelling to improve tracer gas techniques in very open naturally ventilated livestock buildings* (Issue September).
- Vilela, M.O., Gates, R.S., Martins, M.A., Barbari, M., Conti, L., Rossi, G., Zolnier, S., Teles, C. G.S., Zanetoni, H.H.R., Andrade, R.R. & Tinôco, I.F.F. 2019. Computational fluids dynamics (CFD) in the spatial distribution of air velocity in prototype designed for animal experimentation in controlled environments. *Agronomy Research* **17**(3), 890–899. <https://doi.org/10.15159/AR.19.108>
- Zajicek, M. & Kic, P. 2012. Improvement of the broiler house ventilation using the CFD simulation. *Agronomy Research* **10**(SPEC. ISS. 1), 235–242.

## **Psychosocial risks analysis for employees in public administration**

D. Pastare<sup>1</sup>, Z. Roja<sup>1</sup>, H. Kalkis<sup>1,2,\*</sup> and I. Roja<sup>3</sup>

<sup>1</sup>University of Latvia, Ergonomics Research Centre, Raina blvd. 19, LV-1586 Riga, Latvia

<sup>2</sup>University of Latvia, Faculty of Business, Management and Economics, Department of management, Aspazijas blvd. 5, LV-1050 Riga, Latvia

<sup>3</sup>MFD Healthcare group, Vienības gatve 109, LV-1000, Riga, Latvia

\*Correspondence: [henrijs.kalkis@gmail.com](mailto:henrijs.kalkis@gmail.com)

**Abstract.** Nowadays psychosocial risks at work have a serious impact not only on the health of employees, but also on the economic performance of organisations, and this is the biggest challenge in working environment. In Latvia, employees in public administration comprise 11% of the total population. Hence the aim of this study was to analyse the causes of psychosocial risks and the differences in their prevalence among inspectorate officials employed in the State Administration compared to office staff employed by the State Administration. A modified Copenhagen Psychosocial Questionnaire from the Danish National Research Centre for the Working Environment was used to assess psychosocial risks at work. One public administration organisation was selected for the study, which involved 111 staff (60 inspecting officers and 51 office staff). The analysis of the results of the psychosocial risk assessment shows that there are statistically significant differences in the assessment of four out of 11 psychosocial risks to the working environment. The most common psychosocial work environment risk factor among inspectors is the inadequate attitude of management, but the most common risk factor among office employees is the lack of impact on work. To reduce the spread of psychosocial risks more effectively, an individual approach is required for each worker.

**Key words:** public administration, inspectors, office workers, psychosocial risks, work environment.

## **INTRODUCTION**

In Latvia, employees in public administration comprise 11% of the total population. Over the last ten years, psychosocial values, namely, positive relationships in a collective – an employee-respecting management style, which is characterised by dignity, trust, openness and fairness, colleagues and colleagues' support for work-related situations, have become important characteristics of a workplace. Data from the scientific literature shows that employees who are positive, energy-conscious and responsive are more capable of performing their job duties and achieving higher results. Balance between work and family life is a major risk that also affects public administration employees (Kotowska et al., 2010). The work strain predictors in contemporary work environment

frequently are associated with psychosocial risk factors rather than with physical ones (Roja et al., 2017).

The reconciliation between work and family life is closely linked to organisational issues in the work team (flexible work schedule, remote work, working time planning, etc.) and to the psychological climate in the work team, which is to some extent influenced by employee-management, employee-to-employee relationships. (Subramanian, 2017b).

Psychosocial risks at work have a serious impact not only on the health of employees, but also on the economic performance of organisations, and this is the biggest challenge in working environment nowadays (Kortum, 2010). The rapid changes in contemporary labour market have contributed to the spread of these risks. This is mainly due to the rapid entry of information and communication technologies into the labour market, the continued competition between organisations, their restructuring trends, as well as the increase in work intensity. Employees are forced to adapt to dramatic changes and diverse working conditions, which often affect their health and relations in the work team (Eurofound, 2015; Korunka, 2017).

Psychosocial risks are based on psychosocial hazards (work organization, job support, high volume of work, uncertainty about the future, workplace disagreements in the work team) that can adversely affect employees psychologically, physically and socially, causing the following health problems: burnout syndrome, depression, disturbed sleep, mood, fatigue, headache and stomach irritation (Beswick 2006; Chandola 2010; Leka & Aditya, 2010). Some authors suggest that workplace stress management needs to be addressed at national level and the government should not only identify vulnerable populations but also ensure that appropriate preventive measures are in place in each sector to protect the rights of all workers (Maulik, 2017).

The aim of this study was to analyse the causes of psychosocial risks and the differences in their prevalence among inspectorate officials employed in the State Administration compared to office staff employed by the State Administration.

## **MATERIALS AND METHODS**

During the research one public administration organisation was selected for the study, which involved 111 staff members, including 60 inspecting officers and 51 office workers). The main selection criteria were full consent to participate. Altogether were 115 participants planned, but fully participated and answered the questionnaire 111 staff members. Hence the sample consists of 111 employees in the public administration, of which 10.8% ( $n = 15$ ) are males and 89.2% ( $n = 96$ ) females. The age group of 31–40 years includes more females (30.2%,  $n = 29$ ), while age group of 31–40 more males (40%,  $n = 6$ ). Of the participants involved in the study, 45.9% ( $n = 51$ ) are office employees and 54.1% ( $n = 60$ ) are inspecting officers.

The study was approved by the Human Ethics and Institutional Review Board at the University of Latvia in 2019.

A modified Copenhagen Psychosocial Questionnaire (Kristensen et al., 2005) short questionnaire version from the Danish National Research Centre for the Working Environment was used to assess psychosocial risks at work. This questionnaire was modified and adapted to the Latvian work environment, as well as an appropriate work

environment risk assessment system was revised. The questionnaire included the following:

Part 1 – General issues: Gender (female, male), Age (18–30; 3–40; 41–50; 50–60; over 60 years), Profession (office employee; inspecting officer).

Part 2 – A modified Copenhagen Psychosocial Questionnaire. The respondent should respond by selecting one of the given options. A certain value in points is applied to each response. The issues have been prepared in pairs, and each pair of questions is about a particular factor in the psychosocial work environment. A comparison is made between the total assessments provided by respondents for each couple of questions. In questions with five options, the following breakdown of working conditions in relation with psychosocial risks has been developed according to the joint score:

- in the case of a total score of ‘8’ – very good working conditions;
- where the total value of the assessments is ‘6’ or ‘7’ – good working conditions;
- where the total value of the assessments is ‘4’ or ‘5’ – average working conditions;
- in the case of scores of ‘2’ or ‘3’ – poor working conditions;
- if the total score is ‘0’ or ‘1’ – very poor working conditions.

The responses are compared in the groups by the independent feature of the study – type of work. The level of risk is assigned depending on the distribution of respondents (%) whose responses constitute a ‘good’ and ‘very good’ joint assessment:

- if good, very good working conditions are found in 81–100% of respondents – risk level I – neither action nor documentation of psychosocial risk factors are required;
- if good, very good working conditions are found in 61–80% of respondents – risk level II – special measures to reduce psychosocial risks are not needed, however, they need to be monitored;
- if good, very good working conditions have been identified in 41–60% of respondents – risk level III – risk reduction measures are required, but need not be taken immediately; measures should be taken at least within 3–5 months after the risk assessment;
- where good, very good working conditions have been identified in 21–40% of respondents – risk level IV – work must not be carried out until risk reduction or prevention measures have been taken; if it is not possible to interrupt the work, account should be taken of the extent of the consequences of the potential damage and the number of employees, while the measures should be taken within 1–3 months;
- if good, very good working conditions are identified in 1–20% of respondents – V risk level – steps to reduce or eliminate psychosocial risks should be implemented immediately. If the lack of financial means makes it impossible to do so, work should be stopped.

Data processing was performed using descriptive statistical methods, frequency analysis and cross-tabulation with chi-square test to determine the statistical reliability of differences. Results were considered as statistically significant if the significance level (P) was less than 0.05 and 95% confidence interval was calculated for the obtained values. Data analysis was performed using the software SPSS 20.0, Microsoft Excel Office 365 used for charting, the confidence intervals were calculated in the Stats Calculator.

## RESULTS AND DISCUSSION

Analysis of psychosocial risks includes an assessment of the number of employees, whose working conditions in the corresponding position are considered to be good and very good, as well as a risk assessment and an assessment of statistical reliability (see Table 1).

The analysis of the results of the psychosocial risk assessment shows that there are statistically significant differences in the assessment of four out of 11 psychosocial risks to the working environment. For inspectors, the performance of their duties on time corresponds to the risk level I, but for the office staff – to the risk level II.

**Table 1.** Summary of the assessment of psychosocial risk factors

No.	Psychosocial risk factors	Group of position	Good, very good conditions	Level of risk	Significance
1.	Accomplishment of job responsibilities on time	Office employee	66.7% ( <i>n</i> = 34)	II	<i>P</i> = 0.005
		Inspector	85.0% ( <i>n</i> = 51)	I	
2.	Pace of work	Office employee	54.9% ( <i>n</i> = 28)	III	<i>P</i> = 0.336
		Inspector	43.3% ( <i>n</i> = 26)	III	
3.	Emotional factors	Office employee	43.1% ( <i>n</i> = 22)	III	<i>P</i> = 0.373
		Inspector	30.0% ( <i>n</i> = 18)	IV	
4.	Impact on work to be carried out	Office employee	17.6% ( <i>n</i> = 9)	V	<i>P</i> = 0.240
		Inspector	21.6% ( <i>n</i> = 13)	IV	
5.	Provision of information	Office employee	39.1% ( <i>n</i> = 20)	IV	<i>P</i> = 0.023
		Inspector	50.0% ( <i>n</i> = 30)	III	
6.	Upper management attitude	Office employee	25.5% ( <i>n</i> = 13)	IV	<i>P</i> = 0.044
		Inspector	13.3% ( <i>n</i> = 8)	V	
7.	Support from direct management	Office employee	74.5% ( <i>n</i> = 38)	II	<i>P</i> = 0.322
		Inspector	71.7% ( <i>n</i> = 43)	II	
8.	Clarity on work and its objectives	Office employee	74.5% ( <i>n</i> = 38)	II	<i>P</i> = 0.408
		Inspector	78.3% ( <i>n</i> = 47)	II	
9.	Mutual trust within the organisation	Office employee	56.9% ( <i>n</i> = 29)	III	<i>P</i> = 0.013
		Inspector	38.3% ( <i>n</i> = 23)	IV	
10.	Fairness within the organisation	Office employee	33.4% ( <i>n</i> = 17)	IV	<i>P</i> = 0.529
		Inspector	36.7% ( <i>n</i> = 22)	IV	
11.	Impact of time and energy consumption at work on private life	Office employee	45.1% ( <i>n</i> = 23)	III	<i>P</i> = 0.117
		Inspector	35.0% ( <i>n</i> = 21)	IV	

The information provision for inspectors corresponds to the risk level III, but for office staff to the risk level IV. Attitude of the upper management to office staff has been evaluated as the risk level IV and to inspectors as the risk level V. Mutual trust within the organisation has been evaluated by the office staff at risk level III and by inspectors at risk level IV. The data obtained demonstrate that with the risk level V was evaluated the impact of office staff on the work to be carried out and the inappropriate management treatment of inspectors, indicating the immediate need for intervention measures to improve the situation. The risk level IV was determined for inspectors in relation to emotional risk factors, the lack of impact on the work to be carried out, the lack of mutual trust and fairness within the organisation, as well as the impact of time and energy



consumption at work on private life. For office staff, the level of risk of IV has been determined as regards the lack of impact on the work to be carried out, the lack of information provision, inappropriate attitude from senior management, and the lack of fairness within the organisation. Intervention measures should be implemented within 1–3 months.

The risk level I was determined on the issue of inspectors’ performance of duties on time, while for office staff in this case risk level II was found. Nor is it necessary to plan action to mitigate risks regarding the aid from direct management and clarity on work and its objectives, in both cases the risk level II for both inspectors and office staff was found. However, for positions evaluated with risk level II, risks need to be monitored in dynamics and action should be taken in the event of negative changes.

In our research there were 11 factors chosen for the deeper analysis and main results are shown in the figures 1–3 which showed highest group differences. Accordingly to the chosen methodology described in part 2, the grading points were determined from very good working conditions till very poor working conditions.

By analysing the indicator (‘You do the job tasks on time’ and ‘You have sufficient time to perform each job assignment’) in the joint rating groups (see Fig. 1), it is concluded that very good working conditions, respectively, evaluation ‘8’ was found in 8.3% ( $n = 5$ ) for inspection officers and 5.9% ( $n = 3$ ) for office staff, while good working conditions for the score ‘7’ were found to be in 45.0% ( $n = 27$ ) of inspecting officers and 29.4% ( $n = 15$ ) among office employees. Good working conditions at evaluation ‘6’ were found among 31.7% ( $n = 19$ ) inspecting officers and among 31.4% ( $n = 16$ ) of office staff. However, it should be noted that average and poor working conditions are observed among inspectors, with evaluation ‘5’ in 6.7% ( $n = 4$ ) of cases, evaluation ‘4’ – in 5.0% ( $n = 3$ ), but evaluation ‘2’ identifiable by poor working conditions was found in 3.3% ( $n = 2$ ). The observed trend is statistically likely,  $P = 0.005$ .

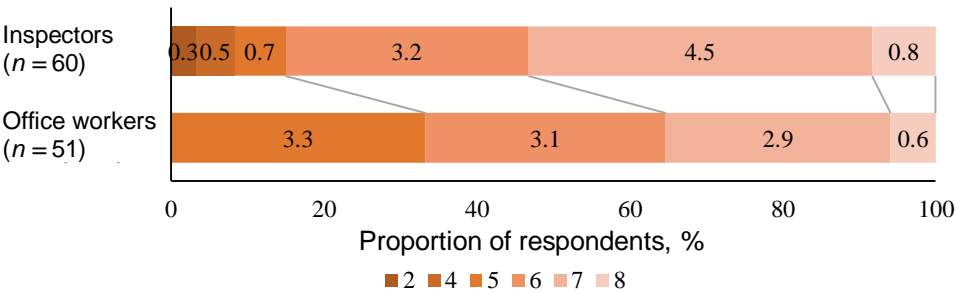


**Figure 1.** Accomplishing job responsibilities on time in the groups of positions (2 – poor; 4, 5 – average; 6, 7 – good; 8 – very good working conditions).

The results could be explained by the fact that inspectors often plan their daily work on their own – it is possible to choose the days and times when inspections are carried out, to draw up letters and inspection acts, while office staff has certain job responsibilities to be carried out within specified time limits. Inspectors are also subjected to different managers, depending on the department in which the inspector works, and, possibly, each of the managers has their own management style as regards

the division of duties, while office staff mostly performs support functions and work duties are performed according to a routine schedule. This corresponds to findings on psychosocial stress impact on management and work productivity (Leka et al., 2003; Haenisch, 2012).

The results of the European Working Conditions Survey show that, on average, 8.0% of employed people in Europe have indicated that there is never enough or rarely enough time to complete the task (Eurofound, 2017).

On the other hand, a study conducted in Latvia in 2014 among employees of the State Administration found that 39.0% of respondents indicated that the amount of work is not adequate and cannot be accomplished in the specified time (State Chancellery, 2014).

In our study, 3.3% of inspectors employed in the public administration have noted poor working conditions (the total amount of the answers forms evaluation '2' — never or rarely work duties have been carried out in time). The results of this study are higher than the European average of 10.0% and significantly lower than the results of the study carried out in Latvia in 2014. By studying the pace of work ('You need to work at an increased pace of work' and 'At an increased pace of work you need to work all day') in the ranking groups, it is concluded that very good working conditions with regard to the pace of work are not identified. Good working conditions (assessment '6' and '7') are seen more frequently among office staff – in 5.9% ( $n = 3$ ) of cases evaluation was '7' and in 25.5% ( $n = 13$ ) of cases – '6', while among inspectors 10.0% ( $n = 6$ ) and 13.3% ( $n = 8$ ) respectively. On the other hand, poor working conditions (assessment '3' and '2') regarding pace of work are seen more frequently among inspectors – 13.3% ( $n = 8$ ) give an assessment of '3' and 10.0% ( $n = 6$ ) '2', while among office staff 15.7% ( $n = 8$ ) and 2.0% ( $n = 1$ ) respectively ( $n = 1$ ). Very poor working conditions in terms of the pace of work have been noted by one inspector (1.7%), very poor working conditions have not been fixed on this issue among office staff. The observed trend is not statistically likely,  $P = 0.336$ .

The possible explanation of the results on this issue is also due to the fact that office staff mainly carry out support functions and are strictly limited in time of performance, which is often disproportionately short, but inspectorate officials can plan their own time in certain duties and, in this case, the results depend on employee's style of work and its timely performance. It should also be noted that there are specific periods during which work must be done, both monthly, quarterly and yearly, and before the end of these periods office staff and inspectorate officials may be exposed to this psychosocial risk factor of the working environment – an increased pace of work. The results of an international study show that, on average in Europe, 21.0% of state administration employees face the need to work at an increased pace of work (three-quarters of working time), while 30.0% of public administration employees face a severe time-limit in their job performance (Eurofound, 2017).

This study shows that employees of the Latvian State Administration are more often confronted with the risk factor of the psychosocial work environment – working at an increased pace of work.

By analyzing the total amount of answer ratings for claims 'You are getting into emotionally burdensome situations' and 'Your job responsibilities include addressing customers' personal problems' (see Fig. 2), it was concluded that good and very good working conditions in terms of emotional conditions were noted only among office

staff – 3.9% ( $n = 2$ ) of the highest number of replies recorded by office staff – overall rating ‘8’, while the score ‘7’, identifiable by good working conditions, was fixed by 21.6% ( $n = 11$ ) of office employees in questionnaires. Among inspectors, good working conditions (‘7’) were mentioned by 15.0% ( $n = 9$ ) of cases. On the other hand, the rating ‘6’ is marked by 17.6% ( $n = 9$ ) of office staff and 15.0% ( $n = 9$ ) by inspectors, respectively. However, it should be noted that among office employees by 1.2 percentage points more frequently were marked very poor working conditions, total evaluation by office employees ‘1’ was found in 3.9% ( $n = 2$ ) of cases, while 1.7% ( $n = 1$ ) was found among the inspectors. The observed trend is not statistically significant in this case,  $P = 0.373$ .

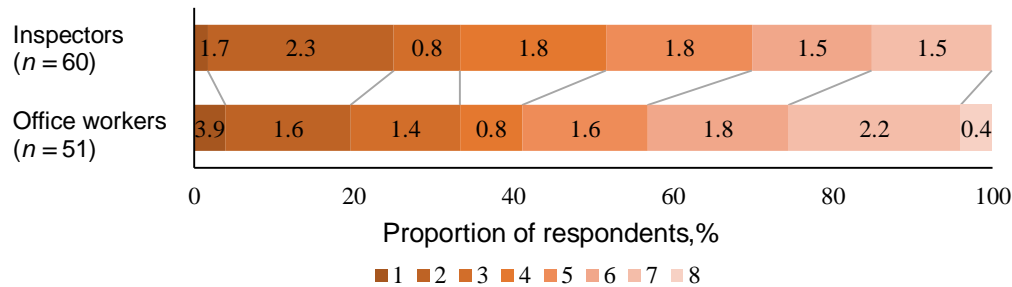


**Figure 2.** Assessment of emotional factors in the groups of positions (1 – very poor; 2, 3 – poor; 4, 5 – average; 6, 7 – good; 8 – very good working conditions).

The results obtained are explained by the fact that, according to the job description, the work with clients is more common among inspectorate officials and the two statements studied in this question group are complementary to each other – dealing with clients, in majority of cases, is related with emotionally burdensome situations. It should also be noted that inspecting officials who exercise control of individuals and control of companies, often face resistance and negative attitudes on the client's side.

The results of the European Working Conditions Survey show that 19.0% of public administration employees face customer discontent and 14.0% of respondents get into emotionally burdensome situations (Eurofound, 2017). When comparing this data to the results of our study, it should be concluded that inspectors involved in the study are experiencing significantly more emotionally burdensome situations and customers' personal problems. The results of this study are also higher than in Europe as a whole among all employees, with 17% of employees experiencing clients' discontent and 11% of employees getting into emotionally burdensome situations.

By analysing employees' responses about their impact on the work to be carried out (‘Overall, you have a major impact on the work to be done’ and ‘You may have an impact on the scope of the tasks entrusted to you’), it is concluded that 3.3% ( $n = 2$ ) of inspectors have recorded very good working conditions, the office staff have not provided such an assessment of this risk factor for the working environment. 3.9% ( $n = 2$ ) of office staff have provided a joint rating of ‘7’, while 13.7% ( $n = 7$ ) of office staff have provided evaluation ‘6’ corresponding to good working environment conditions. Good working conditions for inspectors are in 18.3% ( $n = 11$ , score ‘6’) of cases, evaluation ‘7’ among inspectors has not been provided. It should be noted that

5.9% ( $n = 3$ ) of the total amount of replies from office staff constitute the lowest rating on this issue ‘1’ – poor working conditions. The differences found in this issue are not statistically likely,  $P = 0.240$ . But in some other researches, authors find high coherence between psychological work conditions and its impact on the work content (Nyambura & Ndero, 2016).

The results on this issue vary, as the independent feature of the study is the type of the post, therefore both groups include different levels of staff – middle and lower level managers, as well as office staff under these leaders, inspectors, and senior inspectors. However, it should be noted that managers of different levels should be included in the ‘Office Work’ category, which could be one of the explanations why employees in the office are more likely to have a greater impact on the work to be carried out and its size.

Examining the possibility of affecting the work to be carried out in other studies, it was found out that in European studies of working conditions an average of 69.3% of respondents answered that they can affect the order, volume, speed, and methods (Eurofound, 2017) of the work to be carried out, but in this study, good and very good conditions regarding working impact are noted by 21.6% of inspecting officers and 17.6% by office staff. These figures are, in fact, approximately three times lower for employees of the Latvian State Administration than the average in Europe.

By studying the co-rating of respondents on information provision (‘You are timely informed about important decisions, important changes and future plans in your workplace’ and ‘You are provided with all the necessary information to perform your work duties as best as possible’), it was found out that inspectors are more often informed about changes and plans and inspectors more often have the necessary information which is needed to carry out their job duties comparing with office staff. In the joint assessment they more often mention good and very good working conditions (see page Fig. 3). This group also records very poor working conditions, both among inspectors and office staff, respectively 5.0% ( $n = 3$ ) of inspectors and 3.9% ( $n = 2$ ) of office staff. The observed trend is statistically likely,  $P = 0.023$ . The same approach when psychosocial work conditions influence interaction between work environment and workers has been proved by other authors (Baltes, 2001; Martin, 2005).

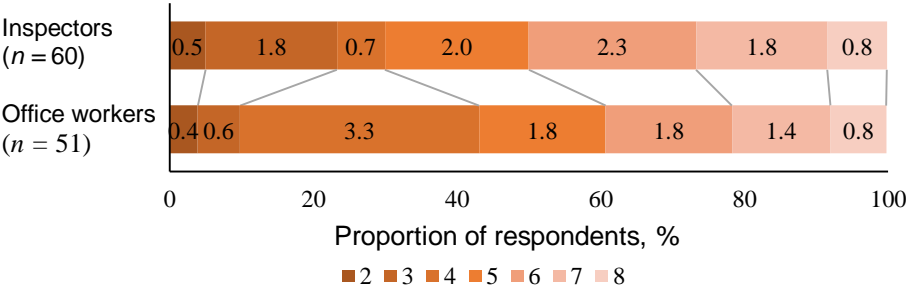


**Figure 3.** Assessment of information provision in the groups of positions (2, 3 – poor; 4, 5 – average; 6, 7 – good; 8 – very good working conditions).

In the public administration, the circulation of information within the framework of the organisation is carried out centralised with the assistance of the internal information system. However, the various results in this block of issues could be

explained by differences in management style and by how quickly the employee receives informal information, thus in this case, the relationship between the employee and management and communication is also important. The reception of the information required for work also depends on the competence and attitude of the head of each department towards the employees under his or her authority.

The results of the National Administration Employees' Engagement Survey show that 41.8% of participants in the study receive sufficient information on changes in the institution and 45.5% of participants receive sufficient information on issues affecting the employee themselves (State Chancellery, 2014). In this study, 49.9% of inspectors and 39.1% of office employees are satisfied with information provision, and working conditions in this matter evaluate as good and very good, results are close to the average of Latvia among employees in the public administration.

When analyzing the question group on direct management support ('How often do your direct management listen to your problems in the performance of job responsibilities?' and 'How often do you get help and support from direct management?') the percentage of total answers, show that 10.0% ( $n = 6$ ) of inspectors do not receive any support from direct management (score '0'), this rate is 2.0% ( $n = 1$ ) among office staff. Poor working conditions regarding receiving support from direct management are also recorded at a total of 9.8% ( $n = 5$ ) of office staff and 10.0% ( $n = 6$ ) of inspectors. However, more than half of the employees in both job groups have indicated positive answers and the total amount of these answers constitutes a good and very good assessment of working conditions. The observed trend is not statistically significant,  $P = 0.322$ .

In analysing this issue, it should be noted that respondents work in different departments with different functions and different managers, and therefore the approach of each manager's work is different, nevertheless, around three quarters of the participants in the study assess the working conditions on this issue as good and very good, which is essentially a positive trend, contrary to the results in the block on the recognition and management's attitude towards employees.

In the European Working Conditions Study, 59.0% of European employees always or frequently receive support from direct management (Eurofound, 2017), but in 2014, a study carried out among employees of the Latvian State Administration shows that support from direct management is received in 60.0% of cases (State Chancellery, 2014). In our study, 71.7% of inspectors and 74.5% of office staff have good or very good working conditions in terms of support from direct management. Figures in Latvia are higher than average in Europe and employees in the State Administration are currently more likely to receive support from direct management.

The analysis of the co-evaluation of the answers on issues of clarity at work ('You have clear objectives of your work' and 'You have a clear view of what is expected from your work') concludes that in both groups, the majority of respondents have good and very good working conditions, however in each of the job groups there are employees whose total answers constitute an assessment 'poor working conditions', 3.3% ( $n = 2$ ) of inspectors and 2.0% ( $n = 1$ ) of office staff have given an assessment of '2', 6.7% ( $n = 4$ ) inspectors and 2.0% ( $n = 1$ ) respectively have provided a joint rating of '3'. This trend is not statistically significant for this psychosocial risk factor,  $P = 0.408$ .

Given that once a year direct management negotiates the objectives of the work with subordinates during the annual performance assessment, the majority of respondents consider the working conditions in this block as good and very good. It is in accordance with Subramanian (2017a) and Sawithri (2017) findings that relationship between management and workers significantly improves decision making and trust levels.

In Latvian State Administration employees' involvement survey, 76.0% respondents know what is expected of the employee, in this study 78.3% of inspectors and 74.5% of office employees have noted good or very good working conditions on this issue, which essentially are close to the results of the State Administration involvement survey.

By studying the differences in the block on mutual trust ('Can you trust the information provided by management?' and 'Do management trust the employees and the fact that the work is done well?'), it appears that there is mutual trust among office staff more frequently than among inspectors. Respectively, 9.8% ( $n = 5$ ) of office staff and 3.3% ( $n = 2$ ) of inspectors' replies represent the maximum rating of '8', while the score of '7' (good working conditions) by 0.6 percentage points is more frequently fixed among inspectors compared to office staff (18.3% ( $n = 11$ ) and 17.6% ( $n = 9$ ) respectively. A joint assessment that is consistent with good working conditions (valuations '5' and '6') is also more common among office staff. The most common assessment among inspectors is '5', 36.7% ( $n = 22$ ) of employees evaluate the working conditions regarding mutual trust as good. It should be noted that 5% ( $n = 3$ ) of inspectors have provided the lowest overall rating '1' in these issues. The observed trend is statistically significant,  $P = 0.013$ . Similar results are represented in Robinson & Griffiths (2005) research, where state chancellery workers are influenced by the organisational changes that results in work related stress, unfriendly attitude from co-workers, low trust level during change process.

The results obtained show that office employees communicate more frequently with managers at different levels due to job responsibilities than inspectorate officials, who mainly communicate with their direct management. Consequently, mutual trust can be seen more frequently.

In the European Working Conditions study, 83.0% of employees agreed that management trusted its employees and that work was done well, and 69.0% agreed that information provided by management could be trusted (Eurofound, 2017). This is also confirmed by the results of the Public Administration Employees Engagement Survey in 2018 (State Chancellery, 2018), which showed that 53.4% of respondents trust the top management, while the results of the 2014 survey showed that 40% (State Chancellery, 2014) employed in the State administration trust the top management. In the same study, good and very good working conditions regarding mutual trust are stated by 38.3% of inspectors and 56.9% of office staff employed in the state administration, indicating that mutual trust among employees in the Latvian State Administration is slightly lower than average in Europe, especially among inspectors.

When assessing fairness in the organisation regarding the question 'Are business conflicts solved fairly?' and 'Are business responsibilities distributed fairly within the company?', it is concluded that the number of responses from both groups of positions is similar in each of the categories. It should be noted that, according to the information provided by respondents, 6.7% ( $n = 4$ ) of inspectors and 3.9% ( $n = 2$ ) of office staff give

evaluation 'very poor working conditions' It is also important that, in total, in terms of fairness within the organisation 31.7% ( $n = 19$ ) of inspectors and 45.3% ( $n = 23$ ) of office staff characterize it as poor. The observed trend is not statistically significant,  $P = 0.529$ .

The results of the investigational block are similar, but inspectors find it a little more common that conflicts are solved fairly and that work responsibilities are also fairly distributed within the organisation and have provided a joint assessment 'good' and 'very good' on these issues. The slight difference in results could be due to the fact that inspectors mainly have defined job responsibilities that are carried out on a daily basis, while additional non-scheduled tasks may be delegated to the office employees (depending on a specific position) for which a specific employee has not been delegated in the organisation. The European Working Conditions Survey states that 71.0% of European employees consider that conflicts within the organisation are being solved fairly and 73.0% believe that work responsibilities are fairly distributed within the organisation (Eurofound, 2017). In this study, good and very good working conditions regarding fairness within the organisation are 36.7% for inspectors and 33.4% for office staff, which are about half as low as average in Europe.

By studying the results of 'Do you feel that your work consumes a lot of energy and has a negative impact on your private life?', it is concluded that inspectors have acknowledged more often that work does not consume much energy and does not affect private life (28.4%,  $n = 15$ ) or have recognised that work consumes energy and affects family life sometimes (45.0%,  $n = 27$ ). However, in the case of inspectors, 3.3% ( $n = 2$ ) of study participants found that work always consumes energy and affects family life, no such response was provided among office staff. The observed trend is not statistically likely,  $P = 0.196$ .

The results on this issue could be explained by the personal characteristics, age, workability and other individual factors of the employee, since employees in the state administration have a certain working time, of course also should be taken into account the results of the block of issues on increased working rates, in which approximately a quarter of respondents rated working conditions as poor and very poor, which shows that these employees often work at an increased rate of work, which also consumes energy accordingly.

When analysing the results concerning the question 'Do you feel that work takes a lot of time and has a negative impact on your private life?', it is concluded that among office employees more often work does not consume so much time that it would influence their family life – 49.0% ( $n = 24$ ) of office staff and 33.3% ( $n = 20$ ) of inspecting officers state that time spent for work does not affect their family life. However, office staff have also expressed a more frequent opinion (24.5%,  $n = 12$ ) that work takes a certain amount of time and has a negative impact on private life compared to inspectorate officials (18.3%,  $n = 11$ ). The observed trend is statistically significant,  $P = 0.044$ .

In analysing the results obtained, it should be taken into account that employees in the state administration predominantly have a defined working time from 8:30 a.m. till 17:00, but considering the specific nature of the work of inspectors, for example in cases of examination of population applications, the inspection may be carried out outside the specified working time, in the same way the work of the office may also be carried out outside the specified working time in order to accomplish it in the scheduled time periods

of performance. The results of the European Working Conditions study show that an average of 86.0% of European employees consider the balance between job responsibilities and family to be appropriate (Eurofound, 2017). The survey on involvement of state administration employees show that 40.5% of public administration employees believe that work and family life are balanced (State Chancellery, 2014). In this study, 33.3% of inspectors and 51.0% of office employees do not have an impact on family life, the results are close to the results of the study carried out in Latvia, but are not comparable to the results of the study carried out in Europe, because in it frequency of the impact of time spent at work is not known as is the case in this study and does not provide a definition of what is appropriate balance.

## CONCLUSIONS

Psychosocial risks at work are significant for those in public administration. The modified Copenhagen Psychosocial Questionnaire short version is a suitable questionnaire for studying psychosocial risks, the causes and the differences in their prevalence at work. The analysis of the results of the psychosocial risk assessment shows that there are statistically significant differences in the assessment of four out of 11 psychosocial risks to the working environment. The most common psychosocial work environment risk factor among inspectors is the inadequate attitude of management, but the most common risk factor among office employees is the lack of impact on work. Results of the research corresponds to the other findings that prove psychological risk connection on work organisation, job support, mutual trust, team work, etc. Future research could be related to studying and analysing the psychosocial risks of the work environment across job groups, including managers at different levels and support staff.

## REFERENCES

- Baltes, B. 2001. Psychological Climate in the Work Setting. *International Encyclopedia of the Social and Behavioral Sciences*. In: *N.J. Smelser & P.B. Baltes (Eds.), International Encyclopedia of the Social and Behavioral Sciences*. Elsevier (Pergamon), New York, NY, **18**, pp. 12355–12359.
- Beswick, J., Gore, J. & Palferman, D. 2006. Bullying at Work: A Review of the Literature. *Health and Safety Laboratory*, WPS/06/04.
- Chandola, T. 2010. Stress at work. British Academy Policy Centre. <https://www.thebritishacademy.ac.uk/sites/default/files/Stress%20at%20Work.pdf>. Accessed 27.10.2019.
- Eurofound. 2015. First findings: Sixth European working conditions survey. <http://www.eurofound.europa.eu/publications/resume/2015/working-conditions/first-findings-sixth-european-working-conditions-survey-resume>. Accessed 25.11.2019.
- Eurofound. 2017. *Sixth European Working Conditions Survey (2017 update)*. Luxembourg: Publications Office of the European Union, 162 pp.
- Haenisch, J.P. 2012. Factors Affecting the Productivity of Government Workers. *SAGE Open* **2**(1), 1–7.
- Kortum, E., Leka, S. & Cox, T. 2010. Psychosocial risks and work-related stress in developing countries: health impact, priorities, barriers and solutions. *International Journal of Occupational Medicine and Environmental Health* **23**(3), 225–238.



- Korunka, C. & Kubicek, B. 2017. Job demands in a changing world of work. In C. Korunka & B. Kubicek (Eds.), *Job demands in a changing world of work: Impact on workers' health and performance and implications for research and practice*. Springer International Publishing. pp. 1–5.
- Kotowska, E.I., Matysiak, A., Styrz, M., Paillhe, A., Solaz, A., Vignoli, D., Vermeylen, G. & Anderson, R. 2010. *Second European Quality of Life Survey: Family life and work*, Office for Official Publications of the European Communities, Luxembourg, pp.1–96.
- Kristensen, T.S., Hannerz, H., Høgh, A. & Borg, V. 2005. The Copenhagen Psychosocial Questionnaire – a tool for the assessment and improvement of the psychosocial work environment. *Scandinavian Journal of Work, Environment & Health* **31**, 438–449.
- Leka, S. & Aditya, J. 2010. *Health impact of psychosocial hazards at work: an overview*. Geneva: World Health Organization, 136 pp.
- Leka, S., Griffiths, A. & Cox, T. 2003. *Work organization and stress: systematic problem approaches for employers, managers and trade union representatives*. World Health Organization. Occupational and Environmental Health Team, 27 pp.
- Martin, A.J., Jones, E.S. & Callan, V.J. 2005. The role of psychological climate in facilitating employee adjustment during organizational change. *European Journal of Work and Organizational* **4**(3), 263–289.
- Maulik, P.K. 2017. Workplace stress: A neglected aspect of mental health wellbeing. *The Indian Journal of Medical Research* **4**(146), 441–444.
- Nyambura, K.J. & Ndero, K. 2016. The Impact of Psychological Climate on Employee Satisfaction: A Case Study. *International Journal of Psychology* **1**(1), 1–22.
- Robinson, O. & Griffiths, A. 2015. Coping With the Stress of Transformational Change in a Government Department. *The Journal of Applied Behavioral Science* **2**(41), 204–221.
- Roja, Z., Kalkis, H., Roja, I., Zalkalns, J. & Sloka, B. 2017. Work strain predictors in construction work. *Agronomy Research* **15**(5), 2090–2099.
- Sawithri, L.D. 2017. The impact of employer-employee relations on employee commitment: a case from Sri Lanka. *Kelaniya Journal of Human Resource Management* **12**(02), 174–192.
- State Chancellery. 2014. *Satisfaction of Public Administration employees with human resources management and its results. Survey results*. Riga: State Chancellery. 32 p. (in Latvian)
- State Chancellery. 2018. Public administration employees' satisfaction with human resource management and its development, results of the survey. Riga: State Chancellery. [https://www.mk.gov.lv/sites/default/files/editor/valsts\\_parvaldes\\_darbinieku\\_iesaistisanas\\_aptauja\\_2018.pdf](https://www.mk.gov.lv/sites/default/files/editor/valsts_parvaldes_darbinieku_iesaistisanas_aptauja_2018.pdf) (in Latvian). Accessed 15.9.2019.
- Subramanian, K.R. 2017. Psychological contract and transparent leadership in organisations. *International Research Journal of Advanced Engineering and Science* **2**(1), 60–65.
- Subramanian, K.R. 2017. Employer Employee Relationship and Impact on Organization Structure and Strategy. *International Journal of Innovative Trends in Engineering* **43**(27), 39–45.

## **A control method for increasing the heat usage efficiency of nearly-zero-energy buildings with heat pumps**

H. Pihlap<sup>1,\*</sup>, A. Annuk<sup>1</sup>, M. Lehtonen<sup>2</sup>, S. Muiste<sup>1</sup>, A. Tooming<sup>1</sup> and A. Allik<sup>1</sup>

<sup>1</sup>Estonian University of Life Sciences, Institute of Technology, Chair of Energy Application Engineering, Kreutzwaldi 56, EE51006 Tartu, Estonia

<sup>2</sup>Aalto University, Department of Electrical Engineering and Automation, Maarintie 8, Espoo, Finland

\*Correspondence: [heino.pihlap@emu.ee](mailto:heino.pihlap@emu.ee)

**Abstract.** In the retrofitting of older buildings with central heating into nearly zero-energy buildings more and more air to water heat pumps are used. These heat pumps are normally connected to heating systems, producing heat only on demand. The greatest demand for heat occurs when the outside temperature and therefore the COP of the pump is lowest. Outside temperature varies during the day, meaning it is possible to save energy by producing and storing heat in a situation where the COP is higher. To determine the periods with higher COP values weather forecast data and COP curves are used. The data enables to rank and select time periods for heat production. This in conjunction with the heat demand curve of the building enables to create an operation schedule for the heat pump. The aim of the study is to develop heat pump control methods for renovated buildings to comply with nearly zero energy building codes. Dependant on the heat pump and weather conditions, up to 10% of the electricity demand for heating can be decreased.

**Key words:** heat demand modelling, heat production scheduling, heating season, optimization, temperature fluctuations.

## **INTRODUCTION**

The operation of heat pumps has been optimized in previous studies for different purposes, for example for the peaks shaving of renewable energy production (Vanhoudt et al., 2014) and voltage control (Mufaris et al., 2013) The coefficient of performance (COP) of the heat pump has been in the focus of few previous studies (Kazjonovs et al., 2014).

To plan the efficient use of an air-to-water heat pump (further described as heat pump), it is essential to know the coefficient of performance (COP) of the particular heat pump. Unfortunately, heat pump manufacturers only scarcely describe COP values, often only at 4–6 specific temperatures, which do not allow for sufficiently accurate predictions of COP values at other temperatures. Consequently, it is necessary to continuously refine the  $COP = f(\text{temp})$  function that characterizes the air to water heat pump COP, using machine learning methods (Xu et al., 2019). Since the efficiency of the air to water heat pump is dependent on the outdoor temperature ( $t$ ), the corresponding coefficient of performance is described as the outdoor temperature function  $COP = f(t)$

(Di et al., 2011). To find the pump COP at various outdoor temperatures, it must be remembered that COP is the ratio of energy consumed to energy produced.  $f(t) = g(t) / h(t)$ , where  $g(t)$  is the energy produced by the pump at the outside temperature  $(t)$  and  $h(t)$  is the energy consumed by the pump at the outside temperature  $(t)$  (Li et al., 2011). Because  $g(t)$  and  $h(t)$  are neither linear nor exponential functions, neither is COP linear or exponential. Depending on the type of air-to-water heat pump, the COP may also be different at the same outdoor temperature, since inverter-type heat pumps control the heat output according to the needs of the building being heated. The change the COP of a heat pump dependant on outside temperature is always one directional.

It is possible to plan the operation of the air to water heat pump (Zhao et al., 2020), by knowing the amount of energy required and the energy that the pump produces at a certain outside temperature and the weather forecast. If the heat pump's productivity is greater than the building's required energy, the excess energy can be stored in a water tank and used later if the heat pump's productivity is less than the building's required energy. The required size of the water tank is determined by the building's energy requirement, the amount of energy stored and the air-to-water heat pump heat capacity (Annuk et al., 2018; Kalder et al., 2018).

The hypothesis of the study is that it is possible to cover the demand by operating the heat pump only during the hours with the highest COP and lower the electricity consumption if the heat pump has a sufficient heating power to cover the buildings energy demand at every outside temperature in the working range of the pump.

Nearly zero energy buildings (NZEBs) have a heat demand limit defined by building codes. An NZEB is defined by an energy consumption per heated floor area and difference between inside and outside temperature lower than  $0.75 \text{ W m}^{-2} \cdot \text{K}$  (Estonian Ministry of Economics and Communication, 2019). The current study uses this limit as an input for the calculations.

The novelty of the study includes the application of control methods in a new situation created by the widespread installation of heat pumps. Previous studies have mostly focused in the optimization of heat pump control on financial savings but the current study focuses on electricity and carbon emission savings.

Like the COP of the pump, it is also necessary to know the efficiency of the building to be heated (Bourdeau et al., 2019). Although NZEBs have limits on the energy consumption of a building, a similar function must be constructed for each individual building that characterizes the amount of thermal energy consumed by the building at a certain outdoor temperature. Unlike air-to-water heat pump COP, the building's COP is a linear function (Deb et al., 2017). However, the physical parameters of a building are not the only factors influencing the heat demand of the building. The number of residents in the building is also important.

The aim of the study is to develop heat pump control methods for retrofitted buildings to comply with nearly zero energy building codes.

## MATERIALS AND METHODS

### System Setup

The study used the following setup (Fig. 1). An internet connection is used to acquire weather forecasts for the scheduling of the operation of the heat pump. The heat

pump supplies energy only to the buffer tank. The energy stored in the buffer tank is used by the heating contours regulated by the indoor controller. The indoor controller operates separately from the heat pump controller.

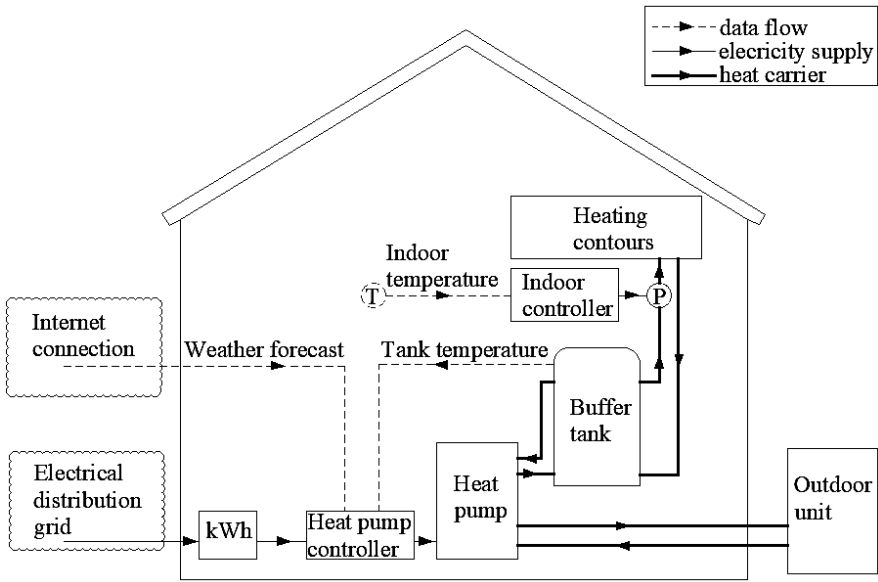


**Figure 1.** The analysed system.

**Air to water heat pump and weather parameters**

Air-water heat pumps nowadays have commonly inverter systems that follow the heating demand of the building directly. The lack of energy storage possibilities restricts the possibilities to optimize the energy use of heat pump. The addition of a thermal storage tank into the heating system of a building equipped with a heat pump enables to optimize the energy use of the heat pump. The optimization is made possible due to the COP change with the change of temperature.

While specific heat pump have different parameters, the COP is always dependant on the outside temperature.

The current study uses certified parameters from heat pump manufacturers (Table 1).

**Table 1.** Heat pump parameters (FSK Heat Pumps and Air Conditioners, 2019)

Temperature (C°)	-25	-20	-15	-7	2	7	15	20	25
Power (W)	3.85	4.95	4.88	4.28	3.4	2.51	2.18	1.98	1.88
COP	1.51	2	2.21	2.52	3.17	4.3	4.95	5.45	5.74

The real COP of an air-to-water heat pump is to a high degree of precision ( $R^2 = 0.999$ ) described by a 6-degree polynomial (Fig. 2).

$$COP(t) = 0.0003t^6 - 0.0072t^5 + 0.0548t^4 - 0.1022t^3 - 0.3638t^2 + 1.6967t + 0.2289$$

Additionally to the COP, also the real power consumption at different temperatures and maximum heating power output is necessary for the modelling of the energy usage optimization strategies (Fig. 3).

$$P_c(t) = -7E-05t^6 + 0.0015t^5 - 0.0158t^4 + 0.1607t^3 - 1.2367t^2 + 3.8598t + 1.0833$$

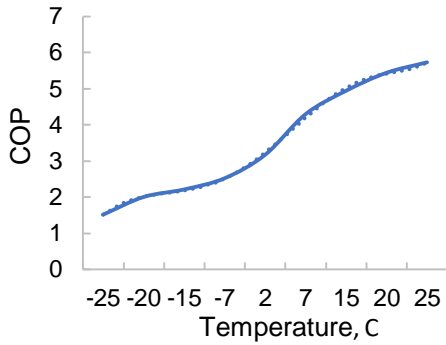


**Figure 2.** Relationship between temperature and COP.

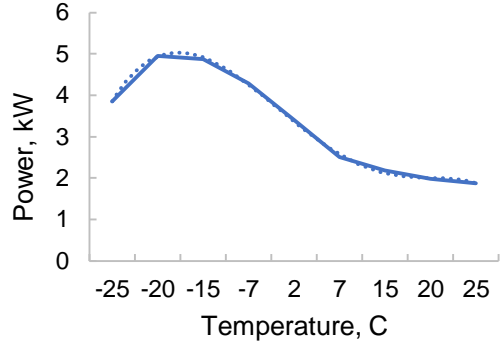


**Figure 3.** Relationship between temperature and power consumption at maximum power output.

On the basis of these relationships (Figs 2 and 3) the heat pumps maximal heating output can be calculated according to the following equation (Eq. 1).

$$P_h(t) = P_c(t) \cdot COP(t) \quad (1)$$

The most frequent temperature range was in 2019 between 0 and 6 C. Coincidentally the change of the COP value is also the largest in this temperature range (Fig. 4). The statistical average temperature in Tartu (Estonia) throughout the heating period (1. October to 4. May) is -1.5 degrees (Estonian Ministry of Economics, 1997). Hourly average outdoor temperatures measured in Tartu are used.

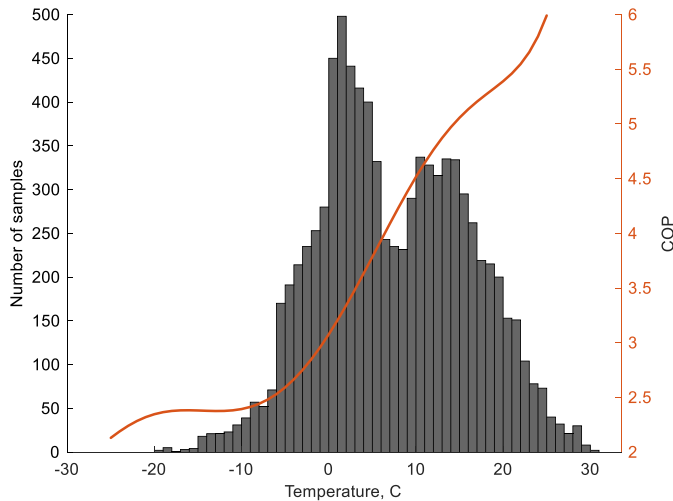


**Figure 4.** Temperature distribution 2019 and COP curve.

### Building parameters

The current study focuses only on the heating demand of the building itself. Some previous has considered to cover separately the domestic hot water demand with heat pumps and ventilation heat exchangers (Torregrosa-Jaime et al., 2018; Yuan et al., 2019). The current study used specifically only the heating load of a building that has the following parameters:

- 1) Heated floor area,  $A = 100 \text{ m}^2$
- 2) Indoor temperature set point,  $t_b = 20 \text{ }^\circ\text{C}$
- 3) Outside temperature,  $t$
- 4) Heating load of the building according to the minimum requirements for nearly zero energy buildings,  $Q_b = 0.75 \text{ W m}^{-2}\cdot\text{K}$  (Estonian Ministry of Economics and Communication, 2019).

The function that determines the heating load of the building ( $P_b(t)$ ) is characterized by the following equation:

$$P_b(t) = A \cdot (t_b - t) \cdot Q_b = 100 \cdot (20 - t) \cdot 0.75(W) \quad (2)$$

A time period was selected during which the energy expenditure is modelled when the different methods are applied (Fig. 5).

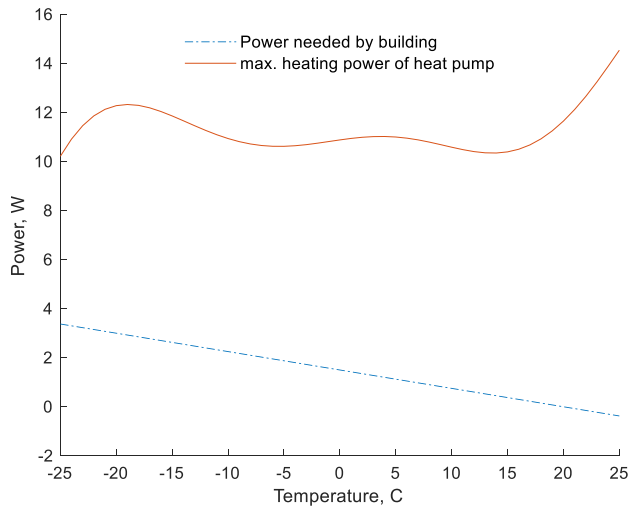


**Figure 5.** Heating demand and maximum heating power of the heat pump in relation to outside temperature.

The Estonian weather conditions may demand heating throughout the year, even in the summer. The changes of heat gains originating from the inhabitants and household equipment are not considered in this research. The heat losses from the heat storage are not considered separately because the tank is located in the building and the losses from the tank don't affect the total heat balance of the building.

### Method I

It is presumed that the heat pump works at full power (on-off regime). Energy is not stored into an accumulation tank and the pump works according to demand. The

figure above (Fig. 5) shows that the output of the heat pump is always higher than the heating demand of the house. This means that the daily consumed electrical energy ( $E_D$ ) for the heat pump can be calculated by the following equation.

$$E_D = \sum_{i=1}^{24} \frac{P_b(t_i)}{COP(t_i)} \quad (3)$$

where  $E_D$  is the electrical energy consumed by the pump, kWh;  $P_b(t_i)$  is the heating demand at the temperature  $t_i$ ;  $COP(t_i)$  is the coefficient of performance at the temperature  $t_i$ .

The yearly energy consumption ( $E_Y$ ) is calculated by adding the daily energy amounts.

$$E_Y = \sum_{j=1}^{365} E_{D_j} \quad (4)$$

The logic of Eq. 4 is also used to calculate the monthly electrical energy demand ( $E_M$ ).

## Method II

A situation is modelled where the needed heat energy is produced with the highest possible COP values. A water tank is used as thermal storage for this purpose and the time frame during which the optimization is made is 24 hours. The presumption is made that the water tank has enough energy stored for the heating demand of the first day of the heating period and the capacity of the storage is large enough to accommodate all the energy needs that can occur during 24 h periods. The hours with the highest COP during a day are often not consecutive hours. The amount of heat to cover the heating demand for each day can be calculated with the following equation:

$$Q_D = \sum_{i=1}^{24} P_b(t_i) \quad (5)$$

The presumption for the model is that algorithm acquires the weather forecasts of the outdoor temperatures for the next 24h at each midnight. On the basis of these forecasts and by using the COP and  $P_b(t)$  values the hours that are most suitable for heat production are selected.

A software is created to calculate the amount of electrical energy that is used for the production of heat. The working principle of this algorithm is described on the following figure (Fig. 6). The software is used to calculate the daily and yearly amounts of electrical energy consumed when the house heating is controlled by Method II.

According to the described algorithm calculations were made with the MatLab programming language. Previous research has measured the effectiveness of heat pump control through the increase in seasonal COP (Pospíšil et al., 2019). The effectiveness of the method in this study was measured with the decrease of consumed energy in relation to the total electrical energy consumption.

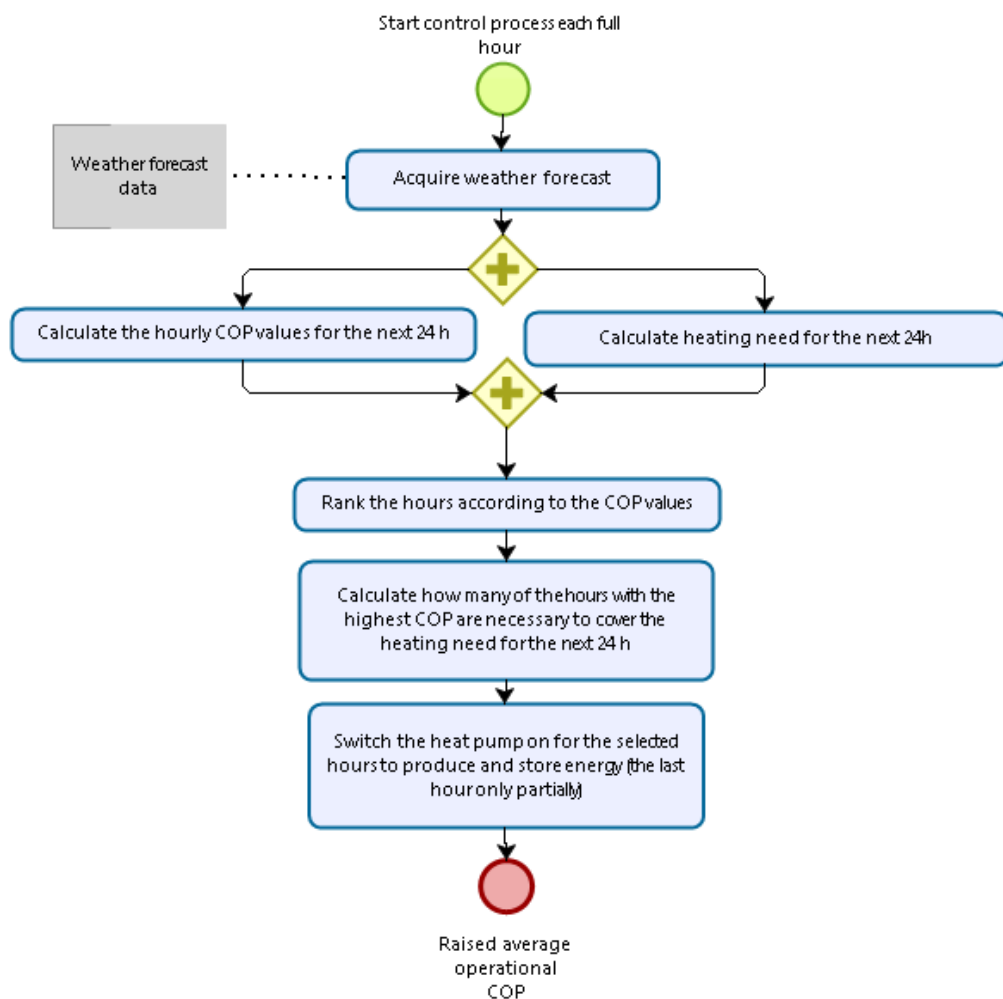


**Figure 6.** Flow chart of the second method.

## RESULTS AND DISCUSSION

### Method I

The modelling was made with the outdoor temperature data from the years 2018 and 2019. The yearly energy consumption of the air-to-water heat pump was calculated according to Eqs (3) and (4). The results are the following  $E_{YI}(2018) = 2,870$  kWh and  $E_{YI}(2019) = 2,600$  kWh.

Also the monthly electrical energy consumption values were calculated according to the logic given above. The modelling results on a monthly basis are given on the following figure (Fig. 7).



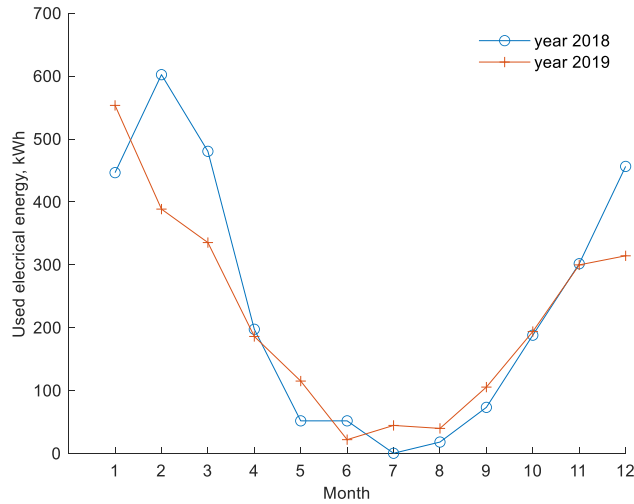


**Figure 7.** Modelled electrical energy usage with Method I.

### Method II

The model used the same input data like Method I, with the outdoor temperature data from the years 2018 and 2019 and based on the Method II given in Fig. 5 the yearly energy consumption of the air-to-water heat pump was calculated. The results are the following  $E_{YII}(2018) = 2,645.56 \text{ kWh}$  and  $E_{YII}(2019) = 2,331.8 \text{ kWh}$ . The comparison of the results from the different methods, Method II (optimized energy usage) and Method I (non-optimized energy usage) are presented in the following figures (Figs 8 and 9).

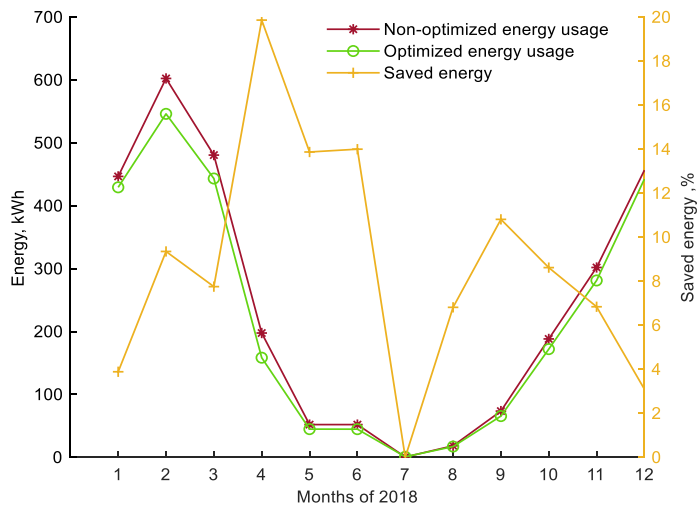


**Figure 8.** Comparison of non-optimized and optimized electrical energy usage and resulting Savings in 2018.

Energy savings ( $E_s$ ) in the years 2018 and 2019 of Method II in comparison to Method I are the following:  $E_s = E_{YI}(2018) - E_{YII}(2018) = 224,5 \text{ kWh}$ , which amounts to 7.82% of the non-optimized energy expenditure and  $E_s = E_{YI}(2019) -$

$E_{YII}(2019) = 268.27 \text{ kWh}$ , which makes up 10.3% of the non-optimized electricity expenditure.

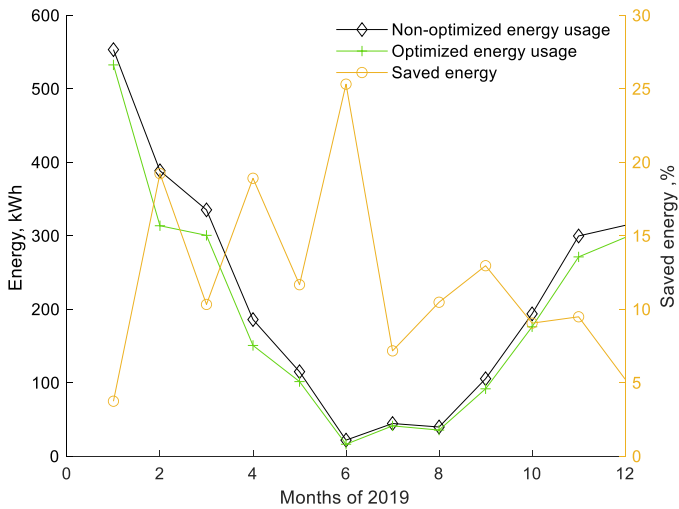


**Figure 9.** Comparison of non-optimized and optimized electrical energy usage and resulting Savings in 2019.

Since the COP is a function of the outdoor temperature, then the saved amount of energy is dependent on the speed and amplitude of the temperature changes. Larger changes enable larger energy savings when using the control methods described above.

The results (Fig. 9) show that the largest proportional savings can be achieved at the beginning and end of the heating period, when the largest changes in outdoor temperature occur between night and daytime.

The relative energy savings per month in 2018 and 2019 are given in the figure below (Fig. 10).

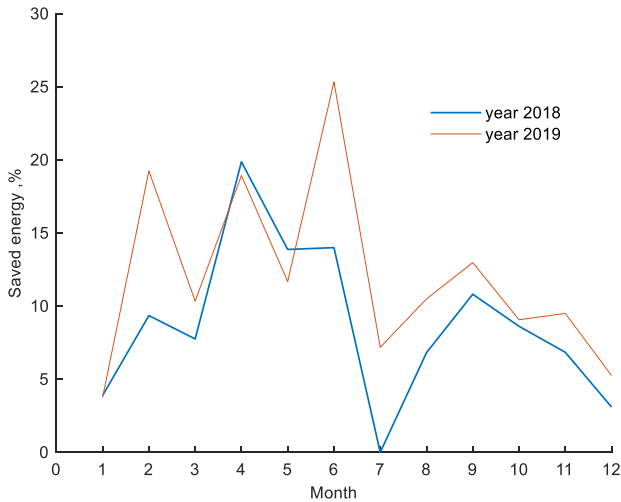


**Figure 10.** Comparison of relative energy saving per month during 2018 and 2019.

The theoretically achieved energy savings of 268.27 kWh per building during the year 2019 and the average CO<sub>2ekv</sub> emissions in the Estonian Electricity consumption of 889 g kWh<sup>-1</sup> (Tranberg et al., 2019) would enable the reduction of emissions by 238 kg CO<sub>2ekv</sub> per year per building. The method has a significant potential for energy and CO<sub>2ekv</sub> savings, for example, 164,000 households in Estonia still used wood fuels as a heating source for their living space, which most likely will be replaced in the future by heat pumps (Maasikmets et al., 2016).

The authors presume that the findings of this study can be generalized to all air to water heat pumps. While specific heat pump have different parameters, the COP is always dependant on the outside temperature.

Future research in this field will use more complex control models including the specified heat demand curve. Further research will also include the use of renewable energy produced on site for heat pumps.

## CONCLUSIONS

The use of air-to-water heat pumps is increasing and the optimization of their operation enables significant energy savings and makes it possible to achieve European Union climate ambitions. Air to water heat pump installers should consider including more storage tanks into the heat pump systems. The main advice for heat pump manufacturers is to give out more information about the COP curves of their products and for the users to be more knowledgeable to ask for more information about the COP curves in the selection process. This enables the more effective design of heating systems with heat pumps.

The method requires as an input the total energy demand and weather forecast during a chosen period not the distribution of the demand inside the period. The main factor that determines the energy savings in practice is the precision of the weather forecasts. A more accurate weather forecast enables to the prognosis of the productivity of the heat pump and heating demand of the building at any given time. The continuous measurement and calculation of the COP of the heat pump would be necessary for the optimization of an air-to-water heat pump in real conditions.

By shifting the heat production inside a day to the hours with higher heat pump COP values, the electricity consumption can be significantly reduced, with this method by 7.82%. 10.3% dependant on the weather conditions. The described method enables energy savings regardless of the characteristic of the heating demand.

**ACKNOWLEDGEMENTS.** The authors express their gratitude for the research funding by the Estonian Ministry of Education and Research through the Estonian Centre of Excellence in Zero Energy and Resource Efficient Smart Buildings and Districts, ZEBE, grant TK146 funded by the European Regional Development Fund.

## REFERENCES

- Annuk, A., Jõgi, E., Lill, H., Kalder, J., Hovi, M., Pihlap, H., Jasinskas, A., Härm, M., Trashchenkov, S. & Allik, A. 2018. *Augmentation of Self-Consumption of Electricity by Using Boilers and Batteries for Residential Buildings* 7, 256–260.

- Bourdeau, M., Zhai, X.Q., Nefzaoui, E., Guo, X. & Chatellier, P. 2019. Modeling and forecasting building energy consumption: A review of data-driven techniques. *Sustainable Cities and Society* **48**(2), 101533. <https://doi.org/10.1016/j.scs.2019.101533>
- Deb, C., Zhang, F., Yang, J., Lee, S.E. & Shah, K.W. 2017. A review on time series forecasting techniques for building energy consumption. *Renewable and Sustainable Energy Reviews* **74**, 902–924. <https://doi.org/10.1016/j.rser.2017.02.085>
- Di, Y., Di, Y., Wang, Y. & Wen, L. 2011. Application and analysis of water source heat pump system in residential buildings. *ISWREP 2011 - Proceedings of 2011 International Symposium on Water Resource and Environmental Protection* **3**, 2425–2428. <https://doi.org/10.1109/ISWREP.2011.5893758>
- Estonian Ministry of Economics. (1997). *Methodology of Calculation of Heating Demand*. 1–19.
- Estonian Ministry of Economics and Communication. 2019. *Minimum requirements for energy performance* **6**, 1–8.
- FSK Heat Pumps and Air Conditioners. 2019. *Air-to-Water Heat Pump Parameters*. Available at <https://www.fsk.ee/ohk-vesisoojuspumbad/ohk-vesi-inverteriga-mudelid/869>
- Kalder, J., Annuk, A., Allik, A. & Kokin, E. 2018. Increasing solar energy usage for dwelling heating, using solar collectors and medium sized vacuum insulated storage tank. *Energies* **11**(7). <https://doi.org/10.3390/en11071832>
- Kazjonovs, J., Sipkevics, A., Jakovics, A., Dancigs, A., Bajare, D. & Dancigs, L. 2014. Performance analysis of air-to-water heat pump in Latvian climate conditions. *Environmental and Climate Technologies* **14**(1), 18–22. <https://doi.org/10.1515/rtuct-2014-0009>
- Li, N., Zhang, W., Wang, L., Liu, Q. & Hu, J. 2011. Experimental study on energy efficiency of heat-source tower heat pump units in winter condition. *Proceedings - 3rd International Conference on Measuring Technology and Mechatronics Automation, ICMTMA 2011*, **2**, 135–138. <https://doi.org/10.1109/ICMTMA.2011.321>
- Maasikmets, M., Kupri, H.L., Teinemaa, E., Vainumäe, K., Arumäe, T., Roots, O. & Kimmel, V. 2016. Emissions from burning municipal solid waste and wood in domestic heaters. *Atmospheric Pollution Research* **7**(3), 438–446. <https://doi.org/10.1016/j.apr.2015.10.021>
- Mufaris, A.L.M., Member, N. & Baba, J. 2013. Local control of heat pump water heaters for voltage control with high penetration of residential PV systems. *IEEE 8th International Conference on Industrial and Information Systems*, pp. 18–23.
- Pospíšil, J., Špiláček, M. & Charvát, P. 2019. Using Predictive Control Preferring Power Production. *Energies* **12**, 1–13. <https://doi.org/doi:10.3390/en12173236>
- Torregrosa-Jaime, B., González, B., Martínez, P.J. & Payá-Ballester, G. 2018. Analysis of the operation of an aerothermal heat pump in a residential building using building information modelling. *Energies* **11**(7). <https://doi.org/10.3390/en11071642>
- Tranberg, B., Corradi, O., Lajoie, B., Gibon, T., Staffell, I. & Andresen, G.B. 2019. Real-time carbon accounting method for the European electricity markets. *Energy Strategy Reviews*, **26**(December 2018). <https://doi.org/10.1016/j.esr.2019.100367>
- Vanhoudt, D., Geysen, D., Claessens, B., Leemans, F., Jespers, L. & Van Bael, J. 2014. An actively controlled residential heat pump: Potential on peak shaving and maximization of self-consumption of renewable energy. *Renewable Energy* **63**, 531–543. <https://doi.org/10.1016/j.renene.2013.10.021>
- Xu, X., Wang, W., Hong, T. & Chen, J. 2019. Incorporating machine learning with building network analysis to predict multi-building energy use. *Energy and Buildings* **186**, 80–97. <https://doi.org/10.1016/j.enbuild.2019.01.002>
- Yuan, Y., Lin, W., Mao, X., Li, W., Yang, L., Wei, J. & Xiao, B. 2019. Performance analysis of heat pump dryer with unit-room in cold climate regions. *Energies* **12**(16). <https://doi.org/10.3390/en12163125>
- Zhao, J. & Shan, Y. 2020. A fuzzy control strategy using the load forecast for air conditioning system. *Energies* **13**(3), 1–17. <https://doi.org/10.3390/en13030530>

## **The experimental investigation of the mechanical properties of steel fibre-reinforced concrete according to different testing standards**

A. Ryabchikov\*, M. Kiviste, S.-M. Udras, M. Lindpere, A. Vassiljev and N. Korb

Estonian University of Life Sciences, Institute of Forestry and Rural Engineering, Chair of Rural Building and Water Management, Kreutzwaldi 1, EE51006 Tartu, Estonia

\*Correspondence: alexander.ryabchikov@emu.ee.

**Abstract.** Steel fibre-reinforced concrete (SFRC) is widely applied in the construction of civil infrastructure projects, including the following: industrial floors, slabs, walls, and foundations. The application of steel fibres in the reinforcement of concrete remarkably improves the post-cracking behaviour of such concrete. In order to estimate this property, the energy involved in absorption is measured by using several valid testing standards: EVS-EN 14651:2005, EVS-EN 14488-5:2006, and ASTM C1550-12a. The objective of this study was to carry out a comparable analysis of the results that have been obtained using previously-mentioned standards and to be able to find a more reliable method for the determination of the fracture toughness of SFRC specimens. Experiments were carried out in accordance with the chosen standards. It was concluded that procedure involved in the ASTM standard provides a smaller variability of results with better levels of repeatability, therefore a smaller volume of specimens can be tested in one series in order to achieve reliable results.

**Key words:** SFRC, steel fibres, flexural strength, energy absorption capacity.

### **INTRODUCTION**

SFRC has advantages over traditionally reinforced and pre-stressed concrete structures (Altun et al., 2007; Kiviste et al., 2019) in terms of its use in civil engineering projects. Steel fibres can be added to a concrete mix in order to make it an integral part of any fresh concrete laying. Although research on SFRC has been rather active during the past decade, there is still a need for evidence-based information on certain mechanical properties that are involved in SFRC. Abbass et al. (2018) found that the addition of different content levels and lengths of steel fibres with increasing water-to-cement ratios tended to cause an increase of about 10–25% in the compressive strength of concrete and about 31–47% in its direct tensile strength. An increase in steel fibre content from 0.5% to 1.5% (per volume of concrete) increased flexural strength from 3% to 124% for steel fibre with a smaller aspect ratio of 65, whereas for a higher aspect ratio of 80, a 140% increase in flexural strength was observed when compared to concrete without any steel fibre additives. Han et al. (2019) found that the length of the

steel fibres has a greater effect on the mechanical properties of SFRC than does the maximum size of any coarse aggregate being used.

When it comes to designing SFRC elements it is important to know flexural strength and post-cracking behaviour, which can be estimated by measuring the energy absorption capacity of test specimens (Salehian et al., 2014; Abbass et al., 2018). Changes in concrete compressive strength and flexural tensile strength are quite small at a steel fibre level that is below 3% of the volume of the concrete and are not of any significance when it comes to design purposes (Ryabchikov et al., 2015; Dong & Shi, 2020).

The post-cracking behaviour of SFRC depends upon the type of steel fibres being used, plus the aspect ratio and its distribution within the volume of concrete. Several European standards (EVS-EN 14651:2005; EVS-EN 14488-5:2006) and an American standard (ASTM C1550-12a) have been developed for determining the flexural toughness of SFRC using different specimen types (beams, square slabs, or round panels). Flexural toughness is defined as the energy that is absorbed during the three-point bending of the beam and this equals the area that is under a load-deflection curve (Köksal et al., 2013).

From knowing the area that is under the load-deflection curve it is possible to determine an equivalent flexural strength ( $f_e$ ) according to Japanese Standard JSCE-SF4. This is defined as the stress, which corresponds to the average load value over the area of the load deflection curve. The equivalent flexural strength can be directly used in designing SFRC elements.

The objective of this study was to review, compare, and analyse the flexural behaviour, flexural toughness, and failure modes of SFRC test specimens using the aforementioned European and American standards in order to be able to highlight their advantages and disadvantages.

SFRC test specimens were prepared and tested according to two European standards and one American standard, under which different loading configurations have been applied. According to the EVS-EN 14651:2005 standard, the notched prisms with dimensions of 150×150×600 mm were tested using a scheme that involved three-point bending. According to the EVS-EN 14488-5:2006 standard, steel fibre square slabs with dimensions of 600×600×100 mm were continuously supported on each side and were centrally loaded. Under the American standard, ASTM C1550-12a, round slabs with a diameter of 800 mm and a thickness of 75 mm were pivot-supported at three points and centrally loaded until they fractured. The results were analysed and conclusions were drawn up.

## **MATERIALS AND METHODS**

Experiments with SFRC have been carried out according to three standards, where various forms of specimen shape (beams, square slabs, and round panels) have been used. Specimens were prepared and treated as prescribed in the applicable standards.

### **Experiments with round panels**

The flexural toughness of SFRC was determined according to the ASTM C1550-12a standard, for which round panels have to be tested. Toughness is defined as the energy that is absorbed by the specimen which is equivalent to the area that is under the load-deflection curve between the onset of loading and a specified central deflection

point (Fig. 1, a). Two series of experiments were carried out with round panels. The ingredients of the concrete and data for the specimens are presented in Table 1.

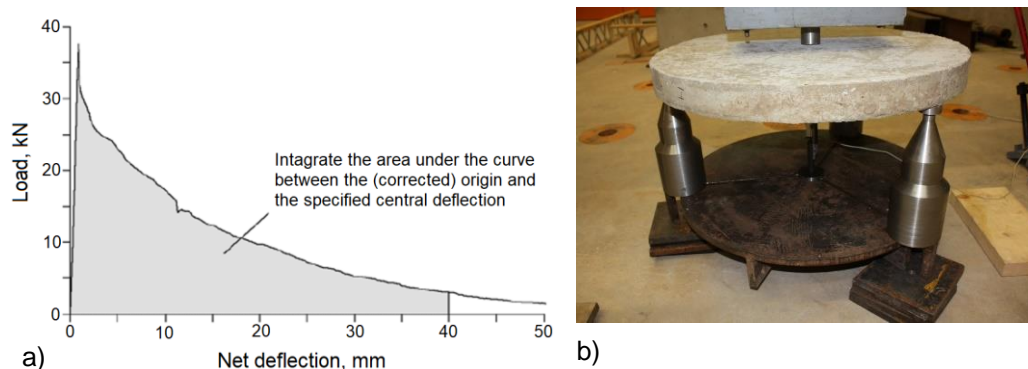


**Figure 1.** Integrating the area under the load-net deflection curve (a) to obtain the energy absorption levels (ASTM C1550-12a), and photo (b) showing the loading of a round plate specimen (Vassiljev, 2013).

Round panels with a nominal diameter of 800 mm were placed on three pivot supports for the bending test (Fig. 1, b). The failure mode for three symmetrically arranged support pivots (Fig. 2) results in low variability levels in the energy that is absorbed by a set of panels up to a specified central deflection point. The nominal thickness of a panel is 75 mm, which strongly influences the panel's performance and has to be measured very accurately. The actual diameter of a specimen should be within the range of 790–810 mm and at a thickness of 70–90 mm. If the actual dimensions of a specimen are different from the nominal dimensions that have been given here then the peak load should be corrected accordingly.

**Table 1.** The ingredients of a round panel specimen (Vassiljev, 2013; Udras, 2016)

	Series 1	Series 2
Cement CEM II/B-M(T-L) 52.5N, kg m <sup>-3</sup>	400	-
Cement CEM-I 42.5N, kg m <sup>-3</sup>	-	383
Sand 0–8, kg m <sup>-3</sup>	1,000	592 (0–5)
Gravel 4–12, kg m <sup>-3</sup>	800	1,110 (8–16)
Superplasticiser, % of cement mass	0.67	-
Water, kg m <sup>-3</sup>	190	230
Water-cement ratio		0.6
Steel fibres HE 1/60, kg m <sup>-3</sup>	48	-
Steel fibres HE 1/50, kg m <sup>-3</sup>	-	70
Strength class of concrete	C45/55	
Average diameter, mm	798 ± 5	798 ± 5
Average thickness, mm	75 ± 1	75 ± 1

Panels were loaded with the hydraulic cylinder, a Lukas LZM 25/200, the deflections were measured with the Ahlborn Almemo FWA050T displacement sensor, and the experimental data were recorded using the Ahlborn Almemo 5690-2 data recorder. The experimental data were further processed on a personal computer.

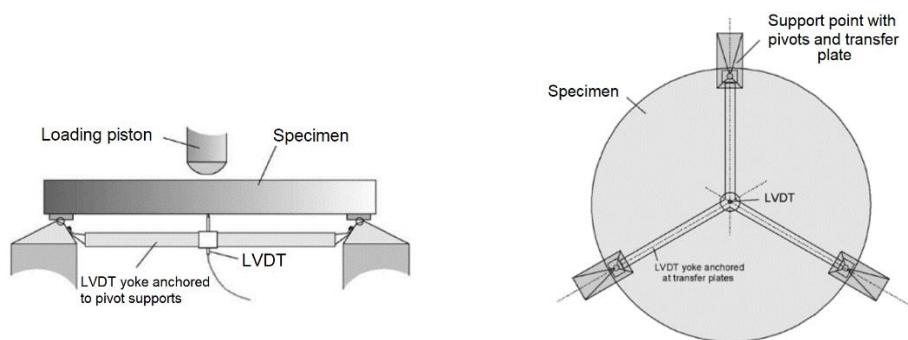


**Figure 2.** Schematic for loading up a round plate specimen (ASTM C1550-12a).

The corrected energy absorption level is calculated for deflection values of 5 mm, 10 mm, 20 mm, and 40 mm according to the formula presented in standard:

$$W = W' \left( \frac{t_0}{t} \right)^\beta \left( \frac{d_0}{d} \right), \quad (1)$$

where  $W'$  is the measured energy absorption level, J;  $t$  is the measured average thickness, mm;  $t_0$  is the nominal thickness of 75 mm;  $d$  is the measured average diameter, mm;  $d_0$  is the nominal diameter of 800 mm,  $\beta = 2.0 - (\delta - 0.5)/80$ ; and  $\delta$  – the specified central deflection at which the capacity to absorb energy is measured, in mm.

### Experiments with the slabs

The energy absorption capacity of fibre-reinforced slab specimens was determined in accordance with the European standard, EVS-EN 14488-5:2006. A square slab is continuously supported along its edges and is loaded at the centre. The load-deflection curve was recorded and the test was continued until a deflection of at least 30 mm was achieved at the slab's mid-span. Five square slabs were cast with dimensions of 600×600×100 mm (Fig. 3, a). Hooked-end steel fibres, HE 75/35, with a dosage of 35 kg m<sup>-3</sup> were used for reinforcing the concrete. The ingredients of the concrete specimens are presented in Table 2.

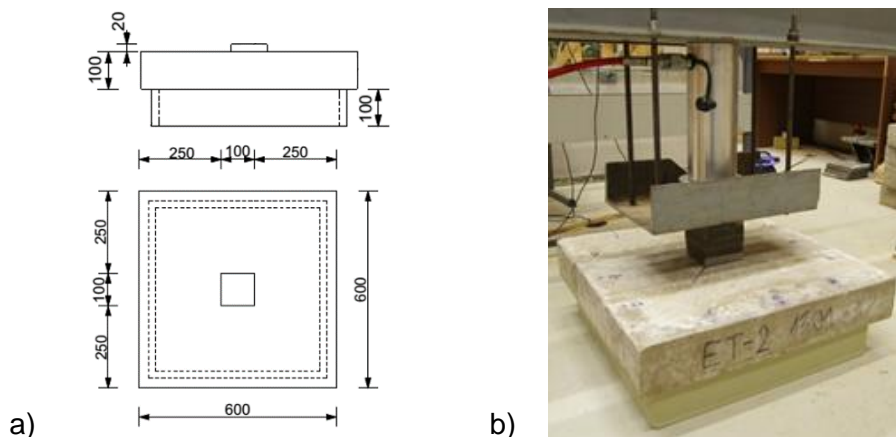


**Figure 3.** Schematic (a) and photo (b) for the loading configuration of a rectangular slab specimen (Lindpere, 2016).



A square rigid frame support (with a thickness of  $20 \pm 1$  mm and internal dimensions of  $500 \pm 2$  mm) was produced so that it could support the slab (Fig. 3, a). Slabs were loaded with the hydraulic cylinder, a Lukas LZM 25/200 (Fig. 3, b), with deflections being measured with an Ahlborn Almemo FWA050T displacement sensor, and test results being recorded with an Ahlborn Almemo 5690-2 data recorder.

The energy absorption capacity was calculated as the area under the load-deflection curve between a deflection of zero and 25 mm.

**Table 2.** The ingredients of a round panel specimen (Lindpere, 2016)

Cement CEM II/B-M(T-L) 52.5R, $\text{kg m}^{-3}$	325
Sand 0-8, $\text{kg m}^{-3}$	1,036
Gravel 4-16, $\text{kg m}^{-3}$	865
Water, $\text{kg m}^{-3}$	180
Steel fibres, $\text{kg m}^{-3}$	35
Strength class of concrete	C25/30
Average length of edge, mm	$600.9 \pm 0.8$
Average thickness, mm	$101.4 \pm 0.3$

### Experiments with the beams

Experiments with beams were carried out in accordance with the EN 14651:2005+A1:2007 standard. The measurements for the specimens were  $150 \times 150 \times 600$  mm. An Instron 3369 universal testing machine with a capacity of 50 kN was applied for the implementation of the three-point bending loading test (Figs 4, a, 4, b). The specimens were loaded at the start of the process so that the deflection increased at a constant rate of  $0.08 \text{ mm min}^{-1}$ . The deflection rate from a value of 0.13 mm was adjusted to a constant rate of  $0.21 \text{ mm min}^{-1}$ . The test was stopped at a deflection point of 5 mm. Deflections were measured by means of a video extensometer with an accuracy level of 0.001 mm at the mid-span of a beam.

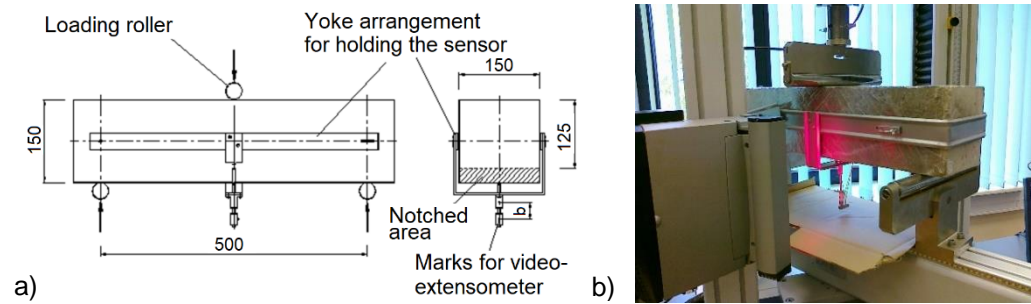


**Figure 4.** Schematic (a) and photo (b) showing the loading of a beam specimen (Ryabchikov et al., 2015).

The yoke arrangement was used for mounting the displacement transducer of a video extensometer and ensuring the accurate measurement of the mid-span deflections, excluding any effects that may have been due to the seating or twisting of the test beam on its supports. Two series of tests were carried out with dosages of  $25 \text{ kg m}^{-3}$  and  $35 \text{ kg m}^{-3}$ . Crimped steel fibres SAVEX 1/50 were used for reinforcement. Specimens were notched at the mid-span of the beam's tensile zone. The width of the notch was 5 mm or less and the height of the fracture section was at  $125 \pm 1$  mm (Fig. 4, a).

The limit of proportionality (LOP)  $f_L$  and residual flexural strength  $f_i$ , corresponding to deflections of 0.47, 1.32, 2.17, and 3.02 mm, were calculated according to the formulas given in the EN 14651:2005+A1:2007 standard.

The equivalent flexural strength  $f_{e,3}$  and  $R_{e,3}$  values were obtained according to the code of the Japanese Society of Civil Engineers – JSCE-SF4. The equivalent flexural strength  $f_{e,3}$  is determined from the area below the load-deflection curve until the measured deflection becomes  $1/150$  of the specimen's span (Fig. 5). The further toughness of the SFRC can be estimated by the equivalent flexural ratio  $R_{e,3} = f_{e,3} f_L^{-1}$  – the higher the value of  $R_{e,3}$ , the higher is the expectation in terms of the beam's load-bearing capacity and toughness. The equivalent flexural strength is calculated at a deflection of 3.33 mm using the formula (2):

$$f_{e,3} = \frac{T_b l}{3.33 b h^2}, \quad (2)$$

where  $T_b$  is the area below the load-deflection curve;  $l$  is the span length;  $b$  is the width of the specimen; and  $h$  is the height of the fracture section.

## RESULTS AND DISCUSSION

The main objective of the study was to provide a review and to carry a comparative analysis of methods for the determination of the residual flexural strength and energy absorption capacity of fibre-reinforced concrete. Experiments were carried out in accordance with two European standards and one ASTM standard. All three standards prescribe the use of different specimen shapes: beams, square slabs, and round panels.

An experimental diagram representing the dependence of the central deflection of a round concrete panel with steel fibres HE 1/60 ( $48 \text{ kg m}^{-3}$ ) on the load is presented in Fig. 6, and a version with steel fibres HE 1/50 ( $70 \text{ kg m}^{-3}$ ) is shown in Fig. 7.

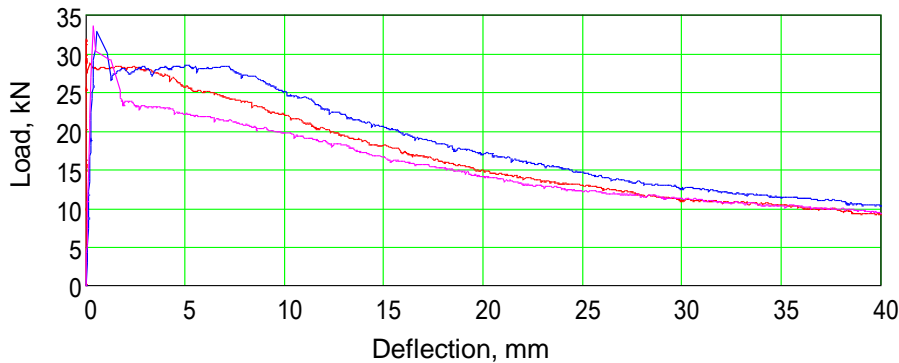


**Figure 6.** The load-deflection curve of a round concrete panel (strength class C45/55) containing steel fibres HE 1/60 with a dosage of  $48 \text{ kg m}^{-3}$  (Udras, 2016).

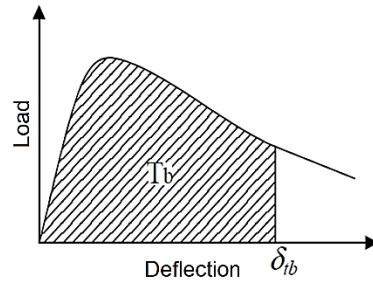


**Figure 5.** Area  $T_b$  for calculating flexural toughness (JSCE-SF4).

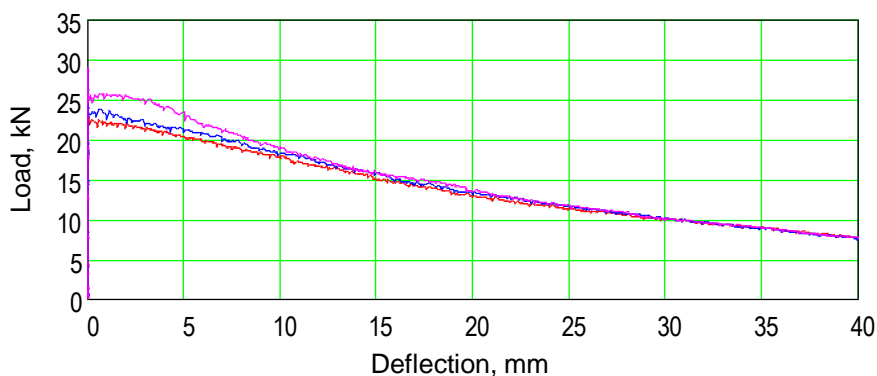


**Figure 7.** The load-deflection curve of a round concrete panel (strength class C25/30) containing steel fibres HE 1/50 with a dosage of  $70 \text{ kg m}^{-3}$  (Vassiljev, 2013).

The calculated average peak load and absorbed energy at the certain central deflections for a round panel for both series of experiments are summarised in Table 3.

Three panels were tested in each test series. The differences between the series were in terms of dosage and in the strength class of the concrete, which mainly affects the peak load value. It can be seen in Figs 6 and 7 that the fluctuation of load deflection curves is higher in the case of a lower fibre dosage.

This was affected by the uneven distribution of fibres in the section fracture and by the difference in the aspect ratio of the fibres.

The load-deflection curves of tested square concrete slabs with measurements of  $600 \times 600 \times 100 \text{ mm}$  and containing steel fibres of the HE 75/50 type with a dosage of  $35 \text{ kg m}^{-3}$  are presented in Fig. 8. The average peak load was  $53.9 \pm 8.7 \text{ kN}$  and the absorbed energy at 25 mm of central deflection was  $571 \pm 99 \text{ J}$ , respectively (Lindpere, 2016). Fig. 8 shows that the peak values within one series of experiments fluctuated within a fairly high range. The peak load is higher than load at first crack and it caused by the amount of fibres bridging the cracks, what is different specimen by specimen. The reason for such behaviour is the chaotic nature of the fibre dispersion and orientation, which was very sensitive to the moulding procedure (Laranjeira, 2010).

Two series of experiments with beams were carried out. The first series was with a dosage of  $25 \text{ kg m}^{-3}$  and the second series was at  $35 \text{ kg m}^{-3}$ . All specimens were notched according to the testing standard, EVS-EN 14651:2005+A1:2007. The load-deflection curve of beams that contained steel fibres of the SAVEX 1/50 type with a dosage of  $35 \text{ kg m}^{-3}$  is presented in Fig. 9. The experimental results are summarised in Table 4.

**Table 3.** Peak load (kN) and energy absorption (J) at the central deflections of a round panel

	Series 1 (Udras, 2016)	Series 2 (Vassiljev, 2013)
Peak load	$32.90 \pm 5.50$	$27.19 \pm 2.33$
5 mm	$133.36 \pm 19.56$	$116.01 \pm 5.03$
10 mm	$253.86 \pm 61.48$	$216.42 \pm 6.41$
20 mm	$439.51 \pm 115.28$	$374.17 \pm 6.13$
40 mm	$681.06 \pm 167.12$	$582.61 \pm 5.36$

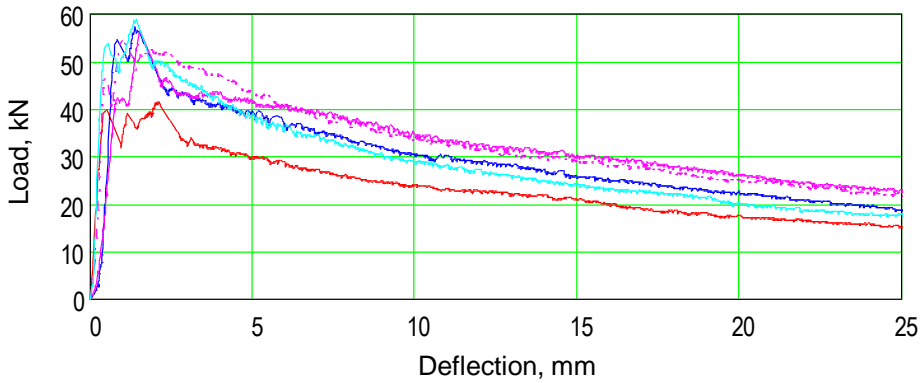


**Figure 8.** The load-deflection curve of a square concrete slab (600×600×100 mm) containing steel fibres HE 75/50 with a dosage of 35 kg m<sup>-3</sup> (Lindpere, 2016).

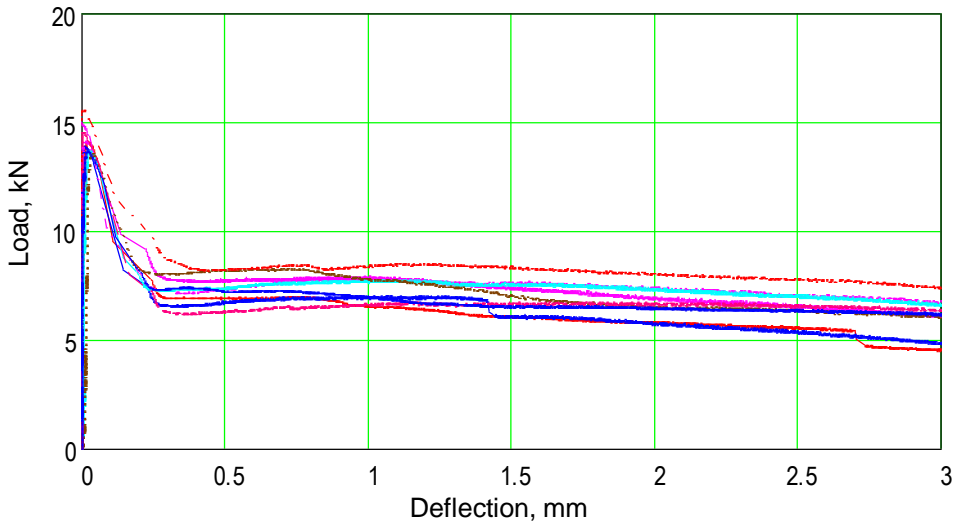


**Figure 9.** The load-deflection curve of concrete beams (150×150×600 mm) which contain steel fibres of the SAVEX 1/50 type with a dosage of 35 kg m<sup>-3</sup> (Korb, 2008).

The fluctuation of the area below the load-deflection curve within one series of experiments is significantly high. In the case of the beam at least twelve specimens had to be tested to obtain reliable results. A lower residual flexural strength and higher deviation was observed in the case of a lower dosage of fibres (Table 4).

**Table 4.** The dimensions of specimens and the results from testing the beams (Korb, 2008).

	Dimensions of the section area (mm)		LOP (MPa)	Residual flexural strength (MPa)		Equivalent flexural strength	
	Height	Width	$f_L$	$f_{0.47}$	$f_{3.02}$	$f_{e,3}$ (MPa)	$R_{e,3}$ (%)
Series 1	125 ± 1	156 ± 1	4.30 ± 0.13	2.20±0.44	1.78±0.35	2.18±0.37	51 ± 8
Series 2	125 ± 1	154 ± 1	4.47 ± 0.13	2.35±0.16	1.94±0.16	2.30±0.15	51 ± 2

The major advantage of the round panel test when compared to the square panel test is the formation of three cracked lines (Fig. 10, a). The large dimension was formed of the cracked area (containing three cracks of a length of 400 mm and a depth of 75 mm), which ensured a certain level of consistency and stability in the experimental results that were obtained (Ciancio et al., 2014). The same tendency was observed in our experiments. When comparing the load-deflection curves of the round panels (Fig. 7) and those of the square slabs (Fig. 8), a higher fluctuation can be seen in the experimental data for the squared slabs. The loading configuration of the round panel is statically determined and the loading configuration of the square slab is statically undetermined. Therefore the crack patterns on the square slabs at the point of failure are different for each tested specimen (Fig. 10, b); therefore the section area and the number of ‘working’ fibres is different every time, which directly affects the absorption capacity of the specimen and the mode of its failure (Salehian et al., 2014).

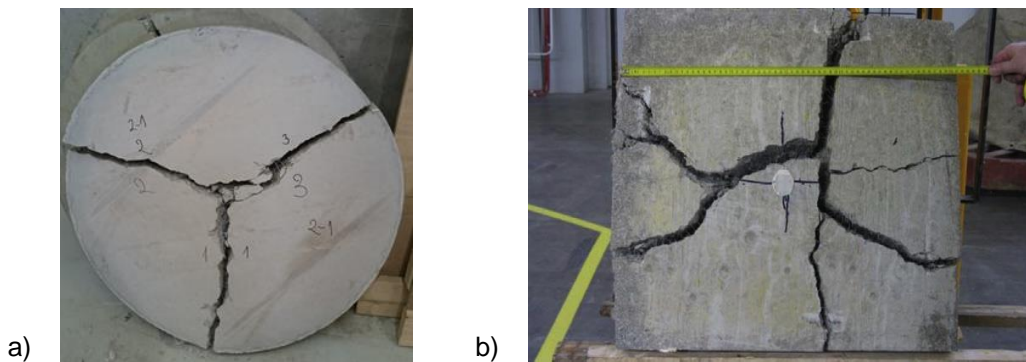


**Figure 10.** Fracture mode for a round panel (a) (Udras, 2016) and for a square slab (b) (Ciancio et al., 2014).

The flexural toughness characterises the structural parameter rather than a material property, and this is dependent upon the dimensions of the sample (Ciancio et al., 2014).

In the case of the beam specimens it is difficult to ensure the uniform distribution of fibres across the entire volume. Therefore, there is a high level of fluctuation in residual flexural strength (Table 4), since a large number of tests should be carried out in order to obtain reliable results. Experiments have demonstrated that the results are more uniform with fibre dosages that start at  $30 \text{ kg m}^{-3}$  (Korb, 2008).

## CONCLUSIONS

The flexural test which covered three shapes (beams, square slabs, and round panels) of steel fibre reinforced specimens according to the recommendations specified in three standards (two European standards and one ASTM) were all carried out and the following conclusions were found:

1. In comparison with the European standard, the experimental results that were obtained by applying the ASTM standard provided a smaller variability in the test results, which means better repeatability, and a greater fracture surface with more fibres. This, in turn, decreased the influence of any uneven distribution of fibres. Therefore less

test specimens were required in order to achieve a reliable result. This meant also that the fracture surface of specimens was measured more accurately.

2. The advantage of a round panel test when compared to a square panel test was the formation of three cracked lines. Therefore a large cracked area was formed, which ensured a greater degree of consistency and stability in terms of the experimental results that were obtained.

3. The application of round panels eliminated the sawing of a notch that was required to prepare the beam specimens. Notched specimens always had only one cracked line at the point of failure, meaning also a smaller cracked area. This, in turn, resulted in a larger variability in the test results.

4. The crack pattern in the square panels at the point of failure was found to be different for each tested specimen. Therefore the section area and the number of 'working' fibres were found to vary somewhat, which in turn directly affected the absorption capacity of the specimen.

5. The limitation in terms of applying the ASTM standard consists of a requirement for preparing a test specimen of relatively large dimensions, which weighs approximately 100 kg.

6. The fibre dosage of 30 kg (or more) per cubic metre of concrete resulted in more uniform residual flexural test results.

ACKNOWLEDGEMENTS. The support is greatly acknowledged of Estonian concrete companies, Savekate AS, Rudus AS, and Betotrade OÜ.

## REFERENCES

- Abbass, W., Khan, M.I. & Mourad, S. 2018. Evaluation of mechanical properties of steel fiber reinforced concrete with different strengths of concrete. *Construction and Building Materials* **168**, 556–569.
- Altun, F., Haktanir, T. & Ari, K. 2007. Effects of steel fiber addition on mechanical properties of concrete and RC beams. *Construction and Building Materials* **21**, 654–661.
- ASTM C1550–12a. Standard Test Method for Flexural Toughness of Fiber Reinforced Concrete (Using Centrally Loaded Round Panel). Developed by Subco mmittee: C09.42
- Ciancio, D., Mazzotti, C. & Buratti, N. 2014. Evaluation of fibre-reinforced concrete fracture energy through tests on notched round determinate panels with different diameters. – *Construction and Building Materials* **52**, 86–95.
- Dong, L. & Shi, L. 2020. The influence of steel fiber on water permeability of concrete under sustained compressive load. *Construction and Building Materials* **242**, 118058.
- EVS-EN 14488-5:2006. Testing sprayed concrete - Part 5: Determination of energy absorption capacity of fibre reinforced slab specimen.
- EVS-EN 14651:2005+A1:2007 Test method for metallic fibre concrete. Measuring the flexural tensile strength (limit of proportionality (LOP), residual).
- Han, J., Zhao, M., Chen, J. & Lan, X. 2019. Effects of steel fiber length and coarse aggregate maximum size on mechanical properties of steel fiber reinforced concrete. *Construction and Building Materials* **209**, 577–591.
- JSCE-SF4. 1984. Methods of tests for flexural strength and flexural toughness of fibre reinforced concrete Japan Society of Civil Engineers.
- Kiviste, M., Lille, H., Linnus, L. & Halgma, R. 2019. Evaluation of retention stresses of prestressing bars of a concrete ribbed panel from agricultural building after 20 years of service. *Agronomy Research* **17(6)**, 2277–2285.

- Korb, N. 2008. *Dependence of mechanical properties of fiber – reinforced concrete on the dosage of fibers*. Thesis of MSc, Estonian University of Life Sciences, Institute of Forestry and Rural Engineering, Tartu, Estonia. 61 pp. (in Estonian).
- Köksal, F., Sahin, Yu., Gencil, O. & Yigit, I. 2013. Fracture energy-based optimization of steel fibre reinforced concretes. *Engineering Fracture Mechanics* **107**, 29–37.
- Laranjeira, F. *Design-oriented constitutive model for steel fiber reinforced concrete*. Universitat Politècnica de Catalunya; 2010.
- Lindpere, M. 2016. *Investigation of mechanical properties of fibre-reinforced concrete slabs*. Thesis of MSc, Estonian University of Life Sciences, Institute of Forestry and Rural Engineering, Tartu, Estonia. 85 pp. (in Estonian).
- Ryabchikov, A., Tamm, V. & Laurson, M. 2015. Investigation of Mechanical Properties of Steel Fibre-Reinforced Concrete. *IOP Conf. Series: Materials Science and Engineering*. IOP Publishing **96**, 012018.
- Salehian, H., Barros, J.A.O. & Taheri, M. 2014. Evaluation of the influence of post-cracking response of steel fibre reinforced concrete (SFRC) on load carrying capacity of SFRC panels. *Construction and Building Materials* **73**, 289–304.
- Udras, S.-M. 2016. *The impact of shape and properties of steel fibres on the flexural strength of fibre reinforced concrete elements*. Thesis of MSc, Estonian University of Life Sciences, Institute of Forestry and Rural Engineering, Tartu, Estonia. 101 pp. (in Estonian).
- Vassiljev, A. 2013. *Investigation of mechanical properties of steel fibre reinforced concrete elements*. Thesis of MSc, Estonian University of Life Sciences, Institute of Forestry and Rural Engineering, Tartu, Estonia. 70 pp. (in Estonian).

## **Tensile properties of wood plastic composites based on plant-filled polyvinyl chloride/poly(3-hydroxybutyrate-co-3-hydroxyhexanoate) matrices**

E.O. Samuilova\*, A.V. Podshivalov, M.I. Fokina, V.S. Chursina,  
I.E. Strelnikova and M.V. Uspenskaya

ITMO University, Faculty of Applied Optics, Kronverkskiy pr., 49, RU197101 Saint Petersburg, Russia

\*Correspondence: samuilova.eo@itmo.ru

**Abstract.** The article considers the obtaining and studying of microcomposites based on polyvinyl chloride (PVC)/poly(3-hydroxybutyrate-co-3-hydroxyhexanoate) (PHBHHx) polymer matrix, filled with a various faction of different natural plant fillers. In work, such plant fillers as wood flour without lignin, spruce flour and rice husk were used. Microcomposites were obtained by melt rolling processing method with subsequent analysis of their morphology and mechanical tensile properties. It is shown that the filler particles were strongly oriented in the direction of the melt rolling process and have a different aspect ratio depending on the filler type. The tensile strength of materials strongly depends on the particle's aspect ratio. When the aspect ratio of the particles is 4.25, the material has a strength value comparable to a pure PVC/PHBHHx matrix.

**Key words:** polyvinyl chloride, polyhydroxyalkanoate, wood-polymer composites, composites morphology, mechanical properties.

### **INTRODUCTION**

Polyvinyl chloride (PVC) is one of the main applicable polymers produced and consumed worldwide after polyethylene and polypropylene. It is widely used to produce packaging and household goods consumed around the world, due to high mechanical properties, thermal stability and low cost (Clough et al., 1996). Life cycle studies of PVC have shown that PVC-based products have high energy uptake and low thermal transfer value, as well as high rigidity. The impact of vinyl products on health and the environment is usually comparable or less than that of alternatives. Despite this, PVC has some lacks that limit its current use. These include a relatively low ability to plastic deformations and non-biodegradability of disposable packaging waste (Amass et al., 1998). The first of these disadvantages of PVC is expressed in the excessive fragility of materials based on it, which can be compensated by the addition of a significant number of additives including heat stabilizers, plasticizers, and shock modifiers. Such additives and fillers, as a rule, have less rigid and mobile chains, which, when they are embedded in between the PVC molecules, leads to an increase in its ductility and processability. Unfortunately, the solution of the problem for non-biodegradability of PVC is not possible,



but a partial solution may be to apply the approach of obtaining semi-biodegradable compositions/blends such as PVC/biodegradable materials (Kann & Padwa, 2014).

Currently, the use of biodegradable polyesters from the family of polyhydroxyalkanoates and their derivatives is relevant as a biodegradable thermoplastic filler. One such polymer is a polyoxy acids copolymer poly(3-hydroxybutyrate-co-3-hydroxyhexanoate) (PHBHHx) with the linear polyester isotactic structure (Kushwah et al., 2016). It is synthesized by different types of bacteria (de Carvalho et al., 2016) as an intracellular stock of carbon and energy in response to physical stress conditions (Kushwah et al., 2016), e.g., nutrient deficiencies (nitrogen, sulfates, etc.). Moreover, an increase in the fraction of 3-hydroxyhexanoate (HHx) in the copolymer composition leads to a decrease in the glass transition and melting temperatures and reduces the rigidity and brittleness of the material (Chang et al., 2014). PHBHHx filling of PVC leads to a decrease in the glass transition temperature of the blend and allows you to get the material with a homogeneous structure and high miscibility of the components (Kann & Padwa, 2014; Sitnikova et al., 2018; Samuilova et al., 2019b).

At the same time, one of the relevant approaches to creating cheap and green semi-biodegradable materials is the creation of wood-based plastic composites (WPCs) (Marcovich et al., 2001; Nunez et al., 2002; Marcovich et al., 2005). To create them, wood and other plants are used as a filler which containing lignocellulose or other plant polysaccharides most often in the form of fibers. One of the disadvantages of such fillers is that they make the material more combustible (Ashori, 2017). In one work (Müller M. et al., 2012), the introduction of wood flour obtained from *Picea abies* into the PVC matrix did not significantly affect the thermal degradation of a material with a similar of destruction temperature of 272 °C for WPC and pure polymer. Probably, this effect is due to the increase in heat resistance of the wood filler when it is inside the polymer matrix. Despite this, this result is not typical for this type of composites (Klyosov, 2010). In this connection, PVC is not the most widespread basis for composites with plant fillers, inferior to polyethylene and polypropylene (Marcovich et al., 2005; Alao et al., 2019). In one of our works (Samuilova et al., 2019a), it was found that the introduction of various amounts of fillers such as wood flour without lignin, spruce flour, and rice husk into a polymer matrix based on a PVC/PHBHHx blend in some cases led to a decrease in the temperature of the degradation of the composite from 251.6 to 232.6 °C (for WPC with pine flour). However, the preparation of the PVC/PHBHHx polymer blend can decrease the processing temperature of composite and can act as actual matrix for the polymer/plant filler composite.

Basically, the WPCs it is necessary to try to keep operational properties of polymeric material on its basis. Especially it concerns the physical and mechanical properties of such materials. As a rule, in such materials, tensile strength and elastic modulus deteriorate significantly with the introduction and increase in the content of plant filler, due to the weak interaction of these fillers with the polymers of the matrix (Ismail H. et al., 1999; Danyadi L. et al., 2007; AlMaadeed M. A. et al., 2013). Moreover, the size of the fraction, the form factor and the processing method of the filler also have a strong influence on the properties of the composite. Currently, there is a lot of research on this topic (Bessa et al., 2017; Alao et al., 2019; Kalalia et al., 2019), but mainly wood polymer composites based on polyethylene or polypropylene were studied. PVC-based composites with plant fillers are not as widely distributed.

This article presents the results of the obtaining and studying of PVC/PHBHHx/plant filler microcomposites filled with various factions of wood flour without lignin, spruce flour, and rice husk. Composites were obtained by melt rolling processing method with subsequent analysis of their morphology and mechanical tensile properties.

## MATERIALS AND METHODS

### Materials

As a macrocomponent of the polymer matrix we used the industrial suspension polyvinyl chloride (PVC) in the form of granules provided by Klekner Pentaplast Rus with containing thermostabilizer mercaptodioctyl 0.2–1.5 wt.%, melt flow modifier 2.0–4.0 wt.% and external lubricant (paraffin) 0.1–0.5 wt.%. PVC contains up to 0.04 wt.% of volatile compounds and has a Fikentscher constant value of 57–58, which is provided by the manufacturer.

Poly(3-hydroxybutyrate-*co*-3-hydroxyhexanoate) (PHBHHx) Aonilex X131A in the form of granules manufactured by Kaneka was used as a biodegradable filler to lower the glass transition temperature and softening of PVC. PHBHHx had an average molecular weight of  $M_w = 500,000\text{--}600,000\text{ g mol}^{-1}$  and a ratio of 3HB/3HH = 95/5. The main thermal properties of the used PVC and PHBHHx were established by us earlier (Sitnikova et al., 2018; Samuilova et al., 2019b) and are presented in Table 1.

To fill the polymer matrix, solid natural fillers based on plant materials, such as wood flour without lignin (WLF) produced by MS Ltd., spruce flour (SF) produced by KFH Agrodom Ltd. and rice husk (RH) produced by Southern Rice Company Ltd were used.

**Table 1.** Thermal properties of the using polymer materials (Sitnikova et al., 2018; Samuilova et al., 2019b)

Material	$T_g$ , °C	$T_f$ , °C
PVC	80.0	141.4
PHBHHx	01.8	< 126.9
PVC/PHBHHx (80/20 wt.%/wt.%)	33.5	113.2

$T_g$  – glass transition temperature;  $T_f$  – flowing temperature.

### Preparation of composites

Composite materials were obtained at different ratios of the mass fractions of the components PVC/PHBHHx/plant filler: 80/20/0, 70/20/10, 60/20/20 and 50/20/30 wt.%/wt.%/wt.%.

Before preparing the polymer composites, the plant fillers were milled for 5 min using a roller mill Brabender (Germany) at a roller speed of 140 rpm to obtain a powder with a narrow particle size distribution relative to the original.

First, PVC and PHBHHx solid granules were premixed with plant filler powder for 5 min using a high-speed mixer Henschel (Germany) until a homogeneous mixture was obtained. To prepare microcomposites, the resulting mixtures of solid components were fed to a laboratory two-roll mill Schwabenthan Polymix 150U and heated to 175 °C to obtain a melt. The heating temperature of the mixtures was chosen between the melting temperature of PVC (Table 1) and the degradation temperature (close to 195 °C) of the PVC/PHBHHx blend. Then the melt was rolled between the rollers at a rotation speed of 24 rpm for 2 min to obtain the material in the form of films. The resulting composites were cooled to room temperature and subjected to thickness measurement using a

standard digital micrometer MCD-25 manufactured by Tehrim (Russia) with a measurement step of 0.001 mm and an error of  $\pm 0.004$  mm. The thickness value ( $d$ ) of the obtained microcomposites was determined as the average value of ten different points in the film area. The average thickness of the films is presented in Table 2.

**Table 2.** Thickness of the obtained composites at varying composition filled with different plant filler

PVC/PHBHHx/ plant filler, wt.%/wt.%/wt.%. .	Thickness with various plant filler $d$ , mm		
	WLF	SF	RH
80/20/0	0.255		
70/20/10	0.368	0.308	0.371
60/20/20	0.416	0.365	0.435
50/20/30	0.411	0.402	0.432

### Light microscopy

Visual analysis of the obtained composites with a plant filler content of 10 wt.% showed that the polymer matrix based on the PVC/PHBHHx blend transmits visible light well and has transparency. To study the materials structure, macrographs were obtained in transmission mode using an optical microscope MBS-9 (Russia) equipped with digital camera.

### Statistical analysis

The morphology of the composites was analyzed using statistical analysis of the obtained macrographs. For this purpose, in the images, particles of plant fillers that do not transmit visible light were segmented relatively to a transparent polymer matrix using ImageJ software v. 1.8.0\_112 (USA) with a rotated rectangle tool. The form factor of the filler particles was calculated as the ratio of the length to the width of the rectangle ( $AR = l w^{-1}$ ). Then, the calculated AR values were distributed according to their frequency and their statistics were determined.

### Mechanical tensile testing

For mechanical tensile testing of the composites, ten samples of each composition were prepared in the form of strips with 10 mm wide and a measuring base length of 50 mm. Mechanical tests of the samples were carried out at a tensile strain rate of  $180 \text{ mm min}^{-1}$  using an electromechanical testing machine Instron 5966 (USA) equipped with the load cell (10 kN capacity) and pneumatic grip system. Signal processing was performed using Bluehill 3 software.

## RESULTS AND DISCUSSION

Fig. 1, a–c shows the results of optical microscopy of PVC/PHBHHx/plant filler microcomposites with a content of 10 wt.% of plant fillers used.

A visual analysis of the morphology of the material with the addition of the WLF filler (Fig. 1, a) shows that most of its particles, obtained by pretreatment, are large in size and have elongated form, close to rectangular. It is also seen in the macrograph that the filler particles are strongly oriented in the direction of the melt rolling process. In the case of the PVC/PHBHHx/SF composite (Fig. 1, b), on average, there is a smaller planar size and a larger number of filler particles compared to using WLF, and the particle shape resembles short fibers. Moreover, the particles are also strongly oriented in the direction of the melt rolling process. In one of the works (Danyadi et al., 2007) according to SEM,

it was noted that when a plant filler is introduced into polymer sheets up to 1 mm thick, the degree of orientation of the filler particles is greater than when filling with a larger thickness. Fig. 1, c shows that the RH filler particles in the PVC/PHBHHx polymer matrix have a relatively large planar size and a shape close to the square. In this case, the direction of the orientation of the particles is difficult to determine. In a general sense, the use of various kinds of plant fillers with the same pretreatment leads to the formation of rectangular particles with different planar size and form factor (aspect ratio). Moreover, the use of the melt rolling method of composite preparation allows the filler particles to be oriented in one direction in the structure of the resulting material.

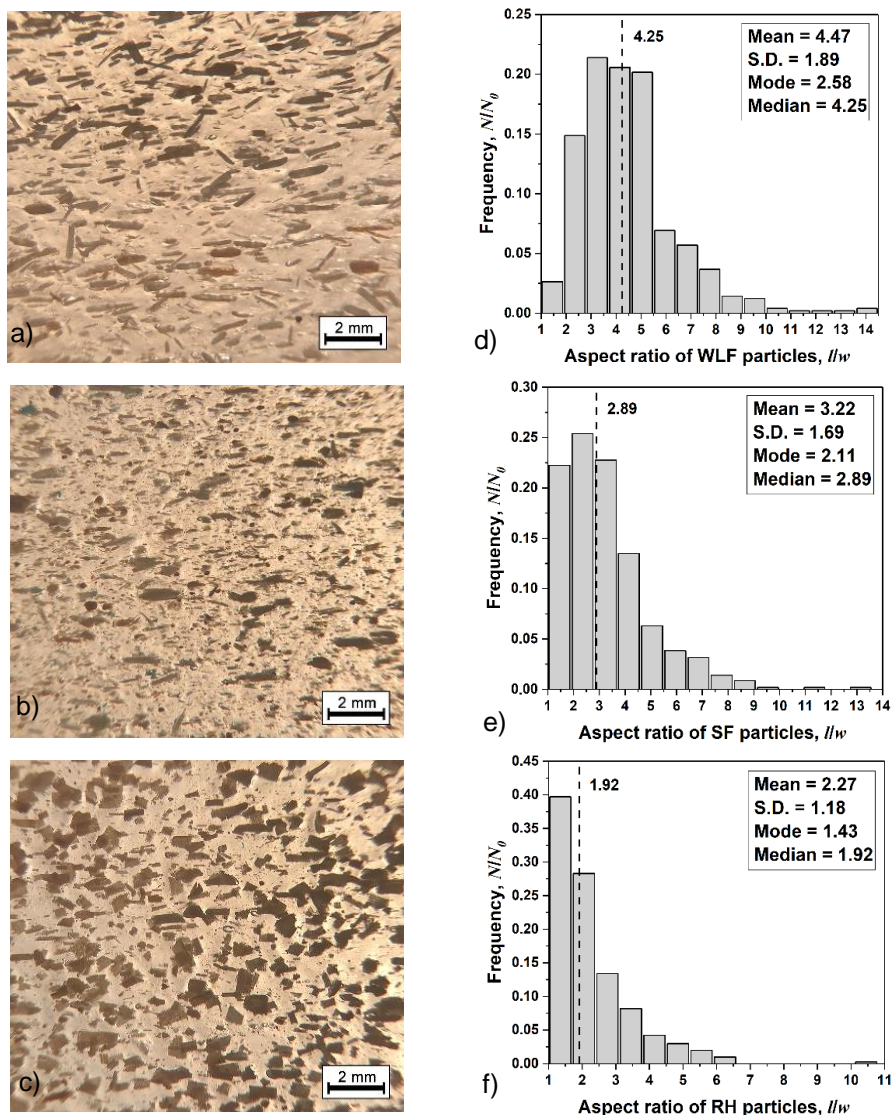


**Figure 1.** Light macrographs of a) PVC/PHBHHx/WLF; b) PVC/PHBHHx/SF and c) PVC/PHBHHx/RH microcomposites at a filler content of 10 wt.% and the corresponding statistical distributions of AR values.

The corresponding results of the statistical analysis of the considered macrographs in the form of statistical distributions of the calculated aspect ratio values (AR) of the filler particles are presented in Figs 1, d – f. The values of central trend measures for distributions are indicated in boxes. The diagrams show that the AR values of the filler particles are not distributed according to the normal law. This feature of the distributions is due to the physical property of the particle form factor, where  $AR \geq 1$ . Moreover, under real conditions, the normality of the AR distribution will decrease when  $AR \rightarrow 1$ . Given these distribution features, the median seems to be the most adequate measure of the central distribution trend. The median values of the distributions of AR values well reflect the results of the visual analysis of macrographs.

Fig. 2 shows the results of mechanical testing of the composites depending on their composition at the addition of the different types of plant fillers. The dependence shows that the introduction of all the considered types of plant fillers into the PVC/PHBHHx polymer matrix leads to a decrease in the tensile strength ( $\sigma$ ) of the material. An increase in the filler fraction in the composition enhances this effect. Similar effects were observed by other authors (Ismail et al., 1999) for WPC from natural rubber/oil palm wood flour where, upon introduction and an increase in the proportion of flour from 0 to 50 wt.%, the tensile strength decreases in the range from 25 to 7 MPa. Also, in another work (Danyadi et al., 2007), when filling a matrix based on polypropylene with wood flour filler,  $\sigma$  value decreases from 25 to 5 MPa. Other authors (AlMaadeed et al., 2013) have shown, that filling the LDPE matrix with such a filler as date palm wood powder in a fraction of 20% led to a reduction in  $\sigma$  value to 9.2 MPa compared to 18.5 MPa for pure LDPE.

The observed behavior of  $\sigma$  value indicates a weak interfacial interaction of the matrix–filler. Using the analysis of SEM and mechanical fatigue of the WPC samples, the (Ismail et al., 1999) showed that with an increase in the content of the plant filler in the composition, its particles aggregate with the formation of stress centers.

It can be seen that the strength of this effect depends on the type of plant filler. In one of the works (Jiang et al., 2017), the authors also observed a different effect of fillers from different raw materials, such as straw fibers, on the mechanical strength of the PVC/straw fiber WPCs. However, the reasons for this behavior are not completely clear. An analysis of the microcomposites morphology showed that the type of filler used is significantly different in terms of the AR value. In this regard, we believe that the  $\sigma$  value of the considered microcomposites is controlled not only by the fraction of the filler in the material composition but also by the AR index of the filler particles.

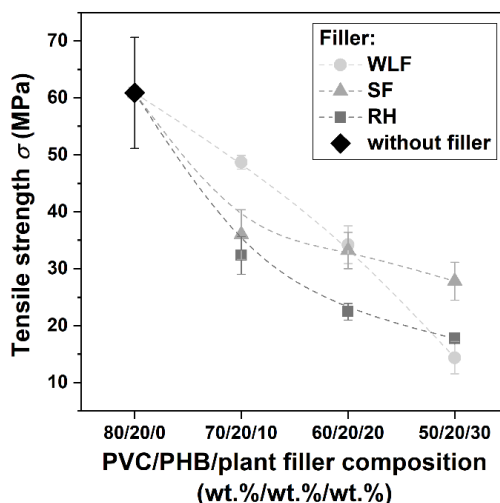


**Figure 2.** Dependence of the tensile strength of PVC/PHBHHx/plant filler microcomposites on the composition at adding of various filler type.

Fig. 3 demonstrates the dependence of the tensile strength of PVC/PHBHHx/plant filler microcomposites at a content of 10 wt.% of plant filler on the median value of the AR index distribution.

The dependence shows that at linear tensile deformations in the direction of melt rolling and, accordingly, the direction of the filler particles orientation (see Fig. 1, a–c) the strength of the material significantly increases with an increase in the AR value. Thus, at AR = 4.25 the energy of the strain deformations is efficiently transferred from the PVC/PHBHHx polymer matrix to the more rigid filler phase, compensating for the weak matrix-filler interfacial interaction. This behavior of the material under tensile strain leads to its reinforcing to  $\sigma = 48.7$  MPa, which is comparable with the range of  $\sigma$  values for a pure polymer matrix PVC/PHBHHx.

An analysis of the elastic deformations of microcomposites under tension depending on their composition with the introduction of various types of plant fillers is presented in Fig. 4.

The graph shows that the introduction of 10 and 20 wt.% of filler in the polymer matrix PVC/PHBHHx leads to an increase in its rigidity. However, the use of RH as a filler has a weak effect on the elastic properties of the polymer matrix, and the use of rigid wood fillers WLF and SF, on the contrary, leads to a significant increase in the stiffness of the material. This behavior of Young's modulus value of microcomposites is caused not only by the form factor of the filler particles but mainly by its type and the value of its own rigidity (Jiang et al., 2017).

Comparing the  $E$  values with the  $\sigma$  values, the concept of the rigidity of microcomposites can be considered as fragility. Similar effects have also been observed for other WPCs (Ismail et al., 1999; Danyadi et al., 2007; AlMaadeed et al., 2013).

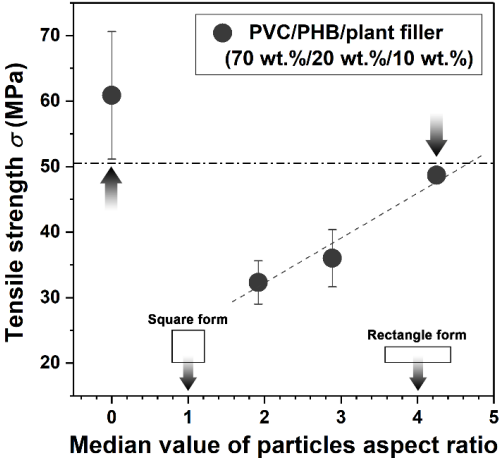


**Figure 3.** Dependence of the tensile strength of PVC/PHBHHx/plant filler microcomposites at a filler content of 10 wt.% on the median of AR value.

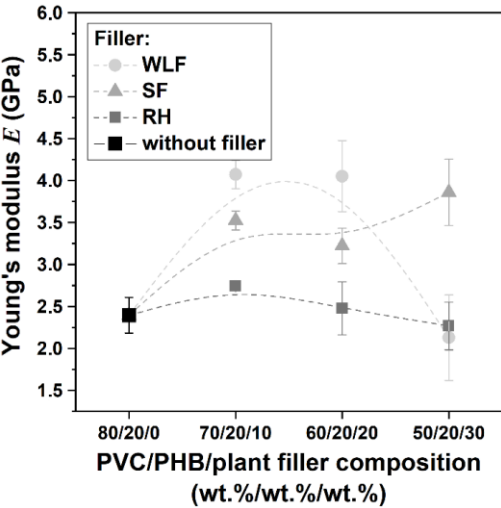


**Figure 4.** Dependence of the Young's modulus of PVC/PHBHHx/plant filler microcomposites on the composition at adding of various filler type.

## CONCLUSIONS

In the course of work, the melt rolling method was used to prepare PVC/PHBHHx/plant filler polymer microcomposites with a ratio of mass fractions of components: 80/20/0, 70/20/10, 60/20/20 and 50/20/30 wt.%/wt.%/wt.%. Materials such as wood flour without lignin, spruce flour, and rice husk were used as plant fillers. It was found that preliminary mechanical processing of the fillers leads to the formation of particles with predominantly of rectangular shape and different aspect ratio. It is shown that the filler particles were strongly oriented in the direction of the melt rolling process. The mechanical analysis of the composites showed that the tensile strength of the PVC/PHBHHx polymer matrix decreases with the introduction and increase in the fraction of filler. However, the strength of materials strongly depends on the aspect ratio of the particles of the filler phase. When the aspect ratio of the particles is 4.25, the material has a strength value comparable to a pure PVC/PHBHHx matrix. The rigidity of the microcomposites depends not only on the composition and aspect ratio of the filler phase particles but also on its type.

**ACKNOWLEDGEMENTS.** This work was carried out on the basis of the International Scientific and Research Institute of Bioengineering of ITMO University with financial support from ITMO University.

## REFERENCES

- AlMaadeed, M.A., Nógellová, Z., Mičušík, M., Novák, I. & Krupa, I. 2013. Mechanical, sorption and adhesive properties of composites based on low density polyethylene filled with date palm wood powder. *Materials and Design* **53**, 29–37.
- Alao, P.F., Kallakas, H., Poltimäe, T. & Kers, J. 2019. Effect of hemp fibre length on the properties of polypropylene composites. *Agronomy Research* **17**(4), 1517–1531.
- Amass, W., Amass, A. & Tighe, B. 1998. A review of biodegradable polymers: uses, current developments in the synthesis and characterization of biodegradable polyesters, blends of biodegradable polymers and recent advances in biodegradation studies, *Polymer International* **47**, 89–144.
- Ashori, A. 2017. Hybrid thermoplastic composites using nonwood plant fibers. In Thakur, V.K., Thakur, M.K., Pappu, A. (eds): *Asokan Pappu Hybrid Polymer Composite Materials: Properties and Characterisation*. Woodhead Publishing, Tehran, 39–56.
- Bessa, J., Mota, C., Cunha, F. & Figueiro, R. 2017. Influence of different thermoplastic polymer/wood ratios on the mechanical and thermal properties of composite materials. *Procedia Engineering* **200**, 480–486.
- de Carvalho, K.C.C., Montoro, S.S.R., Cioffi, M.O.H. & Voorwald, H.J.C. 2016, Polyhydroxyalkanoates and their nanobiocomposites with cellulose nanocrystals In: Thomas S, Shanks R, Chandrasekharakurup S (eds) *Design and applications of nanostructured polymer blends and nanocomposite systems*. Elsevier, Oxford, pp. 261–285.
- Chang, H.M., Wang, Z.H., Luo, H.N., Xu, M., Ren, X.Y., Zheng, G.X., Wu, B.J., Zhang, X.H., Lu, X.Y., Chen, F., Jing, X.H & Wang, L. 2014. Poly(3-hydroxybutyrate-co-3-hydroxyhexanoate)- based scaffolds for tissue engineering. *Brazilian Journal of Medical and Biological Research* **47**(7), 533–539.
- Clough, R.L., Billingham, N.C. & Gillen, K.T. 1996. *Polymer Durability: degradation, stabilization and lifetime prediction*. American Chemical Society, Washington, DC, 599 pp.



- Danyadi, L., Janecska, T., Szabo, Z., Nagy, G., Moczo, J. & Pukanszky, B. 2007. Wood flour filled PP composites: Compatibilization and adhesion. *Composites Science and Technology* **67**, 2838–2846.
- Ismail, H. & Jaffri, R.M. 1999. Physico-mechanical properties of oil palm wood flour filled natural rubber composites. *Polymer Testing* **18**, 381–388.
- Jiang, L., Hea, C., Fua, J. & Chen, D. 2017. Wear behavior of straw fiber-reinforced polyvinyl chloride composites under simulated acid rain conditions. *Polymer Testing* **62**, 373–381.
- Kann, Y. & Padwa, A., 2014 PVC Modification With Biobased Poly(hydroxyalkanoates), *Journal of vinyl & additive technology*, 1–13.
- Kalalia, E.N., Zhanga, L., Shabestarib, M.E., Croyalc, J. & Wanga De-Yi. 2019. Flame-retardant wood polymer composites (WPCs) as potential fire safe bio-based materials for building products: Preparation, flammability and mechanical properties. *Fire Safety Journal*. **107**, 210–216.
- Klyosov, A. 2010, *Wood-polymer composites*. Scientific Foundations and Technologies, St. Petersburg, 736 pp. (in Russian).
- Kushwah, B.S., Singh Kushwah, A.V. & Singh, V. 2016, Towards understanding polyhydroxyalkanoates and their use. *J Polym Res*. **23**(153), 14.
- Marcovich, N.E., Aranguren, M.I. & Reboredo, M.M. 2001, Modified wood flour as thermoset fillers Part I. Effect of the chemical modification and percentage of filler on the mechanical properties. *Polymer* **42**, 815–825.
- Marcovich, N.E., Reboredo, M.M. & Aranguren, M.I. 2005. Lignocellulosic materials and unsaturated polyester matrix composites: Interfacial modifications. *Composite Interfaces* **12**, 3–24.
- Müller, M., Militz, H. & Krause, A. 2012. Thermal degradation of ethanolamine treated poly(vinyl chloride)/wood flour composites. *Polymer Degradation and Stability* **97**, 166–169.
- Nunez, A.J., Kenny, J.M. & Reboredo, M.M. 2002, Thermal and dynamic mechanical characterization of polypropylene-woodflour composites. *Polymer Engineering and Science* **42**, 733–742.
- Samuilova, E.O., Olekhovich, R.O., Sitnikova, V.E., Podshivalov, A.V. & Uspenskaya, M.V. 2019a. Thermal and mechanical properties of wood-PVC composites. In: *19th International Multidisciplinary Scientific GeoConference, SGEM-2019*. **19**(4.1), 561–567.
- Samuilova, E.O., Sitnikova, V.E., Belukhichev, E.V., Strelnikova, I.E. & Uspenskaya, M.V. 2019b. Thermal properties of the polymer composites on the basis of polyvinylchloride and polyhydroxybutyrate. *Izvestia Saint-Petersburg State Technological Institute (Technical University)* **48**(74), 120–125 (in Russian).
- Sitnikova, V.E., Uspenskaya, M.V., Chereneva, S.V., Samuylova, E.O. & Nosenko, T.N. 2018. Thermal properties of polymer composites based on polyvinylchloride film and biopolymer filler. In: *18th International Multidisciplinary Scientific GeoConference. SGEM-2018*, Albena, **18**(5.1), 987–994.



## **Towards a business and production engineering concept for individual beer brewing applying digitalization methodologies**

T. Schlechter<sup>1,\*</sup>, R. Froschauer<sup>1</sup> and A. Bronowicka-Schlechter<sup>2</sup>

<sup>1</sup>University of Applied Sciences Upper Austria, Automotive Mechatronics and Management, Stelzhamer str. 23, AT4600 Wels, Austria

<sup>2</sup>Salzburg Schokolade GmbH, Hauptstraße 14, AT5082 Grödig, Austria

\*Correspondence: [thomas.schlechter@ieee.org](mailto:thomas.schlechter@ieee.org)

**Abstract.** Individualization is a common trend in many fields of production across the industries. Also in the food sector, significant changes can be observed. For many products, individual offerings towards the customer are meanwhile either mandatory or at least help to increase the sales and revenue. Somehow, individual product design and production contradicts scaling effects, which are especially important for food production. On the other hand, as digitalization is implemented in a fairly limited way in the food sector, currently great chances can be observed to build a unique selling proposition and consequently gain market share by implementing appropriate measures to enable a digital food factory. This is where the proposed idea comes into the game. The starting point is the idea to produce individually developed beer and ship it to the individual customer. The beer can be designed on a web page based on typical parameters, like beer type, bitterness, colour, or alcohol concentration. In an expert mode, individual beer creations may be thoughtful, allowing the creation of completely individual recipes (for sure, not guaranteeing the customer a perfect drinking experience). In any way, the data from the web page is directly fed to the brewing equipment in the brewing facility. There, using newly to be developed specialized machines, the individually ordered beer will be produced automatically. In this paper we discuss the individual challenges at each point in the production cycles and propose solutions to those.

**Key words:** digital factory, individual food production, smart manufacturing, gamification, industry 4.0.

### **INTRODUCTION**

There are two trends, which also the food industry cannot withstand: automation of production (Thomas et al., 2017; Morgan & Haley, 2019; Schallmo, 2019; Sonnen, 2019) and individualization of products (Ettl et al., 2015; Neef et al., 2020). Customers request more and more individual products (e.g., cereals (mymuesli GmbH (2020), Zhou & He, 2019) or beer (Beer Engineer (2020))). In the context of competitiveness and efficiency, automation of production needs to be considered as well. The key question arising is: How to automate individual wishes? As long as the definition of the individual request is precise in the form of a formal recipe, this might be directly possible. In general, however, the description from the customer is imprecise and personally biased (Leckner et al., 2003; Kreye, 2018). Furthermore, the quality of raw material and the

production processes underlay natural and statistical fluctuations. Therefore the food industry has a strong demand for approaches dealing with the question how to guarantee the satisfaction of the customer reliably and automated (Shewhart, 2012; Caroco et al., 2018). Developing (a) solution(s) to this problem is challenging, while the path to the solution marks significant milestones in the research field of food technology (Pramanik et al., 2018), as will be shown in the following. For illustrative purposes, we follow a specific real world example for immediate clarification of the argumentation chain, which is the beer brewing process alongside with a digitally transformed brew master involved in the process.

### **Basic Technological Challenges and Implementation Approaches**

The first challenge related to individual beer brewing, for sure, is, to automate the beer production on small batches, e.g., 20–30 litres per brewing cycle. This amount is assumed to be a production quantity, which is possible to be sold to an individual customer within one single sales process. Beer Engineer (2020) use a procedure to create individual beers by creating cuvees from several base beers. However, a very limited amount of different beers can be created and – to be fair – the created beer is not really brewed individually. The customer can choose between Pils and Bock, each with two colour shades. For each of the types five grades of intensity of hops/bitterness and three/four levels of alcohol content and degree of carbonisation can be chosen only. Therefore, alternative approaches need to be developed, which allow micro quantities like 20–30 litres, to be brewed without noticeable manual supervision of the brewing process. For this purpose, newly to be developed brewing equipment needs to be installed. This mainly covers the mechanical setup in a first step.

The scheduling of a single brewing event will be organized by the smart factory on its own, potentially considering premium orders for quicker delivery. The smart production site itself will be completely automated with autonomous logistic infrastructure, secure full connectivity, and production data aware production cycles. This enables a fully remotely accessible real-time status monitoring and control of the production cycle. Any deviation, which can be captured by information technological means, will be detected. As the brewing site will be setup from scratch, early considerations of the latter will not lead to huge implementation efforts, like this would be the case for a retrofitting of an existing brewing site.

Along with the production, additional services to the customer will be derived from the anyway highly automated production site. The customer will be part of the production process, meaning the customer will receive automated feedback on its current process status of his product. Very exemplarily for a specific individual beer the inclusion of the customer could deliver the following information: order received, brewing process started, 1<sup>st</sup> settle time for sugar rest in progress, beer in maturation status. The authors are aware, that there are manifolds of different brewing approaches. The given customer output relates to only one of those many possibilities. As well, this may include: information about continuous ethanolic fermentation/breakdown of the extract, temperature profile, live pictures from brewing process.

The data provided to the customer will be accessible via a secured area on a web page or via a special app. Additionally, the order history along with personally to be added tasting notes of the customer tops the whole story of. The actual extend of usage may be activated on a payment model.

Summarized, the proposed approach may revolutionize the current view on brewing by allowing individualized brewing concepts, as a complete new setup of a brewery does not need to follow hardened process structures of established companies. First initiatives to implement an appropriate machinery are already under investigation at the University of Applied Sciences Upper Austria.

The idea combines a traditional industrial branch with modern technologies and modern business models. Especially this fact puts this research in a charming light. In future extensions, the running production site may be used for interdisciplinary educational purposes as well.

### **Advanced Technological Challenges**

The aforementioned setup covers the automation of idealized process parameters, which can be reliably predicted, straight forward put in operation, and ideally tracked and controlled. However, problems that are more sophisticated pop up once the customers are getting involved as human beings and variations of the used raw material are considered as well. Obviously, fluctuations of quality and properties of per definition equal raw materials influence the appearance of the final product significantly. Examples include: grain and hops are natural products, therefore, every year the actual quality may vary depending on the environmental conditions. Grain, and the resulting malt, may contain more or less or different kinds of stark. Hop may be more or less aromatic and may differ in alpha acid, important for the degree of bitterness. As well, various companies can perform the procedure of malting differently, resulting in different malts from the potentially same grain unintentionally. This may lead to variations in colour and taste using the same recipe. This is not a complete list of potential issues but shall just give a first impression on common problems.

In current systems, a human brew master captures the raw material fluctuations. Applying his/her expertise and experience enables him/her to sustain product quality even in those conditions. In a highly automated production environment, also this brewing master needs to be digitalized, which marks the first extremely challenging field of research to be done. The task of gathering implicit knowledge from experts to automate certain processes is currently accomplished in several domains and often focusses on inspection and quality-preserving process tasks, i.e. OK vs. NOK checks (Puppe, 2012). For continuous production with small lot-sizes these approaches have to be extended to derive production, related parameters at the beginning of a production process (e.g. out of measurement data of raw materials).

Besides capturing the implicit knowledge from the brewing master, also the customers experience has to be involved. Customers are not professional in the field of consumption and therefore are limited in arguing using terminology and relevant parameters of the target field (in this case beer production). Consequently, customers typically use comparative terminology (e.g., should taste like ...) or at least fuzzy linguistic terms (e.g., should be a bit bitter, should be very fruity) instead of hard parameters (e.g., IBU of 30 to uniquely define the bitterness of a beer). This is a well known fact within the food industry. The prove of customer satisfaction in this context is typically performed by a triangular test setup (Sinkinson, 2017; Gatchalian, 1999; TestTriangle, 2020; SSP, 2020). Traditionally, the translation of the customer voice and the food/beer production process is performed using manual polls and surveys processed by human beings. This, however, is inefficient and expensive (cost and time). Therefore,

another part of this research involves the development of a translational model of the customers' demands towards food/beer production process terminology.

The next step is the translation of the hard facts derived from the customer requirements into a recipe, which works as instruction for the automated food production process. Traditionally, a specialist of the individual field of food production performs this step. As the whole process shall be automated, again an artificial instance for recipe derivation needs to be implemented. This procedure is closely linked to the digitalization of the brew master as mentioned before, while at this point traditional deterministic measures can be applied, simplifying the problem. As typically the (typical, usual) parameters of the raw materials and their individual contribution towards the final product are known, this task is easy to a certain extent, as long as the customer demands are within known limits. If the latter cannot be assumed, creative artificial instances have to be developed, which deliver useful recipes fulfilling the customers' demands autonomously. This is especially challenging and not yet well researched in the food production area. For better results, collective knowledge might be used, similar to the approach described above for the customer model.

The final problem to be solved in the process chain is the validation of the product quality with respect to the customer preferences. This step may be considered a feedback loop to crosscheck the measured parameters of the resulting product along the initial customer needs. Traditionally, the brew master, e.g., performs manual testing. Meanwhile, significant advances can be observed in that field, e.g., powered by the measurement equipment of Anton Paar (Paar, 2020). A good show case can be found in the Anton Paar Sudhaus (Sudhaus, 2020). Still, there is a significant need for manual checking and interaction, which inhibits highly automated brewing cycles. For high automation levels, all of those checks have to be performed by a sensor-algorithm combination again involving the digitalization of human senses (Berna et al., 2010; Ciui et al., 2018; Galstyan et al., 2018; Khan et al., 2018; Fraunhofer, 2020). Electric noses and tongues are known (Haugen, 2001; Gorska-Horczyczak et al., 2016; Palmiro et al., 2017; Mohamed et al., 2018; Di Natale et al., 2000), while the processing of the data and the description of the perception is not trivial and not yet very well researched. As stated before, a mapping of the derived perception of the sensor-algorithm setup and the perception of the customer demands need to be performed. Additional difficulties are added to the objective nature of the sensor-algorithm setup perception versus the subjective nature of the customer perception description. Intelligent algorithms need to be integrated to automatically drive this part of the process.

Overall, the described research approach seems simple on first sight: trigger an automated production process based on customer requirements. However, as discussed before, hardly predictable difficulties are introduced by the nature of the problem due to

- Automatically to be considered and detected raw material quality fluctuations
- Automatically to be considered and detected process irregularities
- Transformation of human perception in hard production facts
- Transformation of hard production facts towards human perception
- Including cultural and local individual preferences and deviations of individual perception in the automation process.

Sub-fields of the research are partially investigated, while for major parts no relevant research results are published yet. For instance, the Campus of Senses (Fraunhofer, 2020) deals with the decryption of human perception alongside modelling

this perception by processing data delivered by special sensors for human senses. It intends to digitally recreate human senses, especially the chemical senses of taste and smell. Research here is still at the very beginning. However, we believe our field of research based on this idea may be successful, as we do not need to exactly model human perception to match to the human brain, but to a less complex setup of machinery, the production equipment. Gathering results is very challenging, however, not impossible if drilling the problem down to its actual requirements.

MATERIALS AND METHODS

As described before, several technical challenges need to be mastered to implement the automated production approach described in the introduction. They might be categorized as mechanical, algorithmic, sensing technology, conceptual. Each of the categories are described in the following paragraphs.

Mechanical Setup

The basic mechanical setup for brewing equipment is well known. However, first, the equipment on the market is either large scale (500–2,000 + litres per brewing cycle) and semi-automated (Table 1) or it is small scale (20–50 litres) and basically non-automated. In an optimum case, the temperature ramps and rest times can be programmed. One example of highly automated small scale brewing equipment is the Brumas BrauEule III (Brumas, 2020), another the Brewie+ (Newity 2020). However, significant manual tasks have to be performed.

The main measures to take in this field are therefore as given in the following. A mechanical setup has to be developed, which allows including automation capability in the small-scale equipment already present in large-scale systems (transformation by scaling). Furthermore, new mechanical automation setups have to be developed, where the individual choice of grain, yeast, and hop is automatically chosen from a given portfolio and added as ingredient at the right point in time according to the recipe (new individualization equipment). Especially, the latter mentioned is needed to allow for automation of individual products being an important pillar of the whole concept.

Table 1. Degree of supported automation for large scale brewing

Supported	Not supported
temperature ramps	remove spent grain
grain adding	check cloudiness of to
water adding	be cleared wort
rest times	removal of denaturized
whirlpool	proteins after wort
...	cooking
	...

Sensing Technology

As mentioned in the previous section, some additional sensing technology needs to be included in the setup to allow for automation. Trivially, temperature sensors are needed to precisely and repeatedly enable defined sugar rests and temperature ramps given in the recipe.

Apart from that, it is very important to detect the cloudiness of the wort during the lautering process. At this point, an optical sensor including image processing is foreseen to be installed. While in comparable situations, product quality control by optical sensors

is state of the art, for this specific task not many solutions can be found on the market (e.g., Mettler Toledo (Toledo 2020)). Additional sensors need to be considered for automatically measuring the alcohol and sugar concentration during the fermentation process. While the aforementioned is state of the art within the brewing industry, it is still challenging in the context of producing small batches of maximum 50 litres. This is important to forecast the perfect moment for bottling to achieve the right means of carbonisation. Finally, the individual colour scale of produced beer needs to be checked and aligned to the customer needs before shipping. A visual sensor including image processing again can perform this.

Pushing the overall research complexity further lets us end up with more complex sensors and tasks, which are currently under investigation and not yet available to the open market. This relates to sensors imitating the human's olfaction and degustation. Fraunhofer (2020) is currently performing research in that field in the context of the Campus of Senses. Enablers for this research is, e.g., the so called electronic nose (Di Natale et al., 2000; Haugen, 2001; Gorska-Horczyzak et al., 2016; Palmiro et al., 2017; Mohamed et al., 2018), which allows to digitalize the aforementioned human perceptions. For sure, this part of the research will need some more time before reaching maturity, but is included already now in the consideration of the scope of this research approach. Once the technology is ripe, it will give great top-on benefit on the overall setup.

### **Algorithmic Tasks**

The algorithmic tasks, which have to be performed for sure, are closely related to the sensing devices. As it is the case with the sensor environment, some of the algorithms to be put in field application are state of the art and pure development work. This includes algorithms for temperature ramp implementations, mechanical manipulation tasks and any algorithm related to timing constraints. Those will not be covered in detail here.

Subsequently, there are algorithmic tasks to be performed, which are known to be manageable, however, need some training sequence of algorithms and transformation actions from related areas. This includes, e.g., image processing for cloudiness classification of cleared wort and colour determination of the wort. Furthermore, deriving optimal time-temperature curves for perfect fermentation of the product involving alcohol and rest sugar concentration sensors needs to be considered, but is state of the art.

When it comes to algorithms translating the human perception into a specific recipe including individual actions, the story is a different one. This is also valid to say for algorithms towards a digitalization of the brew master, involving a quality and status check of all raw materials and a cross check of the final product to the customer perception and wishes. The latter involves a third problem to be tackled, which involves the transformation of the digital perception of the electronic nose towards the customer (human) perception – what is needed to validate the product quality w.r.t. the desired result. This part will be the challenging one, which, however, is crucial to make the overall process highly automated. On top of this approach, geographical details about the individual human perception need to be considered as well. As described before, the same type of food and beer will trigger different naming conventions, perception levels, and preferences in different geographical locations. If there is, e.g., a region, where the mostly sold beer type tends to be 'fruity', then a slightly bitter beer might be described

as ‘bitter’, while the same beer in a different region might be considered as ‘slightly bitter’. Including this, algorithms being capable of data analysis and using the intelligence of swarms (in this case distributed beer consumers) needs to be dealt with as well. Concerning the more advanced algorithm application, we identified the following topics of deeper interest.

- **Human Perception to Hard Fact Conversion**
- **Hard Fact to Recipe Conversion**
- **Hard Fact to Human Perception Conversion**
- **Swarm Intelligence Inclusion**

Methodologies we have in mind to solve the problems are deep learning algorithms, fuzzy logic, or variability modelling. Today deep learning methods are broadly accepted for various problems, especially machine vision or voice recognition tasks. A general problem applying machine learning to real world problems is to gather enough valid training data. Therefore, often simulation models as well as statistical data is used to train models. Current research approaches focus on deriving taste and flavour out of online votings in recipe databases and food & nutrition webpages (Teng et al., 2012).

For the proposed approach of individual food production, i.e. individual beer brewing, it is currently hardly possible to gather enough training data to derive accurate recipes out of interviews or surveys from human people. Therefore, we would focus on Fuzzy logic which seems to be an adequate algorithmic approach, as it maps linguistic terms and variables (to be understood very well) into crisp output variables. Those variables represent the direct hard fact output, which can be used to derive the individual recipe. Input parameters might be: beer colour (light, medium, dark), alcohol concentration in %, fruitiness (low, medium, high), bitterness (low, medium, high). Fuzzy output variables might be: weight of hop of specific type (little, some, much), melanoidin malt for colouring (little, some, much). The crisp hard fact output produced by the algorithm may be: take 13 g of a specific hop and 359 g of melanoidin malt in your recipe. Fuzzy inputs and fuzzy outputs are merged by to be developed rules, achieving a deterministic control loop. The advantage is: the definition of input variables is intuitive for the customer while the hard fact output allows direct translation to a specific recipe. The developed rules will then be transformed into a feature model which enables a deterministic mapping of customer features to production assets such as different ingredients. Feature Models are originally used in the field of software engineering to model dependencies between different artefacts (i.e., Functions, Documentation, and Requirements (Kang et al., 1990)). Generally using feature models enables the creation of complete product family and a corresponding decision tree, which will be prompted to customer on the webpage during the configuration process (similar to online car configurators). This approach may also be adoptable to production assets as required for individual food production.

This sounds promising to the authors of this paper and therefore will be one scope of future research.

Optionally, additional information about the local preferences may be included. Knowing the location of the customer allows to sharpen the interpretation of his personal perception. This fact is important for the overall satisfaction of the customer need and needs to be included into the model. The model might be considered being a cognitive sensor deriving own (potentially, e.g., geographically varying) conclusions based on

distributed swarm knowledge and adequate data analysis methodologies. Those are in general well known from social network business cases and can be adopted to the current need within this project.

### **Conceptual Tasks**

The conceptual task involves social interaction with the customer. Gamification is a crucial essence, if the overall approach shall turn to be successful. Gamification can be understood as using game typical elements in a non-game-typical context, e.g., to motivate customers towards purchasing a product. Various approaches are used in the field, which mainly are based on creating some interaction base between the customer and the manufacturer. The customer shall experience some feeling of being entertained while getting involved in the product or being part of the product itself. That way, the frontiers between the actual (mainly physical) product and a virtual product (entertainment, service) disappear. In our context, this includes involving the consumer as observing person in the production process. Along with the (technical, deterministic) individualization processes, an additional ingredient comes into the game. The customer knows at each point during the production what the current status of his personal product is. This leads to more identification with the customer justifying a higher sales price from the customers' point of view. Therefore, both the customers' individual choice of his personal product making and the involvement in the whole production process enables the customer to identify himself with the product he is going to purchase and therefore delivers a unique selling proposition.

## **RESULTS AND DISCUSSION**

The main research work done so far is an analysis of the target market, the current technological state of the art of related fields, and identification of critical pieces in the overall puzzle of issues to be solved.

The outcome is, that the overall concept to be implemented needs to be covered in a heavily multi-disciplinary environment, involving social aspects, economical aspects, sensor and algorithm integration and development along with research in that field, mechanical development, and finally geographical information matching.

This list demonstrates the complexity of the overall project. The initial research described in this paper allows to justify on (none – little – highly) critical issues which need to be targeted.

As highly critical issues we have identified the multi-stage interface between customer wishes, customer wish articulation and transformation towards hard digital facts, validation of the real output product towards the initial customer wishes, and detection and treatment of natural raw material fluctuation.

The main outcome of the analysis is, that one important, critical, but worth to be investigated field is the digitalization of the brew master. This is, as typically the human brew master is able to translate the customer perception into successful recipes including a validation of the latter by tasting events. In addition, the determination of common perception of specific beers is done in the food industry by installing tasting polls with humans. It will be challenging, but still news braking to automate this process.

Along with the successful implementation of the investigated and anticipated field, final results of the applied research to be taken out next will help to introduce significant



changes in the field of food technology. For this reason, further investigation and involvement in this field is promising.

Next steps to be undertaken are to identify both problematic or challenging and in parallel easy to solve tasks. Those may be aligned accordingly in one research and development track and one basic research track. There are for sure more tasks, which can be solved easily but need time and humans as resources, then there are challenging tasks. This conclusion can be taken by reviewing the listed issues in the previous chapter. Still, the less challenging task will need more time to be investigated, therefore the dual split sound reasonable.

To cover the field of challenging tasks, currently a research-funding proposal is under investigation.

## CONCLUSIONS

In this paper we presented our results of state of the art analysis for a beer brewing process, which allows to automate the production of individual customer chosen products. We identified and described specific bottlenecks. The first investigation demonstrates the complexity of the planned project on the one hand, while it discovered the most critical puzzle pieces to focus on as well. Further steps include a deeper analysis of the latter mentioned.

## REFERENCES

- Anton Paar GmbH 2020. <https://www.anton-paar.com/corp-de/>, Access: 02.04.2020.
- Anton Paar Sudhaus GmbH. <https://www.sudhaus.at/>, Access: 02.04.2020.
- Beer Engineer, B.E. GmbH & Co. KG 2020. <https://www.bierzuliebe.de>. Accessed: 28.01.2020.
- Berna, A. 2010. Metal Oxide Sensors for Electronic Noses and Their Application to Food Analysis. *Sensors* **10**(4), pp. 3882–3910.
- Brumas Hausbrauerei 2020. <https://www.brumas.com/brumas>. Accessed 29.01.2020.
- Caroço, R.F., Bevilacqua, M., Armagan, I., Santacoloma, P.A., Abildskov, J., Skov, T. & Huusom, J.K. 2018, Raw material quality assessment approaches comparison in pectin production, *Biotechnol. Prog.* **35**(2). <https://doi.org/10.1002/btpr.2762>.
- Ciui, B., Martin, A., Mishra, R.K., Nakagawa, T., Dawkins, T.J., Lyu, M., Cristea, C., Sandulescu, R. & Wang, J. 2018. Chemical Sensing at the Robot Fingertips: Toward Automated Taste Discrimination in Food Samples. *ACS Sensors* **3**(11), 2375–2384.
- Di Natale, C., Paolesse, R., Macagnano, A., Mantini, A., D'Amico, A., Legin, A., Lvova, L., Rudnitskaya, A. & Vlasov, Y. 2000. Electronic nose and electronic tongue integration for improved classification of clinical and food samples. *Sensors and Actuators B: Chemical* **64**(1), pp. 15–21.
- Ettl, M.R., Oh, S. & Pinchuk, S.G. 2015. Computer-implemented techniques for determining and provisioning real-time individualized product and service offering, US Patent, US10318966B2.
- Fraunhofer IIS/IVV 2020. Campus of the Senses. <https://www.campus-der-sinne.fraunhofer.de/en.html>. Accessed: 28.01.2020.
- Galstyan, V., Bhandari, M.P., Sberveglieri, V., Sberveglieri, G. & Comini, E. 2018. Metal Oxide Nanostructures in Food Applications: Quality Control and Packaging. *Chemosensors*, **6**(2).
- Gatchalian, M. 1999, "Quality assessment through statistically-based sensory evaluation methods", *The TQM Magazine* **11**(6), pp. 389–396. <https://doi.org/10.1108/09544789910287674>

- Gorska-Horczyczak, E., Guzek, D., Molda, Z., Wojtasik-Kalinowska, I., Brodowska, M. & Wierzbicka, A. 2016. Applications of electronic noses in meat analysis. *Food Science and Technology* **36**, 389–395.
- Haugen, J.-E. 2001. *Electronic Noses in Food Analysis*, Springer US, Boston, MA, pp. 43–57.
- Kang, K.C., Cohen, S.G., Hess, J.A., Novak, W.E. & Peterson, A.S. 1990. Feature-oriented domain analysis (FODA) feasibility study, *Technical Report CMU/SEI-90-TR-021*, SEI, Carnegie Mellon University, 161 pp.
- Khan, Z.H., Khalid, A. & Iqbal, J. 2018. Towards realizing robotic potential in future intelligent food manufacturing systems. *Innovative Food Science & Emerging Technologies* **48**, 11–24.
- Kreye, M.E. 2018. Interactions between perceived uncertainty types in service dyads. *Industrial Marketing Management* **75**, 90–99. <https://doi.org/10.1016/j.indmarman.2018.04.014>
- Leckner, T., Koch, M., Stegmann, R. & Lacher, M. 2003. Personalization Meets Mass Customization - Support for the Configuration and Design of Individualized Products, Proc. *Intl. Conf. on Enterprise Information Systems*, pp. 259–264.
- Mohamed, R.R., Yaacob, R., Mohamed, M.A., Dir, T.A.T. & Rahim, F.A. 2018. Food Freshness Using Electronic Nose and Its Classification Method: A Review. *International Journal of Engineering and Technology* **7**(3.28), pp. 49–53.
- Morgan, M.T. & Haley, T.A. 2019. *Chapter 22 - Design of Food Process Controls Systems*, Editor(s): Myer Kutz, Handbook of Farm, Dairy and Food Machinery Engineering (Third Edition), Academic Press, pp. 533–591. <https://doi.org/10.1016/B978-0-12-814803-7.00022-1>
- mymuesli GmbH 2020. <https://www.mymuesli.com>. Accessed: 28.01.2020.
- Neef, C., Luipers, D., Bollenbacher, J., Gebel, C. & Richert, A. 2020. Towards Intelligent Pick and Place Assembly of Individualized Products Using Reinforcement Learning, <https://arxiv.org/pdf/2002.08333.pdf>, Accessed: 02.04.2020.
- Newity Ltd., Brewie+. <https://brewie.org>, Accessed 01.04.2020.
- Palmiro Volpentesta, A., Felicetti, A.M. & Ammirato, S. 2017. Intelligent Food Information Provision to Consumers in an Internet of Food Era. In: *Collaboration in a Data-Rich World*. Luis M. Camarinha-Matos, Hamideh Afsarmanesh, and Rosanna Fornasiero, Editors, Cham, Springer International Publishing, pp. 725–736.
- Pramanik, P.K.D., Pal, S. & Choudhury, P. 2018. Beyond Automation 2018. The Cognitive IoT. Artificial Intelligence Brings Sense to the Internet of Things, Springer International Publishing, Cham, pp. 1–37.
- Puppe, F. 2012, *Systematic Introduction to Expert Systems: Knowledge Representations and Problem-Solving Methods*. Springer Science & Business Media, 364 pp.
- Schallmo, D.R.A. 2019. Selected examples in the context of digital transformation of business models (Ausgewählte Beispiele im Kontext der Digitalen Transformation von Geschäftsmodellen). In: *Digital Transformation Now*. Springer Gabler, Wiesbaden, pp. 9–14 (in German).
- Shewhart, W.A. 2012. The Application of Statistics as an Aid in Maintaining Quality of a Manufactured Product, *Journal of the American Statistical Association* **20**(152), 546–548.
- Sinkinson, C. 2017. *Chapter 7 - Triangle Test*. Editor(s): Lauren Rogers, In Wood head Publishing Series in Food Science, Technology and Nutrition, Discrimination Testing in Sensory Science, Woodhead Publishing, pp. 153–170, <https://doi.org/10.1016/B978-0-08-101009-9.00007-1>.
- Society of Sensor Professionals (SSP) 2020. <https://www.sensorsociety.org/knowledge/sspwiki/pages/triangle%20test.aspx>, Access: 02.04.2020

- Sonnen, J. 2019. Digitalization and Connectivity in Agriculture – Status Quo and Forecast. (Digitalisierung und Vernetzung in der Landwirtschaft – Bestandsaufnahme und Ausblick). In: Frerichs, Ludger (Hrsg.): Jahrbuch Agrartechnik 2018. Braunschweig: Institut für mobile Maschinen und Nutzfahrzeuge, pp. 1–11, <https://doi.org/10.24355/dbbs.084-201901211129-0> (in German).
- Teng, C.-Y., Lin, Y. & Adamic, L.A. 2012. Recipe recommendation using ingredient networks, *WebSci '12: Proceedings of the 4th Annual ACM Web Science Conference*, pp. 298–307.
- Test Triangle 2020. <https://www.testtriangle.com/digital-transformation/customer-experience-management/>, Access: 02.04.2020.
- Thomas, O., Zarvić, N., Brezl, J., Brockschmidt, M. & Fellmann, M. 2017. Lebensmittelindustrie 4.0 – Cyber-physische Produktionssysteme zur sicheren und unverfälschbaren Datenverarbeitung. In: Reinheimer S. (eds) *Industrie 4.0. Edition HMD*. Springer Vieweg, Wiesbaden, pp. 59–69.
- Toledo, M. 2020. [https://www.mt.com/at/de/home/campaigns/product-organizations/pro/eNews\\_Turbidit.html](https://www.mt.com/at/de/home/campaigns/product-organizations/pro/eNews_Turbidit.html). Access: 02.04.2020.
- Zhou, Q. & He, L. 2019, Research on customer satisfaction evaluation method for individualized customized products. *Int J Adv Manuf Technol.* **104**, 3229–3238. <https://doi.org/10.1007/s00170-017-1192-2>

## **Effect of concentrate feeding technology on nutrient digestibility in Latvian Dark-Head lambs**

L. Šenfelde\*, D. Kairiša and D. Bārzdiņa

Latvia University of Life Sciences and Technologies, Faculty of Agriculture, Institute of Animal Science, Street Liela 2, LV-3001 Jelgava, Latvia

\*Correspondence: shenfeldel@gmail.com

**Abstract.** Research has been conducted to evaluate the effect of concentrate feeding technology on nutrient digestibility in Latvian Dark-Head lambs. Twenty-four purebred Latvian Dark-Head lambs (rams) were divided into three study groups (four lambs in each group). Concentrate was offered with different feeding technologies: group 1 – *ad libitum* once per day (ADL); group 2 – five times per day (5TD); group 3 – three times per day (3TD). Lamb live weight at the start of research was 24.6 kg (ADL), 24.1 kg (5TD) and 25.6 kg (3TD), the average age –  $83 \pm 1.4$  days (ADL;  $p < 0.05$ ),  $75 \pm 1.4$  days (5TD) and  $75 \pm 1.6$  days (3TD). Research data were collected over three periods and two repetitions during lamb fattening in July, August and September, 2019. During the data collection period lambs were transferred to cages with slatted wooden floor and a container with a grid under it. The highest concentrate intake in all data collection periods was found in ADL lambs ( $1.25 \pm 0.106$  kg –  $1.75 \pm 0.092$  kg on average per lamb). Hay intake was not equal (90–350 g in average per lamb). The highest average faecal production was found in 3TD and 5TD lambs (F –  $0.98 \pm 0.102$  kg (3TD), S –  $1.13 \pm 0.060$  kg (5TD) and T –  $0.99 \pm 0.070$  kg (5TD)). The least urinal production was found in 3TD lambs ( $0.24 \pm 0.038$  kg (F),  $0.61 \pm 0.078$  kg (S) and  $0.47 \pm 0.033$  kg (T)). Dry matter digestibility was 66.54–80.39%. Faecal consistency was soft for ADL and 5TD lambs and solid for 3TD lambs.

**Key words:** lamb fattening, digestibility, dry matter intake, faecal production, manure.

### **INTRODUCTION**

It is useful to study the different processes in the forestomach (rumen, reticulum, omasum) of ruminants to improve the nutrient breakdown in ruminants and maximize their effect on wool, milk and meat production as well as for meeting animal energy requirements (Slavov, 2017).

Nutrient digestibility denotes the amount of nutrients (part of nutrient intake) used for animal needs and milk, meat and wool production (Spring, 2013). Numerous studies report impact of different factors (forage type and quality, animal breed and age, etc.) on nutrient digestibility and productivity of ruminants (Tripathi et al., 2007; Atkinson et al., 2010; Oguri et al., 2013; Gomes et al., 2014; Zhao & Yan, 2017; Pino et al., 2018; Valério Geron et al., 2019, etc.).

The most appropriate feed ration has been studied for years and scientists have come to the common conclusion that a feed ration with a higher concentrate content and a lower roughage content is best suited for intensive lamb finishing (NRC, 2007). No

data can be found in literature regarding nutrient digestibility in lambs fed the same diet using different feeding technologies. Research results of nutrient digestibility using various feeding technologies could be useful for sheep breeders planning organization of their sheep flock feeding. It would also provide a possibility to determine the labour force necessary for sheep feeding to maximize their productivity.

The research has been conducted to evaluate the effect of concentrate feeding technology on nutrient digestibility in Latvian Dark-Head lambs.

## MATERIALS AND METHODS

The research was carried out at the ram testing station 'Klimpas' of the association 'Latvian Sheep Breeders Association' located in Latvia (57.849789, 25.327707). Twenty-four purebred Latvian Dark-Head ram lambs were used (one born as a single lamb and others as twins or triplets) in two repetitions (twelve lambs in each repetition). In each repetition the lambs were divided into three trial groups (four) lambs per group. Concentrate was offered using different feeding technologies: group 1 – *ad libitum* once per day (ADL); group 2 – five times per day (5TD) and group 3 – three times per day (3TD). Concentrate daily ration was increased during fattening and offered once daily (ADL) or in equal rations daily (5TD and 3TD). Lambs were provided *ad libitum* fresh water and alfalfa hay throughout the research. Concentrate included maize, wheat, soy beans (genetically modified), barley, rapeseed cake, sunflower cake, beet chips, beet molasses, CaCO<sub>3</sub>, seed oil and premix of vitamins and minerals.

Lamb live weight at the start of research was 24.6 kg (ADL), 24.1 g (5TD) and 25.6 kg (3TD), average age –  $83 \pm 1.4$  days (ADL;  $p < 0.05$ ),  $75 \pm 1.4$  days (5TD) and  $75 \pm 1.6$  days (3TD). Lamb live weight was fixed at the beginning of the research and on last day of each data collection period. Electronic scales (accuracy  $\pm 0.01$ ) were used for lamb weighing.

Fattening were organized in two repetitions: 1) from June 15, 2019 to August 16, 2019 (R1); 2) from June 25, 2019 to September 13, 2019 (R2). Research data were collected within three periods (each for five days) and two repetitions within lamb fattening: period 1 (F) from July 1, 2019 to July 5, 2019 (R1) and from July 29, 2019 to August 2, 2019 (R2); period 2 (S) from July 22, 2019 to July 26, 2019 (R1) and from August 19, 2019 to August 23, 2019 (R2); period 3 (T) from August 12, 2019 to August 16, 2019 (R1) and from September 9, 2019 to September 13, 2019 (R2). Research data were compared between average results of each data collection period (F, S and T) in both repetitions.

During fattening lambs were kept on straw bedding in cages placed in an outdoor shed grouped the same way as in the data collection periods (four lambs per group). Cages were equipped with wooden ladder trough, drinkers and hopper trough. For data collection lambs were moved to cages additionally equipped with slatted wooden floor and a container with a riddle under it (Fig. 1). To calculate feed intake the feed refusals were subtracted from the feed offered on the previous day. The data collected about the cage on each data collection day were divided by four to obtain results per lamb (Table 4, 5, 7).

On the first day of fattening lambs were offered 4.00 kg of concentrate and 2.00 kg of hay per group, the amount of concentrate was increased by 160 g per group each subsequent day till concentrate refusals in trough remains under 10% from offered

amount. The offered amount of concentrate remained unchanged when concentrate refusals exceeded 10% from offered amount. The quantity of hay offered remained unchanged.

On the first day of each data collection period only the offered alfalfa hay and concentrate amounts were registered per each cage. Every next day of each data collection period the offered alfalfa hay, feed refusals were weighed and faecal and urine production was collected and weighed additionally per each cage. The results were divided to four (number of lambs per cage) to calculate data of feed and dry matter intake and faecal and urinal production per lamb. Electronic scales (precision  $\pm 0.005$ ) were used for weighing of feed refusals, hay, concentrate, faecal and urine production. Faecal production was placed into a plastic container and kept in a refrigerator under temperatures up to 8 °C until delivery to laboratory. The general feed concentrate (1 kg), alfalfa hay (1 kg) and faecal (2 kg) samples were prepared on the last day of each data collection period.



**Figure 1.** Cages with slatted wooden floor and a container with a grid under it made for data collection (photo from the achieve of project participants): 1 – hopper trough for concentrate feeding in ADL group lambs; 2 – wooden ladder trough for hay; 3 – trough for concentrate feeding in 5TD and 3TD group lambs; 4 – drinker; 5 – slatted wooden floor; 6 – container with a grate for faecal and urine production.

Sample preparation was made in accordance with the standard LVS EN ISO 6498:2012. On the last day of each data collection period all the prepared samples were delivered to the Division of Agronomic analysis of Latvia University of Life Sciences and Technologies Research Laboratory of Biotechnology for making analyses of sample chemical composition. Standards or calculations were used for determination of sample chemical composition (Table 1, 2).

**Table 1.** Chemical components of faecal production and standards used

Chemical component, unit	Standards
Dry matter, %	LVS EN 13040:2008 8.1; 9-11
Nitrogen, % (in natural sample)	LVS EN 13654-1/NAC:2004
Ammonium-nitrogen (N/NH <sub>4</sub> ), g kg <sup>-1</sup>	*FOCT 26180-84, met.2
% of dry matter	
Crude fibre, %	*ISO 5498:1981
Fat, %	*ISO 6492:1999
Ash, %	*LVS EN 13039:2012
P, %	LVS ISO 6598:2001
K, %	LVS ISO 9964-3:2000
pH	LVS EN 13037:2012

\* – unaccredited standard.

**Table 2.** Chemical components of forages and standards used

Chemical component, unit	Concentrate	Hay	Standards
Dry matter, %	indicated	indicated	for hay: LVS NE ISO 6498:2012, 7.5. for concentrate: ISO 6496:1999
% of dry matter			
Crude protein, %	indicated	indicated	LVS EN ISO 5983-2:2009
Bound protein, %	indicated	indicated	* Forage analysis, USA, met. 6:1993
Soluble protein, %	indicated	indicated	* Nor For method – 2006
Protected protein of crude protein, %	indicated	indicated	Calculation
Crude fibre, %	indicated	indicated	ISO 5498:1981
NDF, %	indicated	indicated	LVS EN ISO 16472:2006
ADF, %	indicated	indicated	LVS EN ISO 13906:2008
NEG, MJ kg <sup>-1</sup>	indicated	indicated	TDN=88.9-(ADF*0.779) NEG=(TDN*0.01318)-0.459)*4.184/0.453
ME, MJ kg <sup>-1</sup>	indicated	indicated	TDN=88.9-(ADF*0.779) ME(ruminant)=((TDN*0.2004)*(96-(0.202*CP)))*4.184/0.453/1000 (MJ kg <sup>-1</sup> )
Fat, %	indicated	not indicated	ISO 6492:1999
Ash, %	indicated	indicated	ISO 5984:2002/Cor 1:2005
Ca, %	indicated	indicated	LVS EN ISO 6869:2002
P, %	indicated	indicated	ISO 6491:1998
K, %	indicated	indicated	* LVS EN ISO 6869:2002
Strach, %	indicated	not indicated	LVS EN ISO 10520:2001

\* – unaccredited standard; NDF – Neutral Detergent Fibre, ADF – Acid Detergent Fibre; TDN – Total Digestible Nutrients; NEG – Net Energy used for Growth; ME – Metabolizable Energy.

Daily digested nutrient amount, faecal and urine production excreted into external environment per lamb during the data collection periods were calculated. Results of chemical component analysis of faeces, hay and concentrate were used for calculations of nutrient digestibility in purebred Latvian Dark-Head ram lambs.

Results were calculated using Microsoft Excel. Results obtained in this study are presented as mean values with the standard error of the mean and variation (CV). The results were compared among the data collection periods with *t-test* paired two samples

for means. Significant differences between groups ( $P < 0.05$ ) are marked with different letters of the alphabet in superscripts.

## RESULTS AND DISCUSSION

Laboratory analysis of concentrate chemical components (Table 3) shows low variation in the amount of nutrients in samples, except for bound protein (CV 24.86%) and crude fibre (CV 9.84%). It could be explained by different proportion of nutrients used in concentrate production in different production batches to ensure the necessary amount of protein and crude fibre.

**Table 3.** Forage chemical content

Chemical component, unit	Concentrate		Hay	
	Mean	CV	Mean	CV
Dry matter, %	87.97 ± 0.051	0.13	87.60 ± 1.016	3.10
% of dry matter				
Crude protein, %	21.23 ± 0.067	0.70	9.60 ± 0.395	10.90
Bound protein, %	0.47 ± 0.052	24.86	0.60 ± 0.069	24.40
Soluble protein, %	4.30 ± 0.102	5.30	4.60 ± 0.260	11.40
Protected protein of crude protein, %	72.58 ± 0.369	1.14	30.30 ± 2.673	17.60
Crude fibre, %	5.22 ± 0.230	9.84	32.20 ± 1.146	9.40
NDF, %	15.11 ± 0.219	3.24	59.90 ± 1.633	7.20
ADF, %	7.22 ± 0.061	1.89	36.70 ± 0.951	6.90
NEG, MJkg <sup>-1</sup>	5.90 ± 0.006	0.22	3.10 ± 0.089	7.60
ME, MJ kg <sup>-1</sup>	14.14 ± 0.007	0.11	10.50 ± 0.134	3.40
Fat, %	3.43 ± 0.020	1.30	-	-
Ash, %	7.12 ± 0.017	0.54	5.50 ± 0.214	10.20
Ca, %	1.23 ± 0.015	2.78	0.50 ± 0.042	20.90
P, %	0.58 ± 0.011	4.10	0.20 ± 0.014	16.90
K, %	1.03 ± 0.013	2.79	1.40 ± 0.083	14.00
Starch, %	42.28 ± 0.196	1.04	-	-

NDF – Neutral Detergent Fibre, ADF – Acid Detergent Fibre; NEG – Net Energy used for Growth; ME – Metabolizable Energy.

Hay was prepared at the ram testing station ‘Klimpas’ and preparation process was affected mainly by circumstances of external environment, for example – rain, soil composition or maturity stage. Weather conditions were not recorded during the preparation of the hay, but by comparing the mean nutrient values of hay used in the research and those shown in the summary of chemical analyses and digestibility of forages made in Latvia (Degola et al., 2016) it denotes late hay cutting. Beecher et al. (2018) study results indicate decreased dry matter digestibility of grass in its late maturity stage. It could impact the dry matter digestibility of hay prepared of grass in its late maturity stage as well. As a result the variation of chemical composition of hay was very high (from 3.40% to 24.40%). The lowest variation (3.40%) was fixed for metabolizable energy.

Daily mean concentrate and hay intake per lamb is shown in Table 4. The highest mean concentrate intake per lamb daily in all data collection periods was recorded in ADL lambs (F – 1.25 ± 0.106 kg, S – 1.58 ± 0.043 kg, T – 1.75 ± 0.092 kg). This could



be explained by periods of lamb eating activity. A previous study showed that eating activity of lambs daily was increased: at 02:00–02:59, 08:00–09:59 and 19:00–20:59 (Šenfelde & Kairiša, 2018). The lambs of the ADL group were able to start consuming the desired amount of concentrate in the morning and throughout the day. Although the daily amount of concentrate offered was the same for all groups, at the morning lambs in group 5TD and 3TD received concentrate only partly of daily norm. Thus, in the first half of the day, lambs of group 5TD and 3TD could only consume concentrates partly from the whole daily norm, not as much they wants. Previous researches of 50% Romanov and 50% Dorper crossbred lamb fattening with concentrate using an automatic feeding station showed the concentrate daily intake of 1.13 kg in the first fattening period, 1.50 kg in the middle of fattening and 1.40 kg in the last fattening period (Šenfelde & Kairiša, 2018). Lambs in mentioned research was in the same age and live weight at the start of the research. In the first and second fattening periods it is similar to ADL lambs, but at the end of fattening it is similar to 5TD and 3TD lambs.

**Table 4.** Daily mean concentrate and hay intake per lamb, kg

Data collection period	Concentrate			Hay		
	ADL	5TD	3TD	ADL	5TD	3TD
F	1.25 ± 0.106 <sup>a</sup>	0.65 ± 0.160 <sup>b</sup>	0.71 ± 0.133 <sup>b</sup>	0.13 ± 0.027 <sup>a</sup>	0.22 ± 0.024 <sup>b</sup>	0.35 ± 0.034 <sup>c</sup>
S	1.58 ± 0.043 <sup>a</sup>	1.11 ± 0.129 <sup>b</sup>	1.26 ± 0.096 <sup>b</sup>	0.13 ± 0.034 <sup>a</sup>	0.27 ± 0.027 <sup>b</sup>	0.23 ± 0.032 <sup>b</sup>
T	1.75 ± 0.092 <sup>a</sup>	1.50 ± 0.019 <sup>b</sup>	1.48 ± 0.032 <sup>b</sup>	0.09 ± 0.010 <sup>a</sup>	0.14 ± 0.033 <sup>ab</sup>	0.14 ± 0.015 <sup>b</sup>

<sup>a, b, c</sup> – data with different superscripts are significantly different,  $P \leq 0.05$ .

In the first data collection period significant differences ( $P < 0.05$ ) were found in 5TD ( $0.65 \pm 0.160$  kg) and 3TD ( $0.71 \pm 0.133$ ) lambs compared to ADL ( $1.25 \pm 0.106$ ).

Overall in all data collection periods between all groups there was a varied daily hay intake (from 90 g to 350 g per lamb). ADL lambs had the lowest daily hay intake in all data collection periods (F –  $0.13 \pm 0.027$  kg, S –  $0.13 \pm 0.034$  kg and T –  $0.09 \pm 0.010$  kg). Allen (1997) indicates that ruminants require roughage in their diets to maximize productivity and to maintain health by sustaining a stable environment in the rumen. But also, other researches have to be taken into consideration that increasing dietary roughage in feedlot diets decreases dry mater digestibility (Hales et al., 2014). The results of the research indicate that the hay intake by lambs was in the amount necessary to ensure the functioning of the digestive tract.

Ma et al. (2014) study has shown that increasing the share of concentrates in the ration, and thus the share of dry matter in concentrates, improves the digestibility of total dry matter. These results agree with the results obtained in this study (Table 5, 8). Due to the fact that the undigested amount of dry matter is excreted from the animal's body in the form of faeces, the amount of faeces decreases as the digestibility of dry matter increases. In this study, this is evidenced by the data obtained where the ADL group has the highest dry matter intake (1.10–1.54 kg per lamb daily; Table 5), the highest digestibility (79.63–80.39%; Table 8) and the lowest faecal excretion (0.70–0.94 kg per lamb daily; Table 7).

**Table 5.** Daily mean dry matter intake from concentrate and hay per lamb, kg

Data collection period	Concentrate			Hay		
	ADL	5TD	3TD	ADL	5TD	3TD
F	1.10 ± 0.093 <sup>a</sup>	0.56 ± 0.141 <sup>b</sup>	0.63 ± 0.117 <sup>b</sup>	0.11 ± 0.024 <sup>a</sup>	0.19 ± 0.021 <sup>b</sup>	0.31 ± 0.030 <sup>c</sup>
S	1.39 ± 0.038 <sup>a</sup>	0.98 ± 0.113 <sup>b</sup>	1.11 ± 0.085 <sup>b</sup>	0.11 ± 0.030 <sup>a</sup>	0.23 ± 0.023 <sup>b</sup>	0.20 ± 0.028 <sup>b</sup>
T	1.54 ± 0.081 <sup>a</sup>	1.32 ± 0.016 <sup>b</sup>	1.30 ± 0.028 <sup>b</sup>	0.08 ± 0.009 <sup>a</sup>	0.12 ± 0.029 <sup>b</sup>	0.13 ± 0.013 <sup>b</sup>

a, b, c – data with different superscripts are significantly different,  $P \leq 0.05$ .

Chemical components of faecal production (Table 6) indicate higher nutrient content ( $\text{g kg}^{-1}$ ) at the end of fattening for all groups, except for fat (ADL and 3TD), dry matter (3TD), crude fibre (3TD) and ashes (3TD). The live weight gain by data collection periods is not analyzed in this article, but the increased nutrient content in the faecal production in the last data collecting period (T) could be explained by the fact that the lamb live weight was already close to the maximum in the second data collection period (S) and the nutrient necessity for weight gain decreases in forward.

**Table 6.** Chemical components of faecal production,  $\text{g kg}^{-1}$  of natural sample

Nutrients	ADL			5TD			3TD		
	F	S	T	F	S	T	F	S	T
Dry matter	238.5 ± 27.04	306.0 ± 30.66	317.2 ± 18.63	227.9 ± 25.36	347.8 ± 20.42	340.3 ± 22.37	321.9 ± 27.10	369.0 ± 24.57	287.5 ± 23.87
Nitrogen	8.3 ± 1.09	11.2 ± 1.13	12.6 ± 0.78	6.6 ± 0.91	11.4 ± 0.81	13.6 ± 0.95	9.7 ± 1.28	12.7 ± 0.74	13.2 ± 1.10
Crude fibre	50.3 ± 5.21	69.38 ± 7.20	81.8 ± 5.70	57.7 ± 6.49	91.7 ± 4.28	81.38 ± 5.14	86.5 ± 7.73	89.9 ± 4.44	69.48 ± 5.77
Fat	8.5 ± 0.74	8.7 ± 1.05	6.0 ± 0.34	5.9 ± 0.51	6.5 ± 0.28	6.1 ± 0.40	7.3 ± 0.59	7.4 ± 0.56	6.5 ± 0.54
Ash	39.0 ± 4.88	49.9 ± 5.91	50.3 ± 2.86	35.0 ± 3.78	47.57 ± 4.82	56.0 ± 3.81	43.7 ± 3.41	54.0 ± 5.82	42.3 ± 3.51
P	2.9 ± 0.31	4.1 ± 0.40	5.0 ± 0.29	2.4 ± 0.34	3.5 ± 0.37	4.9 ± 0.32	3.0 ± 0.30	4.8 ± 0.68	3.7 ± 0.31
K	2.6 ± 0.29	3.5 ± 0.42	3.0 ± 0.26	2.6 ± 0.32	3.9 ± 0.22	3.5 ± 0.21	3.7 ± 0.39	4.1 ± 0.21	4.1 ± 0.34
N/NH <sub>4</sub>	1.5 ± 0.24	2.5 ± 0.22	3.1 ± 0.24	1.4 ± 0.33	2.6 ± 0.10	3.0 ± 0.29	2.2 ± 0.41	2.9 ± 0.11	4.3 ± 0.36

The highest daily faecal production (Table 7) per lamb was recorded for 5TD and 3TD lambs (F –  $0.98 \pm 0.102$  kg (3TD), S –  $1.13 \pm 0.060$  kg (5TD) and T –  $0.99 \pm 0.070$  kg (5TD)). The lowest urine production was recorded for 3TD lambs in all data collection periods (F –  $0.24 \pm 0.038$  kg, S –  $0.61 \pm 0.078$  kg and T –  $0.47 \pm 0.033$  kg).

**Table 7.** Daily faecal and urine production per lamb, kg

Data collection period	Faecal production			Urine production		
	ADL	5TD	3TD	ADL	5TD	3TD
F	0.70 ± 0.078 <sup>a</sup>	0.74 ± 0.079 <sup>ab</sup>	0.98 ± 0.102 <sup>b</sup>	0.61 ± 0.138 <sup>a</sup>	0.29 ± 0.021 <sup>b</sup>	0.24 ± 0.038 <sup>b</sup>
S	0.94 ± 0.063 <sup>a</sup>	1.13 ± 0.060 <sup>b</sup>	1.09 ± 0.048 <sup>ab</sup>	0.86 ± 0.116 <sup>a</sup>	0.66 ± 0.112 <sup>ab</sup>	0.61 ± 0.078 <sup>b</sup>
T	0.91 ± 0.073 <sup>a</sup>	0.99 ± 0.070 <sup>a</sup>	0.91 ± 0.076 <sup>a</sup>	0.75 ± 0.077 <sup>a</sup>	0.88 ± 0.070 <sup>a</sup>	0.47 ± 0.033 <sup>b</sup>

a, b, c – data with different superscripts are significantly different,  $P \leq 0.05$ .

Dry matter digestibility of forages (Table 8) was 76.63% – 80.39% (ADL), 66.54% – 76.08% (5TD) and 66.91% – 80.23% (3TD). A lower dry matter digestibility during the S data collection period is observed in all groups. The other studies indicate similar or lower dry matter digestibility results in other sheep breeds. Zhao et al. (2015) indicate 79% dry matter digestibility in Highlander and Texel crossbred lambs for fattening fed *ad libitum* perennial ryegrass (*Lolium perenne*) and 0.5 kg concentrate once daily. Dry matter digestibility in Suffolk purebred lambs fed twice daily with hay and corns ground to particle size from 1 to 3 mm was in the range of 62–65% (Vranic et al., 2017). Dry matter average digestibility in Dorper and thin-tailed Han cross-bred ram lambs fed *ad libitum* mixed diet was 63% (fed twice daily; Ma et al., 2019), 58% (fed once daily; Deng et al., 2012) and 59% (fed once daily; Xu et al., 2015).

**Table 8.** Nutrient digestibility, %

Nutrients	ADL			5TD			3TD		
	F	S	T	F	S	T	F	S	T
Dry matter	80.29	79.63	80.39	75.96	66.54	76.08	71.40	66.91	80.23
Nitrogen	78.73	77.05	76.46	77.17	63.19	70.57	70.30	62.53	71.69
Crude fibre	44.25	37.94	22.59	44.00	27.70	18.65	39.80	25.09	30.93
Fat	77.72	81.61	88.69	77.30	76.33	86.95	73.92	76.34	86.65
Ash	53.77	52.33	55.71	45.75	31.40	45.23	41.93	28.01	58.43
P	55.93	51.56	46.36	50.12	34.91	52.30	45.24	18.12	54.64
K	80.07	77.55	81.86	74.84	67.31	79.41	70.64	67.37	71.99

The results of this research indicated crude fibre digestibility decrease in all groups during the fattening, while digestibility of nitrogen in the all fattening period decreased in ADL and 5TD lambs. In 5TD and 3TD lambs the lowest nitrogen digestibility was in second period when data were collected.

Nutrient digestibility (Table 8) for 3TD lambs compared with 5TD lambs was higher at the end of fattening (T), except for fat and K.

## CONCLUSIONS

Intensive fattening of lambs fed with concentrate offered in a hopper trough ensures low labour necessity and lambs have *ad libitum* access to feed that results in high concentrate and low hay intake. The best dry matter and nitrogen digestibility was in ADL group. The team of authors prefer feeding with *ad libitum* access to forage for lamb fattening. Faecal consistency was soft and extra bedding was necessary.

Low concentrate intake at each feeding time was ensured by feeding lambs five times daily; low hay intake was registered as well. Average dry matter digestibility was not significantly different ( $P > 0.05$ ) and low nutrient content in faecal production was found. 5TD lambs had soft faecal consistency and high urine production.

Lamb fattening by feeding them three times daily resulted in lowest dry matter and nitrogen digestibility in the first data collection period. But compared to the other groups, in the third data collection period dry matter and nitrogen digestibility in 3TD lambs were average. Faecal consistency was solid, visually lambs were dry and clean. Low labour was necessary and hay intake was significantly different ( $P < 0.05$ ) in the first data collection period.

**ACKNOWLEDGEMENTS.** This project was supported by the Ministry of Agriculture of the Republic of Latvia within the framework of project ‘Studies of forage and nutrient digestibility in lambs under different treatments’ No.19-00-SOINV05-000025. The authors would like to gratefully acknowledge the kind support of association ‘Latvian Sheep Breeders Association’.

## REFERENCES

- Allen, M.S. 1997. Relationship between fermentation acid production in the rumen and the requirement for physically effective fiber. *Journal of Dairy Science* **80**, 1447–1462. doi:10.3168/jds.S0022-0302(97)76074-0
- Atkinson, R.L., Toone, C.D. & Ludden, P.A. 2010. Effects of ruminal protein degradability and frequency of supplementation on site and extent of digestion and ruminal fermentation characteristics in lambs fed low-quality forage. *Journal of Animal Science* **88**(2), 718–726. doi:10.2527/jas.2009-2245
- Beecher, M., Baumont, R., O'Donovan, M., Boland, T.M., Aufrere, J., Fleming, C., Galvin, N. & Lewis, E. 2018. Effect of harvesting perennial ryegrass at different levels of herbage mass on voluntary intake and *in vivo* digestibility in sheep. *Grass and Forage Science* **73**, 553–561. doi: 10.1111/gfs.12319
- Degola, L., Trūpa, A. & Aplociņa, E. 2016. *Chemical analyses and digestibility of forages*. Latvia, Jelgava, 52 pp. (in Latvian).
- Deng, K.-D., Diao, Q.-Y., Jiang, C.-G., Tu, Y., Zhang, N.-F., Liu, J., Ma, T., Zhao, Y.-G. & Xu, G.-S. 2012. Energy requirements for maintenance and growth of Dorper crossbred ram lambs. *Livestock Science* **150**(1–3), 102–110. <https://doi.org/10.1016/j.livsci.2012.08.006>
- Gomes, M.J., Guedes, C.M., Silva, S.R., Azevedo, J.M.T. & Dias-da-Silva, A. 2014. Utilisation of high- and low-roughage diets by a local and an exotic breed of sheep: intake, growth and digestive efficiency. *Livestock Science* **167**, 110–120. <http://dx.doi.org/10.1016/j.livsci.2014.04.015>
- Hales, K.E., Brown-Brandl, T.M. & Freetly, H.C. 2014. Effects of decreased roughage concentration on energy metabolism and nutrient balance in finishing beef cattle. *Journal of Animal Science* **92**, 264–271. doi:10.2527/jas.2013-6994
- Ma, T., Deng, K.D., Tu, Y., Zhang, N.F., Jiang, C.G., Liu, J., Zhao, Y.G. & Diao, Q.Y. 2014. Effect of dietary forage-to-concentrate ratios on urinary excretion of purine derivatives and microbial nitrogen yields in the rumen of Dorper crossbred sheep. *Livestock Science* **160**, 37–44. <https://doi.org/10.1016/j.livsci.2013.11.013>
- Ma, T., Wan, F., Yang, D., Deng, K., Yang, K. & Diao, Q. 2019. Growth performance, nutrient digestibility, and slaughter traits of male fattening lambs under different feeding standards. *Animal Nutrition* **5**, 74–79. <https://doi.org/10.1016/j.aninu.2018.07.002>
- NRC. 2007. Nutrient requirements of small ruminants: Sheep, goats, cervids, and new world camelids. 1st ed. Washington, DC: National Academy Press

- Oguri, M., Okano, K., Ieki, H., Kitagawa, M., Tadokoro, O., Sano, Y., Oishi, K., Hirooka, H. & Kumagai, H. 2013. Feed intake, digestibility, nitrogen utilization, ruminal condition and blood metabolites in wethers fed ground bamboo pellets cultured with white-rot fungus (*Ceriporiopsis subvermisporea*) and mixed with soybean curd residue and soy sauce cake. *Animal Science Journal* **84**(9), 650–655.
- Pino, F., Mitchell, L.K., Jones, C.M. & Heinrichs, A.J. 2018. Comparison of diet digestibility, rumen fermentation, rumen rate of passage, and feed efficiency in dairy heifers fed ad-libitum versus precision diets with low and high quality forages. *Journal of Applied Animal Research* **46**(1), 1296–1306. doi:10.1080/09712119.2018.1498788
- Šenfelde, L. & Kairiša, D. 2018. Effect of Automatic Feeding Station use on fattening performance in lambs and intake activity periods. *Agronomy Research* **16**(3), 884–891. <https://doi.org/10.15159/AR.18.132>
- Slavov, T. 2017. Alternatives for optimisation of rumen fermentation in ruminants. *Agricultural Science and Technology* **9**(2), 91–97. doi: 10.15547/ast.2017.02.015
- Spring, P. 2013. The challenge of cost effective poultry and animal nutrition: optimizing existing and applying novel concepts. *Lohmann Inf.* **48**(1), 38–46.
- Tripathi, M.K., Chaturvedi, O.H., Karim, S.A., Singh, V.K. & Sisodiya, S.L. 2007. Effect of different levels of concentrate allowances on rumen fluid pH, nutrient digestion, nitrogen retention and growth performance of weaner lambs. *Small Ruminant Research* **72**(2/3), 178–186. doi: 10.1016/j.smallrumres.2006.10.008
- Valério Geron, L.J., De Souza, A.L., Perosa Zanin, S.F., De Aguiar, S.C., De Souza Santos, I., Da Silva, R.F., Garcia, J., De Moura Zanine, A., Diniz, L.C. & De Jesus Ferreira, D. 2019. Pepper (*Capsicum ssp.*) as a feed additive in sheep rations using two types of inoculum: Effects on in vitro digestibility and fermentation parameters. *Ciencias Agrarias* **40**(6), 3653–3664.
- Vranic, M., Grbeša, D., Bošnjak, K., Mašek, T. & Jareš, D. 2017. Intake and digestibility of sheep-fed alfalfa haylage supplemented with corn. *Canadian Journal of Animal Science* **98**, 135–143. doi: dx.doi.org/10.1139/cjas-2015-0168
- Xu, G.S., Ma, T., Ji, S.K., Deng, K.D., Tu, Y., Jiang, C.G. & Diao, Q.-Y. 2015. Energy requirements for maintenance and growth of early-weaned Dorper crossbred male lambs. *Livestock Science* **177**, 71–78. <https://doi.org/10.1016/j.livsci.2015.04.006>
- Zhao, Y.G., Aubry, A., O'Connell, N.E., Annett, R. & Yan, T. 2015. Effects of breed, sex, and concentrate supplementation on digestibility, enteric methane emissions, and nitrogen utilization efficiency in growing lambs offered fresh grass. *Journal of Animal Science* **93**, 5764–5773. doi:10.2527/jas2015-9515
- Zhao, Y.G. & Yan, T. 2017. Effects of forage type and genotype on nutrient digestibility and energy utilisation efficiency in hill ewe lambs. In Keita, A. & Berckmans, D. (eds): *8th European Conference on Precision Livestock Farming*. Nantes, France, pp. 213–218.

## **Features of the influence of copper nanoparticles and copper oxide on the formation of barley crop**

T. Seregina<sup>1</sup>, O. Chernikova<sup>1,\*</sup>, Yu. Mazhaysky<sup>1</sup> and L. Ampleeva<sup>2</sup>

<sup>1</sup>Academy of law management of the federal penal service of Russia, Sennaya street 1, RU390036 Ryazan, Russia

<sup>2</sup>Ryazan State Agrotechnological University named after P.A. Kostychev, Kostychev street 1, RU390044 Ryazan, Russia

\*Correspondence: [chernikova\\_olga@inbox.ru](mailto:chernikova_olga@inbox.ru)

**Abstract.** In addition to modern methods of agricultural technology, currently the achievements of selection and genetics are widely used, as well as modern nanotechnology and nanomaterials, to improve food production. One of the forms of biologically active nanomaterials is metal nanopowders and their derivatives. The application is carried out in minimal doses that can significantly reduce costs in agricultural production. Improving the yield and quality of crops by optimizing nutrition and plant protection using nanotechnology and nanomaterials will solve not only the problems of increasing the yield and quality of farmed products, but also environmental problems. The purpose of this research was to determine the effect of copper and copper oxide nanoparticles on the formation of a barley crop. Under the conditions of a lysimetric experiment, the effect of presowing treatment of spring barley seeds by nanoparticles of copper and copper oxide on the growth and development of plants, yield, and their nutritional value was studied. The used nanoparticles have the following characteristics: Cu - 40–60 nm, phase composition: Cu - 100%; CuO - 40–60 nm, phase composition: CuO - 100%. A suspension of nanoparticles was obtained by dispersion by ultrasound in an aqueous solution. Nanopowders of copper and copper oxide in the solution contained 0.01 g per hectare seed rate. Barley seeds were soaked 30 minutes before sowing in double distilled water (control variant), as well as in a suspension of nanoparticles. Presowing treatment of barley seeds by Cu nanoparticles contributed to the intensification of growth processes, as well as an increase in green mass. The use of copper nanoparticles contributed to an increase in grain yield by 17.3% compared with the control, while there was no decrease in nutritional value: metabolic energy, feed units, digested protein. Based on the research results, it is preferable to use copper nanoparticles in comparison with copper oxide nanoparticles to obtain a higher barley yield.

**Key words:** copper nanoparticles, copper oxide nanoparticles, linear growth, spring barley yield, nutritional value.

## **INTRODUCTION**

The search and development of techniques that could increase the yield of cultivated plants without increasing fertilizer application rates, as well as improve the quality of agricultural products, is a priority area of modern crop production (Churilov et al., 2013, 2018; Polischuk et al., 2018; Zakharova et al., 2018; Chernikova et al., 2019a,

2019b). One of these areas is the transition to technologies that contribute to optimizing plant nutrition with microelements and stimulators of their growth and development in accordance with the biological requirements of crops, to a strategy for the integrated and differentiated use of genetic, soil-climatic and technogenic factors (Hafeez et al., 2015; Mengmeng Rui et al., 2016; Hlisenikovský et al., 2019; Olkhovskaya et al., 2019).

Adaptive intensification of agriculture requires widespread use of methods of biological correction, which includes non-root feeding by growth stimulants.

Interest in the use of nanoparticles (NPs) in crop production and agricultural practice is associated with their unique properties. Long-term studies of dispersed NP systems have revealed the following features of their biological action:

- metal nanoparticles have low toxicity, by 7–50 times less toxicity of metals in ionic form;
- have a prolonged and multifunctional effect;
- stimulate metabolic processes;
- easily penetrate into all organs and tissues;
- their biological activity is associated with the structural features of the particles and their physicochemical characteristics, etc. (Zeyruk et al., 2019).

The biological activity of metal nanoparticles is directly related to their physicochemical characteristics: particle size, their shape, phase state of particles (Olkhovskaya et al., 2019). As the result, for the successful use of nanoparticles and nanomaterials for the crop industry, their physicochemical properties must be taken into account.

Microelements play an important role in obtaining high yields of good quality spring barley grain. The essential element copper and its oxide were selected to research the influence of NPs of metals on the formation of barley. Copper is a constituent of enzymes that play an important role in redox processes. They improve the intensity of photosynthesis, promote the formation of chlorophyll, have a positive effect on carbohydrate and nitrogen metabolism, and increase the resistance of plants against fungal and bacterial diseases. The protein content in grain increases under the influence of copper (Copper for plants, 2019).

The stimulation was revealed under the action of the dispersed solutions at extremely low concentrations of NPCu (up to  $10^{-17}$  mg L<sup>-1</sup>). The sol treatment of seeds promoted an increase in the degree of their resistance to pathogenic fungi (causing root rots in sprouts) (Maslobrod et al., 2014).

It should be noted that a number of authors (Fedorenko et al., 2020) note the toxic effect of CuO nanoparticles on plant development, which is manifested in changes in tissue and intracellular levels in barley roots. At the same time, there are practically no qualitative changes in plant leaves under the influence of copper in macroand nanodisperse forms. It is shown that the maximum concentration for safe use of copper nanopowder is 100 g ha<sup>-1</sup>, and for copper oxide nanopowder - 10.0 g ha<sup>-1</sup>.

Barley is a culture of versatile use, which has great feed, food, technical and agricultural value. In industrial bakery, barley is sometimes used as a component in the formulation of some varieties of wheat bread. In terms of food, barley remains only a popular cereal crop, which pearl barley and peeled barley groats are obtained from.

Barley is one of the important fodder-grain crops (1 kg of grain contains 1.1 feed units). It is introduced as the main ingredient in most animal feeds. The green mass of

barley in a mixture with legumes (vetch, peas, maple pea, lathyrus) is used for green feed, silage, haylage, hay.

The purpose of this research was to determine the effect of copper and copper oxide nanoparticles on the formation of a barley crop.

MATERIALS AND METHODS

The research was carried out in the lysimeters of the NSRIHEA design with undisturbed soil profile (Fig. 1). The area of stationary field lysimeters is 1.3 m<sup>2</sup>.

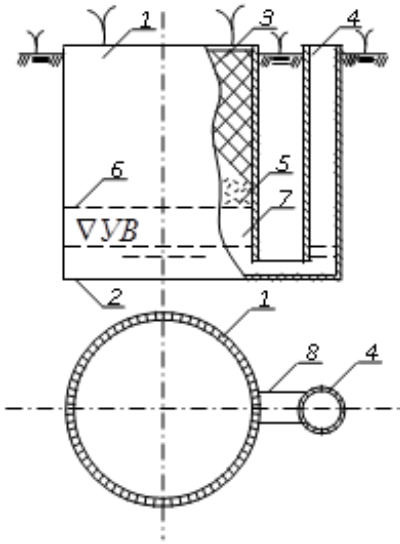


**Figure 1.** Diagram of a water balance lysimeter (legend: 1 – lysimeter case; 2 – lysimeter bottom; 3 – soil monolith; 4 – pocket for water extraction; 5 – gravel packing; 6 – strainer; 7 – groundwater level; 8 – communication channel).

Lysimeters are charged with gray forest soil. Taken soil samples from a depth of 0–25 cm at the beginning of the experiment characterize the soil with a low content of organic matter from 3.8% to 5.4% (on average 4.6% ± 0.6) (Fig. 2).

The acid-base reaction of the soil refers to slightly acidic, pH from 5.3 to 6.4 (on average 5.7 ± 0.1). The supply of soil with mobile nutrients on average was as follows: potassium content - 833.5 mg kg<sup>-1</sup>, total nitrogen - 0.12%, mobile phosphorus - 128 mg kg<sup>-1</sup> that characterizes this soil as medium provided with these elements.



**Figure 2.** Lysimetric experiment on gray forest soil.

According to our research plan, the effect of copper and copper oxide nanoparticles was studied with an optimal concentration of 0.01 g hectare seed rate (Table 1). The experiment was carried out in four replicates.

**Table 1.** The setup of the experiment

Lysimeter number	Variant name	Abbreviation
1, 5, 9, 13	Suspension of nanopowder of copper oxide at a dose of 0.01 g ha <sup>-1</sup>	CuO 0.01
2, 6, 10, 14	Suspension of copper nanopowder in a dose of 0.01 g ha <sup>-1</sup>	Cu 0.01 N <sub>60</sub> P <sub>60</sub> K <sub>60</sub>
3, 7, 11, 15	Suspension of copper nanopowder in a dose of 0.01 g ha	Cu 0.01
4, 8, 12, 16	Control	C



Nanoparticles obtained at the Moscow Institute of steel and alloys by gas-phase chemical reactions. The used nanoparticles are single crystal structures of circular regular shape and have the following characteristics: Cu - 40–60 nm, phase composition: Cu<sup>0</sup> - 100%; CuO - 40–60 nm, phase composition: CuO - 100%. A suspension of nanoparticles was obtained by dispersion by ultrasound in an aqueous solution. Nanopowders of copper and copper oxide contained 0.01 g per hectare seed rate in the solution. Barley seeds were soaked 30 minutes before sowing in double distilled water (control variant), as well as in a suspension of nanoparticles.

Barley spring variety ‘Kati’ was chosen as the object of research (Fig. 3). The species is nutans. The bush is intermediate. The leaf sheath of the lower leaves is without pubescence. The anthocyanin color of the flag leaf ligules is medium - strong, the wax coating on the sheath is weak - medium. The plant has short - medium length. Pyramidal spike - cylindrical, loose - medium density, with medium - strong waxy coating. The awns are



**Figure 3.** Spring barley variety Kati.

longer than spike, serrated, with medium - strong anthocyanin coloration of tips. The first segment of the spike rod has short - medium length, with a slight bend. Sterile spike is from parallel to slightly deflected. The pubescence of the main setae of the weevil is long. Anthocyanin coloration of the nerves of the outer floral scales is weak.

The serration of the internal lateral nerves of the outer floral scales is absent or very weak. The weevil is very large, with an undescended abdominal groove and a covering lodicule. The mass of 1,000 grains is 46–56 g. Grain-fodder. The protein content is 10.9–14.5%. Susceptible to root rot.

Sowing was conducted on April 26, 2019. The technology for growing spring barley in lysimeters imitated the generally accepted one for gray forest soil in this region, but with some features of lysimetric studies.

The grooves were made in the plots with a depth of 3–4 cm; at a distance of 12 cm, the seed rate was distributed at the rate of 55 grains per 1 linear meter (Fig. 4). In the phase, the pips were pulled and 50 pieces were left per 1 linear meter. Agricultural cultivation culture is generally accepted for this zone. Harvesting barley was carried out in a phase of full ripeness. Plants were cut at a height of 1–2 cm from the root neck, placed in bags indicating the number of the variant and repetition.



**Figure 4.** Establishment of lysimetric experiment (sowing barley of Kati variety).

In the laboratory, the above-ground crop was dried to constant weight. After threshing the grain, the refined grain was weighed. Samples were taken from the crop by repetition, numbered, according to the registry, for shipment to the laboratory. A mass of 1,000 seeds, grain moisture, and nutritional value (metabolic energy, feed units, digestible protein) were determined using generally accepted GOST methods.

## RESULTS AND DISCUSSION

Linear plant growth is an important environmental indicator that indirectly characterizes the intensity of cell division or extension. Phenological observations of the growth and development of plants were carried throughout the growing season. This season the weather conditions were unfavorable: temperatures were low for this period, as well as prolonged rains with gusty winds. This fact affected the development of plants and, as a consequence, productivity.

Phenological studies consisted of measuring the height of plants. The observations were carried out in two rows: 3 and 5. The height of the plants was determined by the highest tip, 10 plants of the counting row. The calculation was carried out on 1 plant, calculating the average value for each indicator. There were two of them on barley - 10.05 and 26.07.

The highest linear growth rates of plants on May 10, 2019 were revealed on the variant using copper nanoparticles with the joint application of mineral fertilizers (Table 2). Differences with the control variant were 1.29 cm or 18.14%. It should be noted that the growth and development of plants in the control was uneven and unstable. In variants where copper and copper oxide nanoparticles at a dose of 0.01 g ha<sup>-1</sup> were used for pre-sowing seed treatment, an increase in plant height by 0.61 and 0.22 cm was also observed that amounted to 9.49% and 6.28%.

**Table 2.** Linear growth of barley during presowing treatment of barley seeds by copper and copper oxide nanoparticles

No.	Experiment variants	Plant Height, cm					
		10.05.2019			26.07.2019		
		mean	change cm ±	%	mean	change cm ±	%
1	CuO 0.01	6.43	+ 0.61	9.49%	69.68	+ 0.21	0.30
2	Cu 0.01 N60P60K60	7.11	+ 1.29	18.14%	70.85	+ 1.38	1.95
3	Cu 0.01	6.21	+ 0.22	6.28%	77.01	+ 5.54	9.79
4	C	5.82	-	-	69.47	-	-
	HCP <sub>0.95</sub>	0.9	-	-	3.7	-	-

The linear growth indicators on July 26, 2019 were as follows: the highest plant height was noted on the variant using copper nanoparticles at a dose of 0.01 g ha<sup>-1</sup>. The increase in this indicator compared with the control variant of the experiment amounted to 7.19%. Copper nanoparticles probably contributed to an increase in the adaptive potential of plants that led to the stabilization of growth processes and increased resistance to lodging. The use of copper oxide nanoparticles had practically no effect on plant growth in the last stages of vegetation, and the difference with the control was insignificant 0.21 cm or 0.30%.

Productivity is the most important effective indicator of crop production and agricultural production in general. The yield level reflects the impact of the conditions which the plants are grown in and the quality of the measures taken.

Indicators of linear growth and productivity in our experiment were directly dependent on each other. Thus, the highest yield was noted in the variant with the use of Cu NPs - 44.8 c ha<sup>-1</sup> (Table 3). The mass of 1,000 seeds (Table 4) in this variant was less, however, the number of spikelets and grains in the ear at the time of harvesting was more. Plants during using copper nanoparticles were more resistant to lodging and shedding of seeds that probably led to an increase in this indicator in comparison with the control variant, as well as other experimental variants.

The use of copper oxide nanoparticles and copper nanoparticles together with mineral fertilizers also contributed to an increase in the yield of spring barley. When analyzing the obtained data of the options, it is seen that the yield increases in comparison with the control variant are as follows: CuO 0.01–0.4 c ha<sup>-1</sup> (1.12%), Cu 0.01 N60P60K60 - 3.5 c ha<sup>-1</sup> (9, 02%), Cu 0.01–9.5 c ha<sup>-1</sup> (17.3%).

**Table 3.** The effect of copper and copper oxide nanoparticles on barley yield

No.	Experiment variants	Harvest of main products, c ha <sup>-1</sup>		
		mean	change c ha <sup>-1</sup>	%
1	CuO 0.01	35.7	+ 0.4	1.12
2	Cu 0.01 N60P60K60	38.8	+ 3.5	9.02
3	Cu 0.01	44.8	+ 9.5	17.3
4	C	35.3	-	-
Research accuracy indicators		m = 5% HCP <sub>0.95</sub> = 4.8 c ha <sup>-1</sup>		

**Table 4.** Nutritional value and physical properties of barley grain

No.	Experiment variants	Weight 1,000 grains, g	Moisture, %	Nutritional value 1 kg		
				Metabolic energy E, MJ	Feed units	Digestible protein, g
1	CuO 0.01	66.2	14.2	10.79	1.1	60.0
2	Cu 0.01 N60P60K60	71.7	14.2	10.84	1.1	67.1
3	Cu 0.01	66.0	14.5	10.79	1.1	58.1
4	C	65.4	14.1	10.79	1.1	62.0

One of the most important elements of the crop structure is grain size expressed through the mass of 1,000 seeds. Of course, the mass of 1,000 seeds is the second element of spike productivity after the grain content, but at the same time (Sumina, 2010), this parameter relates to the supply of nutrients, germination ability and seed viability. This indicator is a ‘grading factor’, but it may vary depending on growing conditions. The mass value of 1,000 grains is an indirect indicator of the ‘sufficient balance of the genetic complex’, which is responsible for grain size.

The mass index of 1,000 seeds significantly exceeded the average values (46–56 g), which are characteristic for the features of the Kati variety of spring barley (Table 4). Probably, presowing soaking contributed to the increase of this indicator in all variants of the experiment.

It should be noted that the largest mass of 1,000 seeds was in the variant with the use of copper nanoparticles with the joint application of mineral fertilizers and amounted to 71.7 g that was 6.3 g (8.79%) more in comparison with the control variant of the

experiment. The use of only nanoparticles of copper and copper oxide at a dose of 0.01 g per hectare seed rate also contributed to an increase in this indicator: 0.6 (0.91%) and 0.8 (1.21%) g, respectively.

Digestible protein is a crude protein that is absorbed into the bloodstream and lymph from the digestive tract of cattle. Its amount was in the same stages on all variants of the experiment and ranged from 58.1 to 67.1 g per 1 kg of fodder. Its greatest value was on the Cu 0.01 N60P60K60 variant. It is established that nanoparticles have a huge specific surface, and hence excess surface energy. Copper, as a microelement, shows a synergism with respect to the nitrogen macroelement: a sufficient level of Cu in the soil improves the absorption of N. Probably having a size of 40–60 nm, copper nanoparticles do not penetrate the membrane, while promoting the intensification of nitrogen metabolism in the cell, as a result, the use of these particles together with mineral fertilizers leads to an increase in digestible protein in barley grain and an increase in the mass of the seeds.

In all variants of the experiment, the number of feed units was 1.1 kg that corresponds to the average values that are characteristic for this crop (Table 4).

The amount of energy in the fodder is the most important indicator of its value. The value of this indicator in all variants of the experiment, with the exception of Cu0.01 N60P60K60, was at the same level and amounted to 10.79 MJ. A slight increase was observed during using copper nanoparticles with the joint application of mineral fertilizers and it amounted to 10.84 MJ that is 0.05 MJ more in 1 kg.

The moisture content of the grain is one of the most important indicators of its quality, which was determined immediately after consumption. Water has a strong effect on the grain itself and microorganisms on its surface. Microbes develop faster, the number of ticks and insects increases and also other changes occur on wet grain. Humidity is a factor that shows the proportion of grain nutrients and the duration of its storage. The higher the moisture content in the grain mass, the less it contains nutrients and the faster it spoils. Excessive moisture leads to the activation of physiological, physico-chemical processes. The grain begins to swell, germinate, high molecular weight biopolymers are broken down, the enzymes are activated. The nature and the flowability of grain decrease; it becomes vulnerable to mechanical damage. If the grain remains wet for a long time, its storage and processing become impossible. In any case, grain yield and product quality are reduced during using moist raw materials (Grain moisture, 2019).

The moisture content of the presented samples was within the base humidity, which is from 13.5 to 15%. On average, for all variants of the experiment, it amounted to 14.2%.

## CONCLUSIONS

From the obtained data, it can be concluded that the pre-sowing treatment of barley seeds with copper and copper oxide nanoparticles does not have a toxic effect and contributes to an increase in yield. Pre-soaking of spring barley seeds in suspension with copper nanoparticles at a dose of 0.01 g per hectare seed sowing rate contributed to an increase in the adaptive potential of plants. This played a large role in the formation of the crop: the largest increase was obtained in this experiment variant and amounted to 44.8 kg ha<sup>-1</sup> that is 17.3% more in comparison with the control variant.

Such indicators as the mass of 1,000 g of seeds, as well as nutritional value: metabolic energy and digestible protein due to the intensification of nitrogen metabolism were the best in the variant with the use of copper nanoparticles with the joint application of mineral fertilizers.

## REFERENCES

- Chernikova, O., Mazhayskiy, Yu. & Ampleeva, L. 2019. Selenium in nanosized form as an alternative to microfertilizers. *Agronomy Research* **17**(S1), 974–981.
- Chernikova, O., Ampleeva, L. & Mazhayskiy, Yu. 2019. Effect of Selenium Nanoparticles on the Formation of Corn Yield. *Russian Agricultural Sciences* **45**(3), 256–259.
- Churilov, G.I., Polischuk, S.D., Churilov, D.G., Kuznetsov, D., Borychev, S.N. & Byshov, N.V. 2018. Agroecological grounding for the application of metal nanopowders in agriculture. *International Journal of Nanotechnology* **15**(4–5), 258–279.
- Churilov, G.I., Ivanycheva, Y.N., Polischuk, S.D., Nazarova, A.A., Kutsir, M.V. & Churilov, D.G. 2013. Ecological and biological effects of copper and copper oxide nanopowders on phytohormones of vetch and spring wheat. *Nanotechnology* **4**, pp. 43.
- Copper for plants: Available at: <http://www.agrocounsel.ru/med-dlya-rastenij>, 12 January 2019.
- Fedorenko, A.G., Minkina, T.M., Chernikova, N.P., Fedorenko, G.M., Mandzhieva, S.S., Rajput, V.D., Burachevskaya, M.V., Chaplygin, V.A., Bauer, T.V., Sushkova, S.N. & Soldatov, A.V. 2020. The toxic effect of CuO of different dispersion degrees on the structure and ultrastructure of spring barley cells (*Hordeum sativum distichum*). *Environmental Geochemistry and Health*. doi: 10.1007/s10653-020-00530-5
- Grain moisture: Available at: <http://www.agrocounsel.ru/med-dlya-rastenij>, 14 January 2019.
- Hafeez, A., Razza, A., Mahmood, T. & Muhammad Jhazab, H. 2015. Potential of copper nanoparticle to Increase Growth and Yield of Wheat. *Journal of Nanoscience with Advanced Technology* **1**, 6–11.
- Hlisnikovský, L., Čermák, P., Kunzová, E. & Barlóg, P. 2019. The effect of application of potassium, magnesium and sulphur on wheat and barley grain yield and protein content. *Agronomy Research* **17**(5), 1905–1917.
- Maslobrod, S.N., Mirgorod, Yu.A., Borodina, V.G., Borsch, N.A. 2014. Influence of water dispersed systems with silver and copper nanoparticles on seed germination. *Electronic processing of materials* **50**(4), 103–112.
- Mengmeng, Rui, Chuanxin Ma & Yi, Hao. 2016. Iron Oxide Nanoparticles as a Potential Iron Fertilizer for Peanut (*Arachis hypogaea*). *Frontiers in plant science* **7**, pp. 815.
- Olkhovskaya, I.P., Bogoslovskaya, O.A., Yablokov, A.G. & Glushchenko, N.N. 2019. Yield barley yield indicators after presowing treatment of seeds by metal nanoparticles. *Russian nanotechnologies* **14**(1–2), 55–62 (in Russian).
- Polischuk, S.D., Nazarova, A.A., Churilov, G.I., Borychev, S.N. & Byshov, N.V. 2018. Nanopowders of cuprum, cobalt and their oxides used in the intensive technology for growing cucumbers. *International Journal of Nanotechnology* **15**(4–5), 352–369.
- Sumina, A.V. The influence of environmental factors on the mass of 1,000 grains of barley varieties grown in the hollow conditions of Siberia. 2017. *Juvenis scientia* **10**, pp. 4–6.
- Zakharova, O.V., Gusev, A.A., Altabaeva, Yu.V. & Perova, Yu.S. 2018. Biological Effects of Freshly Prepared and 24-h Aqueous Dispersions of Copper and Copper Oxide Nanoparticles on E. coli Bacteria. *Nanotechnol Russia* **13**, pp. 173 (in Russian).
- Zeyruk, V.N., Vasilyeva, C.V., Derevyagina, M.K., O.A. Bogoslovskaya, I.P. Olkhovskaya, I.P., Afanasenkova, E.S. & Glushchenko, N.N. 2019. The effect of presowing treatment of tubers by metal nanoparticles as a part of polymer coating on the incidence of disease and yield of potatoes. *Russian nanotechnologies* **14**(5–6), 65–73 (in Russian).

## **Non-Invasive measurer for methane and carbone dioxide emissions in bovine cattle through TRIZ**

K.L. Silva-Martínez<sup>1</sup>, L. Cruz-Rivero<sup>1,\*</sup>, A. Arrieta-González<sup>1</sup> and  
R. Purroy-Vasquez<sup>2</sup>

<sup>1</sup>TECNM/ ITS-TANTOYUCA, Posgrado e Investigación, Desv. Lindero Tametate  
SN Col. La Morita CP 92100, Tantoyuca, Veracruz, México

<sup>2</sup>TECNM /ITS- Zongolica, Posgrado e Investigación, Km 4 Carretera a la Compañia  
S/N, Tepetlplanapa, CP 95005, Tantoyuca, Veracruz, México

\*Correspondence: lilirivero@gmail.com

**Abstract.** Greenhouse gases (GHG), mainly methane (CH<sub>4</sub>) and carbon dioxide (CO<sub>2</sub>), can be generated in agricultural activities, not only in waste but also in the process of breathing of livestock. The Theory of Inventive Problem Solving (TRIZ) is an innovative Russian methodology that allows finding the solution to a problem raised. This paper presents the use of two TRIZ tools to design a non-invasive prototype that detects CH<sub>4</sub> and CO<sub>2</sub> emitted by cattle in real time. The tools were the matrix of technical contradictions and the nine-screen analysis with which the parameter to be improved (A) was found and the best possible solution to design a prototype that allows quantifying gases for animal welfare, Final Ideal Result (IFR) a wireless module with a sensor system for each of the gases placed on the bovine head, which convert the detected gas into an electrical signal to be sent wirelessly to a range of 1.5 km in free space at a receiver for its visualization representing the parts per million (ppm) of CH<sub>4</sub> and CO<sub>2</sub> that the bovine is generating during the measurement.

**Key words:** cattle, CH<sub>4</sub>, CO<sub>2</sub>, TRIZ.

## **INTRODUCTION**

Methane (CH<sub>4</sub>) is the greenhouse gas (GHG) that has the second greatest effect on climate, after carbon dioxide (CO<sub>2</sub>). The concentration of CH<sub>4</sub> in the atmosphere has almost tripled in the last 150 years. Atmospheric CH<sub>4</sub> has a greenhouse effect at least 20 times more potent than CO<sub>2</sub>. Agriculture, especially animal production, is one of the most important factors influencing greenhouse gases in the atmosphere and causing global warming (Dubeňová et al., 2014).

Livestock is responsible for about 23% of global CH<sub>4</sub> emissions of anthropogenic origin. As there is a need to quantify the amount of GHG emitted by technologies that still consume fossil fuels or GHG generated by aspects such as livestock, several quantifying devices have been designed (Álvarez-Torres et al., 2014).

Latati et al. (2019), has analyzed the phenomenon of Carbon (C) and nitrogen (N) sequestration in plants and soil micro-organisms considered as a major phenomenon against global warming, in his study is highlighted the role that the mixed crop

legumes-cereals have in the reduction of greenhouse gases.

Without proper resolution, system performance is hindered, or suboptimal technologies are chosen. The Theory of Inventive Problem Solving (TRIZ), offers tools and methods to identify and resolve tradeoffs (which it terms contradictions or conflicts). TRIZ recognizes that fundamental performance limits arise when one or more unresolved tradeoffs exist in a system. According to TRIZ, eliminating or reducing the effects of the conflicts is necessary to move to improved system performance. It is here that lies the importance of the use of TRIZ as an element of integration in various environments and in the creation of new products (Blackburn et al., 2012).

Agricultural activities are the third cause of generation of GHG emissions with a contribution of 12% to national emissions, where most of the emissions are generated by enteric fermentation, manure management and by the use of fertilizers in the soils (Santillán et al., 2016).

The main biotic factor at the rumen level in the production of CH<sub>4</sub> are methanogenic anaerobic bacteria. CH<sub>4</sub> is generated by ruminal fermentation of food and surplus hydrogen (H<sub>2</sub>) (Beltrán-Santoyo et al., 2016). Ruminants are contributing to global warming and deterioration of the ozone layer by releasing high amounts of gases into the atmosphere, including carbon dioxide and CH<sub>4</sub> (Carmona et al., 2005).

The recognition of generic types of problems in innovation was the key to developing TRIZ, this theory uses the systemic approach based on knowledge to achieve innovation (Acosta-Flores, 2010). TRIZ was developed to support engineers and natural scientists solving inventive problems by using the knowledge of former inventors (Moehrle, 2005).

The 40 principles of technological innovation and the 39 parameters of contradiction are the most important contribution of TRIZ and these in turn are the basis of the 'Matrix of contradictions'. The 40 principles are generic suggestions for carrying out a specific action, within a technological system, in order to eliminate some technical contradiction (Altshuller, 2006).

The Matrix is made up of 39 parameters of contradiction and 40 principles, these inventive principles were developed when studying more than 200 thousand patents with which it was concluded that only 40 thousand had some inventive solutions, the rest were only direct improvements. Most of the problems analyzed had been solved by applying only forty fundamental principles known as 'principles of inventiveness' (Cordova Ames, 2008).

TRIZ is a balanced approach combining, in the same environment, psychological and technical creativity, is based on essential areas such as: statistical analysis of patents, a synthesis of the main advantages drawn from numerous problem solving techniques and an analysis of the inventor's creative thinking patterns, with the aim of producing a set of strategies for modeling and solving problems (Cortes Robles et al., 2011).

The ability to creatively solve problems has been considered a powerful tool for people and the source of innovation. However, the way of thinking creatively in solving problems, especially in technological fields such as livestock, as proposed by TRIZ, has been difficult to explain, teach and train because the ways of thinking are not well structured (Nakagawa, 2011).

Within the tools of the TRIZ, is the multiscreen analysis where time and space were established as the variables to follow, in the horizontal plane time and in the vertical plane space. For nine-screen analysis space was the system and its assemblies, the super

system and subsystems. On the other hand, time considered it as the present, past and future (Bukhman, 2012).

Another tool proposed in TRIZ is the Field-Substance analysis, in which, to define a technical system, it is necessary to define two substances and one field, and that there are four basic models of technological systems: an incomplete system that requires completed to a new system; a complete but ineffective system that demands improvements to create the desired effect; a complete harmful system which is necessary to eliminate the negative effect and; an effective complete system, it is there that, for the purposes of this study, it is proposed to work with TRIZ tools to design a non-invasive and low cost CH<sub>4</sub> and CO<sub>2</sub> measurer (Acosta-Flores, 2010).

The animal welfare issues faced by the northern Australian beef cattle industry are similar to those faced by extensive livestock production industries in other countries that means that the industry faces significant challenges to assure high standards of animal welfare produced for the frequency of handling, surgical procedures, identification, transportation, including live export and others (Petherick, 2005).

In the northern of Veracruz, Mexico, one of the main activities is cattle ranching, which is why there is an interest in measuring CH<sub>4</sub> and CO<sub>2</sub> emissions. The objective of this research is to design a prototype of measurer of these GHGs in bovine cattle which is non-invasive, aiming the animal welfare.

MATERIALS AND METHODS

With the purposes to design of the prototype, a five years old cow representative female bovine of the European Swiss breed, weighing 480 kg, was taken from ranch from the municipality of Chontla in the north of the state, located between 21° 11' and 21° 40' north latitude; the meridians 97° 52'and 98° 05' west longitude; altitude between 30 and 1,300 m.

For the design of the model, 9 windows or multi-screen analysis (Table 1) and later the matrix of technical contradictions (Table 1) were used for the selection of parameters that determined the factors to be used for the prototype.

Table 1. Multiscreen analysis for the proposed measurement system

	Past	Present		Future
Super-System Level	*Field	**Laboratory	***Field	Field
System Level	Methane meter	Breathing chamber	Electronic measuring module for telemetry	Non-invasive Real-Time Measurement System
Subsystem level	Cannula, valve, collection bags, tubes	Thermal panels, acrylic windows, various materials	Cannula, valve, collection bags, tubes, Electronic module	Set of Components based on the analysis of parameters through TRIZ that allow measure in real time, non-invasive and that seeks animal welfare

\*Berra (2009); \*\*Canul (2017); \*\*\* Berra (2010).



### **Multi-screen Analysis**

Time and space are established as the variables to be followed. Space is the system and its sets, the super system and subsystems. On the other hand, time is considered as the present, past and future (Martínez-Cruz, 2014). This analysis tool of TRIZ is used for the problem exploration and definition which helps in the extension of the scenario of failure for an evolution in the system (Mansoor et al., 2017).

A prototype consisting of a technique for the measurement of enteric CH<sub>4</sub> in cattle using a system containing a fistula surgically placed in the bovine below the transverse process of the first lumbar vertebra, a cannula and collection bags in order to store the gases and then measure them. This prototype requires performing an invasive procedure in the stomach of the cow (Berra et al., 2009).

As a present scenario, a prototype breathing chamber was analyzed for the in vivo measurement of bovine CH<sub>4</sub> production in Mexico, consisting of thermal panels with two acrylic windows, containing an air volume of 9.97 m<sup>3</sup>. In this system the CH<sub>4</sub> mixed in the air samples is quantified with an infrared analyzer (Canul Solis et al., 2017).

Also, as part of the present scenario, we analyzed the prototype electronic module that measures the volume of gas generated in the rumen. Which is a variant of the prototype that uses the fistula in the ruminal cavity, which has a cellular communication system that uses the General Packet Radio Service (GPRS) network to send measured data via the Internet to a server. The server stores this information in a database for further analysis (Berra et al., 2010).

After multi-screen analysis, we proceeded to work with the Matrix of Technical Contradictions to choose the parameters of contradiction that allow the future design of a CH<sub>4</sub> meter in real time.

### **Matrix of Technical (System) Contradictions**

The Technical Contradictions Matrix is one of the tools of TRIZ that allows to use the principles of inventiveness when a technical contradiction in the problem is identified. There are universal principles of invention, which can serve as a basis for creative innovations and technological advances. Once the problem of inventiveness or technological innovation was completely defined and what was wanted to be determined, the Matrix was used, which has as premise that the technical contradictions are those in which an element 'A' of the technological system to be improved, the same system conflicts with another 'B'.

When performing the analysis of parameters related to the prototype design, it was determined that the appropriate combination of parameters based on what the matrix of contradictions provides is:

- Parameter A: Level of automation.
- Parameter B: Stability of an object.

What is desired to improve is the level of automation so that the prototype can be used in the field, taking care of the welfare of the animal and making measurements in real time was identified as (Bukhman, 2012):

- Parameter 38 at the Automation Level: which is the capacity for that an object or technological system perform the function for which it was designed without human intervention. The lowest level of automation will be that of a manually operated object,

the highest level of operation being that in which the object or a system functions independently of the human being, monitoring its own operation.

- Parameter 13. Stability of the composition of an object: is Integrity of the object or system. Composition of an object is the exact combination of elements providing the structure of the object. Stability of the composition of an object is the exact combination of elements during the given period of interest.

Considering these two parameters, the analysis was performed on the matrix which resulted in the use of inventive principles 18 and 1.

Improving Features	Worsening Feature												
	1	2	3	12	13	14	17	18	27	28	29	38	39
1: Weight of moving object	*	-	15 8	10 14 1 35	28 27 6 29	19 1	1 3	28 27 28 35 26 35 35 3					
			29 34 35 40	19 39 18 40 4 38	<u>32</u>	11 27 35 26 26 18 18 19 24 37							
2: Weight of stationary	-	*	-	13 10 26 39 28 2	28 19	19 32	10 28 18 26 10 1	2 26	1 28				
				29 14 1 40	10 27 32 22	<u>35</u>	8 3	<u>28</u>	35 17	<u>35</u>	15 35		
3: Length of moving object	8 15	-	*	1 8	1 8	8 35	10 15	<u>32</u>	10 14 28 32	10 28 17 24 14 4			
	29 34			10 29 15 34	29 34	<u>19</u>		29 40	<u>4</u>	29 37 26 16 28 29			
12: Shape	8 10	15 10 29 34	*	33 1	30 14 22 14 13 15	10 40 28 32 32 30 15 1	17 26						
	29 40 26 3	5 4		18 4	10 40 19 32	<u>32</u>	<u>16</u>	<u>1</u>	<u>40</u>	<u>32</u>	34 10		
13: Stability of the object	21 35 26 39 13 15 22 1	*		17 9	35 1	32 3	-	<u>13</u>	<u>18</u>	1 8	23 35		
	2 39	1 40	1 28	18 4	<u>15</u>	<u>32</u>	27 16			<u>35</u>	40 3		
14: Strength	1 8	40 26 1 15	10 30 13 17	*	30 10 35 19 11 3	3 27	3 27	<u>15</u>	29 35				
	40 15 27 1	8 35	35 40	<u>35</u>	<u>40</u>	<u>16</u>			10 14				
17: Temperature	36 22 22 35 15 19 14 22 1 35	10 30	*	32 30 19 35 32 19	<u>24</u>	26 2	15 28						
	6 38	<u>32</u>	<u>9</u>	19 32	<u>32</u>	22 40	21 16 3 10	<u>24</u>	19 16	<u>35</u>			
18: Illumination intensity	19 1	2 35	19 32 32 30 32 3	35 19 32 35	*	-	11 15 3 32	2 26	2 25				
	<u>32</u>	<u>32</u>	<u>16</u>	<u>27</u>	<u>19</u>	<u>32</u>	<u>10</u>	<u>16</u>					
27: Reliability	3 8	3 10	15 9	35 1	-	11 28 3 35	11 32	*	32 3	11 32	11 13 1 35		
	10 40 8 28	14 4	16 11			<u>10</u>	<u>13</u>		11 23	<u>1</u>	<u>27</u>	29 38	
28: Measurement accuracy	32 35 28 35 28 26 6 28	32 35 28 6	6 19	6 1	5 11	*	-	28 2	10 34				
	26 28 25 26 5 16	<u>32</u>	<u>13</u>	<u>32</u>	28 24	<u>32</u>	1 23	10 34	28 32				
29: Manufacturing precision	28 32 28 35 10 28 32 30 30 18 3 27	19 26 3 32	11 32	-	*	26 28 10 18							
	13 18 27 9	29 37	<u>40</u>			<u>1</u>		18 23	32 39				
38: Extent of automation	28 26 28 26 14 13 15 32 18 1	25 13 26 2	8 32	11 27 28 26 28 26	*	5 12							
	18 35 35 10 17 28 1 13	<u>19</u>	<u>19</u>	<u>32</u>	10 34 18 23	35 26							
39: Productivity	35 26 28 27 18 4	14 10 35 3	29 28 35 21	26 17 1 35	1 10	18 10 5 12	*						
	24 37 15 3	28 38 34 40	22 39	10 18 28 10 19 1	10 38 34 28 32 1	35 26							

**Figure 1.** Matrix of Technical (System) Contradictions.

- Principle 1: Segmentation. Fragmentation. Micro level transition. Divide an object or a system into separate parts. Make an object easy to disassemble. Increase the degree of fragmentation or segmentation.

- Principle 18 Mechanical vibration. Generation of a oscillating or vibratory system. Increase the frequency of vibration. Use the resonant frequency of an object. Use electrical parts instead of mechanical vibrators. Use ultrasonic and electromagnetic fields.

## RESULTS AND DISCUSSION

Considering the principles set by TRIZ and laws and stages of systems evolution, it is intended to eliminate those elements that are harmful to livestock but continue to perform their function. To this end, it was proposed to use sensors to measure GHG emissions. By obtaining these principles of inventiveness, we have the guideline to design the non-invasive and automated prototype that measures in real time the emissions of CH<sub>4</sub> and CO<sub>2</sub> from cattle. As Final Ideal Result IFR an adjustable harness was developed (Fig. 2) which included MQ4 micro sensors for CH<sub>4</sub> and MQ7 for CO<sub>2</sub>, an Arduino micro controller programmed in C++ and an Xbee module which recorded the measurements in portable computer equipment, which allowed to obtain the measurement without the need to manipulate the animal avoiding to perform surgical procedures in this one being able to carry out the measurement in field.

According with the principle of segmentation proposed in TRIZ's contradiction matrix, the prototype design was segmented into two parts, one transmitter and one receiver wirelessly connected with radio frequency communication using a range between 865 MHz and 2.4 GHz, (Fig. 3). These modules used the network protocol called IEEE 802.15.4 to create FAST POINT-TOMULTIPOINT (point-to-multipoint) networks, or PEER-TO-PEER (peer-to-peer) networks, designed for applications requiring high data traffic, low latency and predictable communication synchronization. The prototype was placed on the specimen (Fig. 4), and the CH<sub>4</sub> and CO<sub>2</sub> emissions in ppm were recorded for 30 minutes. The data obtained were sent with the transmitter wirelessly to the receiver for display in digital form; the measurements were 25 minutes per experimental unit for 3 consecutive weeks, with a sampling frequency of 1 second; CH<sub>4</sub> gas values ranged from 301.99 ppm to 197.37 ppm, while CO<sub>2</sub> ranged from 1,701.83 ppm to 1,169.47 ppm.

In Argentina it has been tried a technique for collecting the gas produced in the rumen by a 2 cm in diameter fistula, through which the gas flows to a container nylon balloon type fixed to the back, in this case a Holstein cow of 550 kg. Once the gas has been collected for periods of 24 h, its CH<sub>4</sub> concentration is determined at intervals of 6 h. The daily gas production was on average 911.7 L and the concentration of CH<sub>4</sub> varied from 20 to 32% and represented on average 247 L d<sup>-1</sup> (Bonilla-Cárdenas & Lemus-Flores, 2012).



**Figure 2.** Data Emitter.



**Figure 3.** Data Receiver.

The prototype developed by the National Institute of Agricultural Technology (INTA) only performs the measurement of CH<sub>4</sub> gas, this being a robust, heavy and invasive prototype, this to contain a probe that is entered inside the rumen of the cow.

The prototype of the INTA sends the data through a GPRS chip to a database, where the relationship of food type with CH<sub>4</sub> gas volume in L was analyzed.

For GPRS operation only the chip was registered in a telephone company and activated the data packet, this system only works with cellular signal being a problem if applied to a rural area. In contrast, the prototype of this study sends the census data of CH<sub>4</sub> and CO<sub>2</sub> gas by means of Radio Frequency (RF) system, which works in places where there is no cellular signal, another characteristic of this device is that the gas readings CH<sub>4</sub> and CO<sub>2</sub> are received in parts per million (ppm).



**Figure 4.** Prototype testing.

INTA developed another device called a backpack cow, where it placed a probe inside the rumen of the cow and connected it to a backpack of cylindrical form located on the upper parts of the back of the ruminant, in this way the gas was encapsulated inside the rucksack of the cow obtaining between 400 and 450 L of CH<sub>4</sub> gas within 24 hours (Berra, 2010).

While the quantifying prototype performed in this study detects two gases CH<sub>4</sub> and CO<sub>2</sub> being a non-invasive prototype as it performs the measurement of gases through two sensors MQ7 and MQ4 through the exhalation of the bovine however this prototype is segmented in two parts to reduce the size and weight and thus not cause discomfort to the animal.

In the prototype of the gas chamber, were obtained measurements of 173.2 L per d of CH<sub>4</sub>, while an emission factor was 17.48 L of CH<sub>4</sub> per kg of dry matter consumed (Canul et al., 2017).

## CONCLUSIONS

With the support of TRIZ, it was possible to find the best approximation of a measurer prototype of CH<sub>4</sub> and CO<sub>2</sub> emissions from cattle, thanks to the adequate selection of parameters and design methodologies. The IFR is a light, non-invasive prototype that does not cause harm to the animal.

For some authors specializing in the management of livestock species, the timely and responsible management of animals when making evaluations or measurements is vital. There are invasive or harmful methods that increase stress in livestock and this can be harmful at the time of consumption of the derivatives thereof.

Using TRIZ helps to expand the panorama in terms of innovation, since it allows to find the solution in a precise way to the problem raised, finding the IFR.

TRIZ is a tool that is not well exploited in Mexico, and even more so in the livestock sector. This is why, with this work, we intend to present an alternative for the design of material and equipment for livestock activities to facilitate the achievement of results.

ACKNOWLEDGEMENTS. Tecnológico Nacional de México (TECNM), Instituto Tecnológico Superior de Tantoyuca (ITSTa) and Francisco Osorio Cruz.

## REFERENCES

- Acosta-Flores, J.J. 2010. The field-sustance analisys (El análisis campo-sustancia). *Ingeniería, Investigación yY Tecnol* **11**(2), 247–252 (in Spanish).
- Altshuller, G. 2006. And suddenly the inventor Appeared, *TRIZ, the Theory of inventive problem solving*. (2nd ed.), Worcester. MA: published by Technical Innovation Center, Inc
- Álvarez-Torres, E., Álvarez-Iglesias, J. & Fleitas-Jiménez, S. 2014. Super-contaminal to estimate the GHG emitted or not emitted for diferents vías (Súper-contaminal para calcular la cantidad de gases efecto invernadero (GEI) emitidos o dejados de emitir por diferentes vías). *Ingeniería agrícola* **4**(4), 50–55 (in Spanish).
- Beltrán-Santoyo, M.A., Álvarez-Fuentes, G., Pinos-Rodríguez, J.M. & Contreras-Servín, C. 2016. Emission of methane in bovine milk production systems in the San Luis Potosí Valley, Mexico (Emisión de metano en los sistemas de producción de leche bovina en el valle de Ssan Lluís pPotosí, Mméxico). *Agrociencia* **50**, 297–305 (in Spanish).
- Berra, G., Bualó, R.A., Finster, L., Zeitune, G. & Valtorta, S.E. 2010. Use of Telemetry to Measure Gas Production in the Rumen (Uso de la Telemetría para Medir la Producción de Gas en el Rumen). *FAVE Sección Ciencias Veterinarias* **9**(1), 49–55 (in Spanish).
- Berra, G., Finster, L. & Valtorta, S.E. 2009. A simple technique for measuring enteric methane emissions in cows (Una técnica sencilla para la medición de emisiones de metano entérico en vacas). *FAVE Sección Ciencias Veterinarias* **8**(1), 49–56 (in Spanish).
- Blackburn, T.D., Mazzuchi, T.A. & Sarkani, S. 2012. Using a TRIZ framework for systems engineering trade studies. *Systems Engineering* **15**(3), 355–367.
- Bonilla-Cárdenas, J.A. & Lemus-Flores, C. 2012. Emission of enteric methane by ruminants and their contribution to global warming and climate change (Emisión de metano entérico por rumiantes y su contribución al calentamiento global y al cambio climático). *Revista Mexicana de Ciencias Pecuarias*, 215–246 (in Spanish).
- Bukhman, I. 2012. TRIZ Technology for Innovation. Cubic Creativity Company
- Canul Solis, J.R., Piñeiro Vázquez, A.T., Arceo Castillo, J.I., Alayón Gamboa, J.A., Ayala Burgos, A.J., Aguilar Pérez, C.F. & Ku Vera, J.C. 2017. Design and construction of low-cost respiration chambers for ruminal methane measurements in ruminants. *Revista Mexicana De Ciencias Pecuarias* **8**(2), 185–191. <https://doi.org/10.22319/rmcp.v8i2.4442>
- Carmona, J., Bolívar, D. & Giraldo, L. 2005. Methane gas in livestock production and some alternatives to measure its emissions and reduces its impact at an environmental and productive level (El gas metano en la producción ganadera y alternativas para medir sus emisiones y aminorar su impacto a nivel ambiental y productivo). *Revista Colombiana de Ciencias Pecuarias. Colombian Journal of Animal Science and Veterinary Medicine* **18**(1), 49–63 (in Spanish).
- Córdova Ames, W. 2008. TRIZ, the systematic thinking and innovation tool (TRIZ, la herramienta del pensamiento e innovación sistemática). *Contabilidad Y Negocios* **3**(6), 11 (in Spanish).

- Cortes Robles, G., Machorro Rodriguez, Á., Negny, S. & LeLann, J.M. 2011. The TRIZ-CBR synergy: a knowledge based innovation process. *Int. J. Manufacturing Technology and Management* **22**(3), 233–246.
- Dubeňová, M., Šima, T., Gálik, R., Mihina, Š., Vagač, G. & Boďo, S. 2014. Reduction of nitrous oxide and carbon dioxide in the pig barn piggery by different ventilation system intensities. *Agronomy Research* **12**(1), 207–214.
- Latati, M., Rebouh, N.Y., Aouiche, A. & Laouar M. 2019. Modeling the functional role of the microorganisms in the daily exchanges of carbon and nitrogen in intercropping system under Mediterranean conditions. *Agronomy Research* **17**(2), 559–573. <https://doi.org/10.15159/ar.19.050>
- Mansoor, M., Mariun, N., Toudeshki, A., Abdul Wahab, N.I., Mian, A. U. & Hojabri, M. 2017. Innovating problem solving in power quality devices: A survey based on Dynamic Voltage Restorer case (DVR). *Renewable and Sustainable Energy Reviews* **70**, 1207–1216. <https://doi.org/10.1016/j.rser.2016.12.022>
- Martínez-Cruz, J.R. 2014. The windos of TRIZ, applications (Las ventanas de TRIZ, aplicaciones). *Ciencia UANL* **17**(66), 70–72 (in Spanish).
- Moehrle, M.G. 2005. What is TRIZ? From conceptual basics to a framework for research. *Creativity and innovation management* **14**(1), 3–13.
- Nakagawa, T. 2011. Education and training of creative problem solving thinking with TRIZ/USIT. *Procedia Engineering* **9**, 582–595. <https://doi.org/10.1016/j.proeng.2011.03.144>
- Petherick, J.C. 2005. Animal welfare issues associated with extensive livestock production: The northern Australian beef cattle industry. *Applied Animal Behaviour Science* **92**(3), 211–234.
- Santillán, V.S., Barra, J.D.E., Paz, F. & Cárdenas, L.O.A. 2016. Greenhouse Gas Emissions in Agricultural Systems in Mexico. *Terra Latinoamericana* **34**(1), 83–96.

## Investigation in fuel consumption of a hybrid and conventional vehicle

R. Šmigins\*, V. Pīrs and D. Berjoza

Latvia University of Life Sciences and Technologies, Faculty of Engineering, Motor Vehicle Institute, J. Čakstes blvd 5, LV3001 Jelgava, Latvia

\*Correspondence: [ruslans.smigins@llu.lv](mailto:ruslans.smigins@llu.lv)

**Abstract.** During the last decade the introduction of more environmentally friendly technologies were raised more rapidly by the decline in the global fossil energy resources and the increased negative environmental impact of conventional vehicles. One of such technology is the hybrid, which is currently making the transition from conventional vehicle with internal combustion engine to an electric vehicle. At this time there exist a lot of offers of such vehicles from different manufacturers, but there do not exist many researches connected with real hybrid performance in different road cycles and conditions allowing evaluate its real economical performance.

This research was realized with the aim to evaluate performance and fuel consumption of hybrid electric vehicle and its conventional internal combustion engine analogue in laboratory conditions. Tests were realized with two new Toyota Yaris vehicles in Alternative Fuels and Research Laboratory on chassis dynamometer MD-1750 using AVL KMA Mobile system. The results showed better adaptation of Toyota Yaris Hybrid to urban operation, demonstrating 21.3% lower fuel consumption than Toyota Yaris conventional gasoline vehicle, accordingly 7.29 and 8.84 L (100 km)<sup>-1</sup>.

**Key words:** hybrid, testing, driving cycle, operating time.

### INTRODUCTION

During the last decade ecological aspect of conventional vehicles (CV) with internal combustion engines become more actual based on ecological changes worldwide. Carbon dioxide (CO<sub>2</sub>) emissions, which are considered as the main reason for the development of these processes, in transportation accounts 24% of direct CO<sub>2</sub> emissions from fuel combustion (Tracking transport, 2019). In that case many different solutions have been analyzed during the last decade for the improvement of exhaust emissions from existing vehicles, including use of different alternative fuels (advanced biofuels, biomethane, etc.) and mixes with conventional fuels, as also putting attention on electrification. Despite to this, global transport emissions still increasing, for example by 0.6% in 2018, highlighting the main reasons for such an increase – car buyer demand for larger and heavier vehicles, as also raising road freight demand with the raise of global gross domestic product (Tracking transport, 2019). This was also a stimulus for EU, moving towards low and zero-emissions vehicles, in 2019 adopt CO<sub>2</sub> emission standards for heavy-duty vehicles setting targets for reduction the average emissions from new lorries for 2025 and 2030 (Regulation 2019/1242, 2019).

Electrification or use of battery electric vehicle (BEV) has been considered as a solution by car manufacturers in emission reduction, which could be observed in increase of the range of electric vehicles from almost all largest brands. Basically it is done by the fact that BEV does not produce harmful emissions from the point of driving (Krumbholz & Koteck, 2019). At the moment most aggressive adaptation of battery-electric transportation could be observed in places, where air pollution and traffic congestion problems are critical, for example, in China, where market share of BEV reached 3.39% in 2018 (Statista, 2020) confirming China as the biggest market for electric vehicles in the world. Despite to positive examples, globally switching to this type of vehicles is not as rapid as it would be desirable due to many unresolved problems concerning vehicle price, distance traveled, lack of infrastructure, etc.

Therefore, hybridisation of the vehicles could be transitional pathway allowing to reduce emissions and fuel consumption better than other technologies and/or fuels at the moment. The most important advantage of hybrid electric vehicle (HEV) is existence of more than two energy sources (Taymaz & Benli, 2014) and at least one of them can deliver electrical energy. Based on that different hybrid constructions are applied in automotive industry, which could be divided based on the complexity of the powertrain and the connection between the internal combustion engine and the vehicle wheels: mild, full and plug-in hybrid electric vehicle (Piechottka et al., 2018). If the mild hybrid electric technology incorporates small changes in conventional vehicle, and usually it do not have high power energy storage, then full hybrid technology incorporates higher electric motor capacity and battery package, as also more complex control system (Benajes et al., 2019). Depending on the connection between the internal combustion engine and the wheels full hybrid could be divided in such architectures: series, parallel and series-parallel (Liu et al., 2019). One of the most common type is parallel hybrid technology, where the electric motor is used, when it is more efficient, for example, for vehicle starting, but internal combustion engine is used in conditions, when it is more efficient, for example, at higher speed. Additionally battery is generated during operation of internal combustion engine. Therefore it is possible to reach higher overall efficiency, improve total emissions, and reduce fuel consumption, as also reduce total costs of the vehicle compared to other hybrid technologies. Besides of that electricity there is not a primary alternative fuel – there could be used also natural gas or bioethanol for internal combustion engine operation in such way making it more environmentally friendly.

Regarding the use of HEV a number of research works have been done in last few years more attention putting on emissions and fuel consumption in road tests in real driving conditions or cycles, which are more valid in exact country's traffic conditions, as also there are some researches on simulation of hybrids in different testing conditions.

Huang (Huang et al., 2019) has tested two pairs of hybrid and conventional gasoline vehicles (Lexus NX and Toyota Alphard) with the same dimensions, weight, suspension system and exhaust after-treatment technology in real-driving conditions. He has found that HEVs could save 23%–49% fuel than conventional internal combustion engine vehicles, reporting main advantage of HEVs under urban driving conditions with low speeds and stop-and-go traffic. According to emissions he concluded that hybridisation of the vehicle powertrain may not bring the expected benefits to urban air quality as testing of HEVs demonstrated no reduction in hydrocarbon (HC) emissions and higher carbon monoxide (CO) emissions compared to conventional internal combustion engine vehicles.



Researchers from Thailand (Pitanuwat & Sripakagorn, 2015) confirmed previously mentioned benefit of HEVs in relation to conventional vehicles. Road tests with four experienced drivers concerning driving styles and additional vehicles (HEV and CV) showed that HEVs are capable of reduction of fuel consumption by 46% in suburban and – 26% in highway traffic, but increase of fuel consumption even 2 times compared to CV, if aggressive driving style is practised. This was also confirmed in other review (Thomas et al., 2017) concerning HEV, where aggressiveness associated with higher levels of acceleration and braking, and higher speeds as well.

Research (Orecchini et al., 2018) on comparison of two different versions of Toyota Yaris vehicles – hybrid and 1.5 gasoline – showed that rapid reduction in fuel consumption for hybrid is realized for low and medium speeds, while such advantage is reduced with increase of speed reaching almost the same fuel consumption for both vehicles at 90 km h<sup>-1</sup>. Experimental campaign was realized on road in urban, mixed, extra-urban and highway test path with participation of 30 drivers.

Not all results are ambiguous, but it seems that hybridisation has a potential in reduction of CO<sub>2</sub> emissions and fuel consumption, but confidence should be gained in case of cycles corresponding to Latvian road and traffic conditions. Therefore, the objective of this study was to evaluate the potential of commercially produced hybrid version of a light duty vehicle with an analogue gasoline version of the same model in order to find the benefits of a hybrid.

## MATERIALS AND METHODS

For the comparable tests were selected two Toyota Yaris vehicles representing hybrid and gasoline versions of the same model. The main difference between models could be observed in capacity of fuel tank and total mass, which usually is characteristic for HEVs as they are equipped with batteries. Main characteristics of both vehicles are shown in Table 1.

**Table 1.** Specifications of the test vehicles

Parameter	Yaris Gasoline	Yaris Hybrid
Engine	1.5P Dual VVT-iE	1.5 HSD
Capacity, cm <sup>3</sup>	1,496	1497
Max power, kW at rpm	82 at 6,000	54 at 4,800
Max torque, Nm at rpm	136 at 4,400	111 at 3,600
Motor Generator power, kW	-	45
Motor Generator torque Nm	-	169
Transmission	Automatic, CVT	Automatic, CVT
Mass		
Empty, kg	1,040–1,145	1,075–1,165
Total, kg	1,545	1,565
Fuel tank, L	42	36
Fuel consumption (WLTP), L (100 km) <sup>-1</sup>		
Combined cycle	4.8	3.6
Urban cycle	6.0	3.3
Extra urban cycle	4.1	3.6
Max. speed, km h <sup>-1</sup>	175	165
Acceleration, 0–100 km h <sup>-1</sup> , s	11.2	11.8

HEV engine uses a high-expansion ratio Atkinson cycle, variable valve timing-intelligent system, electric throttle control system, intelligent and exhaust gas recirculation system employing a highly efficient EGR cooler.

Tests were realized in Alternative Fuels and Research Laboratory on chassis dynamometer MD-1750. The key parameters of dynamometer allows measure power in range till 1,700 HP and maximum speed of vehicle can reach 300 km h<sup>-1</sup>; the brake mechanism is powered by electromagnetic eddy currents. Dynamometer allows to simulate road and air resistance, as well as experiments in different driving cycles.

Fuel consumption measurements were realized with AVL KMA Mobile system, which is a high precision measurement system for vehicle fuel consumption measurements on the road and on chassis dynamometers.

Before tests each car was placed on a chassis dynamometer MD-1750 and fastened with straps and anchors. Each car used in tests has a single fuel line fuelling system. The fuel pump is located in the fuel tank, so it is not necessary to use the fuel meter pump module and the meter switched in line, in the fuel supply line. Before connecting to the AVL KMA Mobile fuel meter, the equipment was rinsed from the previous fuel using 0.8–1.0 l of the fuel used for experiments (E95). Both vehicles were warmed up before the tests, therefore cold tests were not realized. Testing was carried out based on method showed in Fig. 1. Firstly, experiments were performed at a steady speed, then – at cycles: IM-240 and Jelgava cycle. The IM-240 belongs to the combined cycle type (Giakoumis, 2016), where the first part of the cycle simulates urban driving conditions, but the second part – relatively simulates driving in non-urban area. This 240 second test cycle represent a 3.1 km route with an average speed of 47.3 km h<sup>-1</sup> and a maximum speed of 91.2 km h<sup>-1</sup>. The IM240 cycle is used for emission testing of in-use light duty vehicles in inspection and maintenance programs.

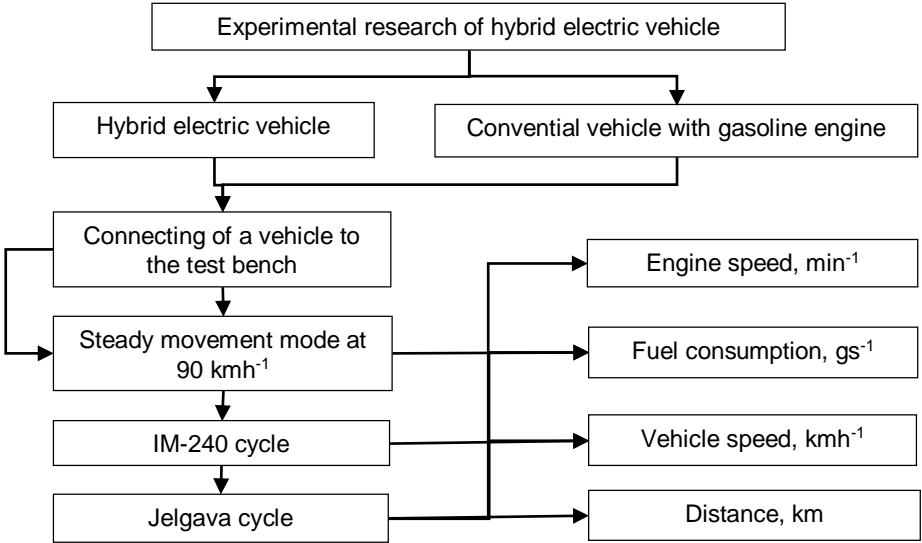


**Figure 1.** Sequential scheme of the experiment.

The Jelgava cycle is a driving schedule that represents the real driving conditions in the city Jelgava. This 360 second test representing 2.3 km route with an average speed – 23.3 km h<sup>-1</sup> and maximum speed – 50.0 km h<sup>-1</sup>. This cycle is developed at the Alternative Fuels and Research Laboratory and describes the car's movement in urban conditions, where are a lot of crossings, traffic lights, pedestrian crossings and other road and traffic elements. Cycle development methodology is already developed and approved at the Faculty of Engineering of Latvia University of Life Sciences and Technologies in previous studies investigating the use of biofuels (Dukulis & Pirs, 2009).

After realization of both cycle trips, repeats were started again with a steady speed mode. At least 5 repeats were performed for each vehicle. If some significant deviations from the movement speed during the cycle were observed, the experiment was scrapped and repeated. The first series of experiments were conducted with a Toyota HEV and the second one with a conventional gasoline powered car. The basic connection scheme of experimental vehicles to the equipment is shown in Fig. 2.

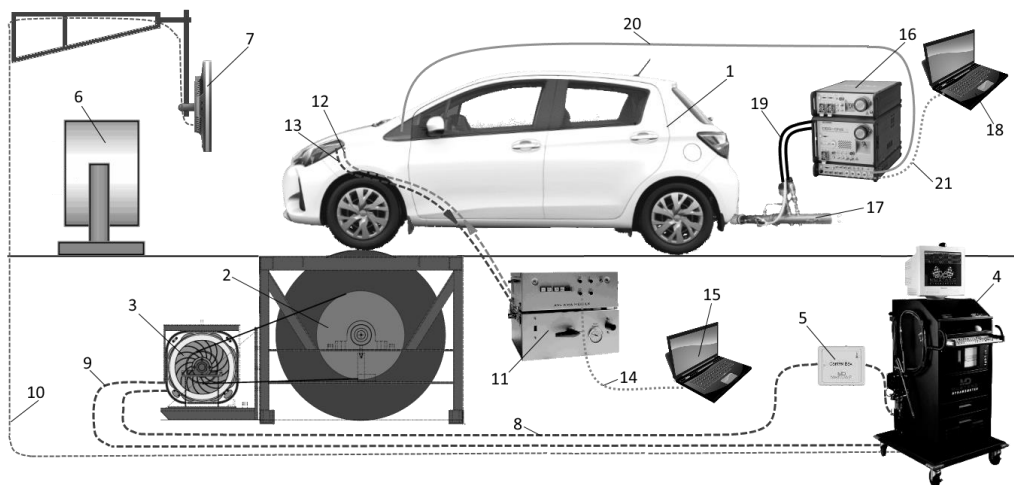


**Figure 2.** Connection scheme of equipment sensors to experimental vehicles.

1 – experimental car; 2 – chassis dynamometer Mustang MD-1750; 3 – power absorber unit (PAU); 4 – Mustang chassis dyno control module & PC with special software; 5 – dynamometer control box; 6 – air blower; 7 – test cycle simulation screen; 8 – dyno control circuit; 9 – Mustang dyno data communication cable; 10 – screen communication cable; 11 – fuel measuring device AVL KMA Mobile; 12, 13 – fuel lines; 14 – fuel measuring device data communication cable; 15 – fuel measuring system PC with special software & data recording; 16 – HORIBA portable emissions measurement system (PEMS); 17 – exhaust flow meter unit; 18 – PEMS PC with special software & data recording; 19 – heated gas sample lines; 20 – OBD data communication cable; 21 – PEMS data communication cable.

Necessary information was taken from the OBD socket of the vehicle (for the exhaust emission measurement system), chassis dynamometer and the fuel consumption meter. The results were stored on three computers, and all data was processed and synchronized after the experiment.

The experiments have also been carried out in a complex research getting many additional data, as also variation of exhaust components. This article summarises and

analyses information only on fuel consumption in different modes and the operating time of the internal combustion engine of HEV.

### RESULTS AND DISCUSSION

Fig. 3 summarizes fuel consumption results of HEV and CV with gasoline engine. Results could be interpreted as highly precise, as variation coefficient for HEV was obtained between 1.52% and 3.10%, while in case of CV this value varied between 0.64% and 0.81%. HEV has a slightly higher coefficient of variation due to the specific action of the hybrid drive in the run-in and braking processes, which may vary between repeats of one group of experiments.

The lowest fuel consumption,  $5.34 \text{ L (100 km)}^{-1}$  for HEV was obtained in IM-240 cycle, while the highest,  $7.29 \text{ L (100 km)}^{-1}$ , was obtained during Jelgava cycle. Driving at a steady speed, HEV at  $90 \text{ km h}^{-1}$  consumed  $5.39 \text{ L (100 km)}^{-1}$ . The highest fuel consumption in Jelgava's driving cycle is explained by its rapid acceleration and frequent breaking. IM-240 cycle is a combined driving cycle with a relatively small running speeds, allowing to achieve best economic indicators.

For a CV with an Otto engine, the lowest fuel consumption of  $5.33 \text{ L (100 km)}^{-1}$  was achieved at a steady speed of  $90 \text{ km h}^{-1}$ , when the electric drive of HEV is not used. During the driving cycles there could be observed benefits of hybrid technologies, when HEV in IM-240 cycle achieves 14.7% lower fuel consumption than CV. An even more important effect has been achieved during Jelgava cycle, when HEV consumed 17.5% less fuel than CV.

Comparing the experimental data with those given in technical characteristics from the manufacturer, such low fuel consumption rates was not achieved in any mode, and the average fuel consumption in combined driving cycle for HEV is about 32.6% higher. In case of CV this number is 21.8% higher.

A separate study has been carried out to find out running time of internal combustion engine from the total cycle time. Fig. 4 summarises the average speed of the HEV Toyota Yaris during IM-240 cycle and the average engine rotation frequency during this cycle.

For a CV, the engine speed during driving is proportional to the speed of movement depending on the gear engaged. As shown in Fig. 4, during the analysis of the first 50 seconds of the cycle in the area of low speed in the run-in mode the internal combustion engine has reached 1,860 rpm and then switched off. Further movement of the vehicle was carried out by an electric motor until the moment, when acceleration begins in the 42th second. At this stage of acceleration the internal combustion engine is switching on

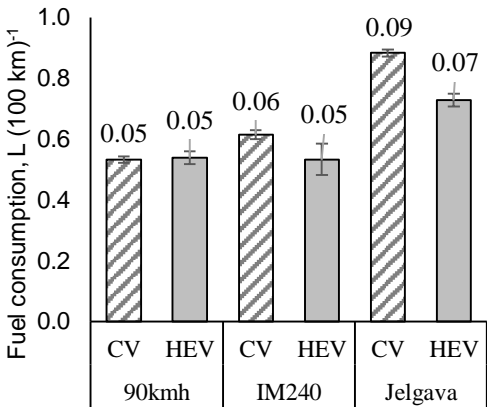


**Figure 3.** Fuel consumption of Toyota Yaris HEV and CV in different cycles.

again, but reaching a steady speed, it switching off again. A detailed analysis of these regularities during IM-240 and Jelgava cycle is shown in Table 2.

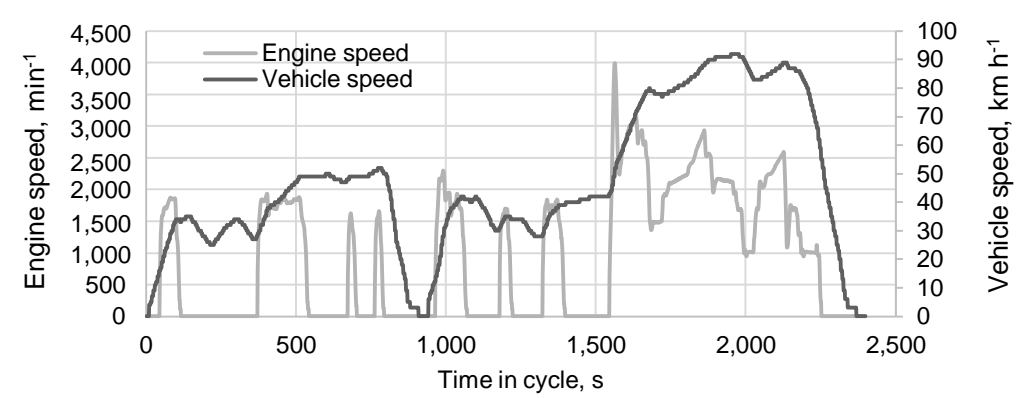


**Figure 4.** Toyota Yaris HEV speed and engine rotation frequency in cycle IM240.

**Table 2.** Movement time (s) of HEV in test cycles

Total time	Time in movement	Time with operating engine	Time in movement, % from total	Time with operating engine, % from total	Time with operating engine, % from time in movement
IM-240 cycle					
240	233.36	135.31	97.23	56.38	57.98
Jelgava cycle					
360	290.18	140.26	80.60	38.96	48.33

The total cycle time of IM-240 is 240 seconds, while for Jelgava cycle this is 360 seconds. From the total cycle time in IM-240 about 233.36 seconds have been spent in motion, while in Jelgava cycle it was about 290.18 seconds.

A comparative analysis has been performed for Toyota Yaris, with a hybrid drive and automatic transmission, experimenting in Jelgava and IM-240 driving cycles. Engine operating time in IM-240 cycle is shown in Fig. 5.

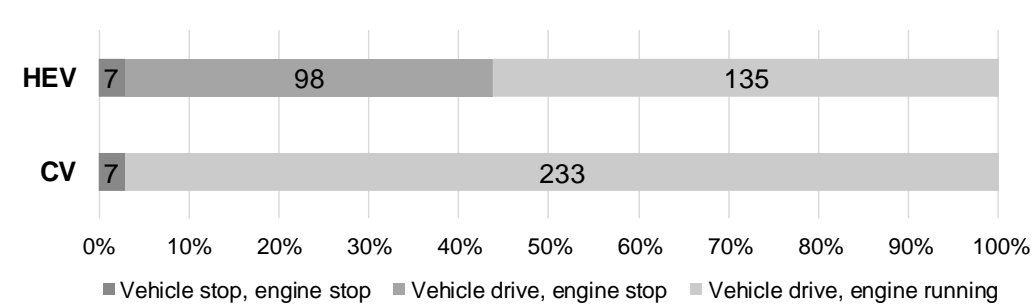


**Figure 5.** Internal combustion engine operating time for test vehicles in cycle IM240.

During IM-240 cycle, CVs as also HEVs internal combustion engine has been operated all time, except 7% of the time in the initial and final part of the cycle. HEV has not been operated for 98 seconds in this cycle and its movement was provided by an electric motor at this time. Remaining operation of 135 seconds of internal combustion engine was also observed. Engine operating time in Jelgava cycle is shown in Fig. 6.

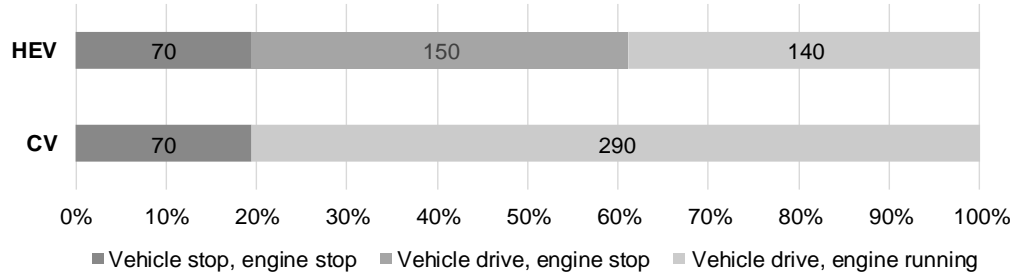


**Figure 6.** Internal combustion engine operating time for test vehicles in Jelgava cycle.

During development of Jelgava cycle, movement took place in the area of intensive traffic with several traffic lights therefore standing of the car is 70 seconds from the cycle total time for both the HEV and CV. The HEV has not operated for 150 seconds from the total time, which can provide a significant fuel economy. In comparison to IM-240 cycle, Jelgava cycle has provided a higher (percentage) non-operating time for the internal combustion engine.

The following steps of the study are intended to set the inductive loop of the power meter on the battery lines for the HEV, which will ensure instantaneous measurement recording for charging or discharging of the battery. This will allow to record the electricity generated during the braking – recovery process.

### CONCLUSIONS

1. HEV consumes 1.1% more fuel than a similar design car with a conventional Otto engine without a hybrid at a steady speed of 90 km·h<sup>-1</sup>.
2. Fuel consumption for the Toyota Yaris Hybrid is 5.34 L (100 km)<sup>-1</sup>, which is 15% less than for the conventional CVT vehicle, which shows 6.14 L (100 km)<sup>-1</sup>, in IM-240 combined cycle.
3. The fuel consumption in Jelgava cycle is higher due to the typical urban traffic. During these tests, Toyota Yaris Hybrid demonstrated 21.3% lower fuel consumption than Toyota Yaris CVT, accordingly 7.29 and 8.84 L (100 km)<sup>-1</sup>.
4. A higher percentage reduction in fuel consumption in Jelgava cycle shows better adaptation of HEV to urban operation. During steady motion in extra urban traffic, HEV does not demonstrate its economical benefits over conventional CVT transmission vehicle.
5. Depending on the mode of movement simulated in two different cycles, Toyota Yaris Hybrid's internal combustion engine may not operate up to 52% of the total travel time, sparing the environment and saving energy resources. In driving conditions with a

smaller proportion of urban traffic, internal combustion engine of HEV has been running for longer time than in urban traffic.

6. During analysis of the HEVs engine speed and movement speed curves, it is possible to determine operating time of the internal combustion engine, however, it is appropriate to use in the next tests the current and direction meter for the battery of HEV to find out the amount of energy produced during the regeneration phase.

## REFERENCES

- Benajes, J., Garcia, A., Monsalve-Serrano, J. & Martinez-Boggio, S. 2019. Optimization of the parallel and mild hybrid vehicle platforms operating under conventional and advanced combustion modes. *Energy Conversion and Management* **190**, 73–90. doi: 10.1016/j.enconman.2019.04.010
- Dukulis, I. & Pirs, V. 2009. Development of driving cycles for dynamometer control software corresponding to peculiarities of Latvia. In: *15th international scientific conference Research for rural development*. Latvia University of Agriculture, Jelgava, pp. 95–102.
- Giakoumis, E.G. 2016. *Driving and Engine Cycles*. Springer, 408 pp.
- Huang, Y., Surawski, N.C., Organ, B., Zhou, J.L., Tang, O.H.H. & Chan, E.F.C. 2019. Fuel consumption and emissions performance under real driving: Comparison between hybrid and conventional vehicles. *Science of The Total Environment* **659**, 275–282. doi: 10.1016/j.scitotenv.2018.12.349
- Krumbholc, M. & Kotek, M. 2019. Analysis of operation parameters of electric and gasoline vehicle in real driving. *Agronomy Research* **17**(S1), 1089–1096. doi: 10.15159/ar.19.035
- Liu, Z., Ivanco, A. & Onori, S. 2019. Aging characterization and modeling of nickel-manganesecobalt lithium-ion batteries for 48V mild hybrid electric vehicle applications. *Energy Storage* **21**, 519–527. <https://doi.org/10.1016/j.est.2018.11.016>
- Orecchini, F., Santiangeli, A., Zuccari, F., Ortenzi, F., Genovese, A., Spazzafumo, G. & Nardone, L. 2018. Energy consumption of a last generation full hybrid vehicle compared with a conventional vehicle in real drive conditions. *Energy Procedia* **148**, 289–296. doi: 10.1016/j.egypro.2018.08.080
- Piechottka, H., Küçükay, F., Kercher, F. & Bargende, M. 2018. Optimal powertrain design through a virtual development process. *World Electric Vehicles* **9**, 11. doi: 10.3390/wevj9010011
- Pitanuwat, S. & Sripakagorn, A. 2015. An Investigation of Fuel Economy Potential of Hybrid Vehicles under Real-World Driving Conditions in Bangkok. *Energy Procedia* **79**, 1046–1053. doi: 10.1016/j.egypro.2015.11.607
- Regulation (EU) 2019/1242 of the European Parliament and of the Council of 20 June 2019. 2019. *Official Journal of the European Union* L198/202, 1–39.
- Statista, Inc. 2020. <https://www.statista.com/statistics/1050120/china-battery-electric-car-market-share/>. Accessed 22.1.2020.
- Taymaz, I. & Benli, M. 2014. Emissions and fuel economy for a hybrid vehicle. *Fuel* **115**, 812–817. doi: 10.1016/j.fuel.2013.04.045
- Thomas, J., Huff, S., West, B. & Chambon, P. 2017. Fuel consumption sensitivity of conventional and hybrid electric light-duty gasoline vehicles to driving style. *SAE Int. J. Fuels Lubr.* **10**(3). doi:10.4271/2017-01-9379
- Tracking Transport 2019. IEA, Paris <https://www.iea.org/reports/tracking-transport-2019>. Accessed 22.1.2020.

## Morpho-physiological effects of Stymjod foliar application on *Dactylis glomerata* L.

J. Sosnowski<sup>1,\*</sup>, K. Jankowski<sup>1</sup>, M. Truba<sup>1</sup>, J. Novák<sup>2</sup>, E. Zdun<sup>1</sup> and  
J. Skrzyczyńska<sup>1</sup>

<sup>1</sup>Siedlce University of Natural Sciences and Humanities, Prusa street 14, PL-08110 Siedlce, Poland

<sup>2</sup>Slovakia University of Agriculture in Nitra, Tr. A. Hlinku street 2, SK94976 Nitra, Slovakia

\*Correspondence: jacek.sosnowski@uph.edu.pl

**Abstract.** The aim of the experiment was to study the effects of foliar application of a growth regulator containing iodine nanoparticles, with the trade name of Stymjod, on morphometrics, photosynthetic activity and chlorophyll content of *Dactylis glomerata* L. The following parameters were determined: the weight of fresh and dry matter of plants, leaves and roots, the number of shoots and leaves, potential (FV/Fm) and effective ( $\Delta F/F_m$ ) quantum efficiency of photosystem, photochemical (qP) and non-photochemical (qN) quenching, as well as chlorophyll a and chlorophyll b content in leaf blades. The pot experiment was carried out in a breeding room. Stymjod was applied at 1.5%, 3% and 4.5% concentrations in the spray solution. It is a nanotechnology-based growth regulator, with easily assimilable forms of mineral and organic ingredients, favorably affecting plant ontogenesis. Plants were treated twice with a single dose of 50 mL of spray per pot. They were sprayed till they were completely covered with the liquid. Distilled water was used to spray control plants. The results were statistically processed using analysis of variance, while the significance of the differences between means was determined with Tukey's test with  $P = 0.05$ . In the experiment it was found that different concentrations of Stymjod in the spray resulted in different response of plants. The best morphological effects were obtained using the concentration of the product exceeding 3%. In the test conditions Stymjod applied to *D. glomerata* increased the efficiency of the photosynthetic apparatus and the content of chlorophyll pigments.

**Key words:** iodine, plant morphology, photosynthetic activity, chlorophyll content.

## INTRODUCTION

Products that contain iodine nanoparticles in their composition and stimulate plant growth and development such as Stymjod and Biojodis are increasingly becoming the topic of research exploring their potential to regulate physiological processes and to increase crop yields (Piotrowski et al., 2016; Romanowska-Duda et al., 2018 and 2019; Sosnowski et al., 2019a; Romanowska-Duda et al., 2020). According to many authors (Strzetelski et al., 2010a, 2010b; Piotrowski et al., 2016; Romanowska-Duda et al., 2018) the dose and form of iodine have a significant effect on plant mineral composition. Forms



of water-soluble iodine are most easily taken up by the root system, but the best effects are achieved with foliar application as iodine together with water penetrates through pores in plant cuticles.

Chlorophyll fluorescence used as a physiological parameter has found wide use, such as a genetic marker of barley productivity (Planchon et al., 1989). It is also used to assess the ripeness of cabbage and coriander seeds (Jalink et al., 1998; Górnik et al., 2013), making use of the fact that the maturation process is directly related to the amount of chlorophyll monitored by the measurements of the maximum photosystem II efficiency. Górnik & Lachuta (2017) found that changes in the maximum photosystem II efficiency ( $F_v/F_m$ ) in sunflower seedlings were associated with their growth. In addition, chlorophyll fluorescence was also proposed as a marker of plant reaction to herbicides (Dayan et al., 2012; Silva et al., 2014). It has been found that damage to cells by a glyphosate herbicide in *Raphanus sativus* L. resulted in changes in the value of fluorescence. Żebrowska & Michałek (2014) used the parameters of photosynthetic activity of strawberry leaves to assess their physiological condition and the level of macronutrients provided by a fertilizer. However, in the available literature there are not many reports on the effects of plant growing methods on changes in the maximum photosystem II efficiency. There is therefore a need for research on the possibility of applying the maximum photosystem II efficiency measurements as a marker of plant reaction to various growing methods and growing conditions, including the use of substances stimulating plant growth and development. The literature points to the possibility of applying the maximum photosystem II efficiency to assess Stymjod effects on the physiological condition of sorghum (Romanowska-Duda et al., 2019), or effects of *Ecklonia maxima* extract on *Medicago × varia* T. Martyn (Sosnowski et al., 2019b).

One of the most important perennial fodder grasses is *D. glomerata*, successfully grown in northern Africa, western and central Europe and in temperate and tropical Asia. With a large variety of ecotypes this species has an unusual ability to adapt to local soil and climatic conditions (Hultén, 1968; Tolmachev et al., 1995). Due to its good nutritive properties, high production efficiency and high tolerance to abiotic stress, *D. glomerata* has been widely used as forage for more than 100 years, especially in North America, Europe (Baležentienė & Mikulionienė, 2006; Maiksteniene & Arlauskienė, 2006; Aavola, & Karelson, 2010) and Japan (Mitui, 1981; Casler et al., 2000).

It is worth noting, however, that at high doses of mineral nitrogen *D. glomerata* tends to accumulate nitrate nitrogen, an undesirable forage component, in the aboveground parts. The use of products containing active iodine in its composition can help to reduce mineral nitrogen fertilization, without production losses. This is because such products applied to plants can improve the absorption of nutrients from the soil and increase their content in tissues. Therefore, they may be recommended to organic plant production, also because their use increases the amount of iodine in the food ration (Romanowska-Duda et al., 2018).

The aim of the experiment was to study the effects of foliar application of a growth regulator with the trade name of Stymjod containing iodine nanoparticles on morphometrics, photosynthetic activity and chlorophyll content of *D. glomerata*. To meet the objectives of the research, the effects of different concentrations of Stymjod on the following characteristics were determined: the weight of fresh and the dry weight of plants, leaves and roots, the number of shoots and leaves, the maximum ( $F_v/F_m$ ) and

actual ( $\Delta F/F_m$ ) photosystem II efficiency, photochemical (qP) and non-photochemical (qN) quenching coefficients, as well as chlorophyll a and chlorophyll b content in leaf blades.

## MATERIAL AND METHODS

A pot experiment was conducted in 2017 in the breeding room of the Department of Grassland and Green Area Creation, Siedlce University of Natural Sciences and Humanities. The conditions of the experiment were as follows: the temperature of  $24 \pm 2$  °C (in light) and  $16 \pm 2$  °C (in darkness); soil moisture with 60% of field water capacity; the intensity of light of  $200 \mu\text{mol m}^{-2} \text{s}^{-1}$ , obtained with high pressure sodium lamps; the photoperiod of 16 hours in light. *D. glomerata* var. Borna was used as a test plant grown in pots with a height of 300 mm and the 200 mm diameter of the base. The experiment was replicated three times and completely randomized with control units. The pots were filled with 5 kg of medium loam soil, sampled from the plough layer. Soil pH in KCl (6.3) was determined together with the concentration of  $\text{N-NO}_3$  ( $1.4 \text{ mg kg}^{-1} \text{ DM}$ ),  $\text{N-NH}_4$  ( $60.9 \text{ mg kg}^{-1} \text{ DM}$ ), and organic carbon,  $\text{C}_{\text{org}}$  ( $17.1 \text{ g kg}^{-1}$ ).

In mid-March, 10 *D. glomerata* seeds were planted in each of the pots at a depth of 1.5 cm. After germination and the three-leaf stage, a negative selection was carried out, leaving three plants with the largest number of leaves. In the experiment different doses of Stymjod were applied with the following variants:

- Control – plants treated with distilled water;
- 1.5% – plants treated with 1.5% concentration of Stymjod;
- 3.0% – plants treated with 3% concentration of Stymjod;
- 4.5% – plants treated with 4.5% concentration of Stymjod.

There were four replications in the experiment. The plants were treated twice: during the six-leaf stage and ten-leaf stage, using 50 mL of the solution per pot each time. According to Romanowska-Duda et al. (2019) Stymjod is a product with organic and mineral components, obtained using cold plasma in nano-technology. It consists of optimal composition of macro and micronutrients as well as iodine nanoparticles. Iodine molecules activate cell metabolism, with plants responding with an intensive growth and development and an increased resistance to biotic and climatic factors. The chemical composition of Stymjod (Romanowska-Duda et al. 2019):

- basic components:  $\text{N-NO}_3^-$  ( $1,231 \text{ mg L}^{-1}$ ), P ( $6,652 \text{ mg L}^{-1}$ ),  $\text{K}^+$  ( $62,720 \text{ mg L}^{-1}$ ),  $\text{Ca}^{2+}$  ( $943 \text{ mg L}^{-1}$ ),  $\text{Mg}^{2+}$  ( $11,570 \text{ mg L}^{-1}$ );
- microelements: Fe ( $18.9 \text{ mg L}^{-1}$ ), Mn ( $886 \text{ mg L}^{-1}$ ), Cu ( $682 \text{ mg L}^{-1}$ ), Zn ( $1,476 \text{ mg L}^{-1}$ ), B ( $576 \text{ mg L}^{-1}$ );
- other components: humic acids 3.3%, organic substances (including amino acids) 56.8%,  $\text{I}_n^+$ : aqueous iodine concentrate 0.0025%.

In the experiment the following parameters were determined: the number of stems per pot, the number of leaves per pot, fresh and dry weight of plants ( $\text{g pot}^{-1}$ ), fresh and dry weight of stems ( $\text{g pot}^{-1}$ ), fresh and dry weight of leaves ( $\text{g pot}^{-1}$ ), fresh and dry weight of roots ( $\text{g pot}^{-1}$ ).

Additionally, other parameters were determined: the leaf greenness index (SPAD), the maximum photosystem II efficiency ( $F_v/F_m$ ), the actual photosystem II efficiency ( $\Delta F/F_m$ ), the photochemical quenching coefficient (qP) and the non-photochemical

quenching coefficient (qN). The content of chlorophyll a and b in *D. glomerata* leaves was also measured. All measurements were carried out when the plants were harvested, on the 15th day after the second Stymjod treatment. The SPAD measurement was conducted with the SPAD-502 portable meter, Minolta, Japan.

### **Chlorophyll content determination**

Chlorophyll a and b content was determined with the Arnon et al. (1956) method modified by Lichtenthaler & Wellburn (1983). The material was collected from each plant at the full flowering stage, with 40–50% flowers open. As for the photosynthetic pigments, the optical density of supernatants was determined with the Marcel Mini spectrophotometer (is produced by the Polish company Marcel) with the wavelengths of 440, 465 and 663 nm. Next, the results were calculated according to the following formulas:

– chlorophyll a content:  $[12.7(E_{663}) - 2.69(E_{645})]$  w/v;

– chlorophyll b content:  $[22.9(E_{645}) - 4.68(E_{663})]$  w/v;

where E – extinction at a particular wavelength; v – amount of 80% acetone (cm<sup>3</sup>) used for extraction; w – sample weight (g).

### **Photosynthetic activity determination**

Photosynthetic activity of plants was determined by the measurement of chlorophyll fluorescence induction using the PAM 2000, Heinz Walz GmbH, Effeltrich, Germany. The following parameters were determined:

- the maximum photosystem II efficiency (Fv/Fm) in the dark-adapted state (Bolh r-Nordenkamp &  quist, 1993);
- the actual photosystem II efficiency in the light-adapted state ( $\Delta F/F_m$ );
- qP – the photochemical quenching coefficient;
- qN – the non-photochemical quenching coefficient (Van Kooten & Snel, 1990).

All measurements were recorded during the growing season, using well developed *D. glomerata* leaves in 6 replications. By taking the measurements the leaf-clip holder 2030-B, a light emitting diode at 650 nm, and the standard intensity of 0.15  $\mu\text{mol m}^{-2} \text{s}^{-1}$  PAR were used. In the dark-adapted state leaves were kept in darkness for 15 minutes.

### **Statistical analysis**

The results were processed statistically using analysis of variance, and the differences between means were tested with Tukey's HSD test,  $P < 0.05$ . In tables means marked with the same letters are not significantly different. The Statistica 13-2017.3 software package was used to conduct all calculations.

## **RESULTS AND DISCUSSION**

According to the results (Table 1) the concentration of Stymjod in the spraying liquid significantly affected the number of *D. glomerata* shoots. The largest number was in plants treated with 4.5% concentration. The average value was 25 per pot and it was greater than the number of shoots in control by about 42%. The use of 1.5% and 3% concentrations did not significantly affect the number of shoots compared to control. Stymjod treatment significantly affected the number of leaf blades developed by plants.

The most leaves were on units with the concentrations of 3 and 4.5%, with the average number of 258 per pot, which was greater by about 35% than the number of leaf blades in the control plants. The concentration of 1.5% did not affect this parameter considerably. A similar trend was also observed with fresh and dry leaf weight. The highest values of these characteristics were in plants treated with 3 and 4.5% concentrations. In addition, according to the dry weight of 100 leaf blades, the largest amounts of leaves were produced by *D. glomerata* treated with the highest concentration of Stymjod, which translated into higher fresh and dry plant weight. The largest fresh and dry plant weight (212 and 40 g per pot, respectively) was on pots with the highest concentration of the product. The use of the 3% Stymjod concentration also contributed to an increase in the value of the above parameter. The statistical analysis did not show a significant variation in the fresh and dry weight of the plant root system. The concentrations used in the experiment did not affect the development of the rhizosphere. Compared to the control units the lowest concentration of the product did not significantly affect any of *D. glomerata* characteristics.

The effect of a substance containing iodine nanoparticles on the increase in crop yields are reported by Gaurilčikienė et al. (2008) and Sosnowski et al. (2019). According to Smoleń (2009), foliar use of Biojodis increased the yield of the Chopin cabbage variety by 4.5% compared to control, and the yield of the Arivist variety by as much as 12%.

**Table 1.** The effect of Stymjod on morphometric parameters of *D. glomerata*

Characteristic	Stymjod concentration			
	control	1.5%	3%	4.5%
	(pieces pot <sup>-1</sup> )			
Shoot number	17.6 (± 1.1) b	17.2 (± 1.4) b	19.8 (± 1.7) b	25.0 (± 2.5) a
Leaf number	191 (± 18) b	213 (± 22) b	254 (± 25) a	262 (± 24) a
	(g pot <sup>-1</sup> )			
Leaf fresh weight	67.8 (± 4.1) b	77.4 (± 6.9) b	97.4 (± 6.0) a	118 (± 8.7) a
Leaf dry weight	12.5 (± 1.1) b	13.3 (± 1.3) b	19.5 (± 1.4) a	22.4 (± 2.2) a
Root fresh weight	80.5 (± 18) a	71.8 (± 11) a	67.7 (± 17) a	93.5 (± 21) a
Root dry weight	16.1 (± 1.4) a	14.2 (± 1.6) a	12.2 (± 1.2) a	17.6 (± 2.1) a
Plant fresh weight	148 (± 21) c	149 (± 22) c	165 (± 29) b	212 (± 31) a
Plant dry weight	28.6 (± 2.2) c	27.5 (± 2.0) c	31.7 (± 2.7) b	40.0 (± 3.2) a
	(g)			
Dry weight of 100 leaves	6.54 (± 0.52) c	6.24 (± 0.70) c	7.68 (± 0.31) b	8.55 (± 0.83) a

Standard deviation (± SD).

In the cultivation of pickled cucumber the same product increased the yield of fruits by 10%. Substances containing iodine have had a beneficial effect on the yield of cereals. Gaurilčikienė et al. (2008), who conducted studies involving spring barley treated with a Biojodis foliar spray, a product containing iodine nanoparticles, found that the average yield of barley increased by 3.2% compared to control. The effect of increased concentrations of Stymjod on the growth of plant aboveground biomass was noted in the studies of Romanowska-Duda et al. (2018). The authors found that sorghum plants responded very well to the growing concentrations of Stymjod. Concentrations of 1.5 and 3% significantly increased plant growth, the leaf greenness index, According to the

authors Stymjod increased the yield by improving the parameters of plant physiological activity. In addition, they also pointed out that the morphological effects of Stymjod on sorghum plants were in line with the general recommendation of its manufacturer. It indicates that Stymjod increases the growth of biomass, improves plant resistance to adverse weather conditions and relieves the negative effects of stress.

The impact of Stymjod on chlorophyll a and b content in *D. glomerata* leaves (Table 2) was statistically significant. In the leaves of control plants the chlorophyll content was 172 mg 100 g<sup>-1</sup> per fresh weight, but upon the treatments of 3% and 4.5% solutions the chlorophyll an increased accordingly to 227 and 225 mg 100 g<sup>-1</sup> per fresh weight. The average increase in chlorophyll a content compared to control was 31.4%. A similar difference of 30.8% was recorded for chlorophyll b. According to the literature (Yokoya et al., 2007; Zhao et al., 2016) these photosynthetic pigments are responsible for collecting light and moving the absorbed light to photosynthetic reaction centres; their concentration is associated with the effectiveness of photosynthesis. Increasing the content of these pigments may be one of the causes of an increase in photosynthetic activity (Zhao et al., 2016). Similarly, in the present studies *D. glomerata* leaves responded to Stymjod application with a higher content of photosynthetic pigments and an increased photosynthetic activity.

**Table 2.** The effect of Stymjod on chlorophyll pigment content (mg 100 g<sup>-1</sup> of fresh weight) and SPAD leaf greenness index in *D. glomerata* leaves

Characteristic	Stymjod concentration			
	Control	1.5%	3%	4.5%
Chlorofil a	172 (± 11.2) c	198 (± 18.1) b	227 (± 20.1) a	225 (± 21.1) a
Chlorofil b	91 (± 10.4) b	119 (± 12.3) a	120 (± 11.7) a	118 (± 10.1) a
SPAD	39.8 (± 4.1) c	44.1 (± 5.0) b	47.7 (± 3.8) a	49.7 (± 3.9) a

Standard deviation (± SD).

According to Netto et al. (2005) and Stankowski et al. (2019) the SPAD index is a good parameter for diagnosing the integrity of the photosynthetic system in leaves, and thus can help with advanced interpretations of the photochemical process. In addition, the content of chlorophyll in leaves depends on many factors, one of which is the availability of nitrogen to the plant. According to the above authors SPAD readings lower than 40 indicate some impairment of the photosynthesis process. In the present experiment (Table 2) SPAD values for *D. glomerata* were between 39.8 for control and 49.7 for plants treated with the highest concentration of Stymjod. Each concentration resulted in a significant increase in the SPAD value, compared to control. According to the research of other authors (Netto et al., 2005; Uddling et al., 2007) the relationship between chlorophyll concentration and SPAD values determined for coffee, birch, wheat and potato was statistically significant. For all species the relationship was nonlinear with a rising slope as the SPAD grew. The relationship between chlorophyll concentration and SPAD values for coffee, birch and wheat were strong ( $r^2 = 0.9$ ), while for potatoes it was weaker ( $r^2 = 0.5$ ). For birch and wheat the relationship was very similar when chlorophyll levels were expressed with a unit of measurement for leave surface area, but it differed when expressed with a unit of measurement for fresh weight. In addition, the relationship values between chlorophyll concentration and SPAD values of wheat for two different varieties and during two different growing seasons were

similar. The curved shape of those relationships matched the simulated effect of uneven chlorophyll distribution on the leaf surface and its rotatory dispersion, causing deviations from linearity in the upper and low SPAD range, respectively.

Fluorescent measurements of *D. glomerata* leaves showed that the effect of Stymjod on the maximum photosystem II efficiency ( $F_v/F_m$ ) in the dark-adapted state was statistically significant (Table 3). Stymjod application resulted in an increase from  $F_v/F_m$  of 0.549 on the control units, to  $F_v/F_m$  exceeding 0.6 for plants treated with different concentrations (1.5% – 0.618, 3% – 0.647, 4.5% – 0.644); the average percentage increase was 26.6%. On the other hand, the actual photosystem II efficiency ( $\Delta F/F_m'$ ), determined under the same conditions, was on average 28.9% higher for leaves of plants treated with Stymjod. According to et al. (1997) such an increase indicates growing demand of plants for products constituting assimilatory power and a lack of disruption in the growth and development process.

**Table 3.** The effect of Stymjod on photosynthetic activity of *D. glomerata* leaves

Characteristics	Stymjod concentration			
	Control	1.5%	3%	4.5%
The maximum photosystem II efficiency ( $F_v/F_m$ )	0.549 ( $\pm 0.02$ ) b	0.618 ( $\pm 0.03$ ) a	0.647 ( $\pm 0.03$ ) a	0.644 ( $\pm 0.03$ ) a
The actual photosystem II efficiency ( $\Delta F/F_m'$ )	0.398 ( $\pm 0.01$ ) a	0.512 ( $\pm 0.02$ ) a	0.509 ( $\pm 0.02$ ) a	0.518 ( $\pm 0.03$ ) a
The photochemical quenching coefficient (qP)	0.537 ( $\pm 0.02$ ) a	0.543 ( $\pm 0.02$ ) a	0.549 ( $\pm 0.03$ ) a	0.556 ( $\pm 0.03$ ) a
The non-photochemical quenching coefficient (qN)	0.108 ( $\pm 0.01$ ) c	0.120 ( $\pm 0.03$ ) b	0.141 ( $\pm 0.03$ ) a	0.138 ( $\pm 0.04$ ) a

Sstandard deviation ( $\pm$  SD).

In addition, an increase in  $F_v/F_m$  means activation of PSII due to the absence of photoinhibition in plant cells with nitrogen deficiency. That is, the energy consumed for the transport of electrons is not reduced. At the same time, an increase in the activity of PSII reaction centres of nitrogen-rich cells indicates a high activity of the photosynthetic apparatus and increased light-energy conversion efficiency (Nishiyama et al., 2006). It is therefore worth pointing out that Stymjod treatment of *Dactylis glomerata* L. may have resulted in better nitrogen nutrition of plant cells, as evidenced by increases in photosynthetic parameters such as the maximum ( $F_v/F_m$ ) and the actual ( $\Delta F/F_m'$ ) photosystem efficiency of leaves. The use of Stymjod also contributed to an increase in the non-photochemical quenching coefficient (qN). As the data in Table 3 indicates, it increased by 23.2% compared to control pots. However, no statistically significant effect of the product on the photochemical quenching coefficient (qP) of leaves was recorded. The literature (Laisk et al., 2014; Körner et al., 2015) points to a very large impact of the genetic conditions of plants on the value of fluorescence parameters, which may explain the lack of differentiation of qP values under the effect of Stymjod.

## CONCLUSIONS

Stymjod applied at the concentration of 4.5% significantly increased the number of shoots, leaf blades and dry weight of 100 leaf blades, which translated into greater fresh and dry *D. glomerata* weight. There was no effect of Stymjod on the increase in fresh and dry root weight relative to the control pots. Under the research conditions, *D. glomerata* treated with Stymjod, regardless of the concentration, was characterized by better efficiency of the photosynthetic apparatus. This is evidenced by, among others, the values of the maximum photosystem efficiency ( $F_v/F_m$ ), the actual photosystem efficiency ( $\Delta F/F_m$ ) and of the non-photochemical quenching coefficient ( $q_N$ ). All of the Stymjod concentrations increased the photosynthetic activity of plants, resulting from an increase in the content of photosynthetic pigments and the value of the SPAD leaf greenness index. Beneficial effects of Stymjod application to *D. glomerata* and the possibility of decreasing mineral nitrogen doses without negative physiological consequences for plants were observed in the research.

**ACKNOWLEDGEMENTS.** The research carried out the theme No 357/13/S was financed by the science grant of the Ministry of Science and Higher Education.

## REFERENCES

- Aavola, R. & Karelson, J. 2010. The dynamics of botanical composition of pure and mixed grass swards on peaty soil. *Agronomy Research* **8**(Special Issue III), 513–522.
- Arnon, D.J., Allen, M.B. & Whatley, F. 1956. Photosynthesis by isolated chloroplast. IV General concept and comparison of three photochemical reactions. *Biochimica et Biophysica Acta* **20**, 449–461.
- Baležientienė, L. & Mikulionienė, S. 2006. Chemical composition of galega mixtures silages. *Agronomy Research* **4**(2), 483–492.
- Bolhår-Nordenkamp, H.R. & Öquist, G. 1993. Chlorophyll fluorescence as a tool in photosynthesis research. *Photosynthesis and production in a changing environment*, 193–206.
- Casler, M.D., Fales, S.L. & McElroy, A.R. 2000. Genetic Progress from 40 Years of orchardgrass breeding in North America measured under Hay Management. *Crop Science* **40**, 1019–1025.
- Dayan, F.E. & Zaccaro, M.L. de M. 2012. Chlorophyll fluorescence as a marker for herbicide mechanisms of action. *Pesticide Biochemistry and Physiology* **102**, 189–197.
- Gaurilčikienė, I., Supronienė, S. & Ronis, A. 2008. The impact of the biological agent Biojodis on the incidence of pathogenic fungi in winter wheat and spring barley. *Zemdirbyste-Agriculture* **95**(3), 406–414.
- Górník, K. & Lachuta, L. 2017. Application of phytohormones during seed hydropriming and heat shock treatment on sunflower (*Helianthus annuus* L.) chilling resistance and changes in soluble carbohydrates. *Acta Physiologiae Plantarum* **39**, 118.
- Górník, K., Janas, R. & Grzesik, M. 2013. Chlorophyll fluorescence of coriander seeds as maturation meter. *Episteme* **20**, 317–322.
- Hultén, E. 1968. Flora of Alaska and Neighboring Territories. Stanford Univ. Press, pp. 1011–1025.
- Jalink, H., van der Schoor, R., Frandas, A., van Pijlen, J.G. & Bino, R.J. 1998. Chlorophyll fluorescence of *Brassica oleracea* seeds as a non-destructive marker for seed maturity and seed performance. *Seed Science Research* **8**, 437–443.

- Körner, O., Rosenqvist, E. & Ottosen, C.O. 2015. Using the quantum yields of photosystem II and the rate of net photosynthesis to monitor high irradiance and temperature stress in chrysanthemum (*Dendranthema grandiflora*). *Plant Physiology and Biochemistry* **90**, 14–22.
- Laisk, A., Oja, V., Eichelmann, H. & Dall'Osto, L. 2014 Action spectra of photosystems II and I and quantum yield of photosynthesis in leaves in State 1. *Biochimica et Biophysica Acta Bioenergetics* **1837**(2), 315–325.
- Lichtenthaler, H.K. & Wellburn, A.R. 1983. Determinations of total carotenoids and chlorophyll a and b of leaf extracts in different solvents. *Biochemical Society Transactions* **11**, 591–592.
- Maiksteniene, S. & Arlauskienė, A. 2006. The effect of agricultural management systems on the weed incidence in cereals. *Agronomy Research* **4**(Special issue), 281–285.
- Mitui, K. 1981. Handbook of Herbage Crops and Grasslands. *Youkendo*, Tokyo, 99. 49–57.
- Netto, A., T., Campostrini, E., de Oliveira, J.G. & Bressan-Smith, R.E. 2005. Photosynthetic pigments, nitrogen, chlorophyll a fluorescence and SPAD-502 readings in coffee leaves. *Scientia Horticulturae* **104**, 199–209.
- Nishiyama, Y., Allakhverdiev, S.I. & Murata, N. 2006. A new paradigm for the action of reactive oxygen species in the photoinhibition of photosystem II. *Biochim Biophys Acta* **1757**, 742–749.
- Piotrowski, K., Romanowska-Duda, Z. & Grzesik, M. 2016. How Biojodis and Cyanobacteria alleviate the negative influence of predicted environmental constraints on growth and physiological activity of corn plants. *Polish Journal of Environmental Studies* **25**(2), 741–751.
- Planchon, C., Sarrafi, A. & Ecochard, R. 1989. Chlorophyll fluorescence transient as a genetic marker of productivity in barley. *Euphytica* **42**, 269–273.
- Romanowska-Duda, Z., Grzesik, M. & Janas, R. 2020. The usefulness of nano-organic-mineral fertilizer Stymjod in intensification of growth, physiological activity and yield of the jerusalem artichoke biomass. In: Wróbel M., Jewiarz M., Szlęk A. (eds) *Renewable Energy Sources: Engineering, Technology, Innovation. Springer Proceedings in Energy*. Springer, Cham. doi.org/10.1007/978-3-030-13888-2\_33
- Romanowska-Duda, Z., Grzesik, M. & Janas, R. 2018. Stimulatory impact of Stymjod on sorghum plant growth, physiological activity and biomass production in field conditions. In: Mudryk K., Werle S. (eds) *Renewable Energy Sources: Engineering, Technology, Innovation. Springer Proceedings in Energy*. Springer, Cham. doi.org/10.1007/978-3-319-72371-6\_24
- Romanowska-Duda, Z., Grzesik, M. & Janas, R. 2019. Maximal efficiency of PSII as a marker of sorghum development fertilized with waste from a biomass biodigestion to methane. *Frontiers in Plant Science* **9**, 1920.
- Silva, F., Costa, A., Pereira Alves, R. & Megguer, C. 2014. Chlorophyll fluorescence as an indicator of cellular damage by glyphosate herbicide in *Raphanus sativus* L. plants. *American Journal of Plant Sciences* **5**, 2509–2519.
- Smoleń, S. 2009. The effect of iodine and nitrogen fertilization on the mineral composition of the carrot. *Environmental Protection and Natural Resources* **40**, 270–277.
- Sosnowski, J., Jankowski, K., Truba, M. & Malinowska, E. 2019b. Effect of *Ecklonia maxima* extract on photosynthesis activity and chlorophyll content of *Medicago × varia* Martyn leaves. *Chilean Journal of Agricultural Research* **79**(2), 257–265.
- Sosnowski, J., Toczyska, E. & Truba, M. 2019a. Morphological effects of Stymjod foliar application on *Medicago × varia* T. Martyn. *Journal of Ecological Engineering* **20**(8), 184–191.



- Stankowski, S., Bury, M., Jaroszewska, A., Michalska, B. & Gibczyńska, M. 2019. Effect of multi-component fertilizers on seeds yield, yield components and physiological parameters of winter oilseed rape (*Brassica napus* L.). *Agronomy Research* **17**(5), 2071–2081. <https://doi.org/10.15159/AR.19.186>
- Strzetelski, P., Smoleń, S., Rożek, S. & Sady, W. 2010a. The effect of differentiated fertilization and foliar application of iodine on yielding and antioxidant properties in radish (*Raphanus sativus* L.) plants. *Ecological Chemistry and Engineering A* **17**(9), 1189–1195.
- Strzetelski, P., Smoleń, S., Rożek, S. & Sady, W. 2010b. The effect of diverse iodine fertilization on nitrate accumulation and content of selected compounds in radish plants (*Raphanus sativus* L.). *Acta Scientiarum Polonorum Horticulture* **9**, 65–70.
- Tolmachev, A.I., Packer, J.G. & Griffiths, G.C.D. 1995. Flora of the Russian arctic, Polypodiaceae. *Gramineae* **1**, 330.
- Uddling, J., Gelang-Alfredsson, J., Piikki, K. & Pleijel, H. 2007. Evaluating the relationship between leaf chlorophyll concentration and SPAD-502 chlorophyll meter readings. *Photosynthesis Research* **91**, 37–46.
- Van Kooten, O. & Snel, J.F.H. 1990. The use of chlorophyll fluorescence nomenclature in plant stress physiology. *Photosynthesis Research* **25**, 147–150.
- Yokoya, N.S., Necchi, O.Jr., Martins, A.P., Gonzalez, S.F. & Plastino, E.M. 2007. Growth responses and photosynthetic characteristics of wild and phycoerythrin deficient strains of *Hypnea musciformis* (Rhodophyta). *Journal of Applied Phycology* **19**, 197–205.
- Żebrowska, J. & Michałek, W. 2014. Chlorophyll fluorescence in two strawberry (*Fragaria x ananassa* Duch.) cultivars. *Journal of Central European Agriculture* **15**, 12–21.
- Zhao, L.-S., Su, H.N., Li, K., Xie, B.B., Liu, L.N., Zhang, X.Y., Chen, X.L., Huang, F., Zhou, B.C. & Zhang, Y.Z. 2016. Supramolecular architecture of photosynthetic membrane in red algae in response to nitrogen starvation. *Biochimica et Biophysica Acta* **1857**, 1751–1758.

## **Investigation of dual varying area flapping actuator of a robotic fish with energy recovery**

I. Tipans, J. Viba, M. Irbe and S.K. Vutukuru\*

Riga Technical University, Faculty of Mechanical Engineering, Transport and Aeronautics, Department of Theoretical Mechanics and Strength of Materials, Kipsala street 6B, LV-1048 Riga, Latvia

\*Correspondence: vshravankoundinya1989@gmail.com

**Abstract.** Autonomous under-water vehicles (AUV) performing a commanded task require to utilize on-board energy sources. At the time when on-board power source runs low during operation, the vehicle (AUV) is forced to abort the mission and to return to a charging station. The present work proposes the technique of an energy recovery from surrounding medium. This effect is studied for dual action actuator movement that obtains energy from fluid. It is realized that a flapping or vibrating actuator can be used for energy extraction phenomenon apart from the non-traditional propulsive technique. In the present work a simple dual flapping actuator that can switch between simple flat plate and perforated plate at extreme end positions (angles) by using an efficient mechatronic mechanism that would help in overcoming viscous forces of the operating medium is extensively studied. The main objective of the present article is to develop a new approach for energy gain and recharge power pack of on-board sources from the surrounding medium and to create a robotic fish that would work autonomously by using unconventional drive along with the possibility of energy restoration by using dual varying area type vibrating actuator. At the time of recharge, the robotic fish would project its tail (actuator) out of water and use surrounding medium (air) to scavenge the energy. All the equations describing the process are formed according to classical laws of mechanics. The mechatronic system is explained and the results obtained are discussed in detail for air as the operating fluid to scavenge energy.

**Key words:** energy extraction, flapping tail, robotic fish.

### **INTRODUCTION**

Highly growing wakefulness for carbon-free environment and also a climate friendly energy requirement led to the development of a new concept of renewable energy. Such energy sources are available in abundance (like ocean, air currents).and are very attractive as these sources are mostly readily accessible in nature. Ever since the technique of harmonically oscillating wing of a windmill was used for the process of energy extraction (Mckinney & DeLaurier, 2012), further research in this field was explored by many eminent researchers. Research work in this direction includes entirely passive motion approach (Peng & Zhu, 2009), motion in a definite order approach for wings that are arranged in tandem in the path of oncoming flow for sinusoidal and non-sinusoidal motion (Ashraf et al., 2011) and studies of power extraction through modified

motion oscillating foil (Xie et al., 2014). Considering the shape driven effects, chord-like flexibility and related outcome for power extraction (Jeanmonod & Olivier, 2017) and combined foil effects on energy extraction (Boudis et al., 2018) were performed. It is important to note that as a result of experiments it is demonstrated that flapping foils when subjected to unsteady and turbulent flow are set into self-unsteady motion, and when effectively controlled, maximum energy extraction can be achieved which is similar to high aspect ratio windmills. Relevant performance parameters were analysed (Simpson et al., 2008). Experiments were followed by numerical investigation pertaining to energy extraction performance for a flapping-foil power generator. Experiments were validated and it was concluded that increased pitching amplitude is good for achieving good power output (Lu et al., 2015). Interesting unmanned vehicle using flapping – hydrofoil for the purpose of energy generation in ocean is designed (Sun et al., 2016). Power generation and basic mechanism for the flapping wing along with three different types of flapping power generators are discussed. Most important is the third type which is determined by fully driven motion – the plunge and pitch motion are through fluid and body interactions, and oscillation motion has a controlled mechanism. Power output is measured by connecting viscous damper for the plunge motion (Ashraf et al., 2019). Flapping wing concept to produce power from tidal current is developed by BioSTREAM company in 2019. Initially in the flow, the pitch angle is adjusted and the resulting plunge motion of the fin is forced to drive a gear box where in the flapping motion is then turned into a rotating motion that drives conventional dynamo. Further, a good review of oscillating foil energy converters is available (Xiao & Zhu, 2014).

In the present work, by paying particular attention to aquatic world a new concept of energy extraction, similar to the propulsive technique (Viba et al., 2011) is studied. In addition, the concept of fluid-body interactions phenomenon according to Tipans et al. (2019b) is used in the present article. The dual tail fin model is shown in the Fig.1 and also Dual flapping tail actuator in diving motion from left to right inside water can be seen from Fig. 2. The advantage of flapping / harmonically oscillating flat plates is based on the fact that they are easy to manufacture, maintain and perform effectively even in shallow waters. Flat plates are advantageous in a way that they form early leading-edge vortices (LEV).

## **MATERIALS AND METHODS**

### **Dual actuator actions for diving and charging positions**

As shown in Fig.1, during the diving motion of the robot the tail form is changed from single tail to dual tail with ability to rotate about the axis O (Fig. 3), and the same process continuously repeats thereby achieving the diving force, and that diving force is maintained unceasing (Viba et al., 2010; Viba et al., 2011). The tail fin here consists of two perforated flat plates whose actions are synchronous. The tail fins (perforated plate) under locked position form the single tail and this specific condition is called ‘locked in’ because there is no relative movement of the two perforated plates (tail fin) and the perforations fit in exactly there by forming a complete flat plate, this single tail fin under extreme angles of propulsive strokes change into perforated plate due to relative movement of the plates in that position. The geometry of the two perforated plates is as mentioned (Tipans et al., 2019a). However, the present article only focuses on the novel concept of scavenging energy from surrounding medium and does not refer to robotic

fish docking position or to the method by which the fish is held stationary in the running waters. As already stated, keeping in view the additional advantage of the flat plate structure the same technique of controlled flapping motion is investigated and the present work offers a novel solution for energy recovery from the surrounding medium and at the same time ensuring that the model is practically realizable. It is also anticipated that this switching of flat plate to a perforated (varying area) helps to overcome the viscous nature of the fluid medium and to improve the propulsive stroke performance.

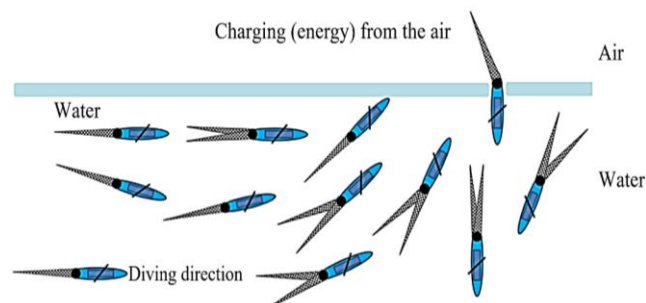


**Figure 1.** Dual tail and single tail fin flapping actuator in diving motion inside water along with the technique of charging from air.

At the time of charging, the single tail fin (locked-in condition) of the fish is extended out of water, and the surrounding medium (air) is used for charging (Fig. 3). The air-flow is assumed to be laminar and is from right to left. The single tail fin at the extreme angles initiates plates relative motion (perforated plates of tail fin) and by the action of wind is set into flapping (curvilinear oscillations) which is required for the energy scavenging Fig. 14. Thereby though dual plates exists as the tail fin for the robotic fish, this article refer more to single tail fin as this particular action of robot is very crucial for the purpose of energy scavenging from the local medium.

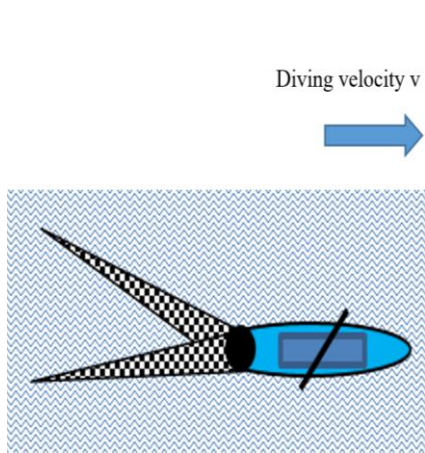


**Figure 2.** Dual flapping tail actuator in diving motion inside water.

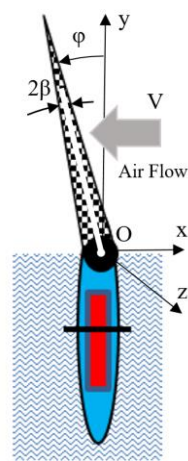


**Figure 3.** Flapping actuator in charging position in air.

The robotic fish prototype with related mechatronic system is shown in the Fig. 15–16. All the calculations performed considering the existing successful robotic fish prototype model. The components and material are so chosen to keep the weight of the robotic fish as low as possible and to be impervious to water. The mechanism of flapping tail fin is tested in wind tunnel, the non-stop flapping of the fin is expected to ensure promising results.

### Mathematical model of the one tail robot horizontal motion in fluid

We consider the motion of a simplified, one-tail actuator for horizontally diving robot (Fig. 3). Assuming a simple linear motion for the robotic fish in water with a mechatronic system, it is possible to come up with a triangular tail with flapping/curvilinear oscillations about the axis O for a given time function. The hull and the tail is described as a mechanical system of one degree of freedom (1 DOF) defined by the coordinate  $x$ . In order to avoid additional movement from the tail rotation leading to instability, it is considered that the rotation axis O coincides with the centre of mass of the tail fin for the robotic fish. Thereby, the differential equation for the robot motion will be (1):

$$(m_0 + m)\ddot{x} = -N_1x - N_2x - b\dot{x}^2 \text{sign}(\dot{x}), \quad (1)$$

where  $m_0$  is a mass of the hull;  $m$  is a mass of the tail;  $\ddot{x}$ ,  $\dot{x}$  are correspondingly the acceleration and velocity of the hull;  $N_1x$  is a fluid interaction component in a pressing zone;  $N_2x$  is a fluid interaction component with the tail in suction zone;  $b\dot{x}^2$  is non-linear interaction of the hull with fluid in rectilinear motion, depending of motion velocity  $v = \dot{x}$  directions;  $b$  is constant.

To determine the vector components  $N_1x$  and  $N_2x$ , the interactions on two infinitely small tail areas in the pressure and suction zones are considered, as shown in Fig. 4. The direction of the angular velocity of the tail rotation as well as the direction of relative motion of the housing must also be taken into account. Since the rotational velocity component of a given area depends on the distances to the axis of rotation, that is expressed by (1) as an integral-differential equation which can be solved approximately by using numerical methods.

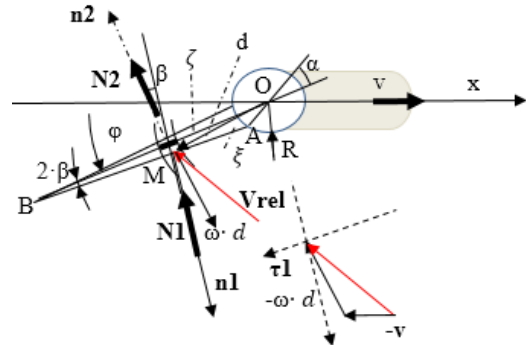


**Figure 4.** Model for tail - fluid interaction calculations.

Before integration, we write analytical link equations (2), (3) at pressing (upstream zone) for triangles OAB and OMB Fig. 4:

$$\xi = \frac{R \sin(\gamma)}{\sin(\alpha + \beta - \gamma)}; \quad (2)$$

$$d = \frac{R \sin(\alpha + \beta)}{\sin(\alpha + \beta - \gamma)}, \quad (3)$$

where  $\xi$ ,  $d$  and  $R$  are shown in Fig. 4, but angle  $\gamma$  is  $\angle$  MOB.

According to engineering calculation method described by (Tipans et al., 2019a) to determine forces  $N1x$  and  $N2x$ , we first find forces in normal direction  $N1$ ,  $N2$  (Fig. 4). They depend on relative velocity projection squares as given by (4), (5):

$$|N1| = B \cdot \rho \left| \int_0^\beta (v \cdot \sin(\varphi - \beta) + \omega \cdot \xi)^2 d\xi \right|; \quad (4)$$

$$|N2| = B \cdot \rho \cdot C \left| \int_R^{R2} (v \cdot \sin(\varphi) + \omega \cdot \zeta)^2 d\zeta \right|, \quad (5)$$

where  $\xi$  is a distance from side AMB and  $d\xi$  is a differential of  $\xi$ , both calculated by (3);  $\zeta$  is a radial distance along OB (Fig. 3);  $C$  is a constant, approximately equal to 0.5 (Tipans et al., 2019).

For the approximate solution of equation (1), the following force equation  $N1x$  and  $N2x$  can be taken as (6) & (7):

$$F1x = |N1| \cdot \text{sign} \left( v \cdot \sin(\varphi - \beta) + \omega \cdot \frac{R + R2}{2} \right) \cdot \sin(\varphi - \beta); \quad (6)$$

$$F2x = |N2| \cdot \text{sign} \left( v \cdot \sin(\varphi) + \omega \cdot \frac{R + R2}{2} \right) \cdot \sin(\varphi) \quad (7)$$

An example of numerical modeling is given below with parameters:  $R = 0.05$  m;  $R2 = 0.25$  m. For the tail fin rotation angle and angular velocity is given by (8), (9) and corresponding graphical results shown in Fig. 5 & Fig. 6 below respectively:

$$\varphi = a[\sin(pt) + 2(\lambda_3)\sin(3pt + \varepsilon_3)]; \quad (8)$$

$$\omega = a[p \cos(pt) + 6p(\lambda_3)\cos(3pt + \varepsilon_3)], \quad (9)$$

where  $\varepsilon_3 = -1.571$ ,  $\lambda_3 = \pm 0.1$ ,  $p = 5$  and  $a = 0.5$ .

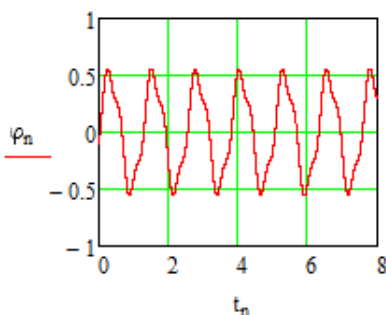


**Figure 5.** Tail rotation angle for varying time.

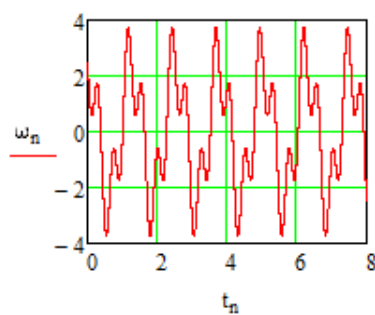


**Figure 6.** Angular velocity for varying time for the tail fin,  $\lambda_3 = -0.1$ .

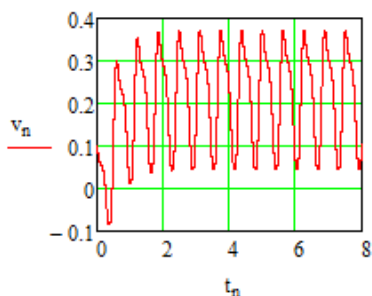


**Figure 7.** Hull velocity ahead.  $\lambda_3 = -0.1$ .

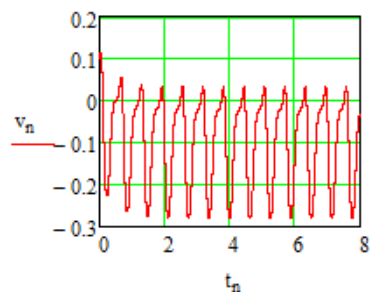


**Figure 8.** Hull velocity in reverse motion.  $\lambda_3 = +0.1$ .

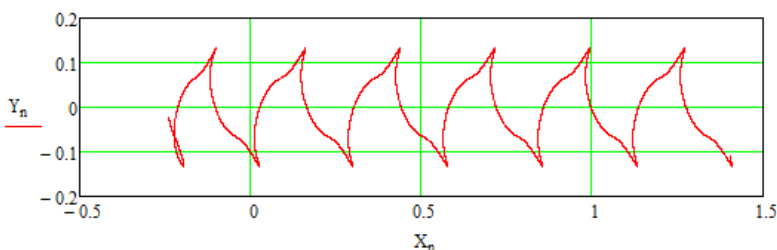


**Figure 9.** Absolute trajectory of tail edge point B, moving forward in plane (X, Y),  $\lambda_3 = -0.1$ .

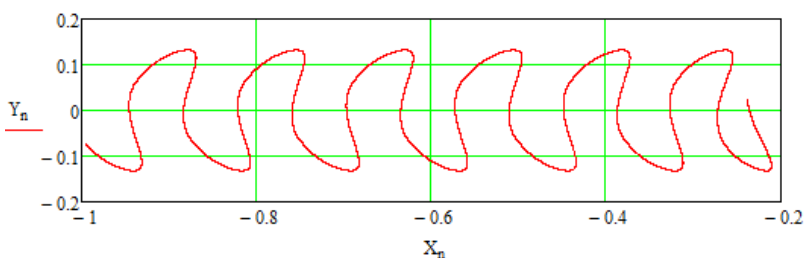


**Figure 10.** Absolute trajectory of tail edge point B, moving backward in plane (X, Y),  $\lambda_3 = +0.1$ .

The following conclusions can be drawn from the results of numerical modelling:

1. Periodic modes start very quickly because the frontal force of the interaction is proportional to the density of the operating medium.
2. By changing the polyharmonic rotation phases, it is possible to move in both directions in the flow (forward and backward).
3. Acquired analytical - numerical relationships can be used in the synthesis of mechatronic engine.

### **Mathematical model for the robot power pack charging with single flapping fin actuator**

In the charging position, the position of robotic fish is static and is not influenced by water currents. The fin (tail), as an actuator, interacts with the flow of air by rotating about a fixed axis  $Oz$  according to the following differential equation (Fig. 3):

$$J_z \ddot{\varphi} = Mwin_z - Mel_z(\varphi) - Mgen_z(\dot{\varphi}), \quad (10)$$

where  $J_z$  is a tail mass moment inertia about rotation axis  $z$ ;  $\ddot{\varphi}$  – angular acceleration;  $\varphi, \dot{\varphi}$  are correspondingly the angle and angular velocity;  $Mwin_z$  is an air flow interaction moment;  $Mel_z(\varphi)$  is a moment from linear or non-linear elastic spring;  $Mgen_z(\dot{\varphi})$  is a linear or non-linear moment from energy generator.

The moment  $Mwin_z$  is determined separately for the pressure and suction zones, similarly to the previous procedure (2)–(7). If the flow-induced pressure and suction zones for the triangular tail do not change direction, the integral-differential equation is simplified. As an example, for a theoretically infinite thin sharp plate  $\beta=0$ ) we obtain (11) – (12):

$$Mwin_z = (1 + C) \cdot B(\omega) \cdot \rho_a \left[ \int_{R1}^{R2} (V \cdot \cos(\varphi) - \zeta \cdot \omega)^2 \cdot \zeta \cdot d\zeta \right]; \quad (11)$$

or

$$\left[ \frac{(R2^4 - R1^4)}{4} \omega^2 + 2 \frac{R1^3 - R1^3}{3} \omega V \cos(\varphi) + \frac{(R2 - R1) V \cos(\varphi)^2}{2} \right], \quad (12)$$

where  $V$  is a flow velocity;  $R1, R2$  are the radial distances of interaction zone;  $C$  is a parameter, explained before;  $B(\omega)$  is a perforated plate area exchange expressed as  $\omega$  function;  $\rho_a$  is an air density.

Eqs (10) and (12) are used for calculating the robot's energy charge. It should be noted that with the help of a mechatronic device, the interaction area of the perforated tail can be changed in the system and that the power charging system can change the generator parameters as well as its optimum control rules.

Modelling results are given below as an example of a relatively small plate. A case with a linear spring and a linear generator characterization in the following form is considered:

$$Mel_z = c \cdot \varphi; Mgen_z(\dot{\varphi}) = b \cdot \dot{\varphi}, \quad (13)$$

where  $c, b$  are the constants.

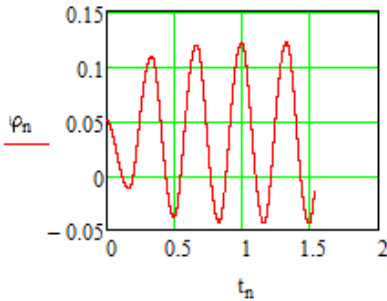


**Figure 11.** Angle of the perforated plate varying with time.

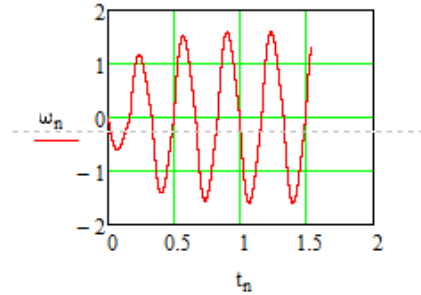


**Figure 12.** Angular velocity of the perforated plate varying with time.



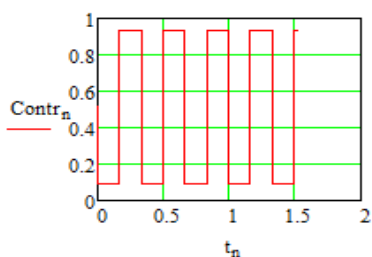


**Figure 13.** Area control action for the perforated plate.

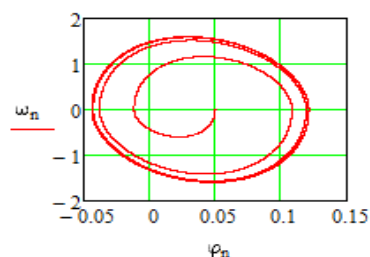


**Figure 14.** Motion in phase plane.

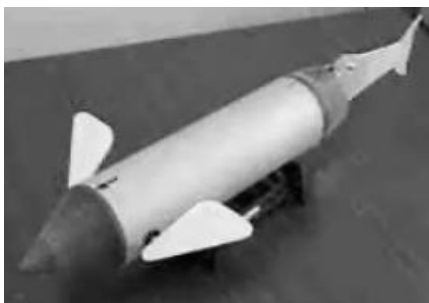


**Figure 15.** Existing Robotic fish prototype. Tail fin without perforated plates.

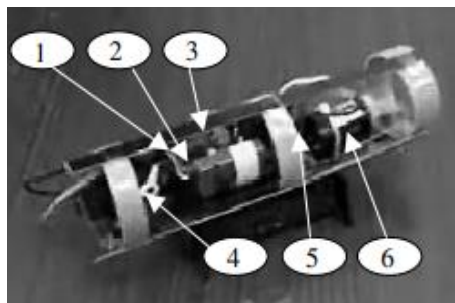


**Figure 16.** Mechatronic system of fish: 1 – Micro controller; 2 – power supply; 3 – signal detector from radio; 4 – attachment for pectoral fins for levelled motion; 5 – direction controller; 6 – velocity control.



**Figure 17.** Robotic fish in action.

The following additional conclusions can be drawn from the results of numerical modelling:

- opening and closing of flat plate perforations can reduce or increase the interaction area;
- it changes forces of interaction, and oscillations are induced in a flexible system; the oscillation is very stable as the periodic cycle is achieved in three to five strokes.

## RESULTS AND DISCUSSION

In this study, the application of dual mechatronic actuator is considered. First, the dual-action actuator in the robot's fish dive motion allows the robot to move back and forth by changing the tail drive phase. Similarly, in future studies, the dual actuator can provide not only rectilinear motion but also steering and floatation. Accordingly, in the mechatronic control of the energy charge mode, the tail interaction area can be changed by opening or closing the perforations. The study shows how in engineering calculations it is possible to obtain relatively simplified differential equations for object rotation and planar motion in fluid. The speed of the hull in forward motion is more as compared to the hull speed in reverse motion as it can be seen from the obtained calculations Fig. 7–8.

Though the calculations involved are for the small, flat perforated plates the same can be extended to plates of any size and geometry. Computer modelling is used instead of practical test for validating the results. The results obtained, discussed in this article ensure that the concept is practically realizable.

## CONCLUSIONS

The dual action actuator ensures the long-term functioning of the underwater robot fish. For this purpose, it shall be possible to switch the mechatronic control system from the movement of the hull dive cycle to the movement of the power refill cycle in the air stream. Energy replenishment is also possible underwater. In this case, the underwater stream should be used. The engineering calculation method proposed in the study allows to analyse the interaction between the motion of different objects and fluids. The method makes it possible to model the complex motion of an object in a fluid, as described by integral differential equations.

**ACKNOWLEDGEMENTS.** This research is funded by the Latvian Council of Science, project 'Creation of design of experiments and metamodeling methods for optimization of dynamics of multibody 3D systems interaction with bulk solids and fluids', project No. lzp-2018/2-0281.

## REFERENCES

- Ashraf, M.A., Joung, J. & Lai, J.C.S. 2011. Numerical Analysis of an Oscillating –Wing wind and hydropower generator. *AIAA Journal* **49**(7), 1374–1386. <https://doi.org/10.2514/1.J050577>
- Ashraf, M.A., Khan, A.A., Miah, Md.S. 2019. An overview of progress in flapping wing power generation. *Conference proceedings of ICMET*, Oman. <http://bps.energy/biostream>.
- Boudis, A., Benzaoui, A., Oualli, H., Guerri, O. & Bayeul –Laine, A.C. & Coutier Delgosha, O. 2018. Energy extraction performance improvement of a flappingfoil by the use ofcombined foil. *Journal of Applied Fluid Mechanics* **11**(6), 1651–1663.
- Jeanmonod, G. & Olivier, M. 2017. Effects of chordwise flexibility on 2D flapping foils used as an energy extraction device. *Journal of fluids and structures* **70**, 327–345.
- Lu, K., Xie, Y., Zhang, D. & Xie, G. 2015. Systematic investigation of flow evolution and energy extraction performance of a flapping –airfoil power generator. *Energy* **89**, 138–147.
- Mckinney, W. & DeLaurier, J.2012. Wingmill: An Oscillating-wing windmill. *Journal of energy* **5**(2), 109.
- Peng, Z. & Zhu, Q. 2009. Energy harvesting through flow-induced oscillations of a foil. *AIP Physics of fluids* **21**(12). doi: 10.1063/1.3275852

- Simpson, B.J., Licht, S., Hover, F.S. & Triantafyllou, M.S. 2008. Energy extraction through flapping foils. OMAE27. *Proceedings of 27th international conference on offshore Mechanics and Arctic Engineering*, pp. 389–396.
- Sun, T., Zhao, J., Yan, X. & Xu, P. 2016. A new flapping – hydrofoil wave power generating unmanned ocean vehicle. OMAE2016, *Proceedings of the ASME 35<sup>th</sup> international conference on ocean, offshore and arctic engineering*.
- Tipans, I., Viba, J., Vutukuru, S.K. & Irbe, M. 2019a. Vibration analysis of perforated plate in non-stationary motion. *Journal of Vibroengineering PROCEDIA* **25**, 48–53.
- Tipans, I., Viba, J., Irbe, M. & Vutukuru, S.K., 2019b. Analysis of Non-Stationary flow interaction with simple form objects. *Agronomy Research* **17**(1), 1227–1234.
- Viba, J., Beresnevich, V., Tsyfansky, S., Grasmanis, B., Yakushevich, V., Eiduks, M., Kovals, E. & Kruusma, M. 2010. Fin type propulsive devices with varying working area of vibrating tail. *Journal of Vibroengineering* **12**(3), 278–286.
- Viba, J., Beresnevich, V., Tsyfansky, S., Kruusma, M., Fontaine, J.G. & Megill, W. 2011. New designs of fin type propulsive devices of robotic fish. *IEEE 15<sup>th</sup> International conference on advanced robotics: New Boundaries for robotics*, pp. 625–630.
- Xiao, Q. & Zhu, Q. 2014. A review on flow energy harvesters based on flapping foils. *Journal of fluids and structures* **46**, 174–191.
- Xie, Y., Lu, K. & Zhang D. 2014. Investigation on energy performance of an oscillating foil with modified flapping motion. *Renewable energy* **63**, 550–557.

## **The co-influence of noise and carbon dioxide on humans in the work and living environment**

A. Traumann<sup>1</sup>, V. Urbane<sup>2</sup>, J. Ievins<sup>2</sup> and P. Tint<sup>3,\*</sup>

<sup>1</sup>Tallinn University of Applied Sciences, Institute of Clothing and Textile, Pärnu mnt. 62, EE10135 Tallinn, Estonia

<sup>2</sup>Riga Technical University, Faculty of Engineering Economics and Management, Institute of General and Civil Safety, Kalnciema 6, LV-1048 Riga, Latvia

<sup>3</sup>Külasema Village Society, EE94744 Muhu, Saaremaa, Estonia

\*Correspondence: [info@piiatint.ee](mailto:info@piiatint.ee)

**Abstract.** The aim of the paper is to investigate the co-influence of noise and carbon dioxide on people in different situations (inside/outside houses/classrooms) depending on the traffic intensity, the fuel used for heating in residential buildings etc.). All the measurements and the questionnaire have been carried out during the autumn of 2019 (at the mean temperature of 5–10 °C). Riga has a more intensive traffic compared to Tallinn and has greater problems of exceeding the permissible noise levels. The levels of carbon dioxide inside classrooms are also very high in Latvia (1,500–2,000 ppm). The concentration of carbon dioxide outside buildings is low in the forest areas (measured in the south of Estonia), being 340–350 ppm. In regional towns, it is 500 ppm (measured in autumn-winter near a busy street). The co-influence of noise and carbon dioxide on the residents has been investigated by using the Weinstein questionnaire. High carbon dioxide levels cause fatigue. Although it was not particularly pointed out by the residents questioned in a panel house with small apartments, the air was considered to be stuffy. The house is situated near a busy street, so the problems with noise are higher. ANOVA statistics has been used for the questionnaire ( $p < 0.001$ ,  $\alpha = 0.93$ ). The decrease of noise and carbon dioxide levels help people stay healthy and the environmental impact from the investigation is emphasising the necessity and providing possibilities to decrease the concentration of CO<sub>2</sub> in the ambient air.

**Key words:** environmental noise, carbon dioxide, risk assessment.

### **INTRODUCTION**

Environmental noise is accumulation of the noise pollution created outdoors. This noise can be produced by transport, industrial and entertaining undertakings. Noise is frequently defined as an 'unwanted sound'. Within this context, environmental noise is mostly available in some form in all zones of human, animal or environmental activities. The special effects in individuals of exposure to environmental noise may differ from sensitive to physiological and psychosomatic (Job, 1988; Guidelines..., 2000; Kivikangur, 2016).

The reduction of the carbon dioxide concentration in the environmental air is an incredible task for innovative people today. One of the origins of carbon dioxide is road transport and avoiding the usage of public transport (electric-based etc.), giving

preference to personal cars. This is also causing high noise levels in the outside environment, predominantly in big cities. The concentration of CO<sub>2</sub> is also high indoors, particularly in schools (Urbane et al., 2004a, 2004b; Wargocki & Wyon, 2013; Vilcane et al., 2015). The dust atoms adsorb on their surface different chemical constituents from the nearby air that also could have an effect on people's health and be the cause of other environmental complications. There are other sources from where the carbon dioxide could be formed indoors, like heating with firewood.

Chemicals that can cause hearing damage and balance troubles when inhaled, swallowed or absorbed through the skin – are found in certain pesticides, solvents and drugs, and the risk of their negative effects progresses when the workers are exposed to elevated noise levels (Sliwincka-Kowalska et al., 2003; Particle..., 2013). OSHA records that one precise kind of hearing loss – speech discrimination dysfunction – is particularly hazardous because the affected worker cannot separate co-workers' voices or notice signals from ambient noise. The research on ototoxicants and their interactions with noise is limited (Air..., 2015).

Do people really percept the risk of the increase of carbon dioxide concentration in the air and noise influence on health? Does the risk perception really exist? (Rundmo & Nordfjaern, 2017). The risk perception and validation have been studied regarding the city transport in Norway. The results do not support the idea that the risk perception could be hypothesized as a thoughtful concept of accident probability assessment and decision of the severity of the consequences. On the basis of the investigated literature, the risk perception related to the noise and air pollution consequences on health has not been studied profoundly.

The aim of the paper is to investigate the co-influence of noise and carbon dioxide on people in different situations (inside/outside houses/classrooms) depending of the traffic intensity, the fuel used for heating in residential buildings, etc.).

Five hypotheses have been formulated and the area to prove them concerning residents in the investigated panel house ( $N = 71$ ;  $N_{\leq 50} = 25$  persons;  $N_{>50} = 46$  persons):

H1. It is hard to concentrate in noisy surroundings.

H2. I get mad when I hear loud music.

H3. I am easily awakened by noise.

H4. I often experience headaches due to noise in my apartment.

H5. I feel the air is not clean. The air in the living-room is stuffy.

The opinions of two groups of people have been compared.

## **MATERIALS AND METHODS**

For measurements of carbon dioxide, the following standard methods have been used: EVS-EN-ISO 7726:2003 'Ergonomics of the thermal environments - Instruments for measuring physical quantities'. The measuring equipment used – TESTO 435. TESTO 435 allows to measure the concentration of CO<sub>2</sub> (0 ppm – 10,000 ppm).

For measurements of noise acoustics, the noise metre TES 1358 (type 1) with the range of 30–130 dB (A) has been used. The methods are presented in ISO 9612: 'System – Guidelines for the measurement and assessment of exposure to noise in a working environment' and ISO 1996-2: 'Acoustics – Description, measurement and assessment of environmental noise – Part 2: Determination of sound pressure levels'.

The noise measurements have been carried out in Riga and Tallinn, as well as in rural areas of Estonia and Latvia, during autumn of 2019. The measured points are presented in Table 1. The air pollutant is carbon dioxide. The noise and carbon dioxide levels have been measured outside and inside the houses. In Riga, the measurements have been carried out in the centre on the city.

**Table 1.** The results of measurements of noise (dBA) and carbon dioxide (CO<sub>2</sub>)

Object	Noise level *± 1 dB	CO <sub>2</sub> level **± 10 ppm	Notes
Apartments in Tallinn			
1) rooms facing a motor road	30.0–33.0*; with opened window: ≤ 60 dB(A)	628**	Impossible to sleep with an opened window
2) rooms facing the courtyard	30.4–31.1	622	
3) environmental data	74–79 (45 cars pass by in a minute) <sup>1</sup>	503	Busy traffic at 6:30 pm
Houses in the rural area in the south of Estonia <sup>2</sup>			
1) houses in the rural area in the south of Estonia <sup>2</sup>	29.0–30.0	1,308	Heating by firewood
2) environmental data around the houses	30.0–31.0	326	Houses in the forest (Figs 6, 7)
Houses on the island Muhu in the west of Estonia <sup>3</sup>			
1) inside the houses	29.0–30.0 Especially from tractors 65 dB(A)	840–900–1,257	Heating by firewood; temperature: 24.4 °C; humidity: 34%
2) environmental data near the houses	29.0–30.0	450–480–543	
Hotel near the Daugava River, Riga, Latvia			
1) inside a hotel	35.0–55.0 (opened window)	535	Heavy traffic, 17.00 (Figs 3, 4)
2) outside in front of the hotel	70.–79.0	487	Heavy traffic
Schools in Latvia			
1) inside the classrooms	35.0–40.0	1,500–2,000	
2) outside	70–79.0 in the capital; 0–60 in the suburbs	513–850	Depending on the season. In summer, the concentration is higher.
In a small car (Skoda-Fabia)			
1) inside the car	Noise from wheels and music: 45.0–55.0	1,348	Temperature inside 18 °C; humidity 51%
2) outside the car	65.0–66.0	487	

\* Uncertainty of measurements; <sup>1</sup> The number of driving cars (mainly private cars) has been counted, using 5 minutes (N = 225); <sup>2</sup> Isolated houses in the forest; <sup>3</sup> Russian-type village houses (10, very near).

An interview method has been used to assess the annoyance caused by noise and impurities of the air (CO<sub>2</sub>) inside the residential building (Fig. 3) and in twenty schools in Latvia. The main type of noise is traffic noise.

In Estonia, the residential buildings have been selected in Tallinn and in rural areas such as the Muhu Island and Otepää in the south of Estonia (Fig. 1). The noise and CO<sub>2</sub> levels have been measured inside and outside the buildings. In Tallinn, the inhabitants of a residential panel type building (Fig. 2) have been asked to fulfil a questionnaire. Ninety questionnaires have been provided, the response rate being 79. Windows of the apartments (of the panel building in Tallinn) face a busy street or a courtyard.

In the qualitative study, the respondents were asked separate questions about annoyance caused by each source of noise, such as: 'How much annoyance do you feel about the individual indoor and outdoor noises?' 'How would you describe your sensitivity to noise?' The reactions to noise in specific situations have been investigated through the questionnaire.

The Weinstein's scale has been used for investigation of sensitivity to noise (Ryu & Jeon, 2011):

1. I cannot concentrate well in noisy surroundings (Int+Ext)\*
2. I complain once I am out of patience due to a noise (Int+Ext)
3. I often desire a quiet environment (Int+Ext)
4. I am annoyed even by low noise levels (Int)
5. There are often times when I want complete silence (Int+Ext)
6. I get mad when I hear loud music (Int)
7. Noise disturbs my concentration when reading a newspaper (Int)
8. I cannot fall asleep easily because of the noise (Int+Ext)
9. I find it hard to relax in a noisy place (Int+Ext)
10. I would not like to live on a noisy street, even if the house/apartment were nice (Ext)
11. I would not like to live across the street from a fire station (Ext)
12. I would not like to live in a house with poor noise insulation (Ext)
13. I am easily awakened by noise (Int)
14. I am confused by noise (Int)
15. Noise during a meal makes me uncomfortable (Int)
16. I feel uneasy when I hear noise (Int)
17. I often experience headaches and/or digestive disorders due to noise (Int)
18. I feel that the air in the room is not clean (Int).

\* *Int- internal*

*Ext- external.*

The last question to find out about the influence of the high carbon dioxide levels has been added to the Weinstein original questionnaire. To evaluate the annoyance of noise and CO<sub>2</sub>, the survey has used a seven-point verbal scale comprised of the following responses: not at all, insignificantly, somewhat, moderately, considerably, highly and extremely. The respondents from the panel-house apartments rated their annoyance and sensitivity to noise. Among the respondents, 55% are from the age group 20–60 years, 20% are retired persons (mean age 76) and 25% are children: Replies of the residents have been divided into two groups: > 50 years old (46 filled forms) and ≤ 50 years old (25 filled forms).

A one-way analysis of variance (ANOVA) has been conducted by using sensitivity scores of each group of indoor and outdoor noises, including carbon dioxide levels).



**Figure 1.** A private house near the Est-Lat border.



**Figure 2.** The investigated residential house is on the right (behind the trees).

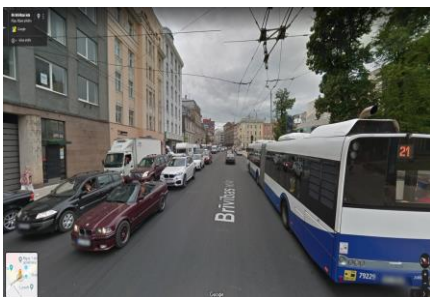


**Figure 3.** The measurement of environmental noise in Riga.



**Figure 4.** Noise and CO<sub>2</sub> investigations in Riga (hotel).

## Theory

The investigations on the co-influence of noise and carbon dioxide on the humans are limited (Sliwinska-Kowalska et al., 2003), but the importance for such investigations are certainly needed due to the increase of the carbon dioxide level in towns and the growing intensity of road transport, particularly in summer.

Millions of workers are wide-opened to noise in the workrooms each day and when uncontrolled, noise exposure may cause an everlasting hearing damage. Investigations show exposure to definite chemicals, called ototoxicants, which may cause hearing loss or stability problems, irrespective of the noise exposure. Substances including certain pesticides, solvents and drugs that contain ototoxicants can undesirably affect the ear, causing hearing loss, and/or affecting the balance (Fig. 4).

Another worldwide exposure is tobacco, consumed by approximately 1.3 billion of the global population (Shafey et al., 2003; Ferrite & Santana, 2005). Tobacco may also affect cochlear blood supply, because it causes peripheral vascular changes, such as increased blood viscosity and reduced available oxygen.

It is widely recognised that exposure to air smog can lead to a wide variety of opposing health effects (Brunekreef & Holgate, 2002). Air pollution is, for example, causing the increased risks of respiratory (Gehring et al., 2013) and cardiac diseases (ESCAPE, 2007). Exposure to ambient air contamination has also been suggested to



increase the depression signs; however, few epidemiological studies have examined these special effects. Exposure to ambient air pollution may be related to the weakened mental health, including depression (Zijlema et al., 2016). Four European general population cohorts have found no consistent evidence for a link between the ambient air pollution (consisting of PM<sub>2.5</sub>, PM<sub>10</sub> & nitrogen dioxide) and the depressed attitude.

The Nordic Expert Group (Johnson & Morata, 2010) published a comprehensive review of occupational exposure to chemicals and hearing loss, summarising the writings on this topic from 1950 to November 2007. The chemicals were chosen based on the widespread indication on their ototoxicity. The review includes medications, organic solvents, metals, pesticide, and polychlorinated biphenyls. Contacts near or below the present occupational exposure limits (OEL) have resulted in hearing deficiencies for the following chemicals: styrene, toluene, carbon disulphide, lead, mercury and carbon monoxide. Another assessment of the effects of ototoxic substances on animals and humans was conducted in 2009 and the results showed that ‘lead, styrene, toluene and trichloroethylene are ototoxic and ethyl benzene, n-hexane and p-xylene are possibly ototoxic at concentrations that are related to the occupational location’. The authors also note that carbon monoxide possibly interrelates and toluene does interact with noise exposure to worsen hearing loss.

Workers are regularly exposed to numerous features and substances that are hazardous to health (Fig. 5), (Campo et al., 2013; Traumann, 2014). In 2005, about 30% of the European workers recounted being exposed to noise during at least a quarter of the time spent in their work environment (Parent-Thirion et al., 2007). Even though occupational noise exposure has long been documented in the US and Europe as the most damaging factor to hearing, the impact of chemical-induced hearing loss on workers should not be undervalued (Morata, 2003).

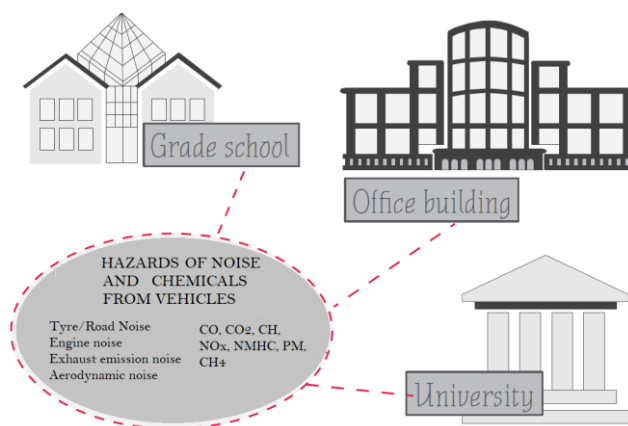


**Figure 5.** The noise and carbon dioxide pollution (Traumann, 2014).

Harmful exposure to ototoxicants (Fischer et al., 2015; Exposure..., 2018) may happen through breath, eating, or skin absorption. Health effects caused by ototoxic chemicals differ grounded on exposure occurrence, strength, length, workstation exposure to other hazards, and individual factors such as oldness. Properties may be transient or everlasting, can affect hearing compassion and result in a standard threshold

shift. As chemicals can affect central portions of the auditory system (nerves in the central nervous system, the routes to the brain), not only do noises need to be louder to be identified, but also they lose clarity. The risk of workplace injuries increase due to the incapacity to hear co-workers, environmental sounds and cautionary signals (Job, 1988).

Industrial ototoxic chemicals have been assessed predominantly through animal studies (Campo et al., 2013). Bergström & Nyström (1986) published the results of the study of hearing quality of 319 Swedish employees. The study reveals that 23% of the workers who were also in contact with chemicals, suffer from hearing impairment. In the studies of Fechter et al. (2004), acrylonitrile was directed internally to rats in a high dose of  $50 \text{ mg kg}^{-1} \text{ d}^{-1}$  for 1–5 days. Acrylonitrile potentiates everlasting noise-induced hearing loss particularly for high-frequency tones and particularly when acrylonitrile and noise are issued repetitively. The outside hair cells (OHCs) are the main objective of toxicity.

Environmental noise is recognised as a key health problem. The challenging health effects (general irritation, speech interference and sleep disorders) of transportation noise are well documented (Guidelines..., 2000). Unlike many other environmental problems, noise pollution is still worsening. In Sweden (Öhrström et al., 2006a, 2006b), the number of persons exposed to traffic noise exceeding the outdoor guidelines ( $L_{Aeq,24h} = 55 \text{ dB}$  and  $L_{Amax} = 70 \text{ dB}$ ) is approximately 2 million or 25% of the population.

People are exposed to noise inside their own homes and from neighbouring houses daily. The noises in residential buildings are numerous, including such things as floor impact sounds, airborne sounds like music and drainage noises from neighbouring units, as well as traffic noises from outside. In addition, ventilation systems and home appliances like refrigerators emit constant, steady noises. Noise in the living environment is an important factor in residential satisfaction (Sliwinska-Kowalska et al., 2003; Nijland et al., 2007; Preventing..., 2018).

## RESULTS

The objects for measurements were as follows:

- a) Apartments in a smoke-free panel house in Tallinn (Fig. 2), 20 m from a busy street, a bedroom facing the driveway or the courtyard. The questionnaire was completed by 71 residents of the panel house (Fig. 2);
- b) House in the countryside (Fig. 1) in the south of Estonia, near the Latvian border;
- c) House(s) on the island (Muhu) in the west of Estonia (countryside);
- d) Hotel and outdoors near the hotel in the centre of Riga, near the Daugava River;
- e) Schools in Latvia;
- f) Inside a small car (Skoda-Fabia).

Carbon dioxide and noise have been measured at all of the measurement objects. The results are provided in Table 1.

Road transport is not the only source of constant noise in Riga. There is also railway, which noise level must be regulated in accordance with the EU Directives. In 2019, the number of complaints from residents of Riga in connection with large-scale road works increased. The highest noise levels in Riga are observed in the morning and evening hours, due to the traffic flow. According to Riga Department of Housing and

Environment, 120,000 people live in areas of acoustic discomfort, due to the noise from roads, the airport, industrial activity in the urban environment (Öhrström et al., 2006a, 2006b; Nijland et al., 2007; NZTA, 2014). Noise above 60 dB can cause cardiovascular diseases and nervous system disorders.

**Investigation of air impurity and noise in isolated houses in South Estonia**

Six isolated houses have been investigated. The results of the carbon dioxide and noise measurements inside the houses are as follows: 1) the elderly home: 873–1,322 ppm; noise: 40.1 dB(A); 2) the private houses: 1,098–1,316 ppm (firewood heating); 521–564 (distance heating) (Figs 6, 7). Outside the houses, the carbon dioxide concentration was from 320–353. The mean data are presented on the figures below. The noise levels differed - in the country area: 35.1 dB(A); in a small town near the investigated private houses - 350 ppm and the noise 65.2 dB (A).

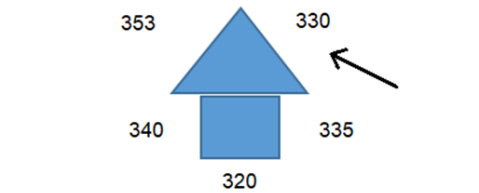


**Figure 6.** Elderly home, outside CO<sub>2</sub> (ppm).

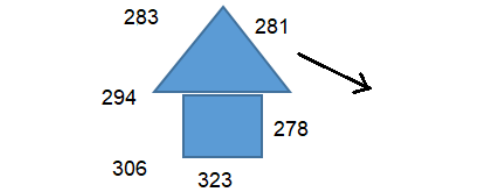


**Figure 7.** Private house, outside CO<sub>2</sub> (ppm).

**Survey of the opinions regarding noise and CO<sub>2</sub> disturbance in residential houses**

A reliability analysis has been conducted to ensure the internal consistency of the sensitivity questionnaire. The Cronbach’s alpha ( $\alpha$ ) was 0.93, indicating that the 18-item questionnaire had high internal consistency. The  $p$ -value was  $< 0.001$ .

The results (Table 2, Fig. 8) show that the inside noise is bothering people mostly on weekends. The inhabitants are mostly disturbed by the traffic noise at night. The investigation was carried out in autumn, but the people told that the noise was more disturbing in summer when windows need to be open as the outside temperature of the air is high and it is difficult to breath. The residents are highly disturbed by the noise when reading newspapers, they cannot fall asleep easily because of noise, and they do not want to live in the house with a poor noise insulation.

**Table 2.** Results of the noise sensitivity survey (Weinstein’s questionnaire)

Question number		7-point scale						
1	2	3	4	5	6	7	8	9
4.6 ± 0.6	2.1 ± 1.6	4.7 ± 1.3	2.4 ± 1.5	3.5 ± 1.5	5.6 ± 1.7	5.9 ± 0.1	5.8 ± 1.2	6.9 ± 0.9
Score, SD								
Question number								
10	11	12	13	14	15	16	17	18
5.2 ± 0.8	6.5 ± 0.5	6.8 ± 0.8	5.2 ± 0.7	5.3 ± 0.7	5.4 ± 0.6	5.8 ± 1.2	4.0 ± 1.4	5.4 ± 0.6

Score, SD

The investigated house was renovated in 2016 (the inside walls were covered with heat- and soundproof material). Carbon dioxide was not very disturbing in autumn. The answer was mostly ‘considerably annoying’.

The questions 2, 4, 5, 17 have low numbers (unsatisfied) as they were assessed as disturbing factors by the older group of residents (age > 50 years). The younger people are more used to listening to music at lunch or reading newspapers.

The two groups of residents (> 50 years (I); ≤ 50 years (II) old) have been compared.

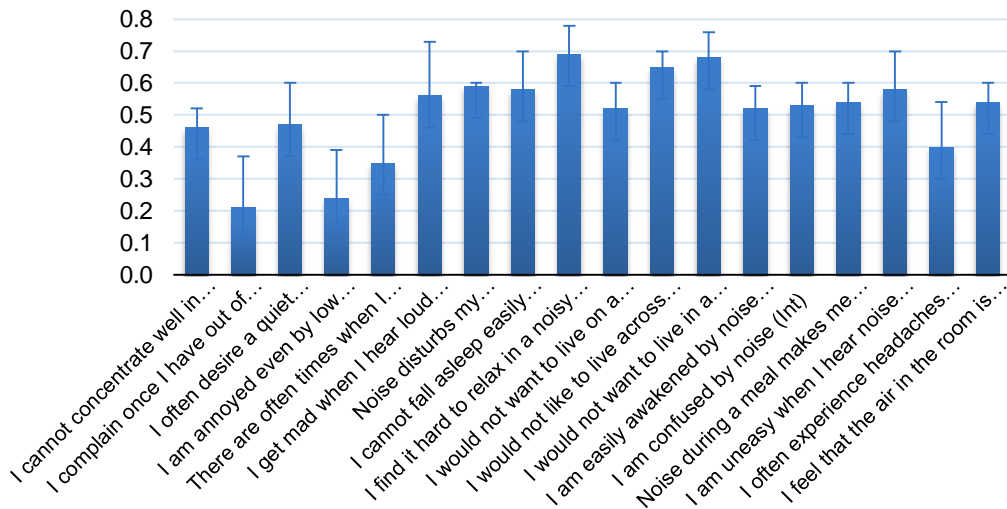


**Figure 8** Results of the noise sensitivity survey according Weinstein's scale.

### Analysis of hypothesis

The hypothesis was proposed to find out about the influence of noise and carbon dioxide on people's health in panel-type apartments (Table 3).

**Table 3.** Statistical analysis of the main hypothesis

Hypothesis and results	Categories	M	SD	t-value
H1 It is impossible to concentrate well in noisy surroundings. <b>Confirmed</b>	Noise and health	5.1 (I) 4.5 (II)	0.6	1.695
H2 I get mad when I hear loud music. <b>Not confirmed</b>	Noise and health	6.2 (I) 4.5 (II)	1.7	0.18
H3 I am easily awakened by noise. <b>Confirmed</b>	Noise and health	5.3 (I) 5.1 (II)	0.7	1.02
H4 I often experience headaches due to noise in my apartment. <b>Not confirmed</b>	Noise and health	5.2 (I) 3.8 (II)	1.4	0.23
H5 I feel the air not clean. The air in the living room is stuffy. <b>Confirmed</b>	CO <sub>2</sub> and health	5.4	0.6	13.40

The young people (≤ 50 of age) are not so sensitive to noise, but they are sensitive to carbon dioxide.

## DISCUSSION AND CONCLUSIONS

The results of the current investigation have indicated that noise and carbon dioxide levels are high in big cities and as Riga is bigger than Tallinn and has more transport (also a railway), the investigated values are higher in Riga, Latvia. The main part of the investigation includes the study of influence of noise on people living in residential buildings near a driveway. It shows that the outside noise disturbs the inhabitants as much as the inside noise created by their neighbours, particularly at weekends.

The results of the Ryu & Jeon (2011) survey specify that the most frequently mentioned indoor noise sources are children jumping and running (67%), i.e. the floor impact noise, and playing musical instruments and people talking, i.e. the airborne noise. The road traffic noise (7%) is the most frequently mentioned outdoor noise (Ryu & Jeon, 2011).

Road noises are not mentioned as a disturbing factor in the Ryu & Jeon (2011) study. In the current study, the road noise is the main disturbing factor. The difference between the two investigations can be explained by different inhabitants in the houses. The panel building in Tallinn (built in the 1960s) is mostly populated by retired people, the proportion of little children is 5.0. All indoor noise sources were recorded at night in the rooms of two apartments with a low background noise level of 25 dBA.

Blocks of flats in Estonia and Latvia have noise-dumping qualities. Tight double windows give higher carbon dioxide levels.

Ryu & Jeon (2011): complaints regarding noises in living environments, including building noises and noises from household electric appliances, are increasing rapidly. The influence of sensitivity on annoyance was greater for indoor noise than for outdoor noise. In addition, different approaches toward indoor and outdoor noises may explain the result of the present study. Outdoor noises initiate from various undetermined sources people are less able to cope with. The correlation coefficients ( $r = 0.29\text{--}0.39$ ) for annoyance between noises are lower than those ( $R = 0.48\text{--}0.59$ ) between various indoor noise sources. The annoyance from indoor noises is greater than outdoor noises. Nijland et al. (2007) found that noises (mainly traffic noises) in residential locations influence the level of satisfaction with the living environment, and noise-sensitive people consider moving out more often. This indicates that a lower noise exposure in a residential space might be an important factor when deciding whether to obtain a house or to move out. The possibilities for moving out (changing the place of living, apartment) depends on the standard of living in the particular country and also on the age of people who would like to move out. In poor countries, it is not very easy to move out, as it funds are needed. Another problem is the age of inhabitants: older people are not able to move out any more.

The decrease of noise and carbon dioxide levels help people staying healthy and the environmental impact from the investigation is focusing the attention on the necessity and possibilities to decrease the concentration of CO<sub>2</sub> in the ambient air.

The future research can be carried out in hot environments and in summer time, when the noise and CO<sub>2</sub> levels in towns and in apartments are higher. It does not concern schools as they have holidays in summer.

Increasingly more investigations of air impurities and the quality of ventilation inside living and working premises are appearing, considering a new type of very dangerous hazards (Corona, Ebola, SARS) for the human health.

## REFERENCES

- Air Quality Guide for Particle Pollution*. 2015. Office of Air Quality and Radiation (6301A). <https://www.airnow.gov/index.cfm?action=pubs.aqguidepart>.
- Bergström, B. & Nyström, B. 1986. Development of hearing loss during long-term exposure to occupational noise- a 20 year follow-up study. *Scand. Audiol.* **15**, 227–234.
- Bruneekreef, B. & Holgate, S.T. 2002. Air pollution and health. *Lancet* **360**, 1233–1242. [https://doi.org/10.1016/S0140-6736\(02\)11274-8](https://doi.org/10.1016/S0140-6736(02)11274-8).
- Campo, P., Morata, T.C. & Hong, O. 2013. Chemical exposure and hearing loss. *Disease-a-Mont* **59**, 119–138. doi: 10.1016/j.disamonth.2013.01.003
- ESCAPE (European Study of Cohorts for Air Pollution Effects). 2007. ESCAPE Homepage. <http://www.escapeproject.eu>
- Exposure to certain chemicals may cause hearing loss*. 2018. Safety+Health. The Official magazine of the NSC Congress & Expo. <https://www.safetyandhealthmagazine.com/articles/16859-exposure-to-certain-chemicals-may-cause-hearing-loss-osha-warns>.
- Fechter, L.D., Gearhart, C. & Shirwany, N.A. 2004. Acrylonitrile Potentiates Noise-Induced Hearing Loss in Rat. *J. Assoc. Res. Otolaryngol.* **5**, 90–98. doi: 10.1007/s10162-003-4028-8
- Ferrite, S. & Santana, V. 2005. Joint effects of smoking, noise exposure and age on hearing loss. *Occup Med.* **55**, 48–53. <https://doi.org/10.1093/occmed/kqi002>
- Fischer, P.H., Marra, M. & Ameling, C.B., Hoek, G., Beelen, R., de Hoogh, K., Breugelmans, O., Kruize, H., Janssen, N.A. & Houthuijs, D. 2015. Air pollution and mortality in seven million adults: the Dutch environmental longitudinal study duels. *Environ. Health Perspect* **123**, 697–704. doi: 10.1289/ehp.1408254
- Gehring, U., Gruzdeva, O., Agius, R.M., Beelen, R., Custovic, A., Cyrus, J., Eeftens, M., Flexeder, C., Fuertes, E., Heinrich, J., Hoffmann, B., de Jongste, J.C., Kerkhof, M., Klümper, C., Korek, M., Mölter, A., Schultz, E.S., Simpson, A., Sugiri, D., Svartengren, M., von Berg, A., Wijga, A.H., Pershagen, G. & Bruneekreef, B. 2013. Air pollution exposure and lung function in children: the ESCAPE Project. *Environ. Health Perspect* <http://dx.doi.org/10.1289/ehp.1306770>
- Guidelines for Community Noise*. 2000. Berglund, B., Lindvall, D.H. & Schwela, D.H. (eds.). World Health Organization (WHO), Geneva, 21 pp.
- Job, R.F.S. 1988. Community response to noise: a review of factor influencing the relationship Between noise exposure and reaction. *J. Acoustic. Soc. Am.* **83**, 991–1001.
- Johnson, A.C. & Morata, T.C. 2010. The Nordic Expert Group for criteria documentation of health risks from chemicals: *Occupational exposure to chemicals and hearing impairment*. University of Gothenburg, Gothenburg, Sweden, p. 142.
- Kivikangur, R. 2016. *Transport noise in detailed plans and environmental impact assessments in Estonia*. Master of Science Thesis, University of Life Sciences, Tartu, Estonia, 86 pp.
- Morata, T. 2003. Chemical exposure as a risk factor for hearing loss. *J. Occup. Environ Med.* **45**, 676–682.
- Nijland, H.A., Hartemink, S., van Kamp, I. & van Wee, B. 2007. The influence of sensitivity for road traffic noise on residential location: does it trigger a process of spatial selection? *J. Acoustic. Soc. Am.* **122**, 1595–1601.
- NZTA. 2014. *Guide to state highway road surface noise*. New- Zealand Transport Agency. <http://www.nzta.govt.nz/assets/resources/road-surface-noise/docs/nzta-surfaces-noise-guide-v1.0.pdf> (Accessed 10.03.2019).
- Parent-Thirion, A., Fernandez Macias, E., Hurley, J. & Vermeulen, G. 2007. *Fourth European Working Conditions Survey*. European Foundation for the Improvement of Living and Working Conditions. Dublin, 139 pp.
- Particle Pollution and Your Health. US EPA Office of Air and Radiation. 2013. [https://www.airnow.gov/index.cfm?action=particle\\_health.index](https://www.airnow.gov/index.cfm?action=particle_health.index)

- Preventing Hearing Loss caused Chemical (Ototoxicity) and Noise Exposure. *Safety and Health Information Bulletin*. 2018. No. 2018–124. US Department of Labor. OSHA. <https://www.osha.gov/dts/shib/shib030818.html>
- Rundmo, T. & Nordfjaern, T. 2017. Does risk perception really exist? *Safety Science* **93**, 230–240.
- Ryu, J.K. & Jeon, J.Y. 2011. Influence of noise sensitivity on annoyance of indoor and outdoor noises in residential buildings. *Applied Acoustics* **72**, 336–340. doi: 10.1016/j.apacoust.2010.12.005
- Shafey, O., Dolwick, S. & Guindon, G.E., eds. 2003. *Tobacco control country profiles*. Atlanta: American Cancer Society. [http://www.who.int/tobacco/global\\_data/country\\_profiles/Introduction.pdf](http://www.who.int/tobacco/global_data/country_profiles/Introduction.pdf).
- Sliwinska-Kowalska, M., Zamysłowska-Szmytko, E., Szymczak, W., Kotyło, P., Fiszer, M., Wesolowski, W. & Pawlaczyk-Luszczynska, M. 2003. Ototoxic effects of occupational exposure to styrene and co-exposure to styrene and noise. *Journal of Occupational and Environmental Medicine* **45**(1), 15–24.
- Traumann, A. 2014. *Improvement of work environment through modelling the prevention of health risks focusing on indoor pollutants*. PhD thesis. Tallinn, Estonia, 80 pp.
- Urbane, V. 2004a. The Problems of an Air Conditioning of the Premises. *Publication in a Scientific Journal of the Series of Scientific Journal of RTU*. <https://ortus.rtu.lv/science/en/publications/2277>. Accessed 9.9.2019.
- Urbane, V. 2004b. The Legislation of Latvian Republic. A Health and a Computer. *Publication in a Scientific Journal of the Series of Scientific Journal of RTU*. <https://ortus.rtu.lv/science/en/publications/2276>. Accessed 9.9.2019.
- Vilcane, I., Urbane, V., Tint, P. & Ievins, J. 2015. The comparison study of office workers' workplace health hazards in different type of buildings. *Agronomy Research* **13**(3), 846–855.
- Wargocki, P. & Wyon, D.P. 2013. Providing better thermal and air quality conditions in school classrooms would be cost-effective. *Building and Environment* **59**, 581–589.
- Zijlema, W.L., Wolf, K., Emeny, R., Ladwig, K.H., Peters, A., Kongsgård, H., Hveem, K., Kvaløy, K., Yli-Tuomi, T., Partonen, T., Lanki, T., Eeftens, M., de Hoogh, K., Brunekreef, B., BioSHaRE, Stolk, R.P. & Rosmalen, G.M. 2016. The association of air pollution and depressed mood in 0,928 individuals from European cohorts. *International Journal of Hygiene and Environmental Health* **219**, 212–219.
- Öhrström, E., Hadzibajramovic, E., Holmes, M. & Svensson, H. 2006a. Effects of road traffic noise and sleep: Studies on children and adults. *Journal of Environmental Psychology* **26**, 116–126.
- Öhrström, E., Skanberg, A., Svensson, H. & Gidlöf-Gunnarsson, A. 2006b. Effects of road traffic noise and the benefit of access to quietness. *Journal of Sound and Vibration* **295**, 40–59. doi: 10.1016/j.jsv.2005.11.034

## **Variable velocity system for evaluating effects of air velocity on Japanese quail**

M.O. Vilela<sup>1,\*</sup>, R.S. Gates<sup>2</sup>, S. Zolnier<sup>1</sup>, M. Barbari<sup>3,\*</sup>, C.G.S. Teles Junior<sup>1</sup>,  
R.R. Andrade<sup>1</sup>, K.S.O. Rocha<sup>1</sup>, I.F.F. Tinôco<sup>1</sup>, C.F. Souza<sup>1</sup>, L. Conti<sup>3</sup> and  
G. Rossi<sup>3</sup>

<sup>1</sup>Federal University of Viçosa, Department of Agricultural Engineering, Av. Peter Henry Rolfs, s/n Campus University of Viçosa, BR36570-900 Viçosa, Minas Gerais, Brazil

<sup>2</sup>Iowa State University, Departments of Agricultural and Biosystems Engineering, and Animal Science, Egg Industry Center, 1202 NSRIC, Ames, IA 50011, USA

<sup>3</sup>University of Florence, Department of Agriculture, Food, Environment and Forestry, Via San Bonaventura, 13, IT50145 Firenze, Italy

\*Correspondence: monique.vilela@ufv.br; matteo.barbari@unifi.it

**Abstract.** This study documents the design and performance of a system to apply different magnitudes of air velocity to Japanese quail, to evaluate the combined effects of velocity, temperature and humidity on bird behaviour, performance and welfare. The system was developed to simulate observed field conditions occurring in regions with high winds where quail are raised in curtain-sided housing. System performance consisted of characterizing air velocity distribution in cages downstream of the air velocity which was directed at the front of the cages. The system consisted of two fans attached to a 25 cm PVC tube, one at each end, with the outlet airflow directed through a continuous slot over the cage front at the feeder. The design and performance of this experimental system was evaluated, with six such systems were built and utilized in research trials. To assess system performance, air velocity was measured at 275 points per cage uniformly arranged along the three dimensions (length, width and height) in eight cages with zero, 1, 2 or 3 m s<sup>-1</sup> nominal velocity setpoints. Spatial distribution of velocity was analysed by mapping and from descriptive statistics, with attention to the zone closest to the feeder where birds must go to eat. There was no significant difference ( $P > 0.05$ ) found in mean paired difference of air speed data measured for pairs of front portion cages with similar velocities. A significant positive correlation was found ( $P < 0.001$ ) between the measured air velocity at paired points in the cages subjected to the same velocity treatment. A comparison of measured mean air velocity to the nominal setpoint values used for experiments indicated that careful attention to outlet adjustment is important, especially at higher nominal velocity setpoint as 3 ( $\pm 0.10$ ) m s<sup>-1</sup> which was difficult to achieve with the system. An example of the use of the deployment of the variable velocity system in controlled environment chambers with Japanese quail is provided.

**Key words:** cold stress, effective temperature, engineering design, heat stress, wind chill.

## **INTRODUCTION**

The thermal environment comprises a complex of factors that interact and combine to influence the effective ambient temperature, i.e., perceived by people, poultry and



livestock (Curtis, 1983; ASHRAE, 2017; ASHRAE, 2019). Air temperature, relative humidity, air velocity, pollutant concentration and solar radiation are the main variables that characterize the microclimate and influence the behaviour welfare of livestock and poultry. According to Dhari et al. (2019), as these variables can interfere in the birds' comfort, the productive performance can also be strongly affected. The bird's welfare and performance can be severely impaired when climatic conditions and air quality are not within appropriate ranges (Rojano et al., 2018). Therefore, for a better understanding of climatic variables combination, various indices have been developed to quantify their impacts, e.g. effective temperature, THI and wind chill index.

Despite all the technological progress of the Brazilian poultry sector, the thermal environment in which birds are housed remains one of the main factors affecting production performance (Vilela, 2016; Freitas et al., 2017) since the buildings are largely open. Thus the type of management and climatic characteristics of each region are important for animal facilities project planning due to environmental needs of the species (Santos et al., 2012), including wind direction and velocity, so that the air velocity may be controlled according to need. The magnitude of air velocity levels inside a building favours convective heat transfer between birds and air (Baêta & Souza, 2010). Within certain limits, air velocity and fresh air exchange control the temperature and relative humidity, and are critical for mitigating the negative effects caused by heat stress in birds (Abreu et al., 2011; Bianchi et al., 2015; Oloyo & Ojerinde, 2019). In addition to convection, air velocity is fundamental to evaporative cooling (Oloyo & Ojerinde, 2019).

Blakely et al. (2007) state that the thermal variations of environment are strongly influenced by air velocity, significantly affecting bird performance. High air velocity decreases the effective temperature; thus, in cold environments the presence of air currents can be harmful. However, in warm environments, elevated air velocity can alleviate heat stress and is the basis for modern tunnel ventilation, as reported by Ruzal et al. (2011), that stated that high velocity ( $3 \text{ m s}^{-1}$ ) positively affects hens egg production in hot environments. According to Dhari et al. (2019), air temperature and velocity are the main factors affecting the physiology and performance of broilers. Vigoderis et al. (2010) evaluated the influence of minimum ventilation on thermal comfort, air quality and broiler performance during winter, using a system consisting of three fans with a flow of  $300 \text{ m}^3 \text{ min}^{-1}$ , positioned close to the ceiling, in parallel to the floor and blowing air into the shed. In these conditions, they concluded the minimum ventilation system significantly reduced the temperature inside the broiler house, reflecting on losses at feed conversion, slaughter weight, and animals' productive efficiency.

The annual growth in Brazilian poultry flock had an increase of 2.9% in 2018, highlighting in hens eggs production, with about 4.4 billion dozen produced (IBGE, 2019). Egg production from Japanese quail (*Coturnix coturnix japonica*) is rapidly expanding in Brazil, with annual growth in the number of quails in excess of 3.9% between 2017 and 2018, (IBGE, 2019), with about 297.3 million dozen eggs produced. Therefore, in order to remain competitive, it is extremely important to pay attention to ventilation conditions in Brazilian poultry houses, so as not to harm the birds comfort. Recently, Brazilian producers have expressed concerns regarding the influence of high air velocity in cooler temperatures on the feeding behaviour and egg production in open poultry houses. Hence, one of the most interest regions for analysis of air velocity influence on bird's welfare and performance is the area closest to the feeder. The importance of studying airflow intensity and distribution in this zone is due to its

influence on the animals' ingestive behaviour, which is an aspect closely related to their performance. In view of the importance of air velocity influence on bird welfare and performance, and considering the practical difficulties often encountered in implementing this type of experiment under field conditions, it was determined to be helpful to develop an air velocity control prototype for use in poultry experiments in controlled environments. Other systems have been developed, such as the system developed by Yanagi et al. (2002), for the measurement and control of temperature, relative humidity and air velocity to evaluate heat stress in birds.

However, a system that provides high air velocity in a controlled fashion over the entire face of a birdcage, especially in the feeder zone, similar to exterior rows of cages in open-sided housing, is not readily available. No similar device could be found in the literature, prompting the design and fabrication. The objectives of this study were to: (1) evaluate the performance of the system to provide nominal air velocity setpoints, (2) to evaluate the uniformity of air velocity at common lines and heights where birds approach the feeder, and (3) to evaluate the repeatability of system performance between prototypes.

## **MATERIALS AND METHODS**

### **Velocity Control System**

The velocity control system was fabricated from a simple length of 25cm diameter PVC tubing, with axial fans (Micro Motor Elgin 1/25 MM – 20B, 60 Hz, 11.93 W) mounted on each end (Figs 1–3), each capable of producing  $950 \text{ m}^3 \text{ h}^{-1}$ . A  $10 \times 100 \text{ cm}$  ( $w \times l$ ) long opening was cut along one side of each PVC tube for air to discharge (Fig. 3) toward the cage. Aluminium angles,  $2 \times 2 \times 110 \text{ cm}$  were fastened to the edges of the opening. This facilitated establishment of an air jet to smooth outflow of air toward the cage. A simple solid-state rheostat was used to adjust the fan motor speeds, hence volumetric flow rate and resultant discharge velocity from the tube. A total of six prototypes were fabricated for use in a series of research trials designed to evaluate the effect of velocity, temperature and humidity on Japanese quail behaviour. A typical setup in one of the climate chambers used is illustrated in Fig. 1.

Four climate chambers were used, one for each nominal velocity level: 0, 1, 2, and  $3 \text{ m s}^{-1}$ . Individual dimensions are  $3.2 \text{ m wide} \times 2.44 \text{ m deep} \times 2.38 \text{ m high}$ , and each climate chamber includes equipment for heating, cooling and humidification as highlighted in Fig. 1. The test facilities are located in the Ambiagro group (Research Center of Environment and Agroindustry Systems Engineering) at the Department of Agricultural Engineering at the Federal University of Viçosa (Minas Gerais, Brazil).

### **Experimental Design**

The velocity control system was designed to provide different mean velocities over the feeding zone of cages, simulating situations of strong winds occurrence that affect the batteries of cages located at the ends of opened aviaries, so that velocity effects on bird behaviour could be investigated. Four nominal velocity levels (setpoints) were evaluated:  $0 \text{ m s}^{-1}$ ;  $1 \text{ m s}^{-1}$ ;  $2 \text{ m s}^{-1}$  and  $3 \text{ m s}^{-1}$  representing still air, low, medium and high air velocities in the feeder area. This system provided an outflow of air from the tube over the feeder and into the cage. For each nominal velocity level, two cages were used as replicates. Fan speeds were adjusted using the average velocity readings from

three points along the length of the tube opening, as depicted in Fig. 2, to obtain the desired nominal velocity setpoint values.



**Figure 1.** Inside view of the climatic chambers, where 1 – air conditioning; 2 – air humidifier; 3 – electronic temperature and relative humidity controller (MT-531R plus); 4 and 5 – ventilation tubes; 6 – air heater; 7 and 8 – cages; 9 and 10 – feeders; 11 and 12 – water tanks.

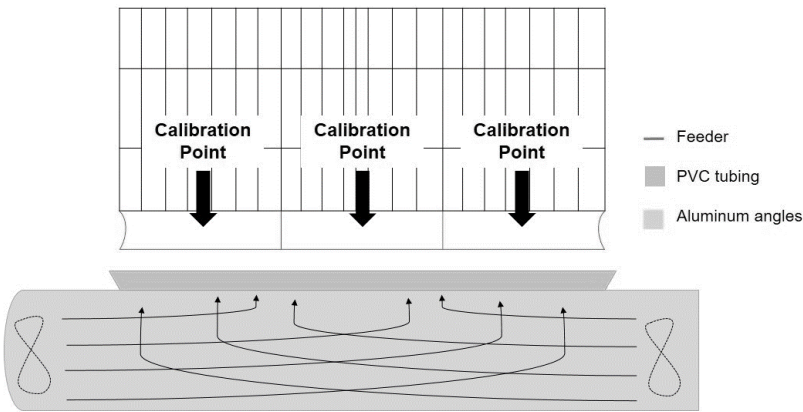


**Figure 2.** Airflow behaviour within the PVC tubes and location of points used for fan velocity adjustment.

A three-dimensional abstraction of the cage system was created, with the origin located at the right rear side of each cage (Fig. 3) with coordinates (x, y, z) referring to lateral, depth and height, respectively. A grid was established, consisting of 275 points/cage within this grid, spaced equidistantly (Fig. 3). Resolution for locating these points was estimated to be  $\pm 10$  mm.

The data collected within the entire cage were useful in order to characterize the distribution of air velocity. However, the main focus was on the velocity in the feeder zone, as is highlighted in Fig. 3. This zone comprises the points located in Lines 3, 4 and 5, measured at 7 points located at the most central portion of the cage (Fig. 3, A). Two

heights, denoted Z0 and Z1, were established for the Line measurements. Z0 is located at the feeder top surface, and Z1 is approximately at the height of the birds when at the feeder.

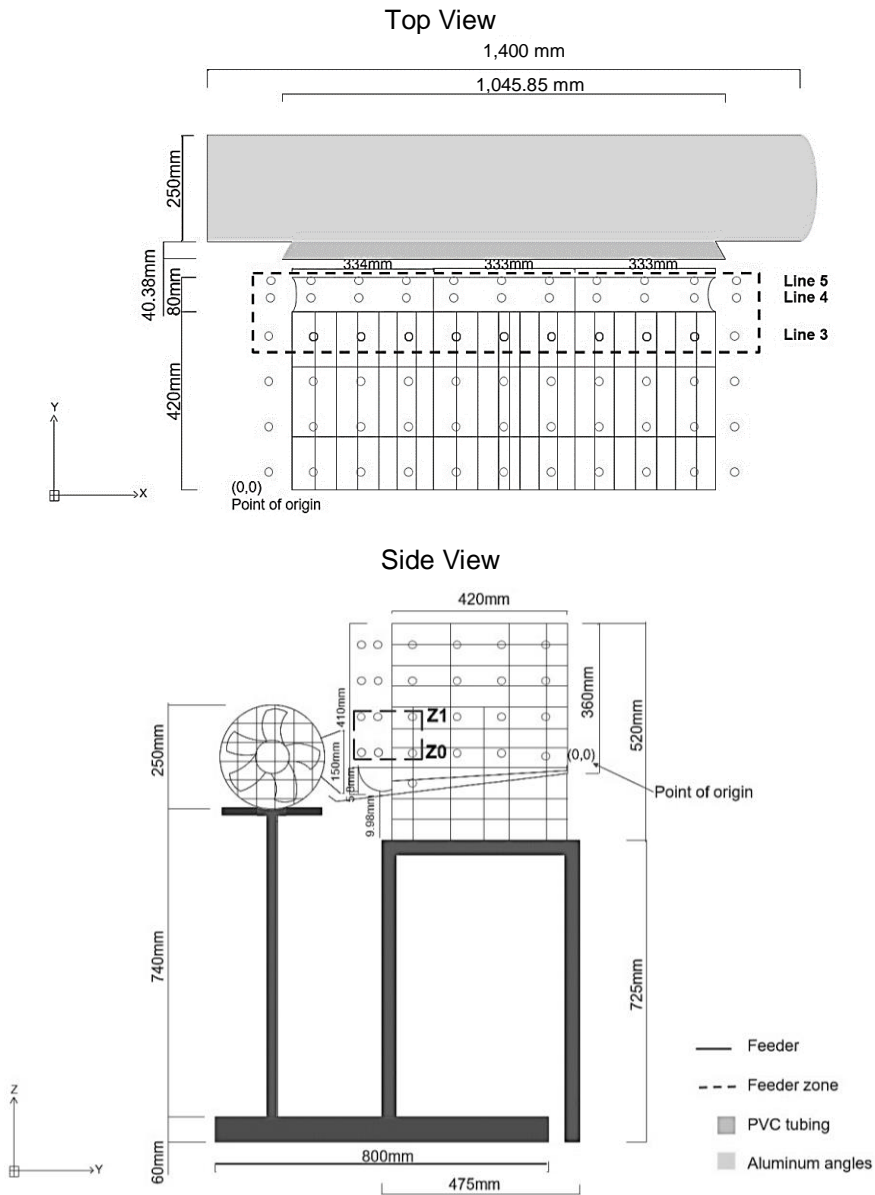


**Figure 3.** Schematic of cage and ventilation control system, with sampling points (275 per cage), Lines (3, 4 and 5) located at different distances from the feeder zone, and heights (Z0, Z1) of primary interest for assessing actual velocities experienced by birds at the feeder. A) Top view. Note the grid includes points located at the exterior of each side of the cage. Line 5 was at the feeder, Line 4 was spaced 40 mm further into the cage, and Line 3 was spaced 115 mm from Line 4. B) Side view, illustrating the location for heights Z0 and Z1 that are used to quantify system performance.

Air velocity was measured using a hot wire anemometer (Testo 425, TESTO INC., Germany) with a 7.5 mm probe diameter, measurement range of 0–20 m s<sup>-1</sup>, display resolution of 0.01 m s<sup>-1</sup>, and 2-s sampling frequency. Velocity measurements at each point were the mean of 30 individual samples taken over a 1-min period to average out fluctuations from turbulence. Care was taken to ensure that the probe tip was oriented perpendicular to the predominant velocity direction, and a single person recorded all measurements to control uncertainty between cages. Air temperature in the climatic chambers during these measurements was 24 °C, considered a comfort average temperature for Japanese quail.

### **Data Analysis**

To evaluate the velocity control system performance and utility for research use, the collected air velocity data were analysed in two different ways.

1) Comparisons between replicate cages subjected to the same velocity set point were made using a paired *t*-test on the mean velocity difference, and a correlations analysis of the collected velocity readings.

2) Spatial distribution of air velocity in the feeder zone was mapped and plotted for assessment of uniformity between replicate cages and between set point velocities.

The velocity difference between identical points in each replicate cage was calculated and subjected to a paired *t*-test to assess if measurements from two replicate cages were different, with the null hypothesis that mean velocity difference was zero. A confidence level of 5% was used. To further assess similarity (or difference) between replicate cages, velocity measurements between cages were subjected to correlation analysis. The Pearson correlation coefficient for velocity measurements between cages was calculated and subjected to a test of significance.

Velocity distribution for each cage was evaluated from boxplots, and maps of spatial distribution were generated using the software SIGMAPLOT® v.12.0. Velocity distribution was analysed at two horizontal plans referring to the area close to the feeder, at high 55 and 142 mm above the floor. These surfaces were named Z0 and Z1, respectively. The velocity distribution maps were generated for each of these plans at each cage, in the zone near the feeder as depicted in Fig. 3.

## **RESULTS AND DISCUSSION**

The two nearest lines to the feeder (Lines 4 and 5 at Z1 height), in combination, best represent the condition in which the birds were exposed due to the fact that they correspond to the zone effectively occupied by the birds during the feeding. Thus, it is possible to observe in Table 1 the actual air velocity to which the animals were submitted when approaching the feeder. The importance of studying the intensity and distribution of airflow near the feeder is associated with its influence on the animals' ingestive behaviour. Thus, Ruzal et al. (2001), studying the air velocity effect on the broilers performance subjected to heat stress (35 °C), concluded that birds exposed to higher air velocities (2.5 and 3 m s<sup>-1</sup>) obtained better results for weight gain, feed intake and feed conversion when compared to birds subjected to 0.5 m s<sup>-1</sup> air velocity. Santos et al. (2018) studied effect of different air velocities on behaviour of Japanese quails and concluded that in heat stress the birds showed a higher frequency of feeding behaviour when subjected to high air velocities. In this same sense, Sevegnani et al. (2005),

working with broilers of the AgRoss strain in the final creation stage, submitted to different heat stress conditions, found that in general, the hotter the environment, the less time spent by birds in the feeder. Barbosa Filho et al. (2007), evaluating the influence of heat stress in laying hens of the Hy-Line Brown line housed in a cage system, observed a reduction of approximately 50% in the frequency of the eating behavioural pattern. On the other hand, when higher air velocities are used in heat stress situations, it is observed that the thermal environment does not significantly influence the animals' ingestive behaviour, since high air velocity ranges favour the body heat exchange through the convection process (Baêta & Souza, 2010).

As shown in Table 1, for the low and medium velocities, the actual mean air velocity achieved in the feeder zone corresponded with the nominal velocity for the experiment. For the highest velocity, the average actual air velocity reached in the feeder area was  $2.3 \text{ m s}^{-1}$ , showing that the desired set point of air velocity was not effective. However, Vilela (2016) and Santos et al. (2017) showed that the developed system can be used for such research because provided with the correct adjustments and considering air velocity levels of up to approximately  $2.5 \text{ m s}^{-1}$ , the mean air velocity was suitable for controlled environments. However, for experimental velocities greater than  $2 \text{ m s}^{-1}$ , an alternative for setting the nominal setpoint or an alternative design would be required, since the used system configuration provided air velocities approximately 23% lower than that desired when the setpoint (experimental velocity) was  $3 \text{ m s}^{-1}$ . Which may end up influencing the behavioural and performance evaluations of poultry, associated with the air velocity applied on them. Vilela et al. (2019) developed a computational fluid dynamics (CFD) model to evaluate the performance of air velocity control prototypes designed for animal and, through this tool, they affirm that it is possible to carry out simulations for improvement of air velocity control system for ranges above  $2 \text{ m s}^{-1}$ , optimizing structural designs to aim animal thermal comfort.

Boxplots of the velocity distribution of all 275-measurement points for each cage by velocity combination are presented in Fig. 4. They demonstrate very consistent velocity distributions between replicate cages at the same set point velocity. Also noteworthy is a positive bias with a long tail at higher velocities, indicative of turbulent conditions. There is a relatively small increase in median velocities with increasing set point values, although upper quartile (Q3) thresholds increased with set point increase. The velocity distributions at each set point in Fig. 4 further indicate that the replicate cages behaved similarly.

Maps of velocity distribution in the cages further illustrate the velocity distribution within a single cage. For brevity, only a one example of the velocity maps for the two cages subjected to  $3 \text{ m s}^{-1}$  velocity set point are provided in Figs 5–6. Clearly delineated in these graphs is the distribution of higher velocities towards the cage front, and over the feeder area in the lower levels (Z1 and Z2), with relatively calm conditions toward the cage backs and at higher levels (Z2 and Z3). The linear distribution across the cage

**Table 1.** Relationship between air velocity set point and mean observed data ( $\pm$  standard deviation) for the combination of values obtained in lines 4 and 5

Air velocity set point ( $\text{m s}^{-1}$ )	Mean observed in lines 4 and 5 (in combination) ( $\text{m s}^{-1}$ )
1. (Low)	$1.1 \pm 0.09$
2. (Medium)	$2.0 \pm 0.22$
3. (High)	$2.3 \pm 0.10$

front is somewhat variable, with lower velocities towards the cage edges and a relatively broad section along the front with highest velocities.

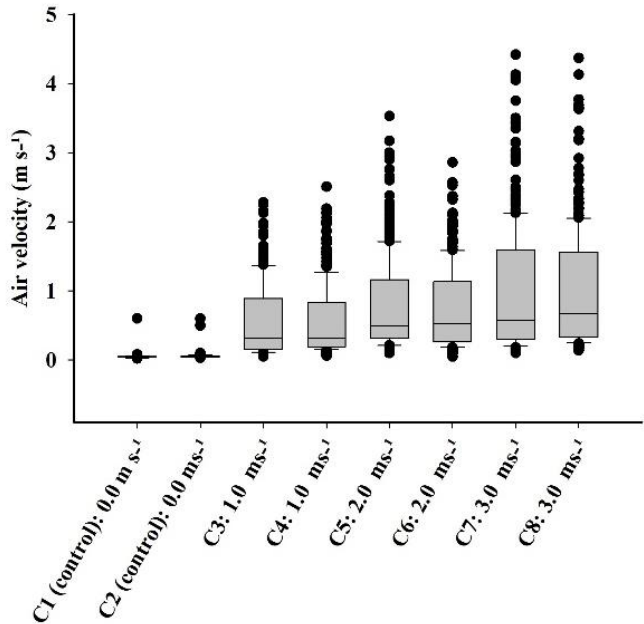


**Figure 4.** Boxplot of air velocity measurements at 275 locations in two replicate cages in still air and 3 controlled velocities. C1 and C2) Control (cages 1 and 2, still air), 0 m s<sup>-1</sup>; C3 and C4) Cages 3 and 4, set point 1 m s<sup>-1</sup>; C5 and C6) Cages 5 and 6, set point 2 m s<sup>-1</sup>; C7 and C8) Cages 7 and 8, set point 3 m s<sup>-1</sup>.

The highest air velocity values were concentrated in the front part of the cages, corresponding to the feeder zone (close to the prototype air outlet), as desired. The tendency was for a decrease in the intensity downstream from this region. Since the cages were relatively open to air circulation, part of the flow was dispersed through lateral and upper openings. As the air velocity influences directly the animal feeding behaviour, it was necessary to highlight the characteristics of the air flow and intensity in the region closest to the feeder, located at the air outlet of the tube. The spatial distribution of air velocity maps in this region are shown in Figs 5–6, for setpoint of 3 m s<sup>-1</sup>, which represents a ‘worst-case’ scenario for the design.

The velocity distribution in both cases tended to be more uniform at bird head level (Z1), whereas, at the lower level, it was seen to diminish more rapidly with depth into the cage. There was a tendency to have a reduced speed on the sides of the cage. This was a consequence of the system design, with two opposing axial fans creating a substantial amount of turbulence within the tube and pushing a larger percentage of air out the centre 80–90% of the opening. The tendency of velocities to diminish rapidly with depth into the cage was also noted by Rocha et al. (2010), in which they verified high velocities along cage fronts in curtain sided buildings exposed to strong wind. Once more, the configuration of the air flow distribution and intensity can be explained by the system design, as it consists of a fan at each tube end, and thus, there is a tendency for

more intense air flow in the central outlet region. In addition, the tube length can be a potential factor for uniformity of air flow distribution.

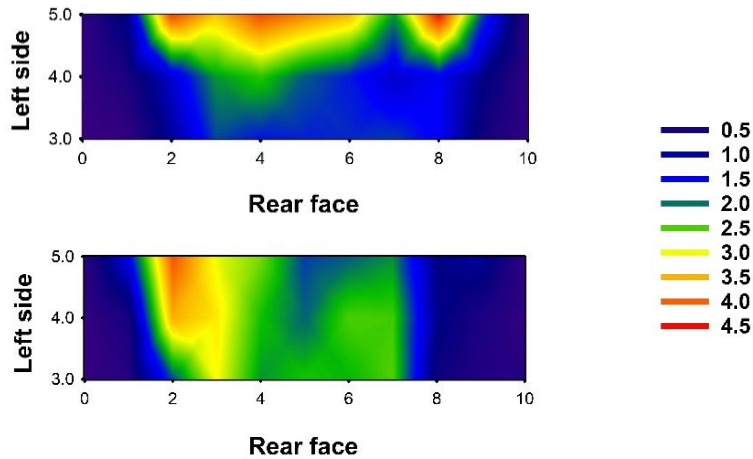


**Figure 5.** Velocity distribution map for the front feeding zone at the two bottom levels in Cage 7 with velocity set point  $3 \text{ m s}^{-1}$ ; A) lowest level, Z0; B) bird head level, Z1.

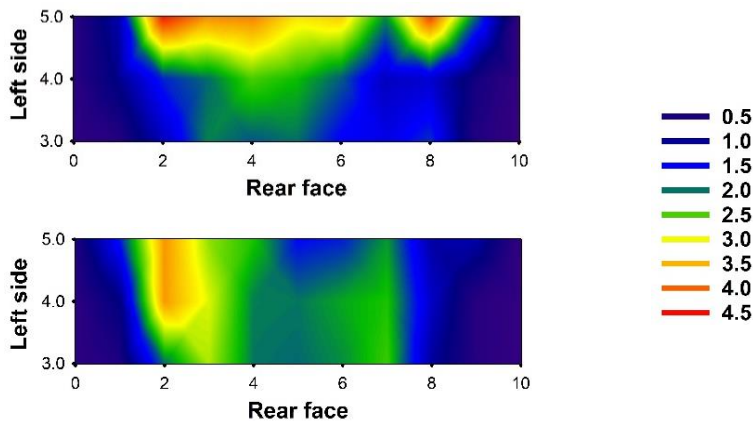


**Figure 6.** Velocity distribution map for the front feeding zone at the two bottom levels in Cage 8 with velocity set point  $3 \text{ m s}^{-1}$ ; A) lowest level, Z0; B) bird head level, Z1.

An assessment of the relative similarity between replicate cages at four different velocity controller settings is provided in Table 2, in which mean differences, standard deviations and probability of significant difference in mean values are tabulated. Mean velocities between the two replicate cages were similar (P values ranging from 0.053 to 0.820). The magnitude of mean differences ranged from 0.0 to  $0.09 \text{ m s}^{-1}$  with standard deviations ranging from 0.02 to  $0.39 \text{ m s}^{-1}$ . Thus, it is concluded that the replicate cages provided suitably similar velocity distributions for each velocity set point tested. However, the mean velocity for the medium and high air velocity setpoint did not achieve the desired values of 2 and  $3 \text{ m s}^{-1}$ , instead averaging 1.1 and  $1.6 \text{ m s}^{-1}$ , respectively.



**Table 2.** Mean ( $\pm$  standard deviation) of velocity measurements in replicate cages, mean ( $\bar{d}$ ) and standard deviation ( $S\bar{d}$ ) of velocity differences between replicate prototypes, and results of a paired t-test for significant difference from zero. Values are for the feeding zone

Nominal Air Velocity Setpoint	Mean Velocity ( $\text{m s}^{-1}$ )		$\bar{d}$	$S\bar{d}$	$t_{\text{calc}}$	$P$
	Prototype 1*	Prototype 2*				
still air (off)	$0.05 \pm 0.01$	$0.05 \pm 0.01$	-0.00	0.02	-0.58	$0.56^{n.s}$
low	$0.95 \pm 0.69$	$0.93 \pm 0.71$	0.02	0.32	0.52	$0.60^{n.s}$
medium	$1.14 \pm 0.89$	$1.04 \pm 0.75$	0.09	0.39	1.97	$0.05^{n.s}$
high	$1.62 \pm 1.19$	$1.61 \pm 1.12$	0.01	0.23	0.23	$0.82^{n.s}$

\* – Prototypes 1 and 2 are replicate systems; *ns* – not significantly different at 5% confidence;  $\bar{d}$  – mean of paired differences;  $S\bar{d}$  – standard deviation of paired difference.

Strong positive correlations were found in velocity at similar points in these replicate cages, as illustrated in Table 3. The overall correlation results for all points in the replicate cages ( $n = 275$ ), by velocity setpoint, demonstrate excellent correlation with the Pearson correlation coefficients exceeding 0.9 for all three velocity set points. Similarly, restricting the analysis to the feeding zone produced similarly high correlation coefficients (0.9 to 0.98). Consequently, it was concluded that replicate cages are adequately similar for experimental purposes, if adjusted carefully at the outset.

**Table 3.** Mean and standard deviation of difference in velocity measurements between replicate prototypes, Pearson’s correlation coefficient, and significance of correlation test

Nominal Air Velocity Setpoint ( $\text{m s}^{-1}$ )	Mean Difference ( $\text{m s}^{-1}$ )	Standard Deviation ( $\text{m s}^{-1}$ )	Correlation Coefficient, $r$	$P$
Results for all sample points ( $n = 275$ )				
low	0.01	0.24	0.893	$< 0.001$
medium	0.05	0.28	0.905	$< 0.001$
high	0.02	0.19	0.976	$< 0.001$
Results for all feeding zone sample points ( $n = 66$ )				
low	0.02	0.32	0.899	$< 0.001$
medium	0.10	0.39	0.900	$< 0.001$
high	0.01	0.23	0.982	$< 0.001$

For purposes of analysing bird behaviour in the feeding zone, it is more practical to restrict the system assessment to the velocity distribution near the feeder. The feeding zone, as depicted previously with Lines in Fig. 3, represents velocity measured at 66 points for the front 3 rows of measurement points and the lower two levels (Z0 and Z1).

For the nominal velocities of 0, 1, 2 and  $3 \text{ m s}^{-1}$  established for each treatment, measured mean values by cage (Table 2) were within measurement error except for the  $3 \text{ m s}^{-1}$  value which were about  $1.6 \text{ m s}^{-1}$ . The higher air velocity was difficult to achieve since airflow became unstable due to turbulence generated by the design. Replicate cages performed very similarly (Table 2) with mean differences of 0.01 to  $0.10 \text{ m s}^{-1}$ . However, the system showed to be capable of providing a reasonable range from still air to  $1.6 \text{ m s}^{-1}$ .

A further examination of the behaviour of air velocity distribution between replicate prototypes is of interest. Since the feeding zone is one of the most important for birds’ behavioural study and the points closest to the side walls did not receive the

same flow intensity found in the centre, a velocity analysis was performed from the three parallel lines closest to the cage centre (Lines 3, 4 and 5), including the seven points distributed within this area. The average air velocity of each Line and their respective range are listed in Table 4.

**Table 4.** Mean ( $\pm$  standard deviation), minimum, and maximum values of air velocity for Lines 5 (closest to air outlet), 4 and 3 (approximately where birds are located to eat) for two cages (Fig. 3, A). Measurements were made at two different heights Z0 (at feeder level) and Z1 (approximately bird height) as shown in Fig. 3, B. Reported velocities are from those observed in each Line for two replicate cages, for three nominal air velocity setpoints representing low, medium and high air velocity at the feeder. Note that velocities for the combination of Z1 and Lines 4 and 5 are most representative of a feeding bird’s location

Nominal Air Velocity Setpoint (m s <sup>-1</sup> )	Matching cages	Lines	Z0	Velocity range (min-max) (m s <sup>-1</sup> )	Z1	Velocity range (min-max) (m s <sup>-1</sup> )
Low (1 m s <sup>-1</sup> )	Prototype 1	3	1.02 $\pm$ 0.4	0.25–1.44	1.24 $\pm$ 0.4	0.20–1.55
		4	1.47 $\pm$ 0.3	0.92–1.97	1.17 $\pm$ 0.5	0.45–1.80
		5	1.99 $\pm$ 0.3	1.25–2.30	1.23 $\pm$ 0.6	0.4–1.95
	Prototype 2	3	1.07 $\pm$ 0.4	0.31–1.57	1.12 $\pm$ 0.5	0.24–1.76
		4	1.73 $\pm$ 0.3	1.16–2.00	1.06 $\pm$ 0.5	0.41–2.01
		5	1.96 $\pm$ 0.3	1.37–2.51	1.04 $\pm$ 0.6	0.31–2.13
Medium (2 m s <sup>-1</sup> )	Prototype 1	3	0.96 $\pm$ 0.4	0.53–1.61	2.00 $\pm$ 0.7	0.51–2.66
		4	0.93 $\pm$ 0.3	0.43–1.52	2.18 $\pm$ 1.0	0.44–3.53
		5	0.91 $\pm$ 0.5	0.35–1.76	2.18 $\pm$ 0.9	0.47–3.17
	Prototype 2	3	1.09 $\pm$ 0.5	0.62–1.93	1.63 $\pm$ 0.5	0.65–2.13
		4	1.17 $\pm$ 0.4	0.59–1.98	1.71 $\pm$ 0.7	0.66–2.57
		5	1.05 $\pm$ 0.5	0.52–1.88	1.91 $\pm$ 0.8	0.61–2.86
High (3 m s <sup>-1</sup> )	Prototype 1	3	1.56 $\pm$ 0.3	0.93–1.80	2.10 $\pm$ 0.7	0.62–3.03
		4	1.71 $\pm$ 0.4	1.22–2.38	2.38 $\pm$ 0.8	0.86–3.50
		5	3.62 $\pm$ 0.7	2.13–4.42	2.31 $\pm$ 1.0	0.82–4.05
	Prototype 2	3	1.66 $\pm$ 0.3	1.14–2.04	2.02 $\pm$ 0.5	0.95–2.78
		4	1.81 $\pm$ 0.5	1.15–2.50	2.33 $\pm$ 0.7	1.20–3.63
		5	3.51 $\pm$ 0.7	2.09–4.37	2.14 $\pm$ 0.8	1.01–3.65

As observed in Tables 3 and 4, the means for the nominal 3 m s<sup>-1</sup> setpoint were substantially lower. This was true regardless of the Line and height (Z0 or Z1) evaluated, except Line 5. This can be attributed to the greater heterogeneity of data induced by turbulence as noted previously. It is found that, in this velocity, there are very low values, generally smaller than 1 m s<sup>-1</sup>, and the highest values are very close to 3 m s<sup>-1</sup>, which means averages always below the expected nominal velocity for treatment. Such unevenness can also be explained by the effect of turbulence. For the nominal velocities of 1 and 2 m s<sup>-1</sup>, the same does not occur in the Z1 height, since there was a higher frequency of values close to and/or above the nominal expectation. This made the average air velocity found in these treatments consistent with the expected.

Examples of research for which these systems were deployed are given in Vilela (2016), and Santos et al. (2017, 2018). To demonstrate the system’s utility, Fig. 7 illustrates the results of a two-velocity test to determine production performance response to air velocity and thermal environment. The two velocities were low and high

(0 and 2.3 m s<sup>-1</sup>) and there were three thermal environments: thermal comfort (TC), dry heat stress (DHS), and humid heat stress (HHS). The following production performance parameters were evaluated: feed intake, water consumption, body weight variation, egg mass and feed conversion.

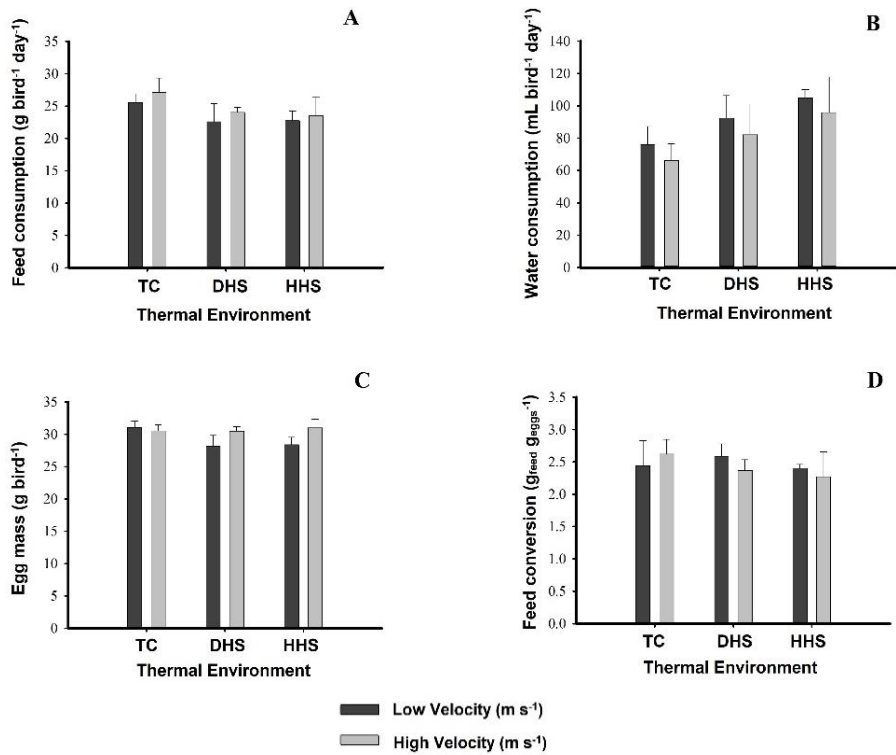


**Figure 7.** Birds' productive performance (mean ± standard deviation) during the experimental period, under thermal comfort (TC), dry heat stress (DHS) and humid heat stress (HHS) environmental conditions, combined with low and high air velocities. A – Feed consumption (g bird<sup>-1</sup> day<sup>-1</sup>); B – Water consumption (mL bird<sup>-1</sup> day<sup>-1</sup>); C – Egg mass (g bird<sup>-1</sup>); Feed conversion (g<sub>feed</sub> g<sub>eggs</sub><sup>-1</sup>).

There was no significant statistical influence of the different environment thermal conditions, of the different air velocity levels and of the interaction of these two factors ( $P > 0.05$ ) on feed intake, egg mass and feed conversion. This result may be related to the imposition of discontinuous stress, where the birds returned to the thermoneutrality conditions at night, which may have favoured the stress recovery process. On the other hand, it was found that these different thermal environments significantly influenced water consumption ( $P = 0.003$ ), representing an increase of 29% and 48% in the birds' consumption exposed to DHS and HHS, respectively.

## CONCLUSIONS

The system provided mean air velocity that was greatest in the zone where birds are housed (Z0 and Z1), as designed.

Replicate cages, using different air velocity control systems, demonstrated similar velocity magnitude and distribution. This was further confirmed with analysis of paired differences in velocity between replicates and with a correlation analysis.

Measured air velocity variation within a cage was substantial, because of the open nature of the cages; however, desired velocity at the feeder zone was achieved, except for the mean air velocity measured in the feeder zone for the 3 m s<sup>-1</sup>, where velocity nominal set point was 2.3 (± 0.10) m s<sup>-1</sup>.

Comparing the mean value of the measured and predetermined air velocity for each treatment, there is a need for greater attention for adjusting the air outlets at higher velocities (e.g. at or above 3 m s<sup>-1</sup>).

**ACKNOWLEDGEMENTS.** Federal University of Viçosa, Iowa State University and University of Florence. This research was supported by the Foundation for Research Support of Minas Gerais (FAPEMIG); Coordination for the Improvement of Higher Education Personnel (CAPES); and National Counsel of Technological and Scientific Development (CNPq).

## REFERENCES

- Abreu, V.M.N., Abreu, P.G., Coldebella, A., Jaenisch, F.R.F. & Silva, V.S. 2011. Evaluation of litter material and ventilation systems in poultry production: I. overall performance. *Brazilian Journal of Animal Science* **40**(6), 1364–1371.
- ASHRAE. 2017. Handbook Fundamentals. Chapter 9: Thermal Comfort. American Society of Heating, Ventilating and Air-Conditioning Engineers. Atlanta, USA, 33 pp.
- ASHRAE. 2019. Handbook HVAC Applications. Chapter 53: Evaporative Cooling. American Society of Heating, Ventilating and Air-Conditioning Engineers. Atlanta, USA, 21 pp.
- Baêta, F.C. & Souza, C.F. 2010. *Environment in Rural Buildings*. 2a. ed. Viçosa: Editora UFV, 269 pp. (in Portuguese).
- Barbosa Filho, J.A.D., Silva, I.J.O., Silva, M.A.N. & Silva, C.J.M. 2007. Evaluation of laying bird behaviors using image sequences. *Agricultural Engineering* **27**, 93–99. (in Portuguese).
- Bianchi, B., Giametta, F., La Fianza, G., Gentile, A. & Catalano, P. 2015. Microclimate measuring and fluid-dynamic simulation in an industrial broiler house: testing of an experimental ventilation system. *Veterinaria Italiana* **51**(2), 85–92.
- Blakely, J.R., Simpson, G., Donald, J., Campbell, J. & Macklin, K. 2007. The Economic Importance of House and Ventilation Management. *The Poultry Engineering, Economics and Management* **49**, 1–4.
- Curtis, S.E. 1983. *Environmental Management in Animal Agriculture*. The Iowa State University Press, Ames, Iowa. 409 pp.
- Dhahri, M., Aouinet, H. & Mhamdi, N. 2019. CFD analysis of the effect of uniformly sheared airflow on natural ventilation in building. *International Journal of Ambient Energy* **1**, 1 – 12.
- IBGE - Brazilian Institute of Geography and Statistics. Municipal Livestock Production. Rio de Janeiro, 2019. <https://www.ibge.gov.br/en/> Accessed 20.10.2019.
- Freitas, L.C.S.R., Tinôco, I.F.F., Baêta, F.C., Barbari, M., Conti, L., Teles Júnior, C.G.S., Cândido, M.G.L., Moraes, C.V. & Sousa, F.C. 2017. Correlation between egg quality parameters, housing thermal conditions and age of laying hens. *Agronomy Research* **15**, 687–693.
- Oloyo, A. & Ojerinde, A. 2019. Poultry Housing and Management. In: *Poultry*. Intech Open, 17 pp.

- Rocha, H.P., Furtado, D.A., Nascimento, J.W.B. & Silva, J.H.V. 2010. Bioclimatic and productive indexes in different poultry houses in Paraíba semiarid. *Brazilian Journal of Agricultural and Environmental Engineering* **14**(12), 1330–1336.
- Rojano, F., Bournet, P.E., Hassouna, M., Robin, P., Kacira, M. & Choi, C.Y. 2018. Assessment using CFD of the wind direction on the air discharges caused by natural ventilation of a poultry house. *Environmental monitoring and assessment* **190**(12), 724.
- Ruzal, M., Shinder, D., Malka, I. & Yahav, S. 2011. Ventilation plays an important role in hens' egg production at high ambient temperature. *Poultry Science* **90**(4), 856–862.
- Santos, M.J.B., Rabello, C.B., Pandorfi, H., Torres, T.R., Santos, P.A. & Camelo, L.C.L. 2012. Factors that interfere with thermal stress in broiler chickens. *Revista Eletrônica Nutritime* **9**, 1779–1786 (in Portuguese).
- Santos, T.C., Gates, R.S., Tinôco, I.F.F., Zolnier, S. & Baêta, F.C. 2017. Behavior of Japanese quail in different air velocities and air temperatures. *Brazilian Agricultural Research* **52**(5), 344–354.
- Santos, T.C., Gates, R.S., Tinôco, I.F.F., Zolnier, S., Freitas, L.C. & Cândido, M.G. 2018. Effect of different levels of air velocity at 35° C on Japanese quail behavior at start of lay. In *10th International Livestock Environment Symposium (ILES X)* (p. 1). ASABE. ILES 2018, Omaha, United States. Paper ILES18-151, 1–5.
- Sevegnani, K.B., Caro, I.W., Pandorfi, H., Silva, I.J.O. & Moura, D.J. 2005. Precision animal production: image analysis to study broiler behaviour under stress conditions. *Brazilian Journal of Agricultural and Environmental Engineering* **9**(1), 115–119.
- Vilela, M.O. 2016. Behavior and performance of Japanese quails under different heat and humidity regimes combined with different levels of air speed. Thesis (*Master Degree in Agricultural Engineering*). Federal University of Viçosa, 103 pp. (in Portuguese).
- Vilela, M.O., Gates, R.S., Martins, M.A., Barbari, M., Conti, L., Rossi, G., Zolnier, S., Teles Jr., C.G.S., Zanetoni, H.H.R., Andrade, R.R. & Tinôco, I.F.F. 2019. Computational fluids dynamics (CFD) in the spatial distribution of air velocity in prototype designed for animal experimentation in controlled environments. *Agronomy Research* **17**, 17890 – 899.
- Vigoderis, R.B., Cordeiro, M.B., Tinôco, I.F.F., Menegali, I., Souza Júnior, J.P.D. & Holanda, M.C.R.D. 2010. Evaluation of the use of minimal ventilation in poultry houses and its influence on the performance of broiler birds in the winter period. *Brazilian Journal of Animal Science* **39**(6), 1381–1386 (in Portuguese).
- Yanagi, T., Xin, H. & Gates, R.S. 2002. A research facility for studying poultry responses to heat stress and its relief. *Applied Engineering in Agriculture* **18**(2), 55–60.

## **Reliability of camera systems to recognize facial features for access to specialized production areas**

J. Vošahlík<sup>1,\*</sup> and J. Hart<sup>2</sup>

<sup>1</sup>Czech University of Life Sciences Prague, Faculty of Engineering, Department of Technological Equipment of Constructions, Kamýcká 129, CZ165 00 Prague, Czech Republic

<sup>2</sup>Czech University of Life Sciences Prague, Faculty of Engineering, Department of Vehicles and Ground Transport, Kamýcká 129, CZ165 00 Prague, Czech Republic

\*Correspondence: [vosahlik@oikt.czu.cz](mailto:vosahlik@oikt.czu.cz)

**Abstract.** The article deals with ergonomics and reliability of camera systems for recognition of facial features and identify person for access to specialized areas. The monitoring of areas relates not only to crime, but it is also an integral part of access to specialized production areas (pharmaceutical production, chemical production, specialized food production, etc.). It is therefore important to adequately secure these premises using the relevant system. One of them is a system based on user identification using specific facial features. For this purpose, there are CCTV systems for recognition of facial features of different price categories (conventional cameras, semi-professional and professional) on the world market. However, problematic situations may occur when identifying. For example, by having the user partially masked face. This research is focusing on the problem. The main goal of the research is establishing the scale of negative impact, in case the identified person has partially masked face, on camera systems recognizing facial features, primarily on recognition time. The results are evaluated in detail. Some camera systems are not suitable in specialized production areas due to their insufficient recognition ability. From all the tested devices, the HIKVISION iDS-2CD8426G0 / F-I camera identification system has proved to be optimal for identification purposes. In the case of designing, it is therefore necessary to choose suitable camera systems that have ergonomics and reliability at a level that will guarantee their sufficient use in the mentioned areas, while decreasing comfort and user-friendliness as little as possible. By measuring the ergonomics and reliability of these CCTV systems, it can be stated that there are statistically significant differences between conventional, semi-professional and professional systems, and it's not just a design change, but also a more efficient recognition method.

**Key words:** security, agricultural buildings, ergonomics, camera systems, face detection.

### **INTRODUCTION**

Nowadays, due to the growing property criminality, it is highly advisable that even agricultural buildings (pharmaceutical production, chemical production, specialized food production, etc) are adequately secured, with respect to the entry to the premises, by authorized individuals only. These agricultural building should be secured for authorized access by face recognition. Especially pharmaceutical or chemical

production. Because in the case of criminality, it can have major negative consequences (chemical leak, escape of viruses and bacteria, steal of medicine, etc) (Hartová & Hart, 2017).

For this purpose, it is congruous to use already existing systems for recognizing a person's identity by recognizing the facial features. These systems are most commonly used as security elements for unauthorized persons to enter a specific building. The camera systems suitable for this purpose include a high-quality video sensor capable of recording in at least Full HD (1080p) in both day and night mode (Hartová et al., 2018; Al-Obaydy & Suandi, 2019).

Elementary camera systems use, for the identity recognition, an additional storage facility which ensures the formula output. More sophisticated camera recording systems utilize an internal software recognition solution along with an internal memory in Micro SSD card format (Mahdi et al., 2017; Tan et al., 2019).

The software solution for recognizing human identity is frequently solved by using the Eigenfaces method, a detection method using Haar's symptoms. Facial recognition represents an extensive and tough task in terms of interference and obstructive recognition. These effects primarily include changes in facial expression, rotation of the angle, distance to the scanned face, and in particular head and face covers. These aspects principally affect the likelihood of false rejection and the time taken to identify an individual (Nagano et al., 2019).

## MATERIALS AND METHODS

The following standard face recognizing camera systems (Fig. 1) were selected for the test series: Netatmo Welcome, HIKVISION model DS-2CD4D36FWD-IZS and a professional model iDS-2CD8426G0/F-I. Netatmo welcome is the cheapest from the mentioned above and is designed primarily for the general public purposes. The semi-professional device is represented by HIKVISION model DS-2CD4D36FWD-IZS. The third tested device is a professional camera system for face recognition of an individual HIKVISION iDS-2CD8426G0/F-I.

The measurement was performed to determine the average time value needed to recognize an individual by the camera system. In order to successfully measure the average time value of the face recognizing camera systems, it was necessary to ensure the most consistent conditions. The room with white walls without disturbing elements (paintings, photographs, animals) was used. The room temperature was maintained at 23 °C

and the light intensity for measurement was determined to be 374 lux with a tolerance of 10% with the CEM DT-3809.



**Figure 1.** Tested recognition camera system (from the left: Netatmo Welcome, HIKVISION iDS-2CD8426G0/F-I, HIKVISION DS-2CD4D36FWD-IZS).

The camera systems were installed on the table and were pointing to the center of the room, which the tested subjects entered. During the testing of the time recognition capabilities of the camera systems, an individual entered the room by opening the door and approaching at a distance of 80 cm opposite the lens. After recording the measured values, the person left the room and waited 30 seconds before repeating the scanning.

To ensure higher accuracy, system stability and equal recognition conditions, a personal computer was used to measure the time needed for the subject recognition by the camera system. For the individual recognition, a timeframe of 10 seconds was set and afterwards the individual recognition was evaluated and set as 'unsuccessful' (the measured time was replaced).

The measurement consisted in recording the necessary time values for recognizing an individual behind the camera system using characteristic facial features. Overall, 5 types of tests were performed:

- The necessary time recognition of an exposed face
- The necessary time recognition of a face with glasses
- The necessary time recognition of a face with a scarf around neck and chin
- The necessary time recognition of a face with a baseball cap
- The necessary time recognition of a face with all previously mentioned elements.

The measurement was performed on 5 subjects (2 men and 3 women). Each test consisted of 10 repeated measurements per person and per device. Each test, to achieve the highest possible correctness, was performed twice. Thus, one series of measurements of one test per device on one person contained 100 measured values. In total, 1,500 recorded readings in compliance with the statistic unpaired t-tests were evaluated on all devices, all subjects and in all tests.

## **RESULTS AND DISCUSSION**

Out of the three compared facial recognition camera systems, the HIKVISION iDS-2CD8426G0 / F-I had the lowest recognition time (Fig. 2) and proved the best recognition ability in all tests performed. In the test without covering the face, the average recognition time was 0.92 sec. In the test with glasses on, the average recognition time was 2.12 sec. In the third test with the scarf covering, the average recognition time was 1.56 sec. In the fourth test, covering the face with a baseball cap, the average time was 3.55 sec. In the last one, by covering all the previous elements, it achieved an average time value of 6.23 sec.

The second tested device, HIKVISION DS-2CD4D36FWD-IZ (Fig. 3), got a moderate average time value. In the first test without covering the face, the device achieved an average recognition time of 1.94 sec. In the second test with glasses on, the average time was 2.91 sec. In the third one, these values reached 2.14 sec. In the fourth test, using a baseball cap, the average recognition time was 3.83 sec. In the last test, the combination of all the previous elements, was an average recognition time of 6.87 sec.

The third tested device, Netatmo Welcome, achieved the slowest recognition times (Fig. 4). In the first test, 2.72 sec without covering the face. In the second test, covering with glasses on, it reached 5.20 sec. The third one, scarf covering test, reached 4.17 sec. In the fourth test with baseball cap, it achieved an average recognition value of 7.24 sec. In the last and most challenging test due to the application of all previous elements, it reached 8.37 sec.



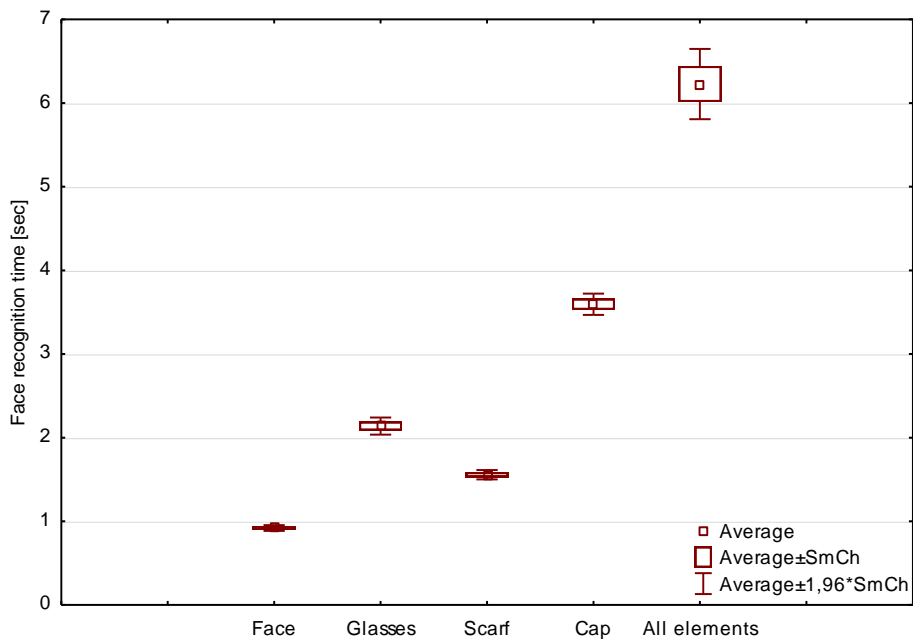


**Figure 2.** Results of average recognition time by HIKVISION iDS-2CD8426G0/F-I.

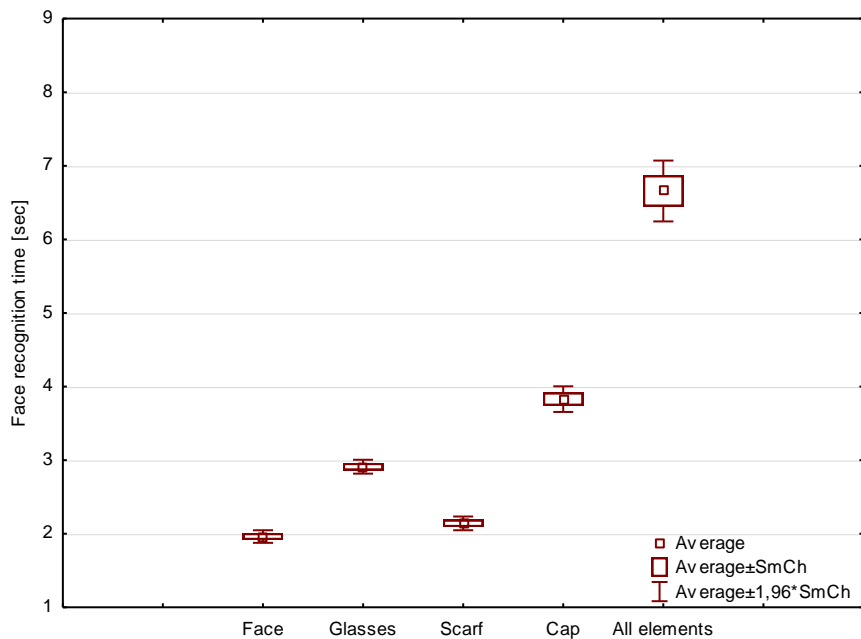


**Figure 3.** Results of average recognition time by HIKVISION DS-2CD4D36FWD-IZ.

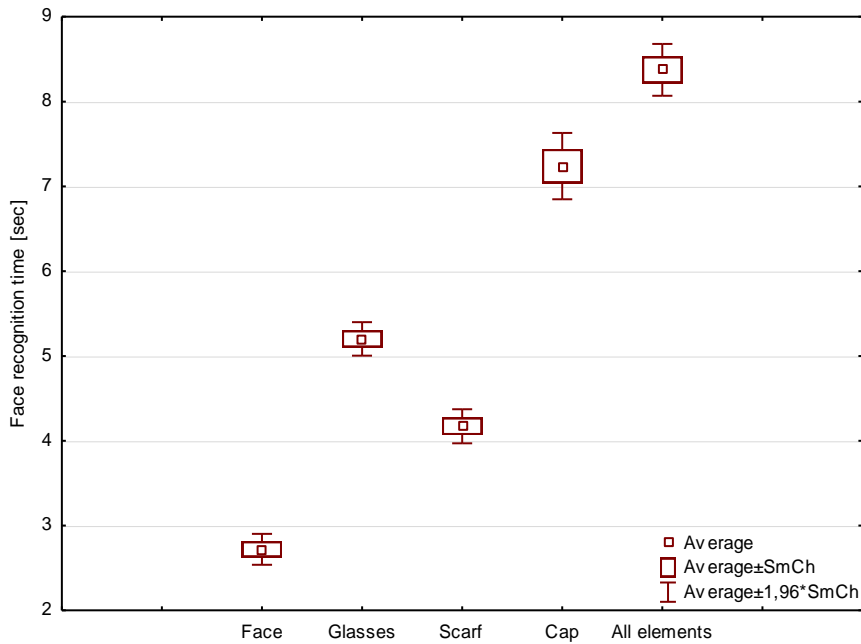


**Figure 4.** Results of average recognition time by Netatmo Welcome.

Unpaired statistical t-tests in Statistica software were applied to the measured values. By applying the measured data according to these tests, the following results were achieved. For all tests carried out, the p-value was less than 0.05 ( $p < 0.05$ ), with the exceptions (Table 1). We can reject the hypothesis of obtaining a similar measurement time for various devices with different face masking except for the tests.

**Table 1.** Results of applied t-tests

Type of camera (group 1 vs. 2)	Type of test	Average time of group 1 (sec)	Average time of group 2 (sec)	t value	p value
C vs. B	All elements vs All elements	6.227	6.657	-1.3339	0.185837
B vs. A	All elements vs Hat	6.657	7.238	-1.9439	0.055509
C vs. B	Glasses vs Scarf	2.137	2.141	-0.0526	0.958074
B vs. A	Glasses vs Face	2.911	2.720	1.7878	0.075633

when A – Netatmo Welcome; B – HIKVISION DS-2CD4D36FWD-IZ; C – HIKVISION iDS-2CD8426G0/F-I.

On these unpaired t-tests, we cannot dismiss the hypothesis of obtaining a similar measurement time on different devices using a different principle of face coverage. Interestingly, HIKVISION iDS-2CD8426G0 / F-I vs. HIKVISION DS-2CD4D36FWD-IZ achieved the highest equality of applied t-tests in the Glasses vs Scarf test type.

The core result in applied unpaired tests using different devices, nevertheless with the same principle of the face covering, is that we always reject the hypothesis with a single exception. This exception, in testing faces covered by all elements, represents the

device HIKVISION iDS-2CD8426G0 / F-I vs. HIKVISION DS-2CD4D36FWD-IZ. In this case the hypothesis definitely cannot be rejected. Both devices disclose similar results at this application, but with the others they significantly differ.

According to the statistic Friedman’s test and Kendall’s conformity test used in software Statistica (Table 2), the conformity assessment of the individual measurement results was clearly determined for uncovered face.

**Table 2.** Applied Friedman’s test and Kendall’s conformity test for uncovered face

Type of test and camera system	Average rank	Sum order	Average	Stan. deviation
Uncovered face A	2.746835	217.000	2.724526	0.069981
Uncovered face B	2.253165	178.000	1.969087	0.418242
Uncovered face C	1.000000	79.000	0.897380	0.172362

The most suitable device according to the average recognition times is HIKVISION iDS-2CD8426G0/F-I with an average rating of 1. The second suitable device according to these tests is HIKVISION DS-2CD4D36FWD-IZS with an average rating of 2.253165. Netatmo Welcome, with an average rating of 2.746835, got unambiguously the last place. The final average values of Friedman’s test and Kendall’s conformity test are demonstrated in the following graph (Fig. 5).

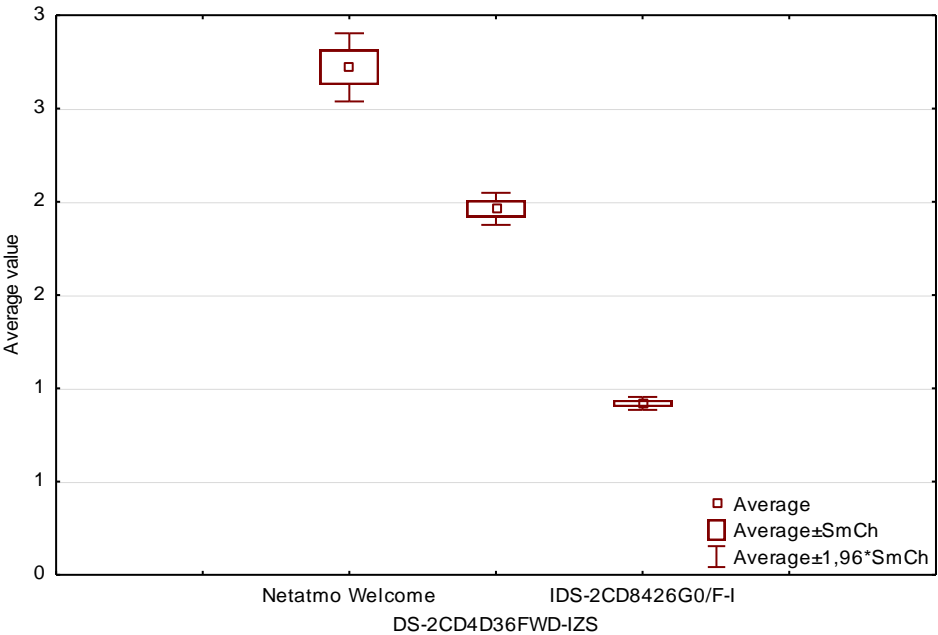


**Figure 5.** Average values of Friedman’s test and Kendall’s conformity test.

For the more results statistic Friedman’s test and Kendall’s conformity test used in software Statistica, the conformity assessment of the individual measurement results was clearly determined for all elements (Table 3).

**Table 3.** Applied Friedman’s test and Kendall’s conformity test for all elements

Type of test and camera system	Average rank	Sum order	Average	Stan. deviation
Covered face by all elements A	2.333333	14.0000	8.182618	0.943636
Covered face by all elements B	1.833333	11.0000	6.396292	1.541099
Covered face by all elements C	1.833333	11.0000	7.435432	1.806244

The most suitable device according to the average recognition times is not clearly determined. For this case of identifying, there are HIKVISION DS-2CD4D36FWD-IZ and HIKVISION iDS-2CD8426G0/F-I at the same level. Netatmo Welcome, with an average rating of 2.746835, got unambiguously the last place. The final average values of Friedman’s test and Kendall’s conformity test are demonstrated in the following graph (Fig. 6).

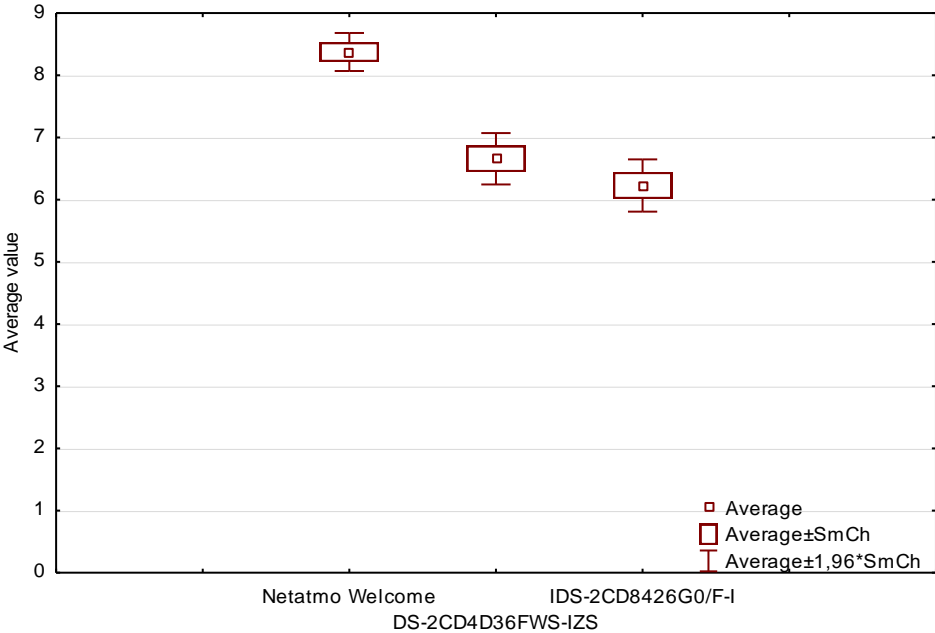


**Figure 6.** Average values of Friedman’s test and Kendall’s conformity test.

According to recent research, the gradual disguising of facial parts during the identification of an individual, leads to a very significant degradation of the ability of these systems to recognize the individual. This has already been described in the article ‘Deep face recognition imperfect facial data’. Such research comprehensively describes face detection and individual identification. It also includes a part of face covering and its partial disposal by the software. This research also recommends having an exposed face without any objects to improve the overall system recognition attributes. (Elmahmudi & Ugail, 2019)

## CONCLUSIONS

The time required for camera systems to recognize facial features increases dramatically when the user is disguised with a facial cover. The measured values evince that when the face is covered, the time required by the person identification device increases and thus negatively affects the process of effective identification of an individual.

In the agri-food complex, it is therefore recommended, according to the results of this measurement, to remove the plaids (masks, gas masks) from the face, as it prevents unambiguous identification of the individual by characteristic facial features. Eliminating this aspect during the identification process, this process will clearly be improved and thus will increase the security against unauthorized entry.

In the agri-food complex, it is therefore recommended, according to the results of this measurement, to remove the plaids (masks, gas masks) from the face, as it prevents unambiguous identification of the individual by characteristic facial features. Eliminating this aspect during the identification process, this process will clearly be improved and thus will increase the security against unauthorized entry.

From among the tested devices, the HIKVISION iDS-2CD8426G0 / F-I camera identification system has proved to be optimal for identification purposes. It had the best individual identification time response. Other tested detectors have been significantly worse than HIKVISION iDS-2CD8426G0 / F-I, therefore are not suitable for securing against unauthorized access to the agri-food complex.

ACKNOWLEDGEMENTS. It is a project supported by the CULS IGA TF ‘The University Internal Grant Agency’ (2019:31170/1312/3113 and 2020:31170/1312/3116).

## REFERENCES

- Al-Obaydy, W.N.I. & Suandi, S.A. 2019. Automatic pose normalization for open-set single-sample face recognition in video surveillance. doi: 10.1007/s11042-019-08414-2
- Elmahmudi, A. & Ugail, H. 2019. Deep face recognition using imperfect facial data. *Future Generation Computer Systems* **99**, 213–225. doi: 10.1016/j.future.2019.04.025
- Hartová, V. & Hart, J. 2017. Comparison of reliability of false rejection rate by monocriterial and multi-criteria of biometric identification systems: *Agronomy Research* **15**(S1), 999–1005.
- Hartová, V., Hart, J. & PRIKNER, P. 2018. Influence of face lighting on the reliability of biometric facial readers: *Agronomy Research* **16**(S1), 1025–1031.
- Mahdi, F.P., Habib, M., Ahad, A.R., Mckeever, S., Moslehuddin, A.S.M., Vasant, P. & Watada, J. 2017. Face recognition-based real-time system for surveillance. *Intelligent Decision Technologies* **11**(1), 79–92. doi: 10.3233/IDT-160279
- Nagano, K., Luo, H., Wang, Z., Seo, J., Xing, J., Hu, L., Wei, L., & Li, H. 2019. Deep face normalization. *ACM Transactions on Graphics (TOG)* **38**(6), 1–16. doi: 10.1145/3355089.3356568
- Tan, J., Niu, L., Adams, J.K., Boominathan, V., Robinson, J.T., Beraniuk, R.G. & Veeraraghavan, A. 2019. Face Detection and Verification Using Lensless Cameras. *IEEE Transactions on Computational Imaging* **5**(2), 180–194. doi: 10.1109/TCI.2018.2889933

## Hydrogen sulfide emissions from cattle manure: experimental study

V. Vtoryi\*, S. Vtoryi and V. Gordeev

Federal State Budgetary Scientific Institution ‘Federal Scientific Agroengineering Center VIM’, Filtrovskoje shosse, 3 p.o. Tiarlevo, Saint Petersburg, RU196625, Russia

\*Correspondence: vvtoryj@yandex.ru

**Abstract.** Animal waste products, manure, in particular, are the sources of gases harmful to human and animal health. Hydrogen sulfide ( $\text{H}_2\text{S}$ ), which is produced from the breakdown of organic matter in animal faeces, is one of them. Its concentration in the cow barn air should not exceed  $5 \text{ mg m}^{-3}$ . A special laboratory setup was designed and the level of hydrogen sulfide emissions from the cow manure was determined depending on the time and manure temperature and moisture content. The most intensive emission of hydrogen sulfide from manure was in the first 24 hours – the increment of  $\text{H}_2\text{S}$  concentration was  $0.168 \text{ mg m}^{-3}$  per hour average. During the next 24 hours, it was  $0.021 \text{ mg m}^{-3}$  per hour. When the manure temperature increased,  $\text{H}_2\text{S}$  concentration increased also; when the temperature manure decreased,  $\text{H}_2\text{S}$  concentration decreased also. In 48 hours, the hydrogen sulfide concentration was  $1.1 \text{ mg m}^{-3}$  at the manure temperature of  $+3.0^\circ\text{C}$ . At the manure temperature of  $+23.4^\circ\text{C}$  and  $21.3^\circ\text{C}$ ,  $\text{H}_2\text{S}$  concentration was  $6.53 \text{ mg m}^{-3}$  and  $4.97 \text{ mg m}^{-3}$ , respectively. The higher was the manure moisture content, the lower was the emission of hydrogen sulfide into the environment. After 24 hours under the manure moisture content of 88.5% and 92.5% and its temperature of  $21^\circ\text{C} \pm 0.3^\circ\text{C}$ , the difference in the hydrogen sulfide concentration was 1.18 times depending on the manure moisture content. The selected regression equations described the dependence of the hydrogen sulfide concentration on the considered factors. The determination coefficients and Student's criteria proved the reliability of the results obtained at the significance level  $P \leq 0.05$ .

**Key words:** hydrogen sulphide, emission, manure, cattle, farm.

### INTRODUCTION

During its lifetime the cattle produces both the products required by human beings and the co-products, which can be applied as organic fertilisers essential for crop growing or, if used inefficiently, become a waste and cause significant damage to the environment. Manure (slurry) have an adverse effect on the livestock house air quality that, in turn, negatively affects the physiological condition and animal welfare in general. In the unfavourable environment their productivity drops – the deviations of the cowbarn climate parameters from the rated values lead to 10–20% lower milk yield, 20–33% lower live weight increment and up to 5–40% higher young animals' mortality (Mishurov & Kuzmina, 2004).

The basic factors, which have the major impact on the barn air quality, are the temperature, relative humidity and air flow rate as well as the content of carbon dioxide, ammonia, and hydrogen sulphide. The emission intensity of the latter elements varies depending on the nutrient supply, animal productivity and physiological condition, and climate factors.

Livestock farms have a negative impact on the environment, increasing the anthropogenic pressure. Annually, they emit 39 billion m<sup>3</sup> of carbon dioxide, 1.8 billion m<sup>3</sup> of ammonia, and 700 thousand m<sup>3</sup> of hydrogen sulfide (Jerebcov, 2017).

Hydrogen sulfide (H<sub>2</sub>S) is a colourless, flammable gas with a characteristic smell of rotten eggs. It is highly soluble in water. H<sub>2</sub>S low concentrations negatively affect the respiratory organs and eyes, reduce the oxygen absorption, and cause the appetite loss. Exceeded permissible H<sub>2</sub>S concentrations may cause paralysis or mortality in humans or animals (Yurkov, 1985; WHO, 2003).

Hydrogen sulfide is formed continuously as a result of breakdown of sulphur-containing proteins in manure, bedding and feed residues. It is also emitted with intestinal gas. It penetrates the human and animal body through the skin and mucous membrane of the respiratory tract.

A dairy farm produces a large quantity of manure (slurry), which includes animal excrement (faeces and urine), bedding, uneaten feed, process water and others. Depending on the cows' productivity and weight, the output of excrement with the average relative moisture content of 88.4% ranges from 50.7 to 107.4 kg per day that can amount to 40 tons per head per year together with bedding (Tekuchev & Chernovol, 2017). This is the main source of hydrogen sulfide in the cow barn. Long-term storage of manure in the cow barns with the poor air exchange contributes to accumulation of hydrogen sulfide in the animal house air in excess of the maximum normalised concentrations (Shi et al., 2019).

Improved manure removal and utilisation technologies may reduce the hydrogen sulfide emissions from manure. Installation of biological filters with 65–96% cleaning efficiency may reduce the anthropogenic pressure on the environment when removing the polluted air from the barn (Krivolapov et al., 2016).

Another promising method in this respect is to use the gases from the barn, hydrogen sulfide included, for plant nutrition in greenhouses adjacent to the cow barns (Gordeev & Gordeeva, 2011; Gordeev & Mironov, 2014). Such application must, however, take into account that hydrogen sulfide is useful for plants only at very low concentrations – it improves their status and the stress factor resistance. At elevated concentrations, the hydrogen sulfide has a suppressing effect on plants (Dooley et al., 2013).

The study was aimed to assess the level of hydrogen sulfide emissions from the cattle manure (slurry) depending on the manure temperature and its storage time. The study findings will be used to justify the environmentally sound technological processes of cattle manure removal, storage and utilisation.

## **MATERIALS AND METHODS**

A laboratory setup was designed for the study as shown in Figs 1–2.

The main part of the laboratory setup was an airtight chamber with a stainless steel trough and a frame above it. The frame had a mounted air temperature and humidity

sensor DVT-0.3.TE with the limit of effective range from +20 °C to +50 °C and a manure temperature sensor T.p/p-420-DIN with the limit of effective range from 0 to 100 °C with a measurement resolution of  $\pm 1$  °C (both manufactured by NPK 'RELSIB', Russia). Hydrogen sulfide concentration was measured by ADT53-1197 sensor of MSR-Electronic GmbH, Germany, with the measurement range from 0 to 100 ppm and a measurement resolution of  $\pm 0.2$  ppm. Under the trough, there was a heating element – a 0.08 kW thermoelectric flexible cable, and a cooling element – a thermoelectric module (Peltier unit) or cool-packs. The real-time analogue signal coming from the sensors was recorded in the memory of the electronic recorder PARAGRAPH PL2 ('Avtomatika', Russia) with the measurement error of 25% installed in the data recording unit and then transferred to Excel tables on the computer for further analysis (Lantsova et al., 2015).

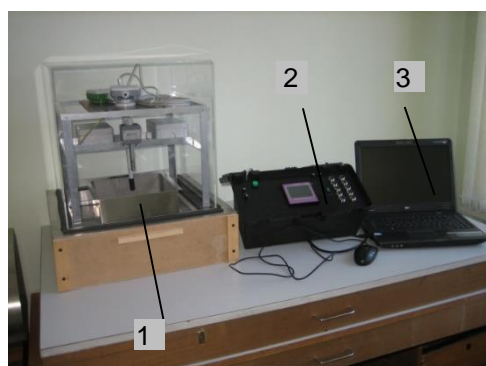


**Figure 1.** General view of the laboratory setup.

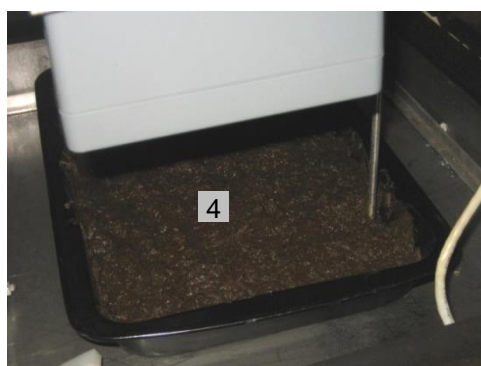


**Figure 2.** Trough with the tested manure sample.

1 – airtight chamber with the sensors of manure temperature and H<sub>2</sub>S concentration; 2 – data recorder; 3 – computer; 4 – trough with manure (slurry).

Fresh manure from a dairy farm was used in the study. This was the semi-liquid manure (slurry) with 85–87% moisture content, the solid bedding (peat) manure with 78% moisture content and the liquid manure with up to 92.5% moisture content. According to the valid classification in Russia, the manure with the relative moisture content below 85% is solid manure, 85–92% moisture content – semi-liquid manure (slurry), 92–97% moisture content – liquid manure, above 97% – manure-bearing wastewater (Khazanov et al., 2008). The mass of each sample was 1 kg. The samples were weighed on SW-1 scales of CAS Corporation, South Korea, with the weighing capacity range from 40 to 5,000 g and 2 g readability.

The experiment duration was 24 or 48 hours. The hydrogen sulfide emission degree was determined by the gas concentration in the airtight chamber. The manure moisture content was determined before placing the sample in the trough using an MX-50 weight hygrometer (A&D Co. LTD, Japan) with a measurement accuracy of 0.02% min<sup>-1</sup> and a display resolution of 0.01%.

The experiments ran as follows. The studied material was placed into the trough 4, which was installed in the chamber of the laboratory setup 1. The chamber was hermetically sealed and additionally thermally insulated from the external environment. Then, the temperature of manure was brought to the specified parameters by either



heating or cooling and the specified time interval was maintained. At the same time, the specified parameters were measured and the sensor readings were recorded in the data recorded 2 with their further processing on computer 3. The recording interval was 10 minutes.

The experimental data were analysed using *Excel* and *Mathcad* software packages; the mathematical expectation and variance of random variables were estimated; the regression models were created, the reliability of which was estimated by the multiple correlation and determination coefficients, and Student's criterion (Valge, 2013; Papez & Kic, 2015).

## RESULTS AND DISCUSSION

The animals excrete waste products throughout 24 hours. These products mix with the bedding material producing manure, accumulate in the animal house and are transported to the long-term storage or processing sites following the adopted technology. The method and conditions of manure accumulation inside the barn affect the degree of the negative impact on animals and personnel (Herbut & Angrecka, 2014).

The microclimate in the premises depends on the type and location of the cow barn, climatic conditions, the cattle housing and tending practices, and manure handling techniques (Angrecka & Herbut, 2014). The permissible concentration of hydrogen sulfide in the livestock farms in Russia is  $5 \text{ mg m}^{-3}$  (Volkov et al., 1986; Management Directive for Agro-Industrial Complex, 2018). When the sufficient air exchange is in place in the barn, the permissible concentration of hydrogen sulfide is not exceeded. Under the poor ventilation and unfavourable climatic conditions, a dangerous increase in the harmful gases content, including the hydrogen sulphide, is possible (Herbut, 2010; Herbut et al., 2013).

The intensity of hydrogen sulfide emission under various internal and external conditions can differ significantly (Maasikmets et al., 2015). According to Shi et al. (2019), the concentration of  $\text{H}_2\text{S}$  in the cow barn is in the range from 0.024 to  $0.151 \text{ mg m}^{-3}$ , with the average value being  $0.092 \text{ mg m}^{-3}$ , and reliably correlates with the sulfur content in feed and manure ( $P \leq 0.05$ ), as well as with the inside temperature ( $P \leq 0.05$ ).

In this regard, it is important to forecast the state of the microclimate in the livestock house for a certain period. Changes in the production technology and weather conditions and the technological equipment failures can result in the above-level maximum permissible concentrations of hydrogen sulfide and lower animals' productivity.

The control models are required to prevent the emergences and to ensure a favorable climate inside the barn. To create such models, the patterns of hydrogen sulfide emission from manure under various conditions must be known. The focus of the study was to identify these patterns.

In the study, the intensity of hydrogen sulfide emission from the cattle manure (slurry) was found to depend on the manure temperature, its moisture content and time.

Fig. 3 shows the time dependence of  $\text{H}_2\text{S}$  concentration during 48 hours under the relatively stable temperature of  $23 \pm 0.6^\circ\text{C}$ , the sample mass of 1 kg and 86.7% moisture content.

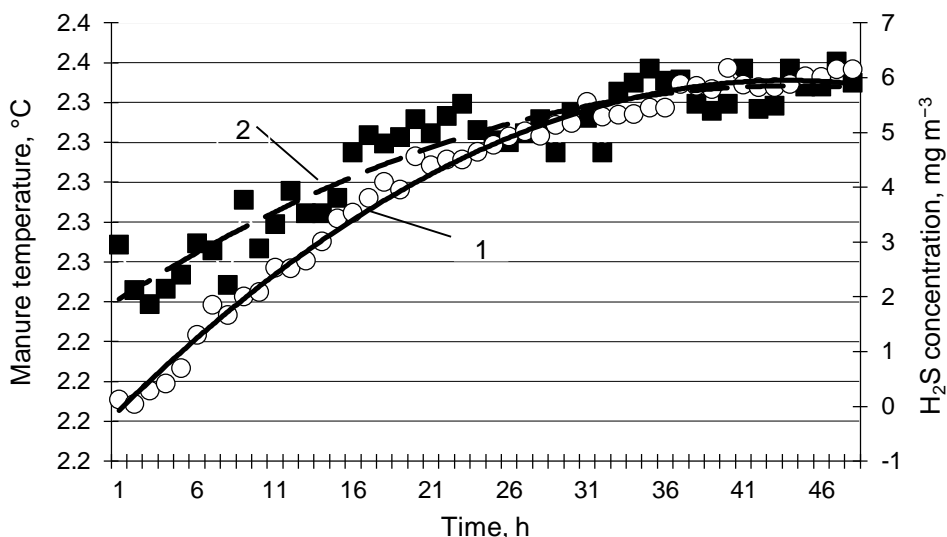


**Figure 3.** Time dependence of H<sub>2</sub>S concentration: 1 – H<sub>2</sub>S concentration, mg m<sup>-3</sup>; 2 – manure temperature, °C.

According to the experimental data exploring, the most intensive hydrogen sulfide emission of from manure was in the first 24 hours. The increment of H<sub>2</sub>S concentration was 0.168 mg m<sup>-3</sup> per hour average; during the next 24 hours it was 0.021 mg m<sup>-3</sup> per hour.

$$K_s = -0.003 \times T_{\text{exp}}^2 + 0.288 \times T_{\text{exp}} - 0.364, R^2 = 0.991 \quad (1)$$

where  $K_s$  – the hydrogen sulfide concentration, mg m<sup>-3</sup>;  $T_{\text{exp}}$  – the experiment duration, hour.

The selected regression equation (1) describes the dependence of hydrogen sulfide concentration  $K_s$  on the experiment duration  $T_{\text{exp}}$  under a slight increase in the manure temperature associated with the course of biochemical processes. The hydrogen sulfide concentration during this period increased from 0.03 to 6 mg m<sup>-3</sup>. The determination coefficient  $R^2 = 0.991$  showed a significant relationship between the dependent and independent variables, and the Student's *t*-test indicated the results reliability at a significance level of ( $P \leq 0.05$ ).

Fig. 4 shows the dependence of H<sub>2</sub>S concentration on time under the low manure temperature in the range from 3.0 °C to 9.7 °C. The bedding manure moisture content was 78%.

The hydrogen sulfide concentration varied from 0.91 mg m<sup>-3</sup> to 2.11 mg m<sup>-3</sup> versus the manure temperature. Under the manure temperature rise, the H<sub>2</sub>S concentration increased; under the decreasing temperature, it also decreased. This is possibly due to a change in the hydrogen sulfide solubility in the water contained in the manure. It is known that the lower is the water temperature, the higher is the hydrogen sulfide solubility (Frog & Levchenko, 1996).

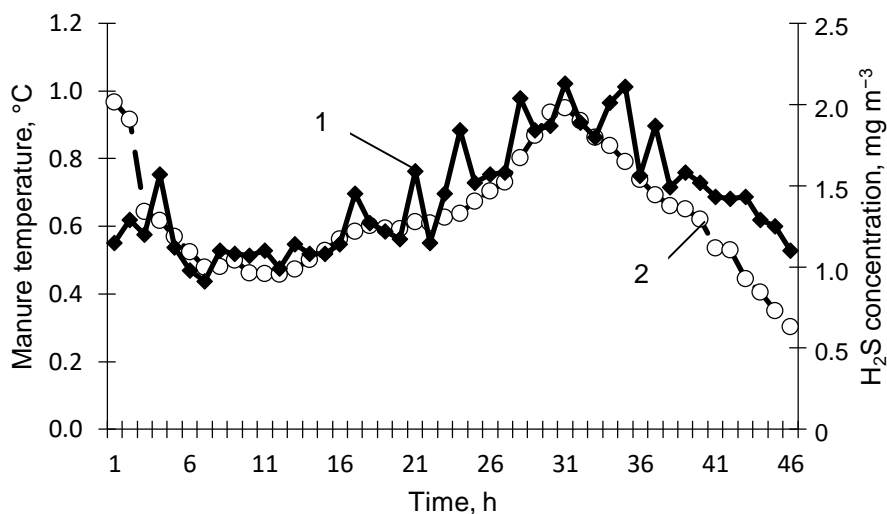


**Figure 4.** Dependence of  $\text{H}_2\text{S}$  concentration on time and manure temperature: 1 –  $\text{H}_2\text{S}$  concentration,  $\text{mg m}^{-3}$ ; 2 – manure temperature,  $^{\circ}\text{C}$ .

Fig. 5 presents the experimental data on the dependence of  $\text{H}_2\text{S}$  concentration on time and the manure temperature. The graphs demonstrate a distinct tendency of the hydrogen sulfide emission intensity to rise with an increase in the manure temperature. The difference in the dependences in Fig. 5 and in Fig. 4 is in the manure temperature and moisture content.

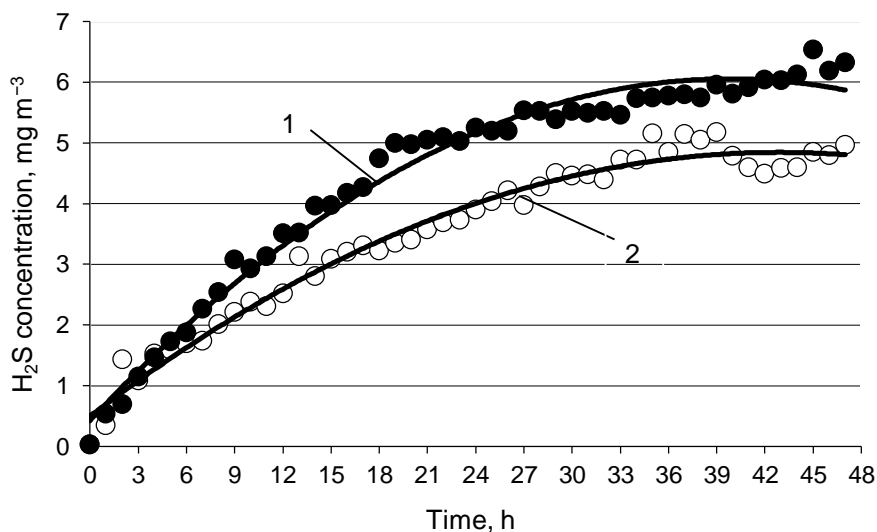


**Figure 5.** Dependence of  $\text{H}_2\text{S}$  concentration on time and manure temperature: 1 – manure temperature of  $+23.4^{\circ}\text{C}$ ; 2 – manure temperature of  $+21.3^{\circ}\text{C}$ .

After 48 hours, the hydrogen sulfide concentration was  $1.1 \text{ mg m}^{-3}$  at the manure temperature  $+3.0^\circ\text{C}$  (Fig. 4) and  $6.53 \text{ mg m}^{-3}$  and  $4.97 \text{ mg m}^{-3}$  at the manure temperature of  $+23.4^\circ\text{C}$  and  $21.3^\circ\text{C}$ , respectively (Fig. 5), with the manure moisture content being 85.6%.

$$K_{s1} = -0.003 \times T_{\text{exp}}^2 + 0.283 \times T_{\text{exp}} + 0.423, R_1^2 = 0.981 \quad (2)$$

where  $K_{s1}$  – the hydrogen sulfide concentration,  $\text{mg m}^{-3}$ , under the manure temperature of  $+23.4^\circ\text{C}$ ;  $T_{\text{exp}}$  – the experiment duration, hour.

$$K_{s2} = -0.003 \times T_{\text{exp}}^2 + 0.283 \times T_{\text{exp}} + 0.423, R_2^2 = 0.975 \quad (3)$$

where  $K_{s2}$  – the hydrogen sulfide concentration,  $\text{mg m}^{-3}$ , under the manure temperature of  $+21.3^\circ\text{C}$ ;  $T_{\text{exp}}$  – the experiment duration, hour.

The selected regression equations (2–3) describe the dependence of the hydrogen sulfide concentration  $K_{s1}$ ,  $K_{s2}$  on the experiment duration  $T_{\text{exp}}$  at the manure temperatures of  $+23.4^\circ\text{C}$  and  $+21.3^\circ\text{C}$ . After 48 hours, the difference in the hydrogen sulfide concentration depending on the manure temperature was 1.31 times. The determination coefficients  $R_1^2 = 0.981$  and  $R_2^2 = 0.975$  showed a significant relationship between the dependent and independent variables, and the Student's *t-test* indicated the results reliability at a significance level of  $P \leq 0.05$ .

Fig. 6 presents the experimental data on the dependence of  $\text{H}_2\text{S}$  concentration on the experiment duration and the manure moisture content. The graphs show the dependence of the increase in  $\text{H}_2\text{S}$  concentration in the setup chamber air with the decrease in the manure moisture content. In this case, the presence of free water in the manure contributed to the dissolution of a larger volume of gas and affected the emission intensity. The manure temperature was  $21 \pm 0.3^\circ\text{C}$ . The experiment duration was 24 hours.

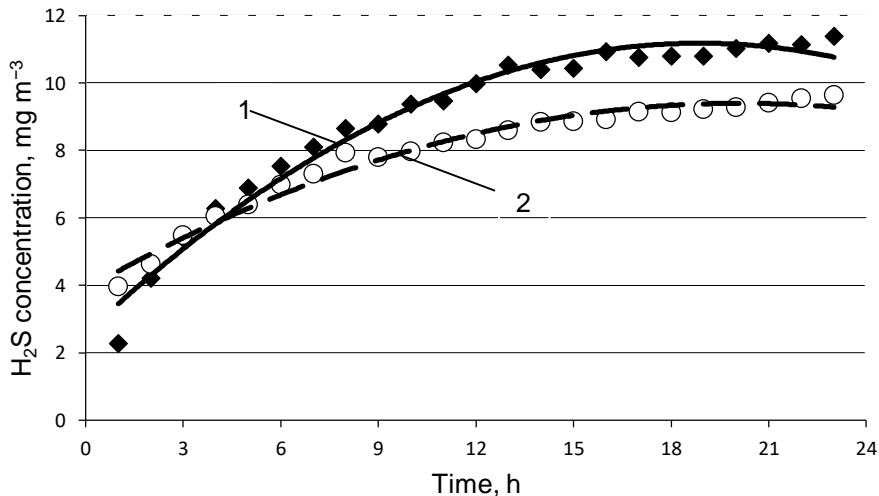


**Figure 6.** Dependence of  $\text{H}_2\text{S}$  concentration on time and manure moisture content: 1 – manure moisture content of 88.5%; 2 – manure moisture content of 92.5%.

$$K_{s1} = -0.024 \times T_{\text{exp}}^2 + 0.912 \times T_{\text{exp}} + 2.558, R_1^2 = 0.975 \quad (4)$$

where  $K_{s1}$  – the hydrogen sulfide concentration,  $\text{mg m}^{-3}$ , under the manure moisture content of 88.5%;  $T_{\text{exp}}$  – the experiment duration, hour.

$$K_{s2} = -0.013 \times T_{\text{exp}}^2 + 0.576 \times T_{\text{exp}} + 3.884, R_2^2 = 0.979 \quad (5)$$

where  $K_{s2}$  – the hydrogen sulfide concentration,  $\text{mg m}^{-3}$ , under the manure moisture content of 92.5%;  $T_{\text{exp}}$  – the experiment duration, hour.

The selected regression equations (4–5) describe the dependence of  $\text{H}_2\text{S}$  concentration  $K_{s1}$ ,  $K_{s2}$  on the experiment duration  $T_{\text{exp}}$  under the manure moisture content of 88.5% and 92.5%. After 24 hours, the difference in  $\text{H}_2\text{S}$  concentration depending on manure moisture content was 1.18 times. The determination coefficients  $R_1^2 = 0.975$  and  $R_2^2 = 0.979$  showed a significant relationship between the dependent and independent variables, and the Student's *t-test* indicated the results reliability at a significance level of  $P \leq 0.05$ .

## CONCLUSIONS

Hydrogen sulfide has a depressing effect on the vital functions of animals and the tending personnel. Its main source in cattle barns is faeces and urine, excreted by animals, mixed with the bedding material and diluted with the process water producing manure (slurry). The amount of hydrogen sulfide released and the air quality in the cow barn depends on the manure accumulation time in the livestock premises and its temperature.

The laboratory study revealed the most intensive emission of hydrogen sulfide from manure to take place in the first 24 hours. Then the process was significantly slowed down. The emission rate was influenced by the manure temperature – the hydrogen sulfide release was more active with the increasing temperature. The relative moisture content of manure also had a certain effect on the hydrogen sulfide emission. The higher was the manure moisture content, the lower was the hydrogen sulfide release into the environment.

The selected regression equations described the dependence of the hydrogen sulfide concentration on the considered factors with a high degree of reliability. They will be subsequently used to simulate the processes of microclimate formation in the cow barns.

## REFERENCES

- Angrecka, S., Herbut, P. 2014. The impact of natural ventilation on ammonia emissions from free stall barns. *Polish Journal of Environmental Studies* **23**(6). 2303–2307.
- Dooley, F.D., Nair, S.P. & Ward, P.D. 2013 Increased Growth and Germination Success in Plants following Hydrogen Sulfide Administration. *PLoS One*, **8**(4), e62048.
- Frog, B.N., Levchenko, A.P. 1996. Water Treatment. Manual for Graduate Students. Moscow: Moscow State University, 680 pp. (in Russian).
- Gordeev, V. & Gordeeva, T. 2011. Ways to reduce anthropogenic load on environment in dairy farming. *Agronomy Research* **9**(S1), 37–41.
- Gordeev, V.V. & Mironov, V.N. 2014. Use of ventilation emissions from animal barn for improvement of plant growth. In: *Engineering for Rural Development. The 13<sup>th</sup> International Scientific Conference*, Jelgava, Latvia, pp. 99–102.

- Herbut, P. 2010. Air movement characteristics inside a cow barn with natural ventilation under no-wind conditions in the winter season. In: *Infrastructure and Ecology of Rural Area*, Krakow, Poland, pp. 159–164.
- Herbut, P., Angrecka, S. 2014. Ammonia concentrations in a free-stall dairy barn. *Annals of Animal Science* **14**(1), 153–166.
- Herbut, P., Angrecka, S., Nawalany, G. 2013. Influence of wind on air movement in a free stall barn during the summer period. *Annals of Animal Science* **13**(1), 109–119.
- Jerebcov, B.V. 2017. The problem of air cleaning in industrial livestock production from hydrogen sulfide. *Era of Science* **9**, 158–172 (in Russian, English abstr.).
- Khazanov, E.E., Gordeev, V.V., Khazanov, V.E. 2008. *Modernization of dairy farms*. GNU SZNIIMESH Rosselkhozacademii, Sankt Peterburg, 375 pp. (in Russian).
- Krivolapov, I.P., Koldin, M.S. & Scherbakov, S.Y. 2016. Research of efficiency of cleaning cart spirit in livestock complexes from ammonia and hydrogen sulfide. *Technologies of food and processing industry of Agro-Industrial Complex – healthy foods* **3**, 9–18 (in Russian, English abstr.)
- Lantsova, E., Vtoryi, V. & Vtoryi, S. 2015. Investigation of water evaporation from cattle manure. In: *Engineering for Rural Development. The 14<sup>th</sup> International Scientific Conference*, Jelgava, Latvia, pp. 590–592.
- Maasikmets, M., Teinemaa, E., Kaasik, A. & Kimmel, V. 2015. Measurement and analysis of ammonia, hydrogen sulphide and odour emissions from the cattle farming in Estonia. *Biosystems Engineering* **139**, 48–59.
- Management Directive for Agro-Industrial Complex. 2018. *Recommended Practice for Engineering Designing of Cattle Farms and Complexes*. RD-APK 1.10.01.01-18. Rosinformagrotekh, Moscow, 166 pp. (in Russian).
- Mishurov, N.P. & Kuzmina, T.N. 2004. *Energy conservation equipment for microclimate maintenance in the livestock houses*. Scientific analytical review. Moscow: FGNU Rosinformagroteh Publishers. Available at: <http://www.norm-load.ru/SNiP/Data/48/48339/index.htm>.
- Papez, J. & Kic, P. 2015. Heating and ventilation in milking parlours. *Agronomy Research* **13**(1), 245–252.
- Shi, Z., Sun, X., Lu, Y., Xi, L., Zhao, X. 2019. Emissions of ammonia and hydrogen sulfide from typical dairy barns in central China and major factors influencing the emissions. *Sci. Rep.* **9**, 13821.
- Tekuchev, I.K. & Chernovol, Yu.N. 2017. Dependence of the excrement volume on a cow's productivity. *Bulletin of VNIIMzH* **1**(25), 40–43. (in Russian, English abstr.)
- Valge, A.M. 2013. *Application of Excel and Mathcad in investigations associated with mechanisation of agricultural production*. SZNIIMESH Rosselkhozacademii, Sankt Peterburg, 200 pp. (In Russian).
- Volkov, G.K., Repnin, V.M., Bolshakov, V.I., Rodin, V.I., Leontev, N.N. 1986. *Livestock Standards for Livestock houses: reference book*. Agropromizdat, Moscow, 303 pp. (in Russian).
- WHO (World Health Organization). 2003. Hydrogen sulfide: Human health aspects. (Concise international chemical assessment document; 53), Geneva, Switzerland. 37 pp.
- Yurkov, V.M. 1985. *Microclimate of livestock barns and complexes*. Rosselkhozizdat, Moscow, 223 pp. (in Russian).

## **Separation of reducing sugars from lignocellulosic hydrolysate: Membrane experiments & system dynamic modelling**

A.R.P.P. Weerasuriya Arachchige\*, L. Mezule and T. Juhna

Riga Technical University, Faculty of Civil Engineering, Department of Water Science and Technology, Paula Valdena street 1-204/205, LV-1048 Riga, Latvia

\*Correspondence: antonrayan@hotmail.com

**Abstract.** Separation of fermentable sugars after hydrolysis of lignocellulosic biomass plays a vital role in second-generation biofuel production. Byproducts and solid fractions generated during pretreatment and hydrolysis can have adverse effects on fermentation efficiency. Previous studies have shown that a maximum of 40% (w/w) of sugar yield can be obtained by sequential UF and NF permeate recovery. This study aimed to introduce a multi-step membrane filtration process to recover fermentable sugars while removing inhibitory bi-products. Fermentable sugar recovery was investigated using a recirculation flow between various stages of separation. The experimental results demonstrated that by introducing NF permeate recirculation to the UF unit a sequential UF/NF system can achieve 60% (w/w%) recovery of reducing sugars. Based on the experimental results, a ‘Simultaneous ultrafiltration and nanofiltration model’ was developed using system dynamics. The model was used to predict the final sugar concentration and sugar yield using sugar permeability in each membrane as the dynamic variability. The model predicts that high sugar permeability (or selective permeability) through the ultrafiltration mostly affects the efficiency of the system, which still is a challenge.

**Key words:** lignocellulosic biomass, fermentable sugars, membrane separation, system dynamic modelling.

### **INTRODUCTION**

The expanding human population and the rapid development of industries are significant causes for high energy demand which leads to many problems such as environmental pollution and depletion of fossil fuel resources (Mahapatra & Kumar, 2019). According to ‘Global Energy Statistical Yearbook 2019’ by the end of the year 2018, total global energy consumption has reached 14,391 million tons of oil equivalent which is a 2.3% increment concerning the year 2017. The repercussions from excessive use of fossil fuel have raised the importance of increasing the share of renewable energy. Driven by these factors the EU Renewable Energy Directive II mandates at least 32% of renewable energy share by the year 2030 (European Union, 2018). Moreover, use of food crops is no more favoured. According to Annex IX of the RED, alternative resources should be used for fuel production.

Lignocellulosic biomass is becoming a valuable resource for bioenergy production due to its high abundance and constant regeneration. In agriculture, after harvesting and processing of crops, the residues are still rich in cellulose and hemicellulose (35%–55%

and 25%–40% by weight, depending on the source) (Adhikari et al., 2018). Currently, most of it is left on the fields, used for soil enrichment or landfilled. However, research has shown that agricultural residues prove to have a great potential towards liquid biofuel production (Blaschek et al., 2010; Nguyenhuynh et al., 2017a). Despite the extensive research, an economically feasible system to produce second-generation bioethanol (Roomi et al., 2017) or any other modern biofuel, which can compete with fossil fuel derivatives is still a challenge.

A typical process for liquid fuel production from lignocellulose consists of pretreatment, hydrolysis, fermentation and subsequent product recovery. Pretreatment is necessary to depolymerise lignin which covers cellulose and hemicellulose. Currently, a wide range of chemical, biological, oxidative and physical methods or their combinations have been used (Kumar & Sharma, 2017). In hydrolysis, the use of enzymes (biological hydrolysis) has been preferred to chemical one, however, commercial enzymes generally contribute to approximately 20% of the total costs in second-generation biofuel production (Tu et al., 2007). Thus, recirculation of enzymes, separation of hydrolysis products and their subsequent concentration to produce carbohydrate concentrations useful for fermentation is of high importance. This can be achieved by the integration of ultrafiltration (UF) and nanofiltration (NF) within the conversion process (Dalecka et al., 2015). Even though there is no effect on the separation of sugars by UF due to high MWCO, it is essential to separate enzymes and use for subsequent hydrolysis reactions (Nguyenhuynh et al., 2017a).

In previous studies, it has been shown that a maximum of 40% yield of sugar recovery from the sugars generated during the pre-treatment and hydrolysis can be recovered (Dalecka et al., 2015). This study aims to determine the maximum sugar yield extractable from the enzymatic hydrolysis of lignocellulose biomass using a laboratory-scale reactor consisting of a subsequent UF-NF filtration system. Laboratory pilot measurements and adjustments in operational system will be combined with the design of system dynamic (SD) model to enable process control. Moreover, mechanically pretreated hydrolysates obtained with laboratory made enzymes from white rot fungi were used as liquids for separation tests. Using the results from pilot experiments, a system dynamic (SD) was developed to model the change of sugar yield over time.

## MATERIALS AND METHODS

### Biomass and enzymes

Dried hay (dry weight (DW):  $92.8\% \pm 1.3\%$ ; 6.02% ash) from semi-natural grasslands was collected and stored at room temperature, then milled by a mechanical cutting mill (Retsch SM100, Haan, Germany) with 1.5 kW drive and a parallel section rotor with a peripheral speed of  $9.4\text{--}11.4\text{ m s}^{-1}$  to obtain particle size  $< 0.5\text{ cm}$ . Lignocellulose degrading enzyme mix was prepared from cultures of *Irpex lacteus* IBB 104 according to a protocol described by Mezule et al. (Mezule et al., 2015).

### Pilot Tests

All experiments and production of hay biomass hydrolysates were performed in a laboratory-scale pilot reactor (Fig. 1). The pilot reactor consists of a hydrolysis reactor with a capacity of 30 L per batch, followed by subsequent filtration units to concentrate sugars extracted in the hydrolysate. Each UF and NF filtration system have one



membrane element particularly selected for protein and sugar rejection respectively. The ground hay was mixed (3% w/v) with 20 L of nano filtered permeate water and boiled in a closed hydrolysis reactor unit until the temperature reached 120 °C, then it was cooled until 37 °C. After cooling, the stock enzyme mixture (25 FPU per mL) was added into the reactor to obtain a final enzyme concentration in the ranges of 0.1–0.4 FPU per mL of reaction liquid. The enzymatic hydrolysis was carried out for 24 hrs at 37 °C. After completion of the hydrolysis, the liquid hydrolysate was pumped into the UF feed tank through a rough filter system (1 micron) to remove biomass particles. Further, the pre-filtered hydrolysate was filtered through an UF membrane where UF permeate was collected in the NF feed tank until a minimum volume (1.5–2 litres) of UF concentrate retains in the UF feed tank. UF feed rate was continuously maintained at 1.5 m<sup>3</sup>hr<sup>-1</sup> at feed pressure of 0.3 MPa. Subsequently, NF filtration of UF permeate was carried out to obtain concentrated carbohydrates. Feed flow rate of NF was maintained 210 L hr<sup>-1</sup> at initial feed pressure of 30 bar. Depending on the type of the experiment, the process flow was modified with either batch or continuous recirculation of NF permeate into the UF feed tank. All the nanofilter circulations were maintained at a constant feed and concentrate flowrates to maintain a constant flux. since flux declination over recirculations or model the fouling effects on the membrane were not addressed in this study. From each unit process step, samples were collected and analysed for the concentration of reducing sugars with the Dinitrosalicylic Acid (DNS) method (Ghose, 1987) according to a previously described protocol (Mezule et al., 2019).

The sugar yield was calculated as the ratio of the amount of sugars collected as NF concentrate in respect to the amount of sugars produced after the hydrolysis (Formula 1):

$$\text{Sugar yield} = \frac{\text{Amount of sugar obtained in NF concentrate (g)}}{\text{Amount of sugar obtained in hydrolysis reactor (g)}} \times 100\% \quad (1)$$

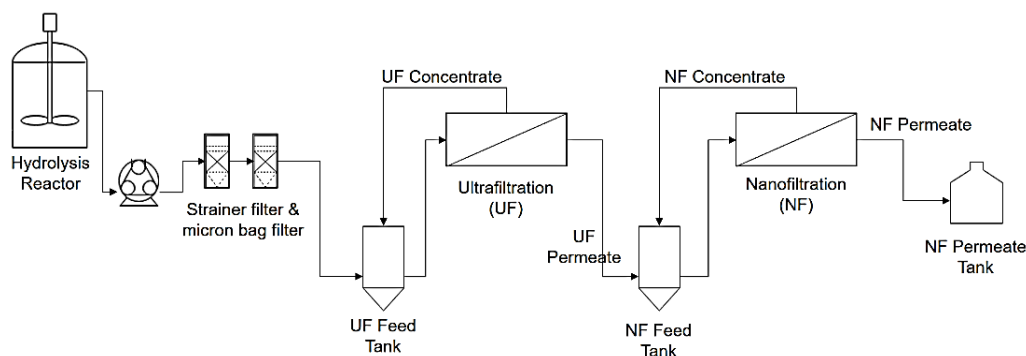


**Figure 1.** Process flow diagram of the pilot (laboratory-scale) reactor.

### System Dynamic (SD) Model

System dynamic modelling has been widely used as a tool for demonstrating the behaviour of a particular system. Though the application of SD is more prevalent among socio-economic aspects, it has also been used to model chemical/biological systems (Park et al., 2014). ‘Stella Architect’ software was used to model a ‘Simultaneous UF & NF filtration process’, which can be used as an empirical model to predict the sugar yield over time in the filtration system.

## RESULTS AND DISCUSSION

Dalecka et al., 2015 has demonstrated that a single pass (one-stage filtration) of the hydrolysate has a high amount of sugar loss and could only recover 24% of the yield produced during hydrolysis. Multistage filtration (secondary waste recirculation after NF and UF) produced the highest sugar yield, which is, 40% from all the produced sugar. From these studies, it was observed that a significant amount of sugar loss occurs as a waste of UF concentrate and waste of wet biomass.

Based on the previous observations, it was assumed that recirculation of NF permeate into UF feed tank will produce higher sugar yield. To test this, an experiment was performed to recirculate equal volume (6 litres) of NF permeate into UF feed tank two times as batch. Sugar yield, which is collected in NF concentrate, was analysed after each recirculation (Fig. 2). Without any NF permeate recirculation, the recovered sugar yield was only 24% of the sugars generated in the hydrolysis. The consecutive recirculations increased the sugar yield. After two recirculations the maximum sugar yield observed was 44%.

From the results, it is conclusive that recirculation of NF permeate into UF concentrate gives a better yield than in a single pass filtration. Since molecular weight pore size of UF is higher than the molecular size of reducing sugars, UF does not have any effect on the separation of sugars (Dey et al., 2018). Hence, sugar separation largely depends on hydraulic recovery. Since UF concentrate consists of high molecular weight proteins such as enzymes, some sugars can adhere to these proteins as well (Qi et al., 2012). Recirculation of NF permeate into UF feed can increase recovery of sugars retained in the UF feed tank as UF concentrate. However, the yield increases at a decreasing rate with each filtration cycle demonstrating the impossibility to obtain 100% recovery. Introduction of diafiltration is an alternative option to increase efficiency with increase circulations (Wagner, 2001), where a buffer solution is used for the extraction of diluted solutes via several recirculations.

Further, the process flow was amended with a continuous recirculation of NF permeate into UF feed tank. The process can be denoted as ‘simultaneous UF and NF’ process. The process resembles an integrated diafiltration where NF permeate is used as the buffer solution for subsequent filtration in UF, eliminating the addition of a different buffer solution. The process flow (Fig. 3) was divided into two systems for the ease of analysis. In system 1, suspended solids were removed, and the hydrolysate was transferred into system 2, where the sugar separation happened. Similar steps were followed for hydrolysis. However, when transferring the hydrolysate (system 1), 5 litres of prefiltered NF permeate was added to recover sugars left in the wet biomass.

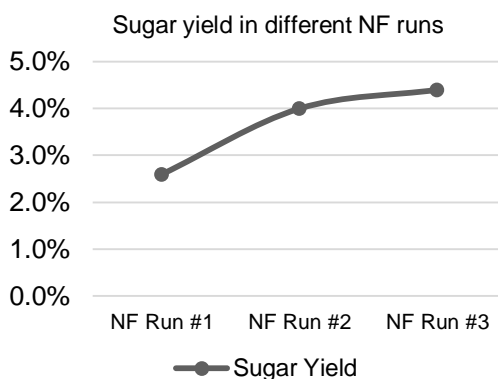


**Figure 2.** Final sugar yields in different NF runs.

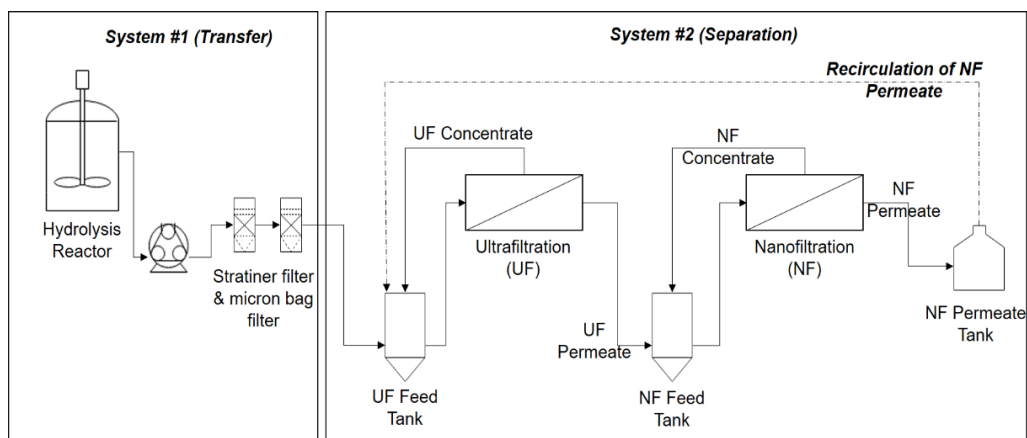


**Figure 3.** Process flow diagram of ‘simultaneous UF and NF filtration’.

After a substantial filtration time, reducing sugar left in each tank was analysed (Table 1).

After the filtration of hydrolysate, the highest sugar yield achieved was 61.63%. The sugar loss wasted as UF concentrate is 3.13 g, which is 0.02% from all the sugars produced. However, most of the sugar waste (24.86%) occurred in system 1 as about 20% (v/v) of the hydrolysate is wasted with wet biomass. To recover this part, extensive washing of the material and physical separation could be introduced. Alternatively, the wet biomass waste produced after hydrolysis and still containing some unrecovered sugar can be used as a valuable feedstock for biogas production by anaerobic digestion; hence the lignocellulose has already partially depolymerised with enzymes (Karuppiyah & Ebenezer Azariah, 2019).

**Table 1.** Average reducing sugars in each tank after ‘simultaneous UF & NF filtration’

Tank	Amount of sugar(g)	Sugar yield
Hydrolysis reactor	141.16	100% *
UF feed tank (before filtration)	106.08	75.14%
UF concentrate (after filtration)	3.13	N/A
NF feed tank (after filtration)	87.00	61.6%

\* 100% yield does not denote full conversion of all biomass oligosaccharides. This represents the value of all released carbohydrates in the current study.

## SD MODEL

A significant problem of the proposed filtration method is the determination of the filtration time. Even though SD has numerous applications, this is the first time it has been used to model a sugar separation process, for the best our knowledge. SD model was built to study the change of sugar yield over time (Fig. 4) to aid the filtration time determination. The model was created and adjusted by using operational data collected from the laboratory pilot studies.

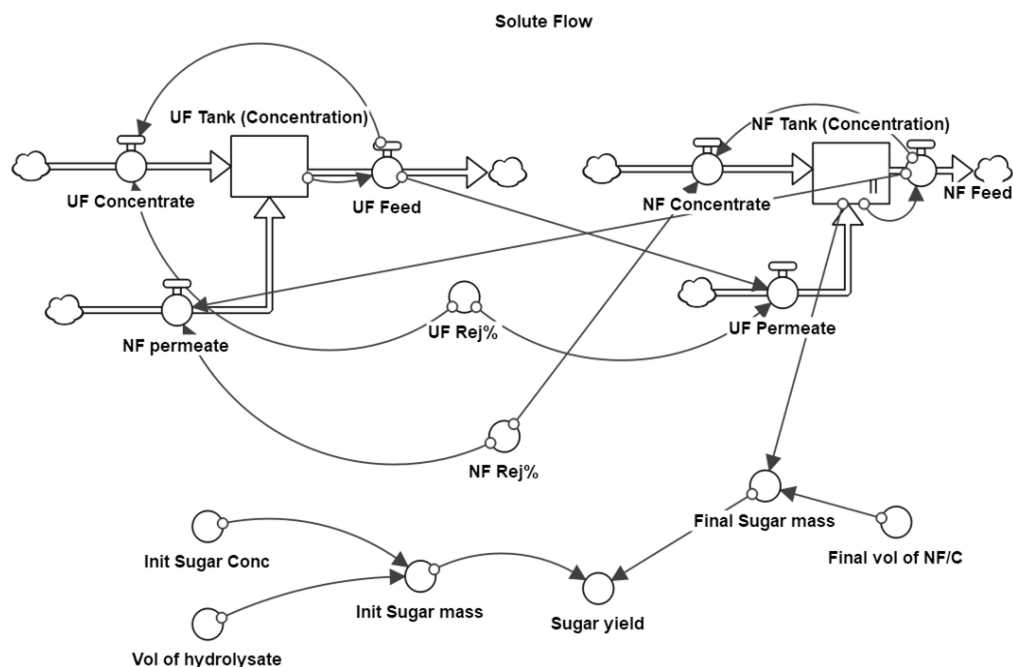


**Figure 4.** System dynamic model.

The validation of the model showed that it is able to predict that sugar yield increases with time at a decreasing rate (Fig. 5). Since the recirculation consumes energy, it is necessary to obtain the correct balance between the desired yield and the energy consumption when operating the system. Furthermore, the model indicates that the sugar permeation from the UF membrane plays a vital role in filtration efficiency.

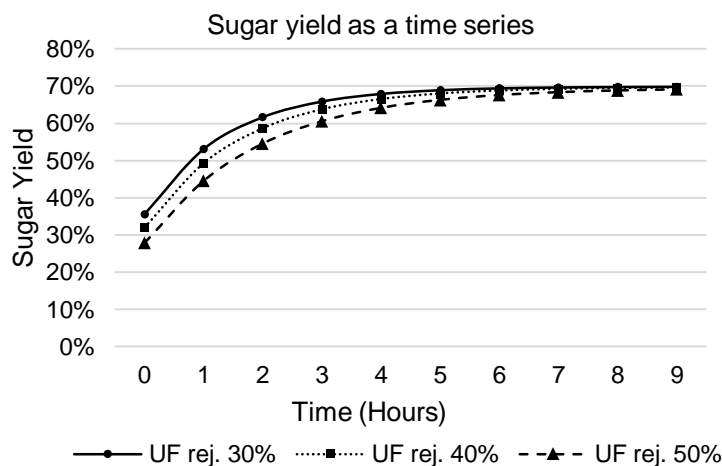


**Figure 5.** Model result (sugar yield as a time series) with different sugar rejections from UF membrane.

As emphasised in this study UF is a vital operation in second-generation biofuel production. Though it has a lower effect in filtering sugars, it is essential to recover enzymes and recirculate to subsequent hydrolysis. The SD model developed for the specific purpose of sugar yield monitoring showed the importance of incorporating a selective UF membrane which has higher permeation for reducing sugars such as submerged UF filters and integrated membrane reactors, which still is a challenge (Rios et al., 2004; Nguyenhuynh et al., 2017b) in recovery processes.

## CONCLUSIONS

The study results demonstrated that a simultaneous UF and NF filtration system can recover 61% of the reducing sugars in lignocellulose hydrolysate, which is produced via enzymatic hydrolysis of biomass agricultural residue. SD model developed and applied for the first time within this study showed that the selection of UF membrane to permeate more sugars has a significant impact on filtration time. The simultaneous UF and NF filtration can be a valuable system when it comes to enzyme recovery and continuous process of sugar recovery. After the sugar separation, the higher molecular weight proteins such as enzymes are collected in the UF tank and will be diluted with the NF permeate. The diluted UF concentrate can be later transferred into the next batch of hydrolysis.

**ACKNOWLEDGEMENTS.** The work has been funded by ERDF Project ‘Zero-to-low-waste technology for simultaneous production of liquid biofuel and biogas from biomass’, No. 1.1.1.1/18/A075. We thank Mr. Martins Strods for technical support.

## REFERENCES

- Adhikari, S., Nam, H. & Chakraborty, J.P. 2018. Chapter 8 - Conversion of Solid Wastes to Fuels and Chemicals Through Pyrolysis. In: Bhaskar, T. et al. (eds) *Waste Biorefinery*. Elsevier, pp. 239–263. <https://doi.org/10.1016/B978-0-444-63992-9.00008-2>
- Blaschek, H.P., Ezeji, T.C. & Scheffran, J. 2010. *Biofuels from Agricultural Wastes and Byproducts: An Introduction*. doi: 10.1002/9780813822716.ch1
- Dalecka, B., Strods, M. & Mezule, L. 2015. Production of fermentation feedstock from lignocellulosic biomass: Applications of membrane separation. *Agronomy Research* **13**(2), 287–293.
- Dey, P., Pal, P., Kevin, J.D. & Das, D.B. 2018 Lignocellulosic bioethanol production: Prospects of emerging membrane technologies to improve the process - A critical review. *Reviews in Chemical Engineering*. doi: 10.1515/revce-2018-0014
- European Union. 2018. Directive (EU) 2018/2001 of the European Parliament and of the Council on the promotion of the use of energy from renewable sources. *Official Journal of the European Union*. pp. 1–128. Available at: <https://eur-lex.europa.eu/eli/dir/2018/2001/oj>.
- Ghose, T.K. 1987. Measurement of cellulase activities. *Pure and applied Chemistry* **59**(2), 257–258. doi: 10.1111/j.1468-2389.1995.tb00038.x
- Karuppiah, T. & Ebenezer, A.V. 2019. Biomass Pretreatment for Enhancement of Biogas Production. *Anaerobic Digestion*. doi: 10.5772/intechopen.82088
- Kumar, A.K. & Sharma, S. 2017. Recent updates on different methods of pretreatment of lignocellulosic feedstocks: a review. *Bioresources and Bioprocessing* **4**(1). doi: 10.1186/s40643-017-0137-9

- Mahapatra, M.K. & Kumar, A. 2019. *Prospects of Renewable Bioprocessing in Future Energy Systems, Biofuels and Biorefineries*. doi: 10.1007/978-3-030-14463-0\_13
- Mezule, L., Berzina, I. & Strods, M. 2019. The impact of substrate–enzyme proportion for efficient hydrolysis of Hay. *Energies* **12**(18). doi: 10.3390/en12183526
- Mezule, L., Dalecka, B. & Juhna, T. 2015. Fermentable sugar production from lignocellulosic waste. *Chemical Engineering Transactions* **43**, 619–624. doi: 10.3303/CET1543104
- Nguyenhuynh, T., Nithyanandam, R., Chong, C.H. & Krishnaiah, D. 2017. A review on using membrane reactors in enzymatic hydrolysis of cellulose. *Journal of Engineering Science and Technology* **12**(4), 1129–1152.
- Nguyenhuynh, T., Nithyanandam, R., Chong, C.H. & Krishnaiah, D. 2017. Configuration modification of a submerged membrane reactor for enzymatic hydrolysis of cellulose. *Biocatalysis and Agricultural Biotechnology* **12**, 50–58. doi: 10.1016/j.bcab.2017.08.013
- Park, S., Kim, B. & Jung, S. 2014. Simulation methods of a system dynamics model for efficient operations and planning of capacity expansion of activated-sludge wastewater treatment plants. *Procedia Engineering* **70**, pp. 1289–1295. doi: 10.1016/j.proeng.2014.02.142
- Qi, B., Luo, J., Chen, G., Chen, X. & Wan, Y. 2012. Application of ultrafiltration and nanofiltration for recycling cellulase and concentrating glucose from enzymatic hydrolyzate of steam exploded wheat straw. *Bioresource Technology* **104**, 466–472. doi: 10.1016/j.biortech.2011.10.049
- Rios, G.M., Belleville, M.P., Paolucci, D. & Sanchez, J. 2004. Progress in enzymatic membrane reactors - A review. *Journal of Membrane Science* **242**(1–2), 189–196. doi: 10.1016/j.memsci.2003.06.004
- Rooni, V., Raud, M. & Kikas, T. 2017. Technical solutions used in different pretreatments of lignocellulosic biomass: A review. *Agronomy Research* **15**(3), 848–858.
- Tu, M., Chandra, R.P. & Saddler, J.N. 2007. Evaluating the distribution of cellulases and the recycling of free cellulases during the hydrolysis of lignocellulosic substrates. *Biotechnology Progress* **23**(2), 398–406. doi: 10.1021/bp060354f
- Wagner, J. 2001. *Membrane Filtration Handbook: Practical Tips and Hints*. Osmonics. Available at: <https://books.google.lv/books?id=3NQJaAEACAAJ>.

## INSTRUCTIONS TO AUTHORS

Papers must be in English (British spelling). English will be revised by a proofreader, but authors are strongly urged to have their manuscripts reviewed linguistically prior to submission. Contributions should be sent electronically. Papers are considered by referees before acceptance. The manuscript should follow the instructions below.

**Structure:** Title, Authors (initials & surname; an asterisk indicates the corresponding author), Authors' affiliation with postal address (each on a separate line) and e-mail of the corresponding author, Abstract (up to 250 words), Key words (not repeating words in the title), Introduction, Materials and methods, Results and discussion, Conclusions, Acknowledgements (optional), References.

### Layout, page size and font

- Use preferably the latest version of **Microsoft Word**, doc., docx. format.
- Set page size to **ISO B5 (17.6 × 25 cm)**, all **margins at 2 cm**. All text, tables, and figures must fit within the text margins.
- Use single line spacing and **justify the text**. Do not use page numbering. Use **indent 0.8 cm** (do not use tab or spaces instead).
- Use font Times New Roman, point size for the title of article **14 (Bold)**, author's names 12, core text 11; Abstract, Key words, Acknowledgements, References, tables, and figure captions 10.
- Use *italics* for Latin biological names, mathematical variables and statistical terms.
- Use single ('...') instead of double quotation marks ("...").

### Tables

- All tables must be referred to in the text (Table 1; Tables 1, 3; Tables 2–3).
- Use font Times New Roman, regular, 10 pt. Insert tables by Word's 'Insert' menu.
- Do not use vertical lines as dividers; only horizontal lines (1/2 pt) are allowed. Primary column and row headings should start with an initial capital.

### Figures

- All figures must be referred to in the text (Fig. 1; Fig. 1 A; Figs 1, 3; Figs 1–3). Use only black and white or greyscale for figures. Avoid 3D charts, background shading, gridlines and excessive symbols. Use font **Arial, 10 pt** within the figures. Make sure that thickness of the lines is greater than 0.3 pt.
- Do not put caption in the frame of the figure.
- The preferred graphic format is Excel object; for diagrams and charts EPS; for half-tones please use TIFF. MS Office files are also acceptable. Please include these files in your submission.
- Check and double-check spelling in figures and graphs. Proof-readers may not be able to change mistakes in a different program.

### References

#### • Within the text

In case of two authors, use '&', if more than two authors, provide first author 'et al.':  
Smith & Jones (1996); (Smith & Jones, 1996); Brown et al. (1997); (Brown et al., 1997)

When referring to more than one publication, arrange them by following keys: 1. year of publication (ascending), 2. alphabetical order for the same year of publication:  
(Smith & Jones, 1996; Brown et al., 1997; Adams, 1998; Smith, 1998)

- **For whole books**

Name(s) and initials of the author(s). Year of publication. *Title of the book (in italics)*. Publisher, place of publication, number of pages.

Shiyatov, S.G. 1986. *Dendrochronology of the upper timberline in the Urals*. Nauka, Moscow, 350 pp. (in Russian).

- **For articles in a journal**

Name(s) and initials of the author(s). Year of publication. Title of the article. *Abbreviated journal title (in italic)* volume (in bold), page numbers.

Titles of papers published in languages other than English, should be replaced by an English translation, with an explanatory note at the end, e.g., (in Russian, English abstr.).

Karube, I. & Tamiya, M.Y. 1987. Biosensors for environmental control. *Pure Appl. Chem.* **59**, 545–554.

Frey, R. 1958. Zur Kenntnis der Diptera brachycera p.p. der Kapverdischen Inseln. *Commentat.Biol.* **18**(4), 1–61.

Danielyan, S.G. & Nabaldiyan, K.M. 1971. The causal agents of meloids in bees. *Veterinariya* **8**, 64–65 (in Russian).

- **For articles in collections:**

Name(s) and initials of the author(s). Year of publication. Title of the article. Name(s) and initials of the editor(s) (preceded by In:) *Title of the collection (in italics)*, publisher, place of publication, page numbers.

Yurtsev, B.A., Tolmachev, A.I. & Rebristaya, O.V. 1978. The floristic delimitation and subdivisions of the Arctic. In: Yurtsev, B. A. (ed.) *The Arctic Floristic Region*. Nauka, Leningrad, pp. 9–104 (in Russian).

- **For conference proceedings:**

Name(s) and initials of the author(s). Year of publication. Name(s) and initials of the editor(s) (preceded by In:) *Proceedings name (in italics)*, publisher, place of publishing, page numbers.

Ritchie, M.E. & Olff, H. 1999. Herbivore diversity and plant dynamics: compensatory and additive effects. In: Olff, H., Brown, V.K. & Drent R.H. (eds) *Herbivores between plants and predators. Proc. Int. Conf. The 38<sup>th</sup> Symposium of the British Ecological Society*, Blackwell Science, Oxford, UK, pp. 175–204.

**Please note**

- Use ‘.’ (not ‘,’) for decimal point: 0.6 ± 0.2; Use ‘,’ for thousands – 1,230.4;
- Use ‘–’ (not ‘-’) and without space: pp. 27–36, 1998–2000, 4–6 min, 3–5 kg
- With spaces: 5 h, 5 kg, 5 m, 5 °C, C : D = 0.6 ± 0.2;  $p < 0.001$
- Without space: 55°, 5% (not 55 °, 5 %)
- Use ‘kg ha<sup>-1</sup>’ (not ‘kg/ha’);
- Use degree sign ‘°’ : 5 °C (not 5 °C).